

NASA Contractor Report 189193

1N-07

160293
P.294

Fuel Injector – Air Swirl Characterization Aerothermal Modeling Phase II

Final Report – Volume II

M. Nikjooy and H.C. Mongia
*Allison Gas Turbine Division
Indianapolis, Indiana*

and

V.G. McDonell and G.S. Samuelsen
*University of California
Irvine, California*

March 1993

Prepared for
Lewis Research Center
Under Contract NAS3-24350



(NASA-CR-189193) FUEL INJECTOR:
AIR SWIRL CHARACTERIZATION
AEROTHERMAL MODELING, PHASE 2,
VOLUME 2 Final Report (General
Motors Corp.) 294 p

N93-25106

Unclas

G3/07 0160293

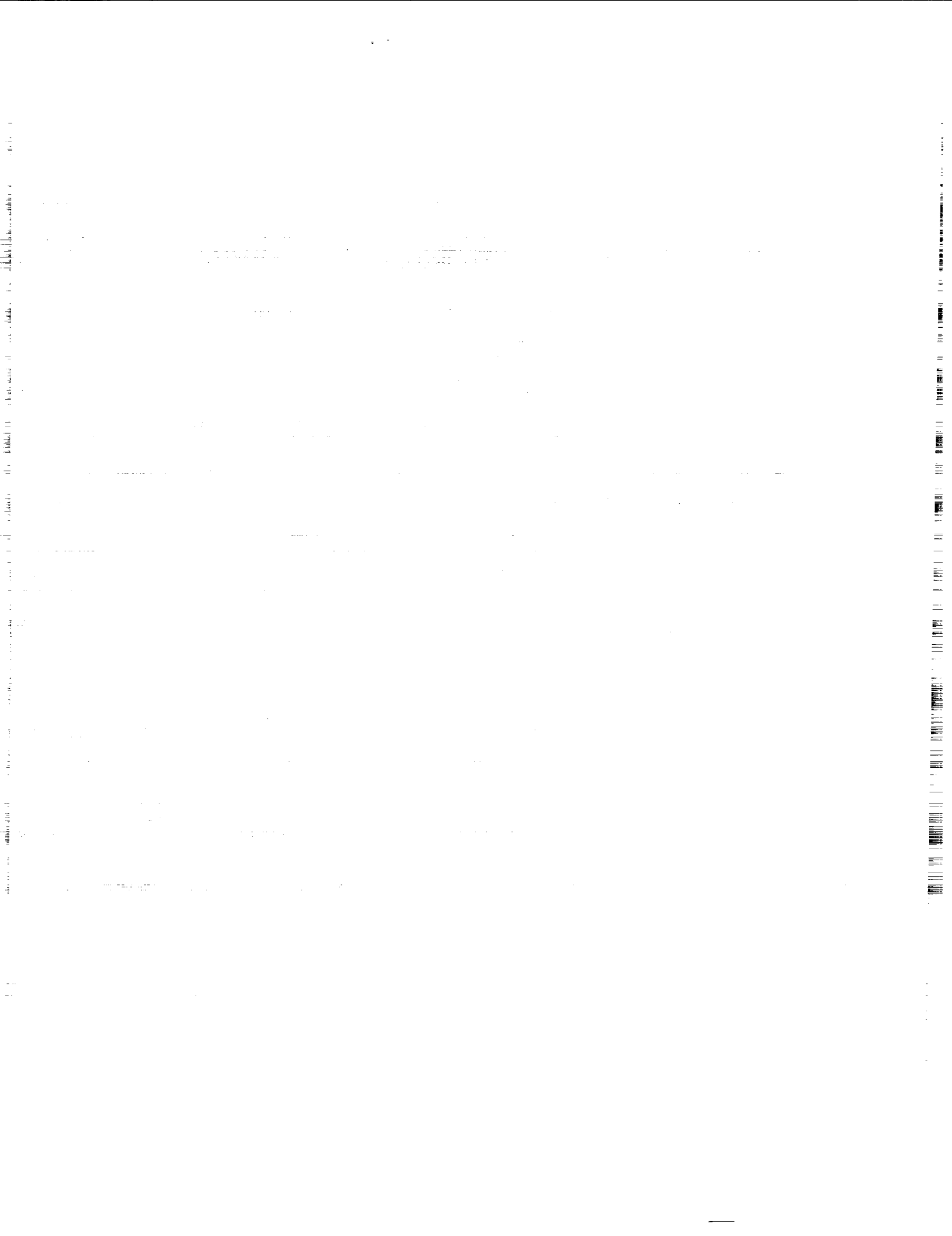


TABLE OF CONTENTS

<u>Section</u>	<u>Title</u>	<u>Page</u>
VOLUME I		
I	Introduction and Summary.....	1
	1.1 Introduction	1
	1.2 Summary	2
II	Selection of Experimental Configuration.....	5
	2.1 Gas Turbine Combustor Flow Field Characteristics	5
	2.2 Idealized Combustor Flow Model	7
	2.2.1 Measurements of Solid-Particle-Laden Flows	7
	2.2.2 Measurements in Sprays.....	8
	2.3 Integrated Modeling/Experimental Approach	11
	2.3.1 Air-Swirler Characterization.....	11
	2.3.2 Fuel Injector and Injector Air Characterization	11
	2.3.3 Combination Fuel-Injector Air-Swirler Characterization	12
III	Experimental Test Facility and Instrumentation	39
	3.1 Test Facility	39
	3.1.1 Unconfined Geometries	39
	3.1.2 Confined Geometries.....	39
	3.1.3 Positioning	40
	3.1.4 Diagnostics Table	41
	3.2 Materials for the Dispersed Phase	49
	3.2.1 Glass Beads	49
	3.3 Flow Systems	53
	3.3.1 Air Delivery	53
	3.3.2 Glass Bead Delivery.....	55
	3.3.3 Methanol Delivery	56
	3.4 Injector/Swirler Assemblies.....	63
	3.4.1 Injector Flow Split Study	63
	3.4.2 Nozzle Symmetry Evaluation	63
	3.4.3 Aerodynamic Swirler	65
	3.4.4 Evolution of Experimental Test Conditions.....	65
	3.5 Diagnostics – Velocity Measurements	88
	3.5.1 Laser Anemometry System	88
	3.5.2 Seeding Systems	90
	3.5.3 Sampling Bias	92
	3.5.4 Validation of Velocity Measurement	92
	3.6 Diagnostics – Particle Size Measurements	112
	3.6.1 Phase Technique – Theory and Limitations.....	112
	3.6.2 Probe Volume Correction	114
	3.6.3 Validation of Technique	114
	3.7 Discrimination Between Phases	126
	3.7.1 Chromatic Discrimination	126
	3.7.2 Amplitude Discrimination	126
	3.7.3 Physical Discrimination	126
	3.8 Vapor Concentration Measurements	133
	3.9 Pressure Measurements in Confined Duct	135
	3.10 Temperature Measurements.....	137
	3.11 Flow Visualization	138
	3.11.1 Photography	138
	3.11.2 High Speed Cinematography	138

TABLE OF CONTENTS (cont)

<u>Section</u>	<u>Title</u>	<u>Page</u>
	3.11.3 Shadowgraph Photography	138
3.12	Data Format	140
IV	Data Presentation and Discussion	145
4.1	Data Case Descriptions	145
	4.1.1 Summary of Data Base	145
	4.1.2 Case Description and Geometries	146
	4.1.3 Data Collection and Reporting Protocol.....	146
	4.1.4 Nomenclature	147
4.2	Single Round Jet	149
	4.2.1 Unconfined Single-Phase Jet – CONF01#2	149
	4.2.2 Unconfined Jet in the Presence of 100-110 Micron Beads at Loading Ratio 0.2 and 1.0 – CONF07#6,#A	150
	4.2.3 Glass Beads in the Unconfined Jet at Loading Ratios of 0.2 and 1.0 – CONF07#5,#3	151
	4.2.4 Effect of Particle Mass Loading in the Unconfined Jet	152
	4.2.5 Unconfined Jet in the Presence of 25 and 105 Micron Beads – CONF13#2	153
	4.2.6 Mixture of 25 and 105 Micron Glass Beads in the Unconfined Jet – CONF13#4	153
	4.2.7 Confined Single Round Jet – CONF04#3	154
	4.2.8 Confined Jet in the Presence of 100-110 Micron Beads at Loading Ratios of 0.2 and 1.0 – CONF10#3,#5	154
	4.2.9 Glass Beads in the Confined Jet at Loading Ratios of 0.2 and 1.0 – CONF10#4,#6	155
	4.2.10 Effect of Particle Mass Loading Ratio in the Confined Jet	155
	4.2.11 Effect of Confinement on Jet	155
	4.2.12 Effect of Confinement on Glass Beads	155
4.3	Single Annular Jet – conf31#2	232
4.4	Single Swirling Annular Jet	239
	4.4.1 Unconfined Case – CONF32#1	239
	4.4.2 Confined Case – CONF34#1	239
	4.4.3 Effect of Swirl	239
	4.4.4 Effect of Confinement	239
4.5	Coaxial Jets	254
	4.5.1 Unconfined Coaxial Jets – CONF02#3	254
	4.5.2 Effect of Coflow on Single Jet	254
	4.5.3 Unconfined Jets in the Presence of 100-110 Micron Beads at Loading Ratio 0.2 – CONF08#1	254
	4.5.4 Glass Beads in the Unconfined Jets at Loading Ratios of 0.2 – CONF08#2	254
	4.5.5 Effect of Coflow on Glass Beads	255
	4.5.6 Confined Single-Phase Coaxial Jets – CONF05#2	255
	4.5.7 Confined Jets in the Presence of 100-110 Micron Beads at Loading Ratios of 0.2 and 1.0 – CONF11#1,#3	255
	4.5.8 Glass Beads in the Confined Jets at Loading Ratios of 0.2 and 1.0 – CONF11#2,#4	255
	4.5.9 Effect of Particle Mass Loading Ratio in the Confined Jet	256
	4.5.10 Effect of Confinement on Coaxial Jets	256
	4.5.11 Effect of Coflow on Confined Jet	256

TABLE OF CONTENTS (cont)

<u>Section</u>	<u>Title</u>	<u>Page</u>
	4.5.12 Effect of Confinement on Glass Beads in Coaxial Jets.....	256
4.6	Coaxial Jets With Swirling Annular Flow	310
	4.6.1 Unconfined Single-Phase Jets – CONF03#3.....	310
	4.6.2 Effect of Swirl on Coflowing Jets	310
	4.6.3 Unconfined Swirling Jets in the Presence of 100-110 Micron Beads – CONF09#4	310
	4.6.4 100-110 Micron Glass Beads in the Unconfined Swirling Jets – CONF09#3	310
	4.6.5 Effect of Swirl on 100-110 Micron Glass Beads in Unconfined Flow	310
	4.6.6 100-110 Micron Glass Beads in the Confined Swirling Jet – CONF12#4	310
	4.6.7 Effect of Swirl on Glass Beads in the Confined Flow	311
4.7	Airblast Injector	339
	4.7.1 Confined Single-Phase – CONF22#1	339
	4.7.2 Gas in the Presence of Confined Methanol Spray – CONF28#2.....	339
	4.7.3 Effect of Spray on Gas Phase Behavior in Confined Spray	339
	4.7.4 Confined Methanol Spray – CONF28#1.....	339
4.8	Airblast Injector With Annular Jet.....	356
	4.8.1 Gas in the Presence of Unconfined Methanol Spray – CONF26#2	356
	4.8.2 Unconfined Methanol Spray – CONF26#1	356
	4.8.3 Confined Single-Phase – CONF23#1	356
	4.8.4 Effect of Coflow on Gas Phase	356
	4.8.5 Confined Methanol Spray – CONF29#1.....	356
	4.8.6 Effect of Coflow on Spray	357
	4.8.7 Effect of Confinement on Spray.....	357

VOLUME II

V	Physical and Mathematical Models	391
	5.1 Single-Phase Flow Models.....	391
	5.2 Two-Phase Flow Models	395
	5.2.1 Dispersed Phase	395
	5.2.2 Continuous Phase	396
	5.3 Mathematical Formulation	399
	5.3.1 Discretization	399
	5.3.2 Power-Law Differencing Scheme	399
	5.3.3 Flux-Spline Differencing Scheme	399
VI	Model Validation	405
	6.1 Single Round Jet	405
	6.1.1 Unconfined Single Round Jet	405
	6.1.2 Confined Single Round Jet	421
	6.2 Unconfined Single Annular Jet	461
	6.3 Single Annular Swirling Jet	491
	6.3.1 Unconfined Annular Swirling Jet.....	491
	6.3.2 Confined Annular Swirling Jet	515
	6.4 Coaxial Jets.....	548
	6.4.1 Unconfined Coaxial Jets.....	548
	6.4.1.1 The k-ε Turbulence Model	549
	6.4.1.2 The Algebraic Second-Moment Closure.....	553

TABLE OF CONTENTS (cont)

<u>Section</u>	<u>Title</u>	<u>Page</u>
	6.4.2 Confined Coaxial Jets	574
6.5	Unconfined Coaxial Jets with Swirling Annular Flow	608
6.6	Airblast Injector	639
VII	Concluding Remarks and Recommendations	655
7.1	Summary of the Present Work	655
7.2	Recommendation	655
Appendix A	Turbulent Flow Equations for the k- ϵ Model	659
Appendix B	Turbulent Flow Equations for DSM Closure	663
Appendix C	Publications Partially Supported by the List of this Study	669

LIST OF ILLUSTRATIONS

<u>Figure</u>	<u>Title</u>	<u>Page</u>
VOLUME I		
2.1-1	Model predictions of flow field around and within combustor	6
2.3.1-1	The flow and geometry test conditions for air-swirler characterization study	14
2.3.1-2	Numerical predictions of the case $m_p/m_s = 0.01$ for air-swirler characterization study; a) velocity vectors b) streamlines c) radial velocity d) kinetic energy	15
2.3.1-3	Numerical predictions of the case $m_p/m_s = 0.06$ for air-swirler characterization study; a) velocity vectors b) streamlines c) radial velocity d) kinetic energy	16
2.3.2-1	The flow and geometry test conditions for fuel-injector characterization study	17
2.3.2-2	Numerical predictions of single-phase flow for fuel-injector characterization study; a) velocity vectors b) streamlines c) radial velocity	18
2.3.2-3	Numerical predictions of two-phase flow without correction of gas turbulent diffusion due to particles of fuel-injector characterization study	19
2.3.2-4	Numerical predictions of two-phase flow with correction of gas turbulent diffusion due to particles of fuel-injector characterization study	21
2.3.2-5	Numerical predictions of two-phase flow without particle dispersion model for fuel-injector characterization study; a) velocity vectors b) streamlines c) kinetic energy	23
2.3.3-1	The flow and geometry test conditions for combination fuel-injector air-swirler characterization study	25
2.3.3-2	Numerical predictions of single-phase flow ($D_p = 0.394$ in.) for combination fuel injector air-swirler characterization study; a) velocity vectors b) streamlines c) radial velocity d) kinetic energy	26
2.3.3-3	Numerical predictions of two-phase flow ($D_p = 0.394$ in.) without correction of gas turbulent diffusion due to the particles for combination fuel-injector air-swirler characterization study	27
2.3.3-4	Numerical predictions of two-phase flow ($D_p = 0.394$ in.) with correction of gas turbulent diffusion due to the particles for combination fuel-injector air-swirler characterization study	29
2.3.3-5	Numerical predictions of single-phase flow ($D_p = 0.197$ in.) for combination fuel-injector air-swirler characterization study	31
2.3.3-6	Numerical predictions of two-phase flow ($D_p = 0.197$ in.) without correction of gas turbulent diffusion due to the particles for combination fuel-injector air-swirler characterization study	32
2.3.3-7	Numerical predictions of two-phase flow ($D_p = 0.197$ in.) with correction of gas turbulent diffusion due to the particles for combination fuel-injector air-swirler characterization study	34
3.1.1-1	Unconfined geometry	42
3.1.2-1	Confined geometry	43
3.1.2-2	Impact of confined duct on probe volume	44
3.1.2-3	Optical access in the confined duct	45
3.1.2-4	Effect of noise on measurement in the confined duct	46
3.1.3-1	Traverse system	47
3.1.3-2	Positioning interface	48
3.1.4-1	Optical table and diagnostic layout	48
3.2.1-1	Monosized glass beads	51
3.2.1-2	Size class discrimination	52
3.3-1	Flow system	57
3.3.1-1	Unconfined screen air manifold	58

LIST OF ILLUSTRATIONS (cont)

<u>Figure</u>	<u>Title</u>	<u>Page</u>
3.3.1-2	Confined screen air manifold	59
3.3.2-1	Particle-laden jet	60
3.3.2-2	Modified screw feeder	61
3.3.3-1	Hydraulic accumulator	62
3.4-1	Ex-Cell-O air-blast atomizer: detail of flow passages through atomizer with outer shroud removed	72
3.4-2	Ex-Cell-O air-blast atomizer: details of atomizer flow passages	73
3.4.1-1	Plenum used for flow split study	74
3.4.2-1	Symmetry of mean spray velocity profiles for three atomizers	75
3.4.2-2	Symmetry of spray SMD profiles for three atomizers	76
3.4.2-3	Measurement locations for detailed symmetry evaluation	77
3.4.2-4	Isopleths of mean axial velocity at an axial location of 50 mm	78
3.4.2-5	Profiles of mean azimuthal velocity at an axial location of 50 mm	79
3.4.2-6	Isopleths of volume flux at an axial location of 100 mm	80
3.4.3-1	Aerodynamic swirler	81
3.4.3-2	Symmetry of swirl vanes	82
3.4.4-1	Original geometries	83
3.4.4-2	Atomizer shroud evaluation: original cap	87
3.5.1-1	Two-component PDPA transmitter	95
3.5.1-2	Two-component PDPA receiver	95
3.5.1-3	Partitioning of the PDPA receiver lens	96
3.5.1-4	Evaluation of signal filtering	97
3.5.1-5	Detail of diffraction grating	98
3.5.2-1	Seeders used in the program: nebulizer based	99
3.5.2-2	Seeders used in the program: fluid bed-type	100
3.5.2-3	Fluid bed output rate	101
3.5.2-4	Seed morphology	102
3.5.2-5	Example of particle response study	103
3.5.3-1	Example of sampling bias in swirling flow	104
3.5.4-1	Setup of instrument comparison	105
3.5.4-2	Cube plots for sensitivity study results at centerline of free jet	106
3.5.4-3	Impact of PMT gain on TSI and PDPA velocity measurement at centerline of free jet	108
3.5.4-4	Impact of frequency shift on TSI and PDPA velocity measurement at centerline of free jet	110
3.6.1-1	Light scattering by a sphere	117
3.6.1-2	Spatial phase shift related to size	118
3.6.2-1	Dependency of probe size on particle size	119
3.6.3-1	Comparison of phase technique to visibility/IV	120
3.6.3-2	Comparison of phase technique to Malvern	121
3.6.3-3	Effect of frequency shift on PDPA and FFT processor measurement of air- assist spray	122
3.6.3-4	Detailed comparison of effect of PMT voltage on uncorrected size distribution measured by PDPA and FFT processor in air-assist spray	124
3.7.3-1	Measurement of seed particles and glass beads in recirculating flow	129
3.7.3-2	Size histograms for two types of seed particles	131
3.7.3-3	Sensitivity of velocity measurements to seed type and sizing enabled/disabled	132
3.8-1	Phase discrimination probe	134
3.9-1	Pressure measurement setup	136
3.11.3-1	Shadowgraph setup	139

LIST OF ILLUSTRATIONS (cont)

<u>Figure</u>	<u>Title</u>	<u>Page</u>
4.2.1-1	Geometry utilized for unconfined single round jet	157
4.2.1-2	Radial profiles of gas phase statistics in unconfined single-phase round jet	158
4.2.1-3	Repeatability and sensitivity of measurements in the unconfined single-phase round jet.....	165
4.2.2-1	Radial profiles of gas phase velocity measurements in unconfined round jet laden with 100-110 micron glass beads with a bead to-gas-mass loading ratio of 0.2	168
4.2.2-2	Radial profiles of gas phase velocity measurements in unconfined round jet laden with 100-110 micron glass beads with a bead-to-gas mass loading ratio of 1.0	173
4.2.3-1	Radial profiles of particle measurements in unconfined round jet laden with 100-110 micron glass beads with a bead-to-gas mass loading ratio of 0.2 ...	178
4.2.3-2	Radial profiles of particle measurements in unconfined round jet laden with 100-110 micron glass beads with a bead-to-gas mass loading ratio of 1.0 ...	183
4.2.4-1	Comparison of gas phase velocities and shear stress in (1) unconfined single-phase round jet, (2) unconfined round jet laden with 100-110 micron particles at mass loading of 0.2, and (3) unconfined round jet laden with 100-110 micron particles at mass loading ratio of 1.0	188
4.2.4-2	Comparison of particle velocities and data rate in unconfined round jet laden with particles at a mass loading ratio of 0.2 and 1.0	190
4.2.5-1	Radial profiles of gas phase velocity measurements in unconfined round jet laden with equal number of 20-30 micron and 100-110 micron glass beads with a bead-to-gas mass loading ratio of 0.2	192
4.2.6-1	Radial profiles of particle measurements in unconfined round jet laden with equal numbers of 20-30 micron and 100-110 micron glass beads with a bead-to-gas mass loading ratio of 0.2	197
4.2.7-1	Geometry utilized for confined single round jet	202
4.2.7-2	Radial profiles of gas phase statistics in confined single-phase round jet	203
4.2.7-3	Repeatability of measurements of mean and fluctuating axial velocity in the confined single-phase round jet	208
4.2.8-1	Radial profiles of gas phase velocity measurements in confined round jet laden with 100-110 micron glass beads with a bead-to-gas mass loading ratio of 0.2	209
4.2.8-2	Radial profiles of gas phase velocity measurements in confined round jet laden with 100-110 micron glass beads with a bead-to-gas mass loading ratio of 1.0	212
4.2.9-1	Radial profiles of particle measurements in confined round jet laden with 100-110 micron glass beads with a bead-to-gas mass loading ratio of 0.2 ...	217
4.2.9-2	Radial profiles of particle measurements in unconfined round jet laden with 100-110 micron glass beads with a bead-to-gas mass loading ratio of 1.0 ...	220
4.2.10-1	Comparison of gas phase velocities and shear stress in (1) confined single-phase round jet, (2) confined round jet laden with 100-110 micron particles at mass loading of 0.2, and (3) confined round jet laden with 100-110 micron particles at mass loading ratio of 1.0	225
4.2.10-2	Comparison of particle velocities and data rate in confined round jet laden with particles at a mass loading ratio of 0.2 and 1.0	227
4.2.11-1	Comparison of mean and fluctuating axial velocities in the confined and unconfined single-phase round jet	229

LIST OF ILLUSTRATIONS (cont)

<u>Figure</u>	<u>Title</u>	<u>Page</u>
4.2.12-1	Comparison of mean and fluctuating axial velocities and data rates for 100-110 micron beads in the round jet with and without confinement for a bead-to-gas mass flow rate ratio of 1.0	230
4.3-1	Geometry utilized for unconfined single-phase annular jet	233
4.3-2	Radial profiles of gas phase statistics in unconfined single-phase annular jet	234
4.4.1-1	Geometry utilized for unconfined single-phase swirling annular jet	240
4.4.1-2	Radial profiles of gas phase statistics in unconfined single-phase swirling annular jet	241
4.4.2-1	Geometry utilized for confined single-phase swirling annular jet	246
4.4.2-2	Radial profiles of gas phase statistics in confined single-phase swirling annular jet	247
4.4.3-1	Comparison of mean and fluctuating axial velocities in the single-phase unconfined annular jets with and without swirl	252
4.4.4-1	Comparison of mean and fluctuating axial velocities in the single-phase swirling annular jet with and without confinement	253
4.5.1-1	Geometry utilized for unconfined coaxial jets	257
4.5.1-2	Radial profiles of gas phase statistics in the unconfined single-phase coaxial jets	258
4.5.1-3	Assessment of repeatability in the unconfined single-phase coaxial jets	263
4.5.2-1	Comparison of mean and fluctuating axial velocities in unconfined single-phase round and coaxial jets	266
4.5.3-1	Radial profiles of gas phase velocity measurements in unconfined coaxial jets with central jet laden with 100-110 micron glass beads at a bead-to-gas mass loading ratio of 0.2	267
4.5.4-1	Radial profiles of particle measurements in unconfined coaxial jets with central jet laden with 100-110 micron glass beads at a bead-to-gas mass loading ratio of 0.2	272
4.5.5-1	Comparison of mean and fluctuating axial velocities and data rates for 100-110 micron beads in the round jet with and without coflow for a bead-to-gas mass flow rate ratio of 0.2	277
4.5.6-1	Geometry utilized for confined coaxial jets	279
4.5.6-2	Radial profiles of gas phase statistics in the confined single-phase coaxial jets	280
4.5.6-3	Assessment of repeatability of mean and fluctuating axial velocities in confined single-phase coaxial jets	285
4.5.7-1	Radial profiles of gas phase velocity measurements in confined coaxial jets with central jet laden with 100-110 micron glass beads at a bead-to-gas mass loading ratio of 0.2	286
4.5.7-2	Radial profiles of gas phase velocity measurements in confined coaxial jets with central jet laden with 100-110 micron glass beads at a bead-to-gas mass loading ratio of 0.2	289
4.5.8-1	Radial profiles of particle measurements in confined coaxial jets with central jet laden with 100-110 micron glass beads with a bead-to-gas mass loading ratio of 0.2	294
4.5.8-2	Radial profiles of particle measurements in confined coaxial jets with central jet laden with 100-110 micron glass beads with a bead-to-gas mass loading ratio of 1.0	297
4.5.9-1	Comparison of gas phase velocity and shear stress in confined coaxial jets with central jet laden with 100-110 micron particles at two particle-to-gas mass loading ratios	302

LIST OF ILLUSTRATIONS (cont)

<u>Figure</u>	<u>Title</u>	<u>Page</u>
4.5.9-2	Comparison of particle velocity and data rate in confined coaxial jets with central jet laden with 100-110 micron particles at two particle-to-gas mass loading ratios	304
4.5.10-1	Comparison of gas phase mean and fluctuating axial velocities in confined and unconfined single-phase coaxial jets	306
4.5.11-1	Comparison of gas phase mean and fluctuating axial velocities in confined single-phase jets with and without coaxial flow	307
4.5.12-1	Comparison of particle axial velocities and data rate in confined and unconfined coaxial jets with the central jet laden with 100-110 micron particles at a particle-to-gas mass loading ratio of 0.2.....	308
4.6-1	Geometry utilized for unconfined round jet with swirling annular flow.....	312
4.6.1-1	Radial profiles of gas phase statistics in the unconfined single-phase coaxial jets with swirling annular air	313
4.6.2-1	Comparison of mean and fluctuating axial velocities in unconfined coflowing jets with and without swirling annular air	318
4.6.3-1	Radial profiles of gas phase velocities in the unconfined jet with swirling annular air flow with the central jet laden with 100-110 micron particles in a particle-to-gas mass loading ratio of 0.2	319
4.6.4-1	Radial profiles of particle velocities in the unconfined jet with swirling annular air flow with the central jet laden with 100-110 micron particles in a particle-to-gas mass loading ratio of 0.2	324
4.6.5-1	Comparison of particle velocities and data rate in unconfined flows with the central jet laden with 100-110 micron particles at a particle-to-gas mass loading ratio of 0.2: free jet versus swirling annular coflow.....	329
4.6.6-1	Geometry utilized for confined round jet with swirling annular air.....	331
4.6.6-2	Radial profiles of particle measurements in confined coaxial jets with swirling annular air with central jet laden with 100-110 micron particles at a particle-to-gas mass loading ratio of 1.0	332
4.6.7-1	Comparison of particle axial velocity and data rate in confined round jet laden with 100-110 micron particles in a particle-to-gas mass loading of 1.0 with and without swirling annular air	337
4.7.1-1	Geometry utilized for the confined methanol spray	340
4.7.1-2	Radial profiles of gas phase statistics in confined single-phase flow from air-blast injector	341
4.7.2-1	Radial profiles of the gas phase measurements in the confined methanol spray	344
4.7.3-1	Comparison of gas phase measurements in the confined air-blast atomizer flow with and without methanol	349
4.7.4-1	Radial profiles of the droplet measurements in the confined methanol spray	352
4.8.1-1	Geometry utilized for unconfined methanol spray with annular coflow	358
4.8.1-2	Radial profiles of the gas phase measurements in the unconfined methanol spray with annular coflow	359
4.8.2-1	Radial profiles of the droplet measurements in the unconfined methanol spray with annular air	364
4.8.2-2	Comparison of the gas phase and droplet velocities in the unconfined methanol spray with annular coflow	368
4.8.3-1	Geometry utilized for the confined methanol spray with annular coflow	370
4.8.3-2	Radial profiles of the gas phase measurements in the confined methanol spray with annular coflow	371
4.8.4-1	Comparison of gas phase velocities in the confined single-phase flow from the air-blast atomizer with and without coflow	376

LIST OF ILLUSTRATIONS (cont)

<u>Figure</u>	<u>Title</u>	<u>Page</u>
4.8.5-1	Radial profiles of the droplet measurements in the confined methanol spray with annular coflow	379
4.8.6-1	Comparison of droplet measurements in the confined methanol spray with and without coflow	383
4.8.7-1	Comparison of the droplet measurements in the methanol spray with and without confinement	386
VOLUME II		
5.3.1-1	Control volume around the grid point P	402
5.3.3-1	One-dimensional condition	402
6.1.1-1	Test facility: unconfined injector only	409
6.1.1-2	Radial profiles of normalized mean axial velocity, turbulence kinetic energy, and shear stress for the single-phase jet	410
6.1.1-3	Radial profiles of normalized rms velocity components and turbulence kinetic energy for the single-phase jet	411
6.1.1-4	Radial profiles of normalized mean axial velocity, turbulence kinetic energy, and shear stress for the single-phase jet; influence of initial ϵ	412
6.1.1-5	Axial distribution of normalized centerline values of gas mean velocity, and particle mean velocity and number density	413
6.1.1-6	Radial profiles of normalized gas axial velocity and particle axial and radial velocity components, LR = 0.2	414
6.1.1-7	Radial profiles of normalized gas turbulence kinetic energy, shear stress, and axial turbulence intensity, and particle axial turbulence intensity at loading ratio, LR = 0.2	415
6.1.1-8	Radial profiles of rms radial and azimuthal velocity components of gas and particles at loading ratio, LR = 0.2	416
6.1.1-9	Radial profiles of normalized gas axial velocity and particle axial and radial velocity components, LR = 1.0	417
6.1.1-10	Radial profiles of normalized gas turbulence kinetic energy, shear stress, and axial turbulence intensity, and particle axial turbulence intensity at loading ratio, LR = 1.0	418
6.1.1-11	Radial profiles of rms radial and azimuthal velocity components of gas and particles at loading ratio, LR = 1.0	419
6.1.1-12	Effect of single-phase and two-phase turbulence models on gas phase turbulence kinetic energy and shear stress for the two loading ratios, LR = 0.2 and LR = 1.0	420
6.1.2-1	Confined round jet geometrical details	428
6.1.2-2	Confined round jet grid layout	429
6.1.2-3	Confined single round jet inlet condition, single phase	430
6.1.2-4	Comparison of predicted mean axial velocity by k- ϵ model with data	431
6.1.2-5	Comparison of predicted turbulent shear stress by k- ϵ model with data	432
6.1.2-6	Comparison of predicted turbulent kinetic energy by k- ϵ model with data	433
6.1.2-7	Comparison of predicted mean axial velocity by k- ϵ and DSM with data	434
6.1.2-8	Comparison of predicted U velocity by ASM with data	435
6.1.2-9	Comparison of calculated streamwise turbulence intensity by ASM with data	436
6.1.2-10	Comparison of calculated radial turbulence intensity by ASM with data	437
6.1.2-11	Comparison of calculated tangential turbulence intensity by ASM with data	438
6.1.2-12	Comparison of calculated U velocity profiles by DSM and ASM with data	439
6.1.2-13	Comparison of calculated streamwise turbulence intensity by DSM and ASM with data	440

LIST OF ILLUSTRATIONS (cont)

<u>Figure</u>	<u>Title</u>	<u>Page</u>
6.1.2-14	Comparison of calculated radial turbulence intensity by DSM and ASM with data	441
6.1.2-15	Comparison of calculated tangential turbulence intensity by DSM and ASM with data	442
6.1.2-16	Comparison of calculated turbulent shear stress profiles by DSM and ASM with data	443
6.1.2-17	Comparison of calculated k by k- ϵ , ASM, and DSM with data	444
6.1.2-18	Comparison of calculated turbulent shear stress profiles by k- ϵ , ASM, and DSM with data	445
6.1.2-19	Measured profiles for continuous phase at the inlet plane (x = 4 mm), particle-laden jet	446
6.1.2-20	Measured profiles for dispersed phase at the inlet plane (x = 4 mm), particle-laden jet	447
6.1.2-21	Comparison of predicted gas phase U velocity profiles by DSM and k- ϵ with data, particle-laden jet	448
6.1.2-22	Comparison of predicted gas phase shear stress profiles by DSM and k- ϵ with data, particle-laden jet	449
6.1.2-23	Comparison of predicted gas phase k profiles by DSM and k- ϵ with data, particle-laden jet	450
6.1.2-24	Comparison of predicted gas phase U velocity profiles by ASM and DSM with data, particle-laden jet	451
6.1.2-25	Comparison of calculated gas phase streamwise turbulence intensity profiles by ASM and DSM with data, particle-laden jet	452
6.1.2-26	Comparison of calculated gas phase radial turbulence intensity profiles by ASM and DSM with data, particle-laden jet	453
6.1.2-27	Comparison of calculated gas phase tangential turbulence intensity profiles by ASM and DSM with data, particle-laden jet	454
6.1.2-28	Comparison of calculated gas phase shear stress profiles by ASM and DSM with data, particle-laden jet	455
6.1.2-29	Comparison of calculated dispersed phase axial velocity (U_p) profiles by k- ϵ with data	456
6.1.2-30	Comparison of calculated dispersed phase axial velocity (U_p) profiles by DSM with data	457
6.1.2-31	Comparison of calculated dispersed phase streamwise turbulence intensity by DSM with data	458
6.1.2-32	Comparison of calculated dispersed phase radial turbulence intensity by DSM with data	459
6.1.2-33	Comparison of calculated dispersed phase tangential turbulence intensity by DSM with data	460
6.2-1	Unconfined annular flow configuration	466
6.2-2	Unconfined single annular jet - grid layout	467
6.2-3	Unconfined single annular jet inlet conditions	468
6.2-4	Comparison of predicted mean axial velocity by DSM with data	469
6.2-5	Comparison of calculated rms axial velocity profiles by DSM with data	471
6.2-6	Comparison of calculated rms radial velocity profiles by DSM with data	473
6.2-7	Comparison of calculated rms tangential velocity profiles by DSM with data	475
6.2-8	Comparison of calculated turbulent shear stress profiles by DSM with data	477
6.2-9	Comparison of predicted mean axial velocity by k- ϵ model with data	479
6.2-10	Comparison of predicted turbulent kinetic energy by k- ϵ model with data	481
6.2-11	Comparison of calculated U velocity by k- ϵ and DSM with data	483

LIST OF ILLUSTRATIONS (cont)

<u>Figure</u>	<u>Title</u>	<u>Page</u>
6.2-12	Comparison of calculated uv profiles by k-ε and DSM with data	485
6.2-13	Comparison of calculated U velocity by k-ε and DSM with data	487
6.2-14	Comparison of calculated uv profiles by k-ε and DSM with data	489
6.3.1-1	Unconfined annular swirling jet geometrical details	496
6.3.1-2	Unconfined annular swirling jet grid layout.....	497
6.1.3-3	Measured profiles at the inlet (x = 3 mm)	498
6.3.1-4	Comparison of calculated mean axial velocity by DSM and k-ε with data	500
6.3.1-5	Comparison of calculated mean tangential velocity by DSM and k-ε with data	501
6.3.1-6	Comparison of calculated axial rms velocity by DSM with data	503
6.3.1-7	Comparison of calculated radial rms velocity by DSM with data	504
6.3.1-8	Comparison of calculated tangential rms velocity by DSM with data	506
6.3.1-9	Comparison of calculated turbulent shear stress profiles by k-ε and DSM with data	507
6.3.1-10	Comparison of predicted mean axial velocity by k-ε with data	509
6.3.1-11	Comparison of predicted mean tangential velocity by k-ε with data.....	510
6.3.1-12	Comparison of predicted turbulent shear stress with data	512
6.3.1-13	Comparison of predicted turbulent kinetic energy with data	513
6.3.2-1	Confined annular swirling jet - geometrical details	521
6.3.2-2	Confined annular swirling jet grid layout	522
6.3.2-3	Measured profiles at the inlet plane (x = 4mm)	523
6.3.2-4	Staggered arrangement of Reynolds stress components	524
6.3.2-5	Inlet dissipation profiles	524
6.3.2-6	Comparison of calculated mean axial velocity by k-ε model using various ϵ_{in}	525
6.3.2-7	Comparison of calculated mean tangential velocity by k-ε model using various ϵ_{in}	527
6.3.2-8	Comparison of calculated turbulent kinetic energy by k-ε model using various ϵ_{in}	529
6.3.2-9	Comparison of calculated turbulent shear stress by k-ε model using various ϵ_{in}	531
6.3.2-10	Comparison of calculated mean axial velocity by DSM using various ϵ_{in}	533
6.3.2-11	Comparison of calculated mean tangential velocity by DSM using various ϵ_{in}	534
6.3.2-12	Comparison of calculated streamwise turbulence intensity by DSM using various ϵ_{in}	535
6.3.2-13	Comparison of calculated turbulent shear stress by DSM using various ϵ_{in}	536
6.3.2-14	Comparison of calculated mean axial velocity using various ϕ , models with data	537
6.3.2-15	Comparison of calculated mean tangential velocity using various ϕ , models with data	538
6.3.2-16	Comparison of calculated U velocity with IP and QI models for confined annular swirling jet	539
6.3.2-17	Comparison of calculated uv profiles with data	540
6.3.2-18	Comparison of calculated streamwise turbulence intensity with measurements	541
6.3.2-19	Comparison of calculated radial turbulence intensity with measurements	542
6.3.2-20	Comparison of the predicted mean and turbulence quantities by ASM and DSM with data	543
6.3.2-21	Comparison of the predicted mean and turbulence quantities by ASM and DSM with data	544
6.3.2-22	Comparison of the predicted mean and turbulence quantities by ASM and DSM with data	545
6.3.2-23	Comparison of the predicted mean and turbulence quantities by ASM and DSM with data	546

LIST OF ILLUSTRATIONS (cont)

<u>Figure</u>	<u>Title</u>	<u>Page</u>
6.3.2-24	Comparison of the predicted mean and turbulence quantities by ASM and DSM with data	547
6.4.1-1	Unconfined coaxial jets geometry	556
6.4.1-2	Measured profiles at the inlet plane ($x = 2$ mm)	557
6.4.1-3	Unconfined coaxial jets grid layout	558
6.4.1-4	Comparison of measurements with mean axial velocity calculations for unconfined coaxial jets	559
6.4.1-5	Comparison of measurements with turbulent kinetic energy calculations	560
6.4.1-6	Inlet dissipation rate profiles	561
6.4.1-7	Profiles of mean axial velocity and turbulent kinetic energy using different inlet turbulent dissipation rate	562
6.4.1-8	Comparison of the $k-\epsilon$ and the ASM predictions of axial velocity using flux-spline with measurements	563
6.4.1-9	Comparison of the ASM prediction of turbulent shear stress with data	564
6.4.1-10	Comparison of the ASM prediction of axial normal stress with data	565
6.4.1-11	Comparison of the ASM prediction of radial normal stress with data	566
6.4.1-12	Comparison of the ASM prediction of tangential normal stress with data	567
6.4.1-13	Radial profiles of normalized mean axial velocity, turbulent kinetic energy, and shear stress for the single-phase coaxial jets	568
6.4.1-14	Radial profile of normalized rms velocity components for the single-phase coaxial jets	569
6.4.1-15	Radial profiles of normalized mean axial velocity, turbulent kinetic energy, and shear stress for the particle-laden coaxial jets	570
6.4.1-16	Measurements of rms gas velocity component for the particle-laden coaxial jets ...	571
6.4.1-17	Radial profiles of normalized particle axial velocity	572
6.4.1-18	Radial profiles of rms of particle velocity components	573
6.4.2-1	Confined coaxial jets – geometrical details	578
6.4.2-2	Confined coaxial jets – grid layout	579
6.4.2-3	Measured profiles at the inlet plane ($x = 4$ mm)	580
6.4.2-4	Comparison of predicted mean axial velocity by $k-\epsilon$ model with data	581
6.4.2-5	Comparison of predicted turbulent shear stress by $k-\epsilon$ model with data	582
6.4.2-6	Comparison of predicted turbulent kinetic energy by $k-\epsilon$ model with data	583
6.4.2-7	Comparison of predicted mean axial velocity by DSM with data	584
6.4.2-8	Comparison of predicted axial rms velocity by DSM with data	585
6.4.2-9	Comparison of predicted radial rms velocity by DSM with data	586
6.4.2-10	Comparison of predicted tangential rms velocity by DSM with data	587
6.4.2-11	Comparison of predicted turbulent shear stress by DSM with data	588
6.4.2-12	Comparison of predicted mean axial velocity by DSM and ASM with data	589
6.4.2-13	Comparison of predicted axial rms velocity by DSM and ASM with data	590
6.4.2-14	Comparison of predicted radial rms velocity by DSM and ASM with data	591
6.4.2-15	Comparison of predicted tangential rms velocity by DSM and ASM with data	592
6.4.2-16	Comparison of predicted turbulent shear stress profiles by DSM and ASM with data	593
6.4.2-17	Comparison of predicted turbulent kinetic energy by $k-\epsilon$, DSM, and ASM with data	594
6.4.2-18	Measured profiles at the inlet plane ($x = 4$ mm)	595
6.4.2-19	Comparison of calculated normalized mean axial velocity of the continuous phase by DSM with data	597
6.4.2-20	Comparison of calculated normalized streamwise turbulence intensity of continuous phase by DSM with data	598

LIST OF ILLUSTRATIONS (cont)

<u>Figure</u>	<u>Title</u>	<u>Page</u>
6.4.2-21	Comparison of calculated normalized radial turbulence intensity of continuous phase by DSM with data	599
6.4.2-22	Comparison of calculated normalized tangential turbulence intensity of continuous phase by DSM with data	600
6.4.2-23	Comparison of calculated normalized shear stress of continuous phase by DSM with data	601
6.4.2-24	Comparison of calculated normalized mean axial velocity of dispersed phase (U_p) by DSM with data	602
6.4.2-25	Comparison of calculated normalized mean radial velocity of dispersed phase (V_p) by DSM with data	603
6.4.2-26	Comparison of calculated normalized streamwise turbulence intensity of dispersed phase by DSM with data	604
6.4.2-27	Comparison of calculated normalized radial turbulence intensity of dispersed phase by DSM with data	605
6.4.2-28	Comparison of calculated normalized tangential turbulence intensity of dispersed phase by DSM with data	606
6.4.2-29	Number density distribution	607
6.5-1	Unconfined axisymmetric swirling coaxial jets geometry	613
6.5-2	Unconfined swirling coaxial jets grid layout	614
6.5-3	Measured profiles at the inlet plane ($x = 4$ mm)	615
6.5-4	Comparison of calculated mean axial velocity by k- ϵ model with data	617
6.5-5	Comparison of calculated mean tangential velocity by k- ϵ model with data	619
6.5-6	Comparison of predicted turbulent kinetic energy by k- ϵ model with measurement	621
6.5-7	Comparison of predicted turbulent shear stress by k- ϵ model with data	623
6.5-8	Comparison of calculated mean axial velocity by k- ϵ and DSM with data	625
6.5-9	Comparison of calculated mean tangential velocity by k- ϵ and DSM with data	627
6.5-10	Comparison of calculated axial rms velocity component by DSM with data	629
6.5-11	Comparison of calculated radial rms velocity component by DSM with data	631
6.5-12	Comparison of calculated tangential rms velocity component by DSM with data	633
6.5-13	Comparison of calculated uv profiles by k- ϵ and DSM with data	635
6.5-14	Comparison of calculated uw profiles by DSM with data	637
6.6-1	Airblast injector flow configuration	643
6.6-2	Airblast injector flow inlet conditions	644
6.6-3	Airblast injector flow grid layout	645
6.6-4	Comparison of calculated mean axial velocity profiles by DSM with data	646
6.6-5	Comparison of calculated rms axial velocity profiles by DSM with data	647
6.6-6	Comparison of calculated rms radial velocity profiles by DSM with data	648
6.6-7	Comparison of calculated rms tangential velocity profiles by DSM with data	649
6.6-8	Comparison of calculated shear stress profiles by DSM with data	650
6.6-9	Comparison of calculated mean axial velocity profiles by k- ϵ with data	651
6.6-10	Comparison of calculated turbulent kinetic energy profiles by k- ϵ with data	652
6.6-11	Comparison of calculated turbulent shear stress profiles by k- ϵ with data	653

LIST OF TABLES

<u>Table</u>	<u>Title</u>	<u>Page</u>
VOLUME I		
3.3-I	Flow system circuit specification	54
3.4-I	Results of flow split test	64
3.4-II	Initial test conditions	66
3.4-III	Impingement testing results	68
3.4-IV	Initial test conditions and changes made	70
3.4-V	Test conditions based on screening tests	71
3.5-I	Milestones in development of UCICL PDPA system	91
3.7-I	Verification of discrimination in the free jet	128
4.1-I	Case numbers used in the tabulated results	145
4.1-II	Quantities measured and diagnostics employed	146
VOLUME II		
5.1-I	Values of constants in the k-e model	392
5.1-II	Values of constants in the ASM and DSM closures	393
6.1-I	Experimental flow conditions at 0.04D downstream of pipe exit	406
6.1-II	Confined single jet experimental flow conditions	421
6.1-III	Confined single jet experimental flow conditions	423
6.2-I	Unconfined single annular jet experimental flow conditions	461
6.2-II	Single annular jet grid definition	462
6.3-I	Unconfined annular swirling jet test configuration	491
6.3-II	Unconfined annular swirling jet grid definition	492
6.3-III	Confined annular swirling jet test configurations	515
6.3-IV	Confined annular swirling jet grid definition	516
6.4-I	Unconfined coaxial jets experimental conditions at 2 mm downstream of pipe exit	548
6.4-II	Confined coaxial jets grid definition	550
6.4-III	Confined coaxial jets experimental conditions at 4 mm downstream of nozzle exit	574
6.5-I	Unconfined swirling coaxial jets experimental conditions	608
6.5-II	Unconfined swirling coaxial jets grid definition	609
6.6-I	Airblast injector flow grid definition	640

1. *Introduction* (100 words)

2. *Background* (100 words)

3. *Methodology* (100 words)

4. *Results* (100 words)

5. *Conclusion* (100 words)

6. *References* (100 words)

7. *Appendix* (100 words)

8. *Summary* (100 words)

9. *Final Remarks* (100 words)

10. *Conclusion* (100 words)

TABLE OF CONTENTS

<u>Section</u>	<u>Title</u>	<u>Page</u>
V	Physical and Mathematical Models	391
5.1	Single-Phase Flow Models	391
5.2	Two-Phase Flow Models	395
5.2.1	Dispersed Phase	395
5.2.2	Continuous Phase	396
5.3	Mathematical Formulation	399
5.3.1	Discretization	399
5.3.2	Power-Law Differencing Scheme	399
5.3.3	Flux-Spline Differencing Scheme	399

V. PHYSICAL AND MATHEMATICAL MODELS

5.1 SINGLE-PHASE FLOW MODELS

In this section, the equations which govern the distribution of the mean quantities are summarized. These equations are derived from the conservation laws of mass and momentum using time averaging and are expressed in tensor notation for steady and constant density flow as

$$\frac{\partial U_i}{\partial X_i} = 0 \quad (5)$$

$$\frac{\partial(U_i U_j)}{\partial X_j} = -\frac{1}{\rho} \frac{\partial P}{\partial X_i} - \frac{\partial}{\partial X_j} (\overline{u_i u_j}) \quad (6)$$

where U_i and u_i are the mean and fluctuating velocities along the X_i direction, respectively, p is the mean pressure, and the bar is used to denote time-averaged quantities.

As a consequence of the nonlinearity of Equation 6, the averaging process used introduces unknown correlations $\overline{u_i u_j}$ which can be made known through the assumption of turbulence modeling.

Three different types of turbulence closures are investigated, namely, the standard k - ϵ model, algebraic second-moment closure (ASM), and differential second-moment closure (DSM).

The k - ϵ model is a simple closure based on the gradient transport relations. In this model, the turbulent fluxes are related to the mean fields through the assumption of an isotropic eddy viscosity and a turbulent Prandtl/Schmidt number as

$$-\overline{\rho u_i u_j} = \mu_t \left(\frac{\partial U_i}{\partial X_j} + \frac{\partial U_j}{\partial X_i} \right) - \frac{2}{3} \delta_{ij} \rho k \quad (7)$$

The eddy viscosity (μ_t) is obtained from the turbulent kinetic energy (k) and its dissipation rate (ϵ) using the relation

$$\mu_t = c_\mu \rho k^2 / \epsilon \quad (8)$$

In order to close the set of Equations 5 through 7, two additional equations governing the transport of k and ϵ are required. These are

$$\rho U_j \frac{\partial k}{\partial X_j} = \frac{\partial}{\partial X_j} \left(\frac{\mu_t}{\sigma_k} + \mu \right) \frac{\partial k}{\partial X_j} - (\overline{\rho u_i u_j}) \frac{\partial U_i}{\partial X_j} - \rho \epsilon \quad (9)$$

$$\rho U_j \frac{\partial \epsilon}{\partial X_j} = \frac{\partial}{\partial X_j} \left(\frac{\mu_t}{\sigma_\epsilon} + \mu \right) \frac{\partial \epsilon}{\partial X_j} - C_{\epsilon 1} \frac{\epsilon}{k} (\overline{\rho u_i u_j}) \frac{\partial U_i}{\partial X_j} - C_{\epsilon 2} \rho \frac{\epsilon^2}{k} \quad (10)$$

where σ_k and σ_ϵ are turbulent Schmidt numbers and $C_{\epsilon 1}$ and $C_{\epsilon 2}$ are model constants. The constants used in this model have been taken from Launder and Spalding (1974^{*}) and are given in Table 5.1-I.

Table 5.1-I.
Values of constants in the k- ϵ model.

C_μ	$C_{\epsilon 1}$	$C_{\epsilon 2}$	σ_k	σ_ϵ
0.09	1.44	1.92	1.0	1.3

The k- ϵ model is the simplest model which is suitable for recirculating flow calculations. It allows the characteristic length scale of a wide range of complex flow fields to be determined. The k- ϵ model has been used with success in the calculation of various free shear flows and recirculating flows with and without swirl (e.g., Rodi, 1980). However, in flows with significant streamline curvature, the isotropic eddy viscosity assumption may not be able to describe the turbulent diffusion effects adequately. The axisymmetric form of the turbulent flow equations is given in Appendix A for the k- ϵ model.

To allow for the nonisotropic behavior of the eddy viscosity and to account for the effect of body forces (e.g., buoyancy, rotation), the k- ϵ model is refined by introducing ASM. This model is based on a simplification of the Reynolds stress transport equation which relates the individual stresses to mean velocity gradient, turbulent kinetic energy, and its dissipation rate by way of algebraic expressions. The ASM model adopted here is based on Rodi's hypothesis (Rodi, 1976) which approximates the convection and diffusion transport of turbulent stresses in terms of the transport of k.

The result can be summarized as

$$a_{ij} = \left(\frac{1 - C_2}{C_1 - 1 + \frac{P_k}{\rho\epsilon}} \right) \left(\frac{P_{ij} - \frac{2}{3}\delta_{ij}P_k}{\rho\epsilon} \right) \quad (11)$$

where

$$P_{ij} = \overline{\rho u_j u_k} \frac{\partial U_i}{\partial X_k} - \overline{\rho u_i u_k} \frac{\partial U_j}{\partial X_k} \quad (12)$$

$$P_k = \frac{1}{2} P_{ii} \quad (13)$$

C_1 and C_2 are model constants and a_{ij} is the nondimensional measure of anisotropy and is given by the following expression

$$a_{ij} = \frac{\overline{u_i u_j}}{k} - \frac{2}{3} \delta_{ij} \quad (14)$$

^{*} References for Section V are listed at the end of the section.

Since the quantities k and ϵ are present in these equations, their transport equations also have to be solved. These are determined by

$$\rho U_j \frac{\partial k}{\partial X_j} = \frac{\partial}{\partial X_j} \left(C_k \rho \frac{k}{\epsilon} \overline{u_j u_n} \frac{\partial k}{\partial X_n} \right) - P_k - \rho \epsilon \quad (15)$$

$$\rho U_j \frac{\partial \epsilon}{\partial X_j} = \frac{\partial}{\partial X_j} \left(C_{\epsilon} \rho \frac{k}{\epsilon} \overline{u_j u_n} \frac{\partial \epsilon}{\partial X_n} \right) + C_{\epsilon 1} \frac{\epsilon}{k} P_k - C_{\epsilon 2} \rho \frac{\epsilon^2}{k} \quad (16)$$

C_k , C_{ϵ} , $C_{\epsilon 1}$, and $C_{\epsilon 2}$ are all model constants and are given in Table 5.1-II.

Table 5.1-II.
Values of constants in the ASM and DSM closures.

$C_{\epsilon 1}$	1.44
$C_{\epsilon 2}$	1.92
C_{ϵ}	0.18
C_k	0.22
C_1	1.8
C_2	0.6
C_{1w}	0.05
C_{2w}	0.006

The k - ϵ and ASM models assume that the local state of turbulence can be characterized by one velocity scale. In order to allow for the different development of the various Reynolds stresses representing various velocity scales in complex flows and to account properly for their transport, models which employ transport equations for the individual stresses must be applied.

The Reynolds stress equations can be written in tensor notation form as

$$\rho U_k \frac{\partial}{\partial X_k} \overline{u_i u_j} - d_{ij} = P_{ij} + \phi_{ij} - \rho \epsilon_{ij} \quad (17)$$

Here, P_{ij} is the production of Reynolds stress $u_i u_j$, ϵ_{ij} represents viscous dissipation, ϕ_{ij} controls the redistribution of turbulence energy among the normal stresses through the interaction of pressure and strain, and d_{ij} stands for turbulence diffusion. Since P_{ij} is exact, it does not need modeling. However, closure assumptions are required for d_{ij} , ϕ_{ij} , and ϵ_{ij} . The assumption of local isotropy allows the dissipation tensor to be approximated by

$$\epsilon_{ij} = \frac{2}{3} \delta_{ij} \epsilon \quad (18)$$

where ϵ is the turbulence energy dissipation rate. The diffusion term is approximated by the gradient-diffusion model of Daly and Harlow (1970)

$$d_{ij} = -\frac{\partial}{\partial X_k} \left(C_k \rho \overline{u_k u_n} \frac{k}{\varepsilon} \frac{\partial \overline{u_i u_j}}{\partial X_n} \right) \quad (19)$$

where C_k is a model constant, and $k = 1/2 \overline{u_i u_i}$ is the turbulent kinetic energy. The pressure redistribution term (ϕ_{ij}) is modeled in three parts: ϕ_{ij1} resulting from purely turbulence interactions known as "return-to-isotropy," ϕ_{ij2} involving interactions between the mean strain rate and turbulence known as "rapid" part, and ϕ_{ijw} representing the effects of rigid boundaries on both ϕ_{ij1} and ϕ_{ij2} . The presence of a rigid wall affects the flow field near that region by impeding the transfer of turbulent energy from the streamwise direction to that normal to the wall, and as a result reduces the relative magnitude of the shear stress. In the present study, Rotta's linear model (Rotta, 1951) for the turbulence part of ϕ_{ij} is adopted

$$\phi_{ij1} = -C_1 \rho \frac{\varepsilon}{k} \left(\overline{u_i u_j} - \frac{2}{3} \delta_{ij} k \right) \quad (20)$$

The simple linear form for ϕ_{ij1} is widely accepted and used despite the fact that the actual "return-to-isotropy" process is highly nonlinear (Bradshaw, 1968). More sophisticated nonlinear forms, such as Lumely and Khayeh-Nouri's proposal (1974) have been suggested, but these have shown no significant improvement over Rotta's proposal. The rapid part is approximated using the simple model suggested by Naot et al. (1970), known as the isotropization production (IP) model

$$\phi_{ij2} = -C_2 \left(P_{ij} - \frac{2}{3} \delta_{ij} P_k \right) \quad (21)$$

A more sophisticated version of ϕ_{ij2} is the linear quasi-isotropic (QI) model (Launder et al, 1975)

$$\phi_{ij2} = -\left(\frac{C_2 + 8}{11} \right) \left(P_{ij} - \frac{2}{3} \delta_{ij} P_k \right) - \left(\frac{8C_2 - 2}{11} \right) \left(D_{ij} - \frac{2}{3} \delta_{ij} P_k \right) - \left(\frac{30C_2 - 2}{55} \right) \rho k \left(\frac{\partial U_i}{\partial X_j} + \frac{\partial U_j}{\partial X_i} \right) \quad (22)$$

where

$$D_{ij} = -\rho \left(\overline{u_i u_k} \frac{\partial U_k}{\partial X_j} + \overline{u_j u_k} \frac{\partial U_k}{\partial X_i} \right) \quad (23)$$

This model includes both the symmetric and antisymmetric mean strain effects on redistribution modeling.

The effects of solid boundaries on pressure redistribution term are included using the wall correction proposed by Launder et al. (1975), or

$$\phi_{ijw} = \frac{k^{1.5}}{\varepsilon X_n} \left[C_{1w} \frac{\varepsilon}{k} \left(\overline{u_i u_j} - \frac{2}{3} \delta_{ij} P_k \right) + C_{2w} (P_{ij} - D_{ij}) \right] \quad (24)$$

where X_n is the normal distance from the wall and the model constants C_{1w} and C_{2w} are specified in Table 5.1-II. The modeled Reynolds stress transport equations in axisymmetric coordinates (x, r) are given in Appendix B.

5.2 TWO-PHASE FLOW MODELS

The mathematical formulations for the particle/flow problems consist of Eulerian conservation equations to the continuous gas phase and Lagrangian equations to discrete particle motion. The continuous gas phase is coupled to the discrete phase by incorporating additional source term.

5.2.1 Dispersed Phase

The model employed for the dispersed phase calculations is based on the stochastic Lagrangian formulation reported by Gosman and Ioannides (1983). In this approach, effects of the gas phase turbulent fluctuations on particle drag and dispersion are considered. Because of the large number of actual particles in the spray, the dispersed phase is characterized by individual spherical particles, termed "computational particles." Each of these computational particles represents a group of particles all having the same initial size, velocity, and temperature. The commonly adopted equation of motion of n-th computational particle in dilute spray, assuming large particle-to-fluid density ratio, is given by

$$\frac{dV_i^n}{dt} = \frac{(U_i - V_i^n)}{\tau_d} + g_i \quad (25)$$

where U_i and V_i are the i th components of instantaneous gas and particle velocity, respectively, g is the gravitational acceleration, and τ_d is the dynamic relaxation time of particle defined as

$$\tau_d = \frac{4D_p\rho_p}{3C_D\rho|U - V^n|} \quad (26)$$

Here, D_p and ρ_p are particle diameter and density, respectively, C_D is the drag coefficient, ρ is the fluid density

$$C_D = (24/Re)(1 + 0.1315[Re]^{0.82-0.05w}), \quad 0.01 < Re \leq 20 \quad (27)$$

$$C_D = (24/Re)(1 + 0.1935[Re]^{0.6305}), \quad 20 < Re \leq 260 \quad (28)$$

where $w = \log_{10}Re$ and the particle Reynolds number (Re) is defined as

$$Re = \frac{\rho|U - V^n|D_p}{\mu} \quad (29)$$

where μ is the fluid viscosity. Integration of acceleration from Equation 25 results in the velocity components of the particle. The position of each particle group can be found by integrating the equation

$$\frac{dX_i^n}{dt} = V_i^n \quad (30)$$

where X_i is the particle position vector. A particle is assumed to interact with an eddy for a characteristic time τ . The interaction time is determined by the minimum of either the residence time (t_r) which is the time required for a particle to cross an eddy or the eddy lifetime (t_e) which is the time that particle remains within the eddy during the whole of its lifetime. The time scales are estimated with the assumption that the characteristic size of an eddy is the dissipation length scale L_e , given by

$$L_e = c_\mu^{1/2} k^{3/2} / \epsilon \quad (31)$$

t_e and t_r are then estimated as

$$t_e = L_e / \sqrt{(2k/3)} \quad (32)$$

$$t_r = L_e / |U - V^n| \quad (33)$$

hence,

$$\tau = \min(t_e, t_r) \quad (34)$$

The velocity fluctuations associated with each eddy are found by making a random selection from the probability density function of velocity. The turbulence is assumed to be anisotropic if the DSM model is applied with fluctuating components having a Gaussian distribution. The standard deviation for each distribution is taken to be its respective root mean square (rms) velocity fluctuation obtained from the Reynolds equations. The distribution is randomly sampled when a particle enters the gas velocity field to obtain the instantaneous gas velocity. However, in the $k-\epsilon$ model, the rms velocity fluctuation is chosen randomly from an assumed isotropic Gaussian distribution with mean square deviation $2/3k$.

5.2.2 Continuous Phase

For high Reynolds number turbulent flow, neglecting the volume fraction of the particle phase, the time averaged mass and momentum equations can be expressed in Cartesian tensor notation as

$$\frac{\partial}{\partial X_i} (\rho U_i) = 0 \quad (35)$$

$$\frac{\partial}{\partial X_j} (\rho U_i U_j) = -\frac{\partial P}{\partial X_i} - \frac{\partial}{\partial X_j} (\rho \overline{u_i u_j}) - S_{pi} \quad (36)$$

where S_{pi} is the interfacial drag force resulting from interaction between particles and the carrier phase.

The interfacial drag force per unit volume is given by

$$S_{pi} = \sum_n \frac{3}{4} \alpha^n C_D \frac{\rho}{D_p} |U - V^n| (U_i - V_i^n) \quad (37)$$

where α^n is the volume fraction of particle group n that passes through the computational cell and is given by

$$\alpha^n = N \frac{\pi}{6} (D_p)^3 / \Delta V \quad (38)$$

Here, N is the number of particles represented by the trajectory n , and ΔV is the computational cell volume.

Two different types of turbulence closures are investigated. One is a simple closure based on the gradient transport relation (Equation 7). Two additional partial differential equations are also needed to obtain k and ϵ (Mostafa and Mongia, 1988). These are

$$\rho U_j \frac{\partial k}{\partial X_j} = \frac{\partial}{\partial X_j} \left(\frac{\mu_t}{\phi_k} + \mu \right) \frac{\partial k}{\partial X_j} - (\overline{\rho u_i u_j}) \frac{\partial U_i}{\partial X_j} - \rho \epsilon - S_{pk} \quad (39)$$

$$\rho U_j \frac{\partial \epsilon}{\partial X_j} = \frac{\partial}{\partial X_j} \left(\frac{\mu_t}{\phi_\epsilon} + \mu \right) \frac{\partial \epsilon}{\partial X_j} - C_{\epsilon 1} \frac{\epsilon}{k} (\overline{\rho u_i u_j}) \frac{\partial U_i}{\partial X_j} - C_{\epsilon 2} \rho \frac{\epsilon^2}{k} - S_{pe} \quad (40)$$

where

$$S_{pk} = \sum_n 2k\alpha^n F^n \left(1 - \frac{\tau_L}{\tau_L + \tau_d} \right) \quad (41)$$

$$S_{pe} = C_{\epsilon 3} \frac{\epsilon}{k} \sum_n 2k\alpha^n F^n \left(1 - \frac{\tau_L}{\tau_L + \tau_d} \right) \quad (42)$$

F^n and τ_L are the interphase friction coefficient and the continuous phase Lagrangian time scale, respectively, given by

$$F^n = \frac{3}{4} C_D^n \frac{\rho}{D_p^n} |U - V^n| \quad (43)$$

$$\tau_L = 0.35 \frac{k}{\epsilon} \quad (44)$$

Another type of closure is based on solving additional transport equations for $\overline{u_i u_j}$ without invoking the gradient transport assumption. The Reynolds stress equation suggested for two-phase flow can be written in tensor notation as

$$\rho U_k \frac{\partial}{\partial X_k} (\overline{u_i u_j}) - d_{ij} = P_{ij} + \phi_{ij} - \rho \epsilon_{ij} + \hat{P}_{ij} \quad (45)$$

where P_{ij} , ϵ_{ij} , and d_{ij} represent production, dissipation, and diffusion of Reynolds stresses (Equations 12, 18, and 19). \hat{P}_{ij} is an extra term that accounts for the generation of turbulence due to the particles motion. The model for \hat{P}_{ij} tensor is suggested as (Lopez et al, 1990)

$$\hat{P}_{ij} = \begin{bmatrix} 4/5 & 0 & 0 \\ 0 & 3/5 & 0 \\ 0 & 0 & 3/5 \end{bmatrix} \hat{P}_i \quad (46)$$

where \hat{P}_i is the turbulence production due to the particles work as they move through the continuous phase and is given by

$$\hat{P}_i = C_3 \sum_n \frac{1}{\tau_d} \rho_p \alpha^n |U - V^n|^2 \quad (47)$$

where $C_3 = 0.02$ is a model constant indicating only 2% of the turbulence created by particles is transferred into the large eddies.

The pressure redistribution, Φ_{ij} , is modeled in three parts. These are: Φ_{ij1} resulting from purely turbulence interaction, Φ_{ij2} involving interactions between the mean strain rate and turbulence, and Φ_{ij3} , as suggested by Lopez et al (1990), representing the effects of particles on both Φ_{ij1} and Φ_{ij2} .

$$\Phi_{ij} = -C_1 \rho \frac{\epsilon}{k} (\overline{u_i u_j} - \frac{2}{3} \delta_{ij} k) - C_2 (P_{ij} - \frac{2}{3} \delta_{ij} P_k) - C_2 (\hat{P}_{ij} - \frac{2}{3} \delta_{ij} \hat{P}_k) \quad (48)$$

The additional unknown, ϵ , is determined by the following equation

$$\rho U_j \frac{\partial \epsilon}{\partial X_j} = \frac{\partial}{\partial X_i} \left(C_{\epsilon 2} \rho \frac{k}{\epsilon} \overline{u_i u_n} \frac{\partial \epsilon}{\partial X_n} \right) + C_{\epsilon 1} \frac{\epsilon}{k} (P_k + \hat{P}_k) - C_{\epsilon 2} \Gamma \frac{\epsilon^2}{k} \quad (49)$$

5.3 MATHEMATICAL FORMULATION

The calculation procedure used in this study is based on the primitive variable formulation of the Navier-Stokes equations. The conservation equations are discretized using a control-volume approach. The coupling between the continuity and momentum equations is handled via the SIMPLER algorithm. The procedure is described in detail in Patankar (1980), Varejao (1979), and Karki et al (1988).

The conservation equations for all dependent variables may be expressed in the following general form

$$\frac{\partial}{\partial X}(\rho U \phi) + \frac{\partial}{\partial Y}(\rho V \phi) = \frac{\partial}{\partial X}\left(\Gamma \frac{\partial \phi}{\partial X}\right) + \frac{\partial}{\partial Y}\left(\Gamma \frac{\partial \phi}{\partial Y}\right) + S \quad (50)$$

where ϕ is the particular variable of interest, Γ is the diffusion coefficient, and S is the source term.

5.3.1 Discretization

Equation 50 can be written as

$$\frac{\partial}{\partial X} J_x + \frac{\partial}{\partial Y} J_y = S \quad (51)$$

where J_x and J_y are the total (convection and diffusion) fluxes defined by

$$J_x = \rho U \phi - \Gamma \frac{\partial \phi}{\partial X} \quad (52a)$$

$$J_y = \rho V \phi - \Gamma \frac{\partial \phi}{\partial Y} \quad (52b)$$

The integration of Equation 51 over the control volume surrounding the grid point P (Figure 5.3.1-1*) gives

$$(J_{x,e} - J_{x,w}) \Delta Y + (J_{y,n} - J_{y,s}) \Delta X = S \Delta X \Delta Y \quad (53)$$

A discretization scheme is needed to relate the flux at each control-volume face to the values of the dependent variable at the neighboring grid points. The results presented in this report have been obtained using the power-law differencing scheme and flux-spline scheme. A brief description of these schemes is presented next.

5.3.2 Power-Law Differencing Scheme

This scheme is based on a curve fit to the exact solution of the one-dimensional convection-diffusion equation without a source. Since this formulation is based on a purely one-dimensional flux balance, it leads to significant numerical errors in the presence either of strong source terms, or of crossflow gradients in multidimensional flows coupled with the grid-to-flow skewness. The flux-spline scheme includes these effects in the interpolation profile between the grid points.

* Figures for Section V appear at the end of each subsection. The figure number identifies the subsection in which the figure is discussed.

5.3.3 Flux-Spline Differencing Scheme

The flux-spline scheme considered here is based on the assumption that within a control volume the total flux in a given direction varies linearly along the coordinate direction. For example, the flux in the x-direction for the control volume around the grid point P (Figure 5.3.3-1) is given by

$$J_x = \rho U \phi - \Gamma \frac{\partial \phi}{\partial x} = J_{x,w} + \left(\frac{J_{x,e} - J_{x,w}}{\Delta x} \right) x \quad (54)$$

The integration of Equation 54 leads to the following expression for the variation of ϕ in the x-direction

$$\phi = a + b \exp(\rho U x / \Gamma) + c x \quad (55)$$

where the constants a, b, and c for a given control volume can be expressed in terms of $J_{x,e}$, $J_{x,w}$, and ϕ_p .

Equation 55 gives the variation of ϕ within a control volume. For two adjacent control volumes the ϕ -profiles are such that they imply the same total flux at the common interface. In addition, these profiles must also give a unique value of ϕ at the common interface. This continuity-of- ϕ (spline continuity) condition for the interface between the grid points W and P can be expressed as

$$J_{x,w} = (D_{x,w} \phi_W - E_{x,w} \phi_P) + B_{x,w} (J_{x,w} - J_{x,e}) + C_{x,w} (J_{x,w} - J_{x,ww}) \quad (56)$$

Here, the expression $(D_{x,w} \phi_W - E_{x,w} \phi_P)$ is identical to that obtained from the lower-order exponential scheme (e.g., Patankar, 1980) which is based on the assumption that the total flux is uniform within a control volume. The extra terms involving B_x and C_x result from the linear variation of flux. For ease of presentation, Equation 56 is rewritten as

$$J_{x,w} = (D_{x,w} \phi_W - E_{x,w} \phi_P) + \hat{J}_{x,w} \quad (57)$$

It should be noted that additional terms such as $\hat{J}_{x,w}$ involve the difference in flux values at adjacent faces of the control volume. That there is a difference in flux indicates the presence of a source term and/or multidimensionality (a change of flux in one direction is felt as a source term in another direction).

Similar expressions can also be derived for fluxes in other coordinate directions. Substituting these expressions in Equation 53 and utilizing the discrete form of the continuity equation, the following discretization equation for ϕ is obtained

$$a_p \phi_p = \sum a_{nb} \phi_{nb} + b + \hat{S} \quad (58)$$

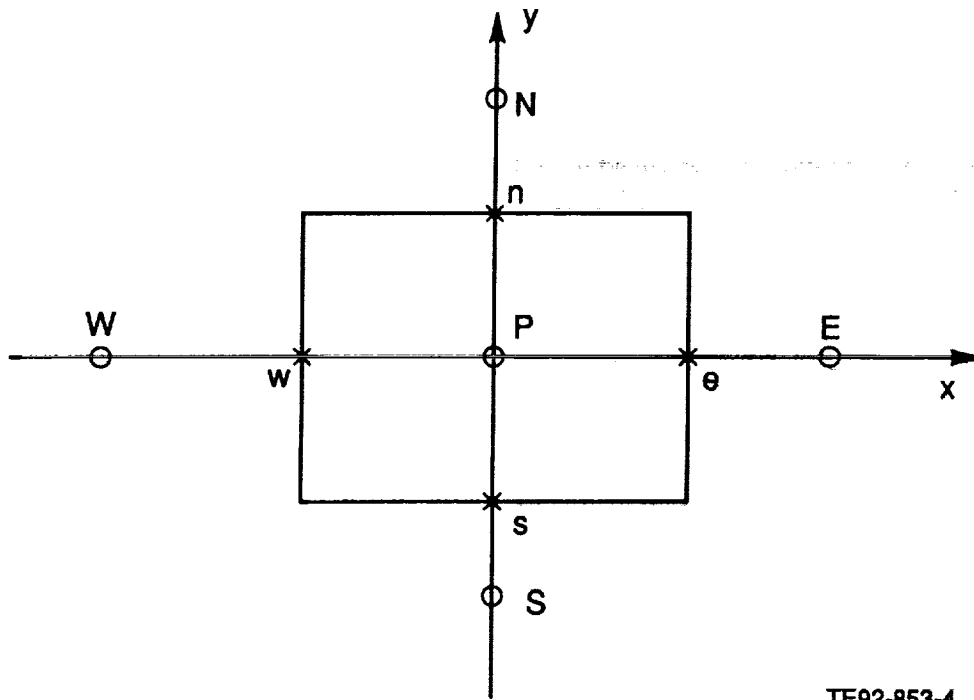
The values of the influence coefficients a_{nb} are identical to the coefficients obtained from the exponential scheme. The contribution of the flux-spline formulation is contained in the term \hat{S} , which is given

$$\hat{S} = (\hat{J}_{x,w} - \hat{J}_{x,e}) \Delta y + (\hat{J}_{y,s} - \hat{J}_{y,n}) \Delta x \quad (59)$$

A two-dimensional situation is governed by three field variables: ϕ , J_x , and J_y . The three sets of equations that determine these variables are

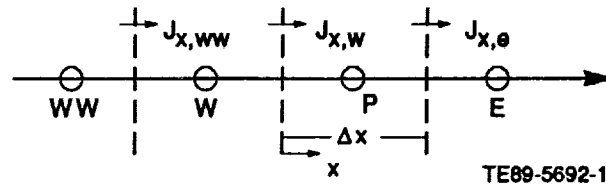
- (1) the conservation equation for ϕ
- (2) the spline-continuity condition in the x-direction
- (3) the spline-continuity condition in the y-direction

The solution of these equations is obtained in an iterative manner. In the beginning, \hat{J}_x and \hat{J}_y are set equal to zero, then the conservation equation for ϕ reduces to the lower-order formulation and can be easily solved. The solution leads to new estimates for the fluxes J_x and J_y from which new \hat{J}_x and \hat{J}_y can be calculated. The ϕ -equation is now solved with the flux-spline contribution to the source term. This process is repeated until convergence is achieved.



TE92-853-4

Figure 5.3.1-1. Control volume around the grid point P.



TE89-5692-1

Figure 5.3.3-1. One-dimensional condition.

REFERENCES

- Bradshaw, P., 1968, "Outlook for 3-Dimensional Procedures," *Proc. AFOSR-IP-Stanford Boundary Layer Conf.*, 1, 427.
- Daly, B. J. and Harlow, F. H., 1970, "Transport Equations of Turbulence," *Phys. Fl.*, 13, 2634-2649.
- Gosman, A. D. and Ioannides, E., 1983, "Aspects of Computer Simulation of Liquid-Fueled Combustors," *J. Energy*, 7 (6), 482-490.
- Karki, K. C., Patankar, S. V., Runchal, A. K., and Mongia, H. C., 1988, "Improved Numerical Methods for Turbulent Viscous Recirculating Flows," *Aerothermal Modeling Phase II Final Report, NASA CR-182169.*
- Launder, B. E. and Spalding, D. B., 1974, "The Numerical Computation of Turbulent Flows," *Computer Methods in Applied Mechanics and Engineering* 3, 269-289.
- Launder, B. E., Reece, G. J., and Rodi, W., 1975, "Progress in the Development of a Reynolds Stress Turbulence Closure," *JFM*, 68, 537-577.
- Lopez de Bertodano, M., et al, 1990, "The Prediction of Two-Phase Turbulence and Phase Distribution Phenomena using a Reynolds Stress Model," *Journal of Fluid Engineering*, 112, 107-113.
- Lumley, J. L. and Khajeh Nouri, B. J., 1974, "Computational Modeling of Turbulent Transport," *Adv. Geophys.*, 18A, 169.
- Mostafa, A. A. and Mongia, H. C., 1988, "On the Interaction of Particles and Turbulent Fluid Flows," *Int. J. Heat Mass Transfer*, 31 (10), 2063, 2075.
- Naot, D., Shavit, A., and Wolfshtein, M., 1970, "Interactions Between Components of the Turbulent Velocity Correlation Tensor," *Israel J. Tech.*, 8, 259-269.
- Patankar, S. V., 1980, *Numerical Heat Transfer and Fluid Flows*, Hemisphere, New York.
- Rodi, W., 1976, "A New Algebraic Relation for Calculating the Reynolds Stresses," *Zeitschrift fuer Angewandte Mathematik and Mechanik*, 56, 219-221.
- Rodi, W., 1980, *Turbulence Models and Their Application in Hydraulics*, International Association of Hydraulic Research, Delft, The Netherlands.
- Rotta, J. C., 1951, "Statistische Theorie Nichthomogener Turbulenz," *Zeitschrift fur Physik*, 129, 547-572.
- Varejao, L. M. C., 1979, "Flux-Spline Method for Heat, Mass, and Momentum Transfer," Ph.D. thesis, University of Minnesota.

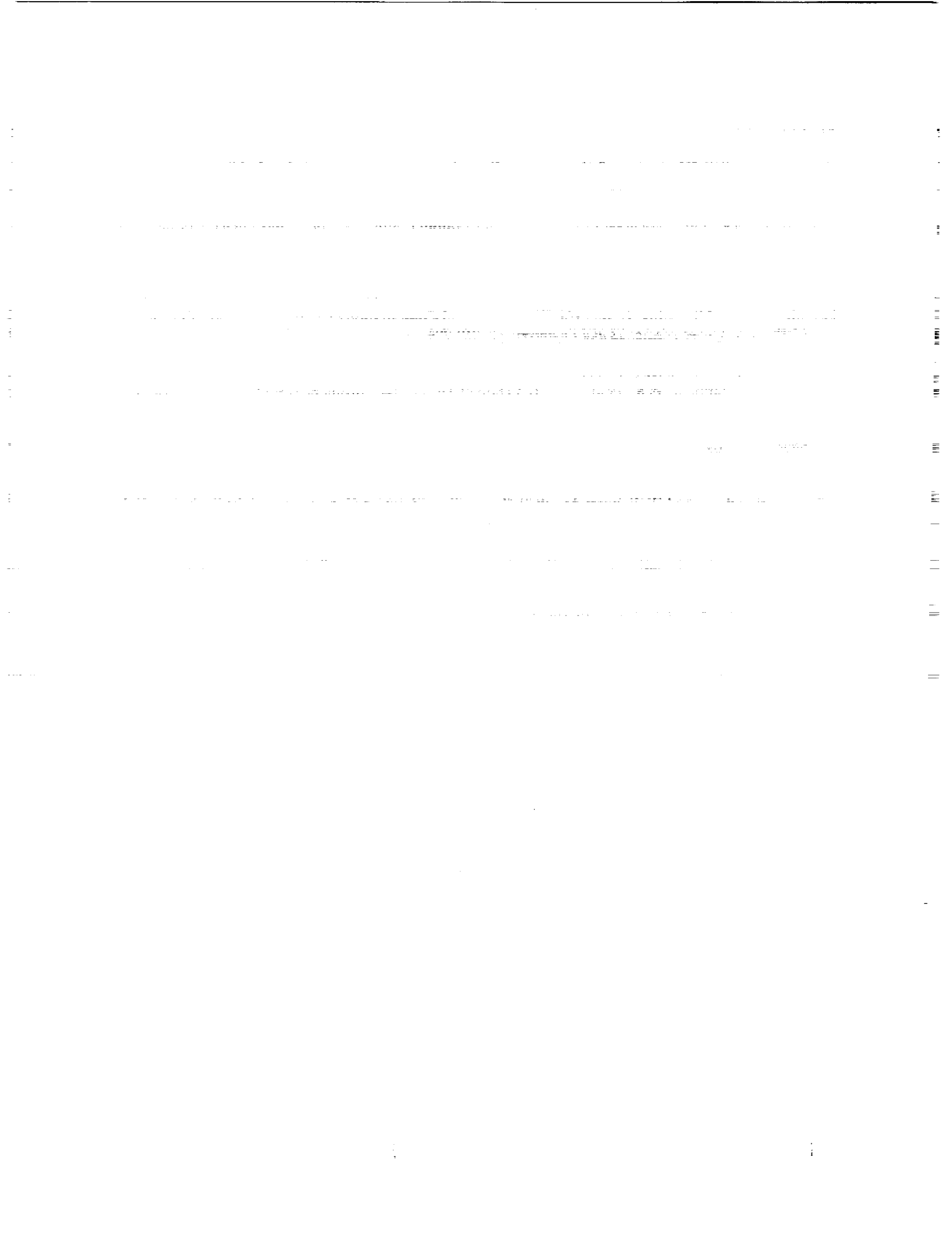


TABLE OF CONTENTS

<u>Section</u>	<u>Title</u>	<u>Page</u>
VI	Model Validation	405
6.1	Single Round Jet	405
	6.1.1 Unconfined Single Round Jet	405
	6.1.2 Confined Single Round Jet	421
6.2	Unconfined Single Annular Jet	461
6.3	Single Annular Swirling Jet	491
	6.3.1 Unconfined Annular Swirling Jet	491
	6.3.2 Confined Annular Swirling Jet	515
6.4	Coaxial Jets	548
	6.4.1 Unconfined Coaxial Jets	548
	6.4.1.1 The k- ϵ Turbulence Model	549
	6.4.1.2 The Algebraic Second-Moment Closure	553
	6.4.2 Confined Coaxial Jets	574
6.5	Unconfined Coaxial Jets with Swirling Annular Flow	608
6.6	Airblast Injector	639

VI. MODEL VALIDATION

This section presents the results of the comparisons of the various models for single-phase and two-phase turbulent recirculating flows. All the experimental data have been fully presented and discussed in Chapter IV. Predictions obtained with each of the turbulence models are discussed and compared with experimental data. The goals of this study require a careful selection of the test cases. They have to provide reliable mean flow and turbulence data in the recirculation and recovery regions. A detailed specification of the flow parameters in the upstream region is also essential since these are used as inlet conditions to start the computations. The test problems used range from simple flows to more complex flows to encompass the range of complexities involved in combustor flows. These are

- single round jet
- single annular jet
- single swirling annular jet
- coaxial jets
- coaxial jets with swirling annular flow
- airblast injector

All data sets meet the criteria for acceptable measurements in terms of adequate experimental facility, appropriate instrumentation, and agreement with generally accepted flow trends.

6.1 SINGLE ROUND JET

This section presents the comparison of computational results with experimental data. Both the confined and unconfined configurations with and without the presence of glass beads are investigated. Benchmark quality data were obtained by using a two-component phase/Doppler technique. The theoretical approach is based on a stochastic Lagrangian treatment for the discrete phase combined with an Eulerian description of the fluid field and using the $k-\epsilon$ or differential second-moment (DSM) closure.

6.1.1 Unconfined Single Round Jet

The case of round jet flow configuration was selected for model validation. The glass bead injector ($D = 25.3$ mm i.d.) with no inlet swirl was directed vertically downward within a 457 mm² wire mesh screen. The sketch of the test section is shown in Figure 6.1.1-1*. Data were obtained at seven axial stations 15, 25, 35, 50, 75, 150, and 300 mm from the exit plane of the injector. In addition, measurements were made close to the exit plane of the retractor to provide initial conditions (Table 6.1-I).

The carrier phase governing equations are solved numerically using the marching finite-difference solution procedure (Spalding, 1978[†]). The present calculations were obtained using a fine grid with 100 cross-stream grid points and marching step sizes limited by 3% of the current radial grid width or an entrainment increase of 3%, whichever is smaller. The ordinary differential equations governing particle motion are solved using a second-order finite difference algorithm. Ten thousand particles are used for the stochastic (ST) treatment, whereas 200 particles are computed when the deterministic (DT) method is compared with the ST.

The calculations start from the first experimental location (1 mm from the nozzle exit) where measured mean and root mean square (rms) velocity profiles for both gas and particles are available. The inlet profile for turbulent kinetic energy dissipation rate is obtained from the measured turbulent kinetic energy, turbulent shear stress, and axial velocity gradient.

* Figures for Section VI appear at the end of each subsection. The figure number identifies the subsection in which the figure is discussed.

† References for Section VI are listed at the end of the section.

Table 6.1-I.
Experimental flow conditions at 0.04D downstream of pipe exit.*

Parameter	Single-phase jet	Particle-laden jet	
		Case 1	Case 2
Gas-phase (air)			
Centerline velocity, $U_{z,0}$, m/s	4.74	4.70	4.20
Density, ρ_1 , kg/m ³	1.178	1.178	1.178
Mass flow rate m_1 , kg/s	0.0021	0.0021	0.0021
Reynolds number $Re = 4m_1/\rho_1 D$	5712	5712	5712
Particle-laden (glass beads)			
Centerline velocity, $V_{z,0}$, m/s		4.41	3.39
Density, ρ_2 , kg/m ³		2500.0	2500.0
Mass flow rate m_2 , kg/s		0.00042	0.0021
Ratio to particle-to-gas mass flow rate, LR		0.2	1.0

* $D = 0.0253$.

Predictions of a single-phase fluid flow field are first compared with data. The performance of the turbulence model in the jet developing region and the effect of the inlet dissipation rate on predicted airflow field are assessed. Both the standard k- ϵ and its modified version (Spalding, 1978) for round jet are employed. In the modified k- ϵ model, the effect of the centerline velocity gradient on c_μ and $c_{\epsilon 2}$ is given by

$$c_\mu = 0.09 - 0.04f_1 \quad (60)$$

$$c_{\epsilon 2} = 1.92 - 0.0067f_1 \quad (61)$$

where

$$f_1 = \left| 0.5R \frac{\frac{dU_c}{dz} - \left| \frac{dU_c}{dz} \right|^{0.2}}{U_c - U_\infty} \right| \quad (62)$$

U_c and U_∞ are the axial velocities of the fluid at the jet centerline and the ambient stream, respectively, and R is the local jet width. This modification allows the attainment of the correct spreading rate of a self-similar round jet.

Figures 6.1.1-2 and 6.1.1-3 relate to the measurements of a single-phase jet and present comparisons with calculations using both k- ϵ models. The results are plotted in a dimensionless form versus r/r_0 , where r_0 is the radius of the nozzle. This way the jet spreading can be seen from the mean axial velocity profiles. The mean axial gas velocities are normalized by the centerline velocity at the inlet of the nozzle, $U_{z,0}$, so that the jet centerline velocity decay can be illustrated in the same figure. All other quantities are normalized by the local mean centerline velocity. Figure 6.1.1-2 presents mean axial velocity, turbulent kinetic energy (k), and shear stress, while Figure 6.1.1-3 shows the three normal stresses and k . The gas rms velocities were calculated using isotropic assumption.

Both models yield good overall agreement with measurements close to the nozzle exit, but for the region downstream, the standard model performs better. In the first region, the decay of the centerline velocity

is very small, therefore, the two sets of model constants are quite the same. When the axial velocity started to decay substantially (at about $Z/D = 5$) c_{μ} and $c_{\epsilon 2}$ of the modified model decrease to values that give the observed spreading rate for self-similar round jets. For instance, at $Z/D = 7$, c_{μ} reduces to a value of 0.064, whereas $c_{\epsilon 2}$ becomes 1.87. These low values decreased the turbulent diffusion and, hence, the decay of the centerline velocity. The modified model also underpredicted the level of turbulence energy. The reason may be attributed to the inlet dissipation rate. Therefore, calculations were made with the standard model, but with two inlet dissipation levels, as given by ϵ_0 and $0.5\epsilon_0$ where ϵ_0 is the dissipation reference conditions obtained from the measured profiles of mean velocity, turbulent kinetic energy, and shear stress at 1 mm downstream of the nozzle exit. As seen from Figure 6.1.1-4, halving the inlet dissipation rate improves the predictions of the kinetic energy of turbulence.

The comparison of two versions of the $k-\epsilon$ model indicates that the results of the standard model agree better with experimental data, especially for the mean axial velocity. Therefore, this model was extended for two-phase flow calculations.

For particle-laden jets, two mass loading ratios (LR), defined as the ratio of particle-to-gas mass flow rate at the inlet plane, LR = 0.2 and 1.0, were considered. To distinguish between the effects of mean and fluctuating gas velocity in particle transport, predictions using ST and DT treatments are compared with the measured data. The main difference between the two treatments is that the first considers the effect of gas turbulence on particle motion, whereas the second completely ignores it.

Figure 6.1.1-5 shows the measured and predicted (ST treatment) distributions of mean centerline velocities and particle number density normalized by their corresponding values at the nozzle exit. Because of the slow decay of the particle mean velocity, there is a momentum transfer from the dispersed phase to the gas which causes an increase in the latter velocity compared with the corresponding single-phase values. This change in the gas-flow properties could also be attributed to the gas turbulence attenuation caused by particles. Gas turbulence attenuation causes a reduction in the jet spreading rate that results in less decay of the gas centerline velocity. Figure 6.1.1-5 (a) shows a progressive increase in the gas centerline velocity with the particle loading ratio LR, which might be explained by the fact that both the momentum transfer and turbulence modulation are proportional to LR. It can be seen from Figure 6.1.1-5 (b) that the particle number density is decaying much faster than the particle velocity. This means that the spreading of the dispersed phase dilutes the particle concentration but does not necessarily decelerate the particles.

Figures 6.1.1-6, 6.1.1-7, and 6.1.1-8 correspond to the measurements of a particle-laden jet with LR = 0.2 and indicate the extent to which the models described allow realistic calculations. Figure 6.1.1-6 presents the mean velocities of both phases, whereas Figures 6.1.1-7 and 6.1.1-8 show the rms values for the particles and gas and the shear stress of the latter. In these calculations, the turbulence model presented for two-phase flows was used. It can be seen from Figure 6.1.1-6 that both ST and DT treatments yield nearly the same results for gas quantities. However, for particle quantities the ST provides good predictions compared with the experimental data, whereas the DT performs quite poorly for the particle flow properties. According to the latter, a particle moves radially due to its initial mean radial velocity and/or the mean radial gas velocity, both of which are very small compared with the axial component. This might explain the narrow distribution of particle mean axial velocity and number density predicted by the DT.

Figure 6.1.1-7 shows comparisons between predicted and measured values of gas turbulence kinetic energy and shear stress. It also presents the rms axial gas velocity and its corresponding value for the particles. If Figure 6.1.1-7 is compared with Figure 6.1.1-2, some reduction in the gas kinetic energy of turbulence caused by the particles could be observed. This phenomenon is more pronounced at LR = 1.0 and will be discussed below in connection with the results of that case. In Figure 6.1.1-8 the comparisons are made for the radial and azimuthal rms velocities of both phases. It is seen that the ST predictions of rms particle velocities are in very good agreement with the data; v_z^2 is somewhat underpredicted near the jet centerline and overpredicted at the outer boundary. This is in agreement with the calculations of Shuen

et al (1983) and Bulzan et al (1987) who studied particle-laden jets under somewhat different flow conditions.

Figures 6.1.1-9, 6.1.1-10, and 6.1.1-11 relate to the measurements of particle-laden jets at $LR = 1.0$ and present comparison with calculations. Figure 6.1.1-9 shows mean axial velocity values for both phases and particle number density, and Figures 6.1.1-10 and 6.1.1-11 show the Reynolds stresses. It can be seen from these figures that the DT is inferior to the ST in predicting particle properties, the same behavior as observed at $LR = 0.2$, which could be attributed to the same physical reasonings discussed in connection with the results of that case.

By comparing Figure 6.1.1-9 with Figure 6.1.1-2, two effects of the particles on the gas mean axial velocity can be observed. First, the mean axial velocity profile at the inlet plane is flatter than the single-phase profile. This is due to the inlet profiles, which correspond to a fully developed pipe flow; the injection tube diameter-to-length ratio was equal to 65.2. At this condition, the particles are leading the fluid near the injector wall region and thus transfer momentum to the gas, which causes the flattening effect. Second, the mean axial gas velocity downstream of the injector is higher than the single-phase value. For instance, at $z/D = 12.45$, an increase of about 20% of the inlet single-phase velocity is caused by the presence of the particles. This phenomenon can be attributed to two effects (Mostafa and Elghobashi, 1985). One effect is the momentum transfer from the particles to the air, since particle velocity becomes greater than gas velocity after a short distance downstream from the injector. The other effect is the modulation of the gas turbulence caused by the particles.

To see how the particles modulate the turbulence structure, the distributions of turbulence kinetic energy and shear stress that are shown in Figure 6.1.1-10 can be compared with the corresponding quantities of single-phase values illustrated in Figure 6.1.1-3. At $z/D = 12.45$, local turbulence intensity is reduced from 20% to 12% at the centerline, which corresponds to a reduction of about 40% of the single-phase value. This turbulence modulation is caused mainly by the fluctuating relative velocity between the particles and the carrier phase. Particles generally cause a reduction in the gas turbulence and an increase in the dissipation rate of that energy. This turbulence attenuation reaches its maximum value at a certain mass loading ratio, when the particle relaxation time becomes very large compared with the gas Lagrangian time scale. The performance of the turbulence model for two-phase flows, which considers this physical phenomenon, is very good compared with the data in Figures 6.1.1-10 and 6.1.1-11.

Figure 6.1.1-12 corresponds to measurements of the gas kinetic energy and shear stress at the two loadings and shows the predictions with the single-phase $k-\epsilon$ model and its version for two-phase flows (Mostafa and Mongia, 1987). In the latter, the turbulence modulation is simulated by introducing extra terms in the turbulence kinetic energy and its dissipation rate equations. Figure 6.1.1-12 shows that the single-phase model does not predict the turbulence modulation caused by the particles in the two cases. However, the two-phase flow model yields fairly good agreement with the data. This result confirms previous findings that the interaction between the gas and particles is indeed due to both relative mean and fluctuating motion between the two phases, and in some cases, the turbulence modulation caused by the particles becomes equally important to the particle dispersion due to gas turbulence.

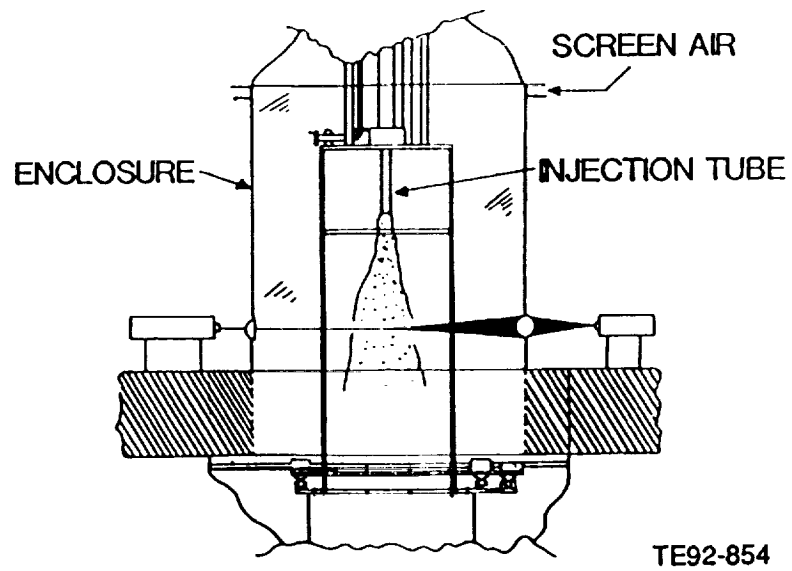


Figure 6.1.1-1. Test facility: unconfined injector only.

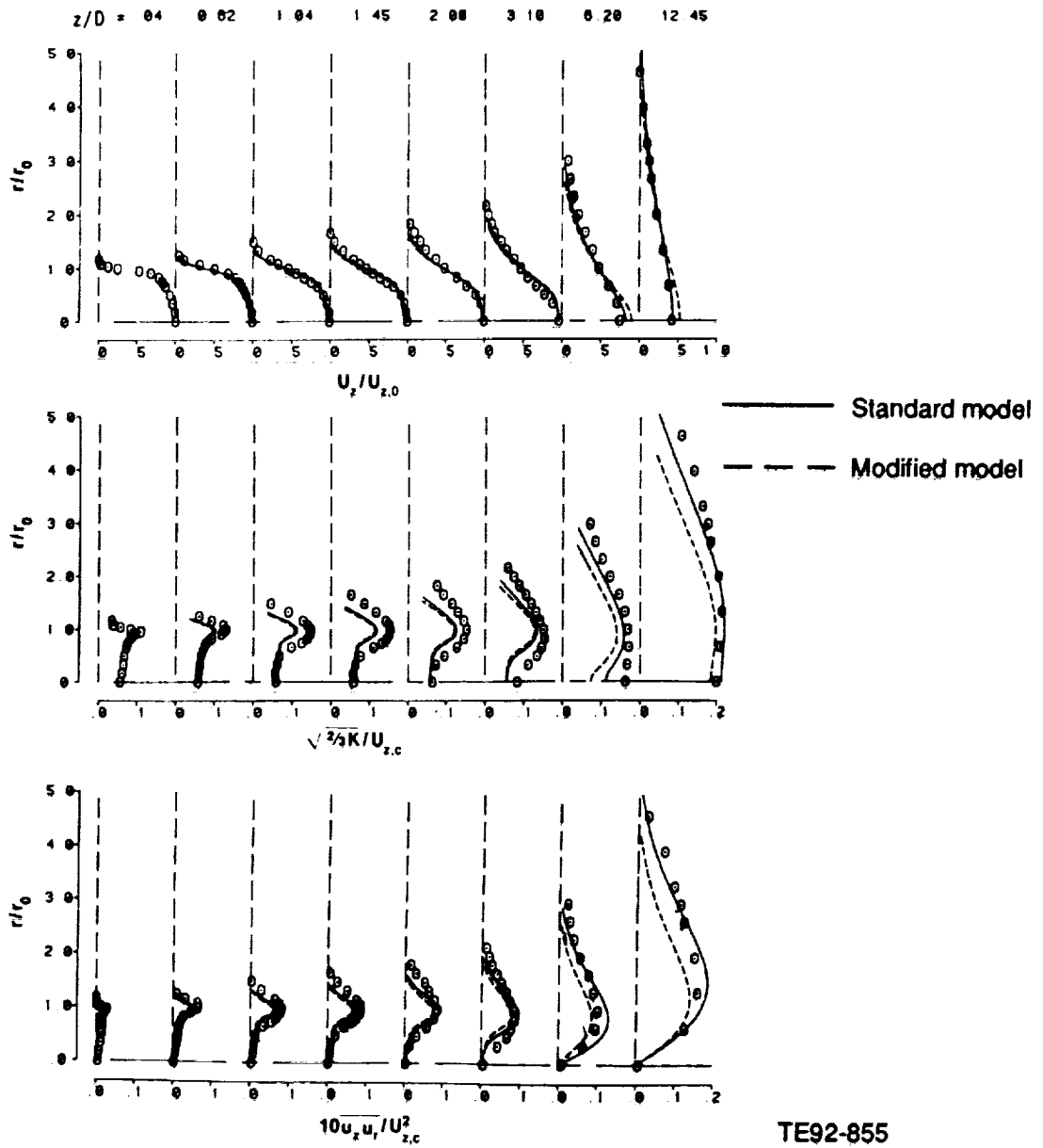
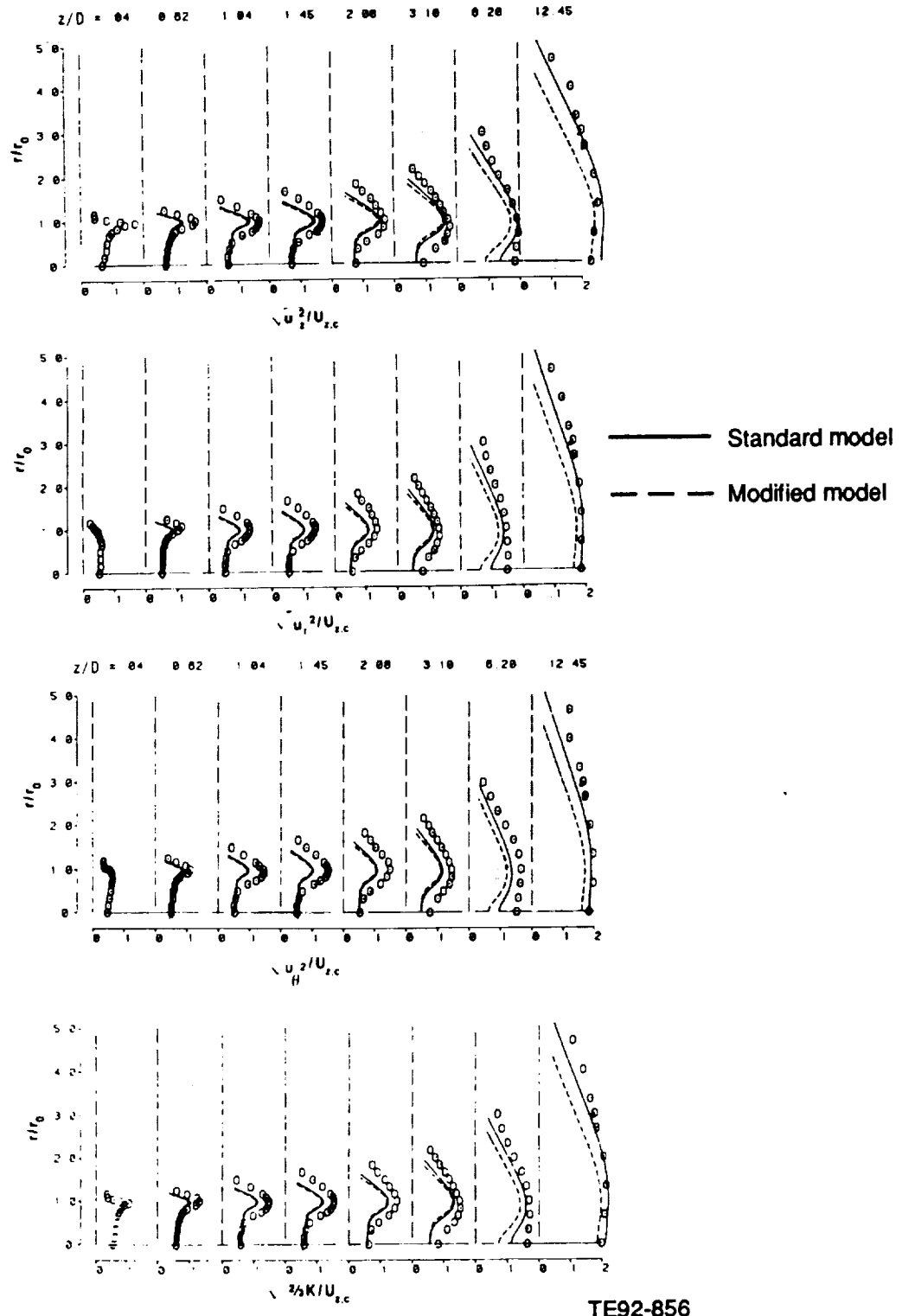


Figure 6.1.1-2. Radial profiles of normalized mean axial velocity, turbulence kinetic energy, and shear stress for the single-phase jet.



TE92-856

Figure 6.1.1-3. Radial profiles of normalized rms velocity components and turbulence kinetic energy for the single-phase jet.

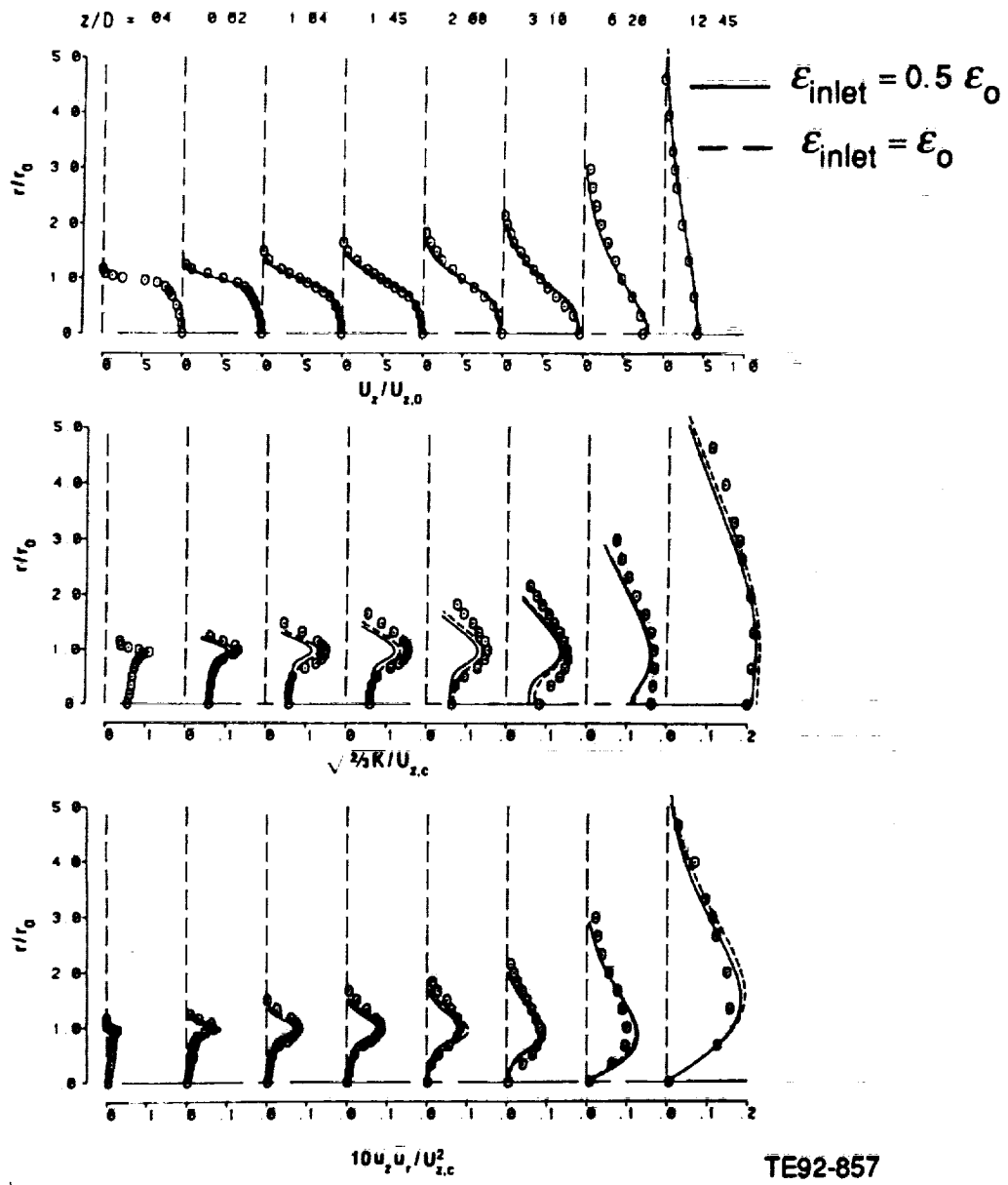
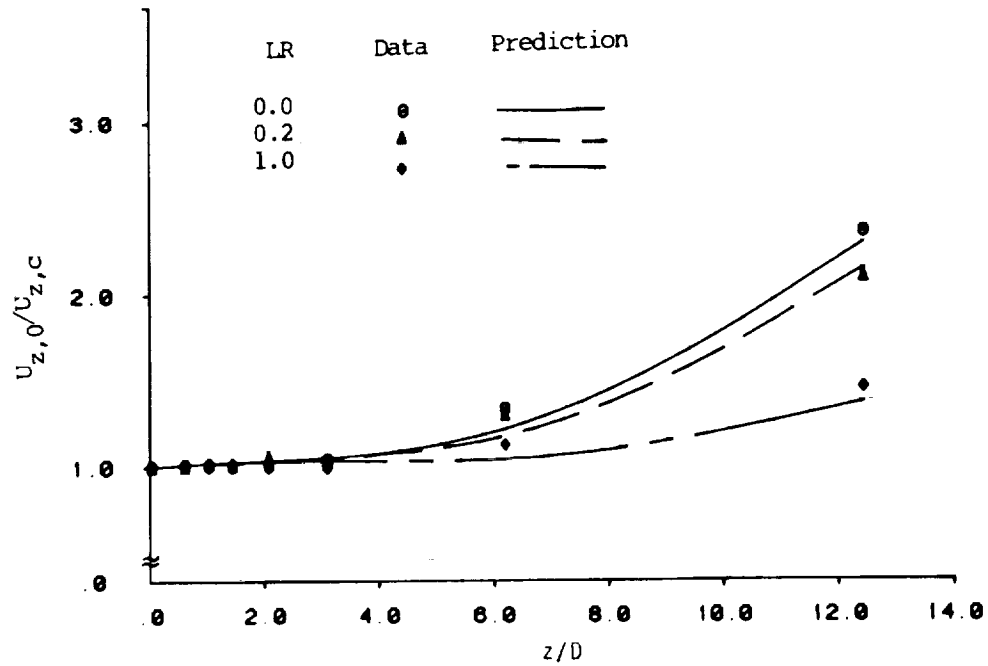
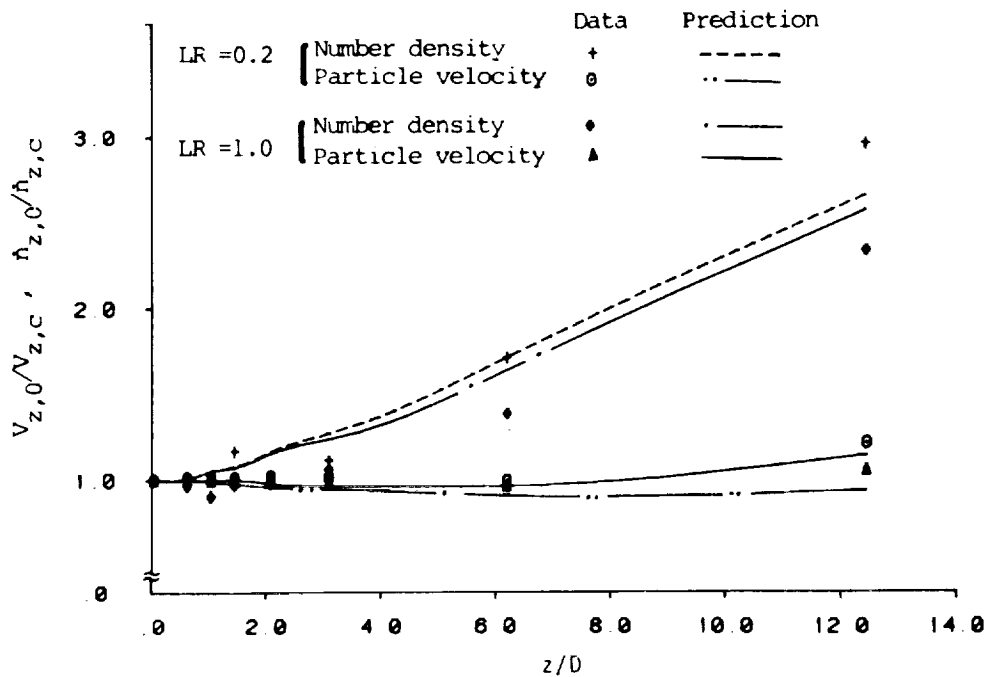


Figure 6.1.1-4. Radial profiles of normalized mean axial velocity, turbulence kinetic energy, and shear stress for the single-phase jet; influence of initial ϵ .



a) Gas phase



b) Particle phase

TE92-858

Figure 6.1.1-5. Axial distribution of normalized centerline values of gas mean velocity, and particle mean velocity and number density.

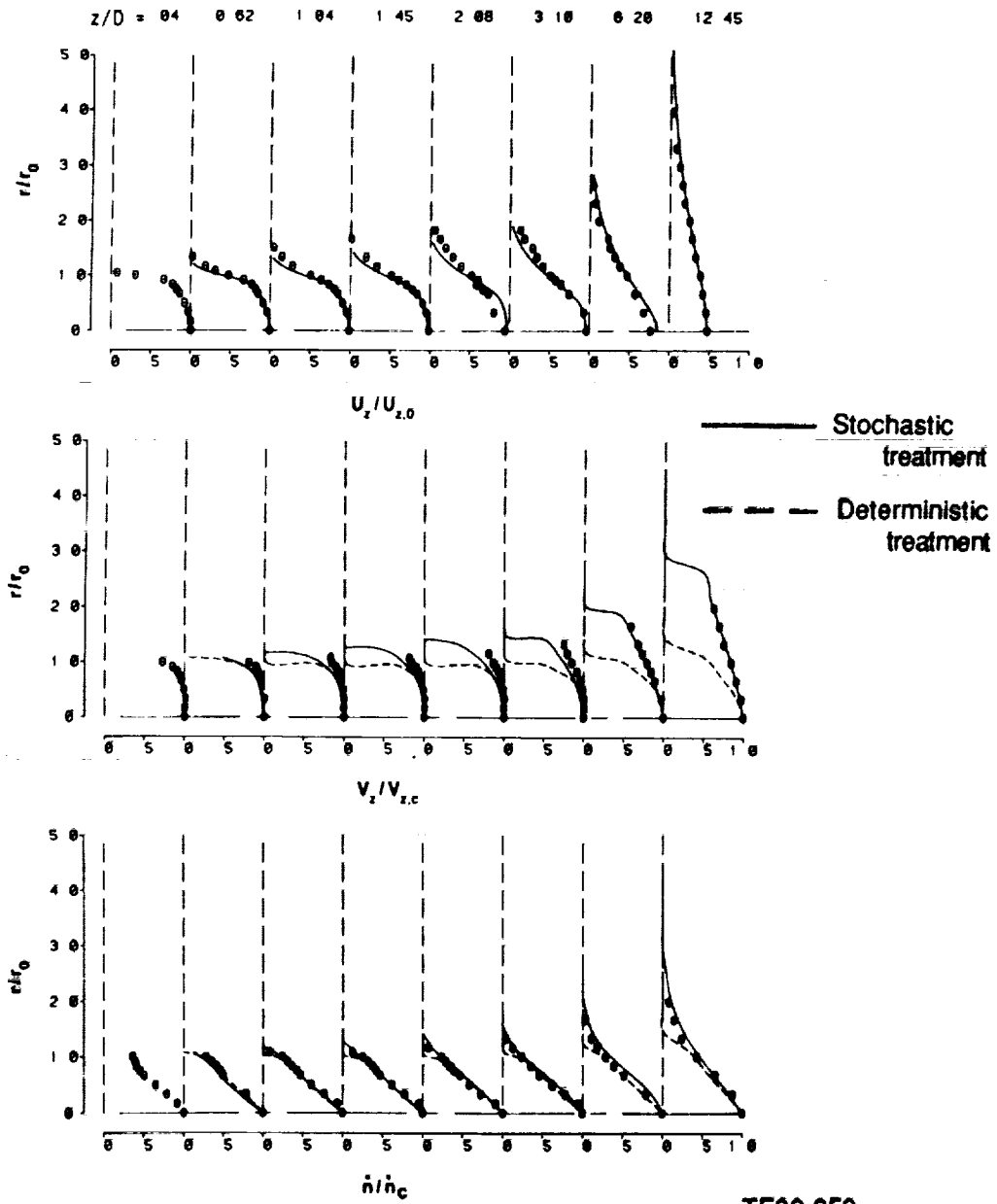


Figure 6.1.1-6. Radial profiles of normalized gas axial velocity and particle axial and radial velocity components, $LR = 0.2$.

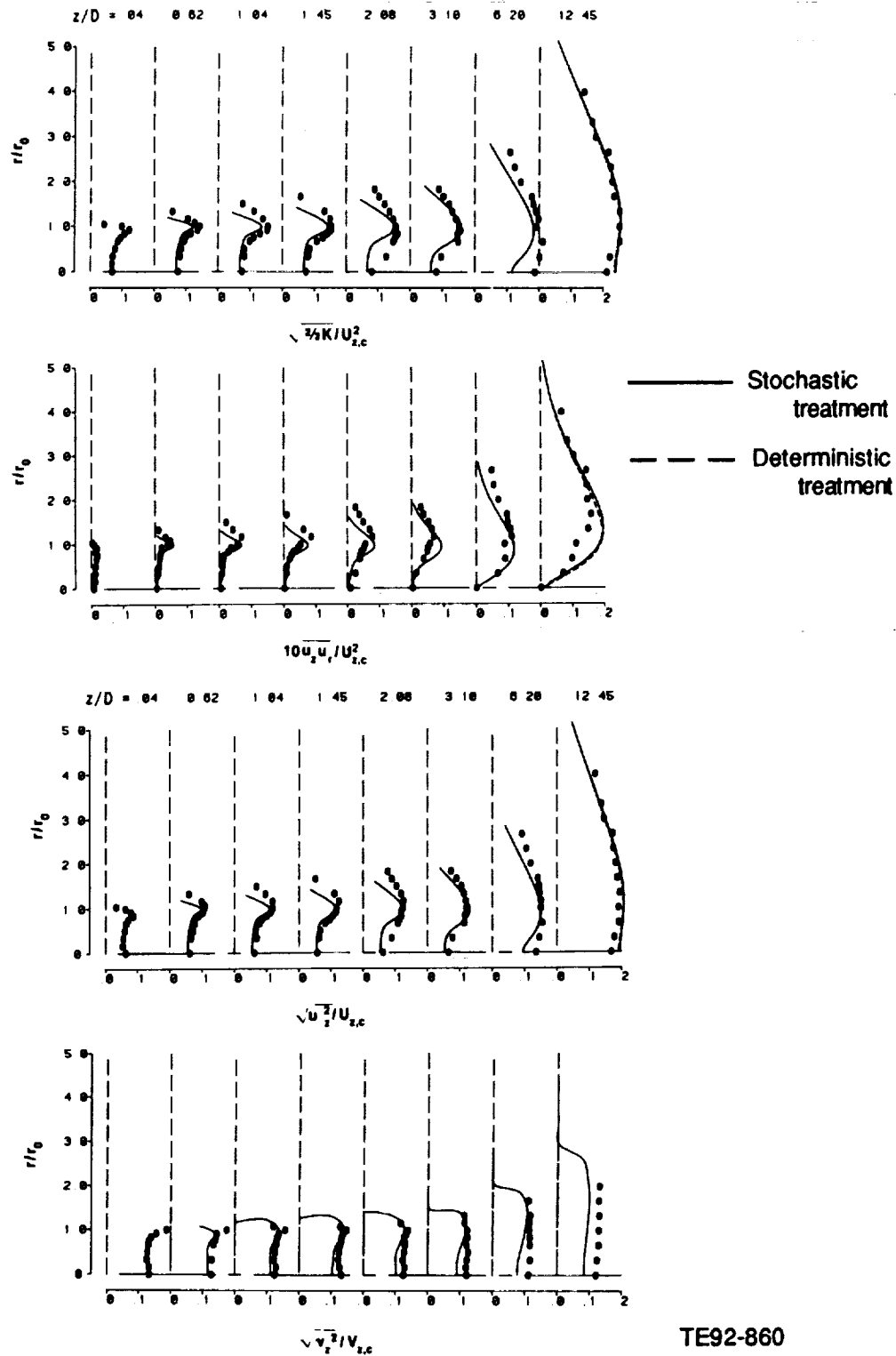


Figure 6.1.1-7. Radial profiles of normalized gas turbulence kinetic energy, shear stress, and axial turbulence intensity, and particle axial turbulence intensity at loading ratio, LR = 0.2.

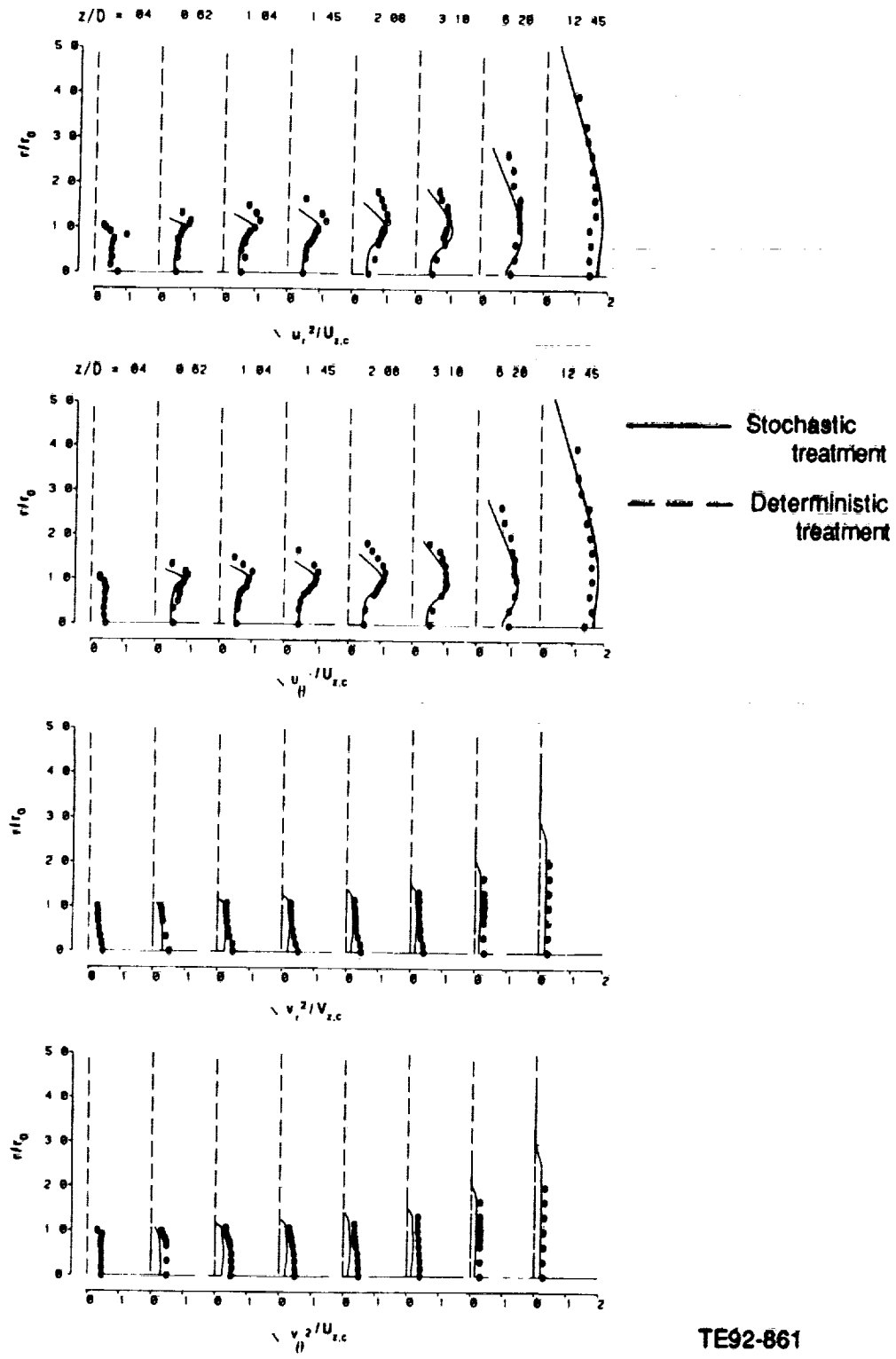


Figure 6.1.1-8. Radial profiles of rms radial and azimuthal velocity components of gas and particles at loading ratio, LR = 0.2.

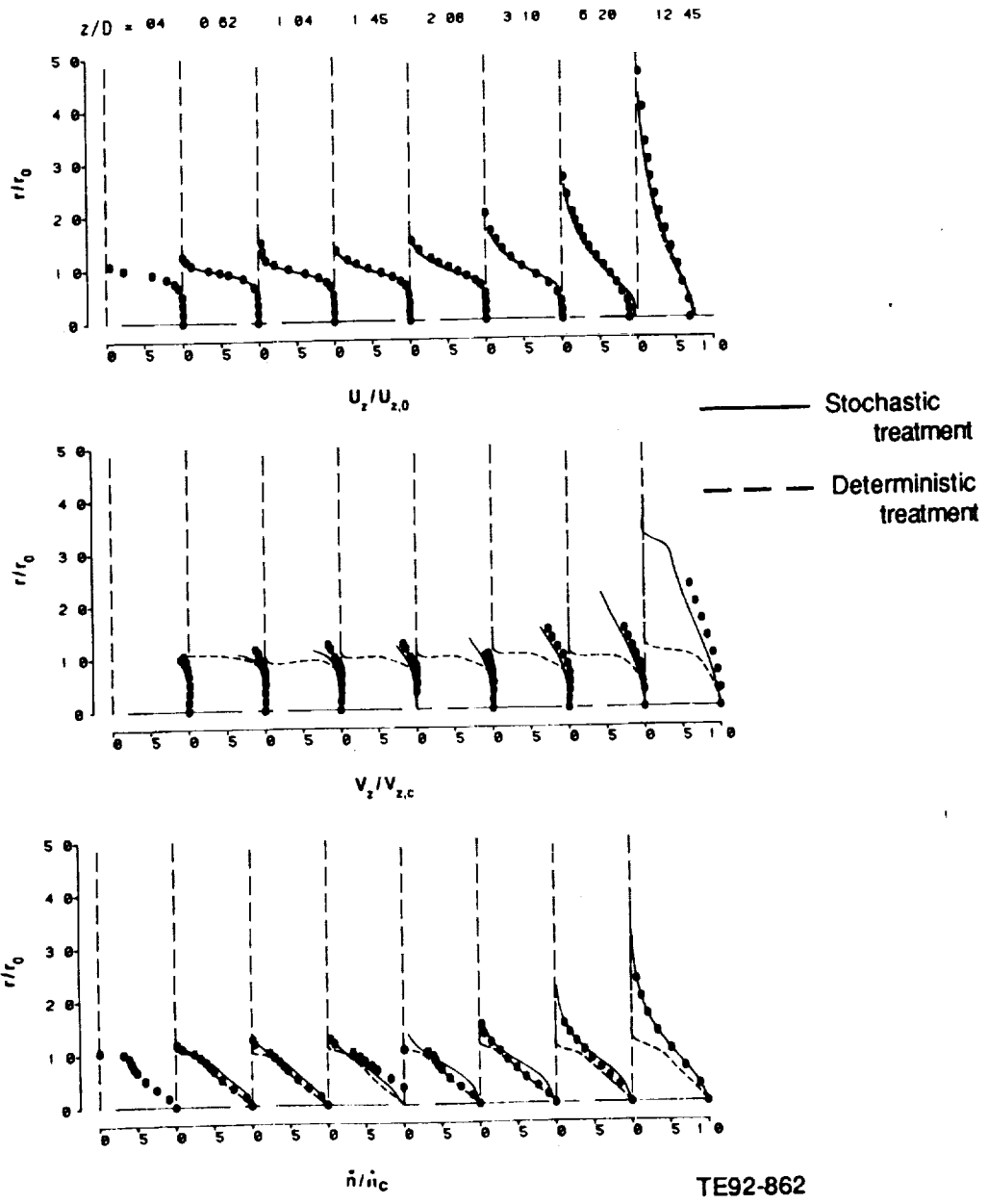
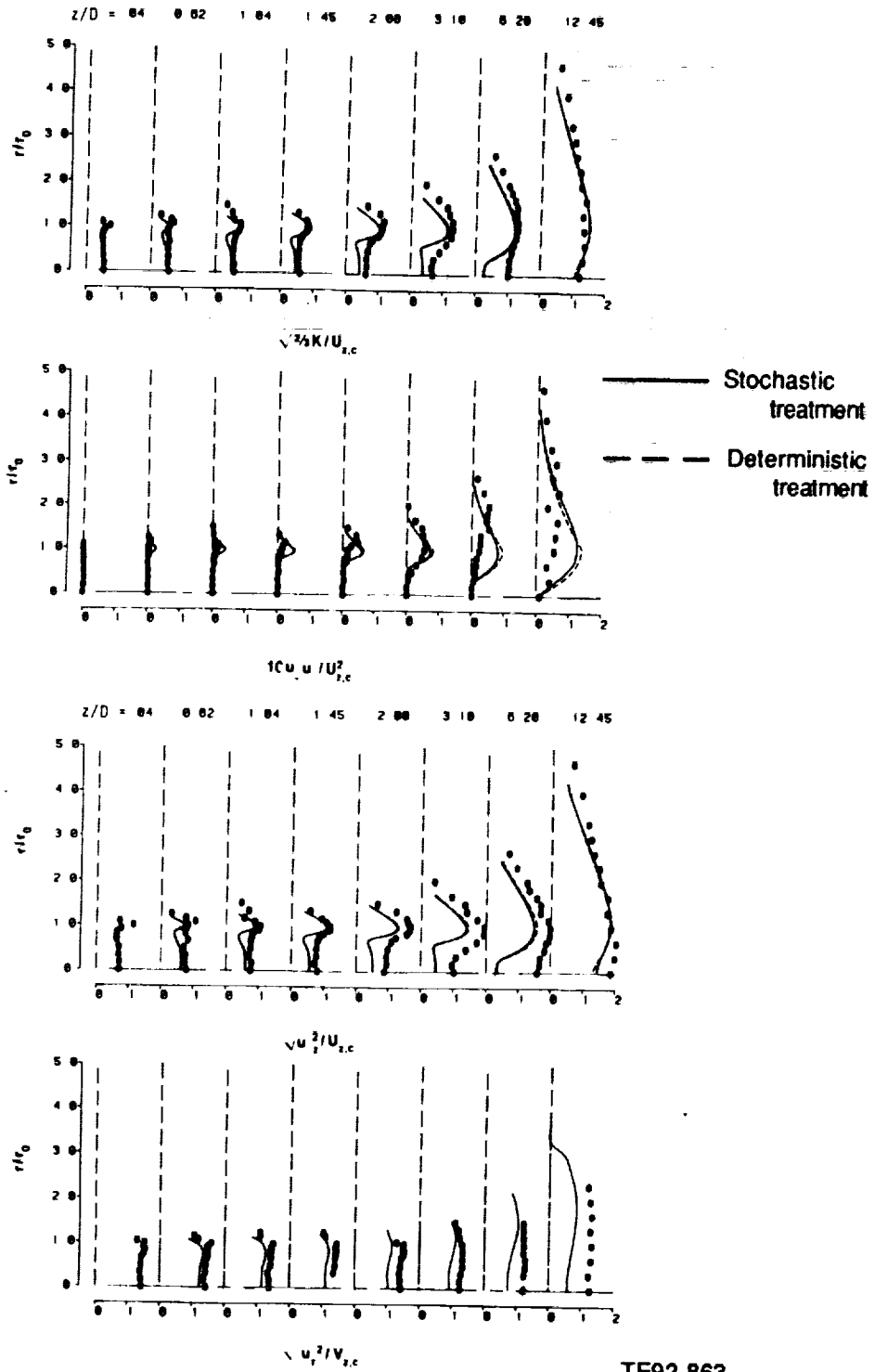
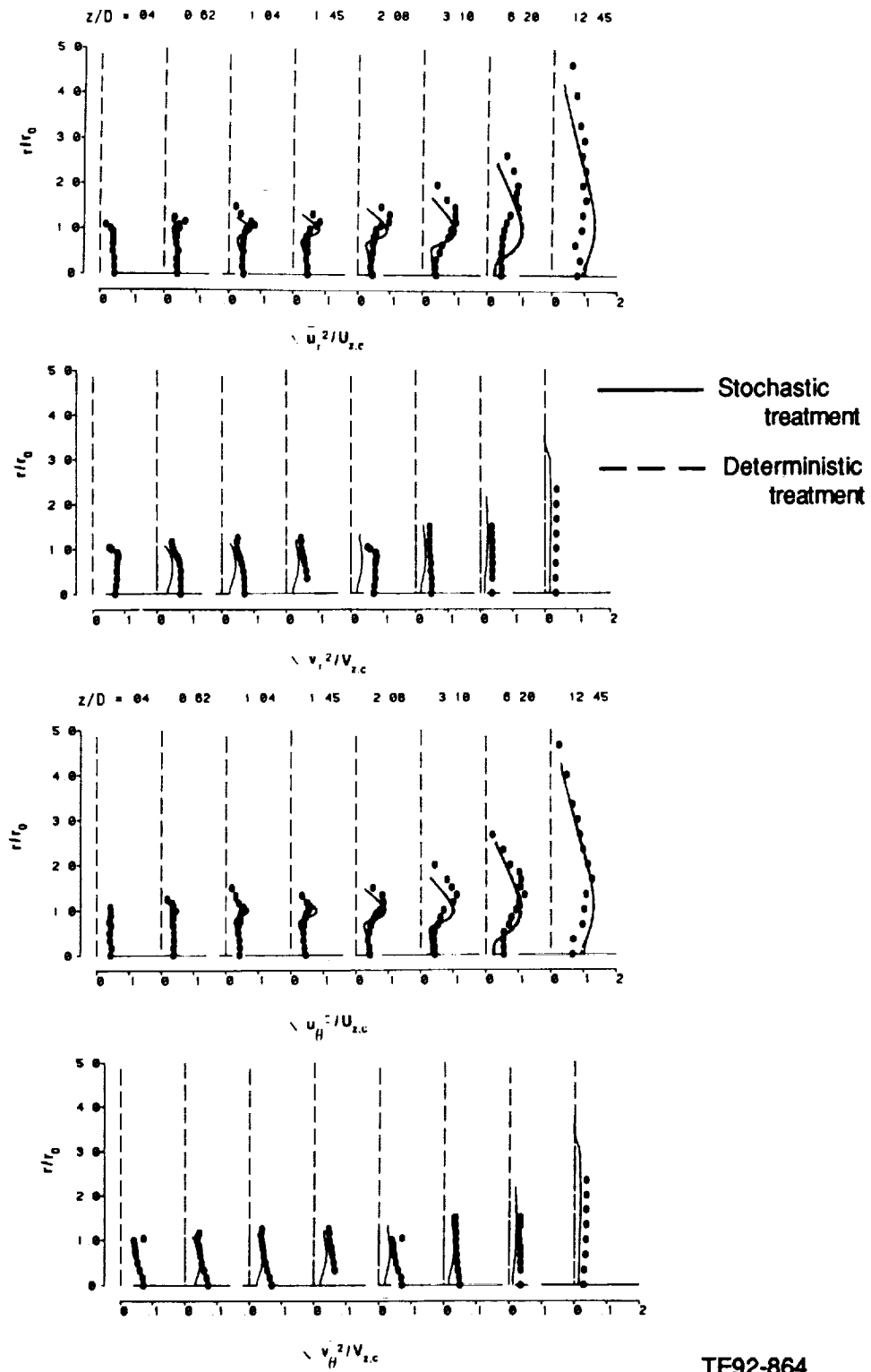


Figure 6.1.1-9. Radial profiles of normalized gas axial velocity and particle axial and radial velocity components, LR = 1.0.



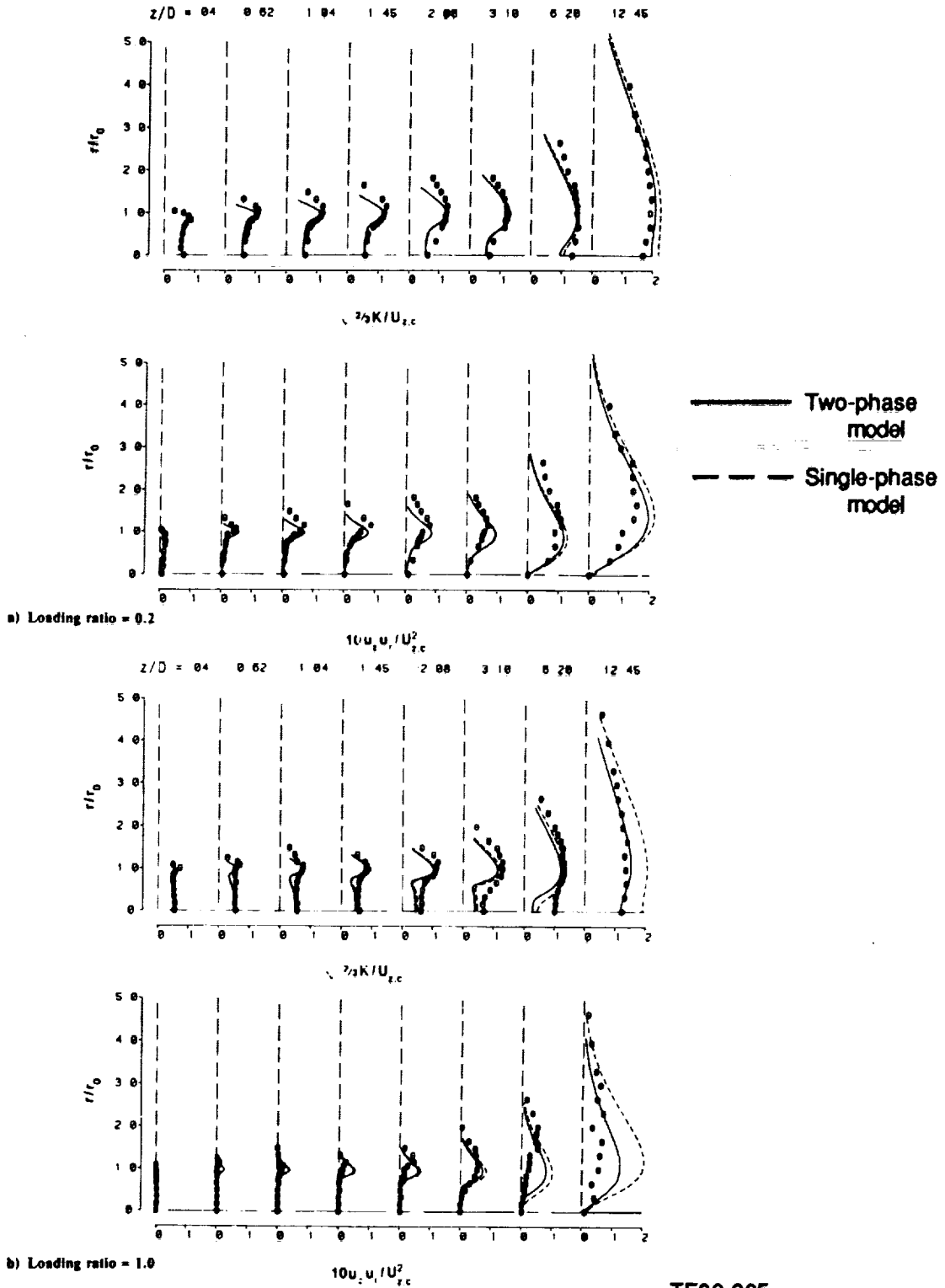
TE92-863

Figure 6.1.1-10. Radial profiles of normalized gas turbulence kinetic energy, shear stress, and axial turbulence intensity, and particle axial turbulence intensity at loading ratio, LR = 1.0.



TE92-864

Figure 6.1.1-11. Radial profiles of rms radial and azimuthal velocity components of gas and particles at loading ratio, LR = 1.0.



TE92-865

Figure 6.1.1-12. Effect of single-phase and two-phase turbulence models on gas phase turbulence kinetic energy and shear stress for the two loading ratios, LR = 0.2 and LR = 1.0.

6.1.2 Confined Single Round Jet

In this section, a numerical study of a confined flow condition is presented. The purpose of this study is to assess the performance of the second-moment closure for confined axisymmetric single-phase and particle-laden flows. The spray model is based on the stochastic-Lagrangian approach. A higher order numerical scheme is employed in the continuous phase. The computational results are compared with detailed experimental data obtained using a two-component phase Doppler technique. A sketch of the test section is shown in Figure 6.1.2-1. The flow conditions used for the cases considered here are given in Table 6.1-II.

The set of governing partial differential equations applied for nonswirling continuous (carrier) phase flow consists of equations for continuity, axial (x) and radial (r) momenta, ϵ , and four Reynolds stress components. The finite volume approach (Patankar, 1980) is used to reduce the continuous equations to a set of coupled discrete equations. The numerical solutions are obtained using the flux-spline differencing scheme, designated FSDS (Varejao, 1979). In this scheme, the total flux is assumed to vary linearly within a computational cell (control volume). This assumption leads to a scheme in which the discretization coefficients are identical to those from the exponential scheme (Patankar, 1980) but there is an additional source which involves the differences in fluxes at adjacent faces of a cell. The presence of this source term enables the flux-spline scheme to respond to the presence of sources and/or multidimensionality of the flow.

The elliptic nature of transfer equations requires that boundary conditions be specified on the four sides of the solution domain. Four kinds of boundaries need consideration: inlet, axis of symmetry, wall, and the outlet. At the inner boundary, which is located at the first measurement plane ($x = 4$ mm), the measured profiles of U, V, W, u^2, v^2, w^2 , and uv are applied. The inlet dissipation rate is prescribed based on the assumption of constant length scale and the turbulent kinetic energy, namely

$$\epsilon = \frac{K^{1.5}}{0.2 R_3} \quad (63)$$

where $R_3 = 76$ mm is the pipe radius. The macrolength scale of $0.2 R_3$ was estimated through the sensitivity analysis.

Table 6.1-II.
Confined single jet experimental flow conditions.

<u>Continuous phase</u>	
Medium	air
Density, ρ	1.17 (Kg/m ³)
Inner jet mass flow rate, m_1	0.0021 (Kg/s)
Dilute jet mass flow rate, m_2	0.0272 (kg/s)
Averaged velocity of inner jet, U_0	3.935 (m/s)
<u>Discrete phase</u>	
Medium	glass beads
Density, ρ_p	2500 (kg/m ³)
Beads diameter, D_p	105 (mm)
Centerline velocity	4.2 (m/s)
Centerline beads rate	90 (1/s)
Mass flow rate	0.00193 (kg/s)
Mass loading beads to air, LR	0.925

At the axis of symmetry, the radial velocity, shear stresses, and radial gradients of other variables are set to zero. All streamwise gradients are presumed zero in the exit plane of the calculation domain, except for axial velocity, which needs to be corrected to satisfy integral mass balance. The conventional logarithmic law, which is based on the local equilibrium assumption, is applied to determine the wall shear stress component. The shear stress is then used as boundary condition for U momentum and uv equations. The boundary conditions for normal stresses are imposed through the modifications of their production terms using the new calculated wall shear stress value.

The coupled equations and boundary conditions are solved numerically in a sequential manner using the staggered grids for velocities and shear stresses. The main advantage of staggering the location of stresses is to enhance the numerical stability, a result of high coupling between the shear stresses and related mean strains. The iteration sequence employs the SIMPLER algorithm (Patankar, 1980) to handle the coupling between the continuity and momentum equations. The algebraic equations are solved using a line-by-line tridiagonal matrix algorithm (TDMA).

The ordinary differential equations describing the dispersed phase are solved using forward numerical integration. The calculations start from the first measurement plane ($x = 4$ mm) where the mean and fluctuation velocity profiles of particles and their rates of injection are available. At the wall, particles are assumed to bounce back with an angle of reflection equal to the angle of incidence.

Numerical iterations are performed over the continuous and dispersed phases until the absolute sums of the normalized mass and momentum of the carrier phase at all internal grid points and the change of the particle source terms are less than 10^{-5} .

The predicted mean and turbulence quantities obtained for a single-phase confined round jet are first compared with the experimental data. The results presented here were obtained using a 61×57 ($x - r$) grid (Figure 6.1.2-2). The x and r grid coordinates are also shown in Table 6.1-III. A finer grid spacing is assigned near the inlet, centerline, and in shear layer. The computational domain extends from the first experimental location ($x = 4$ mm) to 450 mm downstream of the jet exit. Since the measured flow does not show any x dependence at $x > 200$ mm, the specified condition $\partial/\partial x = 0$ at the exit plane of the calculation domain is realistic. Since the computational results did not change using a finer grid, it is therefore assumed that the predicted results are grid independent.

Table 6.1-III.
Confined single jet experimental flow conditions.

STREAMWISE COORDINATES OF THE GRID

I	DX	X	XU
1	0.000E+00	0.000E+00	0.000E+00
2	7.750E-04	7.750E-04	0.000E+00
3	1.625E-03	2.400E-03	1.550E-03
4	2.050E-03	4.450E-03	3.250E-03
5	2.500E-03	6.950E-03	5.650E-03
6	2.700E-03	9.650E-03	8.250E-03
7	2.938E-03	1.259E-02	1.105E-02
8	3.313E-03	1.590E-02	1.413E-02
9	3.888E-03	1.979E-02	1.768E-02
10	4.588E-03	2.438E-02	2.190E-02
11	5.250E-03	2.963E-02	2.685E-02
12	5.775E-03	3.540E-02	3.240E-02
13	6.238E-03	4.164E-02	3.840E-02
14	6.713E-03	4.835E-02	4.488E-02
15	7.063E-03	5.541E-02	5.183E-02
16	7.200E-03	6.261E-02	5.900E-02
17	7.250E-03	6.986E-02	6.623E-02
18	7.288E-03	7.715E-02	7.350E-02
19	7.300E-03	8.445E-02	8.080E-02
20	7.300E-03	9.175E-02	8.810E-02
21	7.288E-03	9.904E-02	9.540E-02
22	7.275E-03	1.063E-01	1.027E-01
23	7.288E-03	1.136E-01	1.100E-01
24	7.300E-03	1.209E-01	1.173E-01
25	7.300E-03	1.282E-01	1.246E-01
26	7.300E-03	1.355E-01	1.319E-01
27	7.300E-03	1.428E-01	1.392E-01
28	7.300E-03	1.501E-01	1.465E-01
29	7.300E-03	1.574E-01	1.538E-01
30	7.300E-03	1.647E-01	1.611E-01
31	7.300E-03	1.720E-01	1.684E-01
32	7.300E-03	1.793E-01	1.757E-01
33	7.300E-03	1.866E-01	1.830E-01
34	7.300E-03	1.939E-01	1.903E-01
35	7.300E-03	2.012E-01	1.976E-01
36	7.300E-03	2.085E-01	2.049E-01
37	7.300E-03	2.158E-01	2.122E-01
38	7.300E-03	2.231E-01	2.195E-01
39	7.200E-03	2.303E-01	2.268E-01
40	7.200E-03	2.375E-01	2.339E-01
41	7.400E-03	2.449E-01	2.412E-01
42	7.400E-03	2.523E-01	2.487E-01
43	7.325E-03	2.596E-01	2.560E-01
44	7.325E-03	2.670E-01	2.633E-01
45	7.275E-03	2.742E-01	2.706E-01
46	7.275E-03	2.815E-01	2.779E-01
47	7.300E-03	2.888E-01	2.852E-01
48	7.450E-03	2.963E-01	2.925E-01

PART 1 OF 3
TE92-899

Table 6.1-III (cont).

49	7.775E-03	3.040E-01	3.001E-01
50	7.975E-03	3.120E-01	3.080E-01
51	8.500E-03	3.205E-01	3.160E-01
52	9.500E-03	3.300E-01	3.250E-01
53	1.000E-02	3.400E-01	3.350E-01
54	1.000E-02	3.500E-01	3.450E-01
55	1.125E-02	3.613E-01	3.550E-01
56	1.375E-02	3.750E-01	3.675E-01
57	1.500E-02	3.900E-01	3.825E-01
58	1.500E-02	4.050E-01	3.975E-01
59	1.500E-02	4.200E-01	4.125E-01
60	1.875E-02	4.388E-01	4.275E-01
61	1.125E-02	4.500E-01	4.500E-01

TRANSVERS COORDINATES OF THE GRID

J	DY	Y	YV
1	0.000E+00	0.000E+00	0.000E+00
2	3.750E-04	3.750E-04	0.000E+00
3	7.500E-04	1.125E-03	7.500E-04
4	8.750E-04	2.000E-03	1.500E-03
5	1.000E-03	3.000E-03	2.500E-03
6	1.000E-03	4.000E-03	3.500E-03
7	1.000E-03	5.000E-03	4.500E-03
8	1.000E-03	6.000E-03	5.500E-03
9	1.000E-03	7.000E-03	6.500E-03
10	1.000E-03	8.000E-03	7.500E-03
11	1.000E-03	9.000E-03	8.500E-03
12	1.000E-03	1.000E-02	9.500E-03
13	1.000E-03	1.100E-02	1.050E-02
14	1.000E-03	1.200E-02	1.150E-02
15	1.000E-03	1.300E-02	1.250E-02
16	1.000E-03	1.400E-02	1.350E-02
17	1.000E-03	1.500E-02	1.450E-02
18	1.000E-03	1.600E-02	1.550E-02
19	1.000E-03	1.700E-02	1.650E-02
20	1.000E-03	1.800E-02	1.750E-02
21	1.000E-03	1.900E-02	1.850E-02
22	1.000E-03	2.000E-02	1.950E-02
23	1.000E-03	2.100E-02	2.050E-02
24	1.000E-03	2.200E-02	2.150E-02
25	1.000E-03	2.300E-02	2.250E-02
26	1.000E-03	2.400E-02	2.350E-02
27	1.000E-03	2.500E-02	2.450E-02
28	1.000E-03	2.600E-02	2.550E-02
29	1.000E-03	2.700E-02	2.650E-02
30	1.000E-03	2.800E-02	2.750E-02
31	1.000E-03	2.900E-02	2.850E-02
32	1.000E-03	3.000E-02	2.950E-02

PART 2 OF 3
TE92-899

Table 6.1-III (cont).

33	1.000E-03	3.100E-02	3.050E-02
34	1.000E-03	3.200E-02	3.150E-02
35	1.250E-03	3.325E-02	3.250E-02
36	1.750E-03	3.500E-02	3.400E-02
37	2.000E-03	3.700E-02	3.600E-02
38	2.000E-03	3.900E-02	3.800E-02
39	2.000E-03	4.100E-02	4.000E-02
40	2.000E-03	4.300E-02	4.200E-02
41	2.000E-03	4.500E-02	4.400E-02
42	2.000E-03	4.700E-02	4.600E-02
43	2.000E-03	4.900E-02	4.800E-02
44	2.000E-03	5.100E-02	5.000E-02
45	2.000E-03	5.300E-02	5.200E-02
46	2.000E-03	5.500E-02	5.400E-02
47	2.000E-03	5.700E-02	5.600E-02
48	2.000E-03	5.900E-02	5.800E-02
49	2.000E-03	6.100E-02	6.000E-02
50	2.000E-03	6.300E-02	6.200E-02
51	2.000E-03	6.500E-02	6.400E-02
52	2.000E-03	6.700E-02	6.600E-02
53	2.000E-03	6.900E-02	6.800E-02
54	2.000E-03	7.100E-02	7.000E-02
55	2.000E-03	7.300E-02	7.200E-02
56	2.000E-03	7.500E-02	7.400E-02
57	1.000E-03	7.600E-02	7.600E-02

PART 3 OF 3
TE92-899

The present calculations have been made using the flux-spline differencing scheme and the calculated results are essentially free of numerical diffusion. Therefore, the discrepancy between the experimental data and the prediction can be attributed to two sources, improper boundary conditions at the inlet plane and the deficiency of the turbulence model. As regards the inlet conditions, all quantities except the dissipation rate, ϵ , were prescribed from the measurement. These profiles are shown in Figure 6.1.2-3 and have been normalized by the inner jet averaged velocity, U_0 , and the pipe radius, R_3 . Above $r/R_3 > 0.5$, the flow field is similar to the plug flow condition created by the strong coflow. This region is not the focus of this study and is not shown in the presented figures. The uncertainties in the derivation of inlet ϵ profile would adversely affect the calculation at downstream locations. It was shown, however, that the use of inlet ϵ derived from the constant length-scale assumption can result in a better prediction (Nikjooy and Mongia, 1991).

A comparison of the normalized axial mean velocity profiles at various locations with data is shown in Figure 6.1.2-4. These results were obtained from the $k-\epsilon$ model. The predictions are in good agreement with measurements. The velocity profiles are flat near the centerline. The experimental data indicate that the centerline velocity constantly decreases. The deceleration in axial velocity is due to the pressure effects. Comparisons of the turbulent shear stress and kinetic energy are presented in Figures 6.1.2-5 and 6.1.2-6. The $k-\epsilon$ model overestimated the maximum level of the turbulent shear stress near the nozzle exit, however, the differences decreased in downstream locations. The agreement between the predicted and experimental values of kinetic energy is not as good as that for the axial velocity. Even though the trends are similar, the predicted kinetic energies are smaller than those derived from the measurements in downstream regions. The mean velocity profiles predicted by $k-\epsilon$ and DSM are also very close, except for some minor differences near the centerline (Figure 6.1.2-7).

Comparisons of the mean and turbulence quantities predicted by the algebraic second-moment (ASM) closure with the measured values are presented in Figures 6.1.2-8 through 6.1.2-11. Effects of the pressure-strain correlation model on mean and turbulence flow fields are analyzed. Two different model constants for C_1 and C_2 have been examined in this study. These are $C_1 = 3.0$, $C_2 = 0.3$ (Gibson and Younis, 1986) and $C_1 = 5.0$, $C_2 = 0.0$ (Donaldson, 1969). The prediction of mean axial velocity profiles using these two models are very similar. There are substantial differences between the measured profiles and the ASM calculation which show more mixing, and hence lower velocity, near the centerline.

The predicted stress components are shown in Figures 6.1.2-9, 6.1.2-10, and 6.1.2-11. Despite the similarities that appeared in the mean velocity field, the Reynolds stress profiles are different in the shear layer and near the centerline zone. The discrepancy observed in the turbulence field between the prediction and the measurement is related in large to the deficiency of the pressure-strain model. At downstream locations, the differences between the calculations have vanished. The turbulence intensities become almost uniform near the centerline indicating a well-mixed flow condition.

Comparisons of the normalized mean axial velocity and Reynolds stresses predicted by DSM and ASM closures with the measured values are presented in Figures 6.1.2-12 through 6.1.2-16. The pressure redistribution model used for these calculations involved only the return-to-isotropy part ($\phi_{ij} = 0$) with a constant $C_1 = 5.0$ in the ϕ_{ij} model. The calculated velocity field predicted by both models is very similar at all axial locations. Some minor differences are observed between the two models at downstream regions. Overall, the prediction is in good agreement with data. Examination of the calculated axial rms profiles indicates that the DSM's results mimic the experimental data better as flow proceeds towards downstream regions. The maximum radial and tangential rms predicted by both models are very close and are slightly underpredicted despite the differences that appeared in their axial components. As regards the turbulent shear stress, the calculated profiles are similar to the exhibited data trend, however, the $k-\epsilon$ model resulted in better prediction (Figure 6.1.2-18).

The calculation for a particle-laden jet was also performed over the same computational domain. The same grid distribution was used. As regards the inlet conditions, all quantities except the dissipation rate, ϵ , were prescribed from the measurement. These profiles are shown in Figures 6.1.2-19 and 6.1.2-20 and have been normalized by the inner jet averaged velocity, U_0 , particles flux at the centerline, N_0 , and the pipe radius, R_3 . The inlet dissipation rate is prescribed based on the assumption of constant length scale and the turbulent kinetic energy (Equation 63).

Comparisons of normalized mean axial velocity, turbulent shear stress, and kinetic energy profiles predicted by $k-\epsilon$ and DSM closure with the measured values are presented in Figures 6.1.2-21, 6.1.2-22, and 6.1.2-23. The predicted velocity result is in excellent agreement with the experimental data. The velocity profiles are quite flat near the centerline. The centerline velocity decreases for about 10% from the inlet plane to station $x = 200$ mm. The deceleration in axial velocity probably results from the pressure effect. The predicted pressure distribution shows a negative radial gradient favoring an outward motion. As a result, the axial velocity is slowing down to satisfy the mass conservation. The predicted turbulent shear stress and kinetic energy profiles are somewhat larger than those calculated by DSM closure. The $k-\epsilon$ model overpredicted the maximum uv and k to station $x = 35$ mm, however, DSM underpredicted the peaks at all the streamwise stations. Overall, the turbulence quantities were qualitatively well predicted and their behaviors are in agreement with the measured profiles, despite the differences that appeared in the shear layer.

Comparisons of the mean and turbulence quantities predicted by the ASM and DSM closures with the experimental data are shown in Figures 6.1.2-24 through 6.1.2-28. The calculated mean field obtained from both models is essentially identical and is in excellent agreement with data. The differences between the prediction and data in the downstream region ($x > 150$ mm) could be related to the diffusion process. This is cleared by noting the underprediction of Reynolds stresses in those regions. Comparisons of the predicted and measured streamwise turbulence intensity profiles show some minor differ-

ences between the ASM and DSM in calculating the peak values. The differences appear to be more significant for single-phase flow than this two-phase case. At most of the locations the turbulence intensity near the centerline was underpredicted. This is due in part to an excessive turbulence dissipation rate at the inlet. Nevertheless, the turbulence intensity profiles obtained from these models are similar to the exhibited experimental trend. The discrepancy observed in the turbulence field between the prediction and measurement is related in large to the deficiency of the pressure-strain model. This has resulted in underprediction of the maximum values of radial and tangential turbulence intensities. The discrepancies between the prediction and measurement are less significant in the case of shear stresses. In the downstream region ($x > 150$ mm), the calculated results deviate from the data in the outer zone. The results demonstrate that the dispersed phase had no significant effects on the continuous phase.

Figure 6.1.2-29 presents the mean velocity of the dispersed phase. In this calculation the two-phase $k-\epsilon$ turbulence model was used. It can be seen that the ST approach provides good predictions compared with the experimental data, whereas the DT treatments perform poorly for the particles' velocity. According to the DT approach, a particle moves radially due to its initial mean radial velocity and/or the mean radial gas velocity, both of which are very small compared with the axial component. This might explain the narrow distribution of particle mean axial velocity predicted by the DT.

Predicted and measured mean particle velocities predicted by the DSM and ST approach along the axis are shown in Figure 6.1.2-30. The calculated velocities are based on the particles' mass flow rate weighted averages. Only a portion of the entire radial section where particles could be found are presented. The predicted axial values are in good agreement with data. Despite the variations observed in the gas phase velocity near the centerline, the particle velocity shows almost no change. This is related to the fact that the particle dynamic relaxation time, τ_d , is very large compared to the turbulent characteristic time, τ . The reason for large τ_d is found in the large particle-to-gas density ratio (2500:1.17). This clearly shows that the inertia force is responsible for the particles' motion and the effects of drag force are marginal. The predicted profiles of mean radial velocity of particles are in qualitative agreement with the data. The radial velocity component, however, is at least one order of magnitude smaller than the axial component. It is, therefore, reasonable to believe that their quantitative disagreement would not severely affect other results.

The agreements between the predicted and measured fluctuating velocities of the particles are not favorable (Figures 6.1.2-31, 6.1.2-32, and 6.1.2-33). The data show similar radial and tangential fluctuating components. On the other hand, the axial rms value is about 1.5 times larger than others. The model has successfully predicted the anisotropy feature of the dispersed flow field. However, all three components are predicted to be higher than the data.

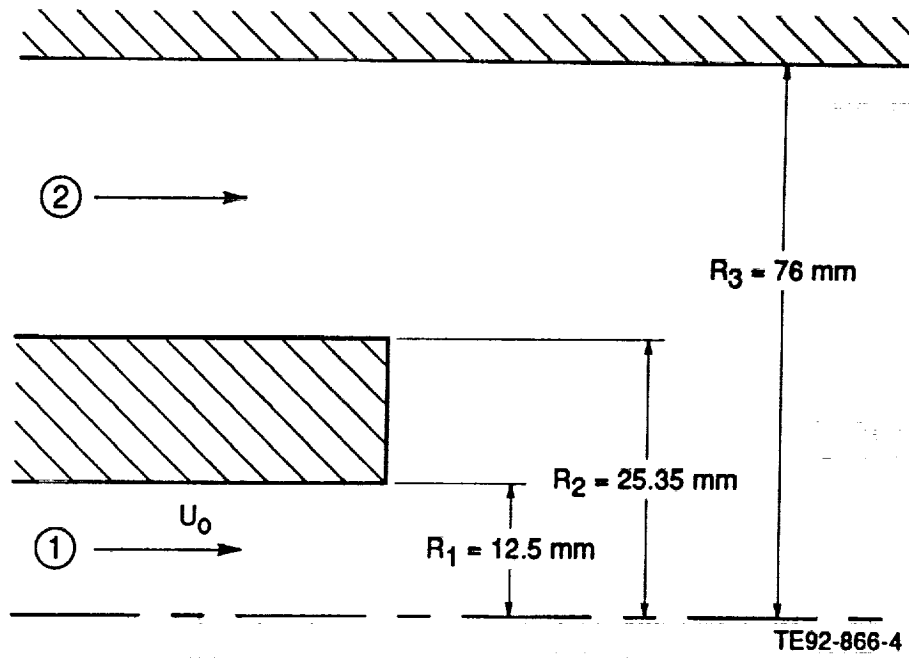


Figure 6.1.2-1. Confined round jet geometrical details.

SINGLE JET

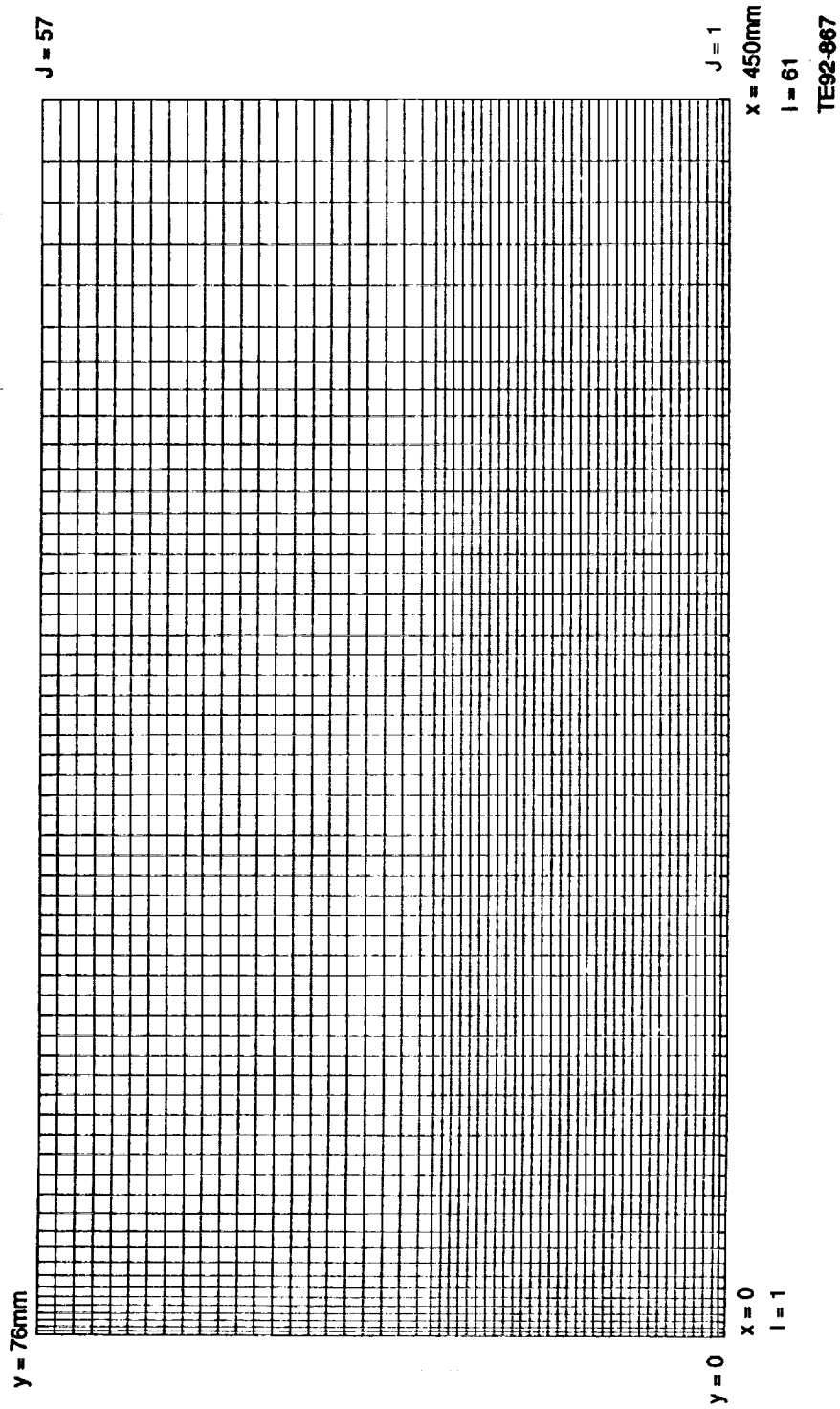
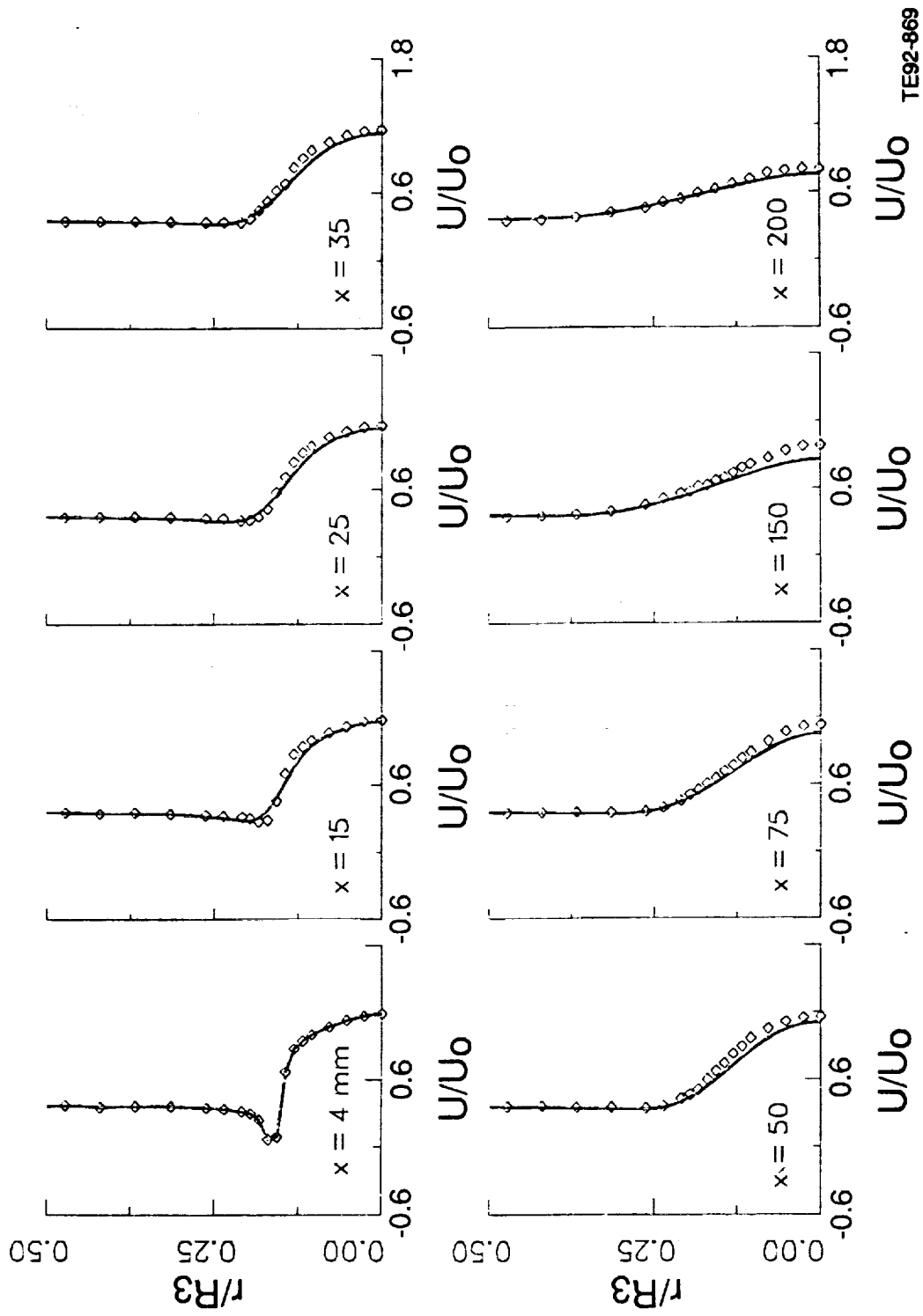


Figure 6.1.2-2. Confined round jet grid layout.



TE92-869

Figure 6.1.2-4. Comparison of predicted mean axial velocity by $k-\epsilon$ model with data.

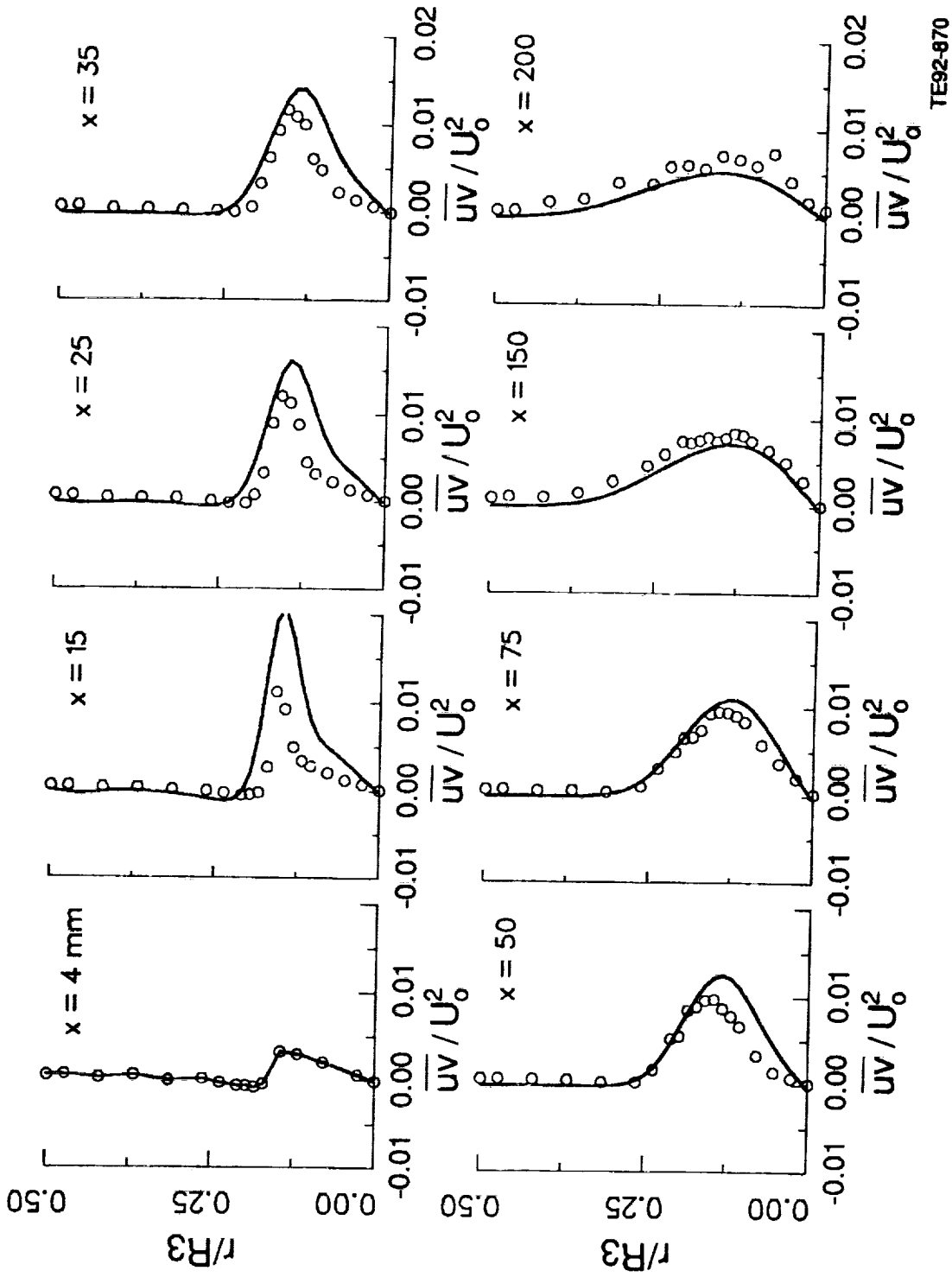


Figure 6.1.2-5. Comparison of predicted turbulent shear stress by k-ε model with data.

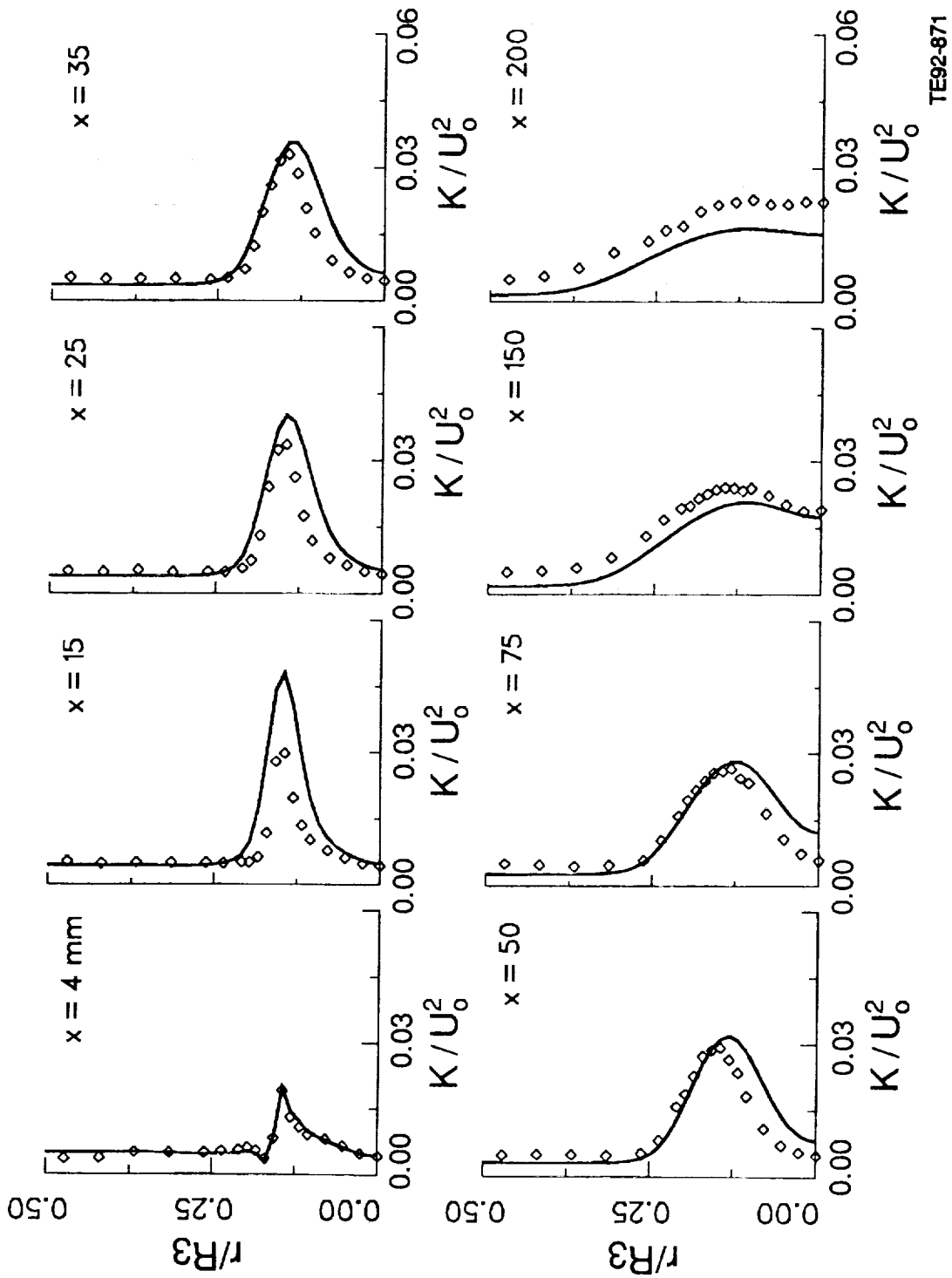


Figure 6.1.2-6. Comparison of predicted turbulent kinetic energy by $k-\epsilon$ model with data.

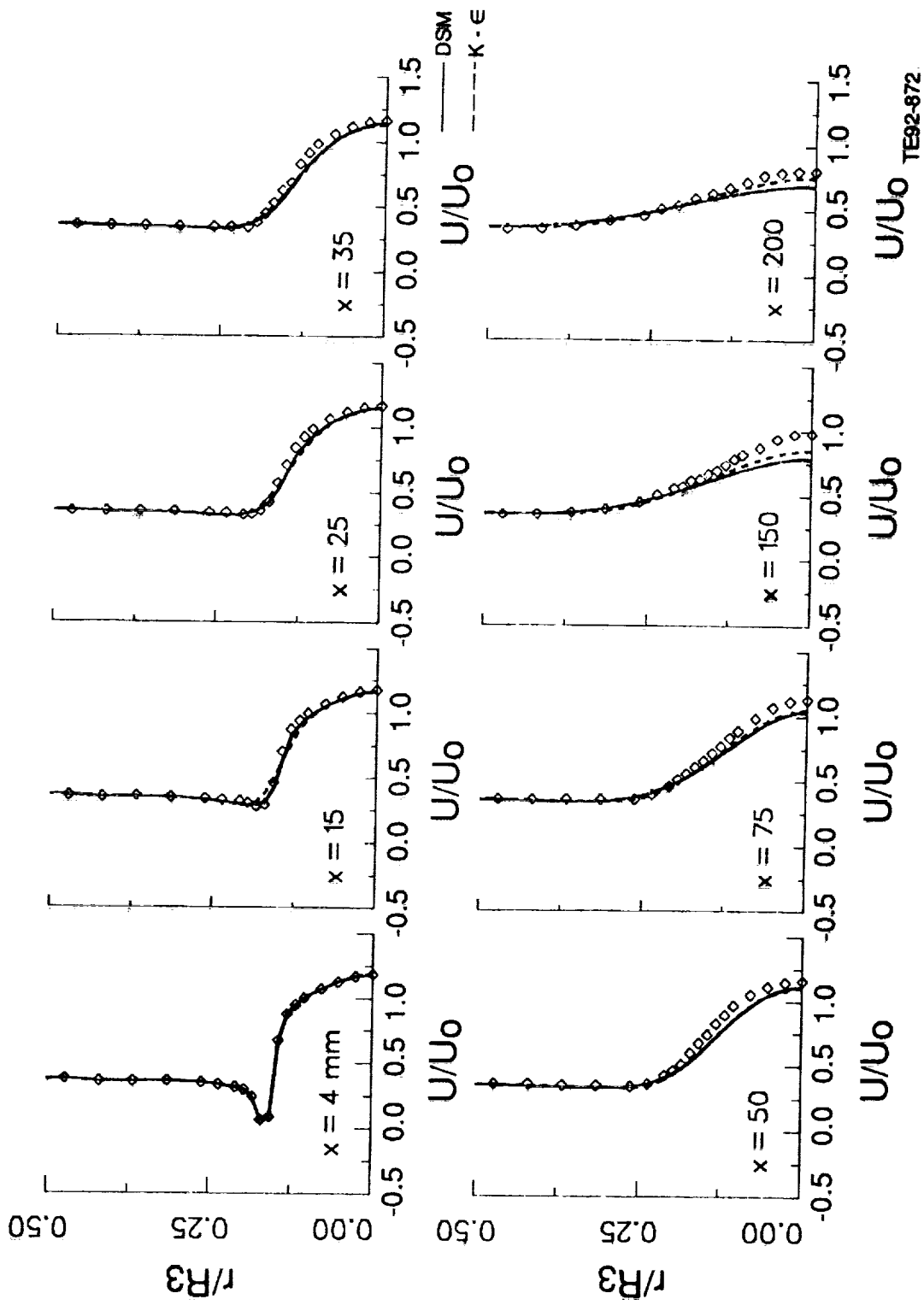


Figure 6.1.2-7. Comparison of predicted mean axial velocity by $k-\epsilon$ and DSM with data.

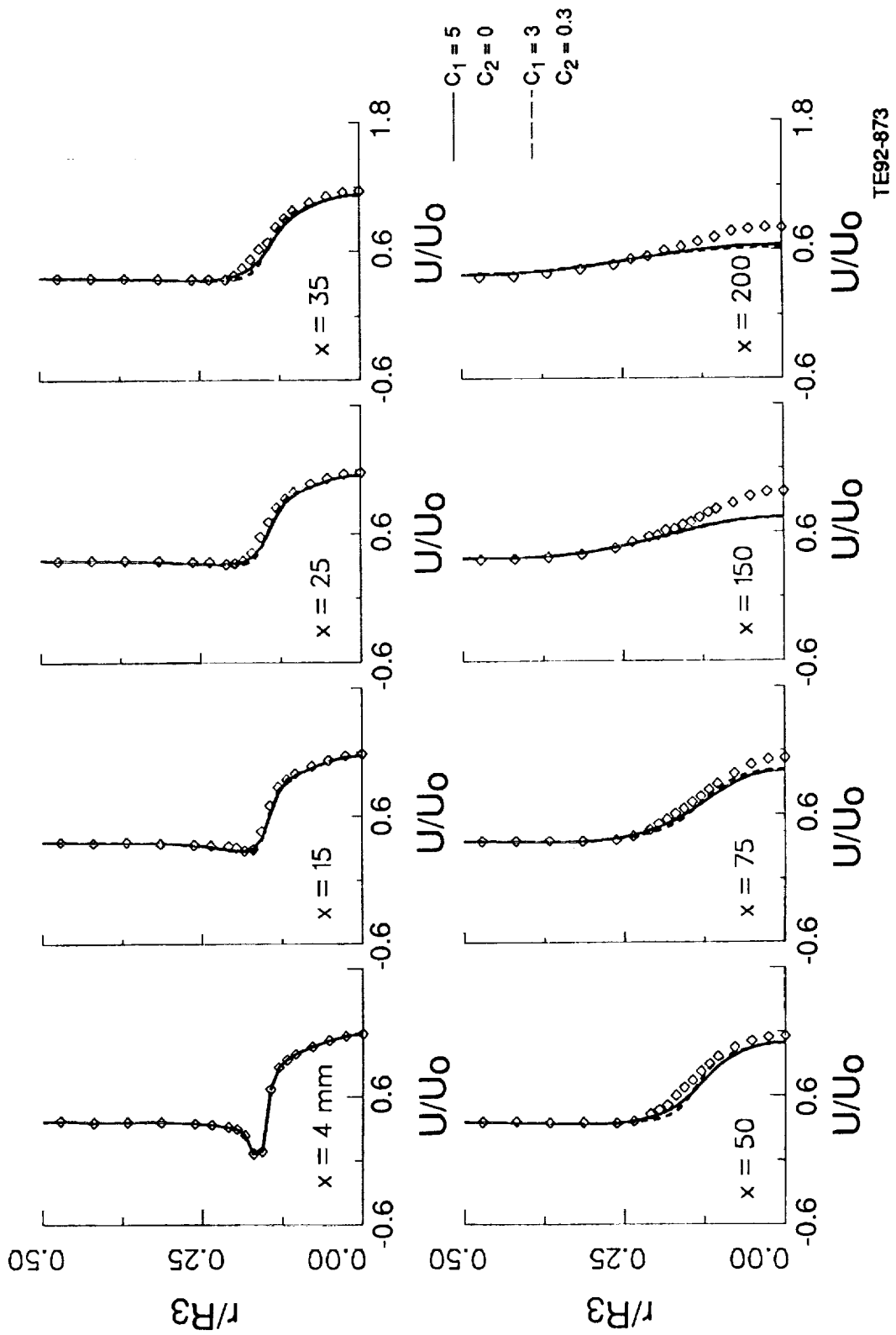


Figure 6.1.2-8. Comparison of predicted U velocity by ASM with data.

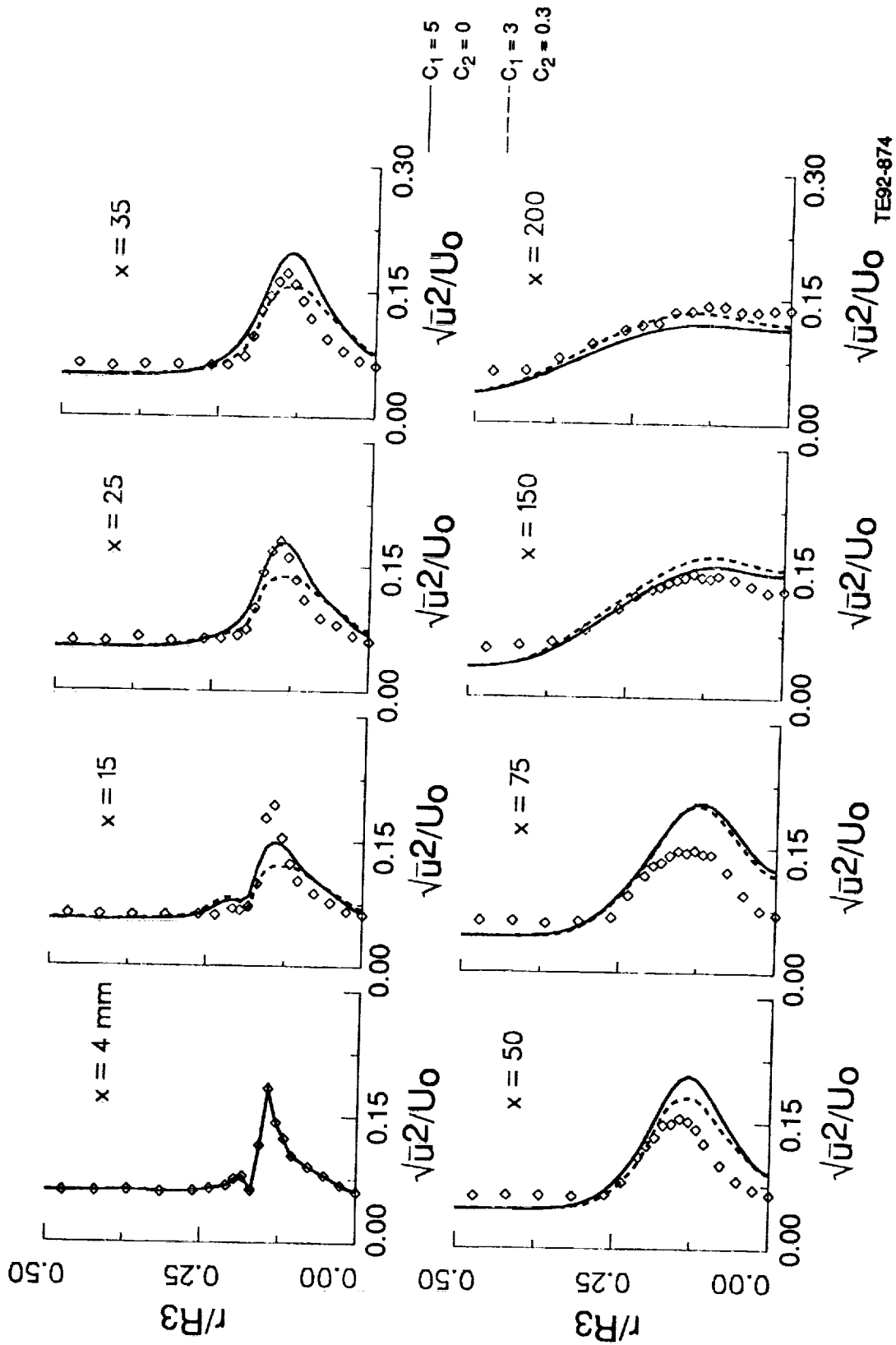


Figure 6.1.2-9. Comparison of calculated streamwise turbulence intensity by ASM with data.

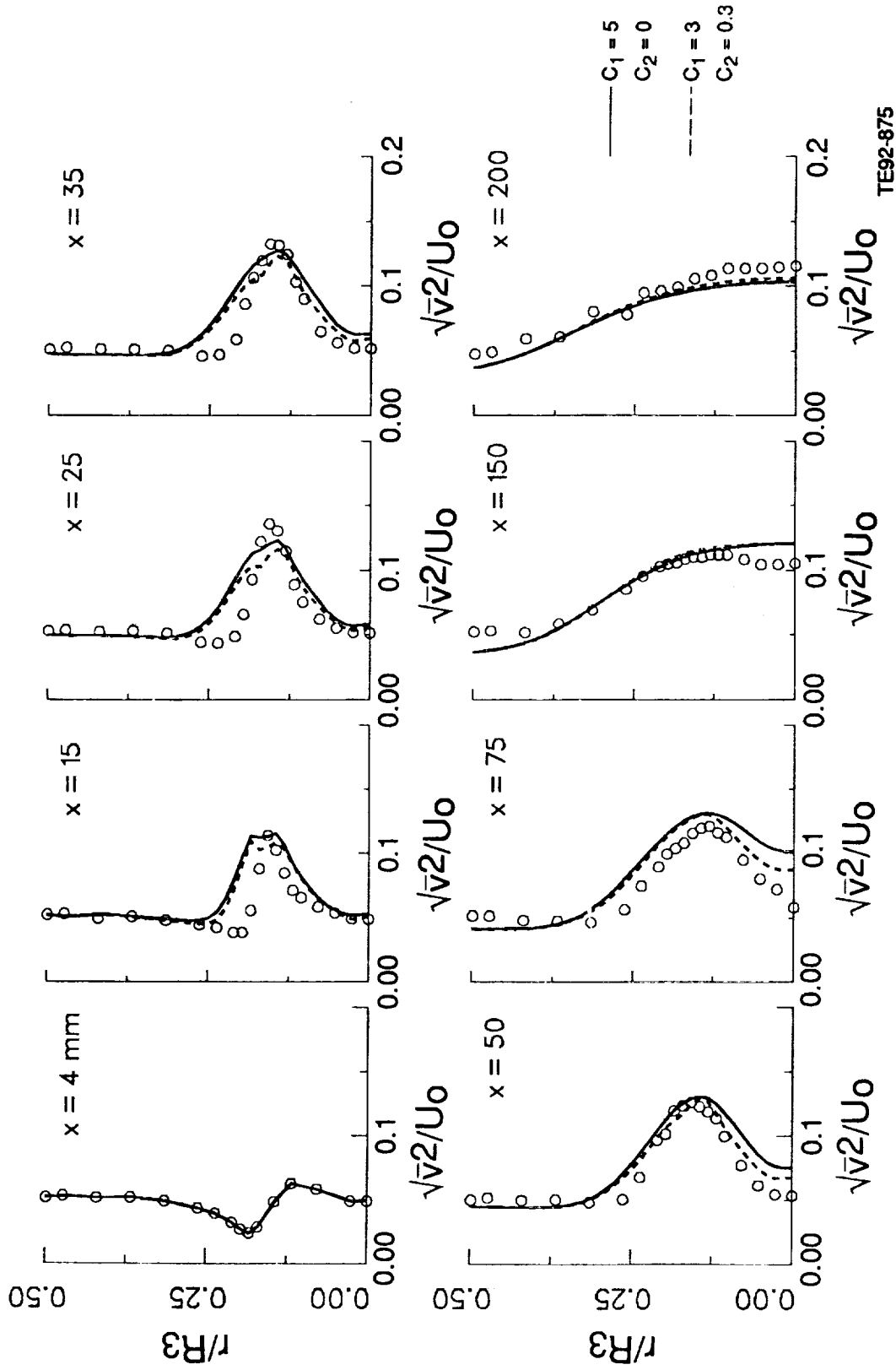


Figure 6.1.2-10. Comparison of calculated radial turbulence intensity by ASM with data.

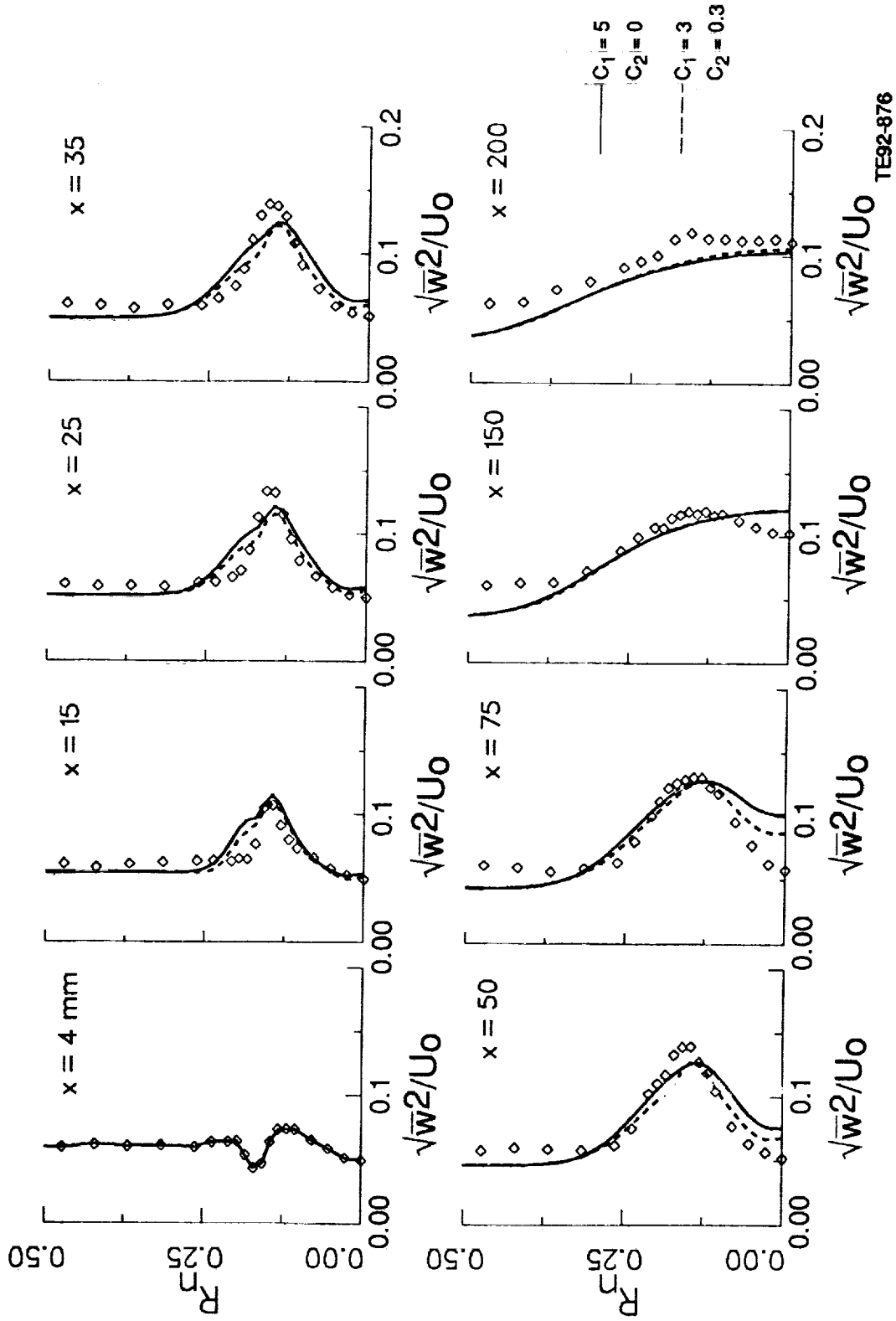


Figure 6.1.2-11. Comparison of calculated tangential turbulence intensity by ASM with data.

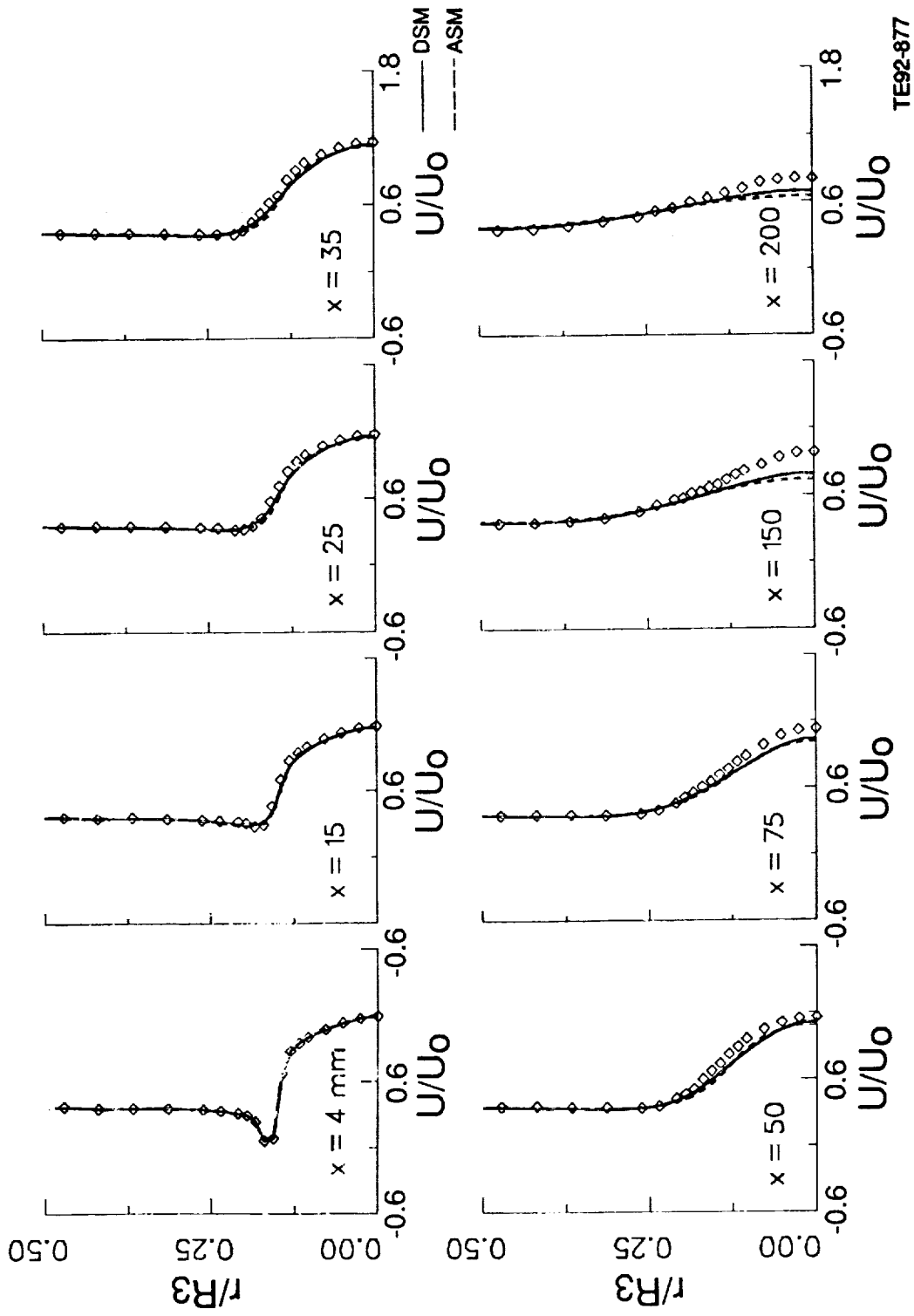
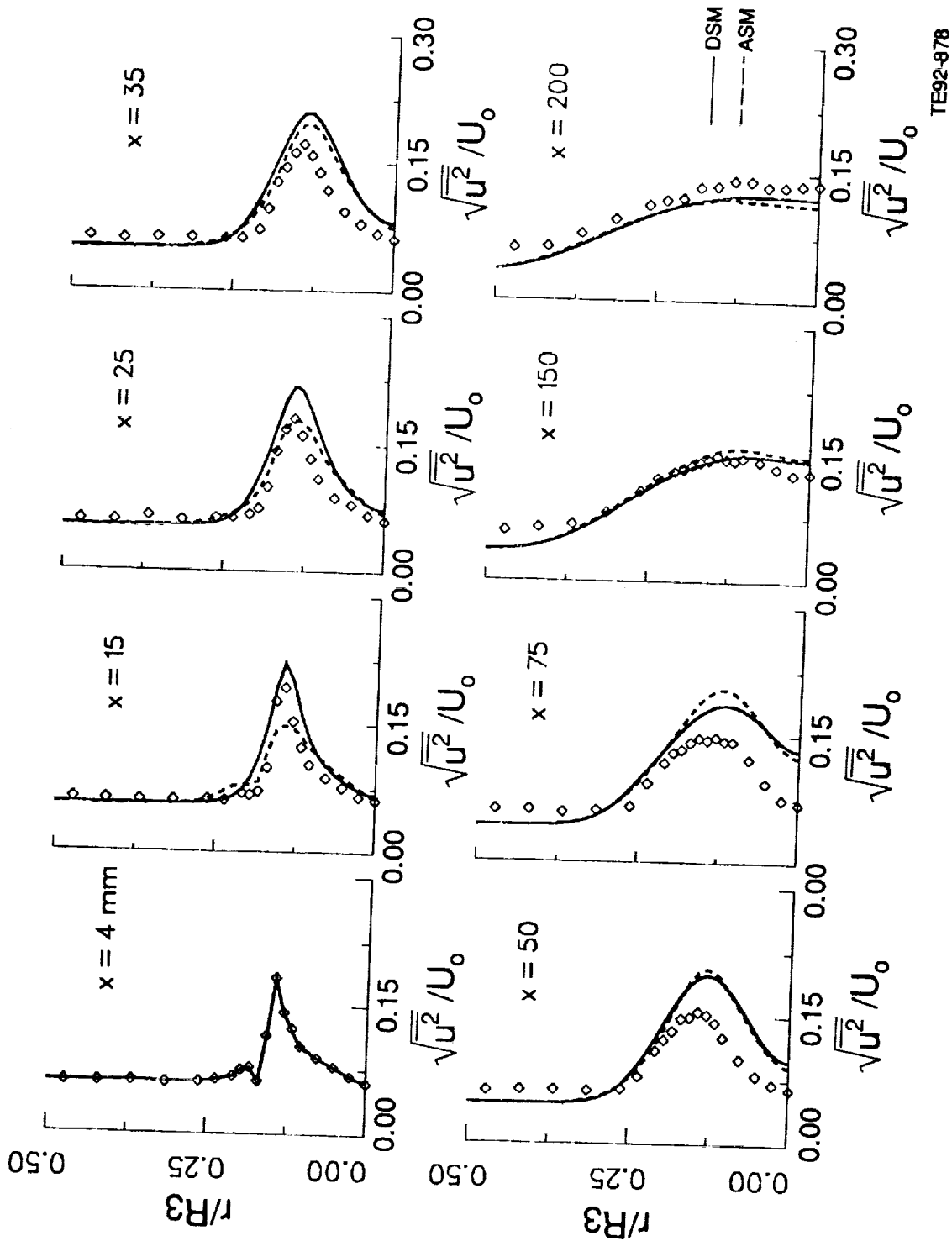


Figure 6.1.2-12. Comparison of calculated U velocity profiles by DSM and ASM with data.



TE92-878

Figure 6.1.2-13. Comparison of calculated streamwise turbulence intensity by DSM and ASM with data.

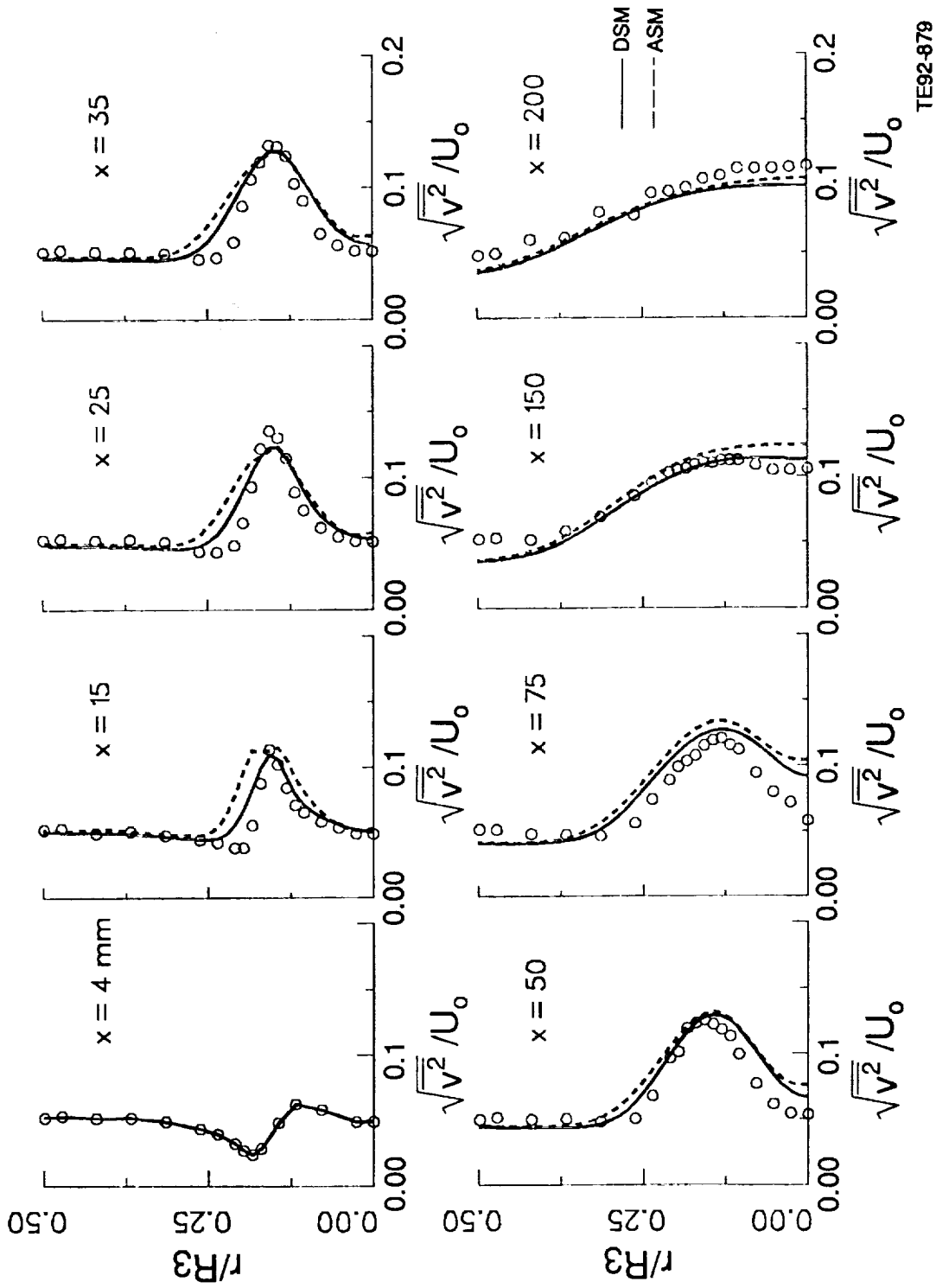


Figure 6.1.2-14. Comparison of calculated radial turbulence intensity by DSM and ASM with data.

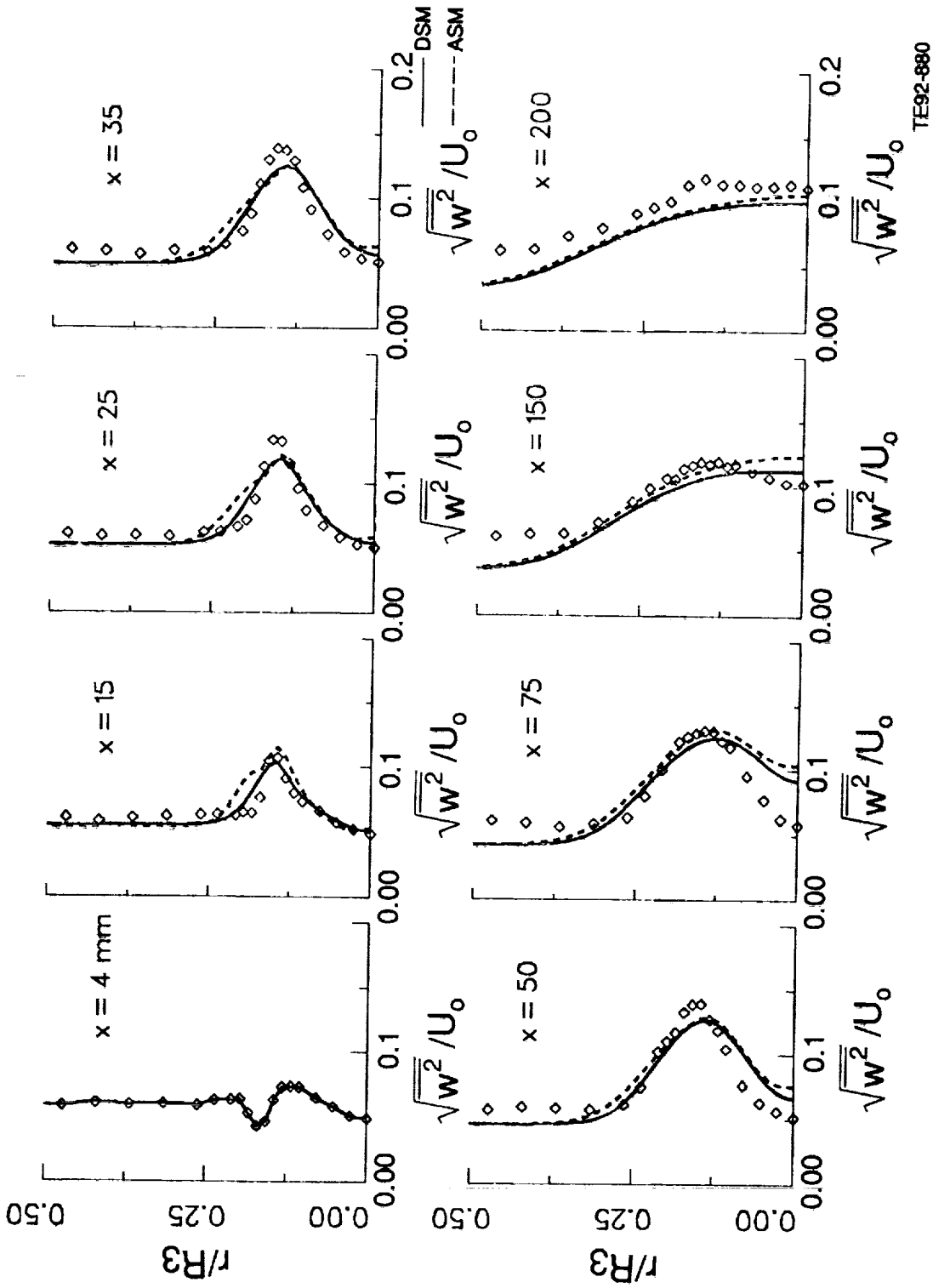


Figure 6.12-15. Comparison of calculated tangential turbulence intensity by DSM and ASM with data.

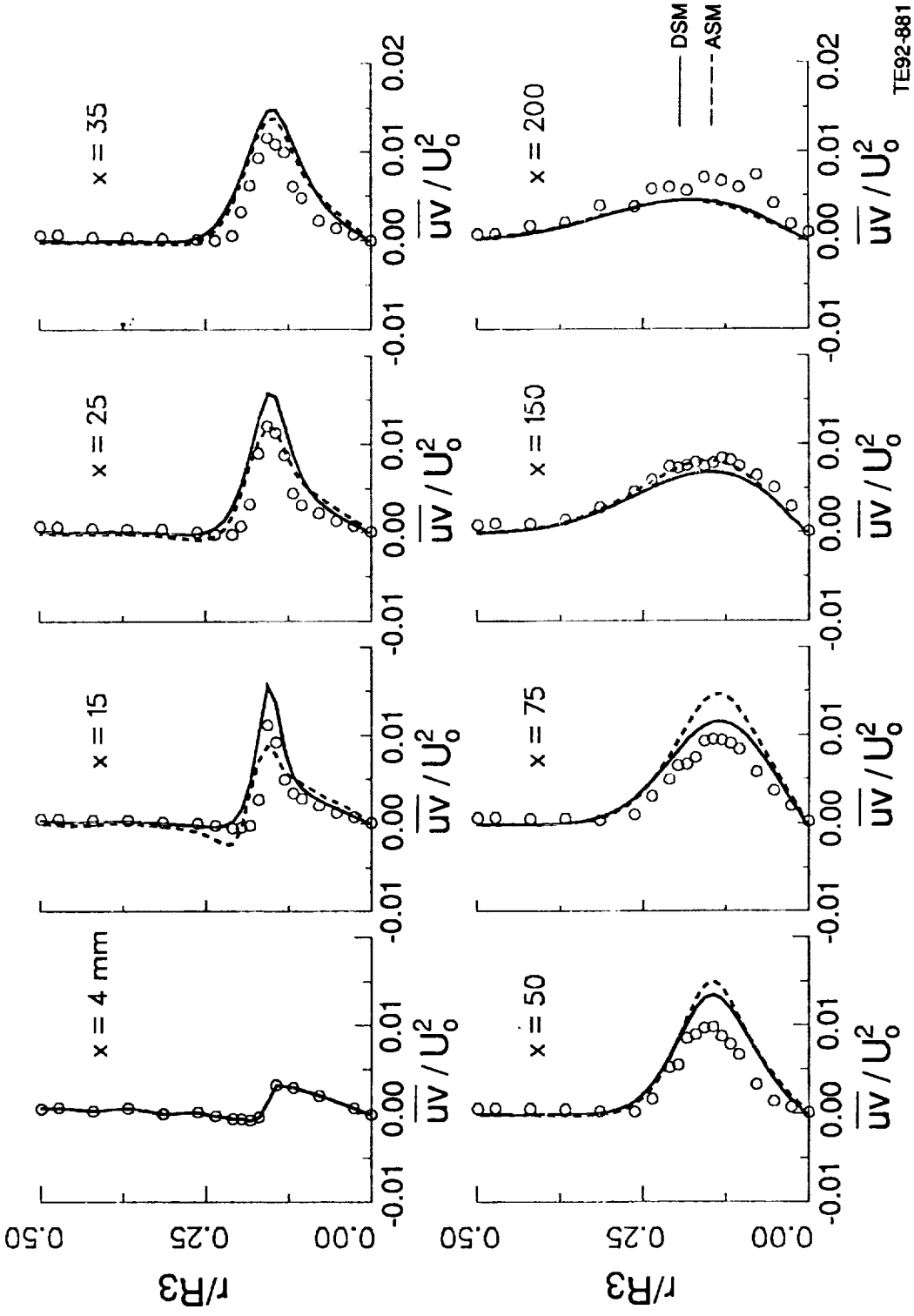


Figure 6.1.2-16. Comparison of calculated turbulent shear stress profiles by DSM and ASM with data.

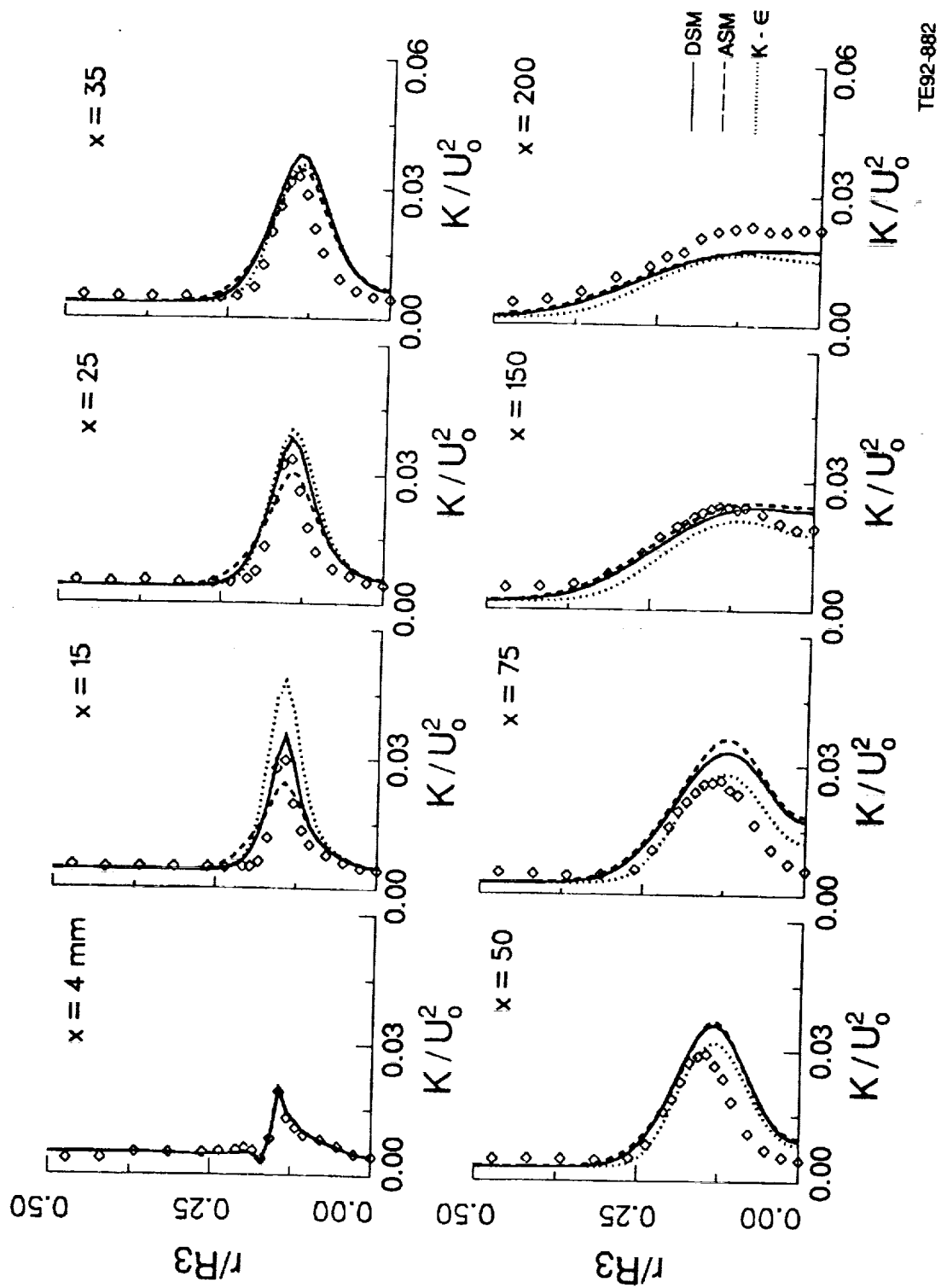
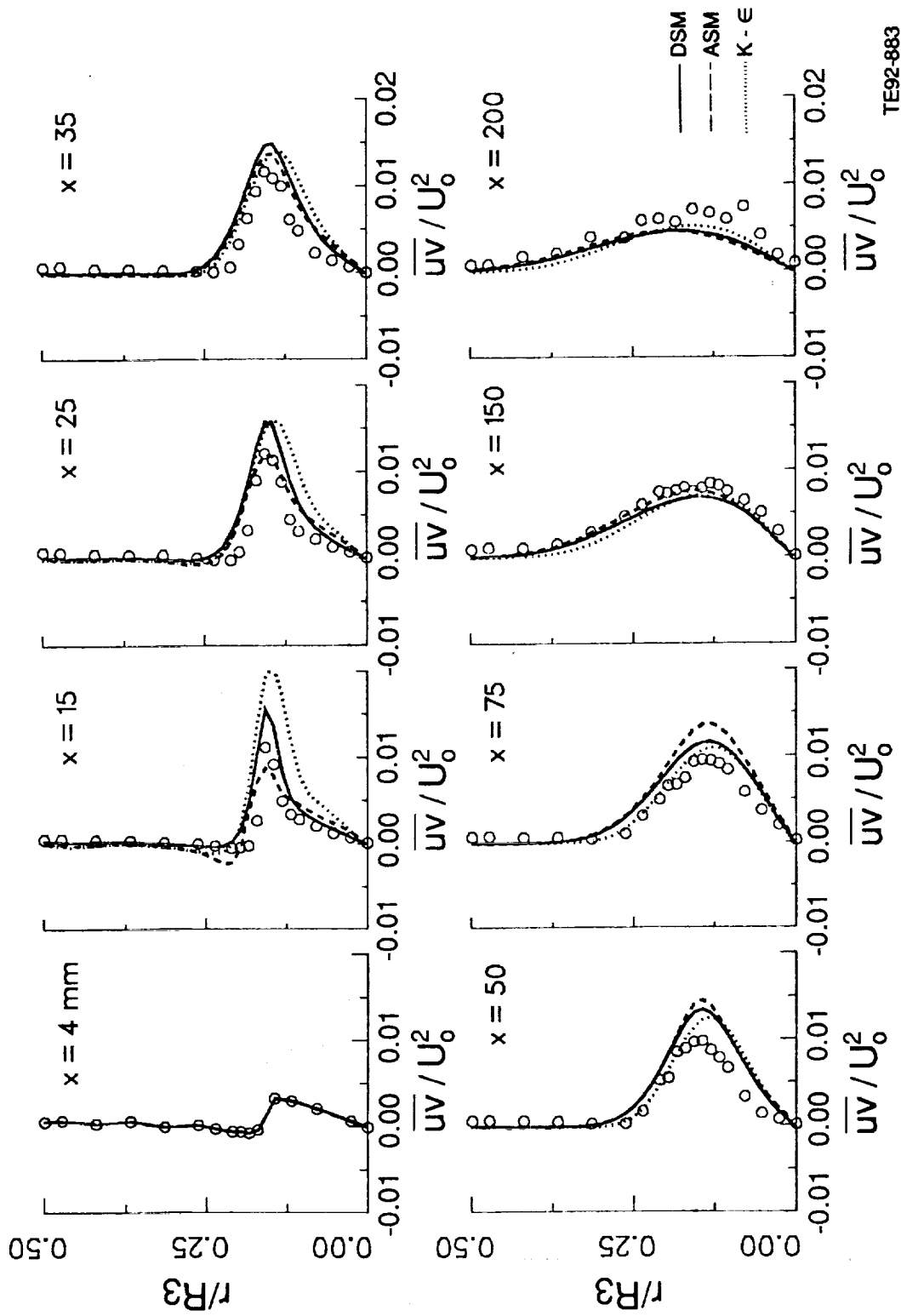


Figure 6.12-17. Comparison of calculated k by $k-\epsilon$, ASM, and DSM with data.



TE92-883

Figure 6.1.2-18. Comparison of calculated turbulent shear stress profiles by k-ε, ASM, and DSM with data.

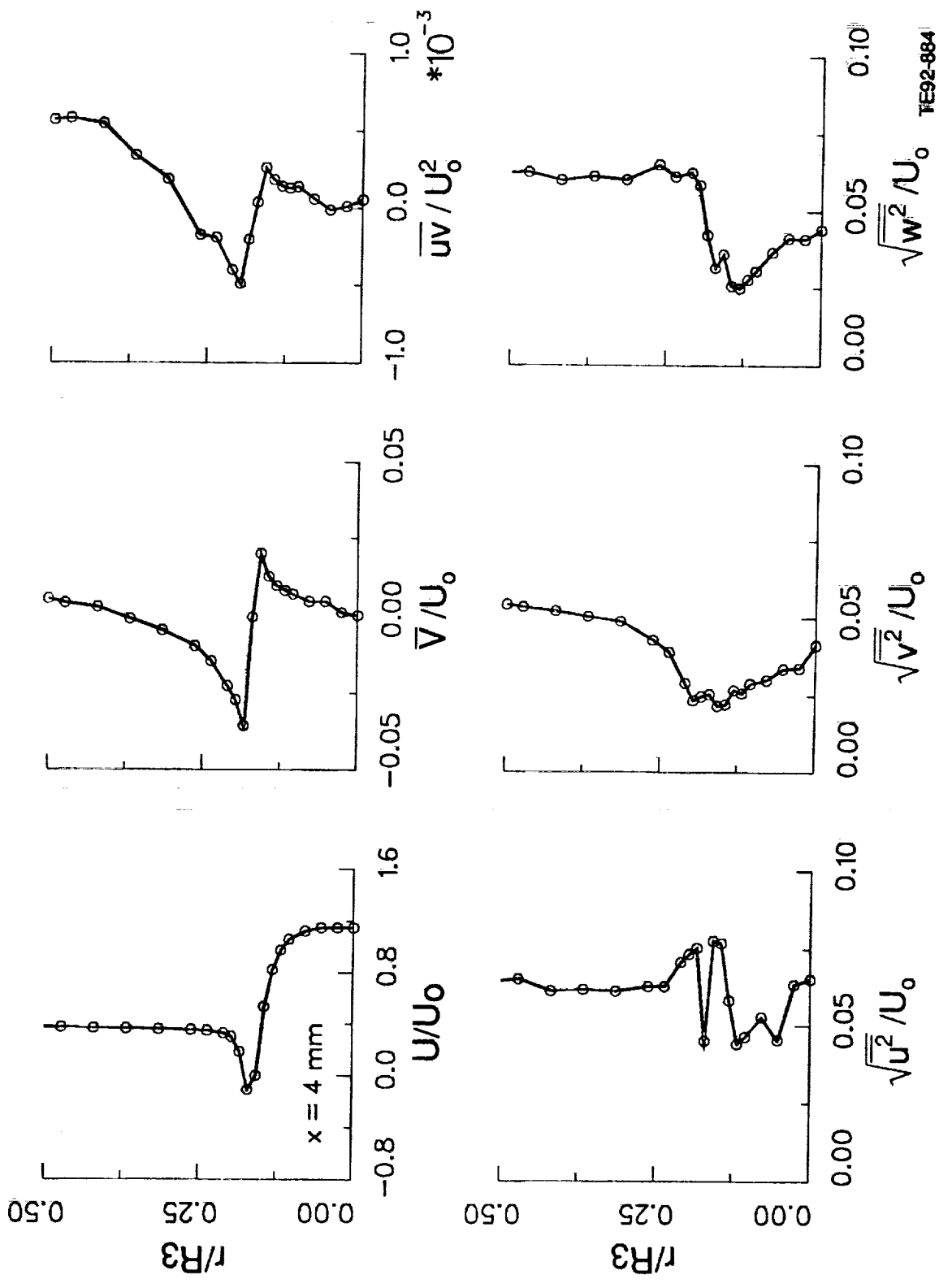
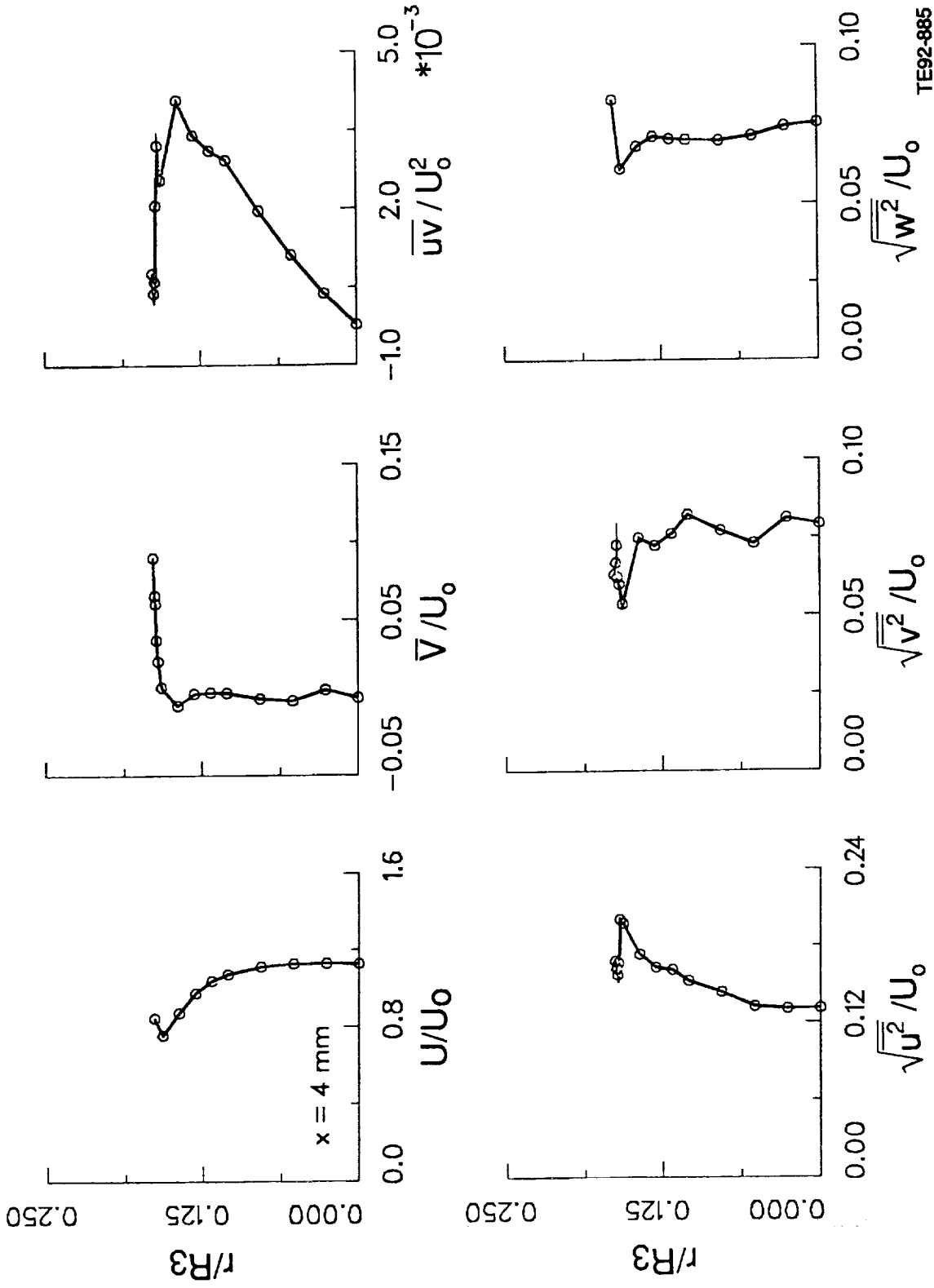
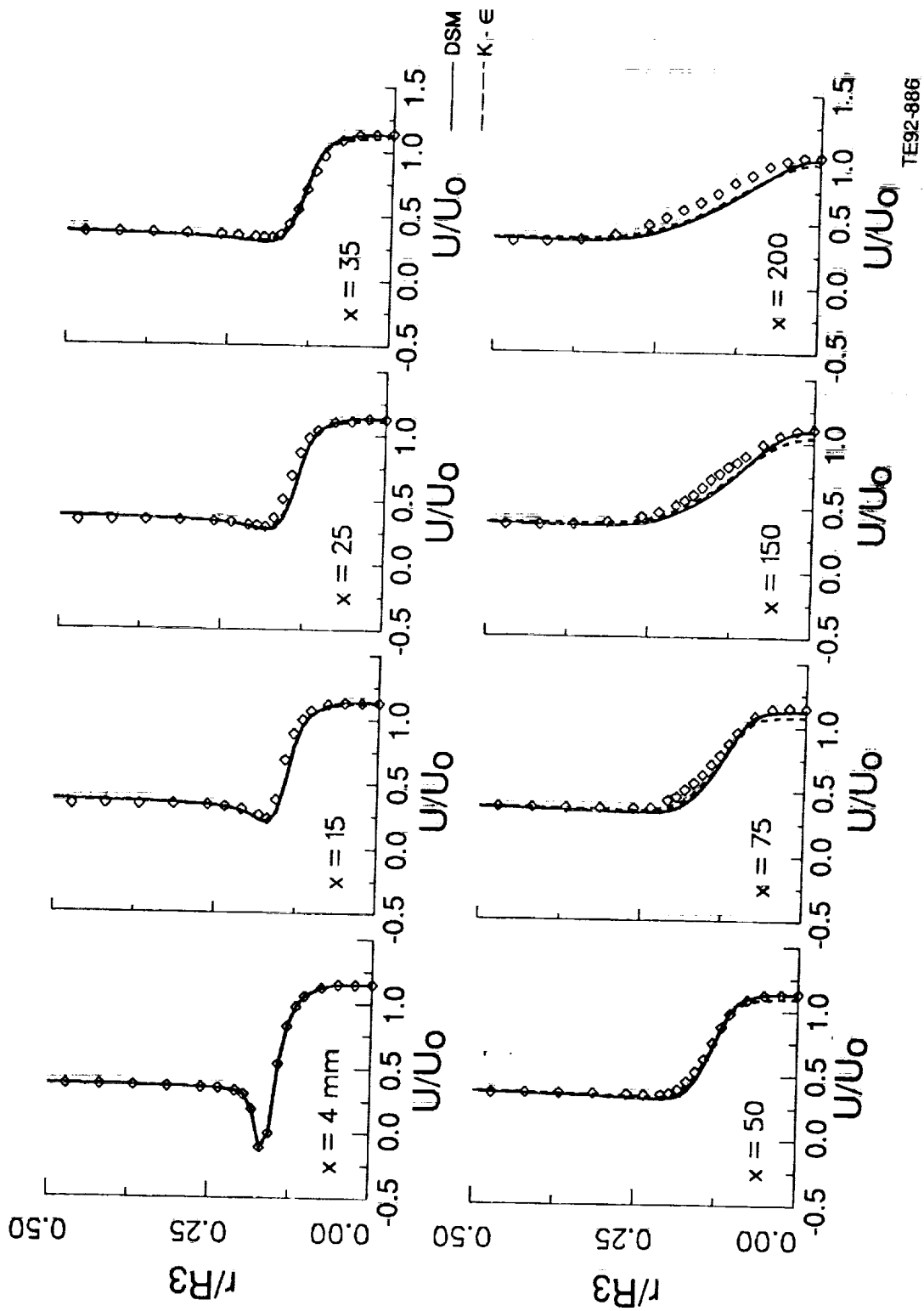


Figure 6.1.2-19. Measured profiles for continuous phase at the inlet plane ($x = 4$ mm), particle-laden jet.



TE92-885

Figure 6.1.2-20. Measured profiles for dispersed phase at the inlet plane ($x = 4$ mm), particle-laden jet.



TE92-886

Figure 6.1.2-21. Comparison of predicted gas phase U velocity profiles by DSM and $k-\epsilon$ with data, particle-laden jet

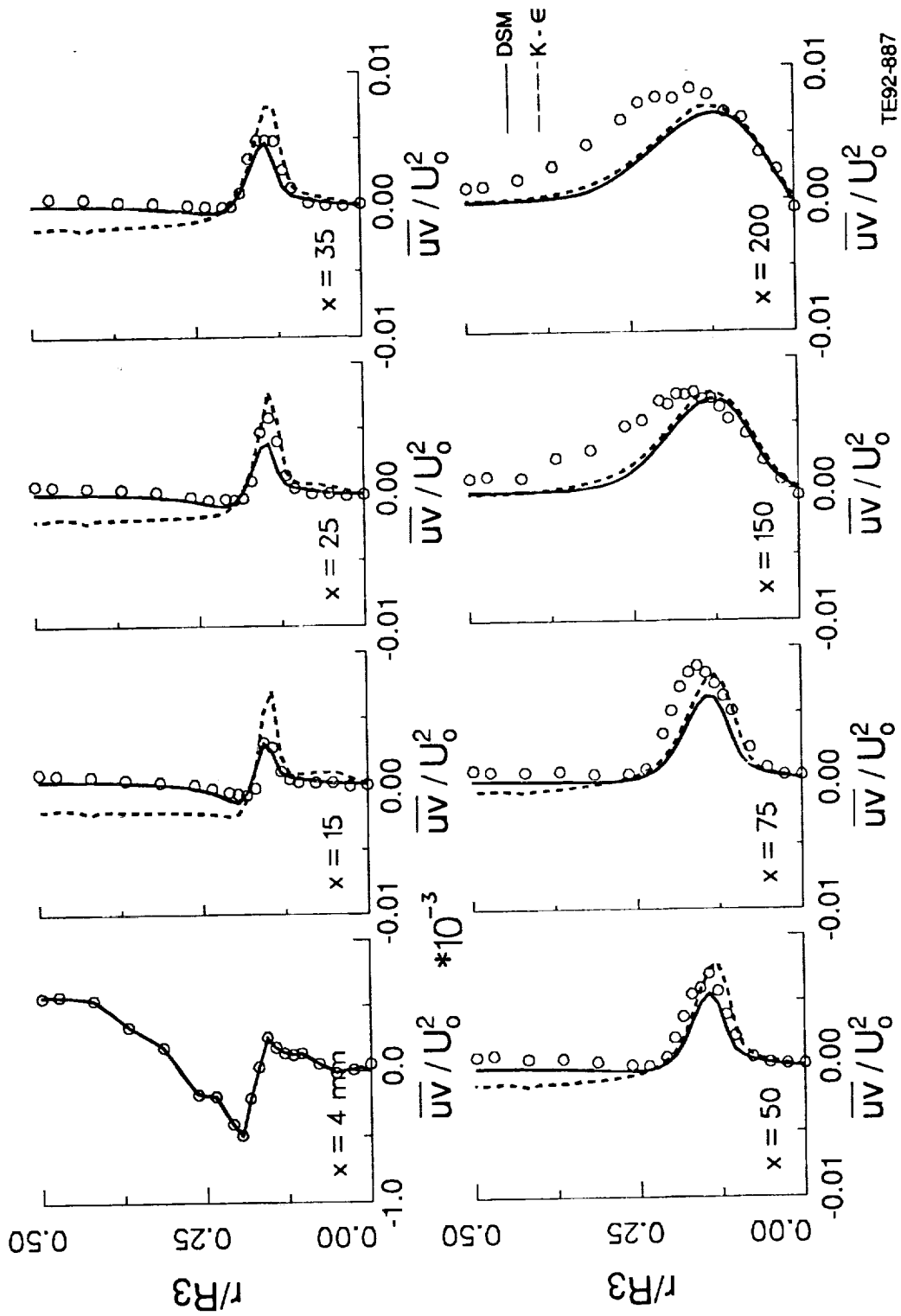


Figure 6.1.2-22. Comparison of predicted gas phase shear stress profiles by DSM and k-ε with data, particle-laden jet.

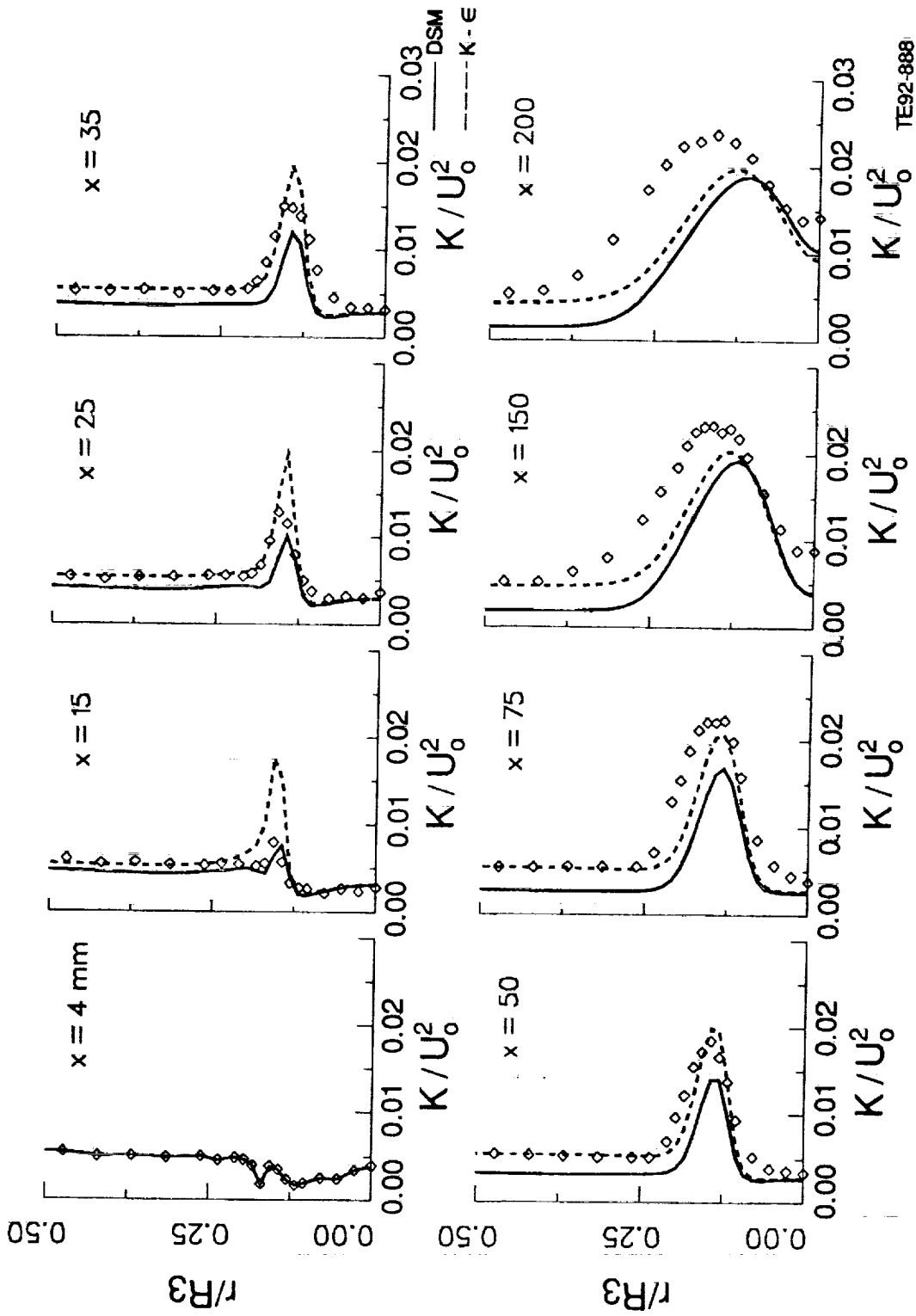


Figure 6.1.2-23. Comparison of predicted gas phase k profiles by DSM and $k-\epsilon$ with data, particle-laden jet.

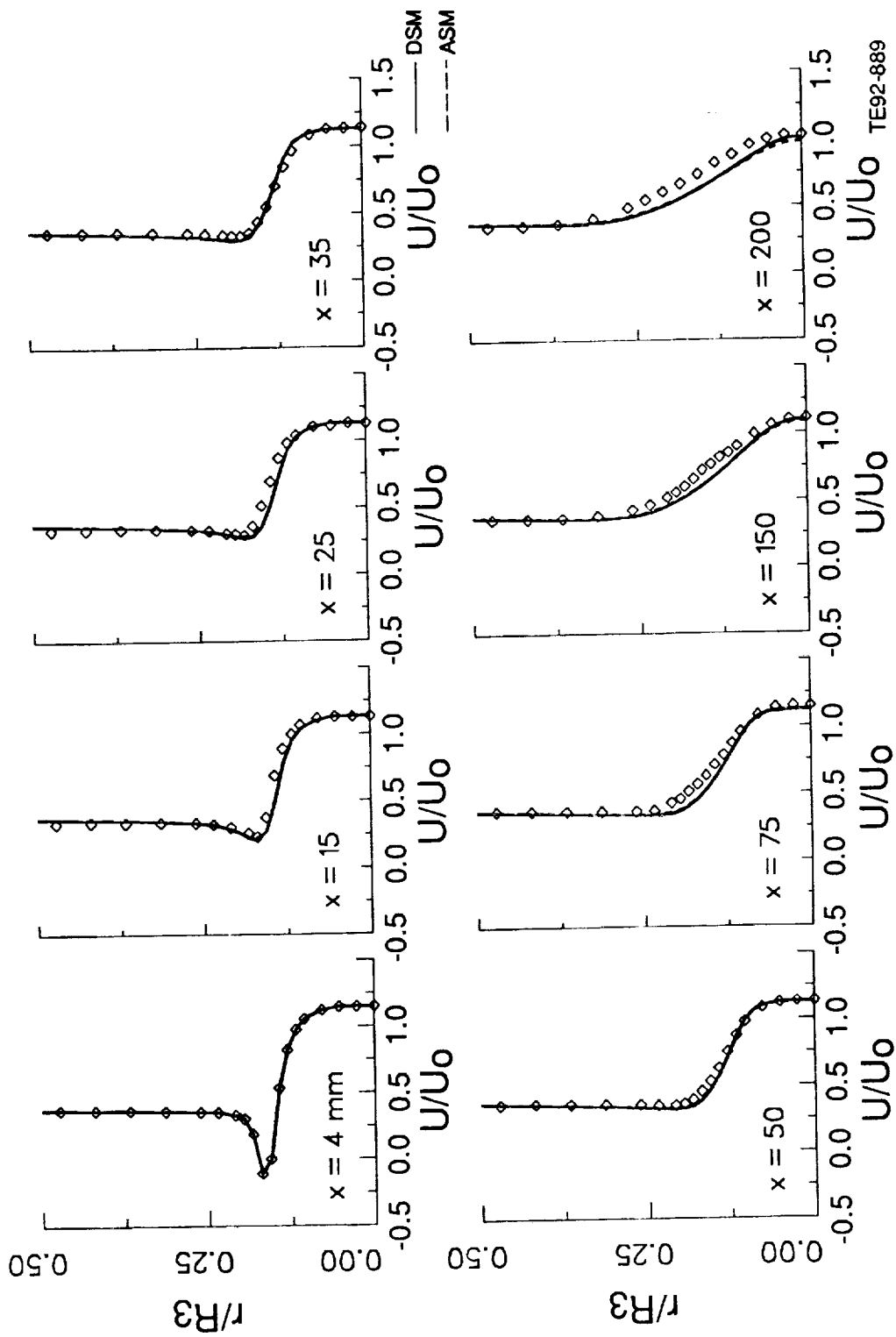
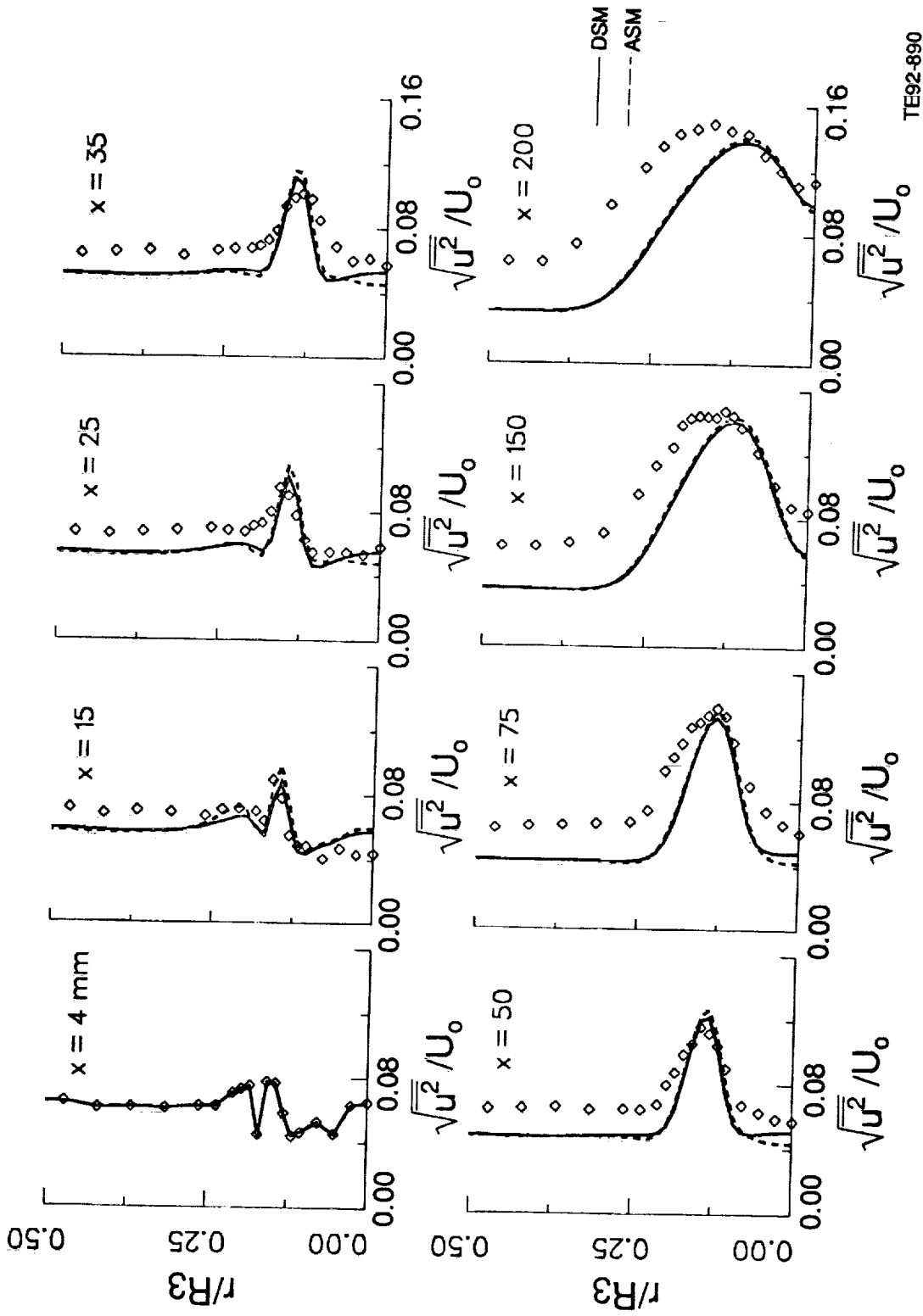


Figure 6.1.2-24. Comparison of predicted gas phase U velocity profiles by ASM and DSM with data, particle-laden jet.

TE92-889



TE92-890

Figure 6.1.2-25. Comparison of calculated gas phase streamwise turbulence intensity profiles by DSM and ASM with data, particle-laden jet.

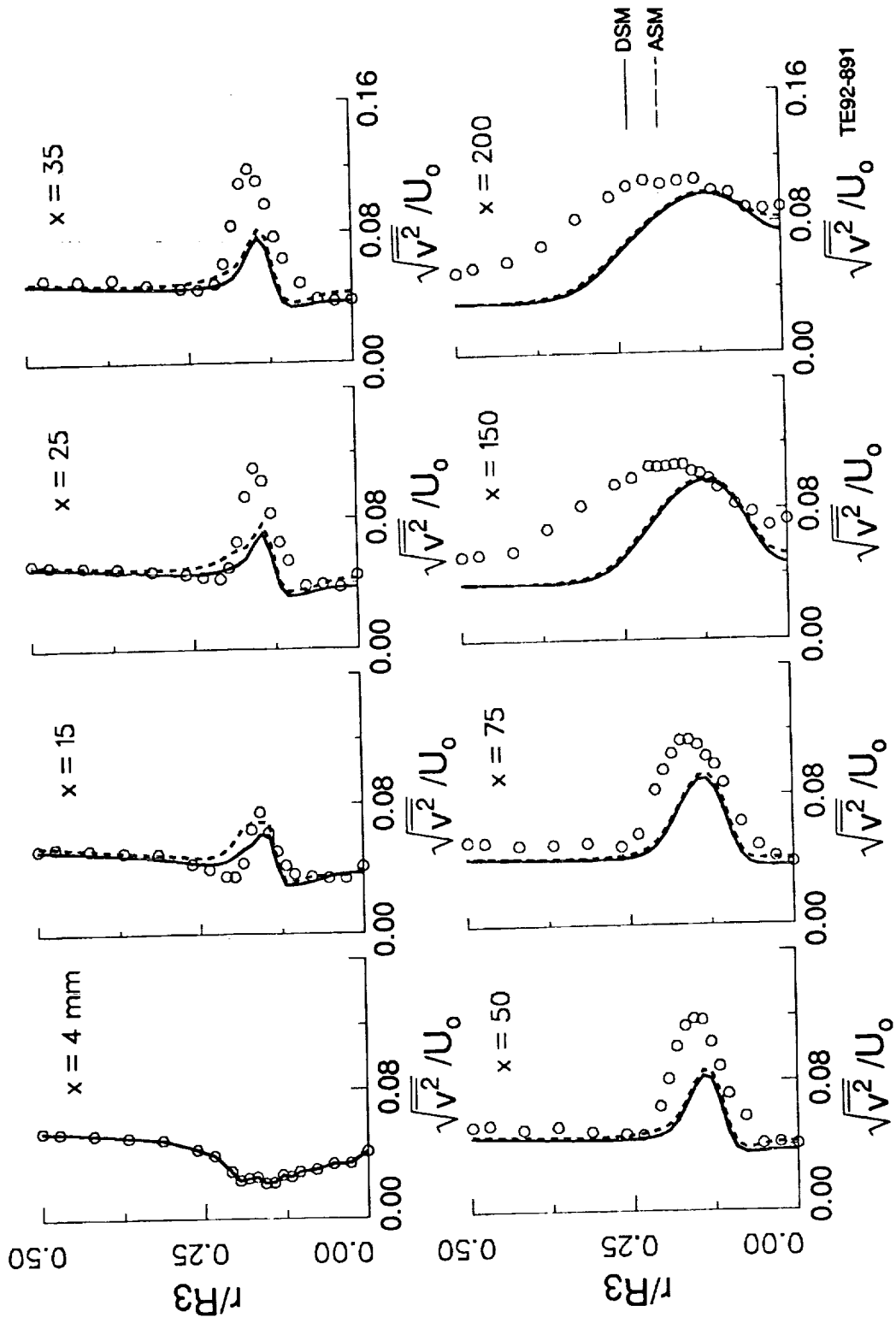


Figure 6.1.2-26. Comparison of calculated gas phase radial turbulence intensity profiles by DSM and DSM with data, particle-laden jet. TE92-891

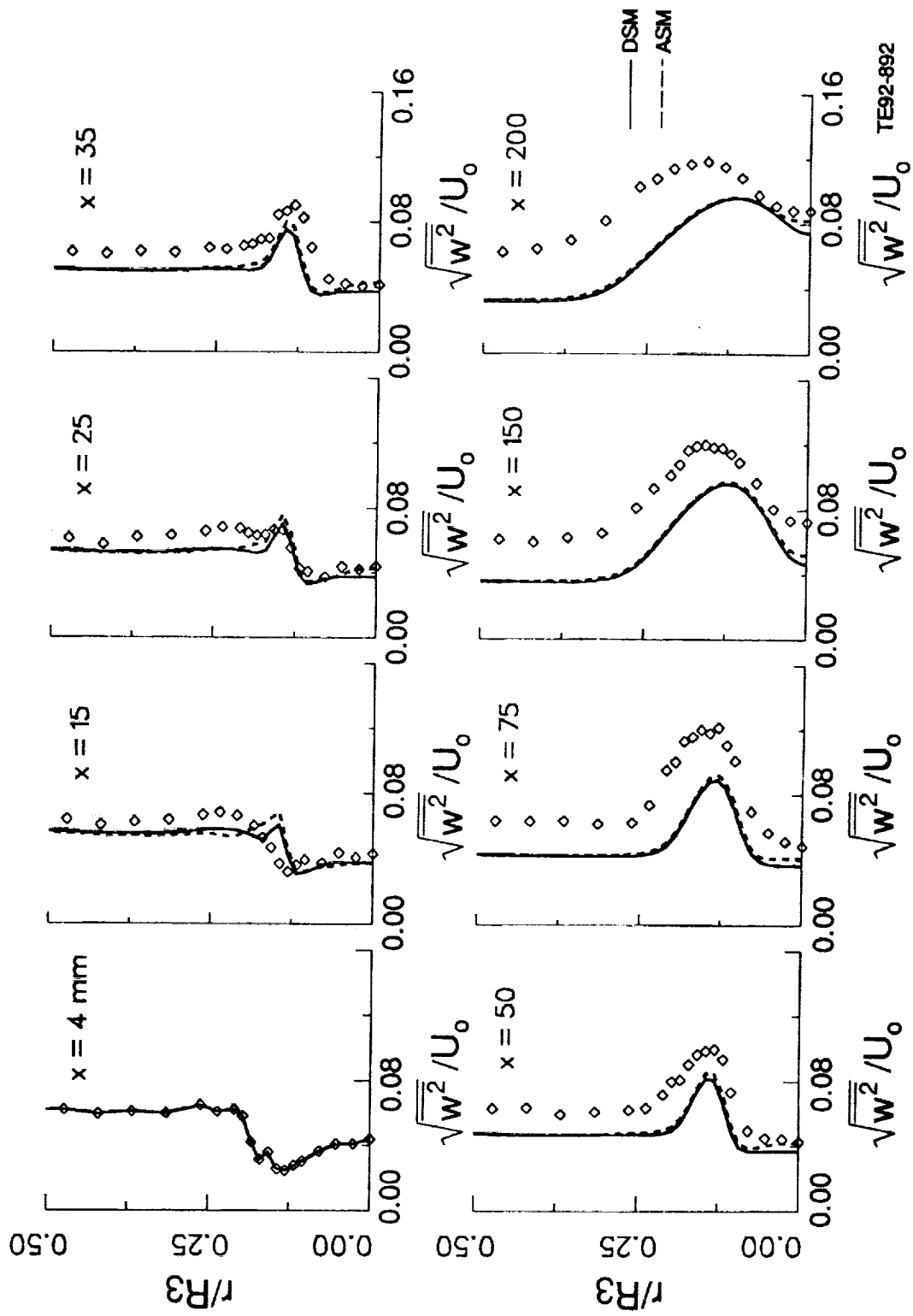
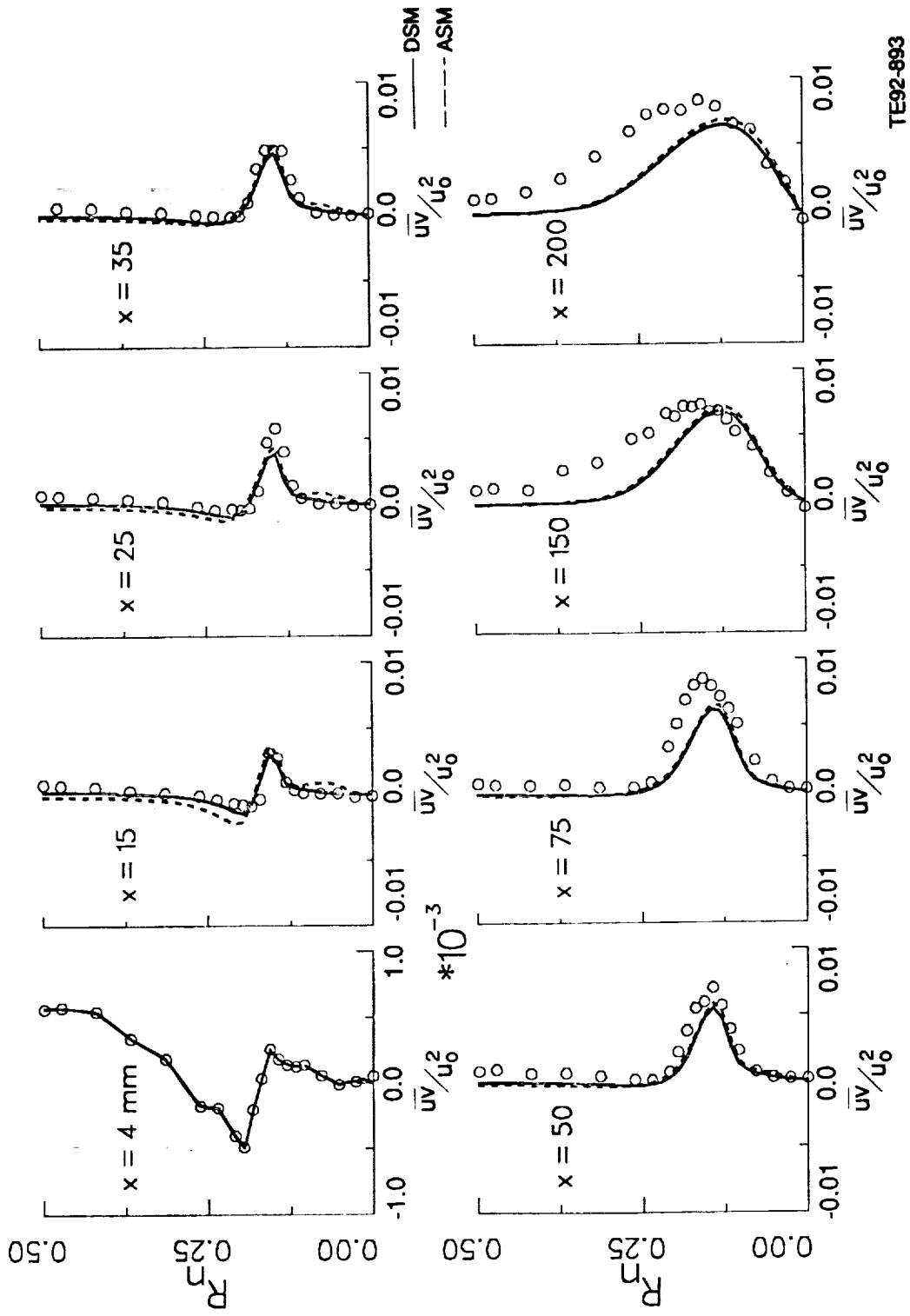
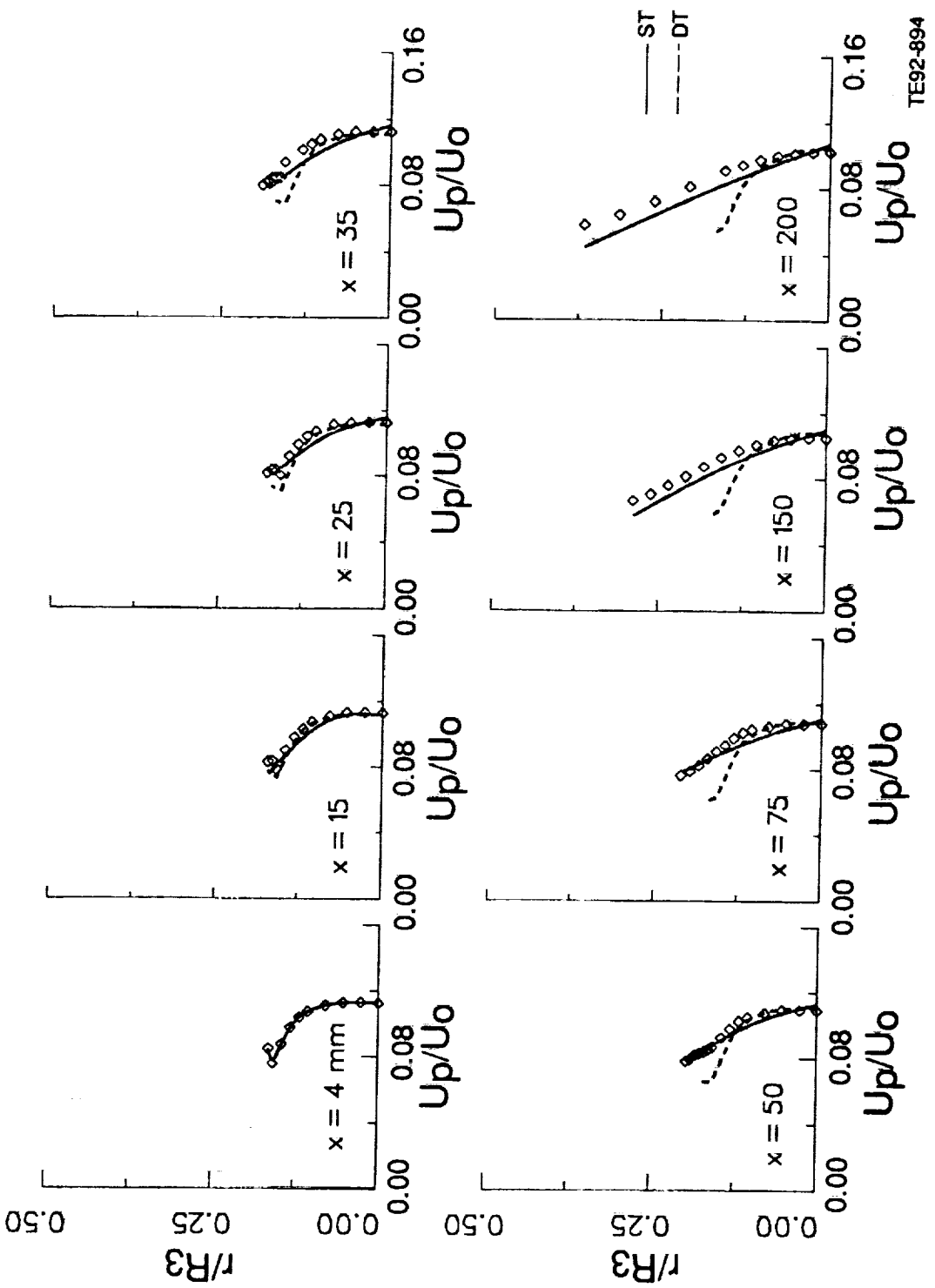


Figure 6.1.2-27. Comparison of calculated gas phase tangential turbulence-intensity profiles by DSM and DSM with data, particle-laden jet.



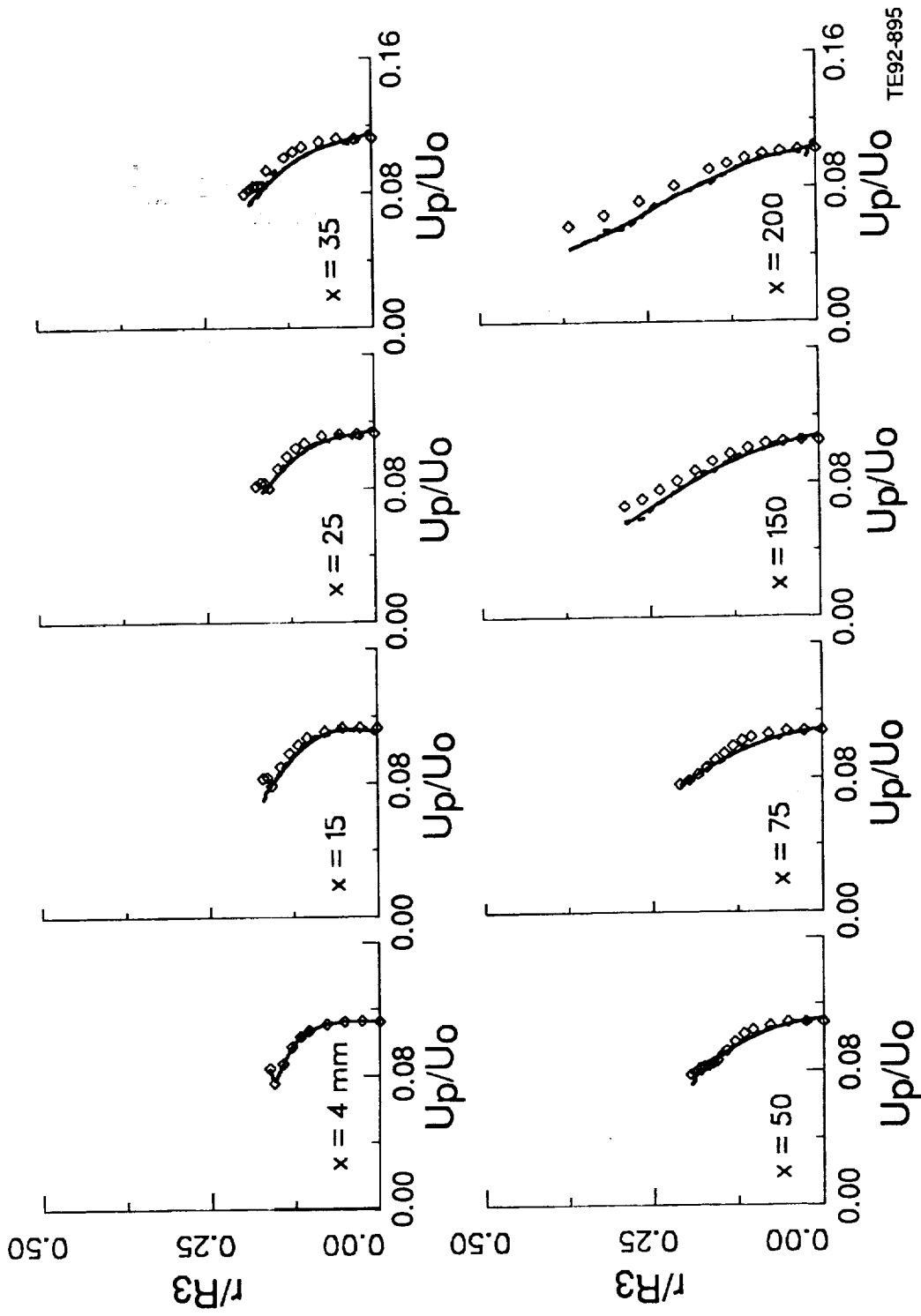
TE92-893

Figure 6.1.2-28. Comparison of calculated gas phase shear stress profiles by ASM and DSM with data, particle-laden jet.



TE92-894

Figure 6.1.2-29. Comparison of calculated dispersed phase axial velocity (U_p) profiles by $k-\epsilon$ with data.



TE92-895

Figure 6.1.2-30. Comparison of calculated dispersed phase axial velocity (U_p) profiles by DSM with data.

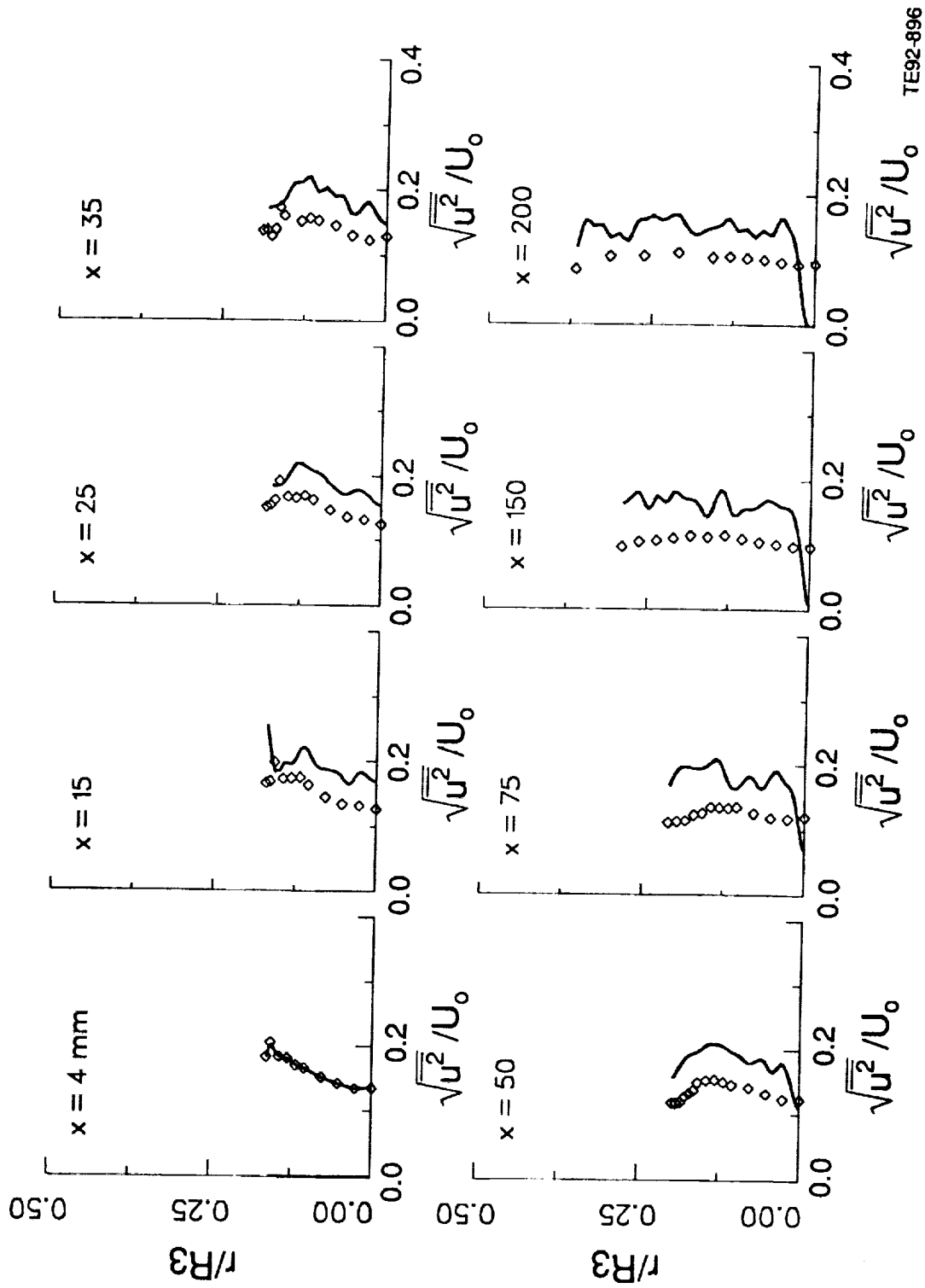


Figure 6.1.2-31. Comparison of calculated dispersed phase streamwise turbulence intensity by DSM with data.

TE92-896

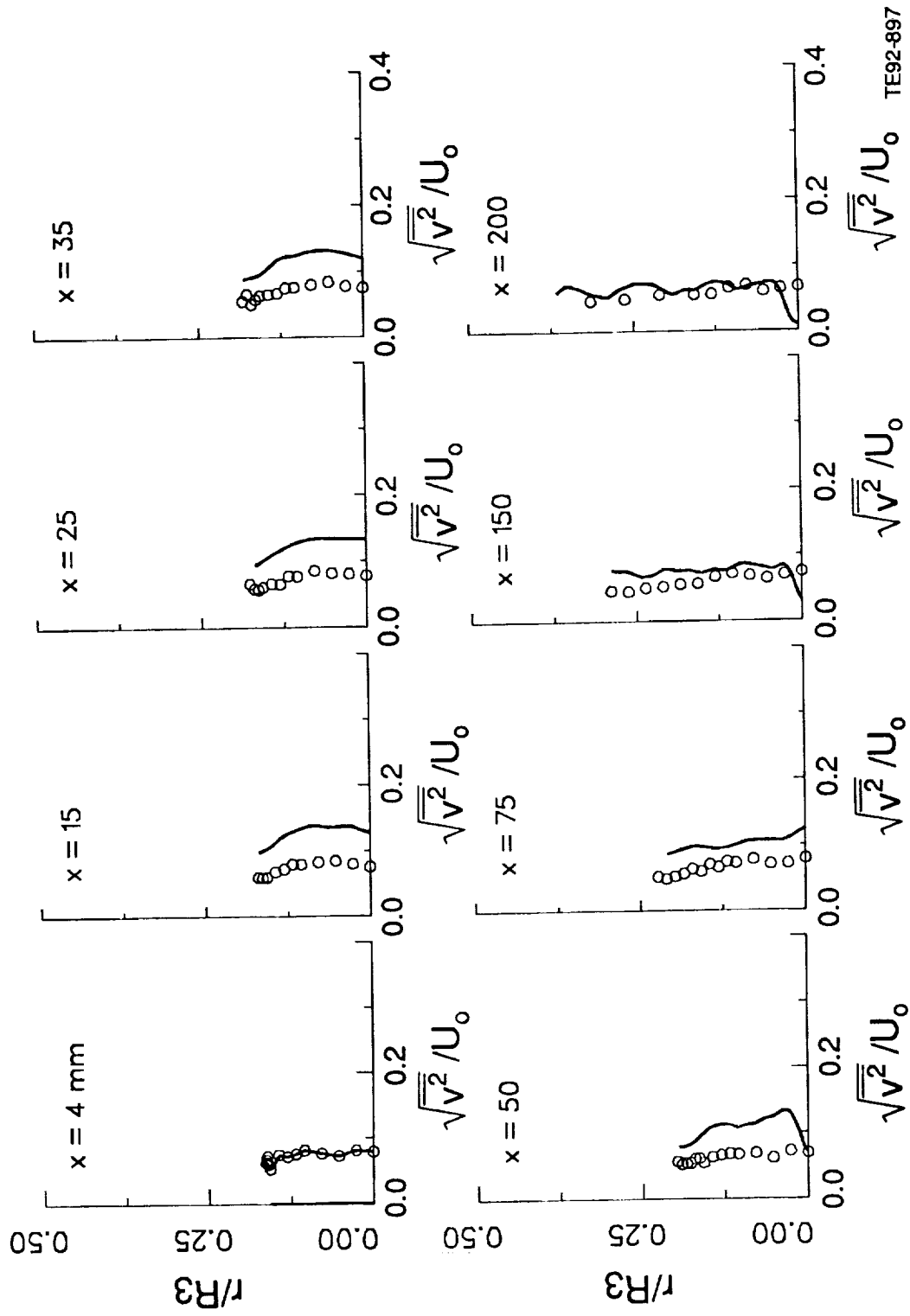


Figure 6.1.2-32. Comparison of calculated dispersed phase radial turbulence intensity by DSM with data.

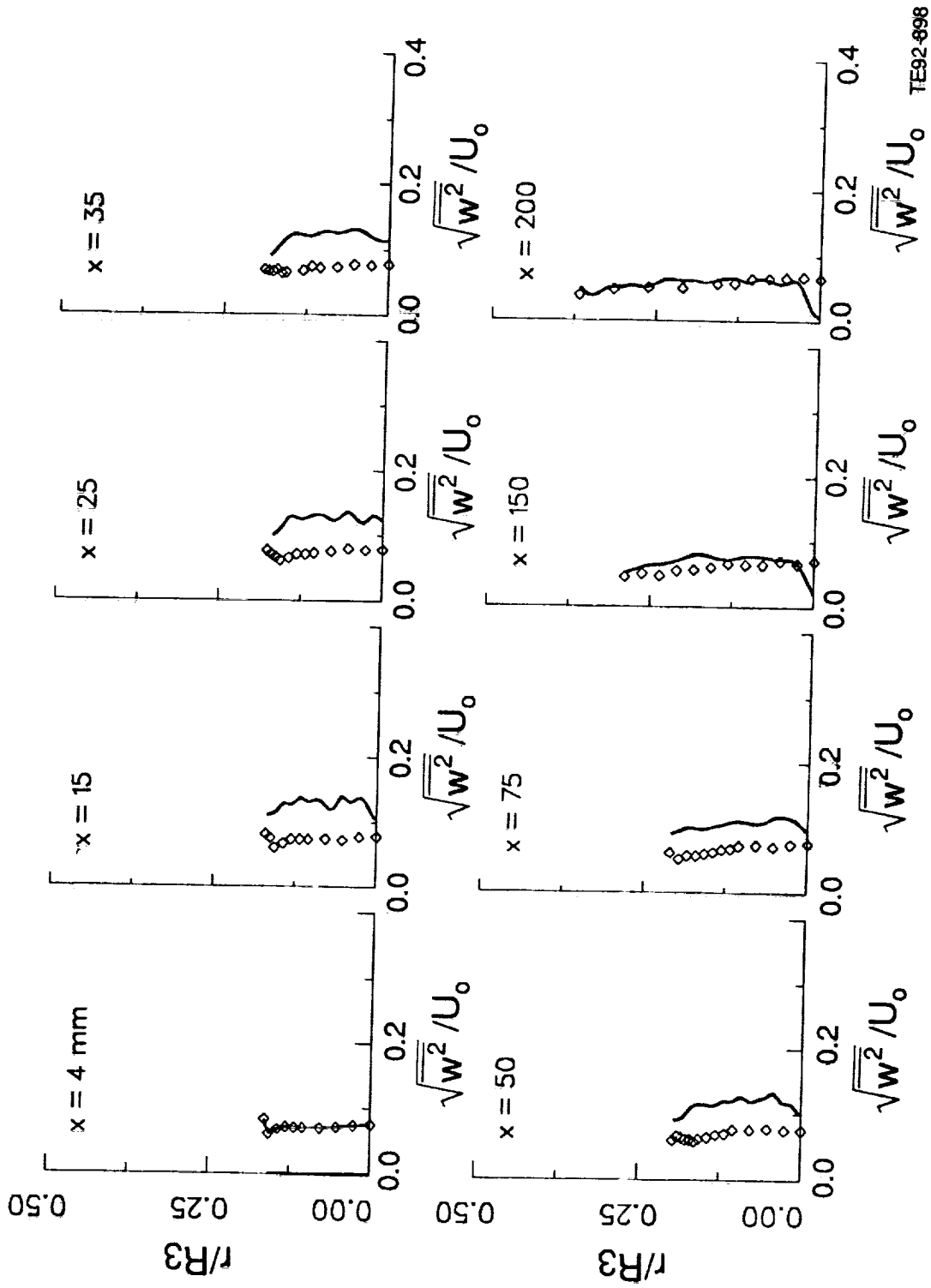


Figure 6.1.2-33. Comparison of calculated dispersed phase tangential turbulence intensity by DSM with data.

TE92-698

6.2 UNCONFINED SINGLE ANNULAR JET

In this section, study of an unconfined annular flow configuration (Figure 6.2-1) is presented. The flow conditions used for the case considered here are given in Table 6.2-I. In this configuration, the test section was directed vertically downward and the annular jet discharged into stagnant air. Measurements have been taken using a two-color, two-component laser anemometer system at eight axial stations: 3, 15, 25, 35, 50, 75, 150, and 300 mm from the exit plane of the jet exit. At each spatial point, the laser simultaneously measured two orthogonal components of velocity. To get all three components, two scans were taken. One was used to measure $U, V, u^2, v^2,$ and uv components and the other was able to measure $U, W, u^2, w^2,$ and uw components. Thus all three mean and rms velocity components, uv and uw were measured along with $U,$ and u^2 was measured twice.

The computational mesh used for all calculations consisted of 61×70 nonuniformly distributed grid points in the axial (x) and radial (r) directions (Figure 6.2-2). The tabulated x and r grid coordinates are shown in Table 6.2-II. A finer grid spacing was used near the inlet, centerline, and in the shear layer. The computational domain extended from the first measurement plane to 450 mm downstream of the nozzle exit. In the radial direction, the entrainment boundary was placed at 170 mm from the axis of symmetry. The convergence criterion used to terminate the iterations was the absolute sums of the mass and momentum residuals at all internal grid points, normalized by inlet mass and momentum fluxes, less than 10^{-3} .

A calculation procedure for elliptic flow requires boundary conditions on all boundaries of the computational domain. Four kinds of boundaries need consideration, namely, inlet, axis of symmetry, outlet, and the entrainment boundary. At the inlet boundary, which was located at the first measurement plane ($x = 3$ mm), the measured profiles of $U, V, u^2, v^2, w^2,$ and uv were applied. These profiles are shown in Figure 6.2-3. Two different approaches were used to prescribe the inlet dissipation rate. The first approach is based on the assumptions of constant length scale and turbulent kinetic energy, namely

$$\epsilon = k^{1.5}/0.20 D_j \quad (64)$$

where D_j is the jet diameter. The second approach, based on the assumption of local equilibrium ($P_k = \rho\epsilon$) for turbulence energy, can be written as

$$\epsilon = 0.3k \frac{\partial U}{\partial r} \quad (65)$$

At the axis of symmetry, the radial velocity, shear stresses, and radial gradients of other variables are set to zero. At the outlet, axial diffusion is neglected for all variables. Along the entrainment boundary, which was placed sufficiently far from the axis of symmetry, the quantity (rV) was assumed zero, and k and ϵ were assigned arbitrary low values yielding an eddy viscosity, $\mu_t = 10\mu$.

Table 6.2-I.
Unconfined single annular jet experimental flow conditions.

R_1	13.82 (mm)
R_2	18.35 (mm)
h	7.0 (mm)
U_0	6.9 (m/s)
Annular flow rate	0.0033 (Kg/s)

Table 6.2-II.
Single annular jet grid definition.

STREAMWISE COORDINATES OF THE GRID

I	DX	X	XU
1	0.000E+00	0.000E+00	0.000E+00
2	7.750E-04	7.750E-04	0.000E+00
3	1.625E-03	2.400E-03	1.550E-03
4	2.050E-03	4.450E-03	3.250E-03
5	2.500E-03	6.950E-03	5.650E-03
6	2.700E-03	9.650E-03	8.250E-03
7	2.938E-03	1.259E-02	1.105E-02
8	3.313E-03	1.590E-02	1.413E-02
9	3.888E-03	1.979E-02	1.768E-02
10	4.588E-03	2.438E-02	2.190E-02
11	5.250E-03	2.963E-02	2.685E-02
12	5.775E-03	3.540E-02	3.240E-02
13	6.238E-03	4.164E-02	3.840E-02
14	6.713E-03	4.835E-02	4.488E-02
15	7.063E-03	5.541E-02	5.183E-02
16	7.200E-03	6.261E-02	5.900E-02
17	7.250E-03	6.986E-02	6.623E-02
18	7.288E-03	7.715E-02	7.350E-02
19	7.300E-03	8.445E-02	8.080E-02
20	7.300E-03	9.175E-02	8.810E-02
21	7.288E-03	9.904E-02	9.540E-02
22	7.275E-03	1.063E-01	1.027E-01
23	7.288E-03	1.136E-01	1.100E-01
24	7.300E-03	1.209E-01	1.173E-01
25	7.300E-03	1.282E-01	1.246E-01
26	7.300E-03	1.355E-01	1.319E-01
27	7.300E-03	1.428E-01	1.392E-01
28	7.300E-03	1.501E-01	1.465E-01
29	7.300E-03	1.574E-01	1.538E-01
30	7.300E-03	1.647E-01	1.611E-01
31	7.300E-03	1.720E-01	1.684E-01
32	7.300E-03	1.793E-01	1.757E-01
33	7.300E-03	1.866E-01	1.830E-01
34	7.300E-03	1.939E-01	1.903E-01
35	7.300E-03	2.012E-01	1.976E-01
36	7.300E-03	2.085E-01	2.049E-01
37	7.300E-03	2.158E-01	2.122E-01
38	7.300E-03	2.231E-01	2.195E-01
39	7.200E-03	2.303E-01	2.268E-01
40	7.200E-03	2.375E-01	2.339E-01
41	7.400E-03	2.449E-01	2.412E-01
42	7.400E-03	2.523E-01	2.487E-01
43	7.325E-03	2.596E-01	2.560E-01
44	7.325E-03	2.670E-01	2.633E-01
45	7.275E-03	2.742E-01	2.706E-01
46	7.275E-03	2.815E-01	2.779E-01
47	7.300E-03	2.888E-01	2.852E-01

PART 1 OF 3
 TE92-1140

Table 6.2-II (cont).

48	7.450E-03	2.963E-01	2.925E-01
49	7.775E-03	3.040E-01	3.001E-01
50	7.975E-03	3.120E-01	3.080E-01
51	8.500E-03	3.205E-01	3.160E-01
52	9.500E-03	3.300E-01	3.250E-01
53	1.000E-02	3.400E-01	3.350E-01
54	1.000E-02	3.500E-01	3.450E-01
55	1.125E-02	3.613E-01	3.550E-01
56	1.375E-02	3.750E-01	3.675E-01
57	1.500E-02	3.900E-01	3.825E-01
58	1.500E-02	4.050E-01	3.975E-01
59	1.500E-02	4.200E-01	4.125E-01
60	1.500E-02	4.350E-01	4.275E-01
61	7.500E-03	4.425E-01	4.425E-01

TRANSVERS COORDINATES OF THE GRID

J	DY	Y	YV
1	0.000E+00	5.000E-04	0.000E+00
2	2.500E-04	7.500E-04	5.000E-04
3	7.500E-04	1.500E-03	1.000E-03
4	1.000E-03	2.500E-03	2.000E-03
5	1.000E-03	3.500E-03	3.000E-03
6	1.000E-03	4.500E-03	4.000E-03
7	1.000E-03	5.500E-03	5.000E-03
8	1.000E-03	6.500E-03	6.000E-03
9	1.000E-03	7.500E-03	7.000E-03
10	1.000E-03	8.500E-03	8.000E-03
11	1.000E-03	9.500E-03	9.000E-03
12	1.000E-03	1.050E-02	1.000E-02
13	1.000E-03	1.150E-02	1.100E-02
14	1.000E-03	1.250E-02	1.200E-02
15	7.500E-04	1.325E-02	1.300E-02
16	5.000E-04	1.375E-02	1.350E-02
17	5.000E-04	1.425E-02	1.400E-02
18	5.000E-04	1.475E-02	1.450E-02
19	5.000E-04	1.525E-02	1.500E-02
20	5.000E-04	1.575E-02	1.550E-02
21	5.000E-04	1.625E-02	1.600E-02
22	5.000E-04	1.675E-02	1.650E-02
23	5.000E-04	1.725E-02	1.700E-02
24	5.000E-04	1.775E-02	1.750E-02
25	5.000E-04	1.825E-02	1.800E-02
26	5.000E-04	1.875E-02	1.850E-02
27	5.000E-04	1.925E-02	1.900E-02
28	5.000E-04	1.975E-02	1.950E-02
29	7.500E-04	2.050E-02	2.000E-02
30	1.000E-03	2.150E-02	2.100E-02
31	1.000E-03	2.250E-02	2.200E-02

PART 2 OF 3
TE92-1140

Table 6.2-II (cont).

32	1.000E-03	2.350E-02	2.300E-02
33	1.000E-03	2.450E-02	2.400E-02
34	1.000E-03	2.550E-02	2.500E-02
35	1.000E-03	2.650E-02	2.600E-02
36	1.000E-03	2.750E-02	2.700E-02
37	1.000E-03	2.850E-02	2.800E-02
38	1.000E-03	2.950E-02	2.900E-02
39	1.500E-03	3.100E-02	3.000E-02
40	2.000E-03	3.300E-02	3.200E-02
41	2.500E-03	3.550E-02	3.400E-02
42	3.000E-03	3.850E-02	3.700E-02
43	3.000E-03	4.150E-02	4.000E-02
44	3.000E-03	4.450E-02	4.300E-02
45	3.500E-03	4.800E-02	4.600E-02
46	4.000E-03	5.200E-02	5.000E-02
47	4.500E-03	5.650E-02	5.400E-02
48	5.000E-03	6.150E-02	5.900E-02
49	5.000E-03	6.650E-02	6.400E-02
50	5.000E-03	7.150E-02	6.900E-02
51	5.000E-03	7.650E-02	7.400E-02
52	5.000E-03	8.150E-02	7.900E-02
53	5.000E-03	8.650E-02	8.400E-02
54	5.000E-03	9.150E-02	8.900E-02
55	5.000E-03	9.650E-02	9.400E-02
56	5.500E-03	1.020E-01	9.900E-02
57	5.500E-03	1.075E-01	1.050E-01
58	5.000E-03	1.125E-01	1.100E-01
59	5.000E-03	1.175E-01	1.150E-01
60	5.000E-03	1.225E-01	1.200E-01
61	5.000E-03	1.275E-01	1.250E-01
62	5.000E-03	1.325E-01	1.300E-01
63	5.000E-03	1.375E-01	1.350E-01
64	5.000E-03	1.425E-01	1.400E-01
65	5.000E-03	1.475E-01	1.450E-01
66	5.000E-03	1.525E-01	1.500E-01
67	5.000E-03	1.575E-01	1.550E-01
68	5.000E-03	1.625E-01	1.600E-01
69	5.000E-03	1.675E-01	1.650E-01
70	2.500E-03	1.700E-01	1.700E-01

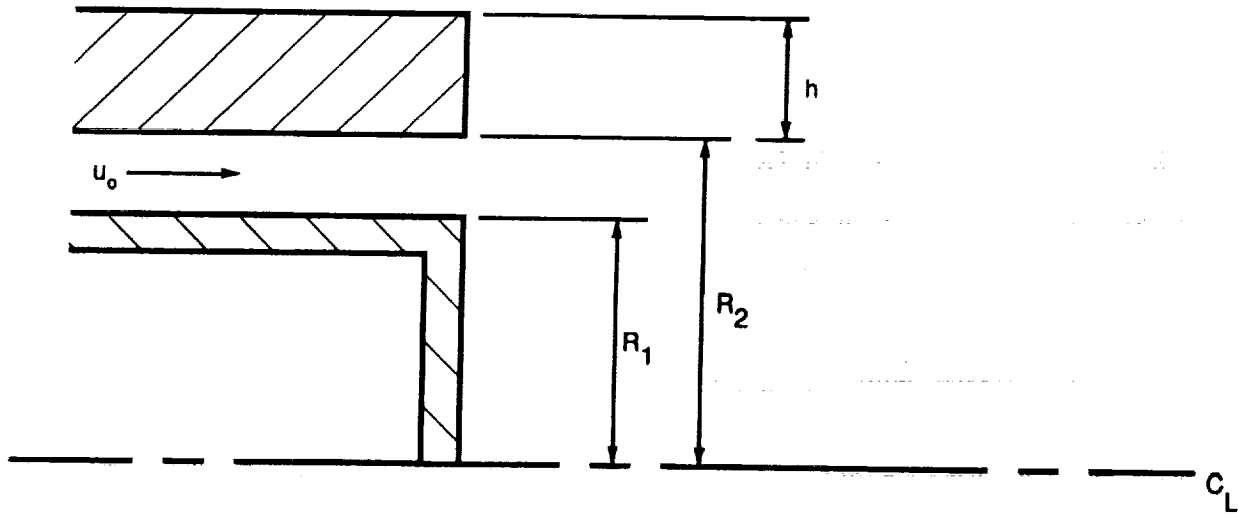
PART 3 OF 3
TE92-1140

In an attempt to assess the importance of inlet turbulence dissipation rate (ϵ_{in}) on mean velocity and stress fields predictions, two different approaches were followed to determine ϵ_{in} (Equations 64 and 65). Comparisons of the calculated mean axial velocity profiles by DSM with the experimental data are illustrated in Figure 6.2-4. The results show differences in the prediction of peak and centerline values in the developing region. The inlet ϵ profile calculated, based on equilibrium assumption (Equation 65), resulted in a closer prediction with data near the inlet plane. Further downstream, the differences between the model and data become more severe. In developing flow region, the experiment shows that the momentum is being transferred towards the centerline, increasing the centerline velocity. However, the model did not simulate this process adequately. As a result, the velocity was underpredicted in the inner region, however, the DSM performed reasonably in the outer region. At downstream ($x > 150$ mm), the calculated velocity field is in good agreement with measurement, although some minor discrepancies appear near the centerline.

Comparisons of the predicted turbulence intensities from the DSM closure are shown in Figures 6.2-5, 6.2-6, 6.2-7, and 6.2-8. When the inlet ϵ distribution is calculated with the constant length scale assumption,

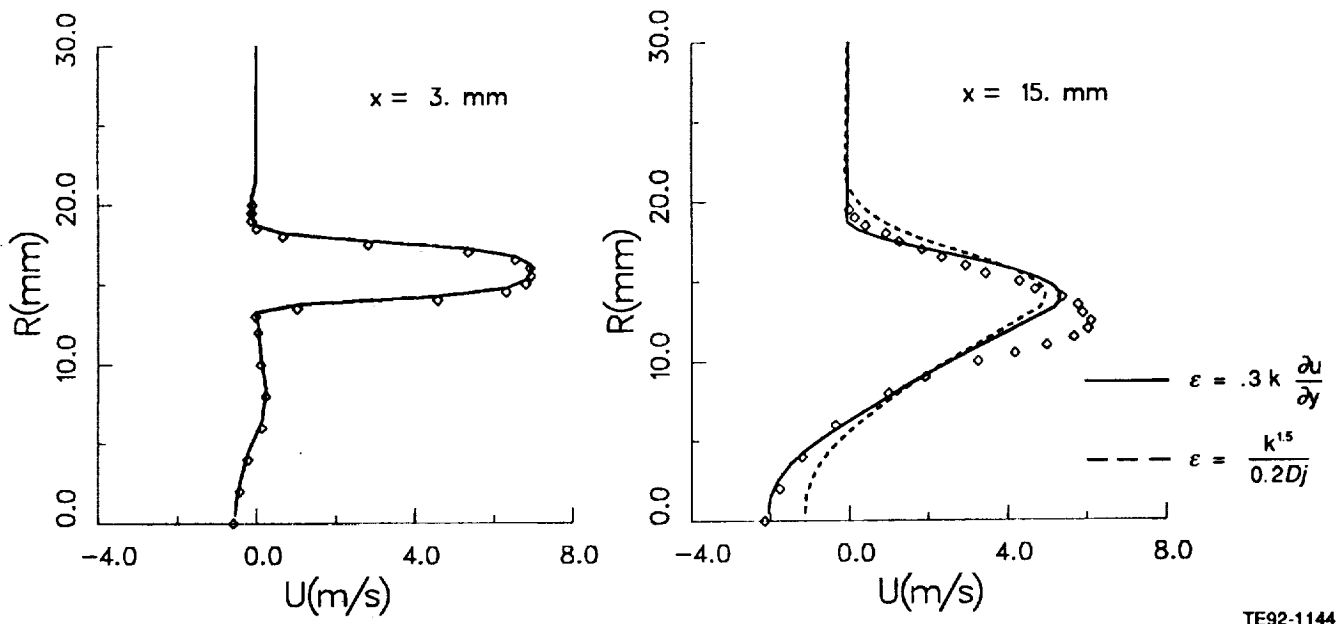
the profiles are closer to the exhibited data trend. A wide disparity exists between this calculation and the calculation with ϵ_{in} obtained from Equation 65. The model indicates a faster mixing in the inner region than is shown by experiment. Numerical study indicates that the inlet ϵ profile is a very important factor in predicting the maximum values of mean and turbulence quantities. The turbulent normal stresses are decreased due to an excessive dissipation rate at the inlet. Comparisons of radial and tangential Reynolds stress components reveal that essentially the same trends are observed for v^2 and w^2 profiles. The effects of the ϵ_{in} on the shear stress profiles are found to be serious near the inlet region where the central recirculation is formed (Figure 6.2-8). In comparison with the data, the calculated values are not in good agreement in the developing flow region. A wide disparity exists between the calculations. The ϵ_{in} derived from constant length scale assumption resulted in more realistic profiles. However, the locations of the maxima and minima have been shifted in the developing region of the flow field.

The predicted mean axial velocity profiles from the k- ϵ model are compared with data in Figure 6.2-9. These results were also obtained using the two different inlet dissipation rate profiles. Similar behavior is also observed here. The major differences between the two calculations appeared in the region where maximum velocity occurs. Both methods are unable to predict the flow in the center region accurately. But the discrepancies are removed as flow proceeds towards the downstream region. Figure 6.2-10 shows the kinetic energy profiles at various axial locations. Again, the behavior of two sets of computations is in closer agreement to each other than to measurement. Most of the differences are seen in the peak and centerline regions. The agreement between the predicted and experimental values of kinetic energy is not as good as that for the axial velocity. Even though to some extent the trends are similar, the predicted kinetic energy levels are smaller than those derived from the measurements. For the ease of comparison, the predicted mean axial velocity and turbulent shear stress profiles from the DSM and k- ϵ models have been compared in Figures 6.2-11 through 6.2-14. Depending on the shape of ϵ_{in} distribution, the discrepancies between the DSM and k- ϵ model predictions can be severe or minor. This clearly demonstrates the importance of inlet profiles, particularly the dissipation rate for turbulence model validation (Sturgess et al, 1983).



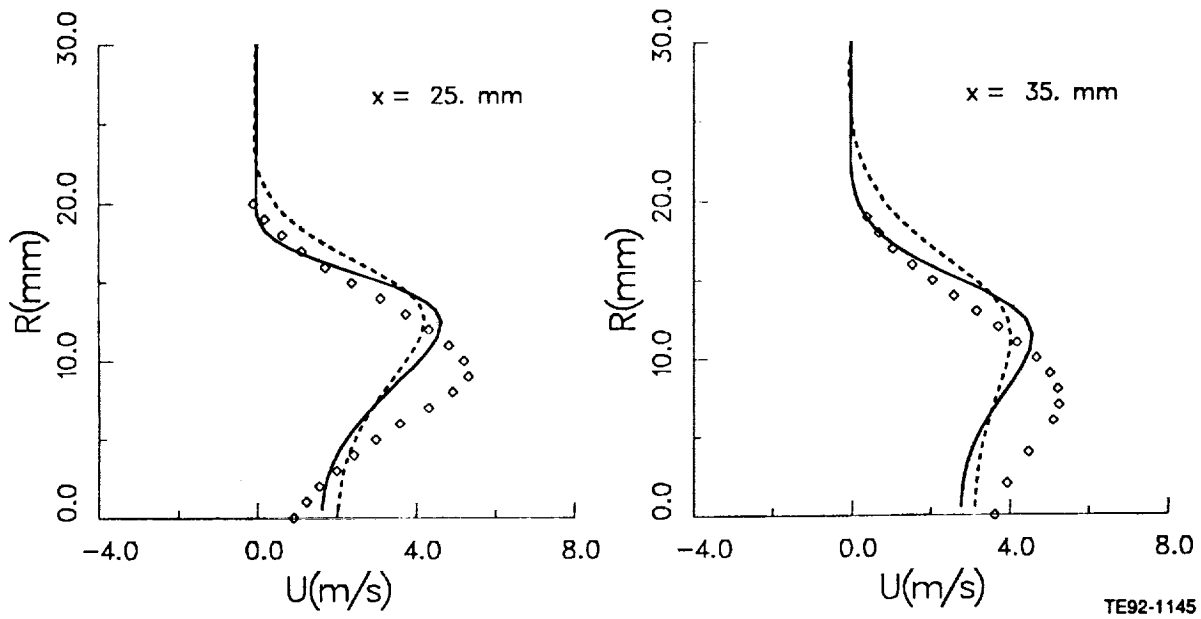
TE92-1141-4

Figure 6.2-1. Unconfined annular flow configuration.



TE92-1144

Figure 6.2-4. Comparison of predicted mean axial velocity by DSM with data (1 of 4).



TE92-1145

Figure 6.2-4. Comparison of predicted mean axial velocity by DSM with data (2 of 4).

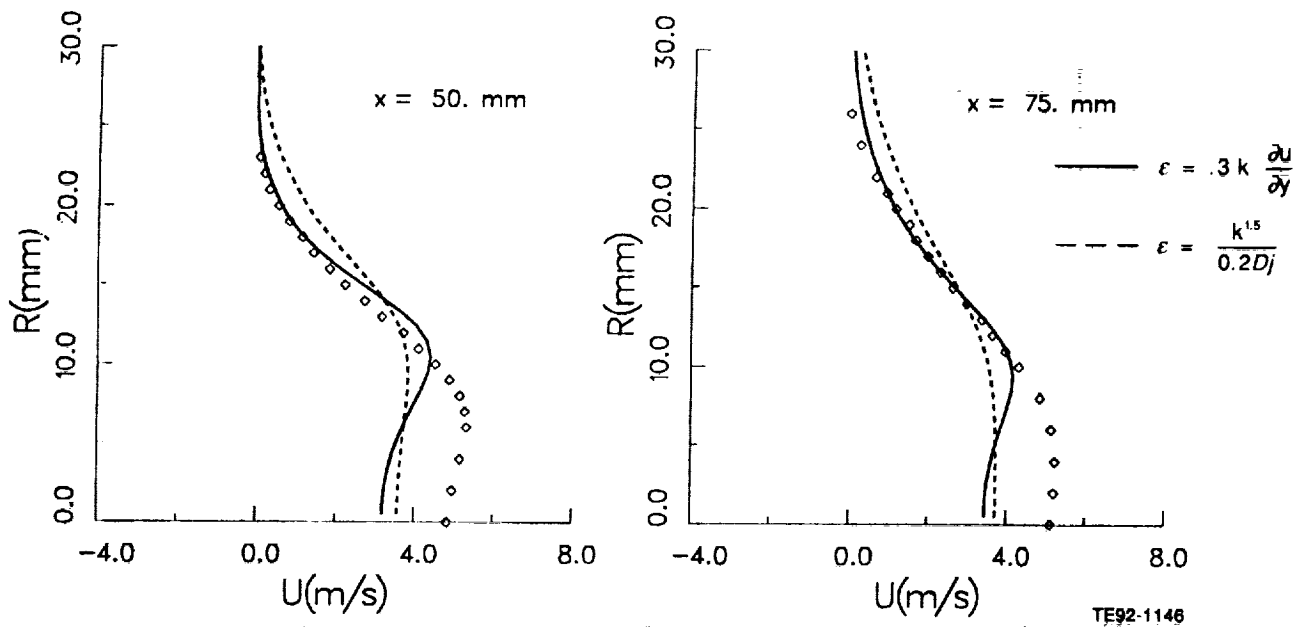


Figure 6.2-4. Comparison of predicted mean axial velocity by DSM with data (3 of 4).

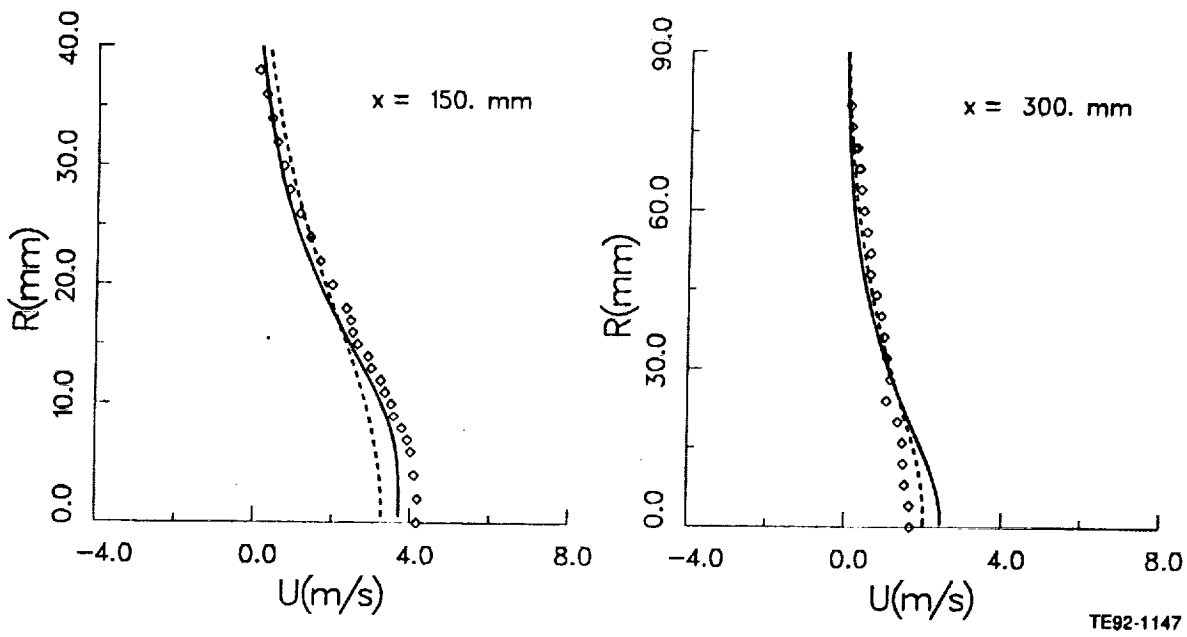


Figure 6.2-4. Comparison of predicted mean axial velocity by DSM with data (4 of 4).

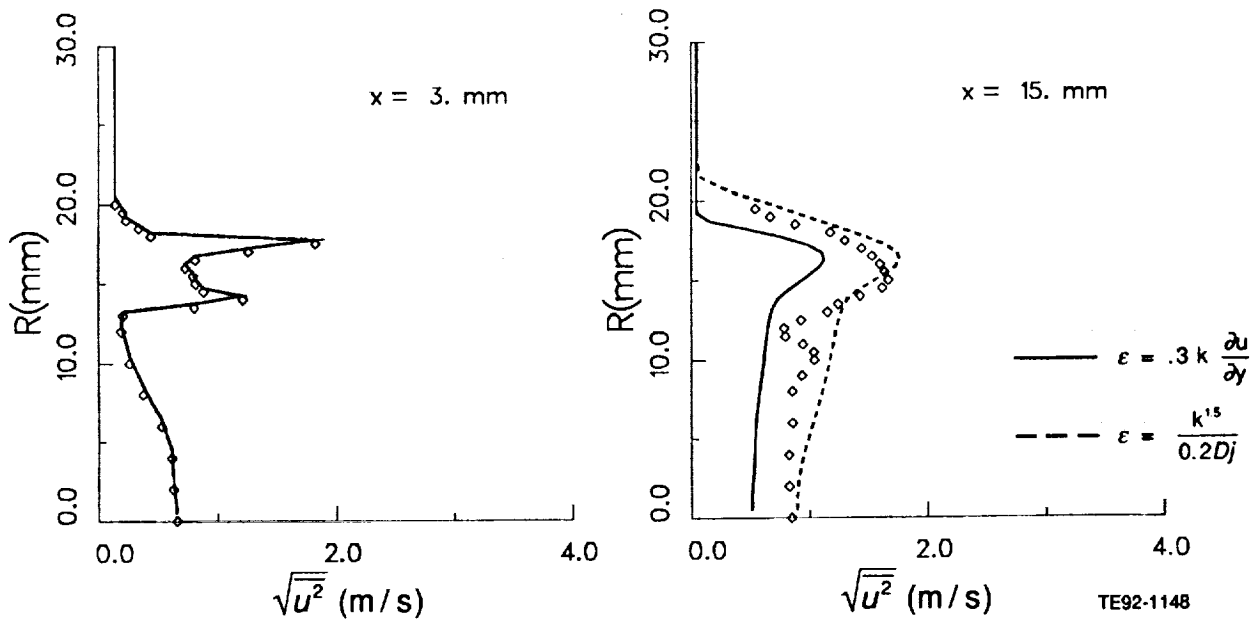


Figure 6.2-5. Comparison of calculated rms axial velocity profiles by DSM with data (1 of 4).

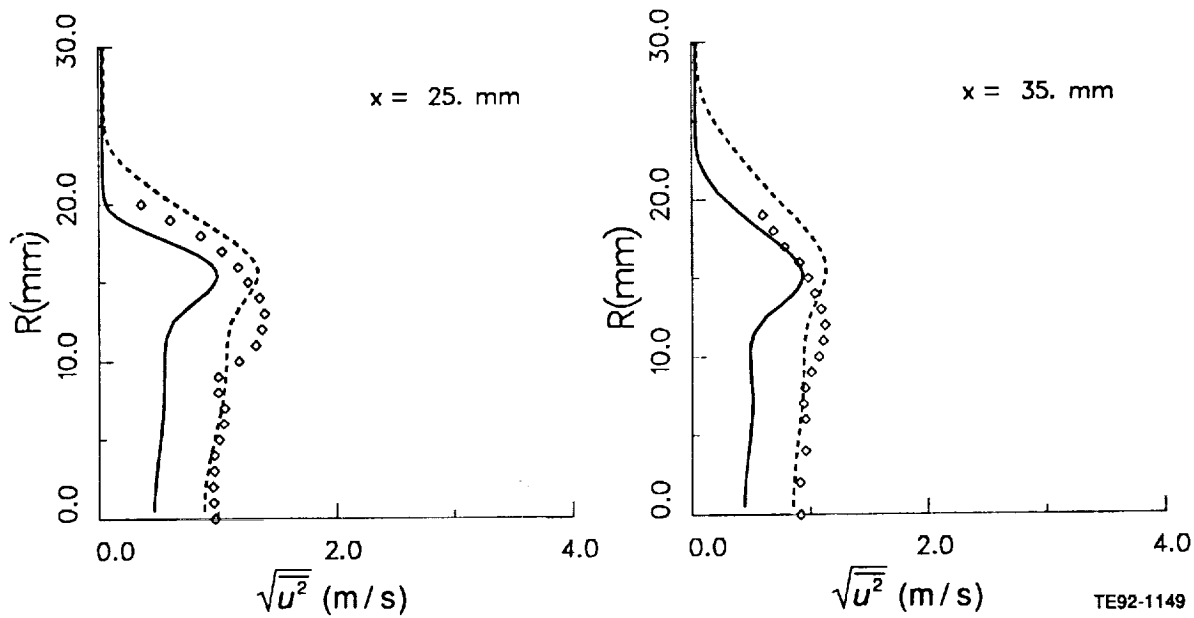


Figure 6.2-5. Comparison of calculated rms axial velocity profiles by DSM with data (2 of 4).

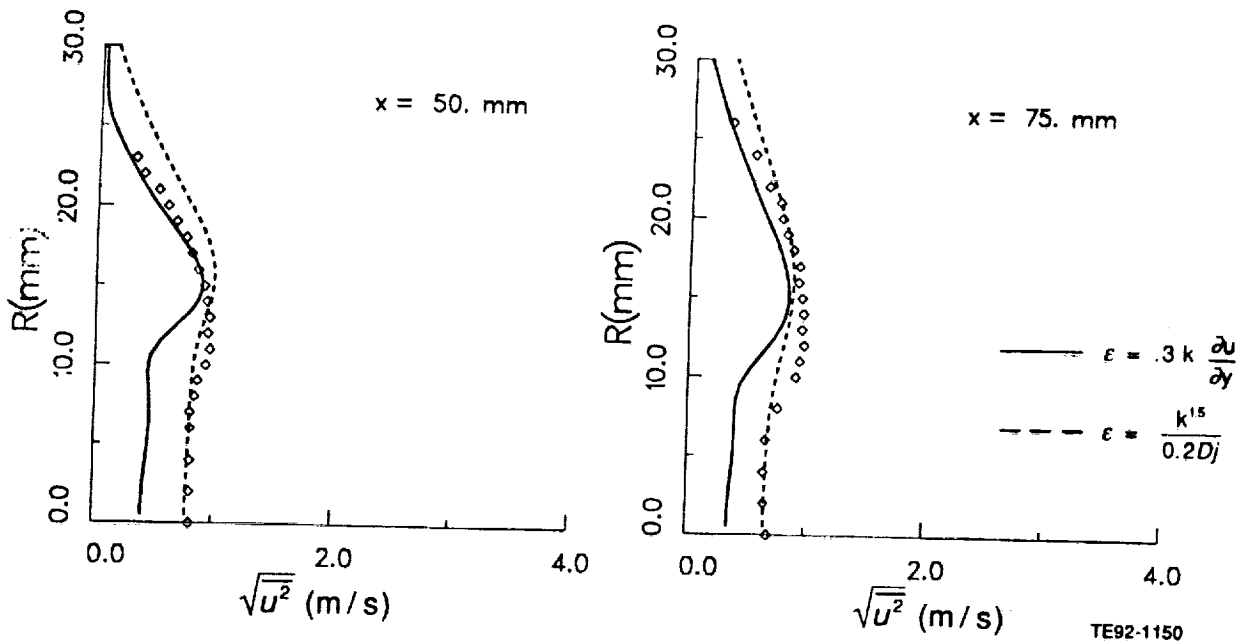


Figure 6.2-5. Comparison of calculated rms axial velocity profiles by DSM with data (3 of 4).

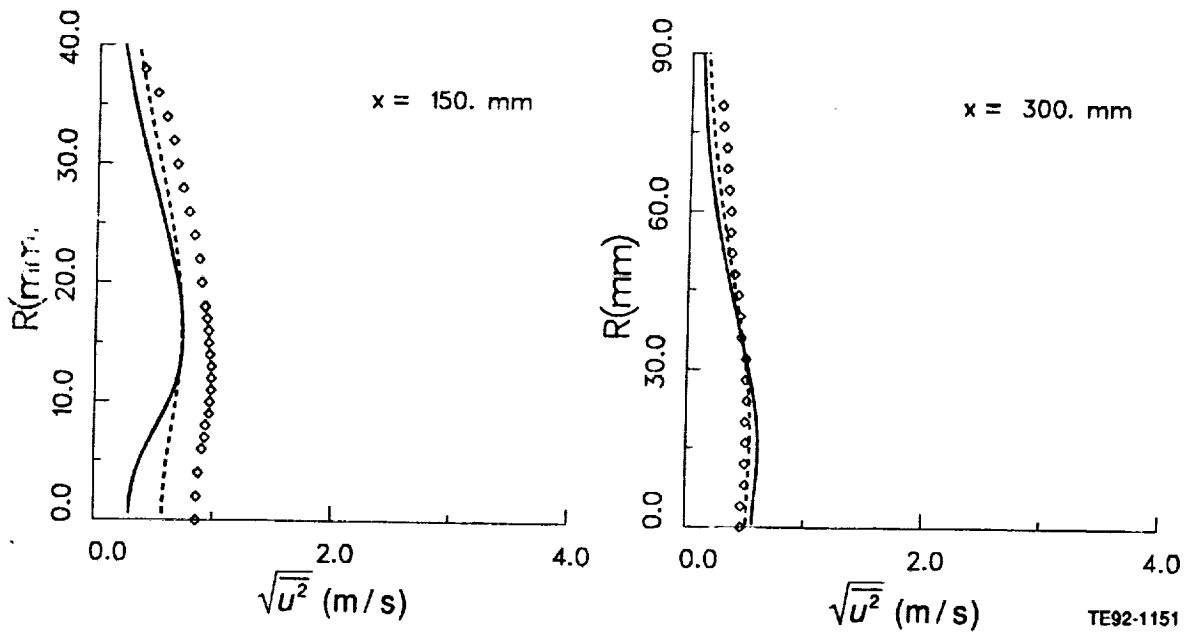


Figure 6.2-5. Comparison of calculated rms axial velocity profiles by DSM with data (4 of 4).

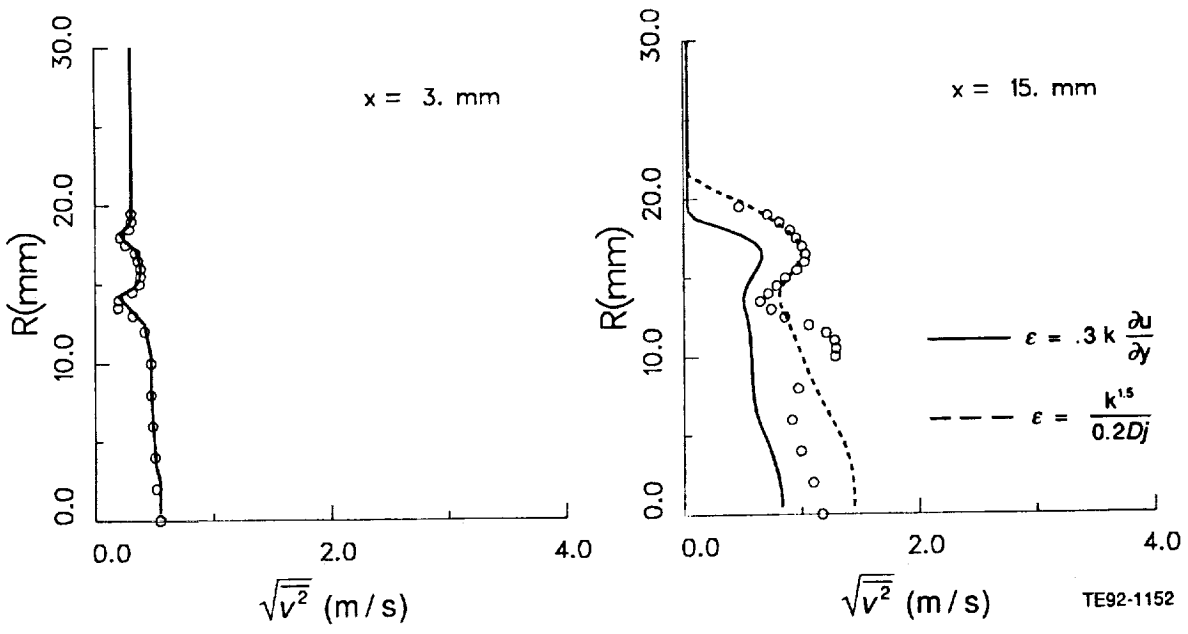


Figure 6.2-6. Comparison of calculated rms radial velocity profiles by DSM with data (1 of 4).

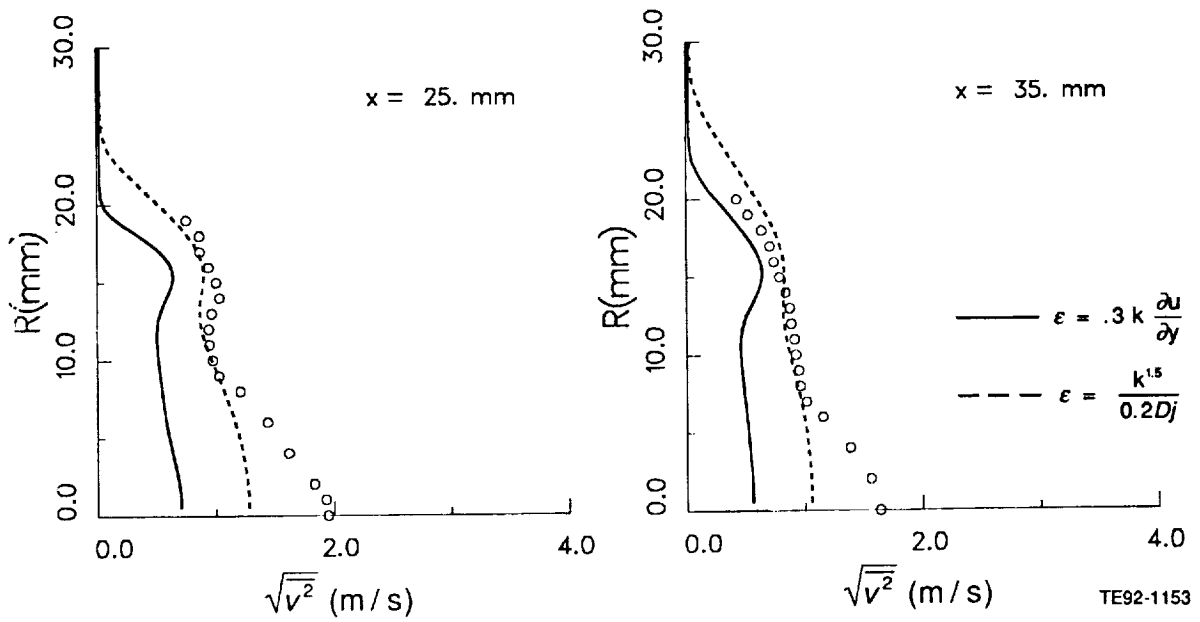


Figure 6.2-6. Comparison of calculated rms radial velocity profiles by DSM with data (2 of 4).

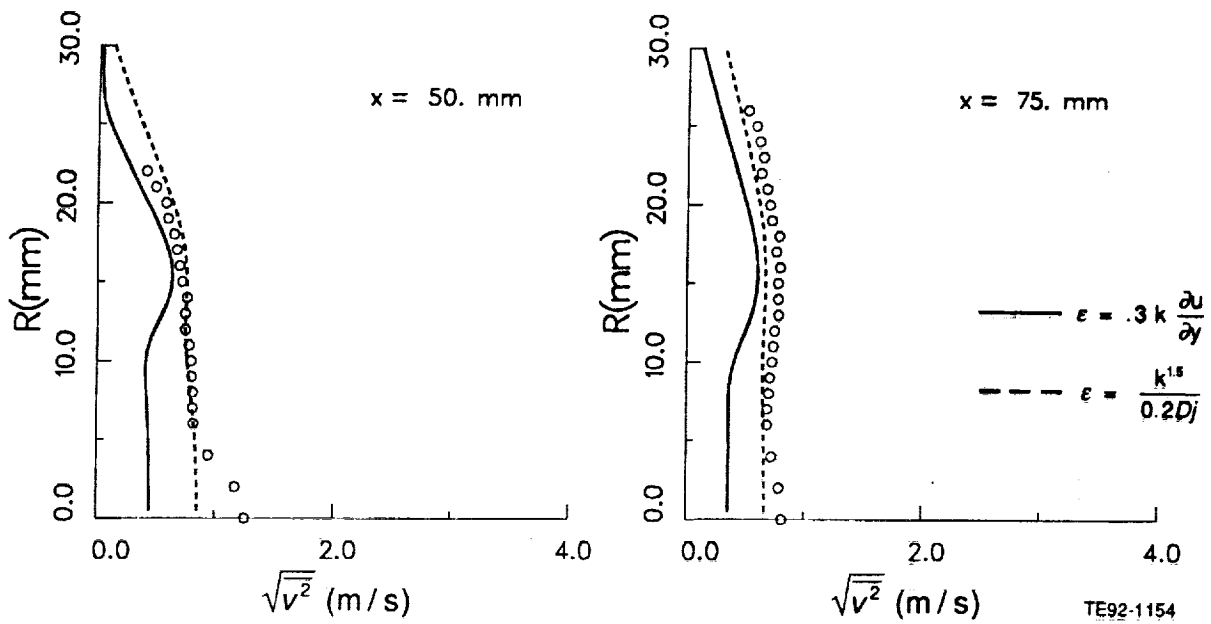


Figure 6.2-6. Comparison of calculated rms radial velocity profiles by DSM with data (3 of 4).

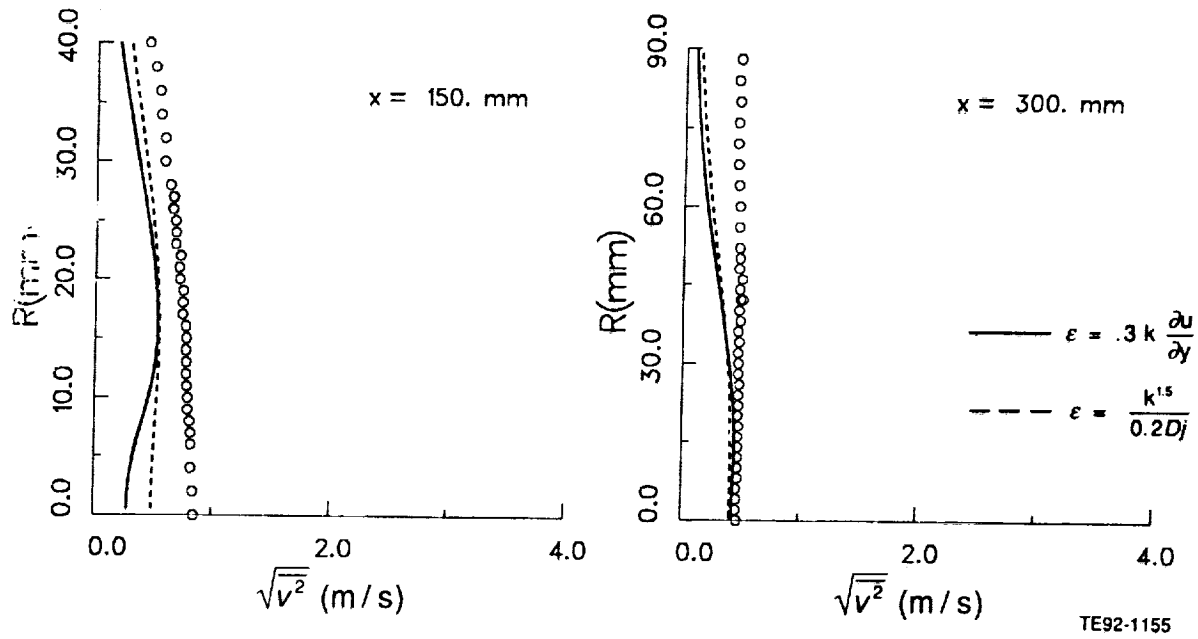


Figure 6.2-6. Comparison of calculated rms radial velocity profiles by DSM with data (4 of 4).

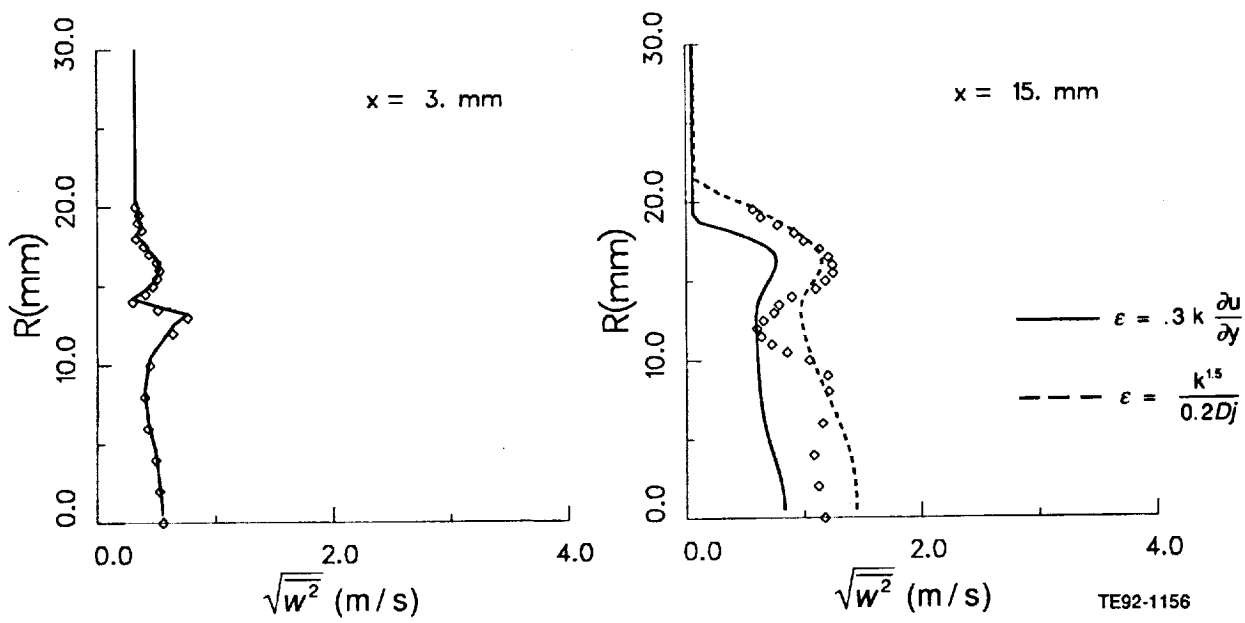


Figure 6.2-7. Comparison of calculated rms tangential velocity profiles by DSM with data (1 of 4).

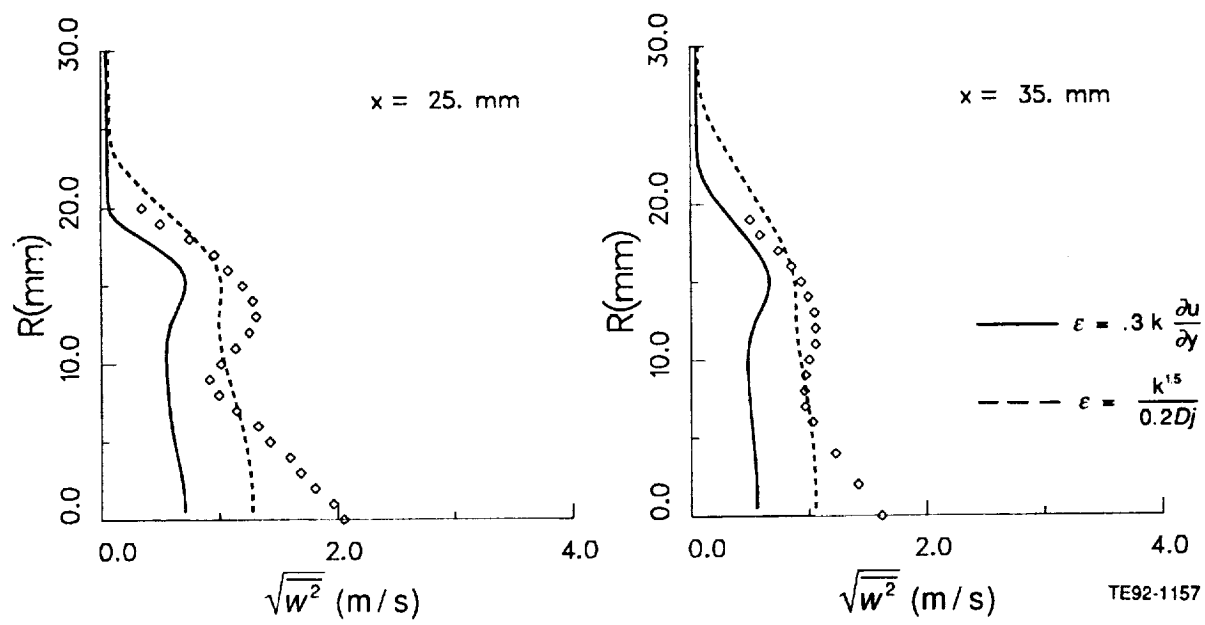


Figure 6.2-7. Comparison of calculated rms tangential velocity profiles by DSM with data (2 of 4).

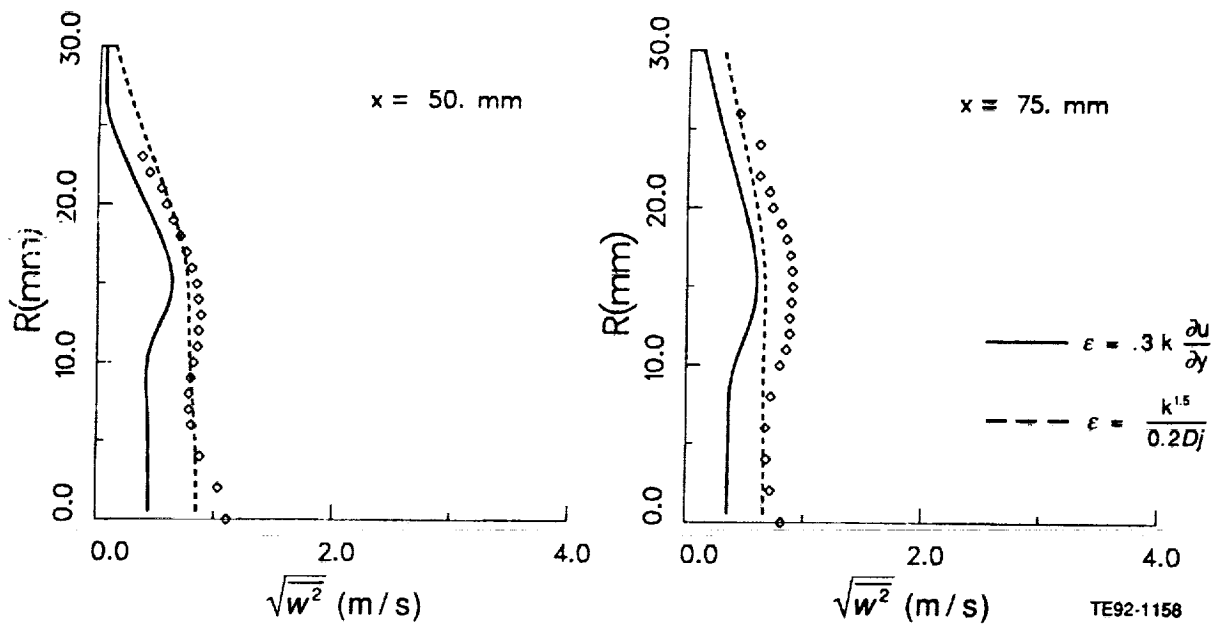


Figure 6.2-7. Comparison of calculated rms tangential velocity profiles by DSM with data (3 of 4).

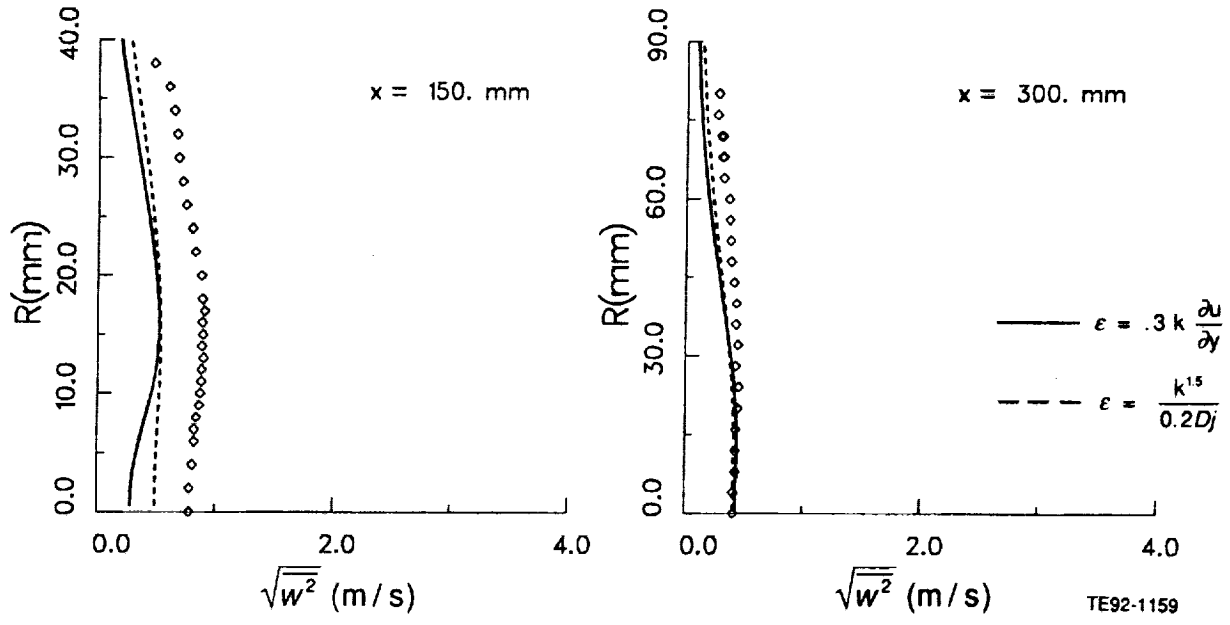


Figure 6.2-7. Comparison of calculated rms tangential velocity profiles by DSM with data (4 of 4).

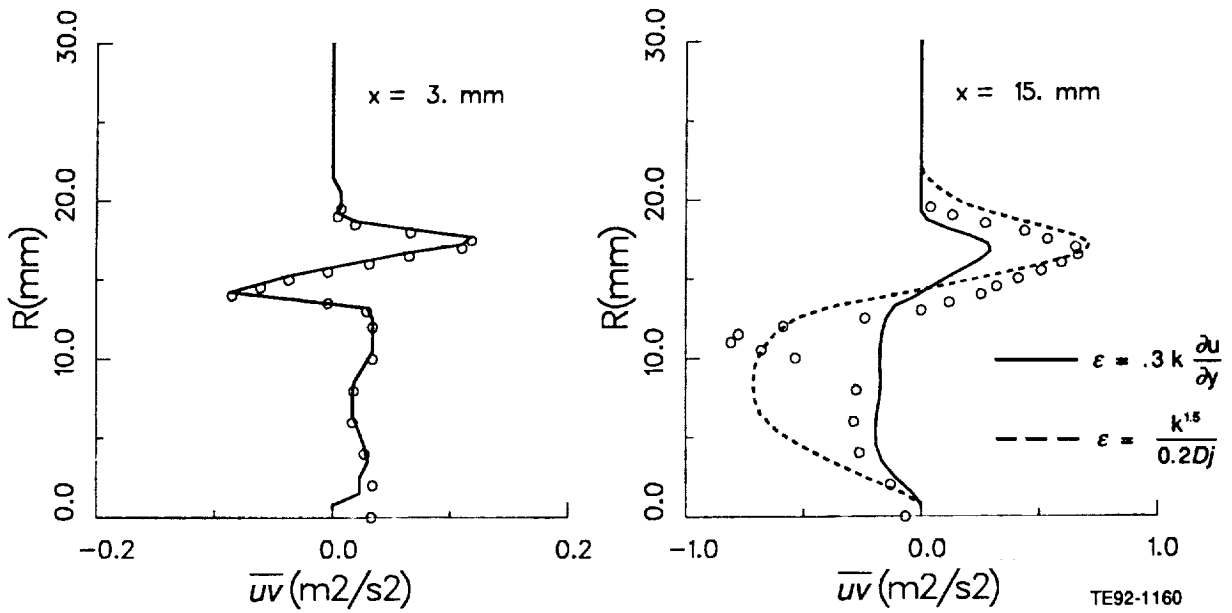


Figure 6.2-8. Comparison of calculated turbulent shear stress profiles by DSM with data (1 of 4).

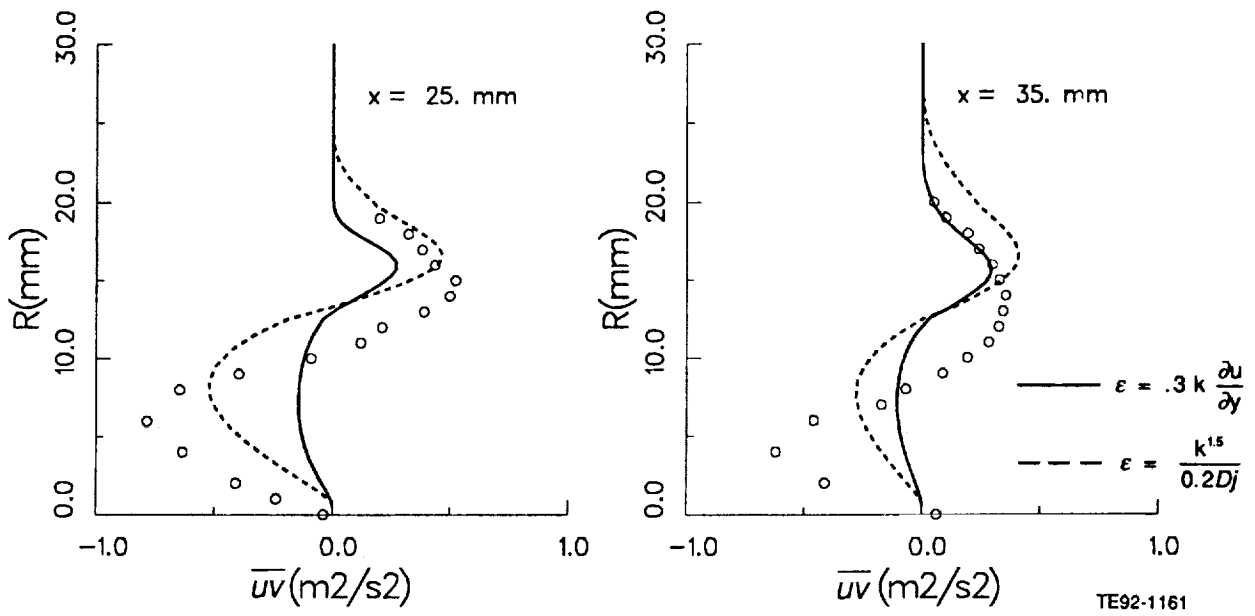


Figure 6.2-8. Comparison of calculated turbulent shear stress profiles by DSM with data (2 of 4).

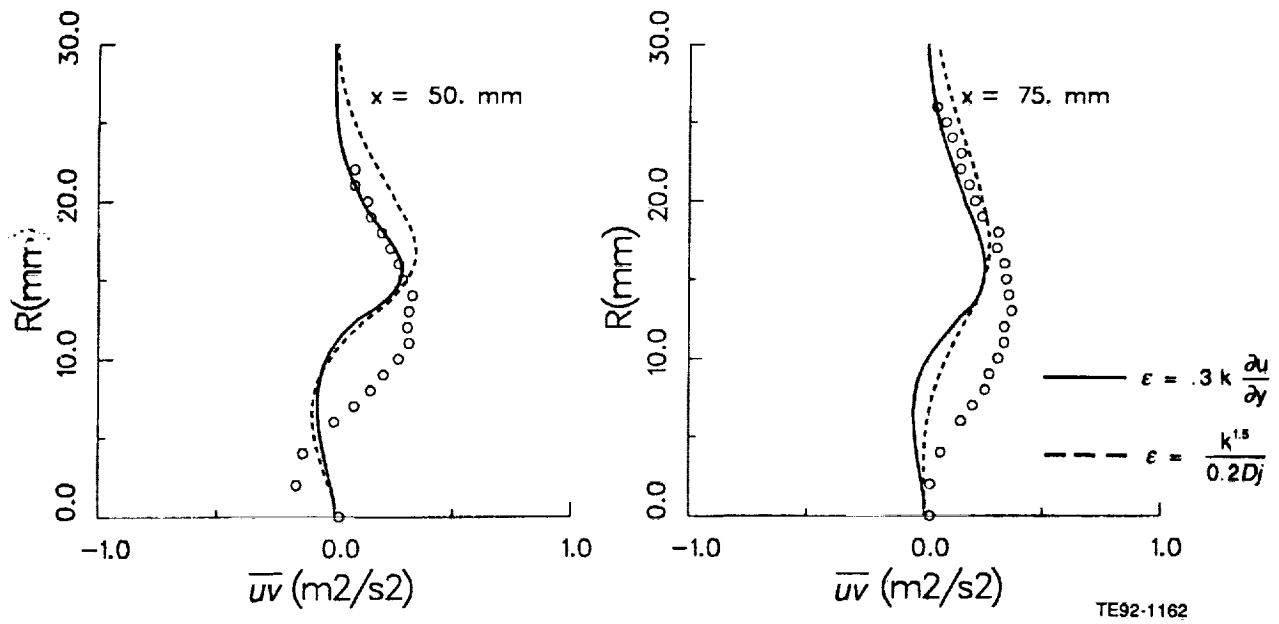


Figure 6.2-8. Comparison of calculated turbulent shear stress profiles by DSM with data (3 of 4).

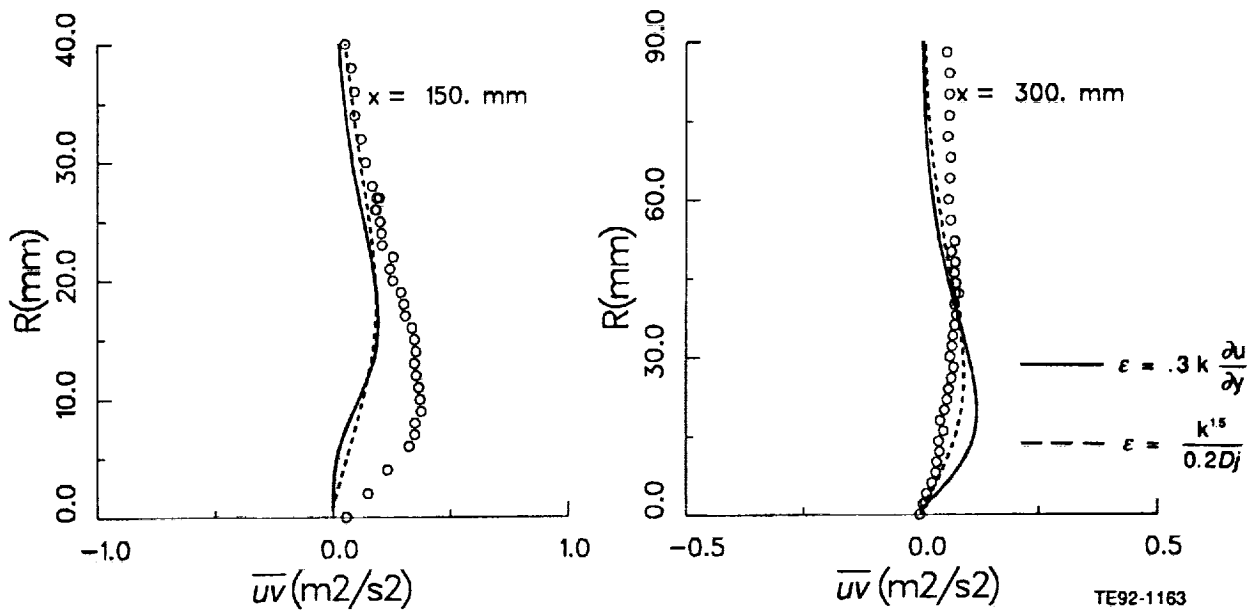


Figure 6.2-8. Comparison of calculated turbulent shear stress profiles by DSM with data (4 of 4).

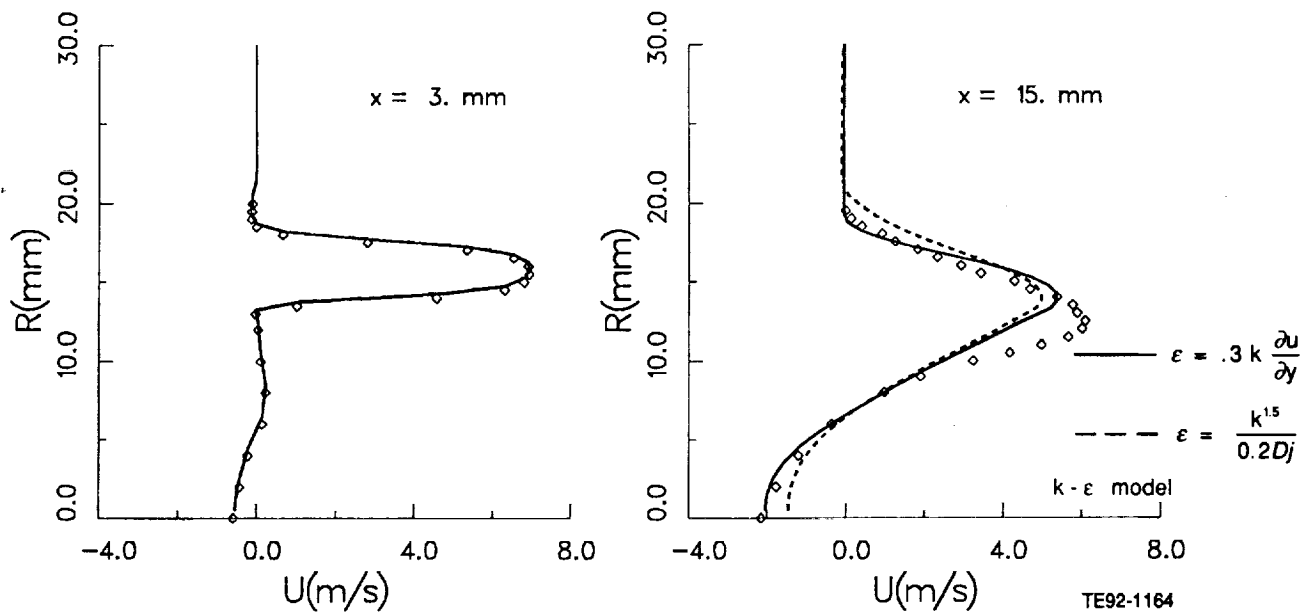


Figure 6.2-9. Comparison of predicted mean axial velocity by $k-\epsilon$ model with data (1 of 4).

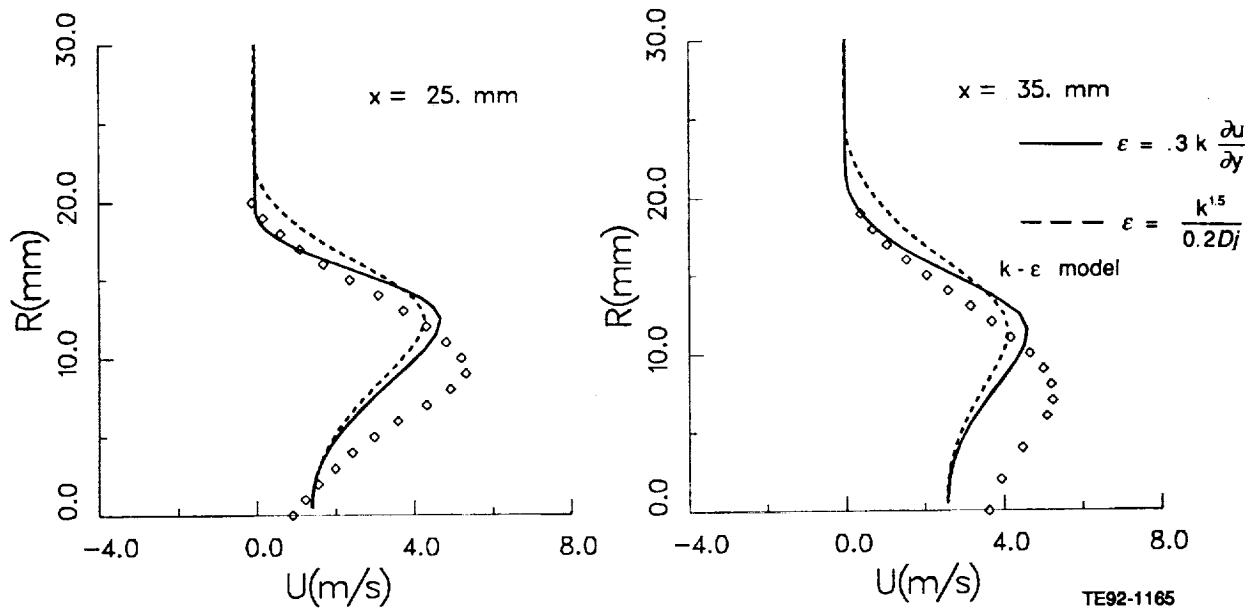


Figure 6.2-9. Comparison of predicted mean axial velocity by $k-\epsilon$ model with data (2 of 4).

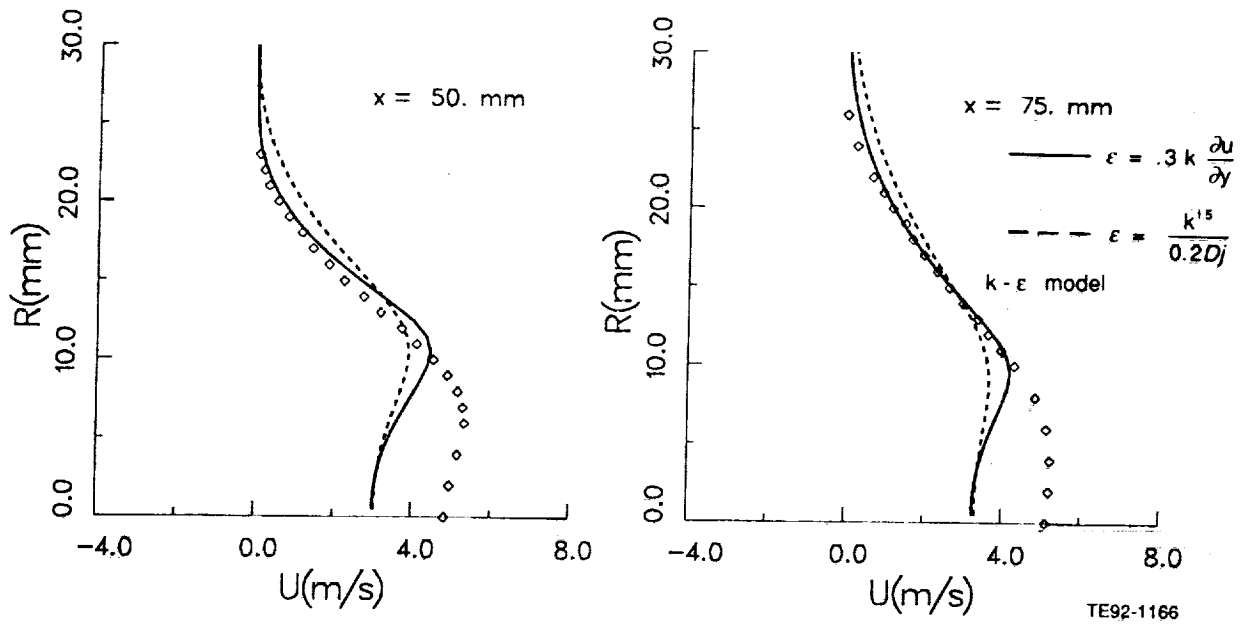


Figure 6.2-9. Comparison of predicted mean axial velocity by $k-\epsilon$ model with data (3 of 4).

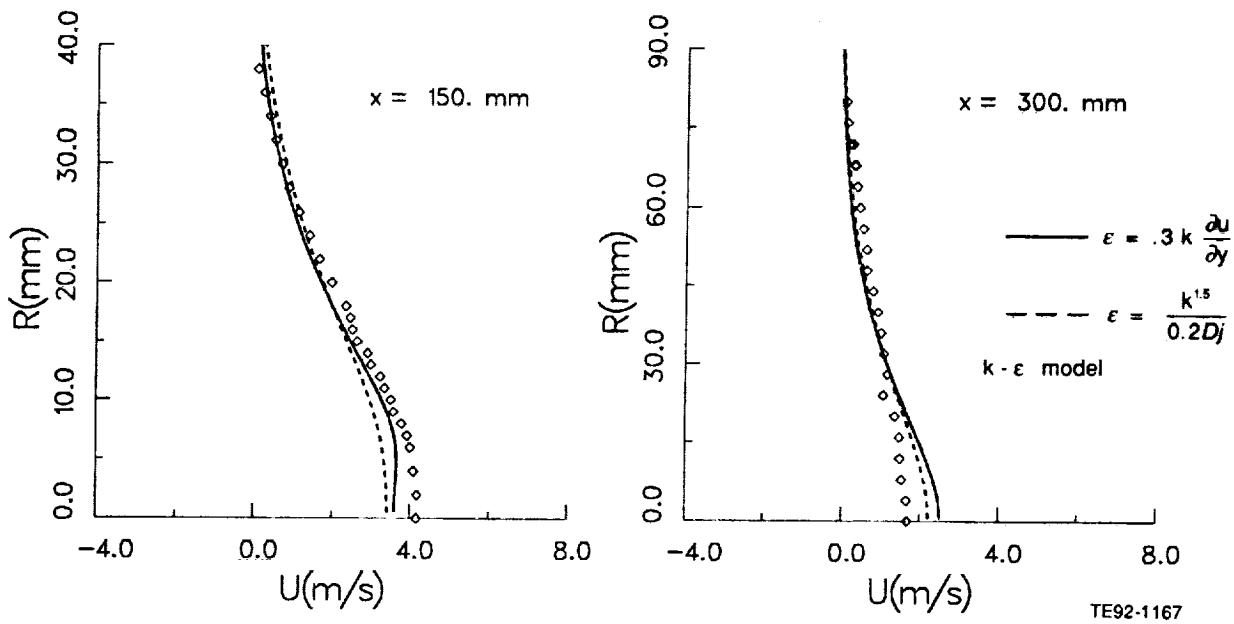


Figure 6.2-9. Comparison of predicted mean axial velocity by $k-\epsilon$ model with data (4 of 4).

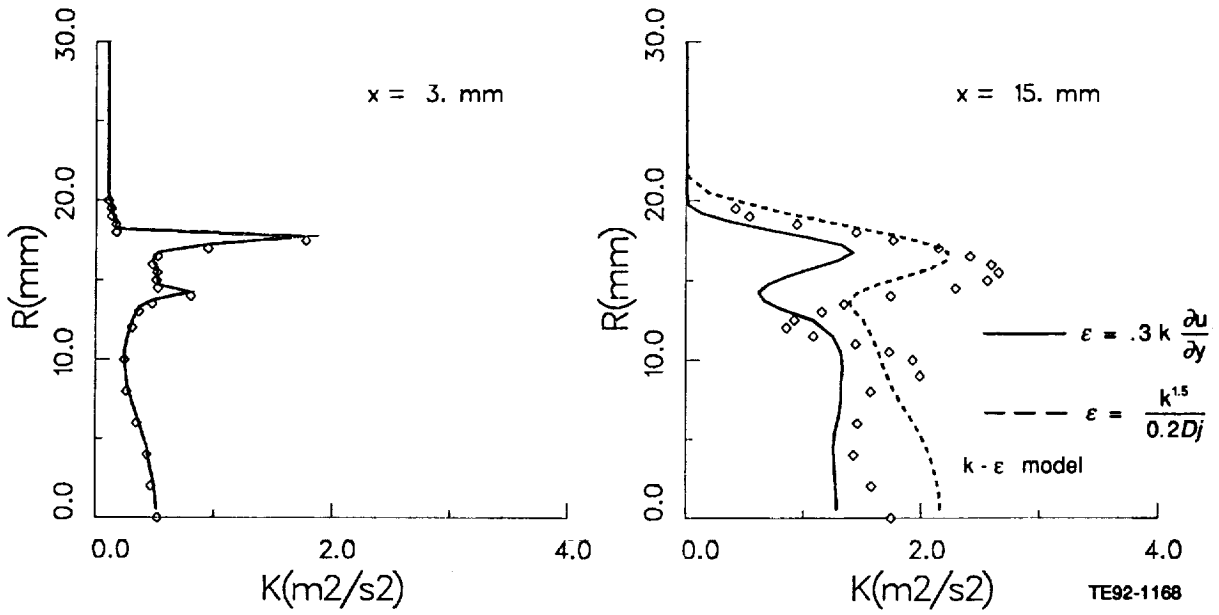


Figure 6.2-10. Comparison of predicted turbulent kinetic energy by k- ϵ model with data (1 of 4).

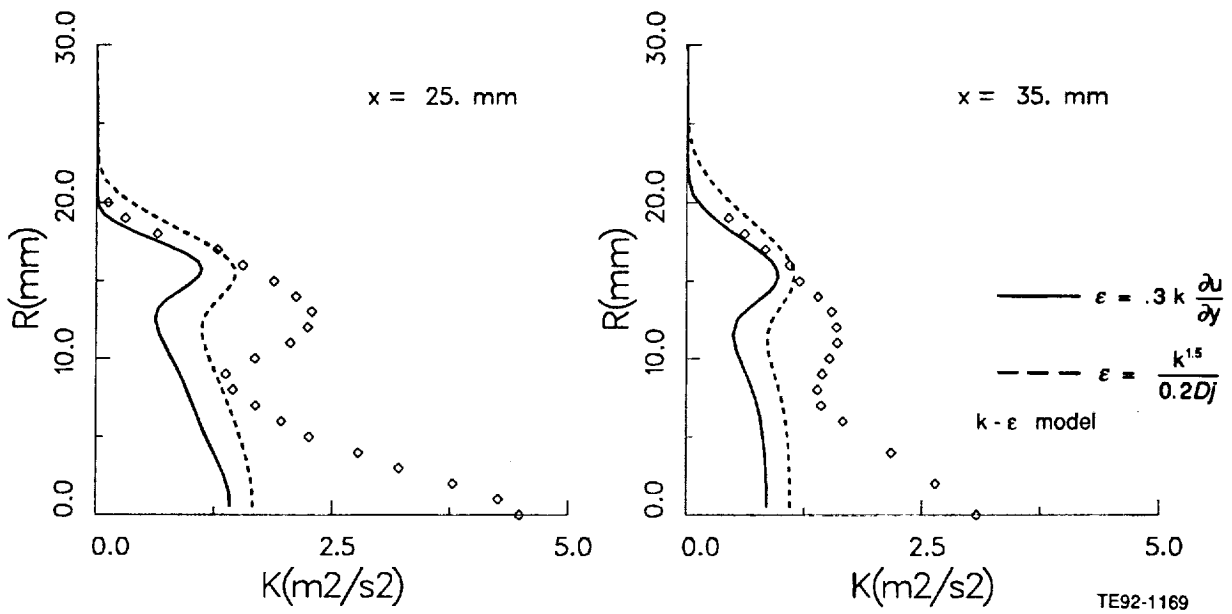


Figure 6.2-10. Comparison of predicted turbulent kinetic energy by k- ϵ model with data (2 of 4).

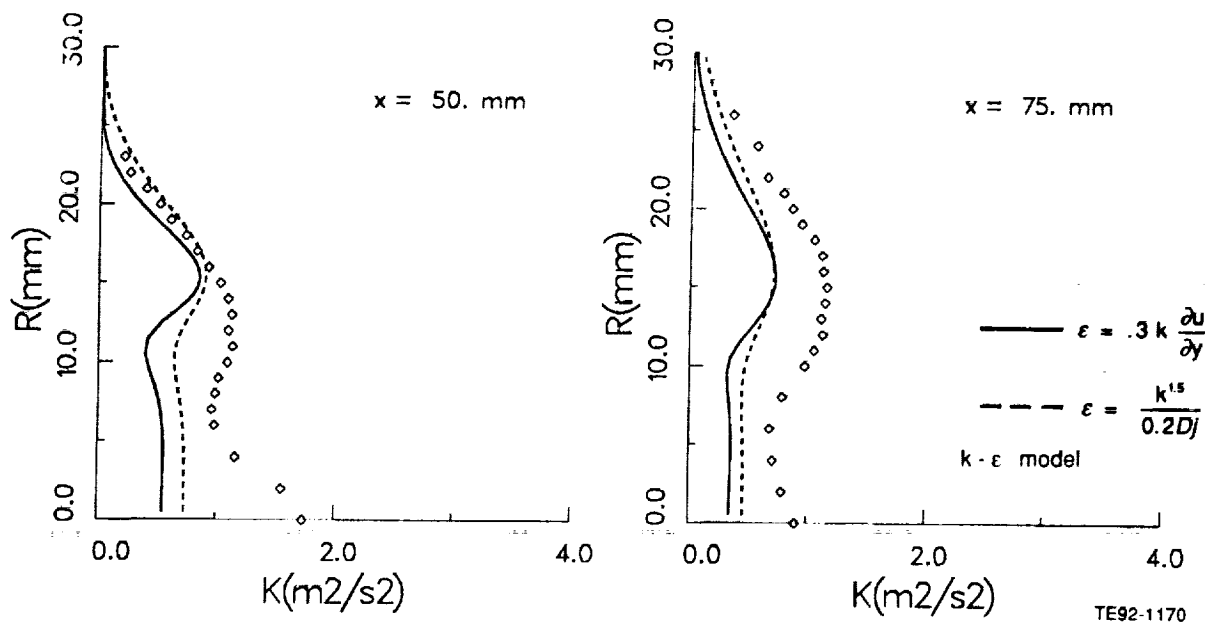


Figure 6.2-10. Comparison of predicted turbulent kinetic energy by k- ϵ model with data (3 of 4).

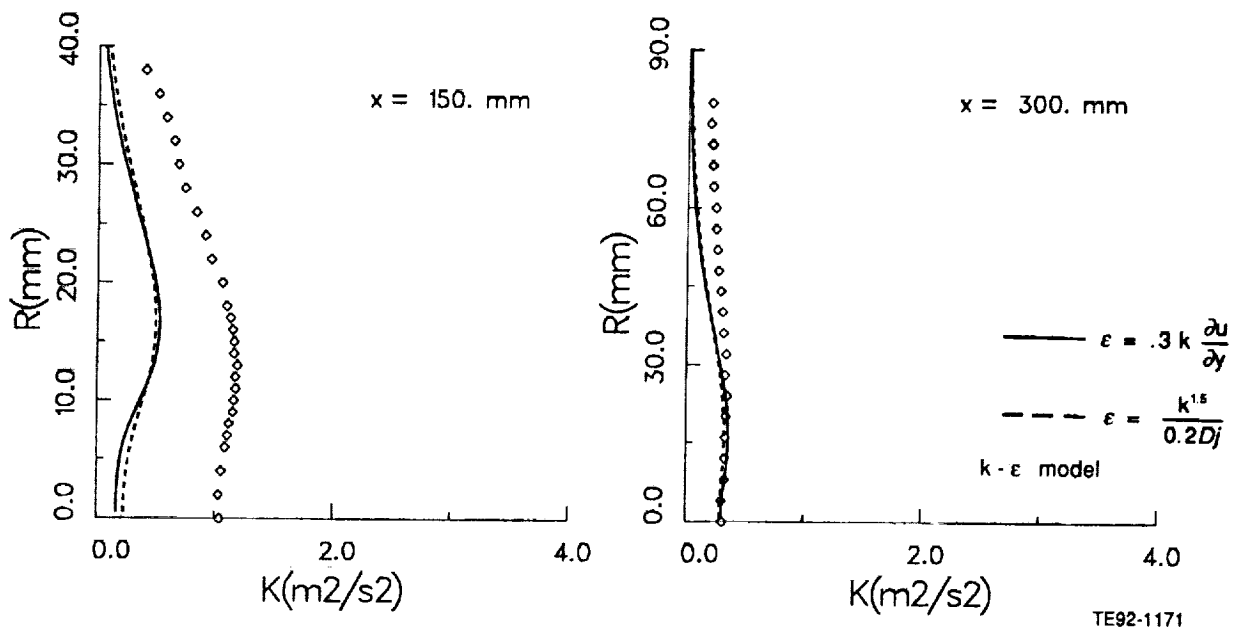


Figure 6.2-10. Comparison of predicted turbulent kinetic energy by k- ϵ model with data (4 of 4).

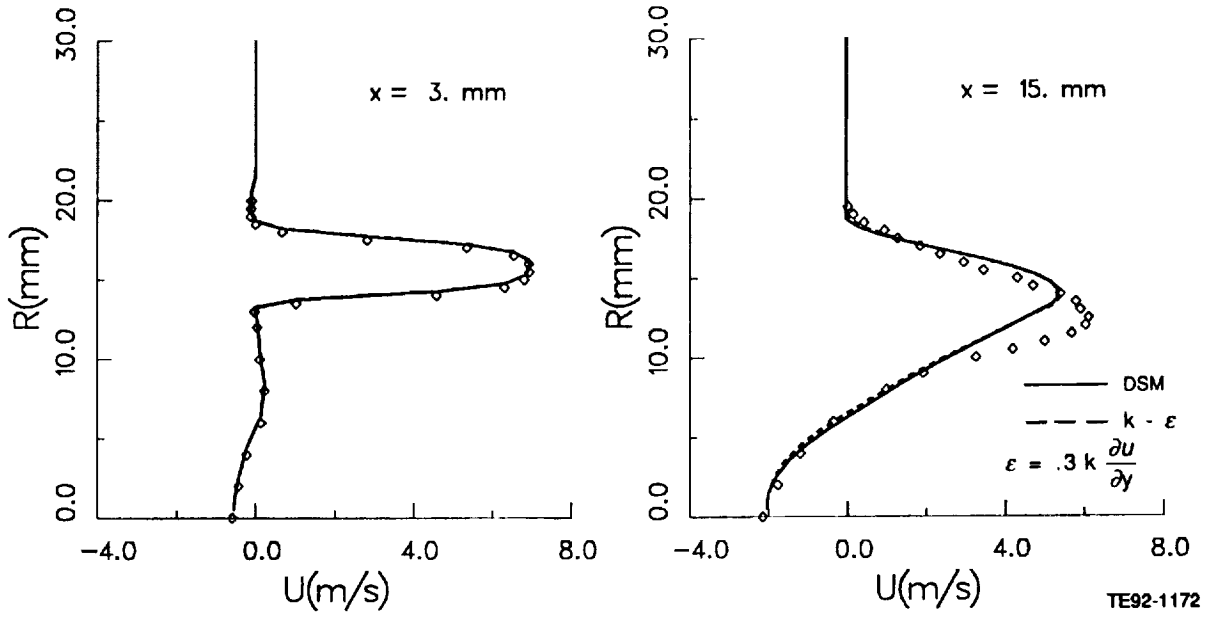


Figure 6.2-11. Comparison of calculated U velocity by k-ε and DSM with data (1 of 4).

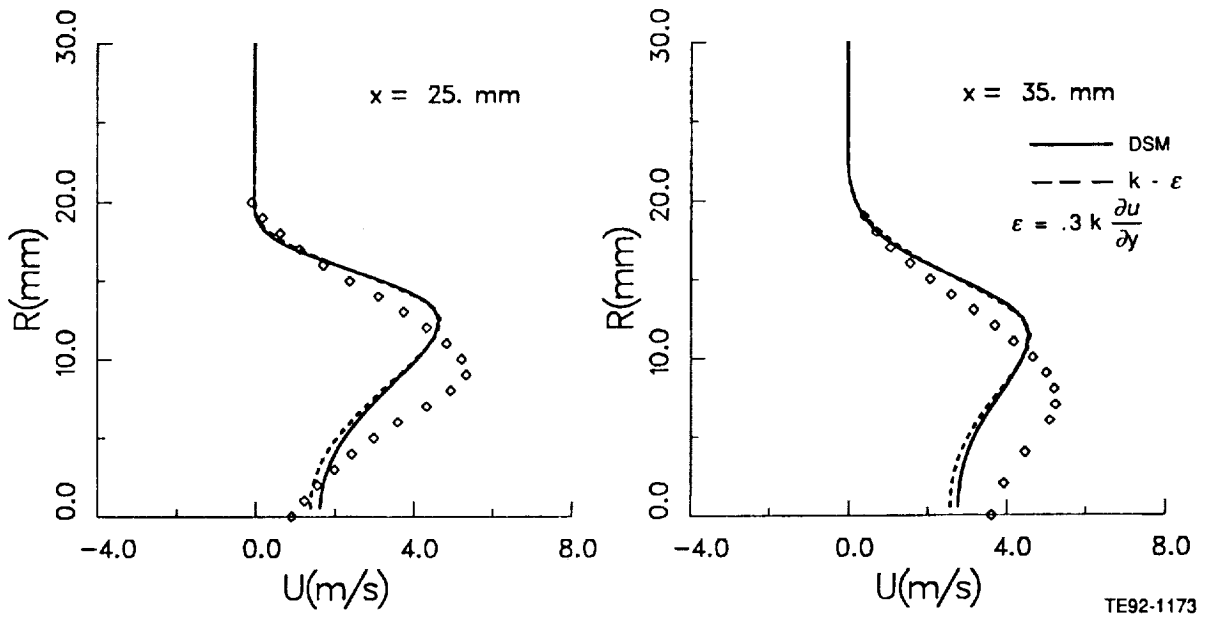


Figure 6.2-11. Comparison of calculated U velocity by k-ε and DSM with data (2 of 4).

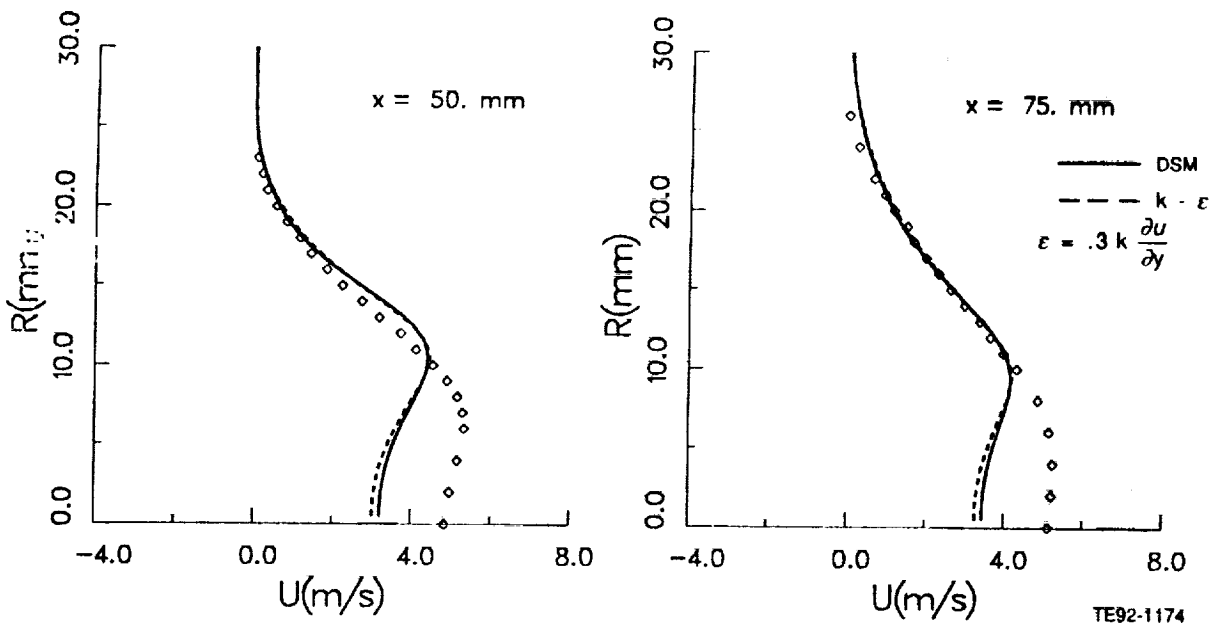


Figure 6.2-11. Comparison of calculated U velocity by k- ϵ and DSM with data (3 of 4).

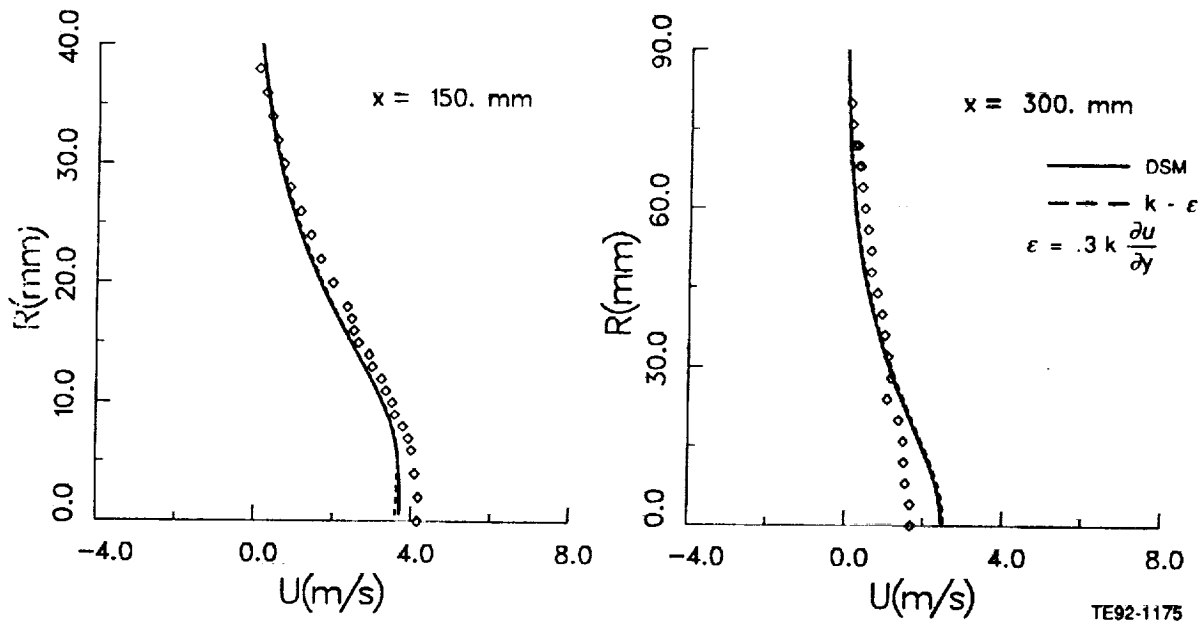


Figure 6.2-11. Comparison of calculated U velocity by k- ϵ and DSM with data (4 of 4).

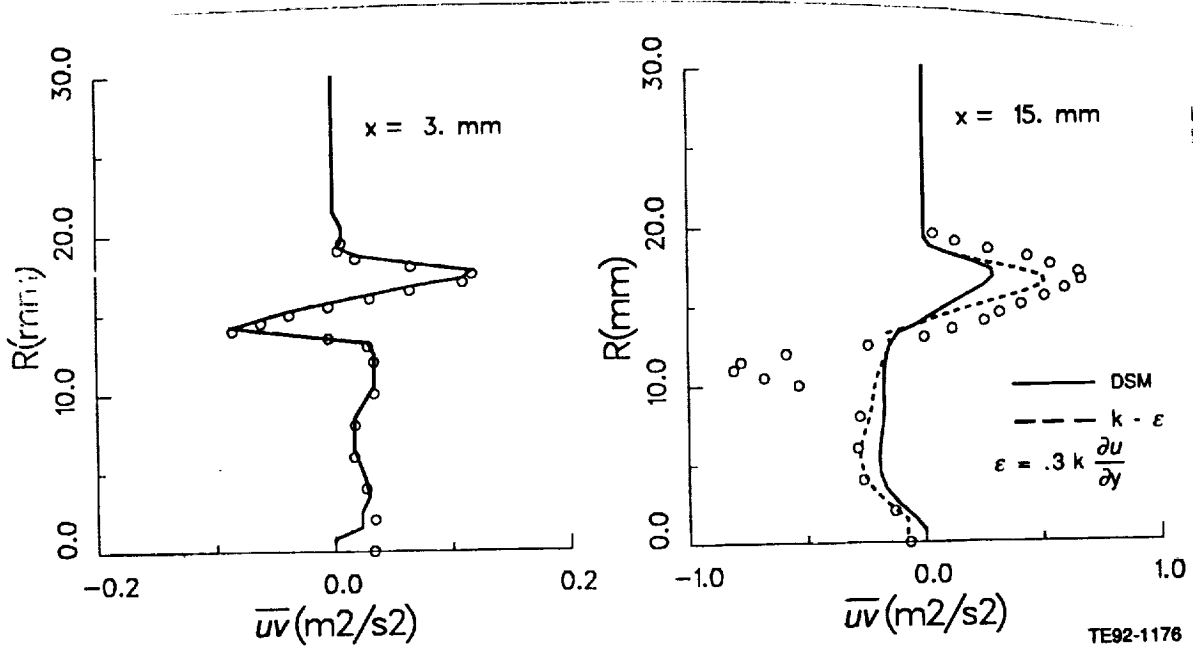


Figure 6.2-12. Comparison of calculated \overline{uv} profiles by $k-\epsilon$ and DSM with data (1 of 4).

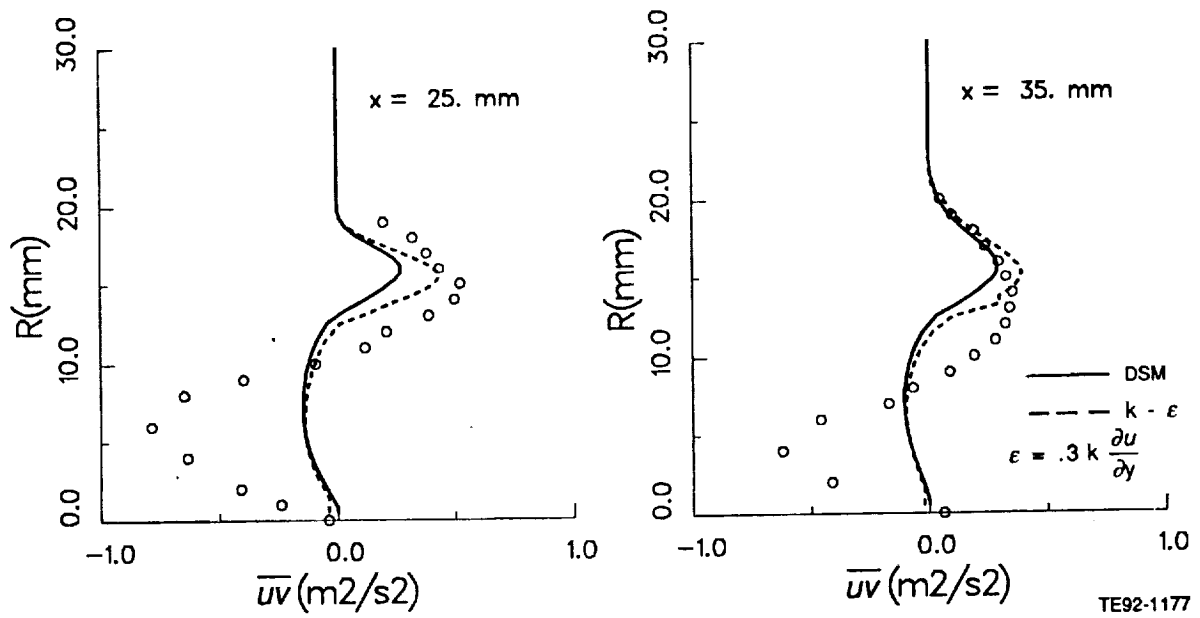


Figure 6.2-12. Comparison of calculated \overline{uv} profiles by $k-\epsilon$ and DSM with data (2 of 4).

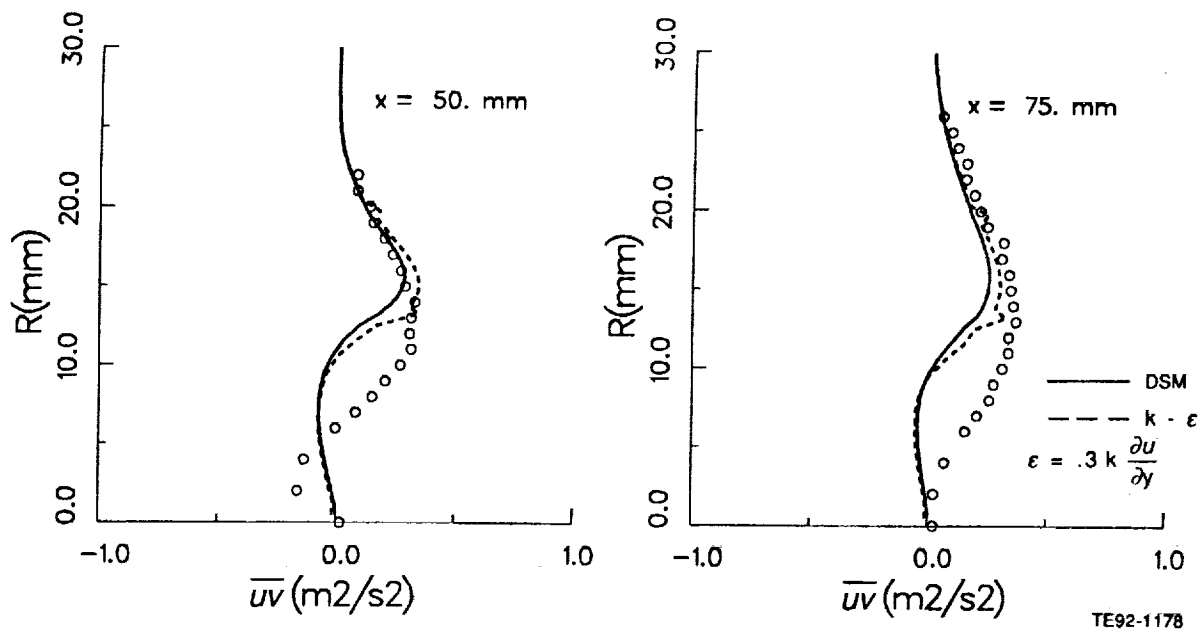


Figure 6.2-12. Comparison of calculated \overline{uv} profiles by $k-\epsilon$ and DSM with data (3 of 4).

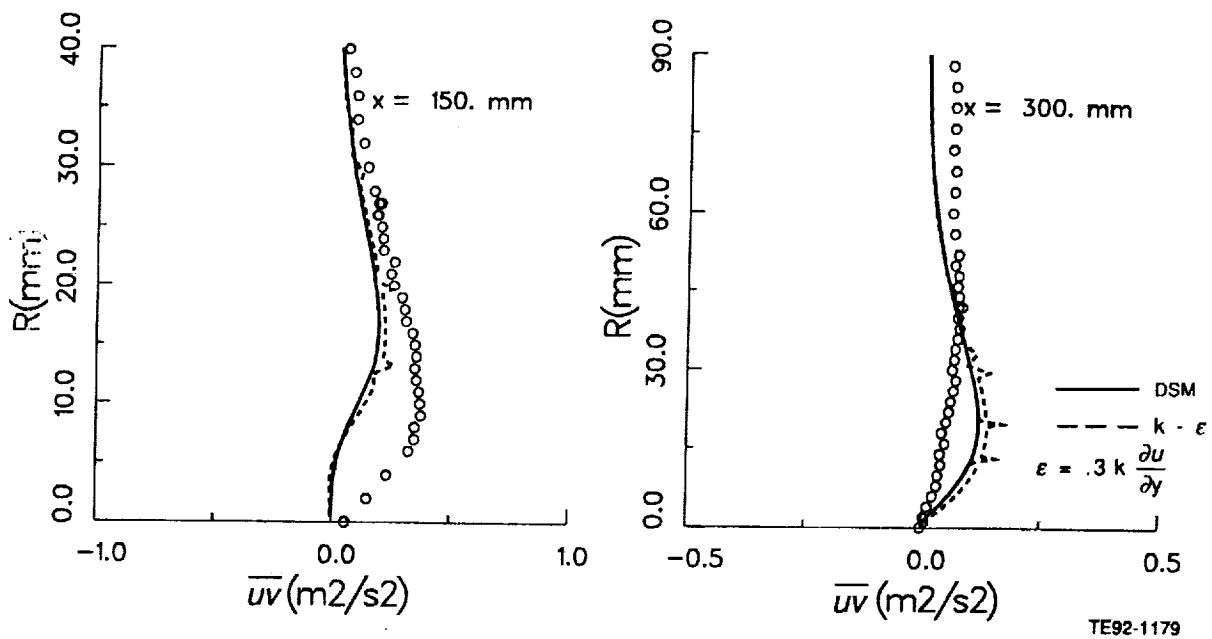


Figure 6.2-12. Comparison of calculated \overline{uv} profiles by $k-\epsilon$ and DSM with data (4 of 4).

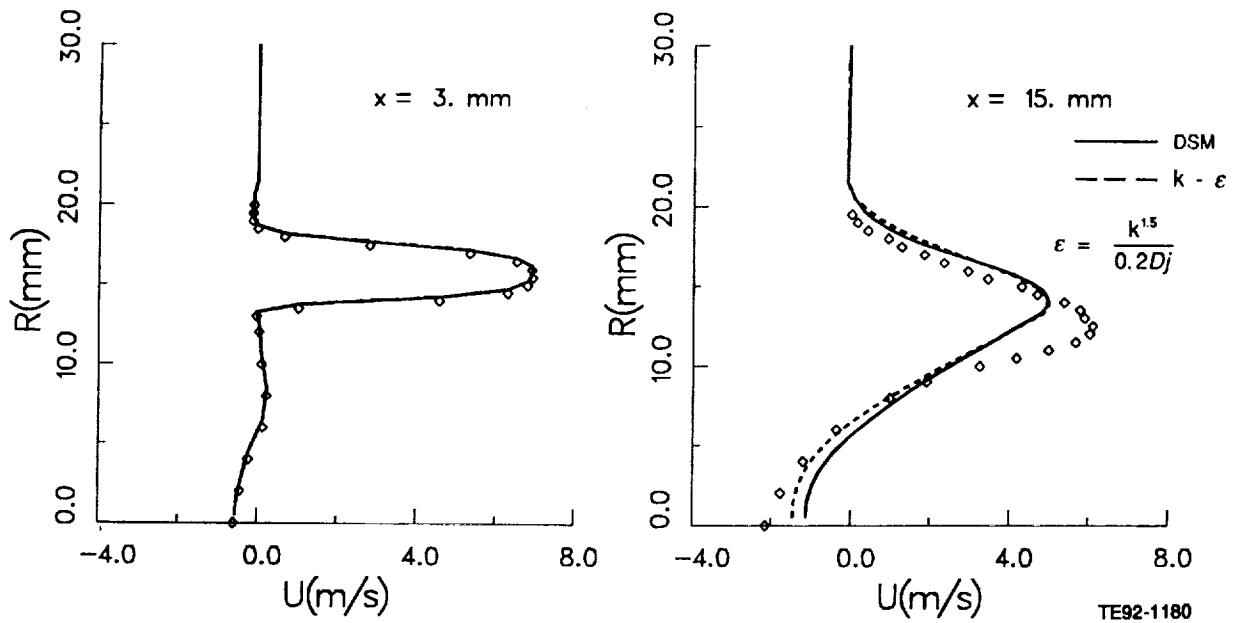


Figure 6.2-13. Comparison of calculated U velocity by k- ϵ and DSM with data (1 of 4).

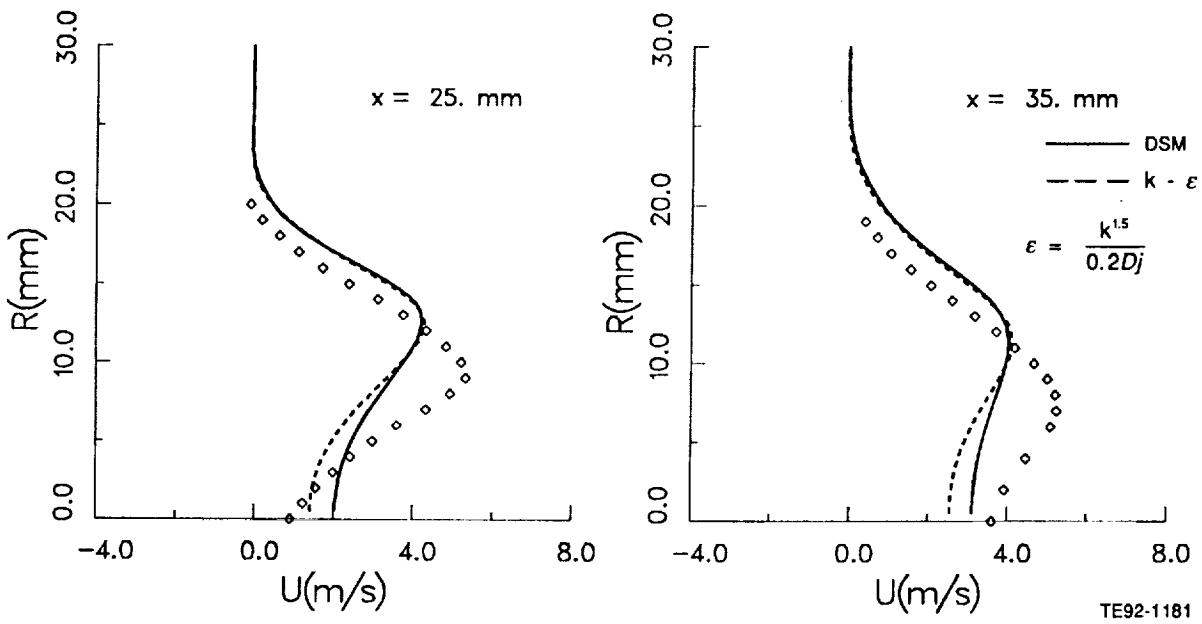


Figure 6.2-13. Comparison of calculated U velocity by k- ϵ and DSM with data (2 of 4).

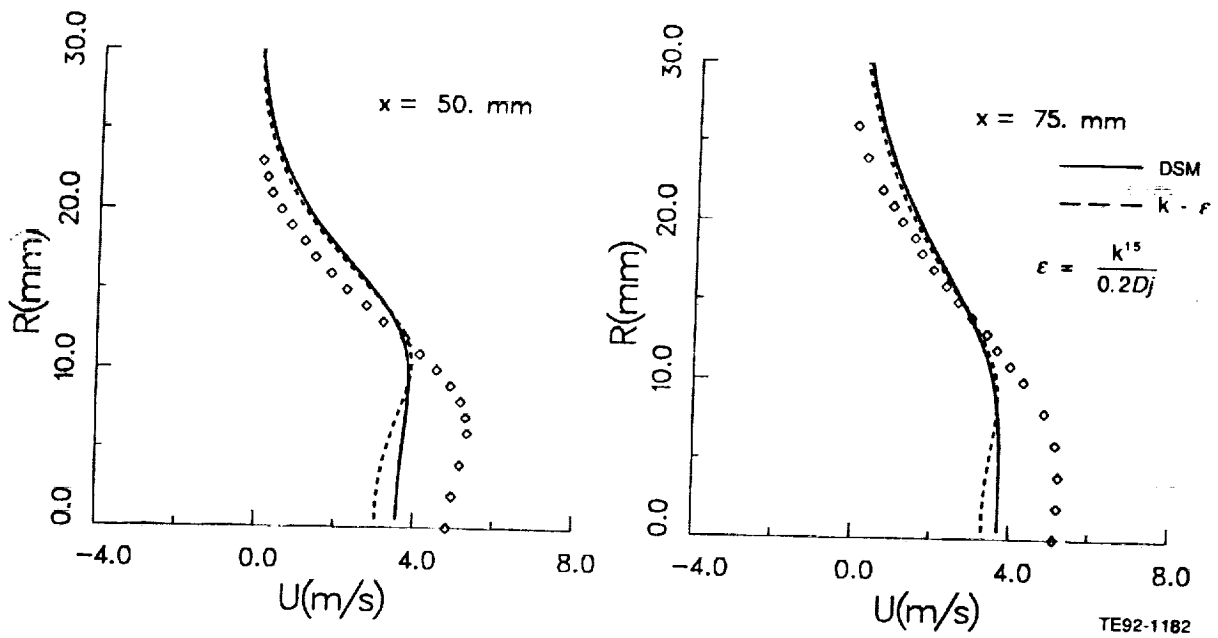


Figure 6.2-13. Comparison of calculated U velocity by k- ϵ and DSM with data (3 of 4).

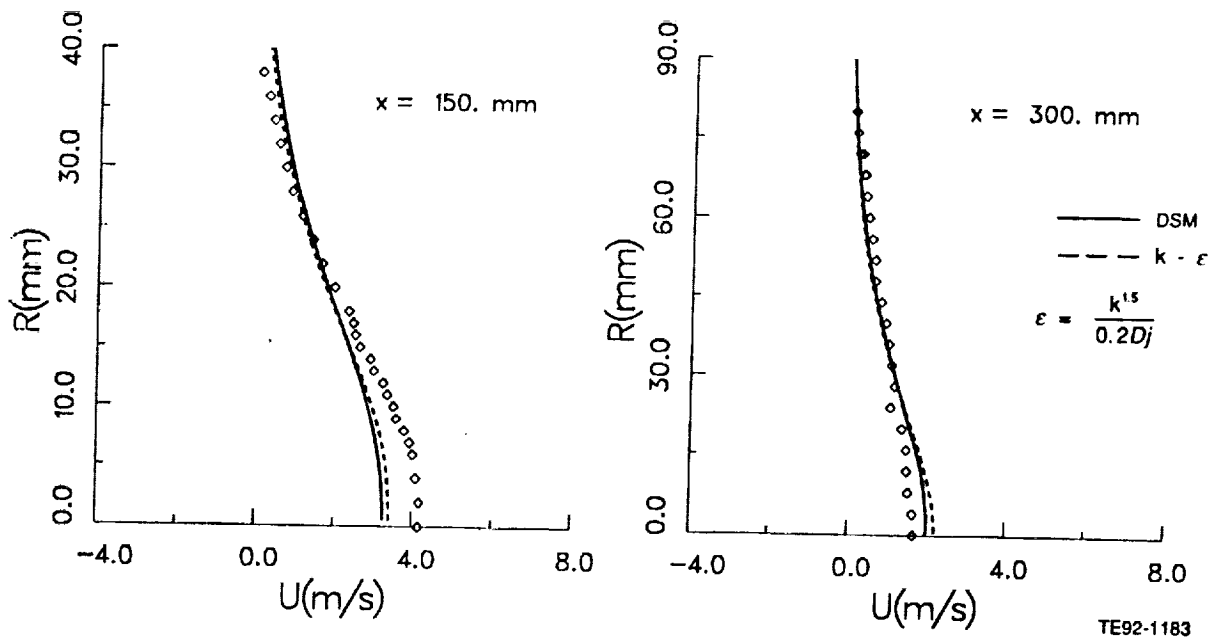


Figure 6.2-13. Comparison of calculated U velocity by k- ϵ and DSM with data (4 of 4).

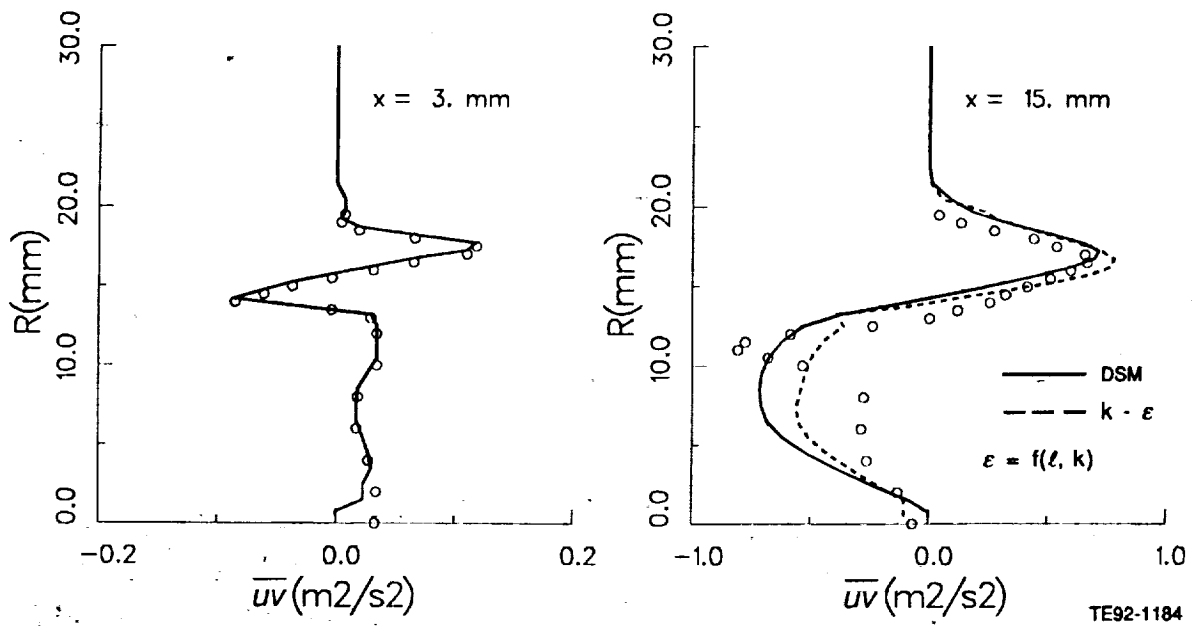


Figure 6.2-14. Comparison of calculated \overline{uv} profiles by $k-\epsilon$ and DSM with data (1 of 4).

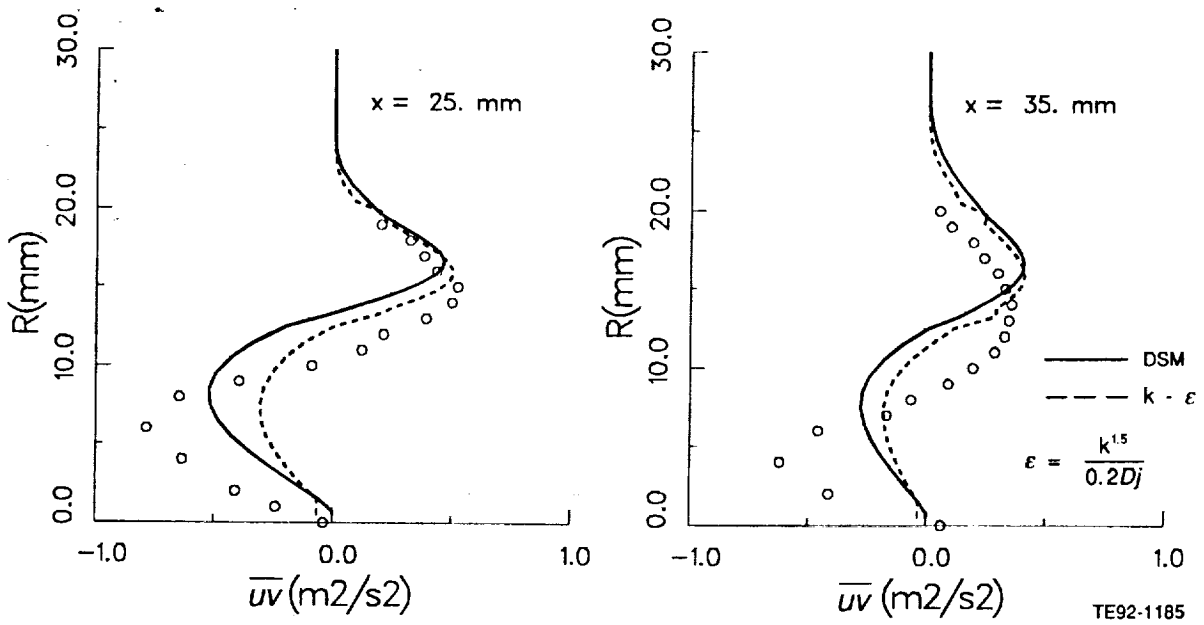


Figure 6.2-14. Comparison of calculated \overline{uv} profiles by $k-\epsilon$ and DSM with data (2 of 4).

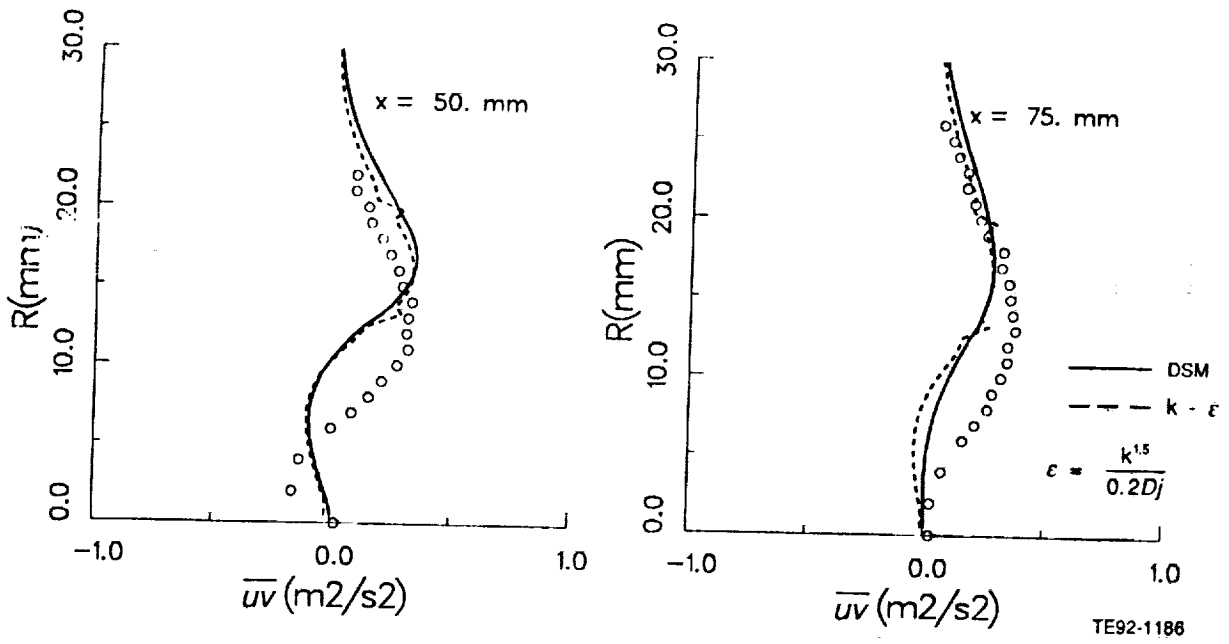


Figure 6.2-14. Comparison of calculated uv profiles by k-ε and DSM with data (3 of 4).

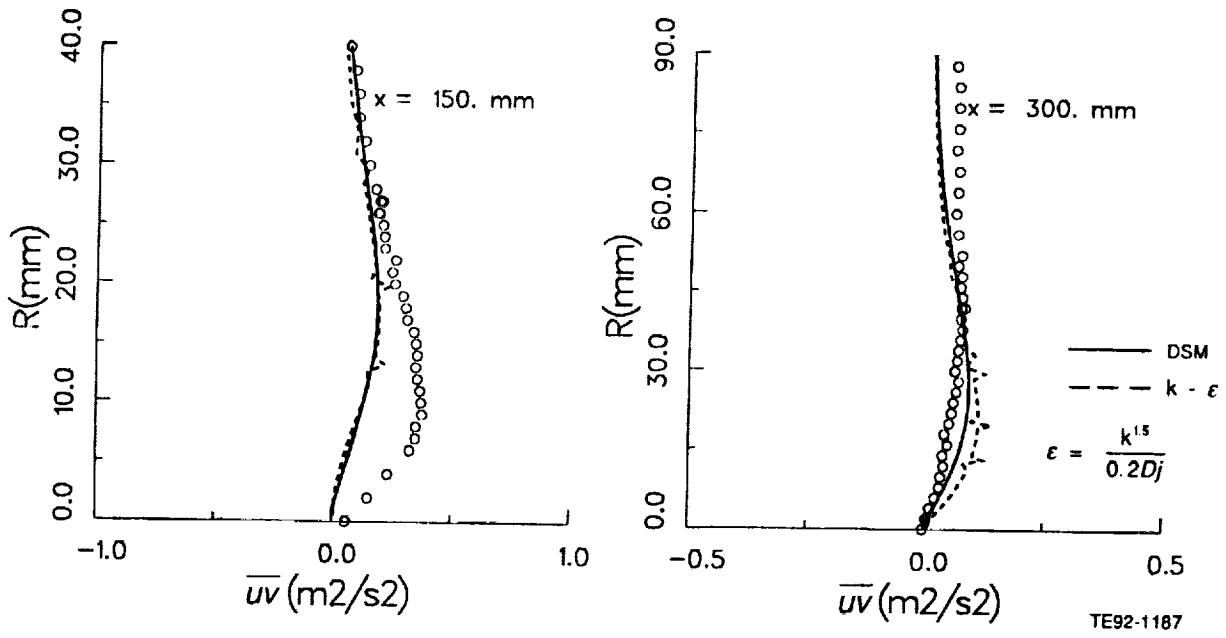


Figure 6.2-14. Comparison of calculated uv profiles by k-ε and DSM with data (4 of 4).

6.3 SINGLE ANNULAR SWIRLING JET

6.3.1 Unconfined Annular Swirling Jet

In this section, computations for an unconfined axisymmetric annular swirling jet are reported. This configuration is the same as the previous one, but with a swirler in the annular passage. In this configuration, an annular jet was directed vertically downward within a 457 mm² wire mesh screen. Experimental data were obtained at eight axial locations 3, 15, 25, 35, 50, 75, 150, and 300 mm from the exit plane of the injector. The flow conditions used for this case are given in Table 6.3-I and the sketch of the test section is shown in Figure 6.3.1-1.

The governing equations were discretized using the control volume approach (Patankar, 1980). The flux-spline differencing scheme was applied for obtaining the numerical scheme. The computational mesh used for all calculations consisted of 61 x 70 nonuniformly distributed grid points in the axial (x) and radial (r) directions. A finer grid spacing was used near the inlet, centerline, and in the shear layer (Figure 6.3.1-2). The tabulated grid points in the axial and radial directions are shown in Table 6.3-II. The computational domain extended from the first measurement plane, located downstream of the nozzle exit at a distance of 3.0 mm to 450 mm.

A calculation procedure for elliptic flow needs boundary conditions on all boundaries of the computational domain. Four kinds of boundaries, namely, inlet, axis of symmetry, outlet, and the entrainment boundary, need consideration. At the inlet boundary located at the first measurement plane, the measured profiles of mean velocities and Reynolds stresses were prescribed. These profiles are shown in Figure 6.3.1-3. The k-profile was obtained from the measured Reynolds normal stress components. The ϵ value at the inlet plane (ϵ_{in}) was derived from the kinetic energy profile and constant length-scale assumption. At the axis of symmetry, shear stresses, radial velocity, and radial gradient of other variables are set to zero. At the outlet, axial diffusion is neglected for all variables. Along the entrainment boundary, the quantity (rV) was assumed constant. In addition, the axial velocity (U) and tangential velocity (W) were assumed to be zero. Turbulent kinetic energy and its dissipation rate were assigned arbitrary low values yielding an eddy viscosity, $\mu_t = 10\mu$.

Predictions of mean axial and tangential velocities obtained from the k- ϵ and DSM are illustrated in Figures 6.3.1-4 and 6.3.1-5. A wide disparity exists between the models' predictions of axial velocity especially near the centerline. There are substantial differences in the capability of the various models to promote or hinder formation of the recirculation zone. With regard to the comparison between measurements and calculations, the trend predicted by the k- ϵ model seems to be better away from the centerline. The maximum velocity was underpredicted by both models. The results of the DSM closure show less radial diffusion process. As a result, in comparison with data, the peak values were all shifted. One of the main reasons for discrepancies between the model and data can be related to the uncertainties in treating the open boundaries. This is clear when the models are applied for confined swirling flow. The k- ϵ model also resulted in slightly better prediction for tangential velocity. An examination of the calculated Reynolds stresses (Figures 6.3.1-6, 6.3.1-7, 6.3.1-8) indicates that the relative performance of the

Table 6.3-I.
Unconfined annular swirling jet test configuration.

R ₁	13.82 (mm)
R ₂	18.35 (mm)
h	7.0 (mm)
U ₀	6.9 (m/s)
Swirl angle	60 deg
Swirl airflow rate	0.0033 (Kg/s)

Table 6.3-II.
Unconfined annular swirling jet grid definition.

STREAMWISE COORDINATES OF THE GRID

I	DX	X	XU
1	0.000E+00	0.000E+00	0.000E+00
2	7.750E-04	7.750E-04	0.000E+00
3	1.625E-03	2.400E-03	1.550E-03
4	2.050E-03	4.450E-03	3.250E-03
5	2.500E-03	6.950E-03	5.650E-03
6	2.700E-03	9.650E-03	8.250E-03
7	2.938E-03	1.259E-02	1.105E-02
8	3.313E-03	1.590E-02	1.413E-02
9	3.888E-03	1.979E-02	1.768E-02
10	4.588E-03	2.438E-02	2.190E-02
11	5.250E-03	2.963E-02	2.685E-02
12	5.775E-03	3.540E-02	3.240E-02
13	6.238E-03	4.164E-02	3.840E-02
14	6.713E-03	4.835E-02	4.488E-02
15	7.063E-03	5.541E-02	5.183E-02
16	7.200E-03	6.261E-02	5.900E-02
17	7.250E-03	6.986E-02	6.623E-02
18	7.288E-03	7.715E-02	7.350E-02
19	7.300E-03	8.445E-02	8.080E-02
20	7.300E-03	9.175E-02	8.810E-02
21	7.288E-03	9.904E-02	9.540E-02
22	7.275E-03	1.063E-01	1.027E-01
23	7.288E-03	1.136E-01	1.100E-01
24	7.300E-03	1.209E-01	1.173E-01
25	7.300E-03	1.282E-01	1.246E-01
26	7.300E-03	1.355E-01	1.319E-01
27	7.300E-03	1.428E-01	1.392E-01
28	7.300E-03	1.501E-01	1.465E-01
29	7.300E-03	1.574E-01	1.538E-01
30	7.300E-03	1.647E-01	1.611E-01
31	7.300E-03	1.720E-01	1.684E-01
32	7.300E-03	1.793E-01	1.757E-01
33	7.300E-03	1.866E-01	1.830E-01
34	7.300E-03	1.939E-01	1.903E-01
35	7.300E-03	2.012E-01	1.976E-01
36	7.300E-03	2.085E-01	2.049E-01
37	7.300E-03	2.158E-01	2.122E-01
38	7.300E-03	2.231E-01	2.195E-01
39	7.200E-03	2.303E-01	2.268E-01
40	7.200E-03	2.375E-01	2.339E-01
41	7.400E-03	2.449E-01	2.412E-01
42	7.400E-03	2.523E-01	2.487E-01
43	7.325E-03	2.596E-01	2.560E-01
44	7.325E-03	2.670E-01	2.633E-01
45	7.275E-03	2.742E-01	2.706E-01
46	7.275E-03	2.815E-01	2.779E-01
47	7.300E-03	2.888E-01	2.852E-01

PART 1 OF 3
TE02-1100

Table 6.3-II (cont).

48	7.450E-03	2.963E-01	2.925E-01
49	7.775E-03	3.040E-01	3.001E-01
50	7.975E-03	3.120E-01	3.080E-01
51	8.500E-03	3.205E-01	3.160E-01
52	9.500E-03	3.300E-01	3.250E-01
53	1.000E-02	3.400E-01	3.350E-01
54	1.000E-02	3.500E-01	3.450E-01
55	1.125E-02	3.613E-01	3.550E-01
56	1.375E-02	3.750E-01	3.675E-01
57	1.500E-02	3.900E-01	3.825E-01
58	1.500E-02	4.050E-01	3.975E-01
59	1.500E-02	4.200E-01	4.125E-01
60	1.500E-02	4.350E-01	4.275E-01
61	7.500E-03	4.425E-01	4.425E-01

TRANSVERS COORDINATES OF THE GRID

J	DY	Y	YV
1	0.000E+00	5.000E-04	0.000E+00
2	2.500E-04	7.500E-04	5.000E-04
3	7.500E-04	1.500E-03	1.000E-03
4	1.000E-03	2.500E-03	2.000E-03
5	1.000E-03	3.500E-03	3.000E-03
6	1.000E-03	4.500E-03	4.000E-03
7	1.000E-03	5.500E-03	5.000E-03
8	1.000E-03	6.500E-03	6.000E-03
9	1.000E-03	7.500E-03	7.000E-03
10	1.000E-03	8.500E-03	8.000E-03
11	1.000E-03	9.500E-03	9.000E-03
12	1.000E-03	1.050E-02	1.000E-02
13	1.000E-03	1.150E-02	1.100E-02
14	1.000E-03	1.250E-02	1.200E-02
15	7.500E-04	1.325E-02	1.300E-02
16	5.000E-04	1.375E-02	1.350E-02
17	5.000E-04	1.425E-02	1.400E-02
18	5.000E-04	1.475E-02	1.450E-02
19	5.000E-04	1.525E-02	1.500E-02
20	5.000E-04	1.575E-02	1.550E-02
21	5.000E-04	1.625E-02	1.600E-02
22	5.000E-04	1.675E-02	1.650E-02
23	5.000E-04	1.725E-02	1.700E-02
24	5.000E-04	1.775E-02	1.750E-02
25	5.000E-04	1.825E-02	1.800E-02
26	5.000E-04	1.875E-02	1.850E-02
27	5.000E-04	1.925E-02	1.900E-02
28	5.000E-04	1.975E-02	1.950E-02
29	7.500E-04	2.050E-02	2.000E-02
30	1.000E-03	2.150E-02	2.100E-02
31	1.000E-03	2.250E-02	2.200E-02

PART 2 OF 3
TE92-1188

Table 6.3-II (cont).

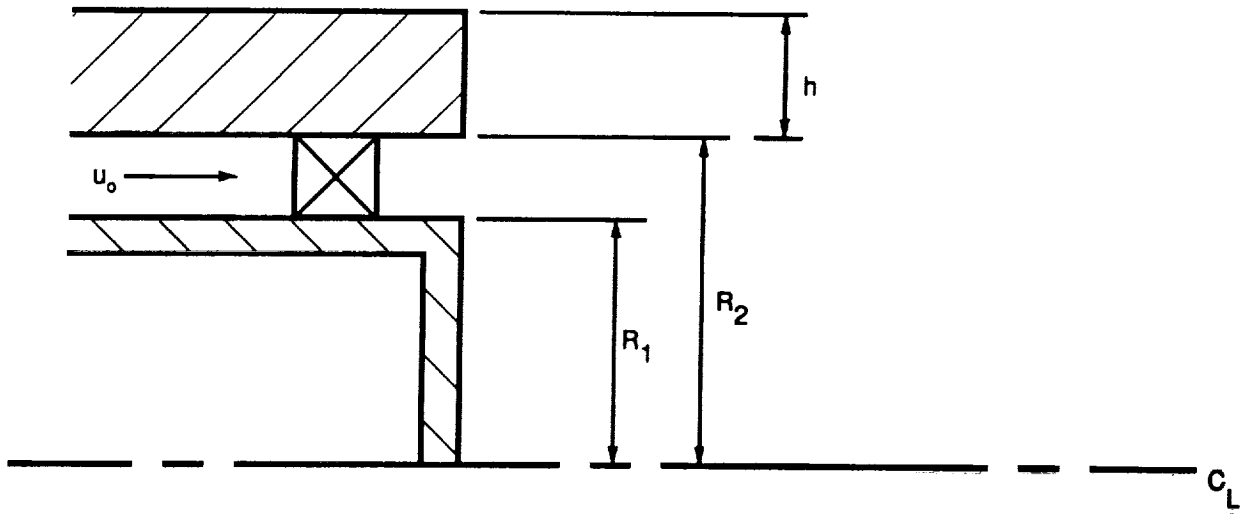
32	1.000E-03	2.350E-02	2.300E-02
33	1.000E-03	2.450E-02	2.400E-02
34	1.000E-03	2.550E-02	2.500E-02
35	1.000E-03	2.650E-02	2.600E-02
36	1.000E-03	2.750E-02	2.700E-02
37	1.000E-03	2.850E-02	2.800E-02
38	1.000E-03	2.950E-02	2.900E-02
39	1.500E-03	3.100E-02	3.000E-02
40	2.000E-03	3.300E-02	3.200E-02
41	2.500E-03	3.550E-02	3.400E-02
42	3.000E-03	3.850E-02	3.700E-02
43	3.000E-03	4.150E-02	4.000E-02
44	3.000E-03	4.450E-02	4.300E-02
45	3.500E-03	4.800E-02	4.600E-02
46	4.000E-03	5.200E-02	5.000E-02
47	4.500E-03	5.650E-02	5.400E-02
48	5.000E-03	6.150E-02	5.900E-02
49	5.000E-03	6.650E-02	6.400E-02
50	5.000E-03	7.150E-02	6.900E-02
51	5.000E-03	7.650E-02	7.400E-02
52	5.000E-03	8.150E-02	7.900E-02
53	5.000E-03	8.650E-02	8.400E-02
54	5.000E-03	9.150E-02	8.900E-02
55	5.000E-03	9.650E-02	9.400E-02
56	5.500E-03	1.020E-01	9.900E-02
57	5.500E-03	1.075E-01	1.050E-01
58	5.000E-03	1.125E-01	1.100E-01
59	5.000E-03	1.175E-01	1.150E-01
60	5.000E-03	1.225E-01	1.200E-01
61	5.000E-03	1.275E-01	1.250E-01
62	5.000E-03	1.325E-01	1.300E-01
63	5.000E-03	1.375E-01	1.350E-01
64	5.000E-03	1.425E-01	1.400E-01
65	5.000E-03	1.475E-01	1.450E-01
66	5.000E-03	1.525E-01	1.500E-01
67	5.000E-03	1.575E-01	1.550E-01
68	5.000E-03	1.625E-01	1.600E-01
69	5.000E-03	1.675E-01	1.650E-01
70	2.500E-03	1.700E-01	1.700E-01

PART 3 OF 3
TE92-1188

model is dependent on the flow region. The results show differences, especially in the prediction of the centerline values. The discrepancy can be the result of the inlet dissipation rate profile. The inlet dissipation rate is a determining factor in predicting the maximum level of turbulence intensity. Comparison of the calculated shear stress profiles with data is shown in Figure 6.3.1-9. In comparison with the measurement, the predicted values by the k- ϵ model are in better agreement, however, the maximum and minimum have not been well predicted.

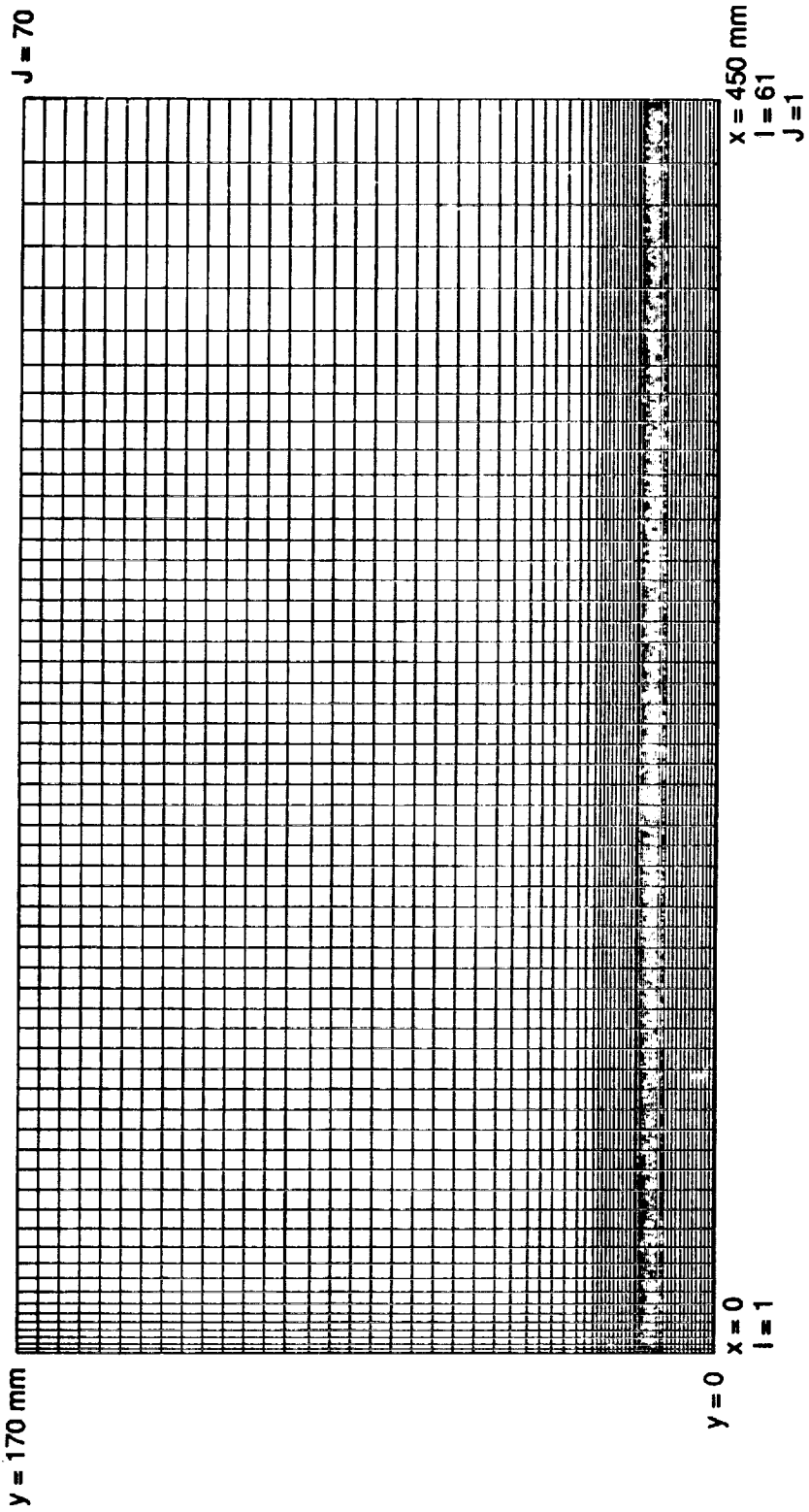
In an attempt to assess the importance of inlet dissipation rate (ϵ_{in}) on flow field, calculations were also made using an alternative ϵ_{in} distribution, which was derived from local equilibrium assumption for turbulence energy (Equation 65). Comparison of the calculated mean axial and tangential velocity profiles by the k- ϵ model with the experimental data are presented in Figures 6.3.1-10 and 6.3.1-11. Numerical experiments indicate that the inlet ϵ profile is the single most important factor in predicting the maximum values of mean and turbulence quantities. This point is now clear by comparing the two sets of results. The major differences between these two conditions are in the peak region. The inlet dissipation rate profile derived from the equilibrium assumption resulted in shorter maximum velocity and smaller recirculation zone to satisfy the global mass conservation. The tangential velocity has also been affected simi-

larly by ϵ_{in} . Figures 6.3.1-12 and 6.3.1-13 show comparisons of turbulent shear stress and kinetic energy profiles. The ϵ_{in} found by equilibrium assumptions resulted in higher shear and energy. These will increase the radial diffusion process, and as a result, the peak velocities will be quickly diminished.



TE92-1189-4

Figure 6.3.1-1. Unconfined annular swirling jet geometrical details.



TE92-1190

Figure 6.3.1-2. Unconfined annular swirling jet grid layout.

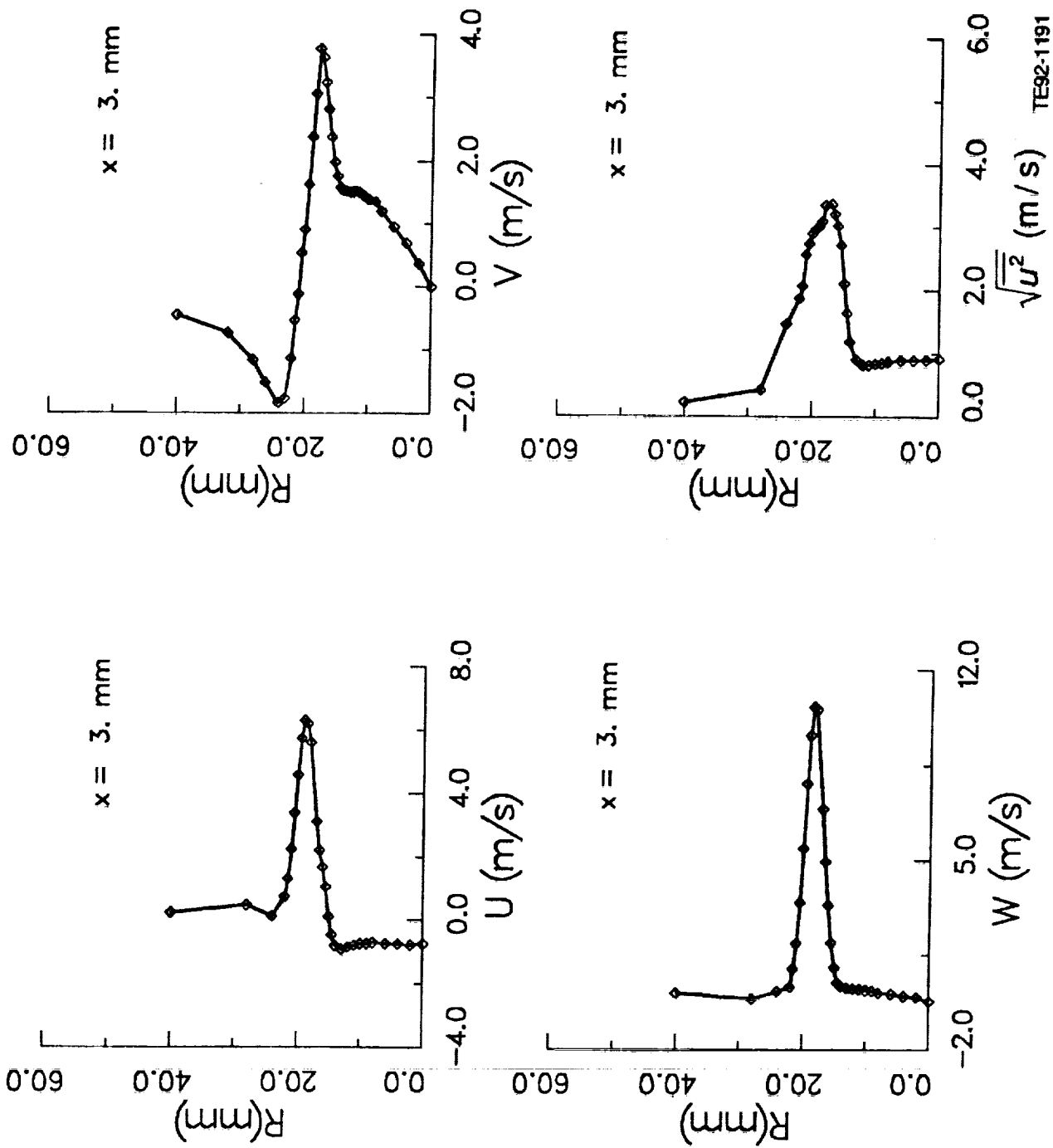


Figure 6.3.1-3. Measured profiles at the inlet ($x = 3 \text{ mm}$)(1 of 2).

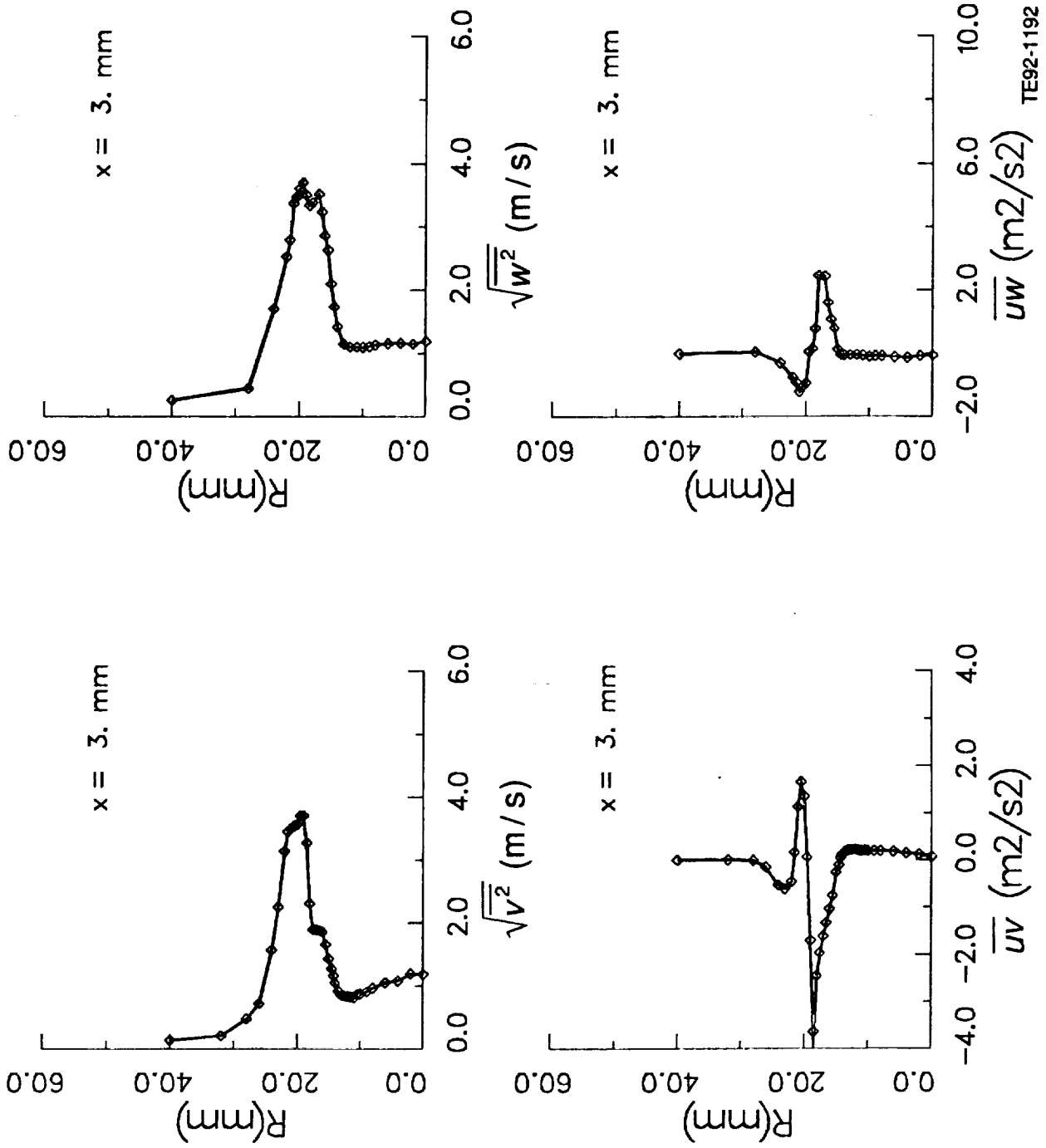


Figure 6.3.1-3. Measured profiles at the inlet ($x = 3 \text{ mm}$) (2 of 2).

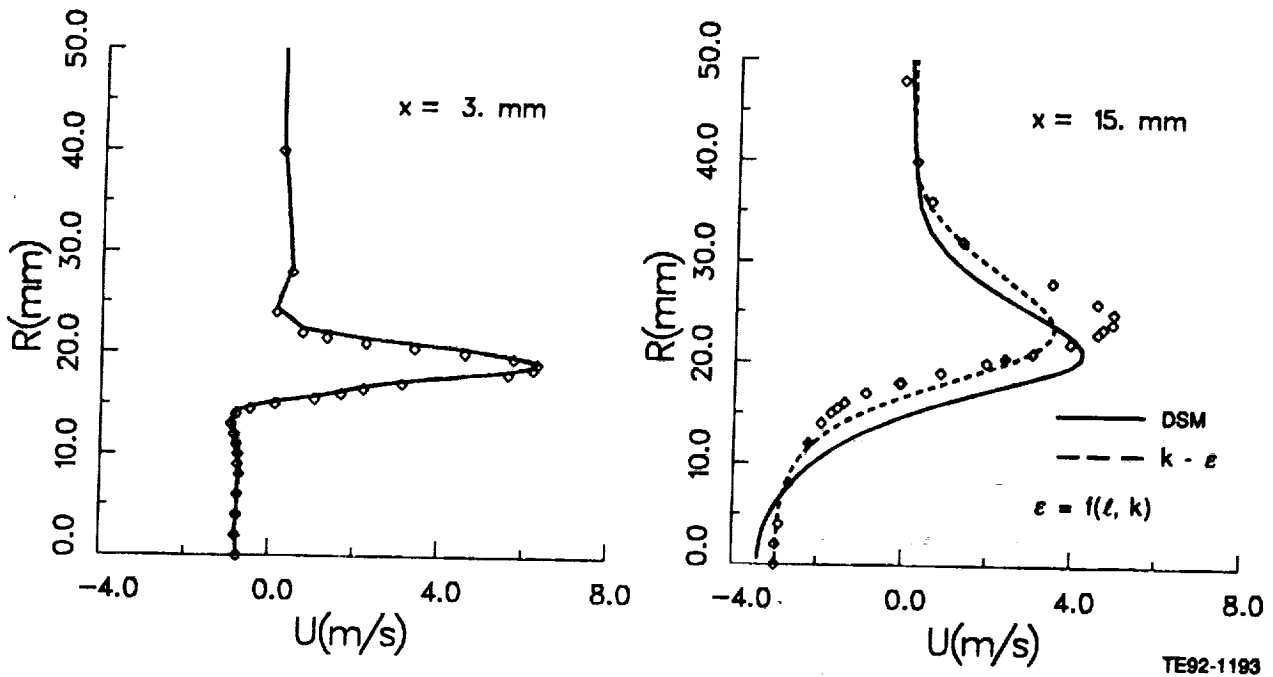


Figure 6.3.1-4. Comparison of calculated mean axial velocity by DSM and $k-\epsilon$ with data (1 of 3).

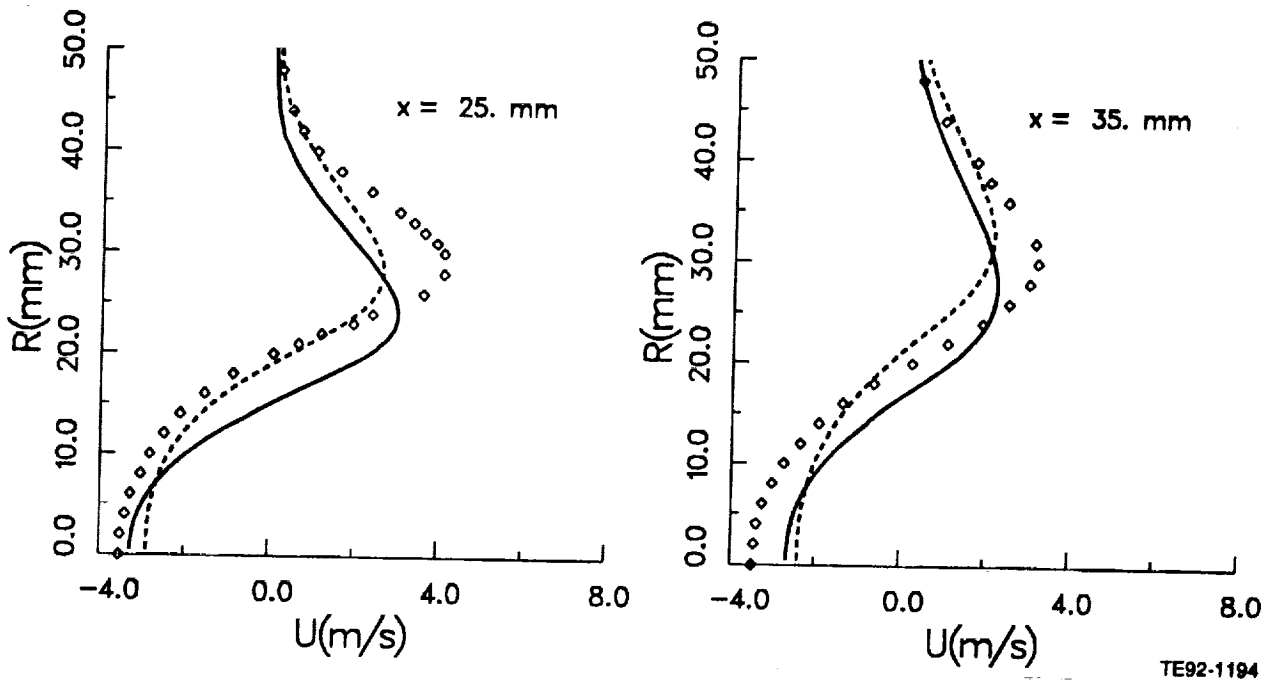


Figure 6.3.1-4. Comparison of calculated mean axial velocity by DSM and $k-\epsilon$ with data (2 of 3).

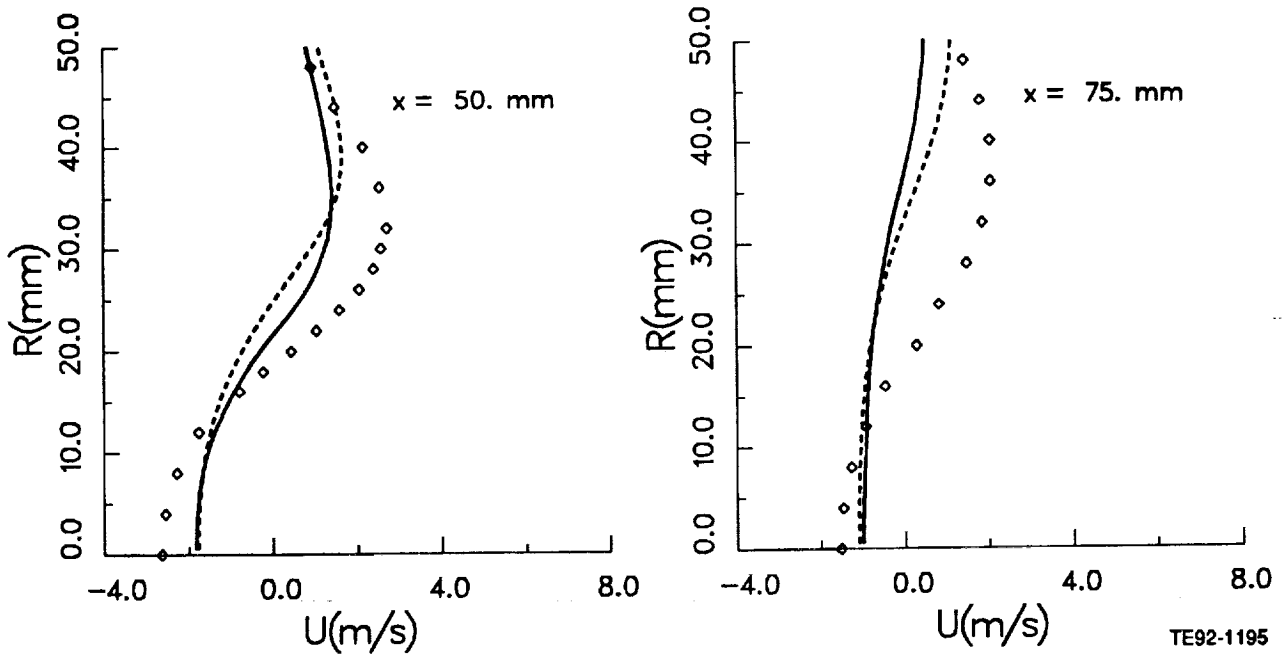


Figure 6.3.1-4. Comparison of calculated mean axial velocity by DSM and $k-\epsilon$ with data (3 of 3).

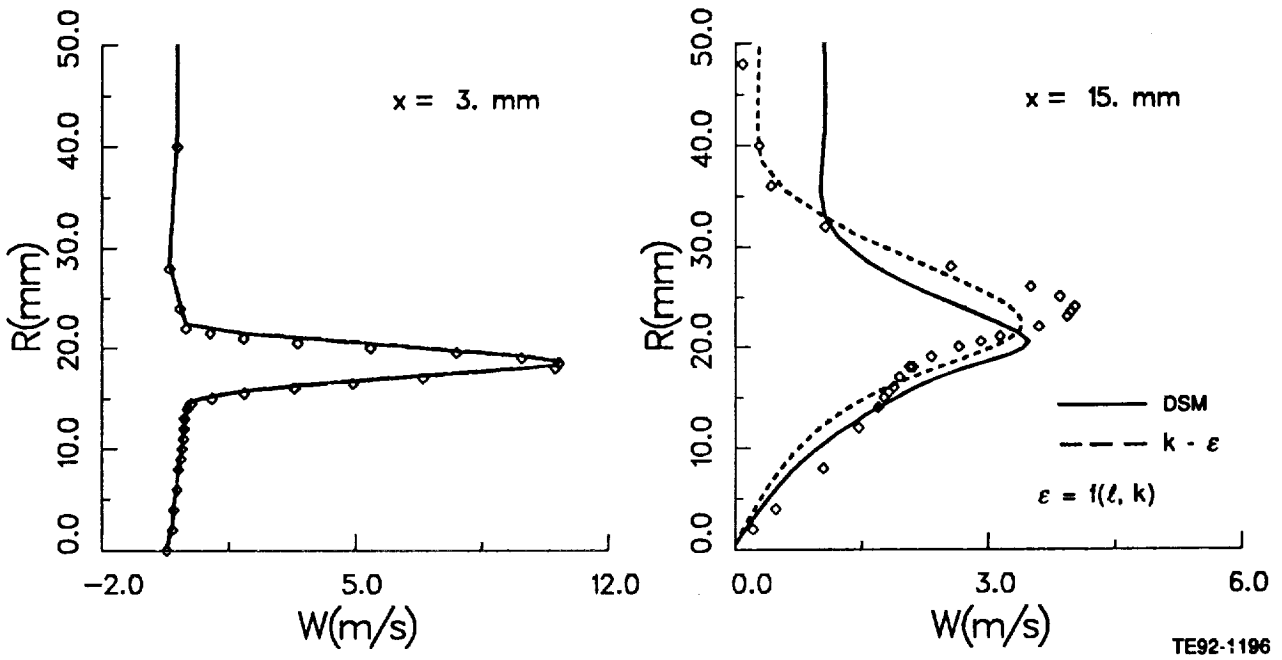


Figure 6.3.1-5. Comparison of calculated mean tangential velocity by DSM and $k-\epsilon$ with data (1 of 3).

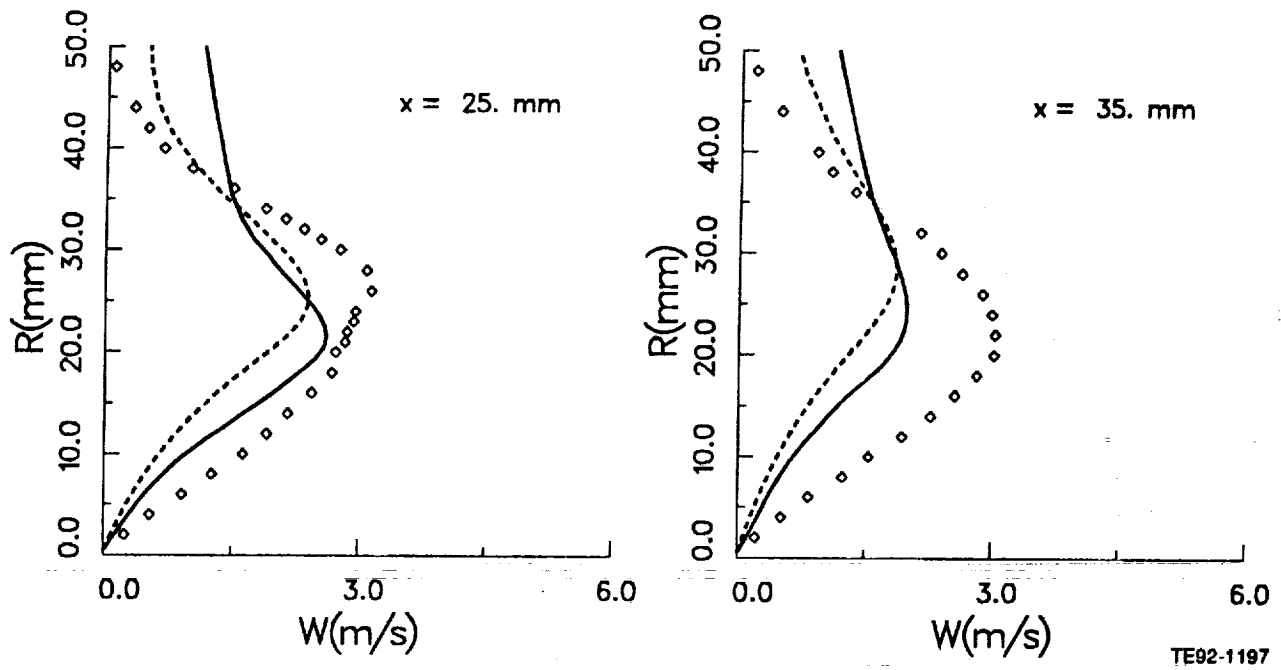


Figure 6.3.1-5. Comparison of calculated mean tangential velocity by DSM and $k-\epsilon$ with data (2 of 3).

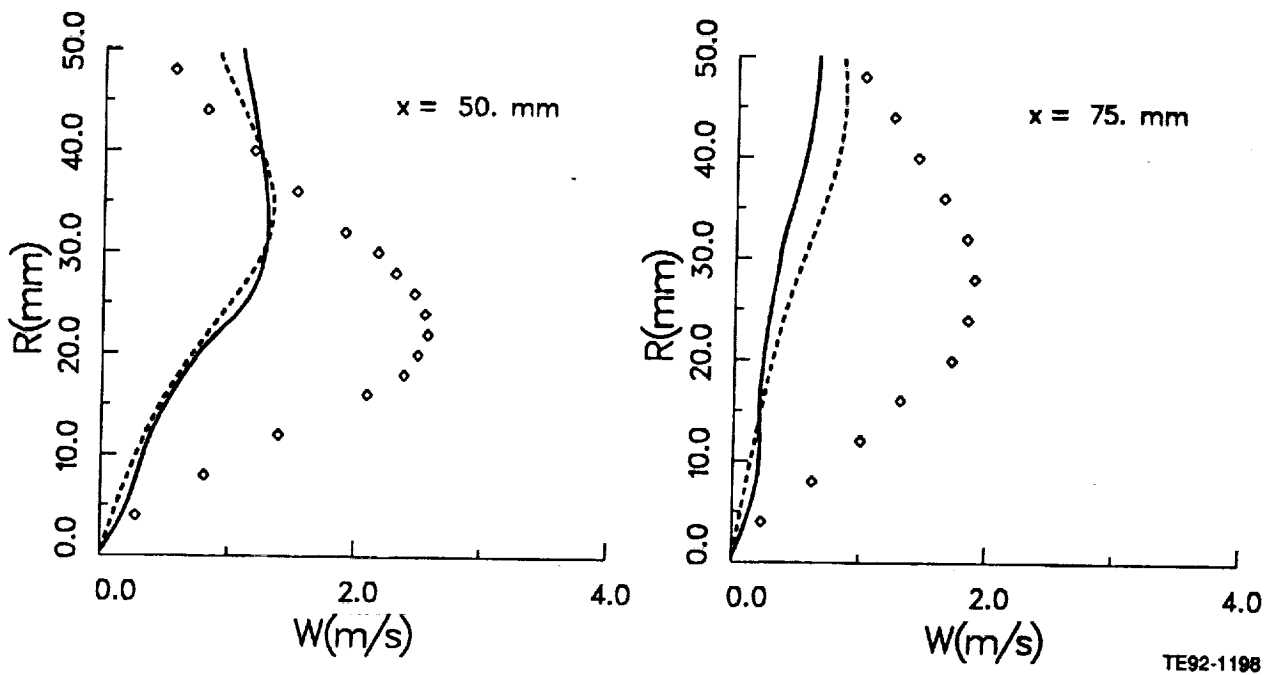


Figure 6.3.1-5. Comparison of calculated mean tangential velocity by DSM and $k-\epsilon$ with data (3 of 3).

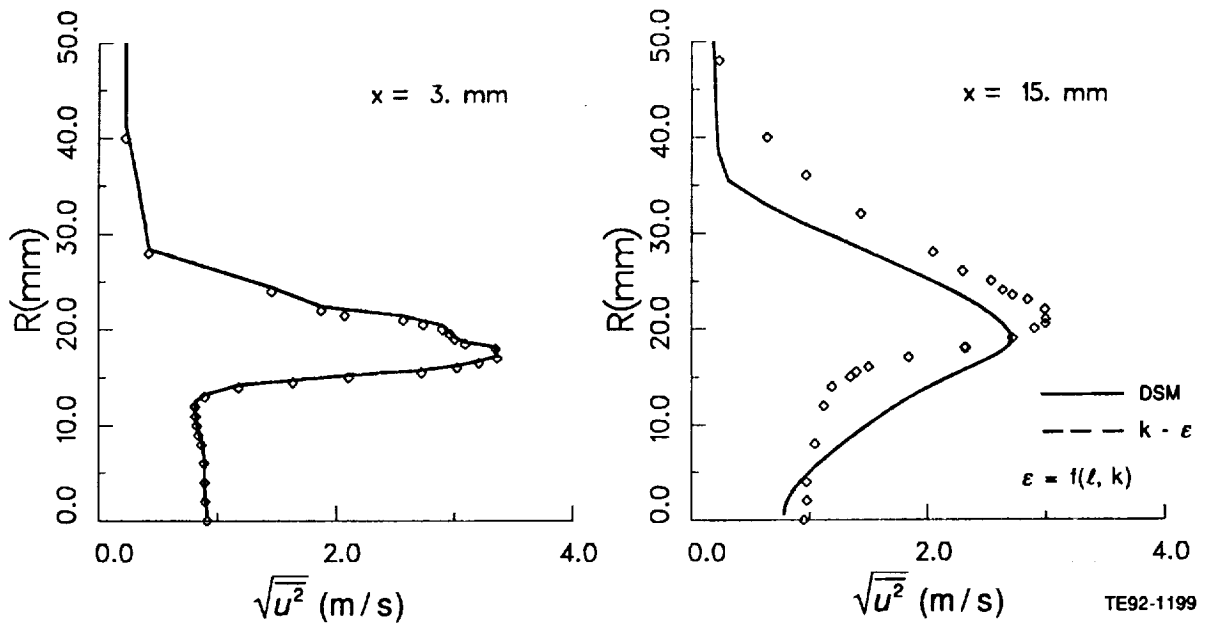


Figure 6.3.1-6. Comparison of calculated axial rms velocity by DSM with data (1 of 3).

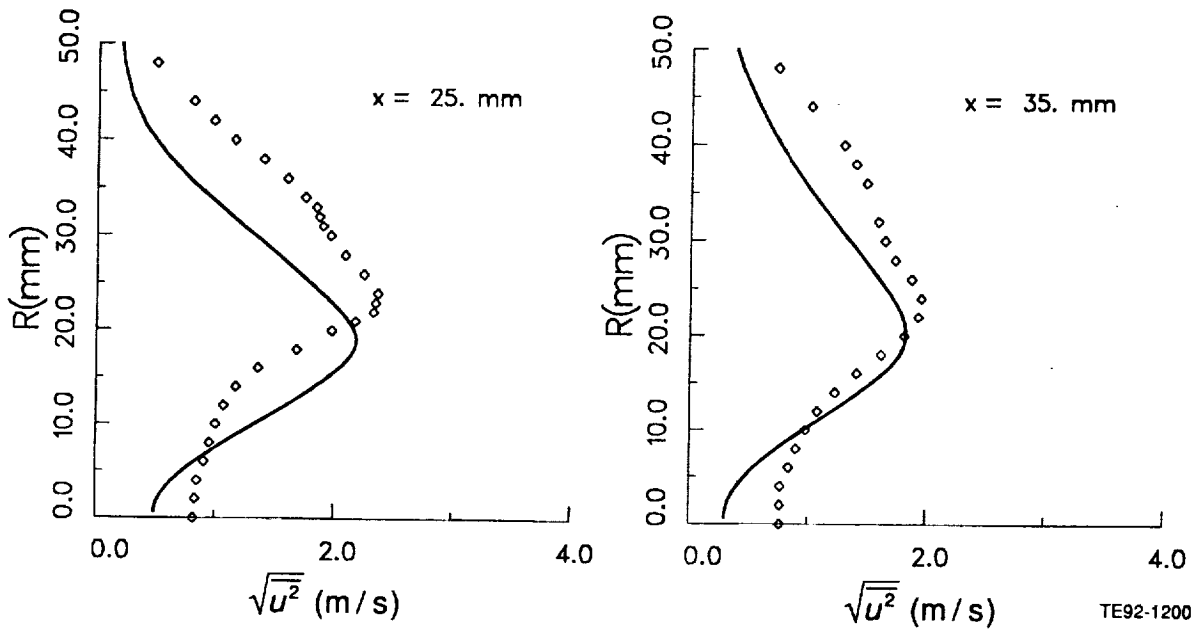


Figure 6.3.1-6. Comparison of calculated axial rms velocity by DSM with data (2 of 3).

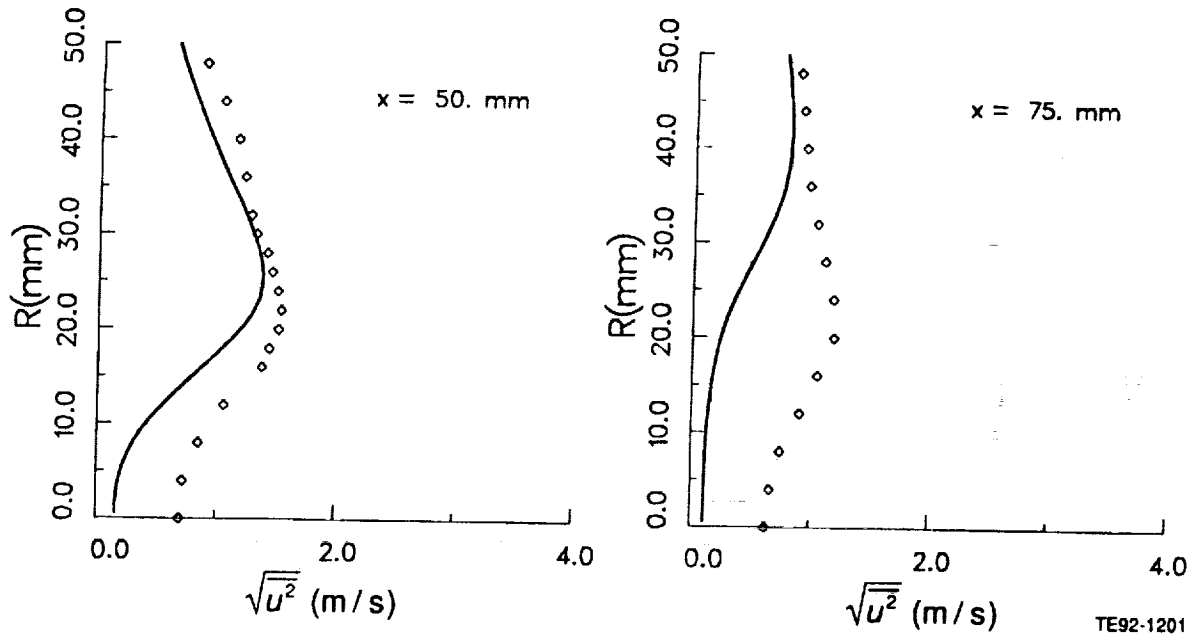


Figure 6.3.1-6. Comparison of calculated axial rms velocity by DSM with data (3 of 3).

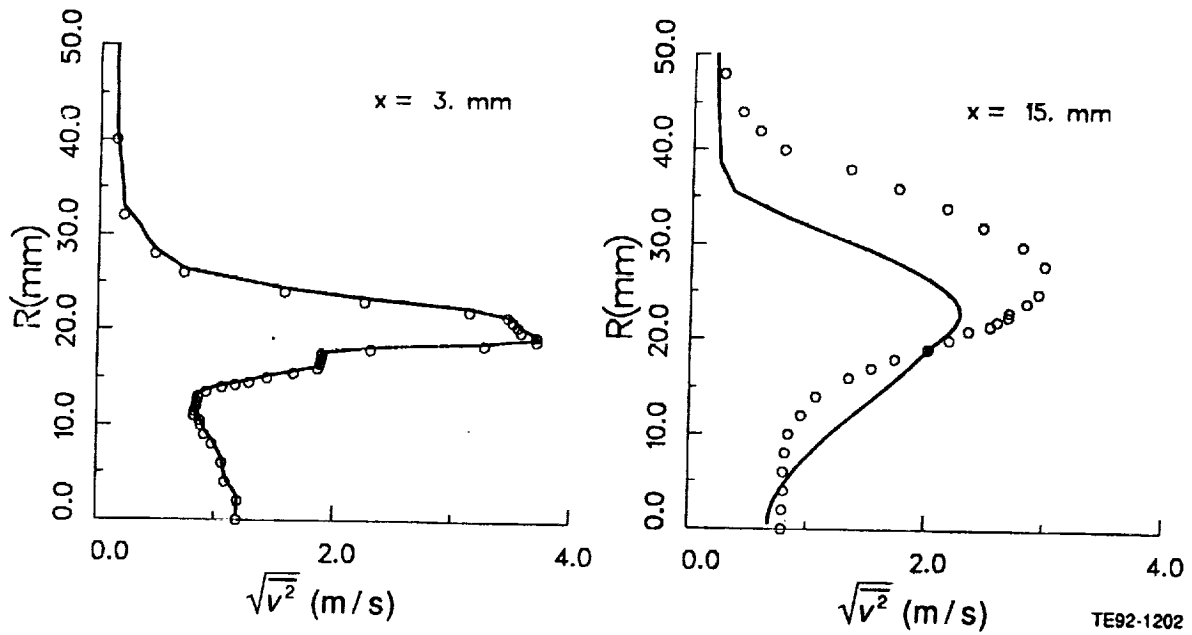


Figure 6.3.1-7. Comparison of calculated radial rms velocity by DSM with data (1 of 3).

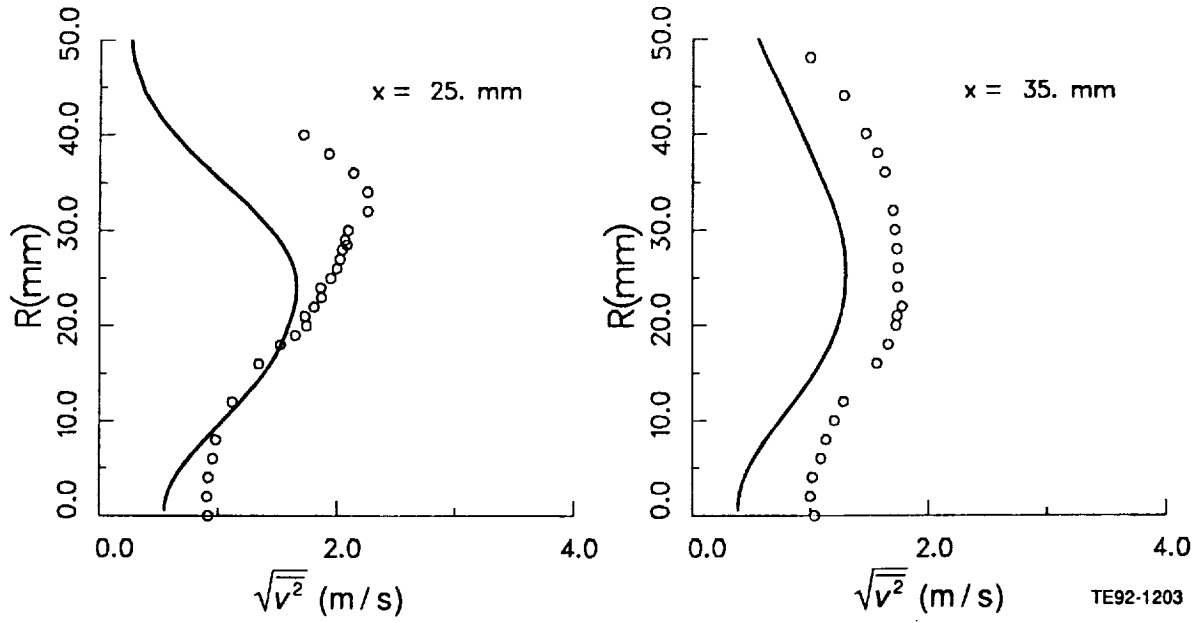


Figure 6.3.1-7. Comparison of calculated radial rms velocity by DSM with data (2 of 3).

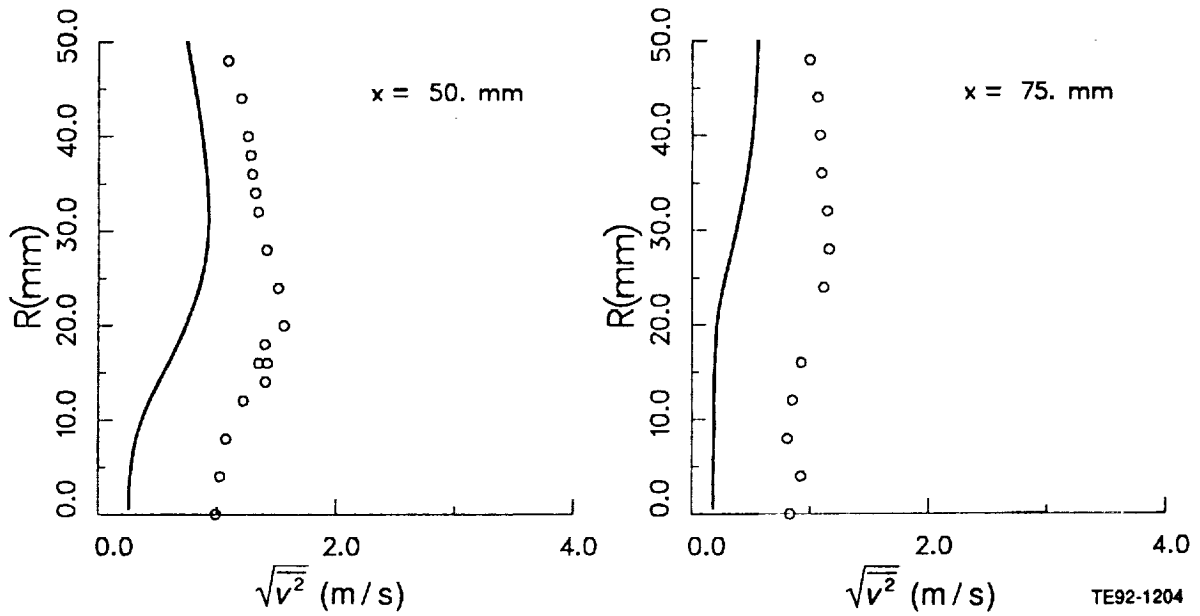


Figure 6.3.1-7. Comparison of calculated radial rms velocity by DSM with data (3 of 3).

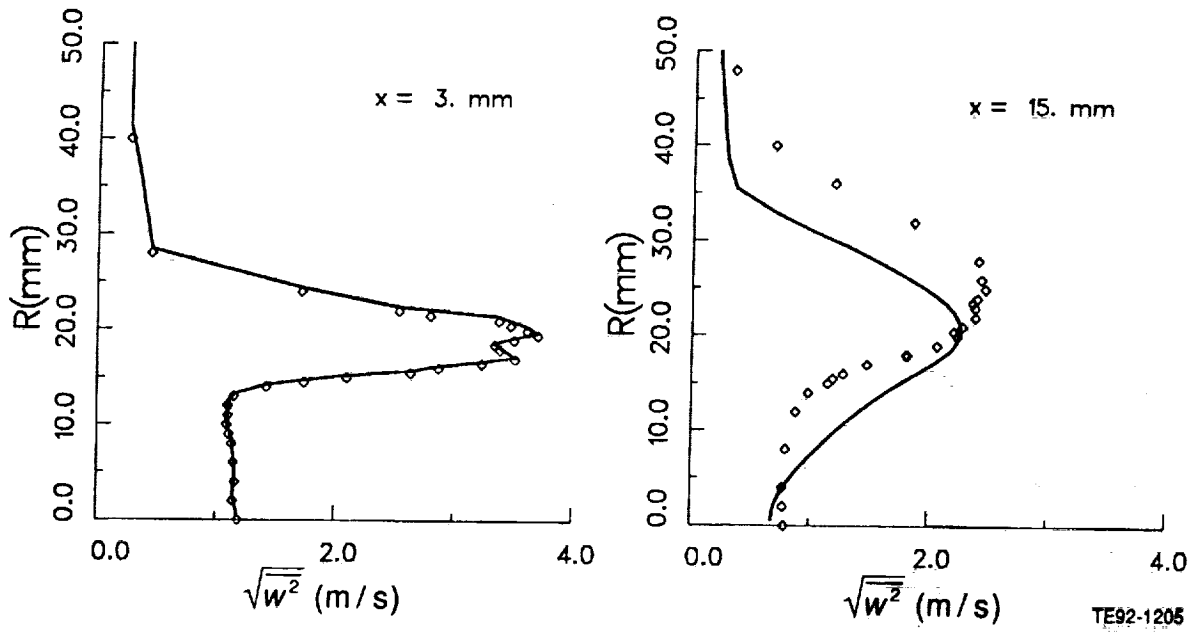


Figure 6.3.1-8. Comparison of calculated tangential rms velocity by DSM with data (1 of 3).

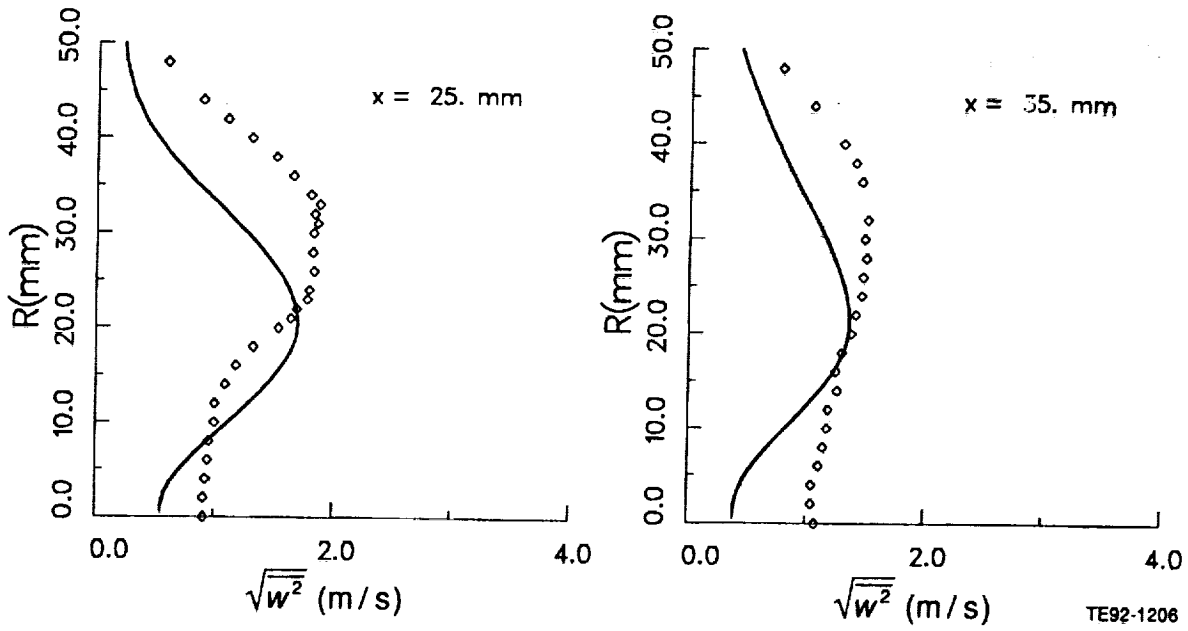


Figure 6.3.1-8. Comparison of calculated tangential rms velocity by DSM with data (2 of 3).

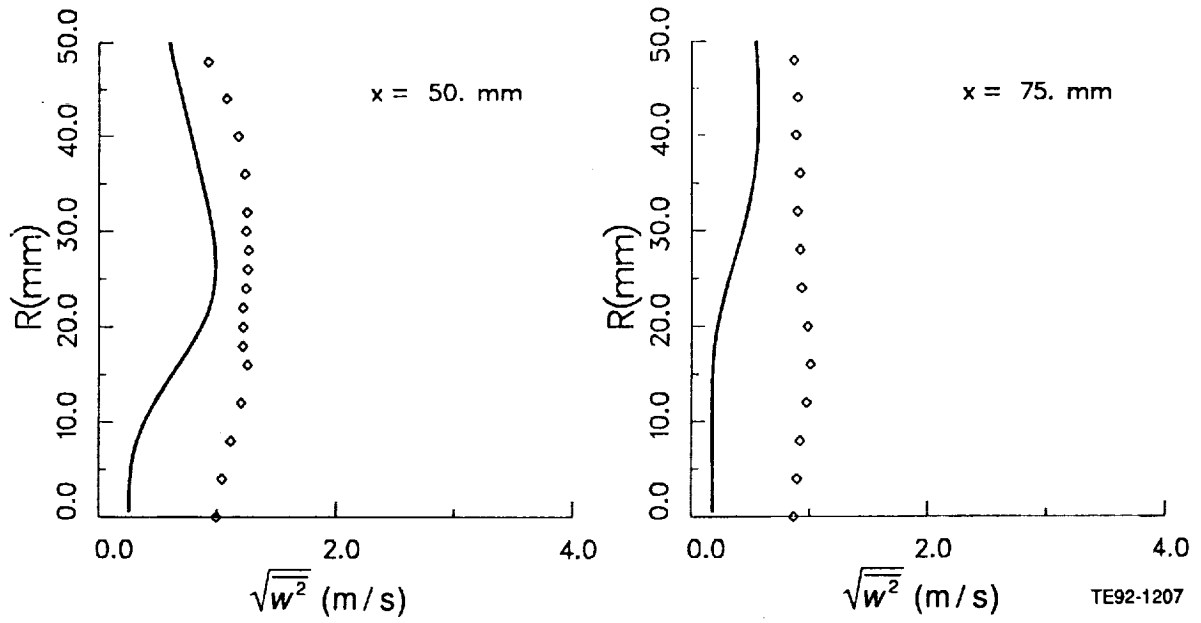


Figure 6.3.1-8. Comparison of calculated tangential rms velocity by DSM with data (3 of 3).

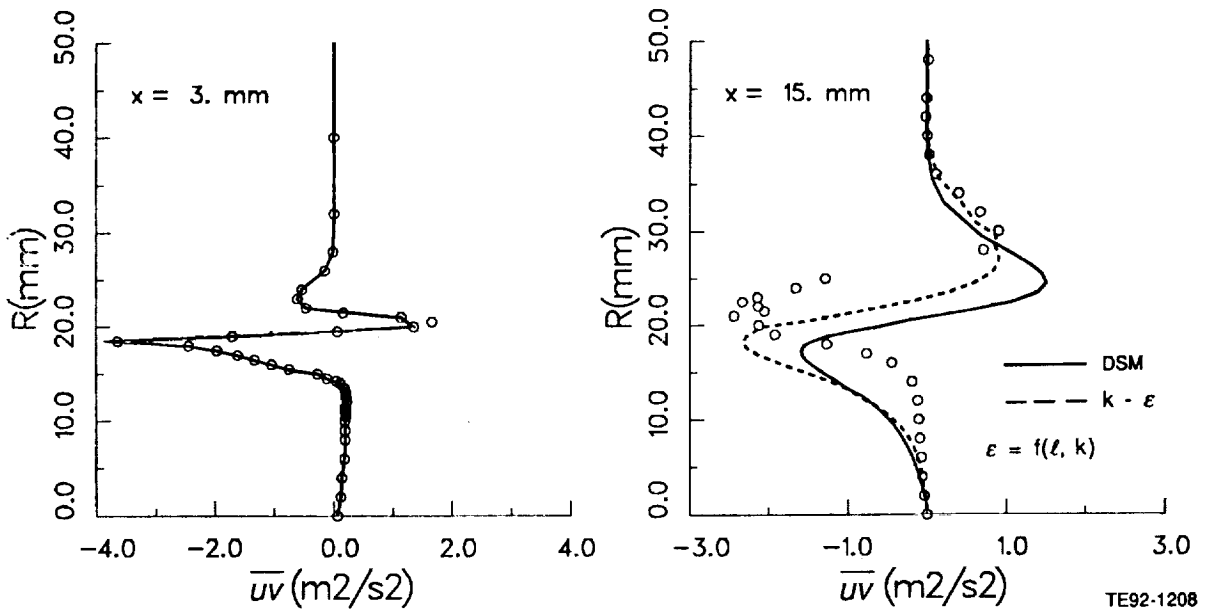


Figure 6.3.1-9. Comparison of calculated turbulent shear stress profiles by $k-\epsilon$ and DSM with data (1 of 3).

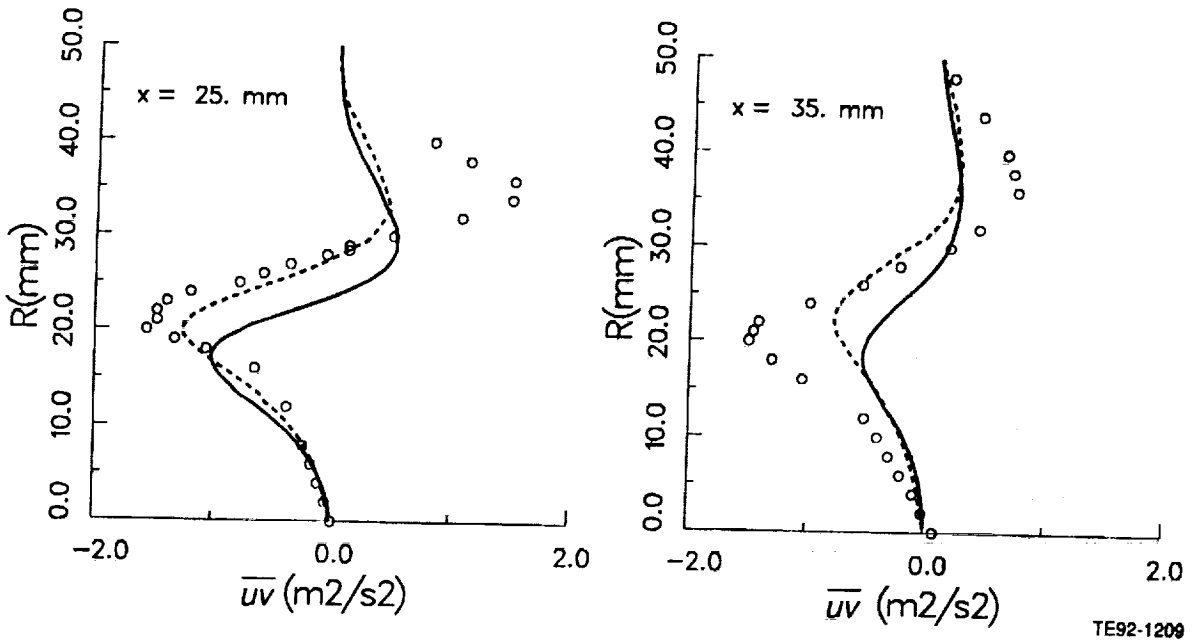


Figure 6.3.1-9. Comparison of calculated turbulent shear stress profiles by $k-\epsilon$ and DSM with data (2 of 3).

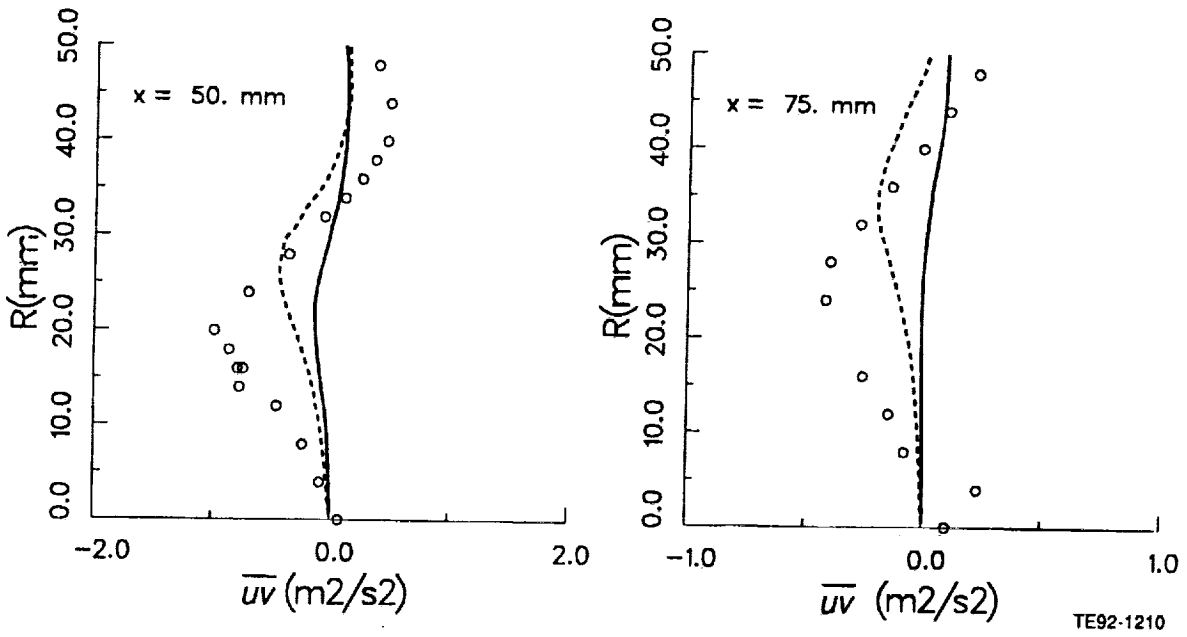


Figure 6.3.1-9. Comparison of calculated turbulent shear stress profiles by $k-\epsilon$ and DSM with data (3 of 3).

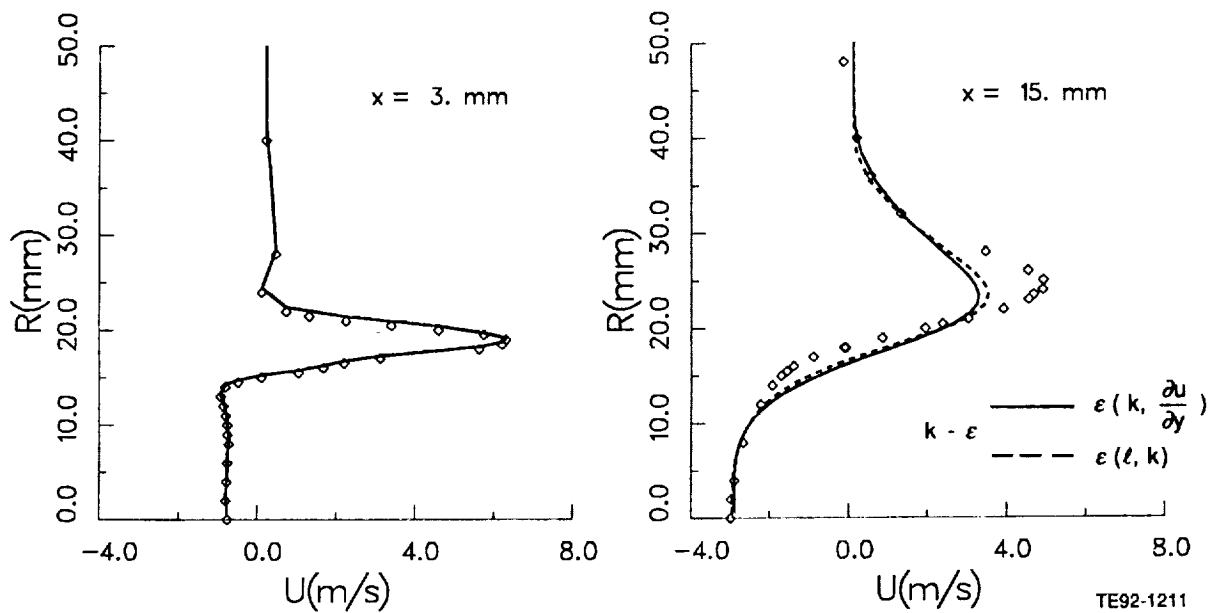


Figure 6.3.1-10. Comparison of predicted mean axial velocity by k- ϵ with data (1 of 3).

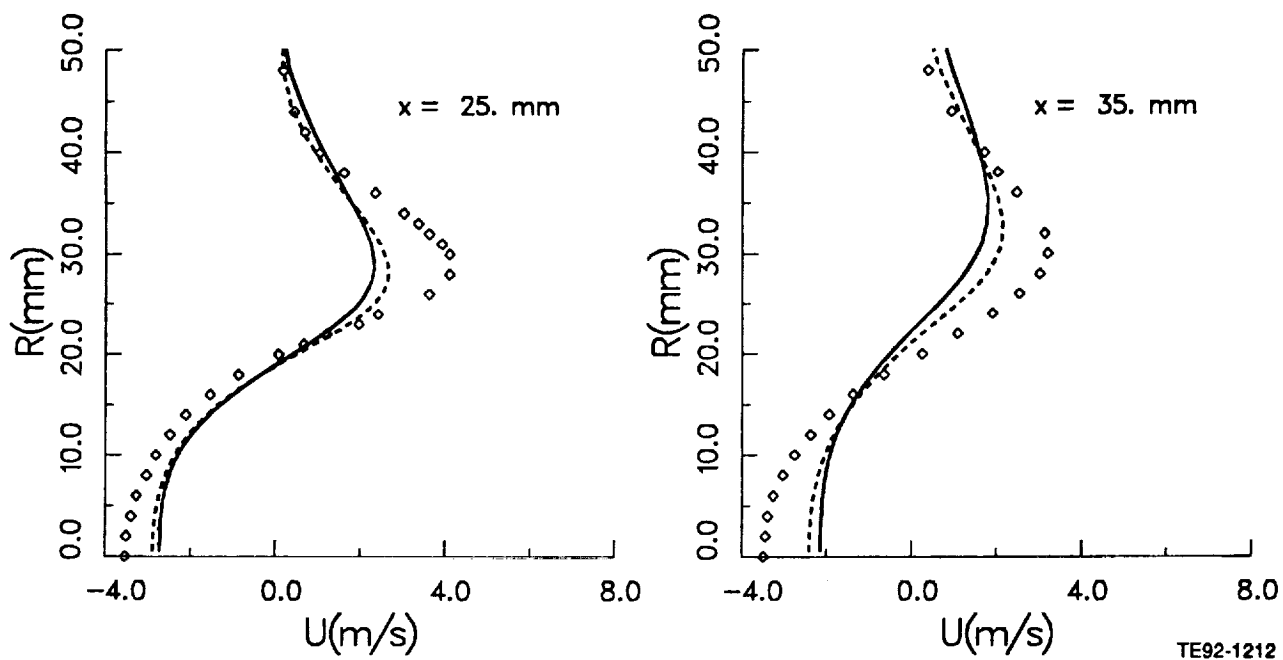


Figure 6.3.1-10. Comparison of predicted mean axial velocity by k- ϵ with data (2 of 3).

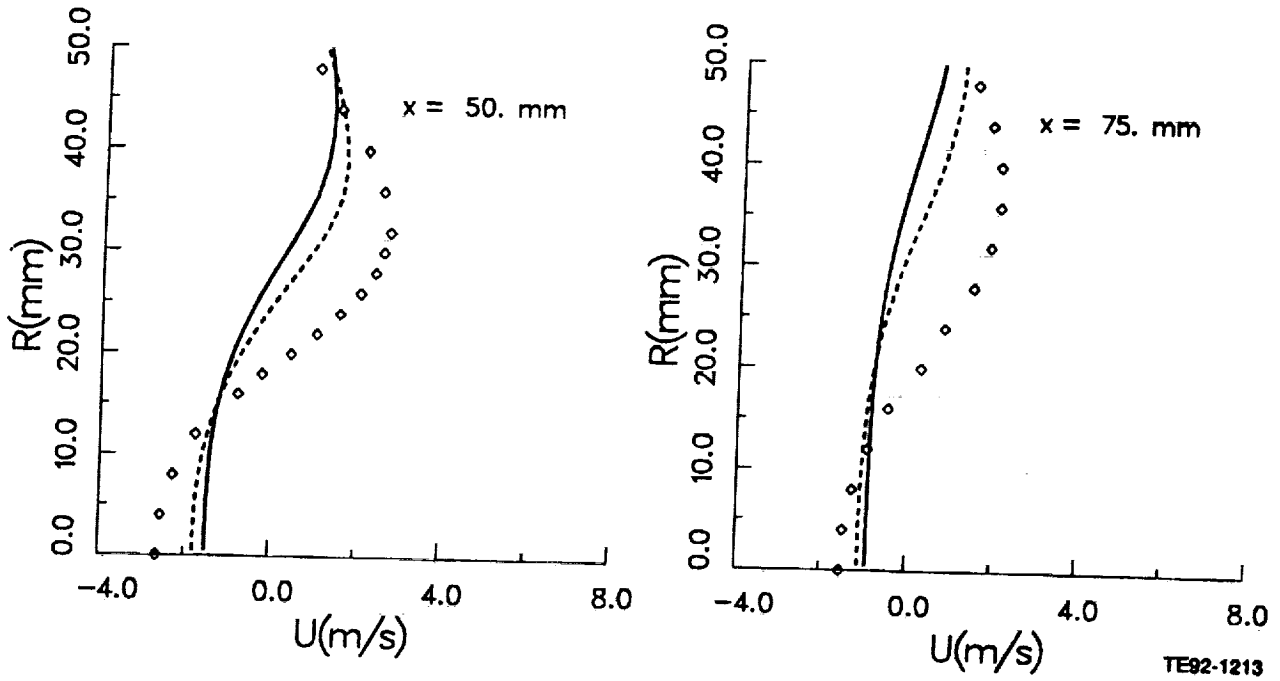


Figure 6.3.1-10. Comparison of predicted mean axial velocity by $k-\epsilon$ with data (3 of 3).

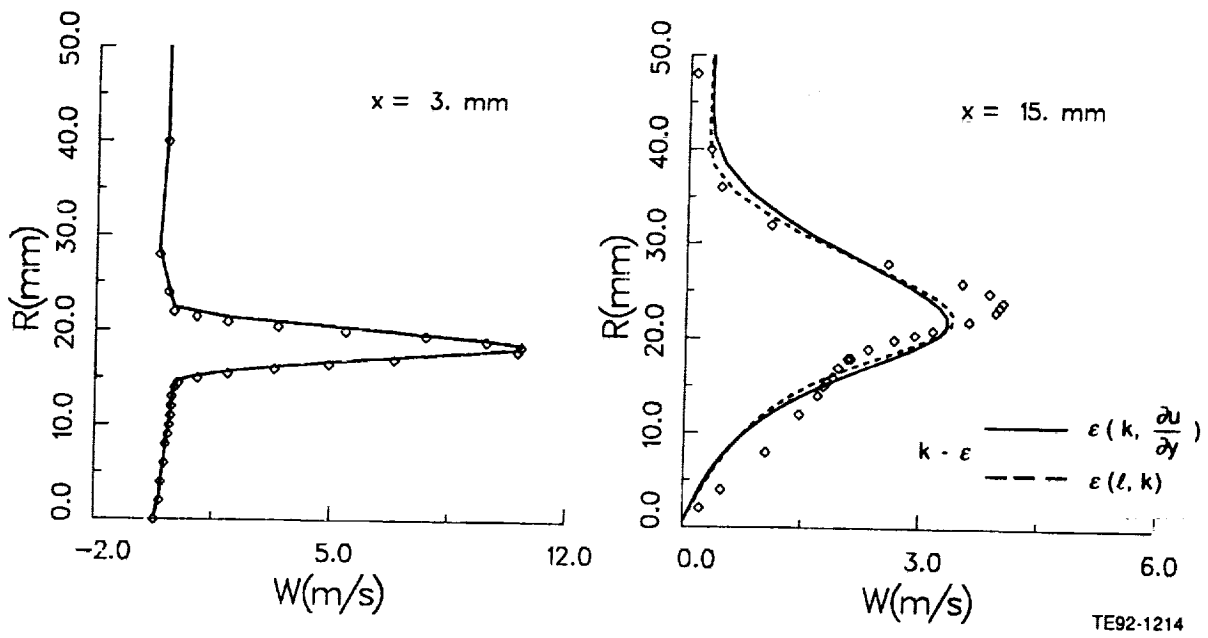


Figure 6.3.1-11. Comparison of predicted mean tangential velocity by $k-\epsilon$ with data (1 of 3).

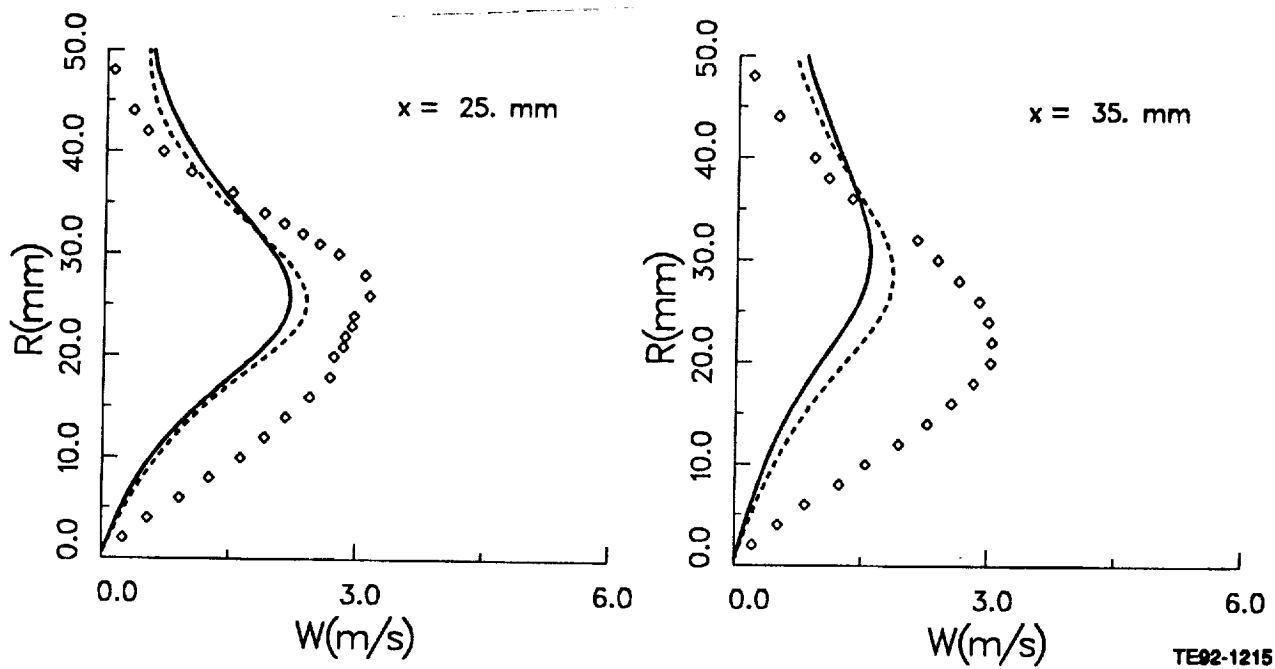


Figure 6.3.1-11. Comparison of predicted mean tangential velocity by k- ϵ with data (2 of 3).

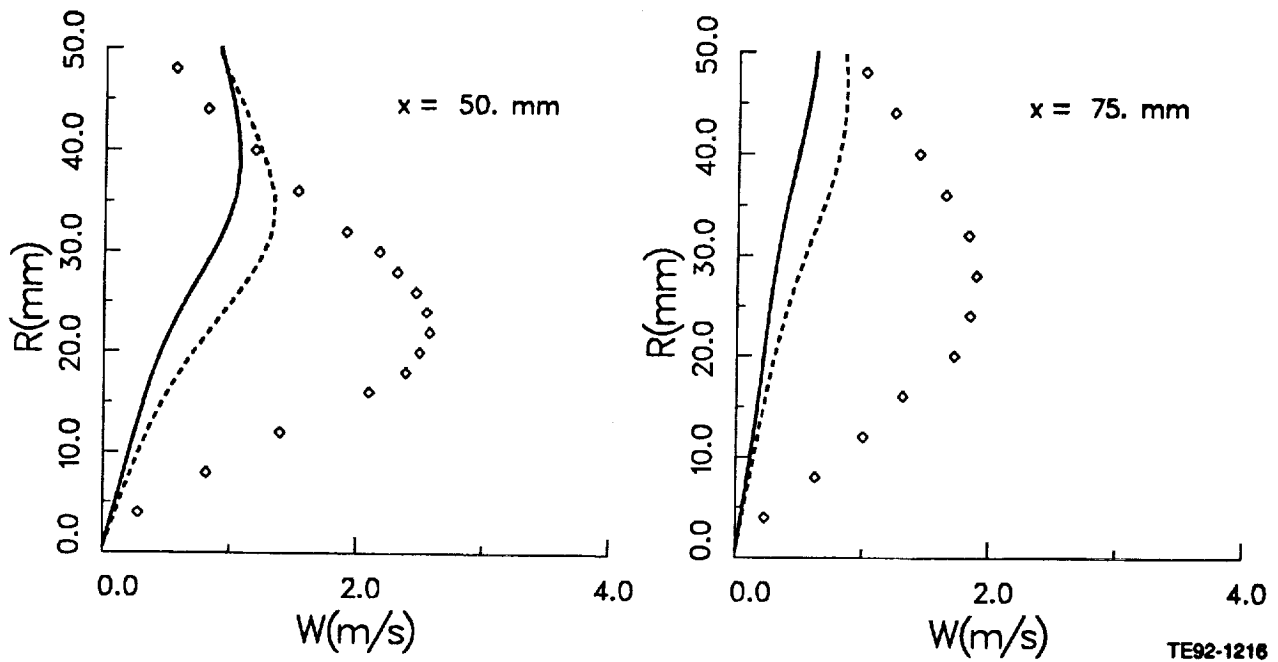


Figure 6.3.1-11. Comparison of predicted mean tangential velocity by k- ϵ with data (3 of 3).

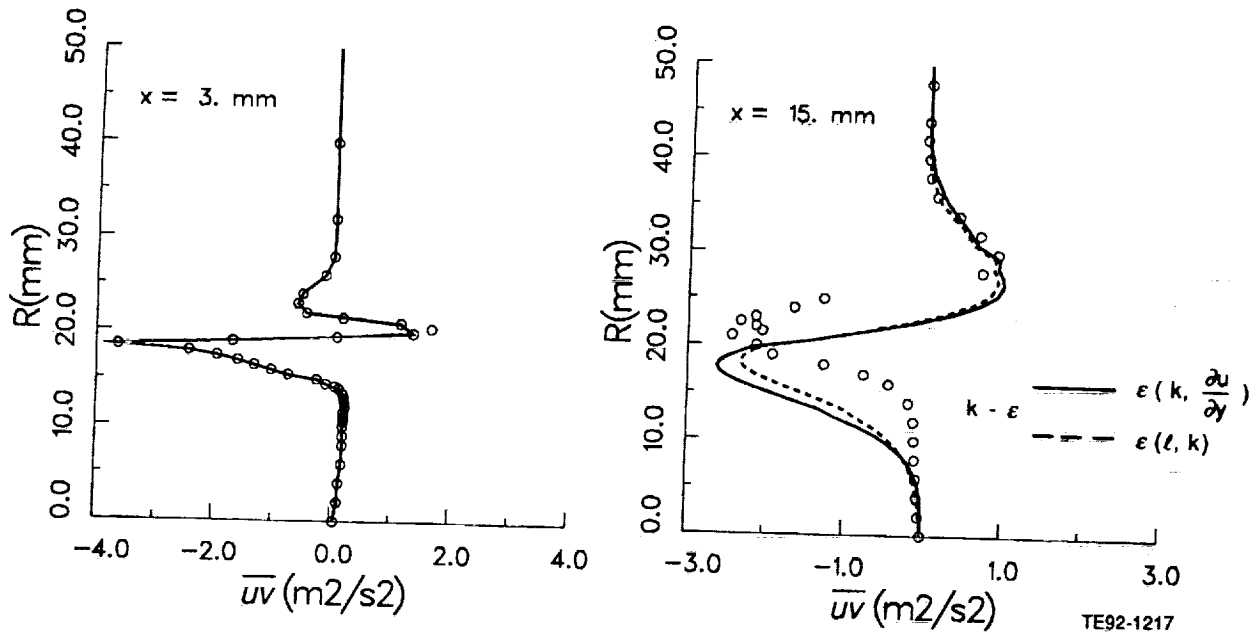


Figure 6.3.1-12. Comparison of predicted turbulent shear stress with data (1 of 3).

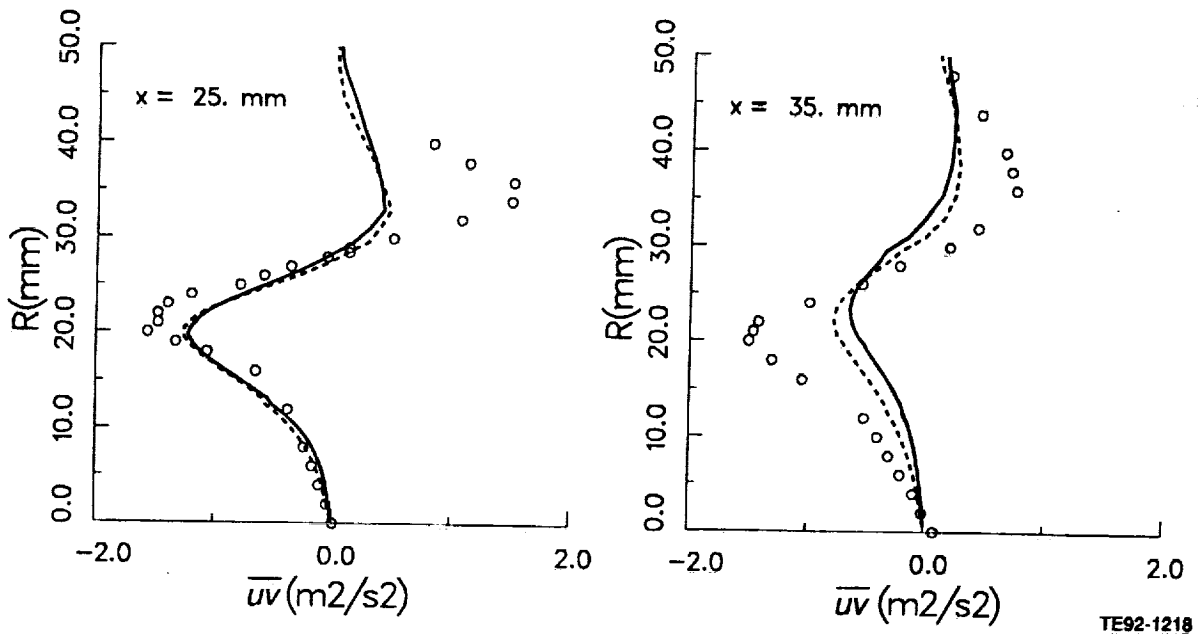


Figure 6.3.1-12. Comparison of predicted turbulent shear stress with data (2 of 3).

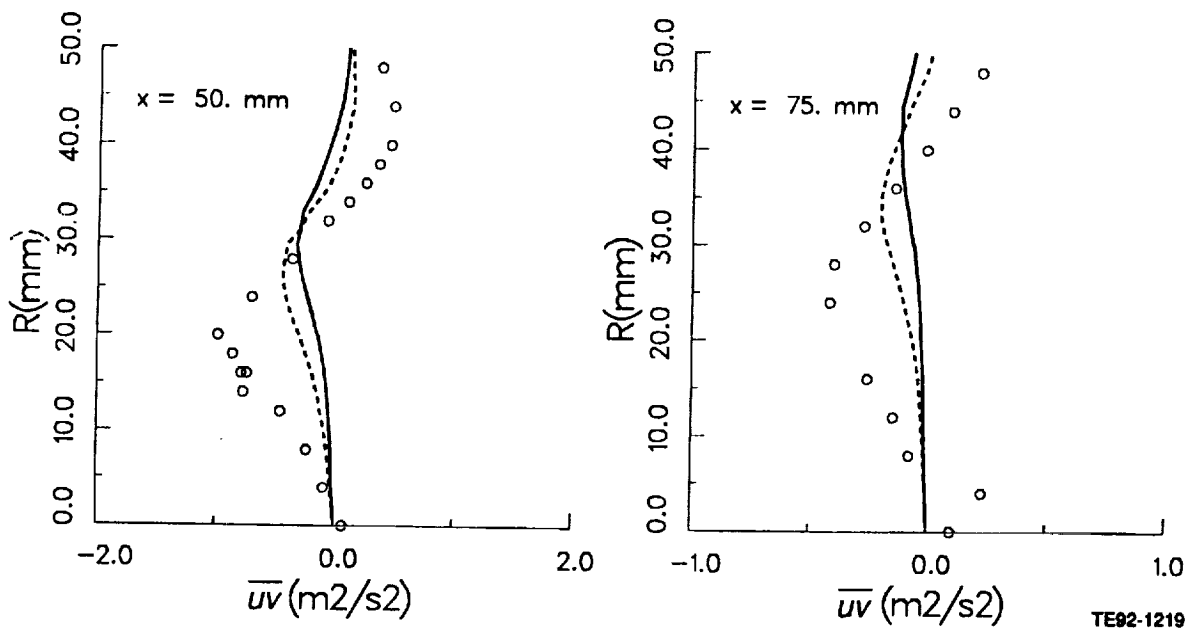


Figure 6.3.1-12. Comparison of predicted turbulent shear stress with data (3 of 3).

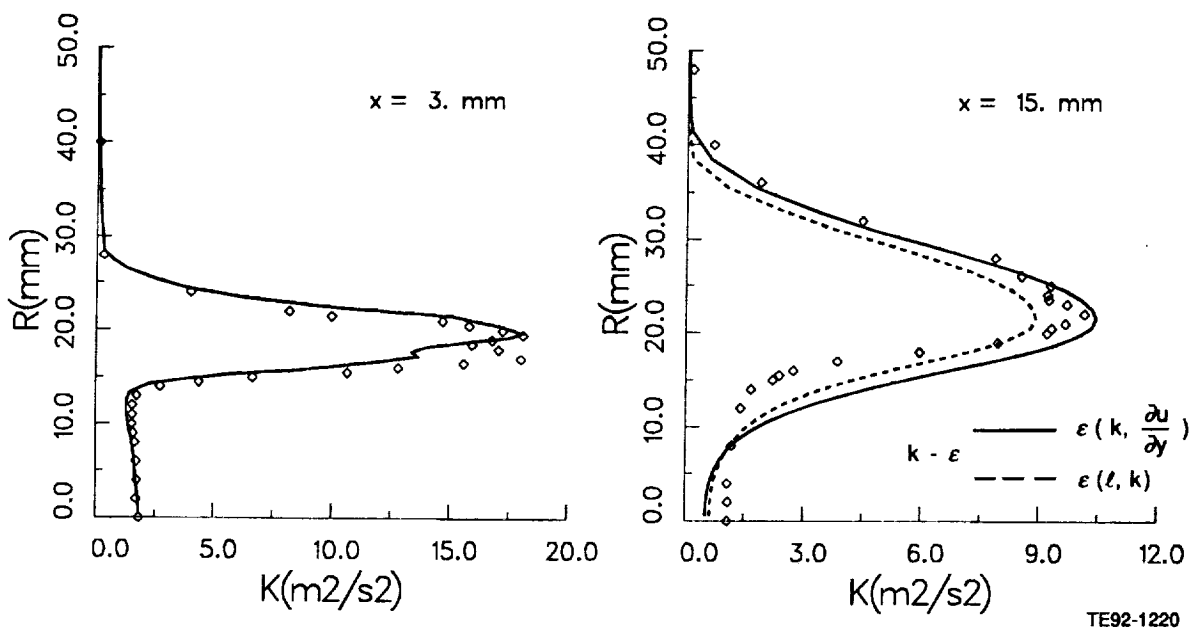
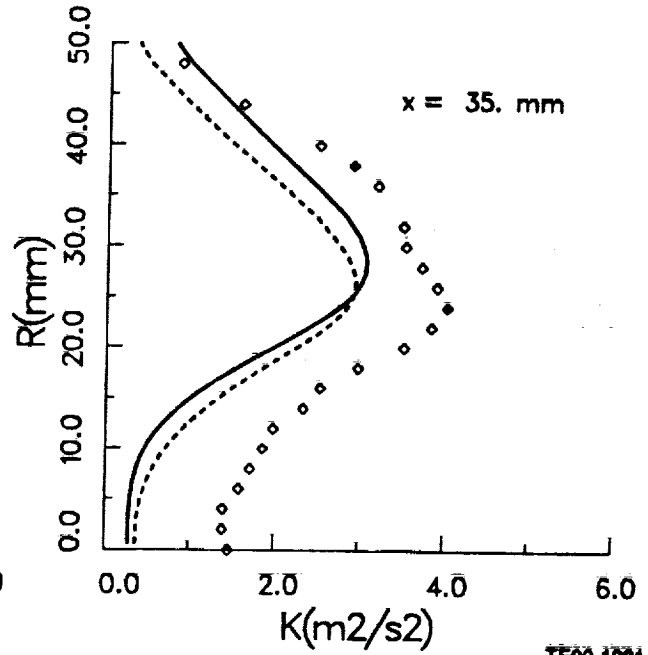
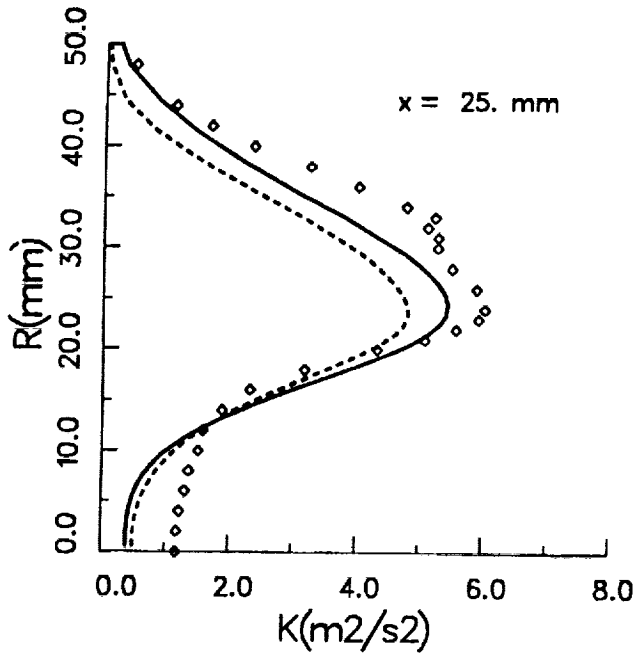
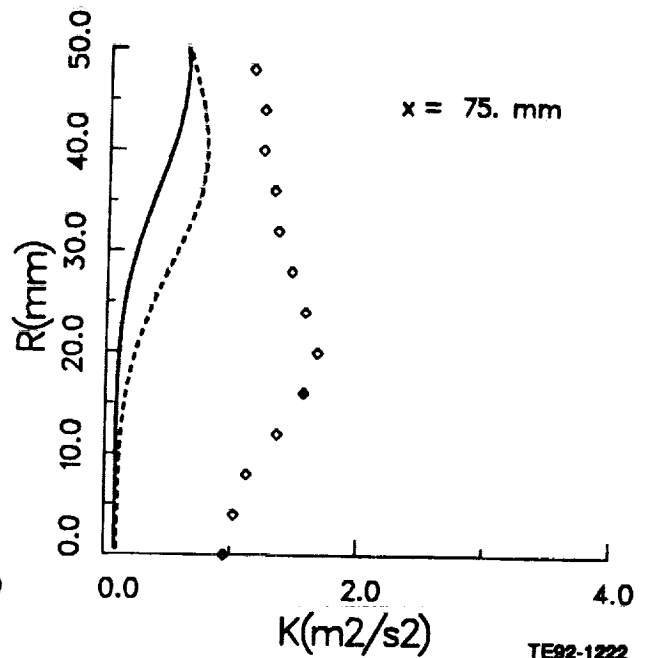
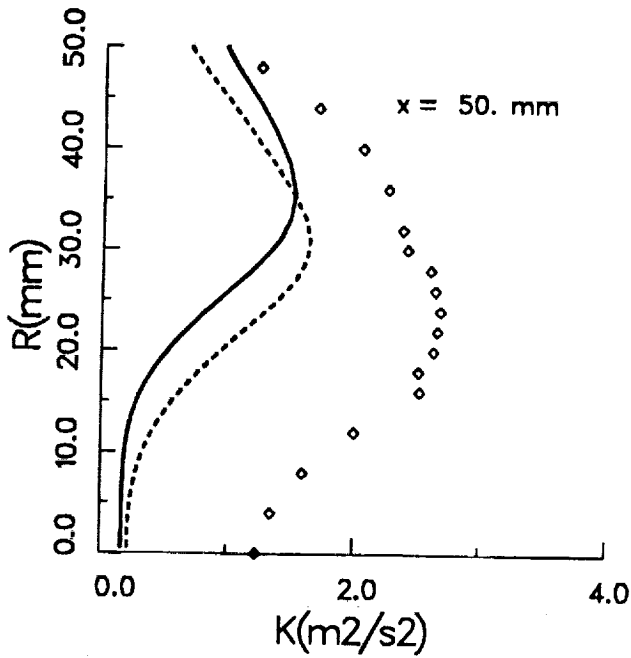


Figure 6.3.1-13. Comparison of predicted turbulent kinetic energy with data (1 of 3).



TE92-1221

Figure 6.3.1-13. Comparison of predicted turbulent kinetic energy with data (2 of 3).



TE92-1222

Figure 6.3.1-13. Comparison of predicted turbulent kinetic energy with data (3 of 3).

6.3.2 Confined Annular Swirling Jet

The predicted mean and turbulence fields obtained from the k-ε, ASM, and DSM closures are compared with the experimental data. The experiments were performed in a modeled laboratory combustor and the complex flow field has an aerodynamically controlled, swirl stabilized recirculation zone. A two-color, two-component laser anemometer system was used to measure the velocity components. At each spatial point, the laser simultaneously measured two orthogonal components of velocity. To get all three components, two scans were taken. One was used to measure U, V, u², v², and uv components, and the other one was able to measure U, W, u², w², and uv components. Thus all three mean and fluctuating velocity components were measured, with U and u² measured twice. Data were obtained at eight axial stations 4, 15, 25, 35, 50, 75, 100, and 150 mm from the exit of the swirler. At each station, between 10 and 20 radial points were scanned, as determined by the desired level of profile resolution. The experimental test parameters are summarized in Table 6.3-III and the sketch of the test section is shown in Figure 6.3.2-1.

A nonuniform grid of 48 x 44 in the axial and radial directions was used for all calculations (Figure 6.3.2-2). A finer grid spacing was used near the inlet, centerline, and in the shear layer. The streamwise and transverse coordinates of the grid points are shown in Table 6.3-IV. The elliptic nature of the transfer equations requires that boundary conditions be specified on the four sides of the solution domain. Four kinds of boundaries need consideration: inlet, axis of symmetry, wall, and outlet. At the inlet boundary, which is located at the first measurement plane (x = 4 mm), the measured profiles of U, V, W, u², v², w², uv, and uw are applied. These profiles are shown in Figure 6.3.2-3. Three different approaches were used to prescribe the inlet dissipation rate. The first approach is based on the assumption of constant length scale and turbulent kinetic energy, namely

$$\epsilon = \frac{k^{1.5}}{0.2 D_j} \quad (66)$$

where D_j is the jet diameter. Here, the macrolength scale of 0.2D_j was estimated through the sensitivity analysis. The second approach is derived from the k-ε eddy viscosity and neglecting the ∂V/∂X term at the inlet to relate the turbulent shear stresses to their corresponding mean strain rates. That is,

$$\epsilon = C_\mu k^2 \frac{\left[\left(\frac{\partial U}{\partial r} \right)^2 + \left(\frac{\partial W}{\partial r} - \frac{W}{r} \right)^2 \right]^{1/2}}{[(\overline{uv})^2 + (\overline{vw})^2]^{1/2}} \quad (67)$$

Table 6.3-III.
Confined annular swirling jet test configurations

R1	13.82 mm
R2	18.35 mm
R3	76.00 mm
h	7.0 mm
U ₀	6.9 m/s
Swirl angle	60
Swirl airflow rate	0.0033 kg/s
Dilute airflow rate	0.272 kg/s

Table 6.3-IV.
Confined annular swirling jet grid definition.

STREAMWISE COORDINATES OF THE GRID

I	DX	X	XU
1	0.000E+00	0.000E+00	0.000E+00
2	7.750E-04	7.750E-04	0.000E+00
3	1.625E-03	2.400E-03	1.550E-03
4	2.050E-03	4.450E-03	3.250E-03
5	2.500E-03	6.950E-03	5.650E-03
6	2.700E-03	9.650E-03	8.250E-03
7	2.938E-03	1.259E-02	1.105E-02
8	3.313E-03	1.590E-02	1.413E-02
9	3.888E-03	1.979E-02	1.768E-02
10	4.588E-03	2.438E-02	2.190E-02
11	5.250E-03	2.963E-02	2.685E-02
12	5.775E-03	3.540E-02	3.240E-02
13	6.238E-03	4.164E-02	3.840E-02
14	6.713E-03	4.835E-02	4.488E-02
15	7.063E-03	5.541E-02	5.183E-02
16	7.200E-03	6.261E-02	5.900E-02
17	7.250E-03	6.986E-02	6.623E-02
18	7.288E-03	7.715E-02	7.350E-02
19	7.300E-03	8.445E-02	8.080E-02
20	7.300E-03	9.175E-02	8.810E-02
21	7.288E-03	9.904E-02	9.540E-02
22	7.275E-03	1.063E-01	1.027E-01
23	7.288E-03	1.136E-01	1.100E-01
24	7.300E-03	1.209E-01	1.173E-01
25	7.300E-03	1.282E-01	1.246E-01
26	7.300E-03	1.355E-01	1.319E-01
27	7.300E-03	1.428E-01	1.392E-01
28	7.300E-03	1.501E-01	1.465E-01
29	7.300E-03	1.574E-01	1.538E-01
30	7.300E-03	1.647E-01	1.611E-01
31	7.300E-03	1.720E-01	1.684E-01
32	7.300E-03	1.793E-01	1.757E-01
33	7.300E-03	1.866E-01	1.830E-01
34	7.300E-03	1.939E-01	1.903E-01
35	7.300E-03	2.012E-01	1.976E-01
36	7.300E-03	2.085E-01	2.049E-01
37	7.300E-03	2.158E-01	2.122E-01
38	7.300E-03	2.231E-01	2.195E-01
39	7.200E-03	2.303E-01	2.268E-01
40	7.200E-03	2.375E-01	2.339E-01
41	7.400E-03	2.449E-01	2.412E-01
42	7.400E-03	2.523E-01	2.487E-01
43	7.325E-03	2.596E-01	2.560E-01
44	7.325E-03	2.670E-01	2.633E-01
45	7.275E-03	2.742E-01	2.706E-01
46	7.275E-03	2.815E-01	2.779E-01
47	7.300E-03	2.888E-01	2.852E-01
48	3.650E-03	2.925E-01	2.925E-01

PART 1 OF 2
 TE92-1223

Table 6.3-IV (cont).

TRANSVERS COORDINATES OF THE GRID

J	DY	Y	YV
1	0.000E+00	0.000E+00	0.000E+00
2	5.000E-04	5.000E-04	0.000E+00
3	1.500E-03	2.000E-03	1.000E-03
4	2.000E-03	4.000E-03	3.000E-03
5	2.000E-03	6.000E-03	5.000E-03
6	2.000E-03	8.000E-03	7.000E-03
7	2.000E-03	1.000E-02	9.000E-03
8	2.000E-03	1.200E-02	1.100E-02
9	2.000E-03	1.400E-02	1.300E-02
10	1.750E-03	1.575E-02	1.500E-02
11	1.250E-03	1.700E-02	1.650E-02
12	1.000E-03	1.800E-02	1.750E-02
13	1.000E-03	1.900E-02	1.850E-02
14	1.000E-03	2.000E-02	1.950E-02
15	1.000E-03	2.100E-02	2.050E-02
16	1.250E-03	2.225E-02	2.150E-02
17	1.750E-03	2.400E-02	2.300E-02
18	2.000E-03	2.600E-02	2.500E-02
19	2.000E-03	2.800E-02	2.700E-02
20	2.000E-03	3.000E-02	2.900E-02
21	2.000E-03	3.200E-02	3.100E-02
22	2.000E-03	3.400E-02	3.300E-02
23	2.000E-03	3.600E-02	3.500E-02
24	2.000E-03	3.800E-02	3.700E-02
25	2.000E-03	4.000E-02	3.900E-02
26	2.000E-03	4.200E-02	4.100E-02
27	2.000E-03	4.400E-02	4.300E-02
28	2.000E-03	4.600E-02	4.500E-02
29	2.000E-03	4.800E-02	4.700E-02
30	2.000E-03	5.000E-02	4.900E-02
31	2.000E-03	5.200E-02	5.100E-02
32	2.000E-03	5.400E-02	5.300E-02
33	2.000E-03	5.600E-02	5.500E-02
34	2.000E-03	5.800E-02	5.700E-02
35	2.000E-03	6.000E-02	5.900E-02
36	2.000E-03	6.200E-02	6.100E-02
37	2.000E-03	6.400E-02	6.300E-02
38	2.000E-03	6.600E-02	6.500E-02
39	2.000E-03	6.800E-02	6.700E-02
40	2.000E-03	7.000E-02	6.900E-02
41	2.000E-03	7.200E-02	7.100E-02
42	2.000E-03	7.400E-02	7.300E-02
43	1.500E-03	7.550E-02	7.500E-02
44	5.000E-04	7.600E-02	7.600E-02

PART 2 OF 2
TE92-1223

where $C_\mu = 0.09$ is a model constant. The third approach, based on the assumption of local equilibrium for turbulence energy ($P_k = \rho \epsilon$), Boussinesque approximation, isotropic effective viscosity, and ignoring streamwise velocity gradient, can be written as

$$\epsilon = \sqrt{C_\mu} k \left[\left(\frac{\partial U}{\partial r} \right)^2 + \left(\frac{\partial W}{\partial r} - \frac{W}{r} \right)^2 \right]^{1/2} \quad (68)$$

At the axis of symmetry, the radial velocity, shear stresses, and radial gradients of other variables are set to zero. All streamwise gradients are presumed zero in the exit plane of the calculation domain except for axial velocity, which needs to be corrected to satisfy integral mass balance. The conventional logarithmic law, which is based on the local equilibrium assumption, is applied to determine the wall shear stress components in the axial and tangential directions. These shear stresses are used as boundary conditions for U and W momentum, as well as for the uv and rw equations. The boundary conditions for normal stresses are imposed through the modification of their production terms using the new calculated wall shear stresses.

The computational domain extends from the first experimental location ($x = 4$ mm) to 300 mm downstream of the jet exit. The reason for this selection was to prevent recirculation at the exit. Since the measured flow does not show any x dependence at $x > 150$ mm, the specified condition, $\partial/\partial x = 0$, at the exit plane of the calculation domain is realistic. The coupled equations and boundary conditions are solved numerically in a sequential manner using the staggered grids for velocities and shear stresses (Figure 6.3.2-4). The main advantage of staggering the locations of stresses is to enhance numerical stability, a result of high coupling between the shear stresses and related mean strains.

The present calculations have been made using the higher order numerical scheme, and the calculated results are essentially free of numerical diffusion. Therefore, the discrepancies between the experimental data and the predictions can be attributed to two sources: improper boundary conditions at the inlet plane and the deficiencies of the turbulence model. As regards the inlet conditions, all quantities except the dissipation rate (ϵ) were prescribed from the measurement. Uncertainties in the derivation of the ϵ profile, however, would adversely affect the calculations at downstream locations. In an attempt to assess the importance of inlet dissipation rate (ϵ_{in}) on flow field prediction, three different approaches (Equations 66, 67, and 68) were followed to determine ϵ values from the measured quantities. The inlet ϵ profiles for these cases are shown in Figure 6.3.2-5 and have been normalized by the inlet mean velocity (U_0) and pipe radius (R_3).

Overall, the major differences among the inlet dissipation profiles appeared in the peak and the centerline regions. Comparisons of the predicted mean velocities and turbulence quantities obtained from the $k-\epsilon$ model with measurement are shown in Figures 6.3.2-6 through 6.3.2-9. It is noted that the use of inlet dissipation calculated from the strain rate and shear stress resulted in higher peak and centerline velocities in upstream planes. However, the recirculation region has been better predicted as flow proceeds towards the downstream region. There are significant differences among the calculated turbulent kinetic energy and shear stress profiles. The main discrepancy has arisen in prediction of the maximum values in the shear layer.

Comparisons of the predicted mean velocities and Reynolds stresses profiles using the DSM closure are presented in Figures 6.3.2-10 through 6.3.2-13. These profiles have been normalized by the inlet velocity and pipe radius. Above $r/R_3 > 0.5$, the flow field is similar to plug flow created by the strong coflow. This region is not the focus of our study and is not shown in the figures. The use of ϵ_{in} profiles derived from the constant length-scale assumption (Equation 66) and the equilibrium assumption (Equation 68) resulted in similar predictions outside the recirculation zone. However, the calculated flow field with ϵ_{in} obtained from the shear stress and strain rate (Equation 67) showed somewhat different behavior. This is related mainly to the maximum value of the inlet ϵ , which has been changed considerably. The variations of the ϵ_{in} profiles near the centerline also affect the prediction of the reverse flow region, although the Reynolds stresses and dissipation rate are significantly smaller near the centerline, compared to the shear region. The uncertainties in the evaluation of velocity gradients may lead to errors in ϵ_{in} values as well. It must be pointed out that, in a similar nonswirling jet configuration, the flow field was found to be less sensitive to the magnitude of ϵ_{in} . The differences between the ϵ_{in} calculated by various methods were larger for the swirling flow case than the nonswirling case. The effects of ϵ_{in} on shear stress are serious near the inlet, where the central recirculation is formed. In comparison with the data, the locations of the maximum and minimum have been shifted in the developing region of the flow field. In the outer part of

the recirculation zone, where the effect of coflow is more pronounced, and near the axis of symmetry, where the velocity gradient is negligible in the radial direction, the discrepancies among the calculations are in fact diminished. The peak values are the main differences that appear using various inlet ϵ distributions. When the inlet ϵ are found from Equations 66 and 68, the predicted turbulence intensity profiles are similar to the exhibited data trend. However, a wide disparity exists between these calculations and the calculations with ϵ_{in} obtained from Equation 67. The turbulent normal stresses are decreased due to an excessive dissipation rate at the inlet. This results in an insufficient diffusion effect and therefore an inaccurate prediction of the velocity profile.

Effects of the pressure-strain correlation model on mean and turbulence fields are also analyzed. The inlet dissipation rate is calculated using a constant length-scale assumption (Equation 66). The relative merits of the four different pressure redistribution models on ASM closures have been examined in detail by Nikjooy and So (1987). Their results indicate that the inability of the second-moment closure to correctly resolve the turbulence field could be attributed, to a large extent, to the modeling of the ϕ_{ij} term. For swirling flows, the redistribution of turbulence by fluctuating pressure is bound to be different from that for the corresponding nonswirling flows. A vast range of values have been suggested for C_1 and C_2 by different researchers. However, most choices of C_1 and C_2 gather close to the line $(1 - C_2)/C_1 = 0.23$ (Launder, 1989). For a simple shear flow in local equilibrium condition the Reynolds stresses are a function of $(1 - C_2)/C_1$ only. The original work of Naot et al (1970) neglected the return to isotropy process (ϕ_{ij1} model constant). Conversely, Donaldson's proposal (1969) totally ignores the ϕ_{ij2} process and just includes a contribution from the ϕ_{ij1} process, with a large model constant of $C_1 = 5$. Recently, Gibson and Younis (1986) argued that, for swirling flows, the constants for ϕ_{ij} models should be modified. They proposed a simple modification of model constants, $C_1 = 3.0$ and $C_2 = 0.3$, a choice that emphasizes ϕ_{ij1} more than ϕ_{ij2} . This choice is based on the observation that swirling flows are better predicted with this combination. These values were used for the calculations shown in Figures 6.3.2-10 through 6.3.2-13.

Three different model constants for C_1 and C_2 have been examined in this study. These are $C_1 = 3.0$ and $C_2 = 0.3$ (Gison and Younis, 1986), $C_1 = 1.8$ and $C_2 = 0.6$ (Launder, 1989), and $C_1 = 5.0$ and $C_2 = 0.0$ (Donaldson, 1969). The predictions of mean axial and tangential velocity profiles using these three models are shown in Figures 6.3.2-14 and 6.3.2-15. There are substantial differences between the measured profiles and the calculations with the second model, which shows less mixing near the centerline, causing the reverse flow to persist. There is, correspondingly, a slowing down in the diminution of the swirl velocity. As a result, unrealistic recirculation length has been predicted. The mean velocity fields predicted by the Gibson and Younis' model and Donaldson's model are almost identical and are in complete accord with experiment near the centerline, while the swirl velocity is well predicted at most of the locations. With a constant $C_2 = 0$ ($\phi_{ij2} = 0$), the results obtained for $C_1 = 1.5 - 10$ were all nearly the same. But with $C_2 \neq 0$, convergence was obtained only for certain combinations of C_1 and C_2 satisfying $(1 - C_2)/C_1 = 0.2 - 0.35$. However, the results were different. This seems to suggest that for $C_2 = 0$ results are insensitive to C_1 , but when $C_2 \neq 0$ the combination of C_1 and C_2 is important. It must be pointed out that the slow part of the pressure-strain rate term by itself did not fully account for all of the stress-component interactions. Therefore selection of an appropriate model for ϕ_{ij} is crucial for swirling flow calculations. A more sophisticated version of ϕ_{ij2} is the linear quasi-isotropic (QI) model (Equation 22). This model (Equation 22) includes both the symmetric and antisymmetric mean strain effects on redistribution modeling. The QI model achieves reasonable success in thin shear flows but shows no significant advantage over the isotropization production (IP) model to swirling flows. Comparison of mean axial velocity profiles that resulted from the IP and QI models at location of 35 mm is shown in Figure 6.3.2-16. The solutions were obtained for $C_1 = 1.8$ and $C_2 = 0.6$. Some minor improvements are observed near the centerline. However, the QI model still gives inferior results in comparison with the Gibson and Younis' model. This indicates that the additional linear terms, in the present form, did not result in superior predictions. Similar observations were made for tangential velocity and Reynolds stress components.

The predicted stress components are shown in Figures 6.3.2-17 through 6.3.2-20. Despite the significant differences that appeared in the mean velocity fields, the Reynolds stress profiles are nearly the same. This can be explained by noting that the momentum equations consist of the Reynolds stress gradients. Although the stresses look similar, careful examination reveals differences in their gradients. Thus any minor variation in the Reynolds stress gradients will result in significant changes in mean velocities. To verify this point, a calculation was made using the Reynolds stresses obtained from one solution ($C_1 = 5$ and $C_2 = 0$) and the mean velocities from another solution ($C_1 = 1.8$ and $C_2 = 0.6$). By freezing the stresses' field and solving only the momentum equations, the velocity field corresponding to $C_1 = 5.0$ and $C_2 = 0$ was obtained. This clearly shows that the differences in the Reynolds stress gradients are responsible for differences in the velocity field.

Comparisons of the mean and turbulence quantities predicted by the ASM and DSM closures with the measured values are presented in Figures 6.3.2-21 through 6.3.2-24. The results have been shown for four streamwise locations, namely, $x = 15, 25, 35,$ and 50 mm. The pressure redistribution model used for these calculations involved only the return-to-isotropy part ($\phi_{ij2} = 0$) with a constant $C_1 = 5.0$ in the ϕ_{ij1} model. In general, the results of the ASM and DSM are very similar in the near field ($x \approx 15$ mm). At subsequent downstream locations, there are substantial differences between the two models in the prediction of centerline velocity and the recirculation length. Use of the ASM promotes earlier decay of the centerline velocity relative to the DSM and fails to display the size of the experimental recirculation zone. The reason is attributed to the turbulent diffusion process, which depends on the Reynolds stress gradients. Despite the fact that the predicted normal stresses look similar, their gradient profiles are different. In the outer flow region, the ASM and DSM predict similar axial velocity distributions. With regard to the comparison between measurements and calculations, the predictions by ASM seem to be slightly better than DSM for tangential velocity. Examination of the calculated u^2 profiles indicates that the ASM's results mimic the experimental data better as flow proceeds toward the downstream region. The maximum turbulence intensity predicted by both models is very close and is slightly underpredicted by both models only at $x = 25$ mm. As regards the turbulent shear stresses, uv and uw , the calculated profiles are similar to the exhibited data trend. The measurement shows a constant increase of the uw values near the centerline from $x = 15$ mm to $x = 75$ mm, except at $x = 25$ mm. This sudden change is considered to be an experimental error. Overall, the shear stresses were qualitatively well predicted and their behaviors are in agreement with the measured profiles, although the maximum values were shifted slightly. In general, apart from the centerline velocity profile, the ASM closure performed a reasonable job in predictions of the tangential velocity and Reynolds stress components.

The present study serves to illustrate three very important points in the development of turbulence closures for calculation of complex swirling flows. First, the inlet ϵ profile was found to be highly influential on the stress field prediction. The mean velocity field, to some extent, is affected by the choice of ϵ_{in} especially in the recirculation zone. Second, the model assumptions for the pressure-strain correlations are not very satisfactory and need improvement. The return-to-isotropy part of the ϕ_{ij} by itself could predict important features of the flow. However, the rapid part, ϕ_{ij2} , was found to be influential for swirling flow, and the emphasis should be placed on developing a better combination of ϕ_{ij1} and ϕ_{ij2} . Finally, the ASM closure appeared to be unsuitable for prediction of the central recirculation zone. The ASM application, however, resulted in good tangential velocity and stresses profiles. In general, for such cases, a DSM closure is more suitable.

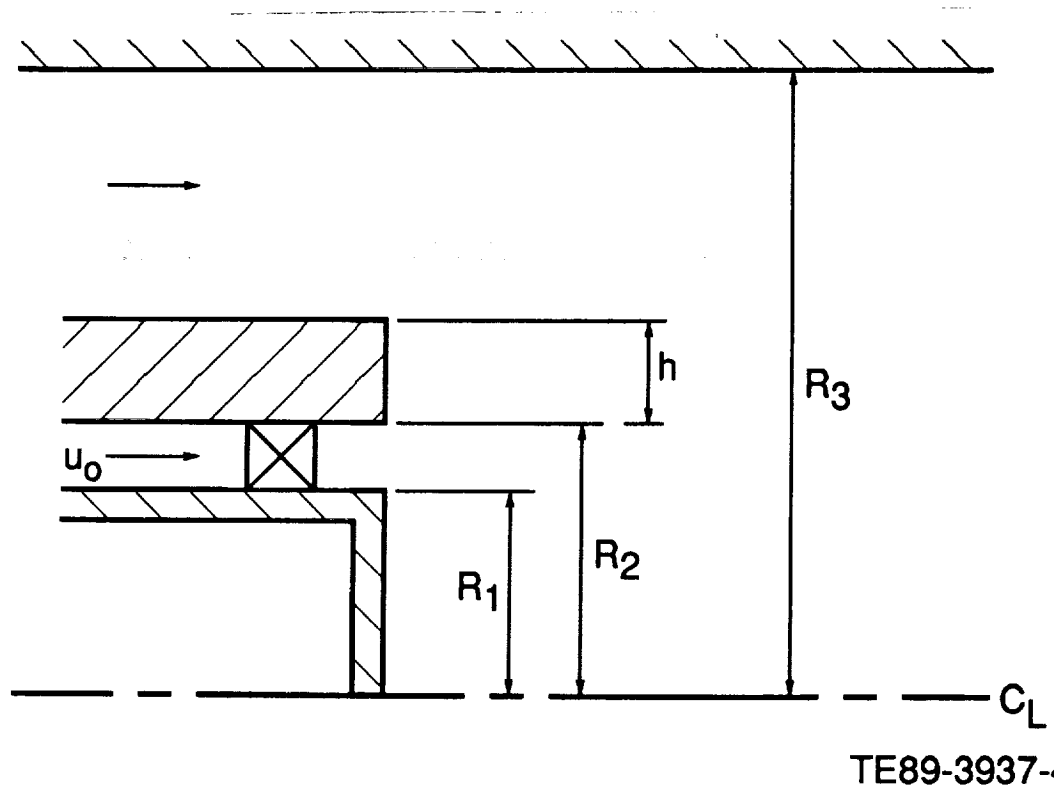
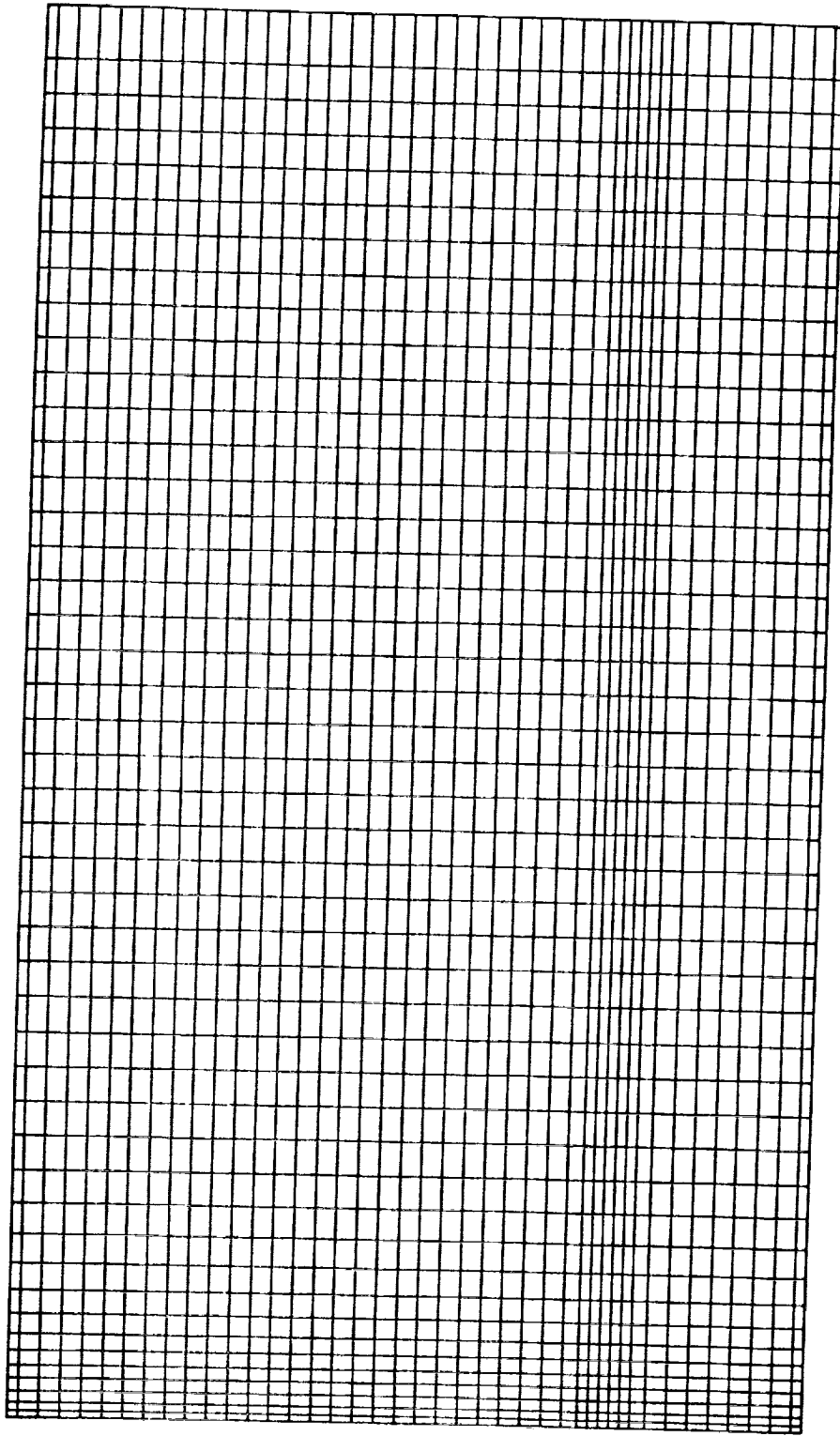


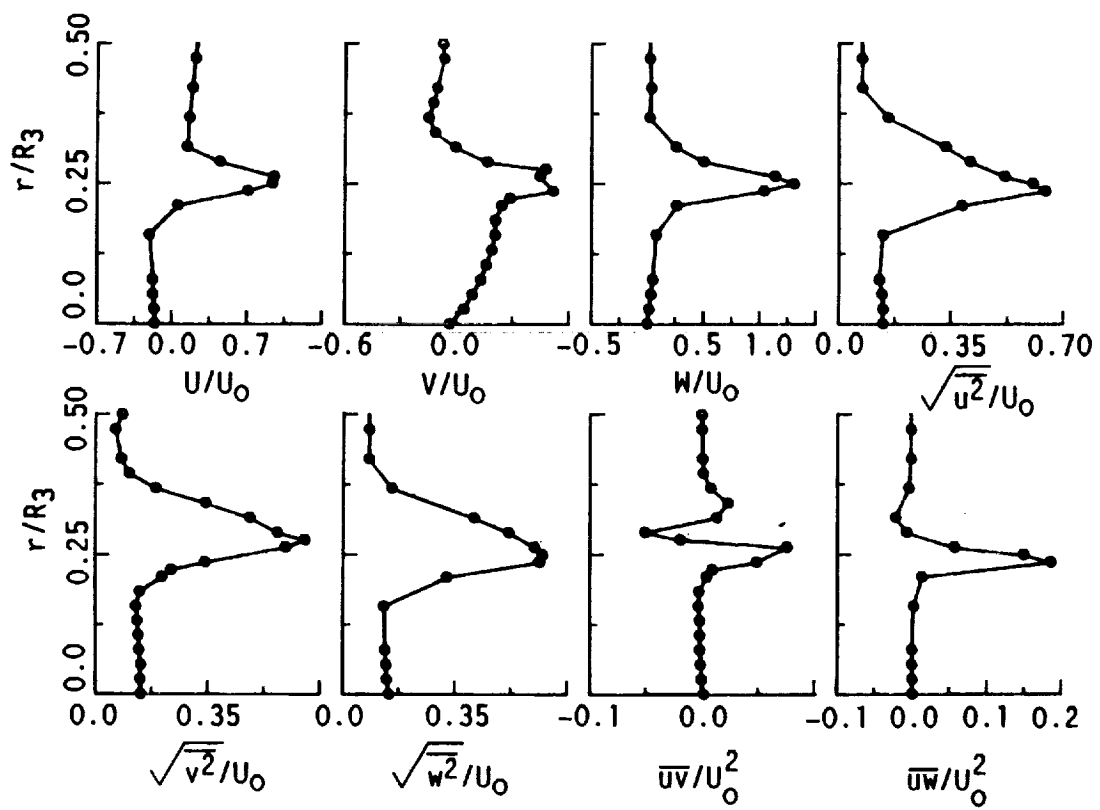
Figure 6.3.2-1. Confined annular swirling jet - geometrical details.

TE89-3937-4



TE92-1224

Figure 6.3.2-2. Confined annular swirling jet grid layout.



TE89-3938

Figure 6.3.2-3. Measured profiles at the inlet plane ($x = 4\text{mm}$).

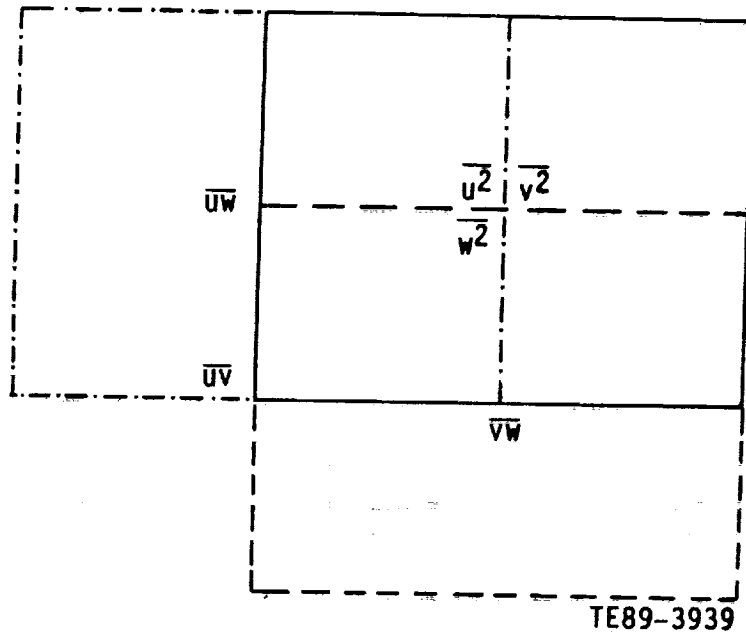


Figure 6.3.2-4. Staggered arrangement of Reynolds stress components.

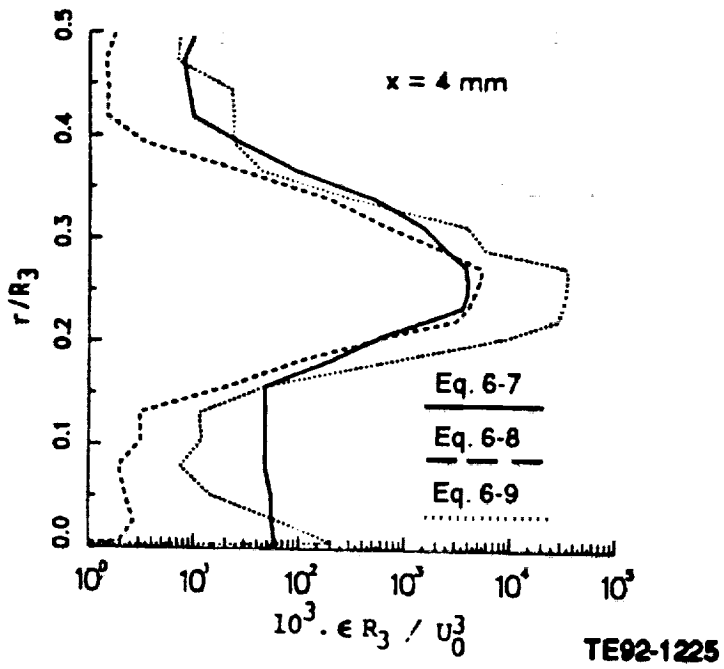
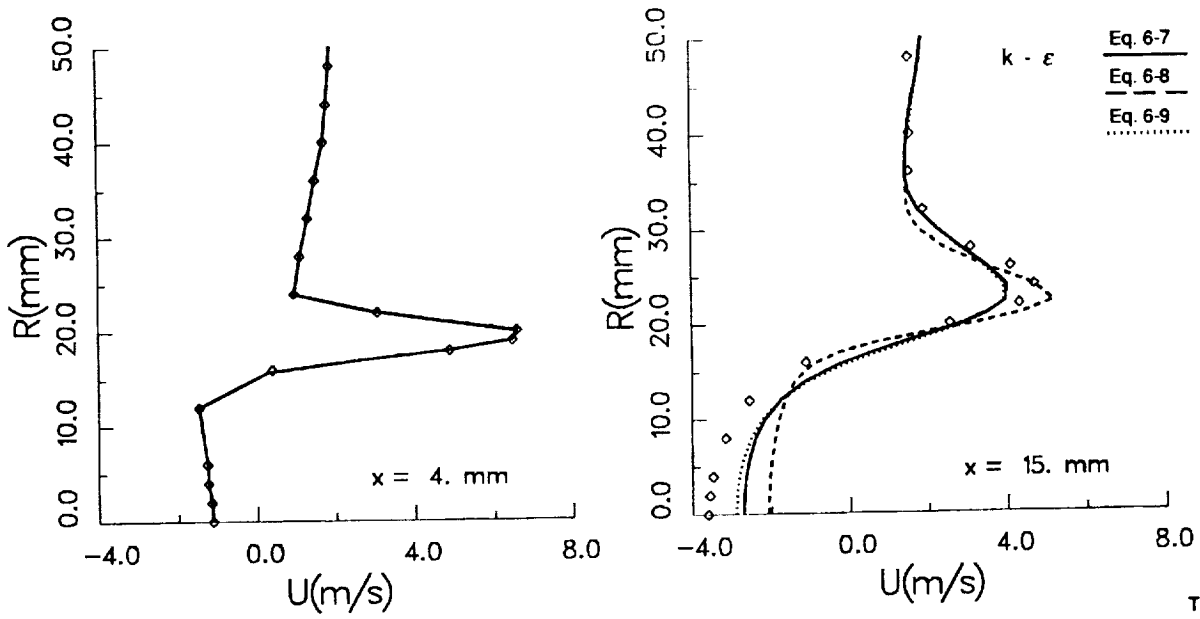
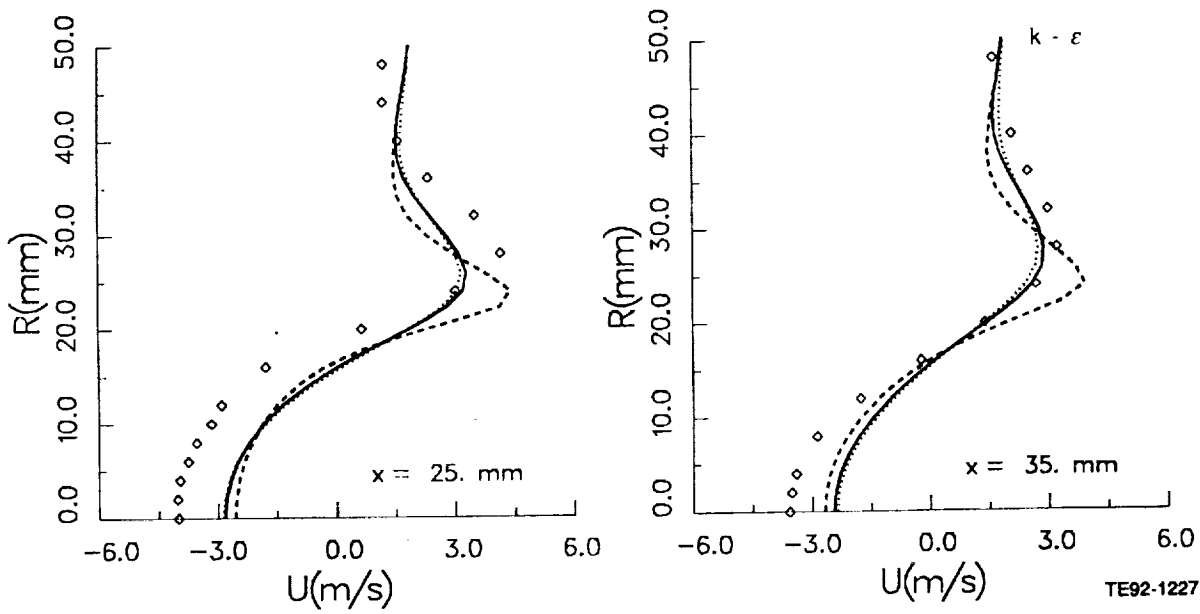


Figure 6.3.2-5. Inlet dissipation profiles.



TE92-1226

Figure 6.3.2-6. Comparison of calculated mean axial velocity by $k-\epsilon$ model using various ϵ_{in} (1 of 4).



TE92-1227

Figure 6.3.2-6. Comparison of calculated mean axial velocity by $k-\epsilon$ model using various ϵ_{in} (2 of 4).

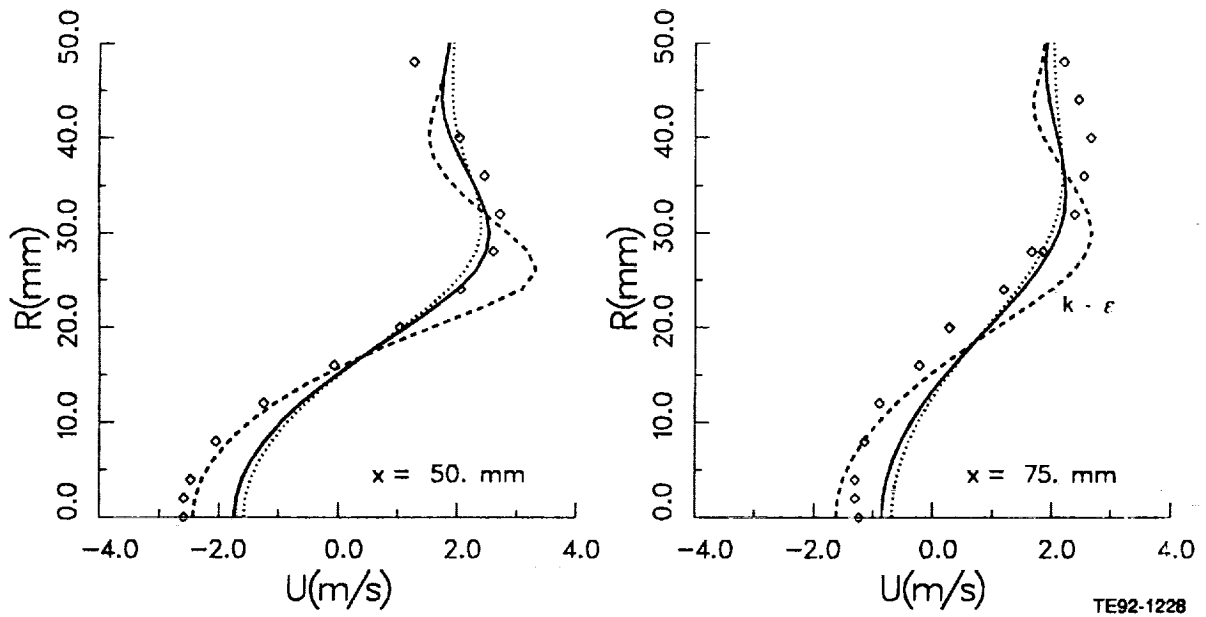


Figure 6.3.2-6. Comparison of calculated mean axial velocity by $k-\epsilon$ model using various ϵ_{in} (3 of 4).

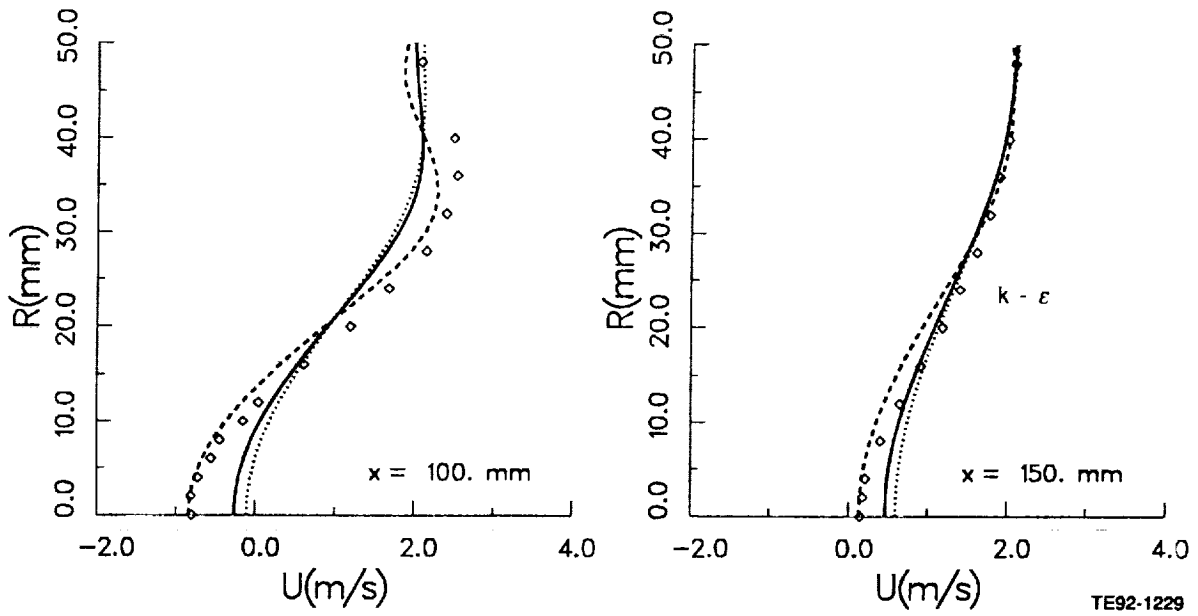


Figure 6.3.2-6. Comparison of calculated mean axial velocity by $k-\epsilon$ model using various ϵ_{in} (4 of 4).

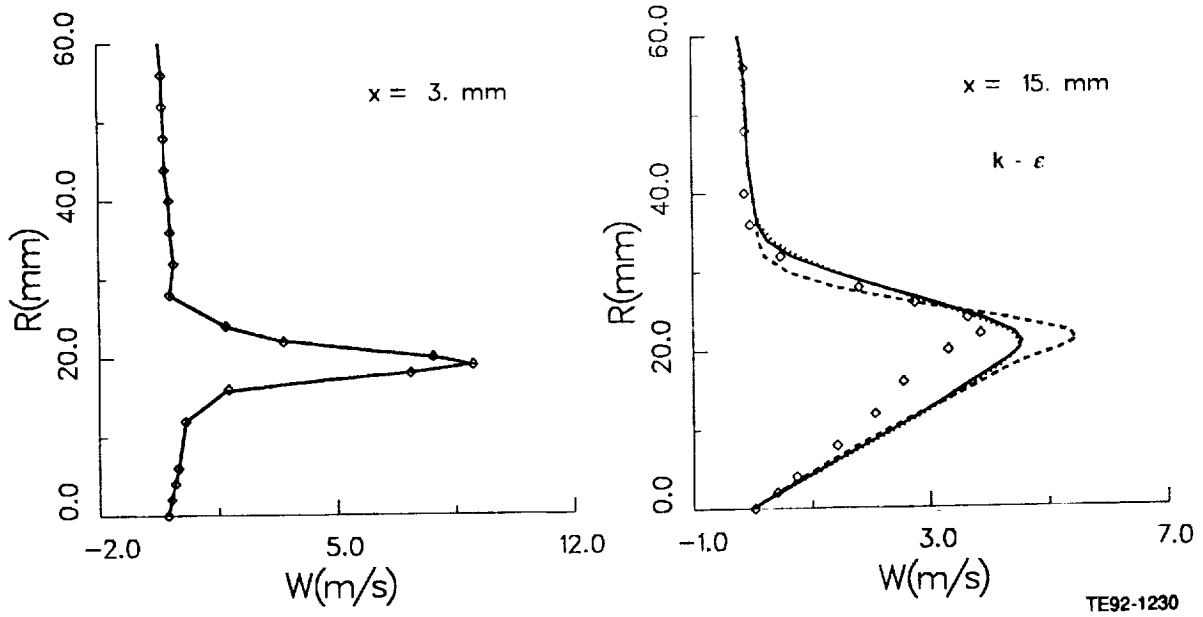


Figure 6.3.2-7. Comparison of calculated mean tangential velocity by k- ϵ model using various ϵ_{in} (1 of 4).

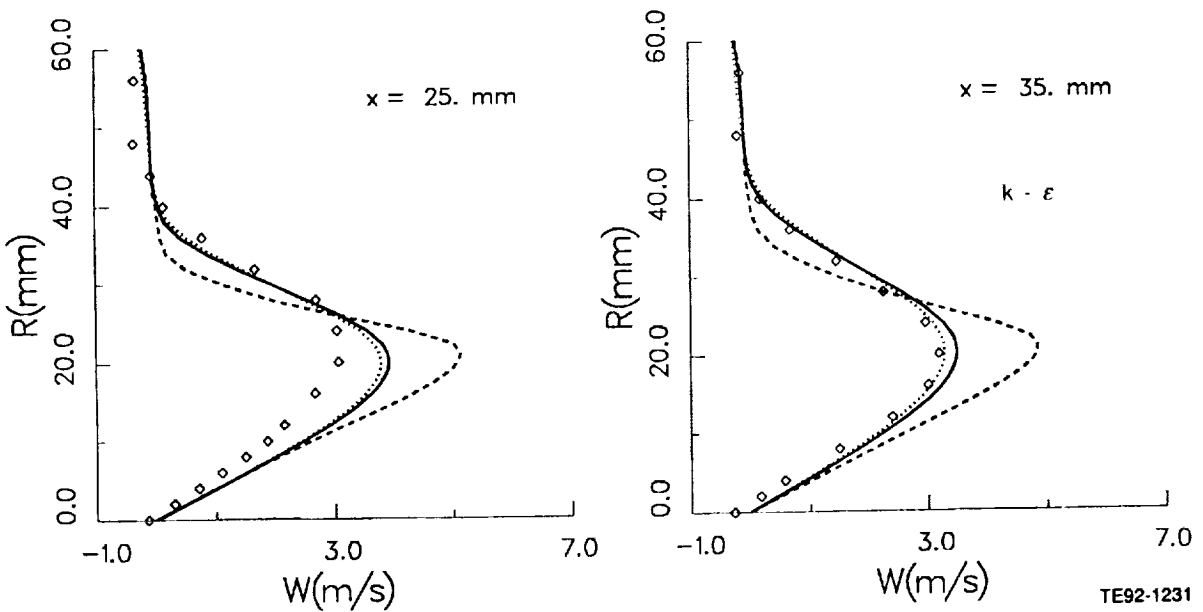


Figure 6.3.2-7. Comparison of calculated mean tangential velocity by k- ϵ model using various ϵ_{in} (2 of 4).

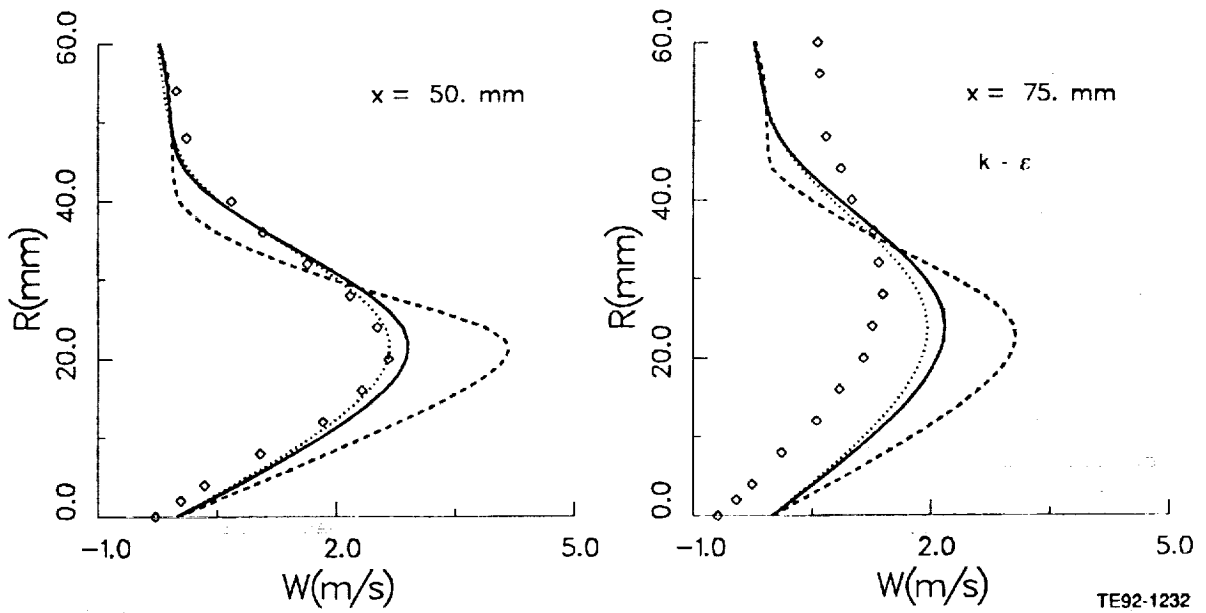


Figure 6.3.2-7. Comparison of calculated mean tangential velocity by $k-\epsilon$ model using various ϵ_{in} (3 of 4).

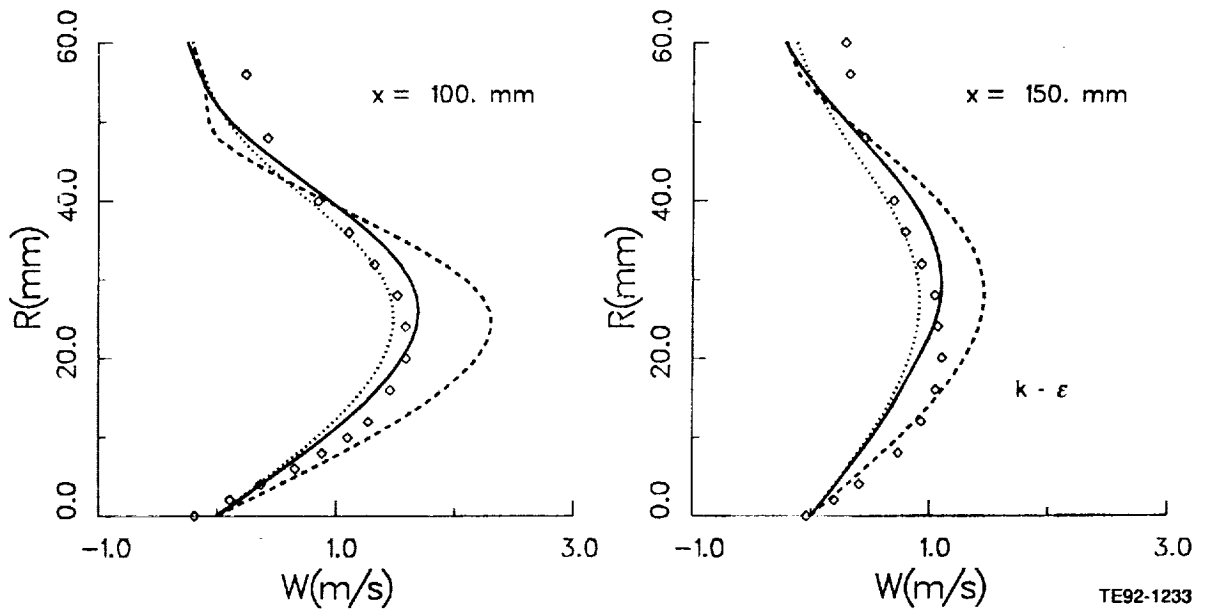


Figure 6.3.2-7. Comparison of calculated mean tangential velocity by $k-\epsilon$ model using various ϵ_{in} (4 of 4).

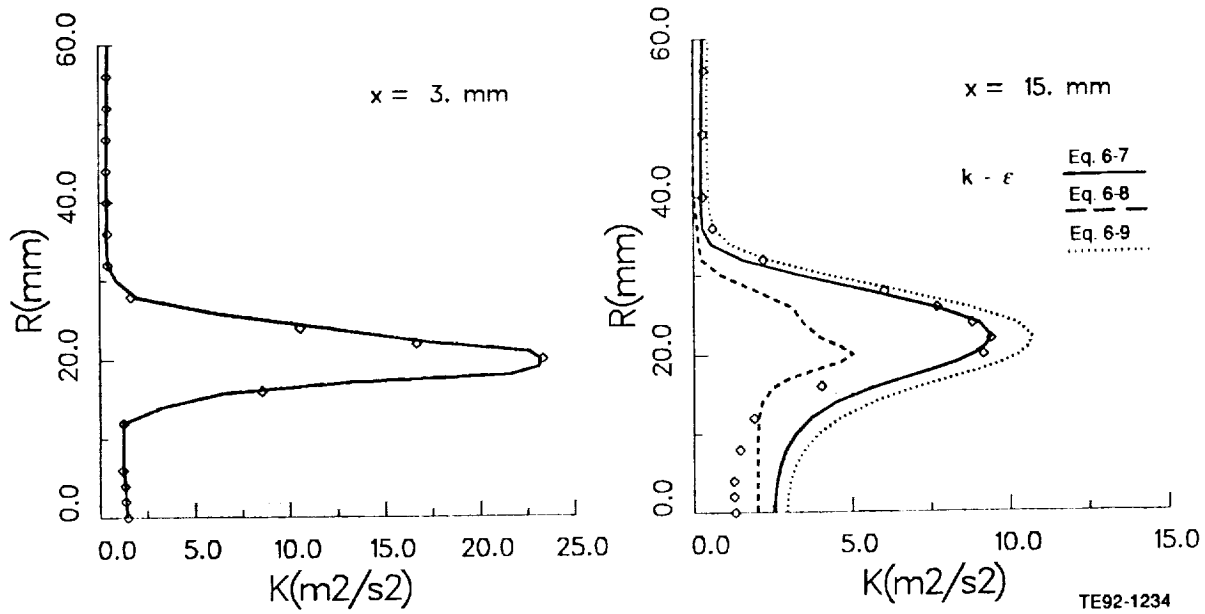


Figure 6.3.2-8. Comparison of calculated turbulent kinetic energy by $k-\epsilon$ model using various ϵ_{in} (1 of 4).

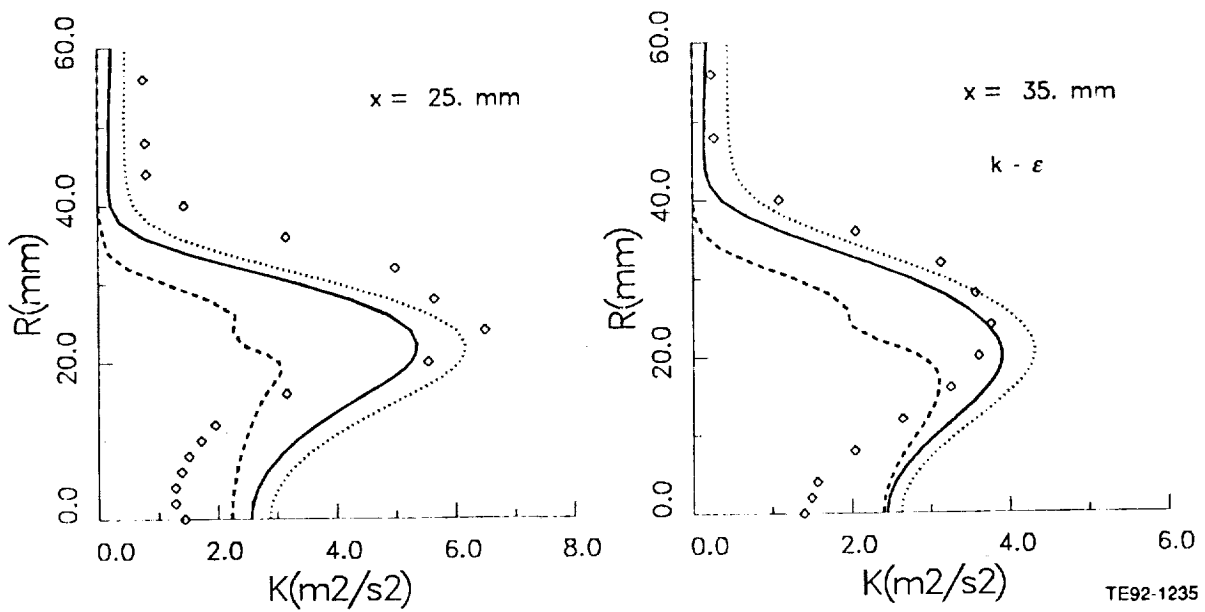


Figure 6.3.2-8. Comparison of calculated turbulent kinetic energy by $k-\epsilon$ model using various ϵ_{in} (2 of 4).

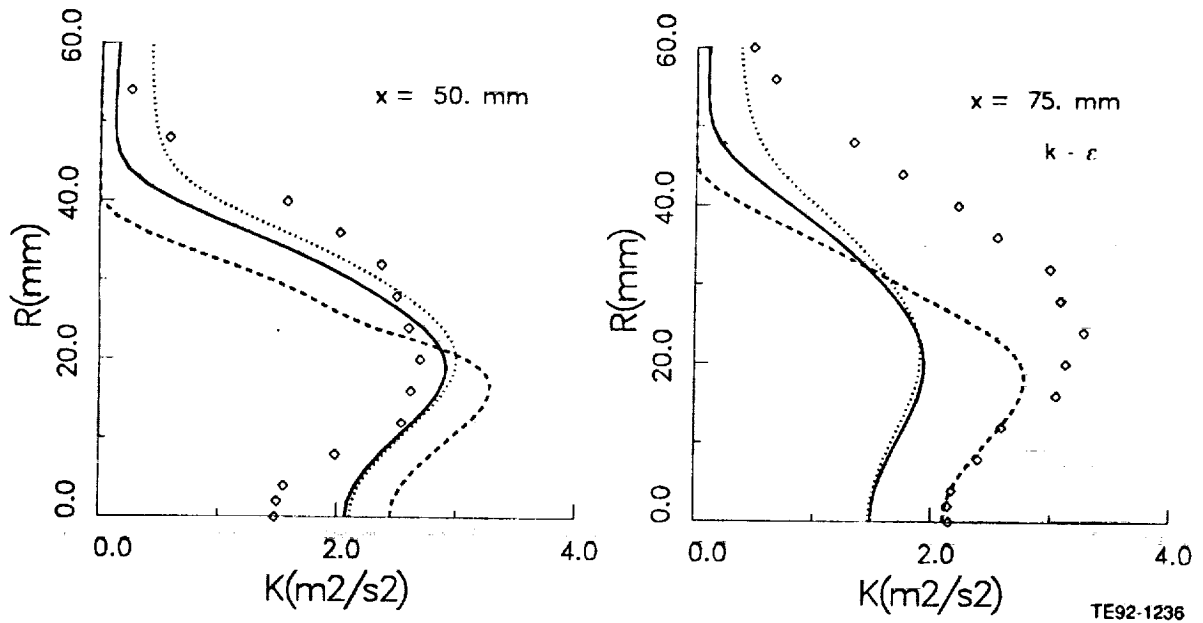


Figure 6.3.2-8. Comparison of calculated turbulent kinetic energy by k- ϵ model using various ϵ_{in} (3 of 4).

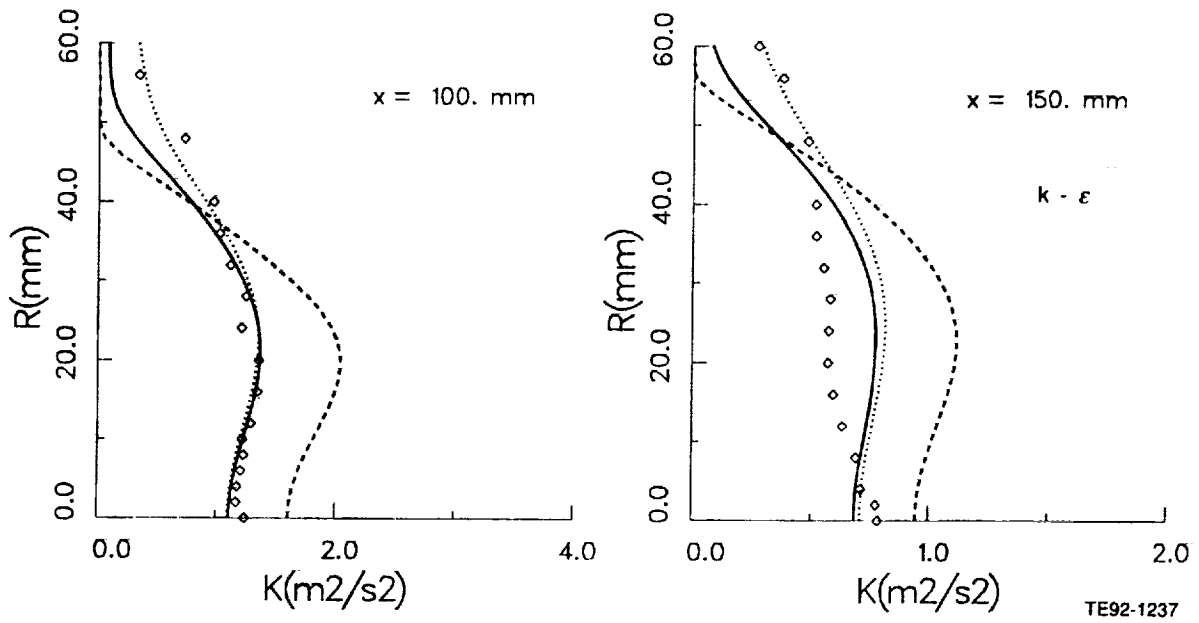


Figure 6.3.2-8. Comparison of calculated turbulent kinetic energy by k- ϵ model using various ϵ_{in} (4 of 4).

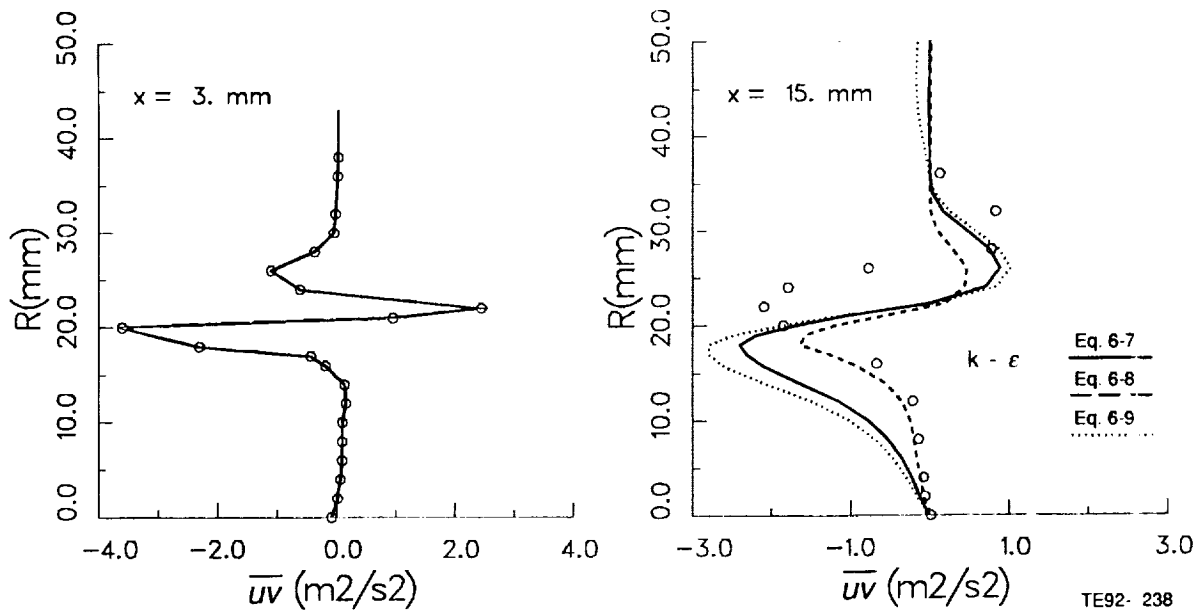


Figure 6.3.2-9. Comparison of calculated turbulent shear stress by k- ϵ model using various ϵ_{in} (1 of 4).

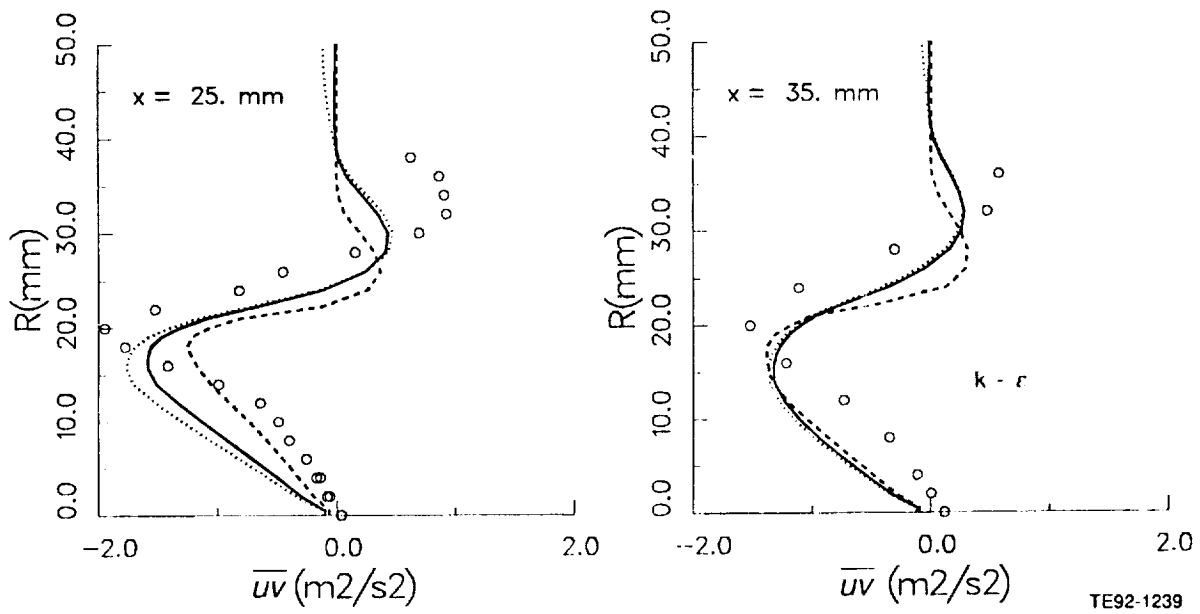


Figure 6.3.2-9. Comparison of calculated turbulent shear stress by k- ϵ model using various ϵ_{in} (2 of 4).

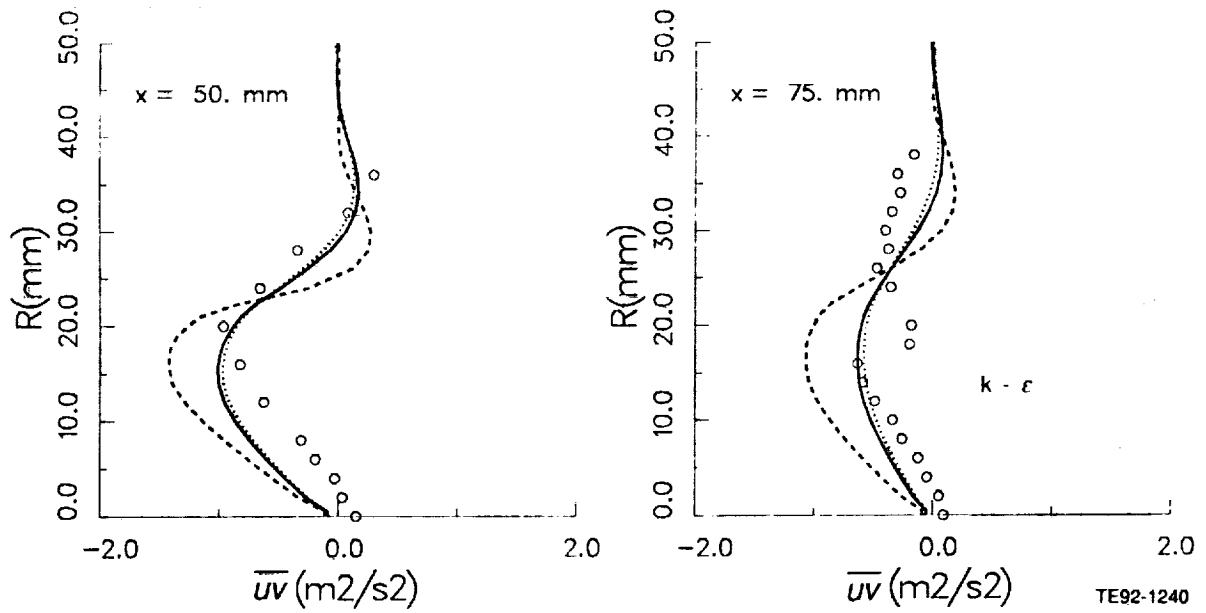


Figure 6.3.2-9. Comparison of calculated turbulent shear stress by $k-\epsilon$ model using various ϵ_{in} (3 of 4).

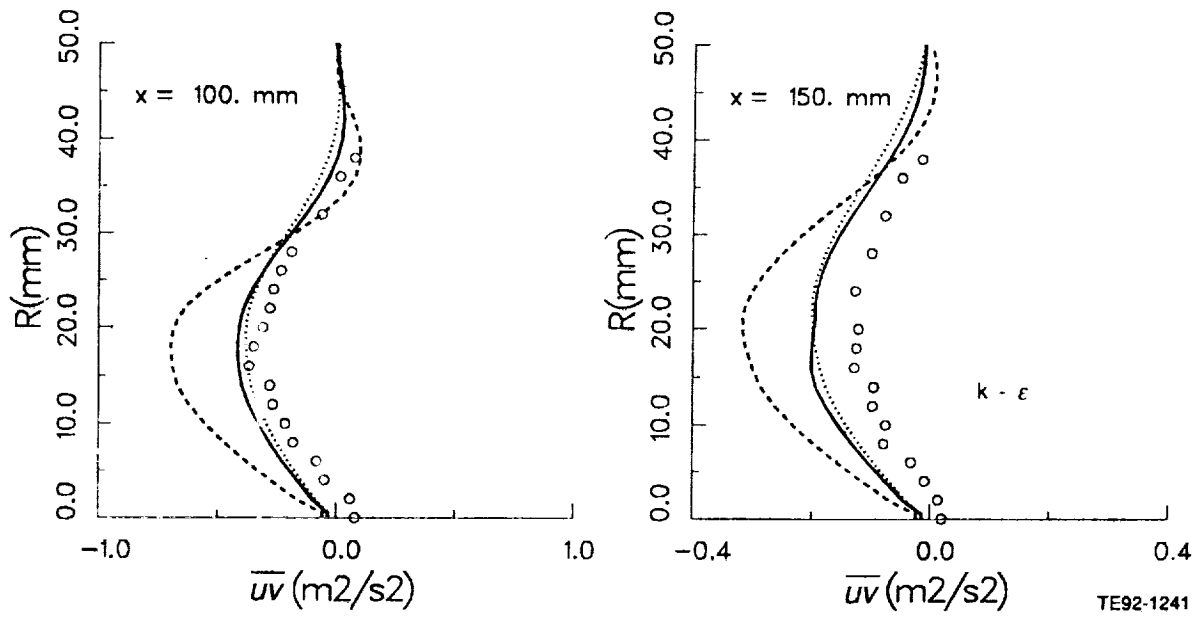


Figure 6.3.2-9. Comparison of calculated turbulent shear stress by $k-\epsilon$ model using various ϵ_{in} (4 of 4).

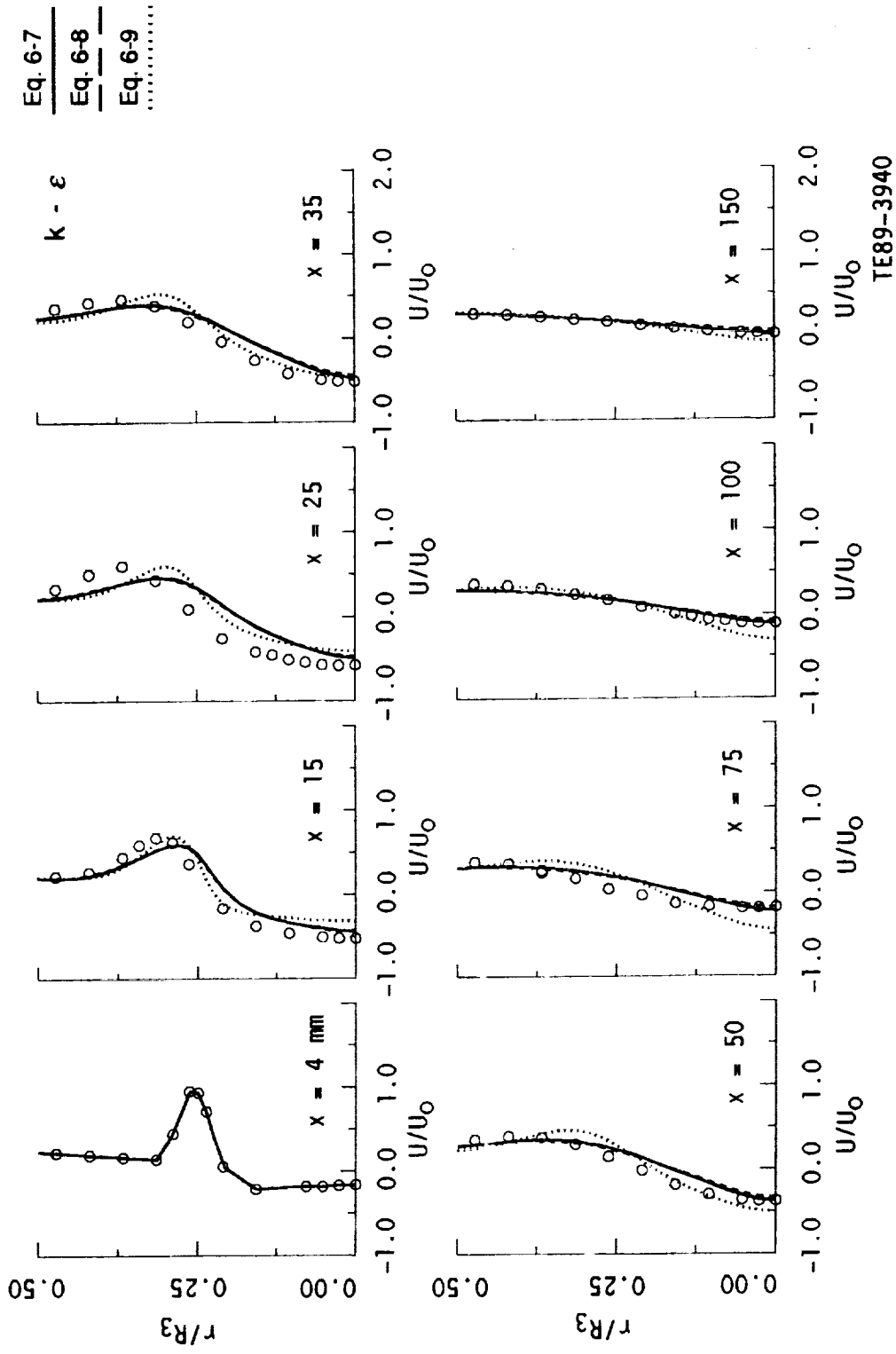


Figure 6.3.2-10. Comparison of calculated mean axial velocity by DSM using various ϵ in.

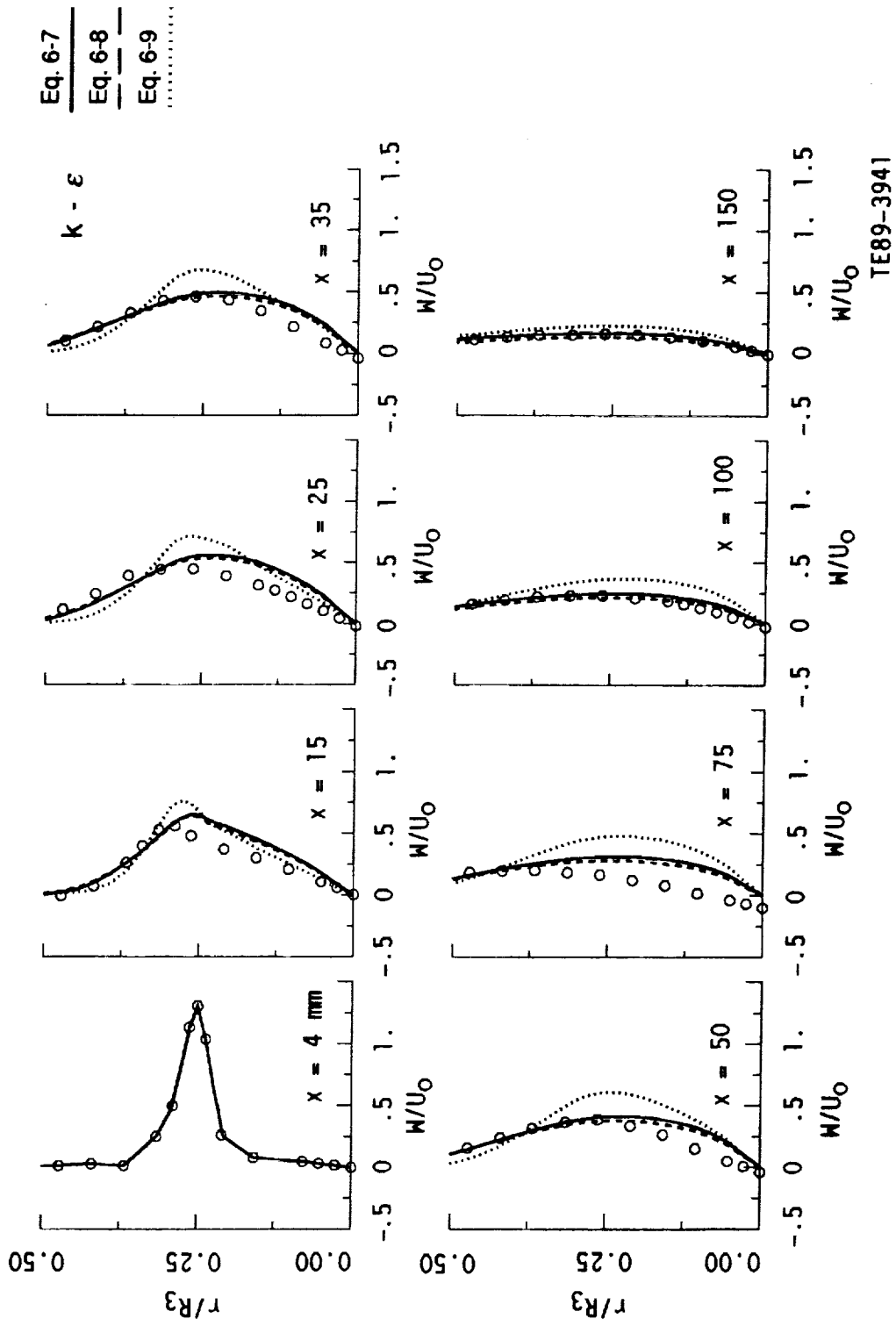
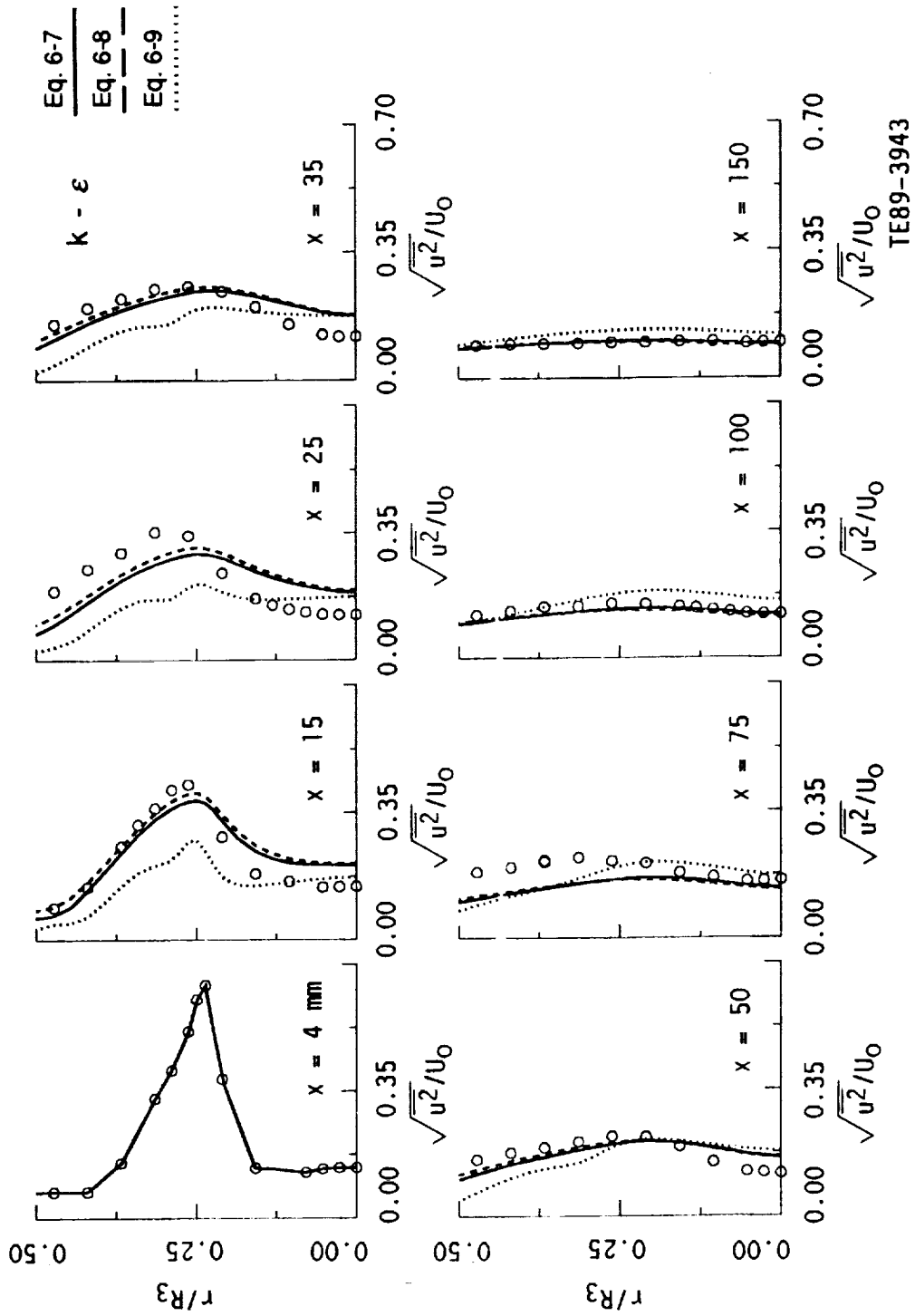


Figure 6.3.2-11. Comparison of calculated mean tangential velocity by DSM using various ϵ in



TE89-3943

Figure 6.3.2-12. Comparison of calculated streamwise turbulence intensity by DSM using various ϵ in.

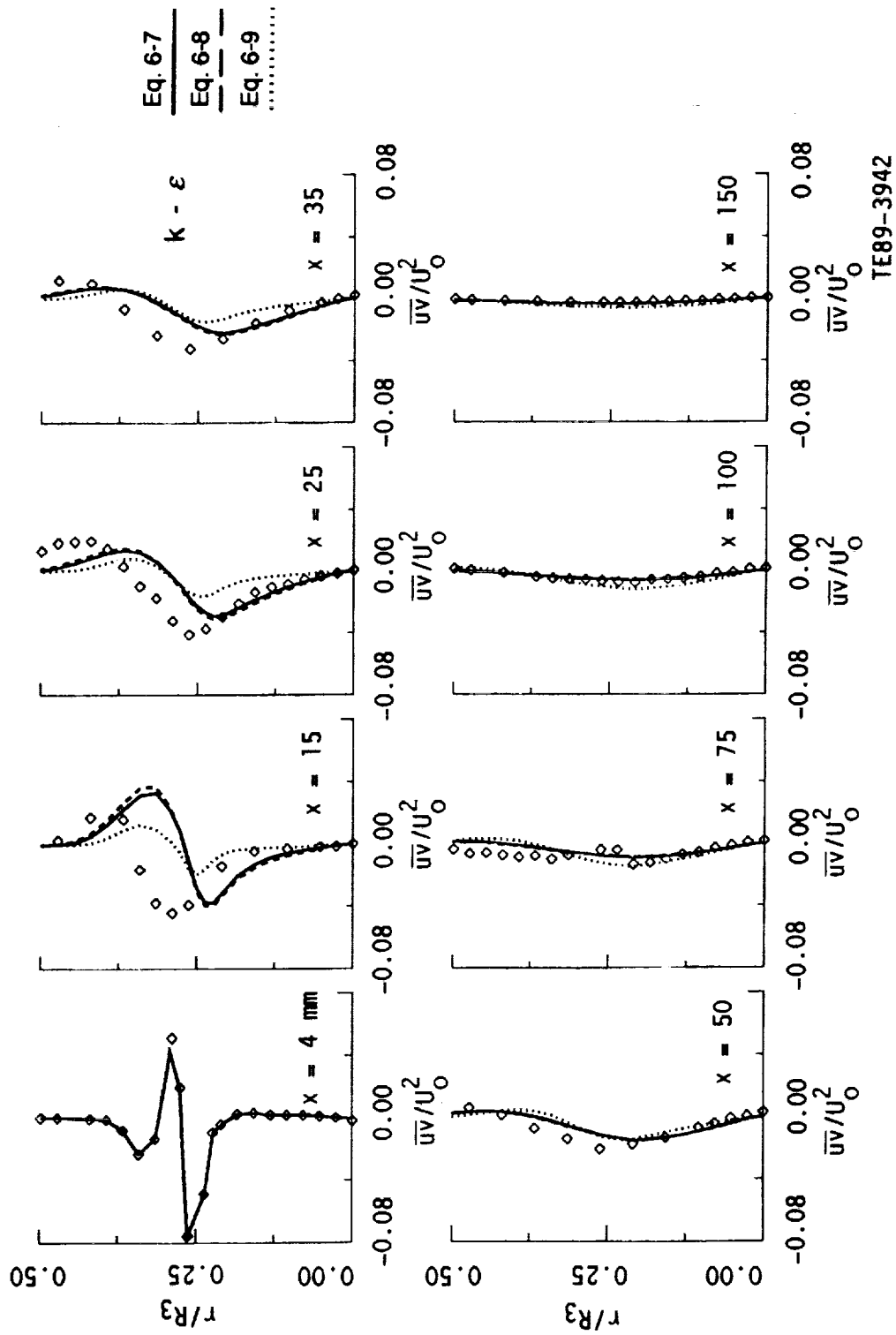


Figure 6.3.2-13. Comparison of calculated turbulent shear stress by DSM using various ϵ_{in} .

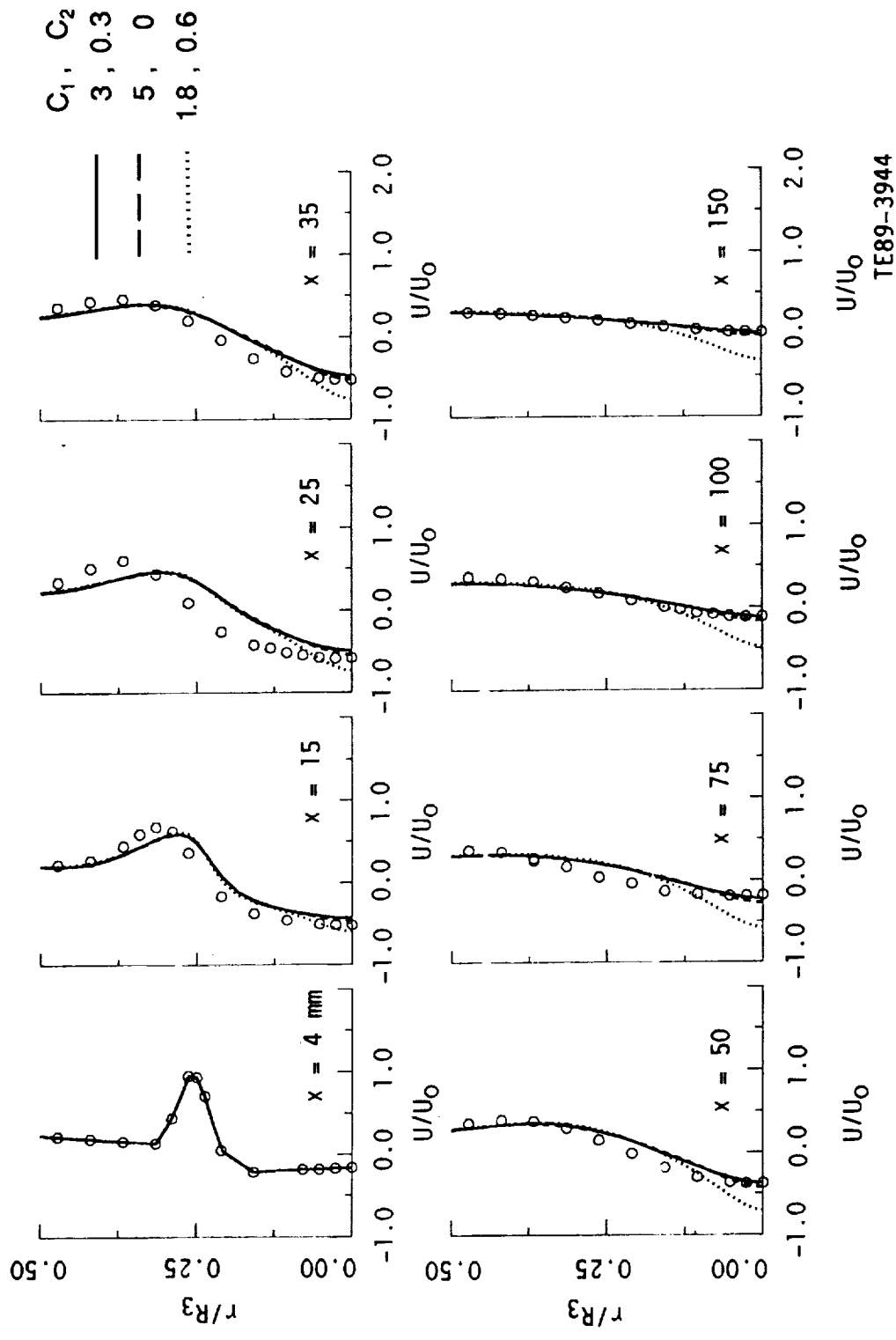
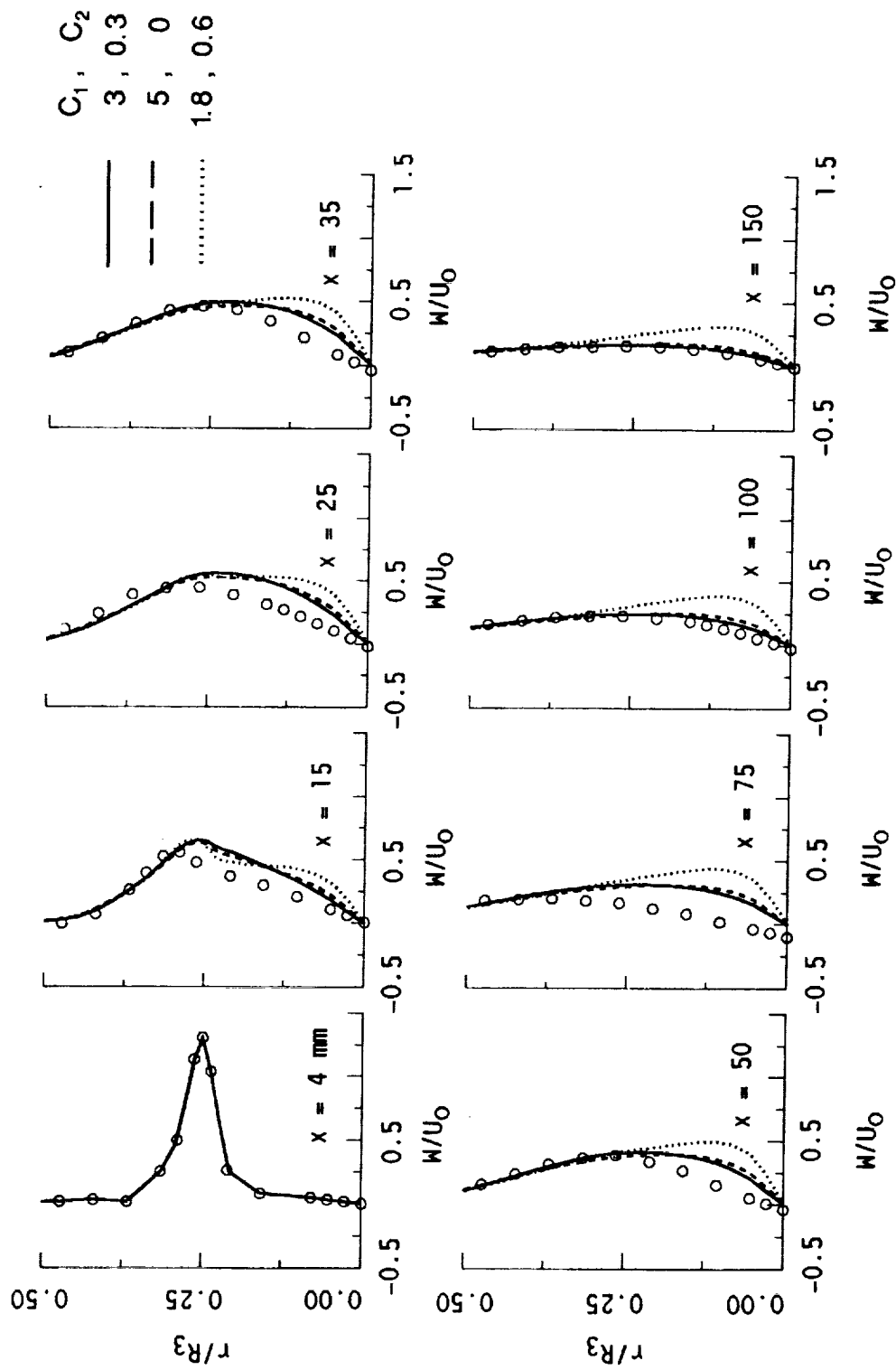


Figure 6.3.2-14. Comparison of calculated mean axial velocity using various ϕ , models with data.



TE89-3945

Figure 6.3.2-15. Comparison of calculated mean tangential velocity using various ϕ , models with data.

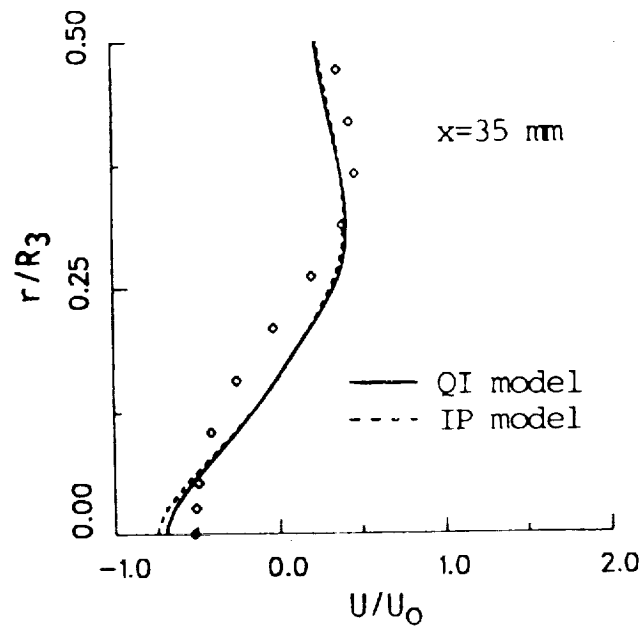
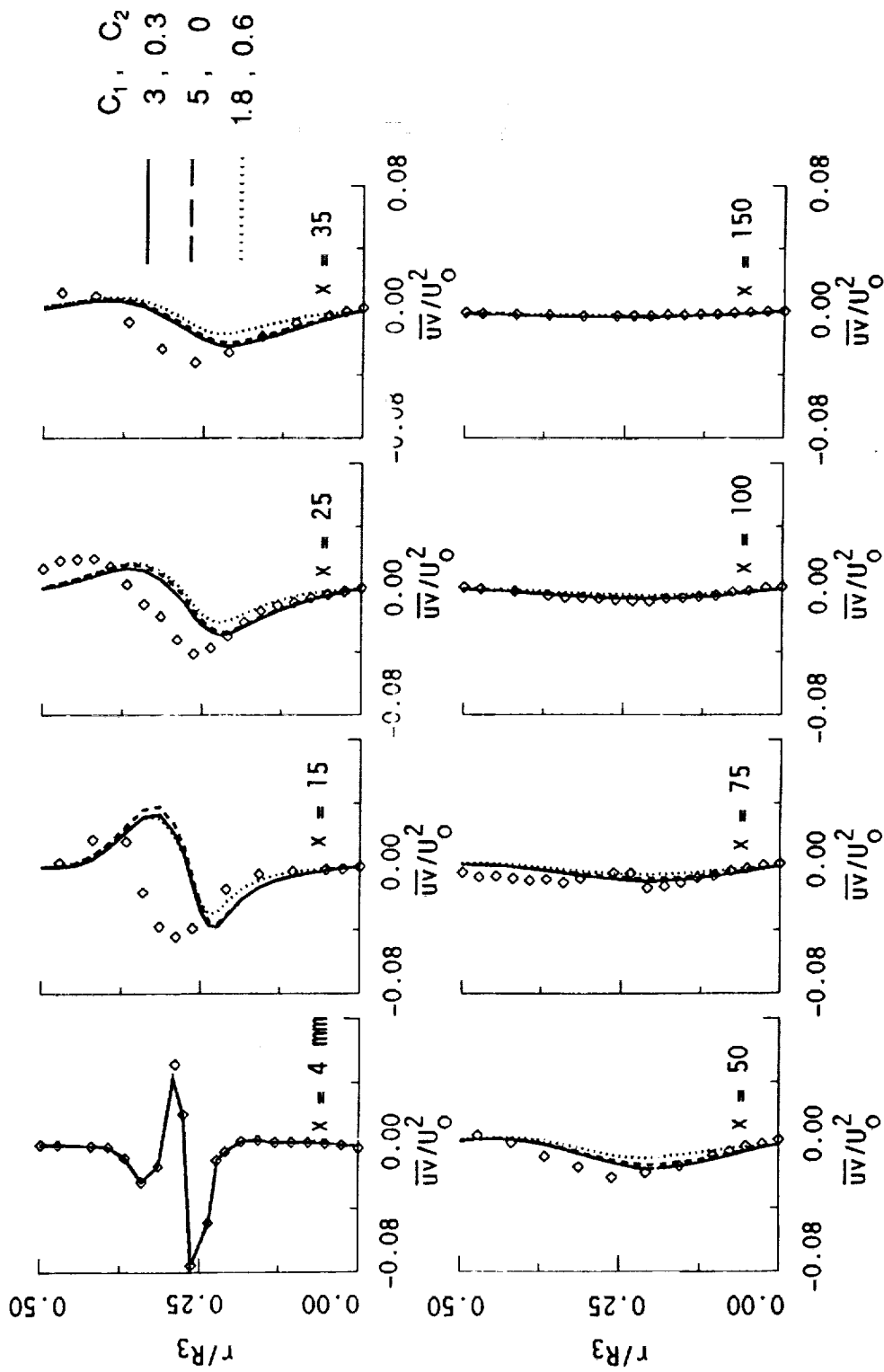


Figure 6.3.2-16. Comparison of calculated U velocity with IP and QI models for confined annular swirling jet.



TE89-3946

Figure 6.3.2-17. Comparison of calculated uv profiles with data.

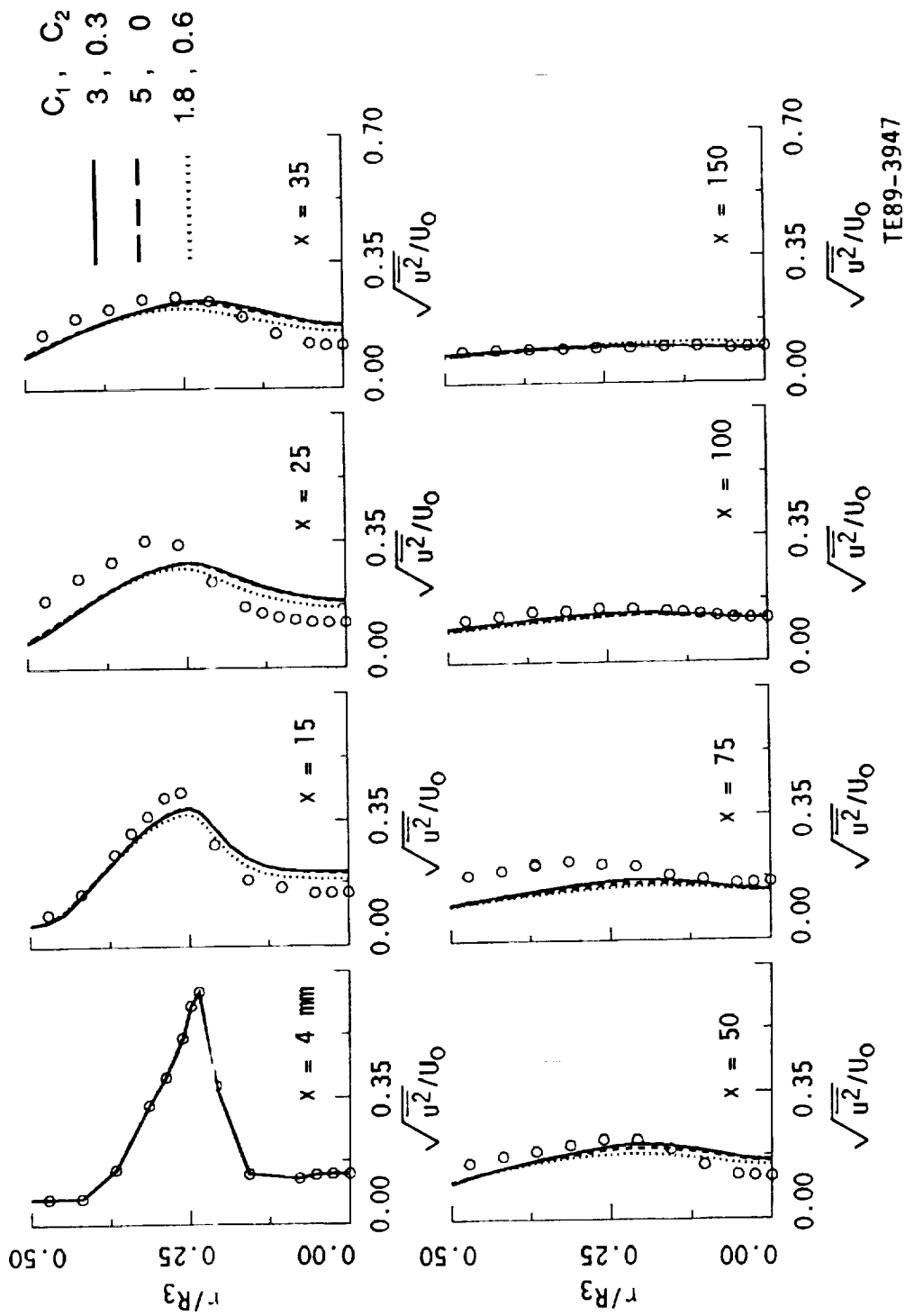
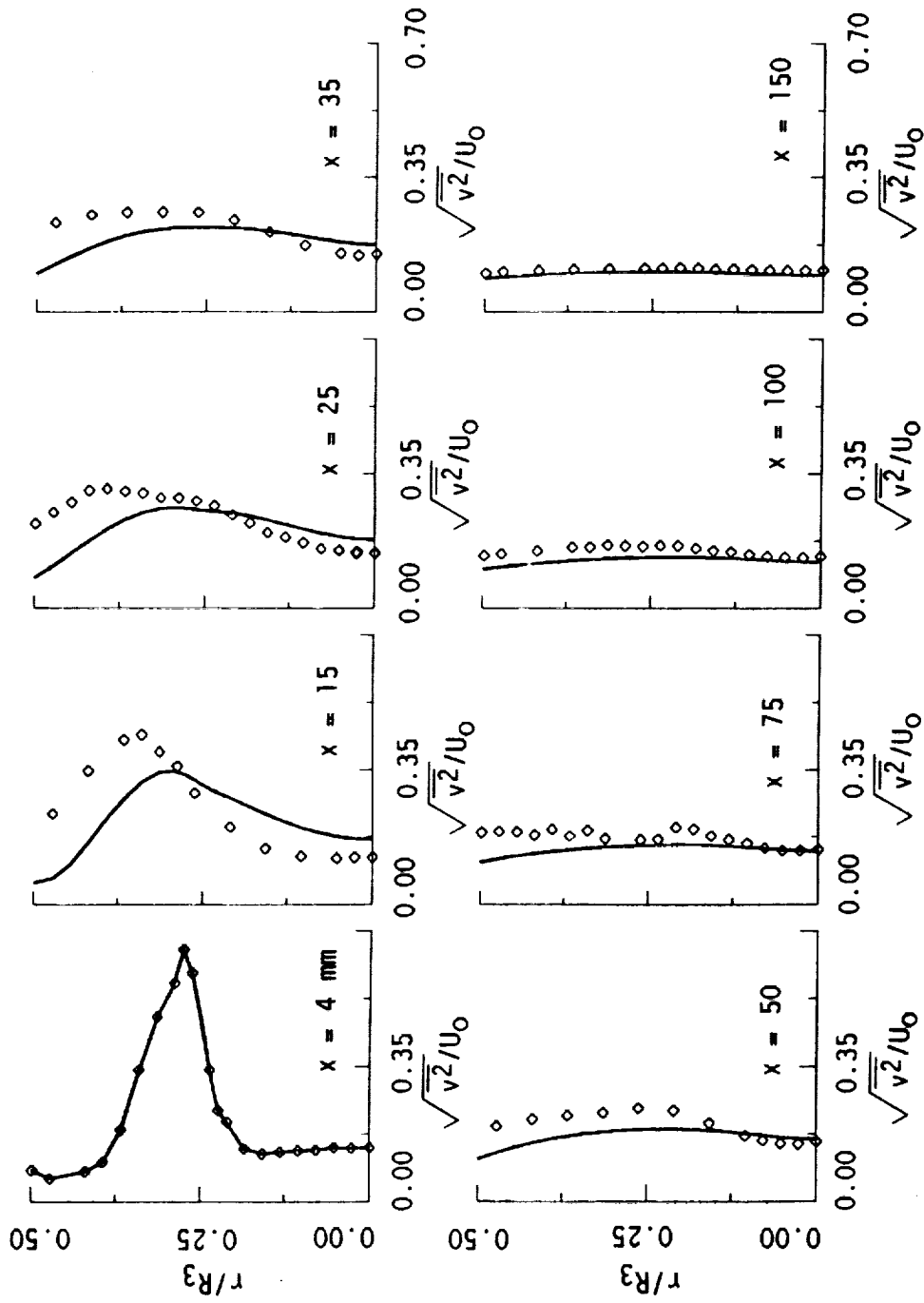


Figure 6.3.2-18. Comparison of calculated streamwise turbulence intensity with measurements.



TE89-3948

Figure 6.3.2-19. Comparison of calculated radial turbulence intensity with measurements.

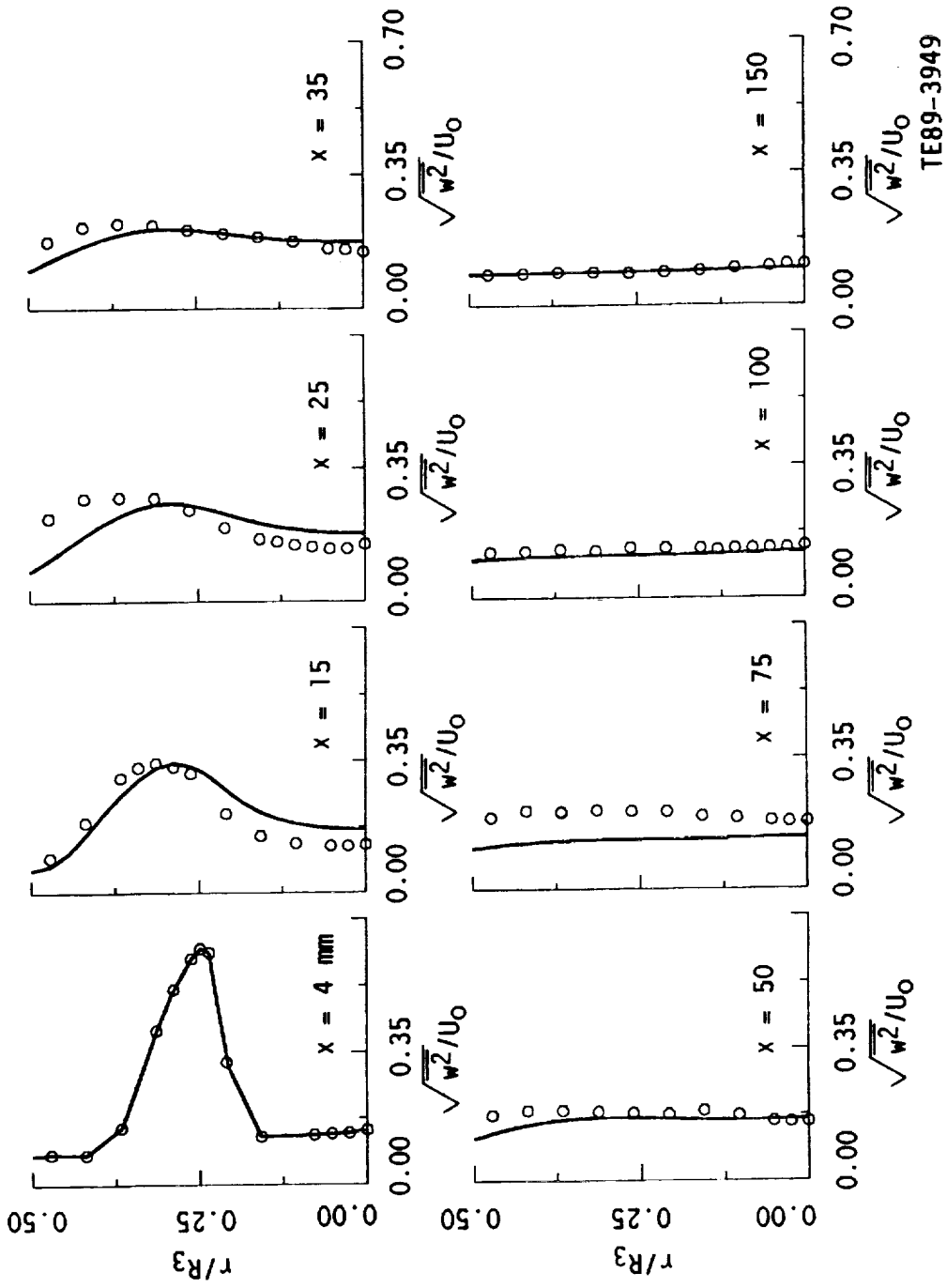


Figure 6.3.2-20. Comparison of the predicted mean and turbulence quantities by ASM and DSM with data.

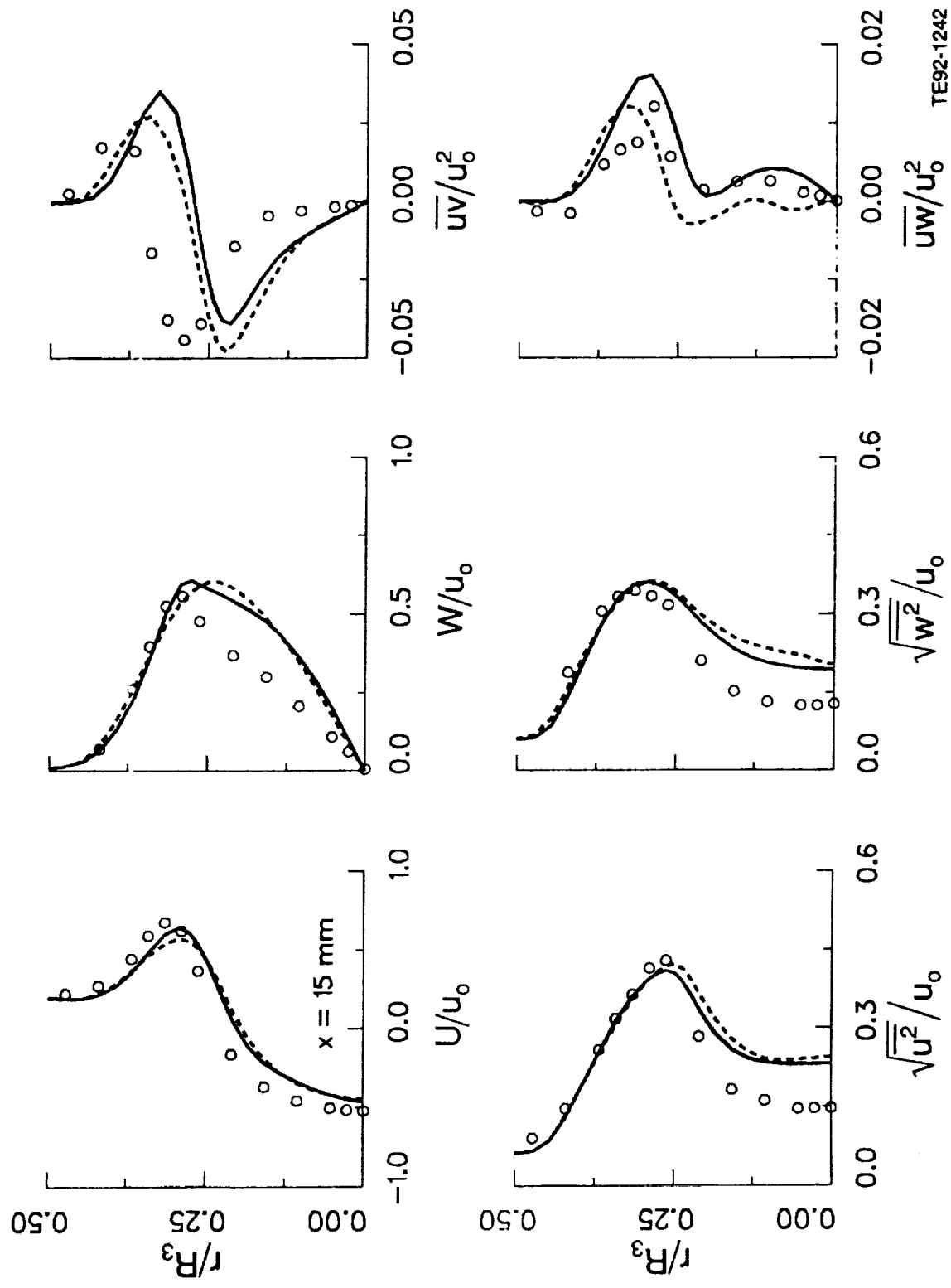


Figure 6.3.2-21. Comparison of the predicted mean and turbulence quantities by ASM and DSM with data.

TE92-1242

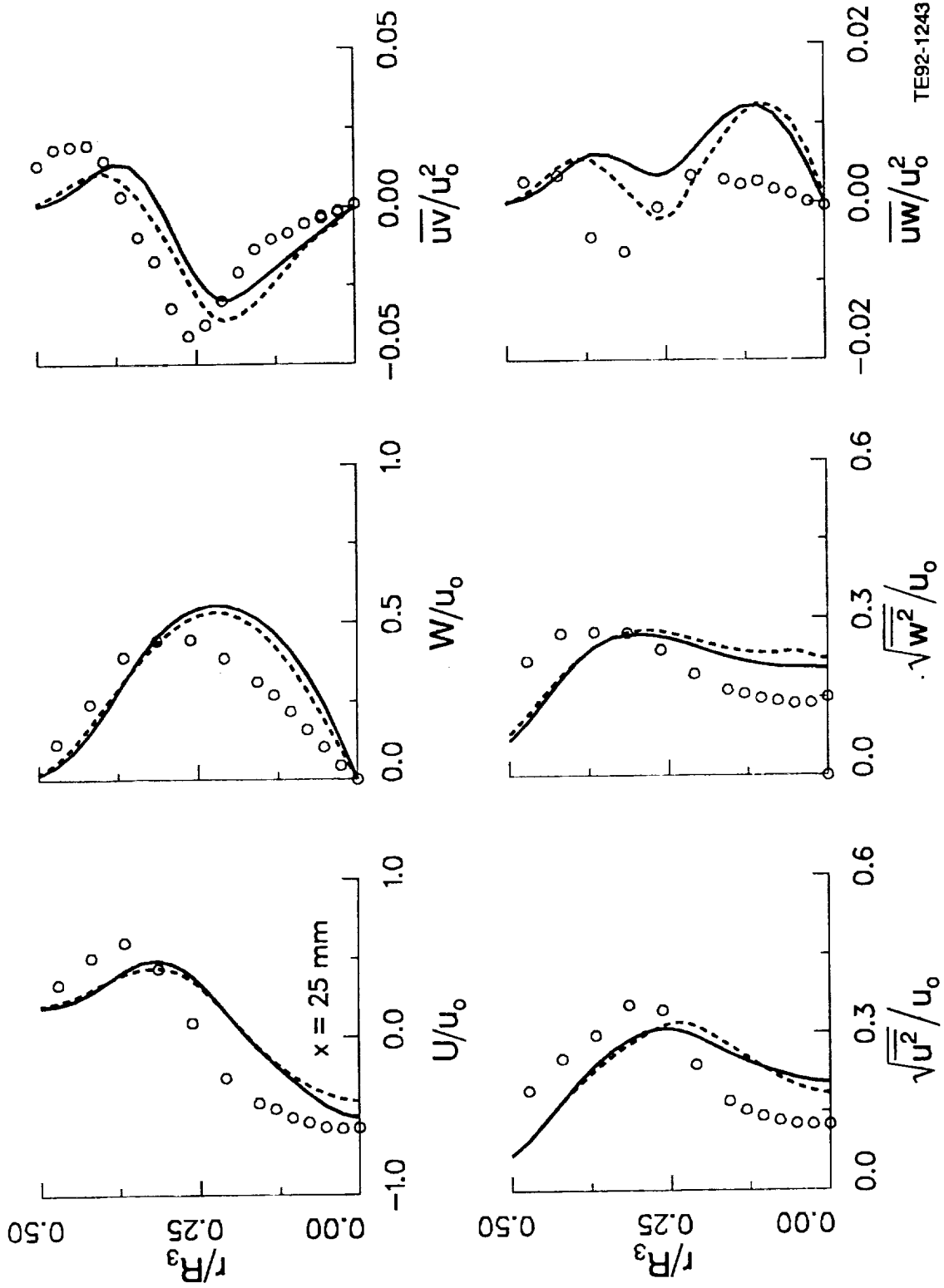


Figure 6.3.2-22. Comparison of the predicted mean and turbulence quantities by ASM and DSM with data.

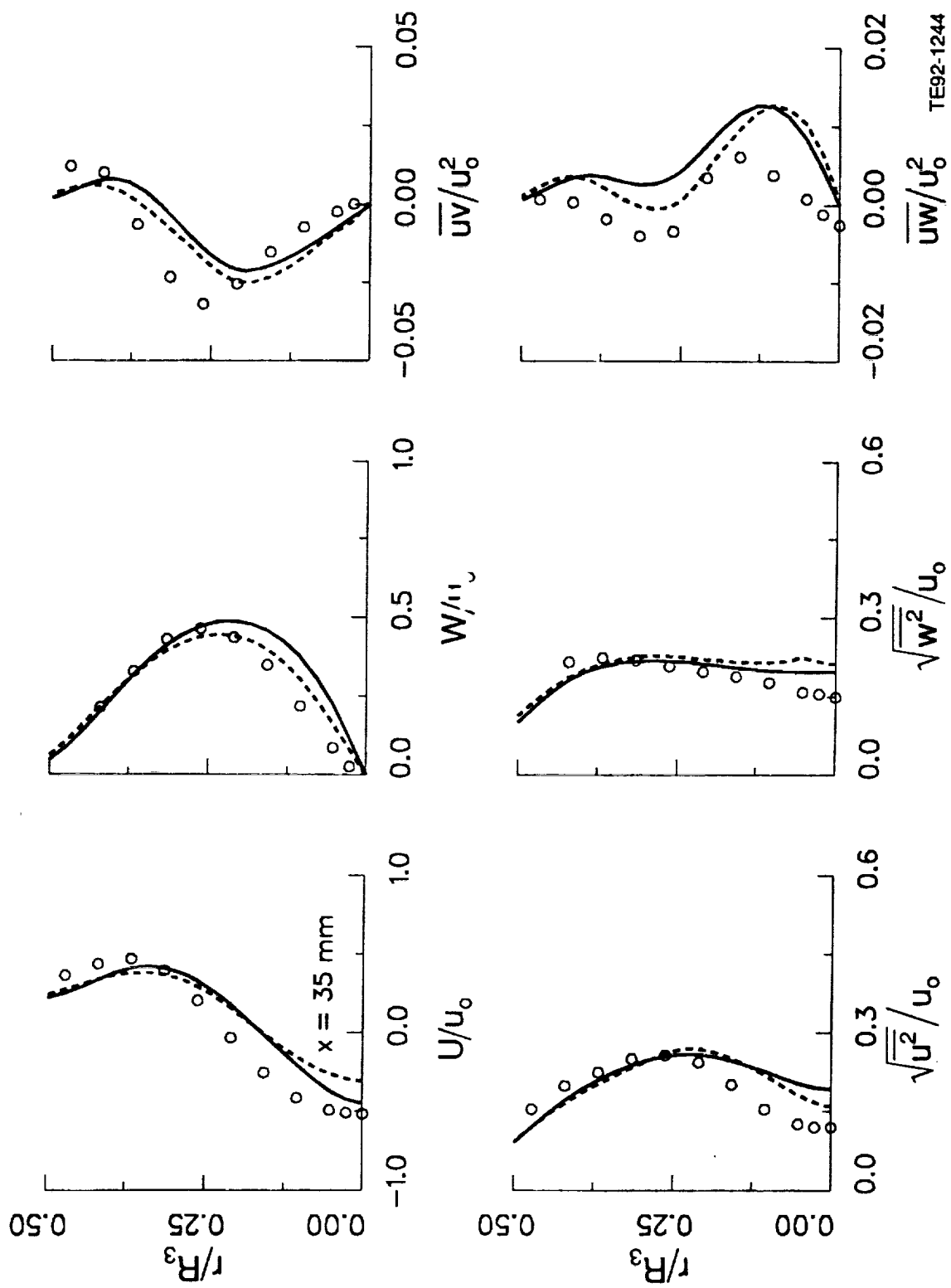


Figure 6.3.2-23. Comparison of the predicted mean and turbulence quantities by ASM and DSM with data.

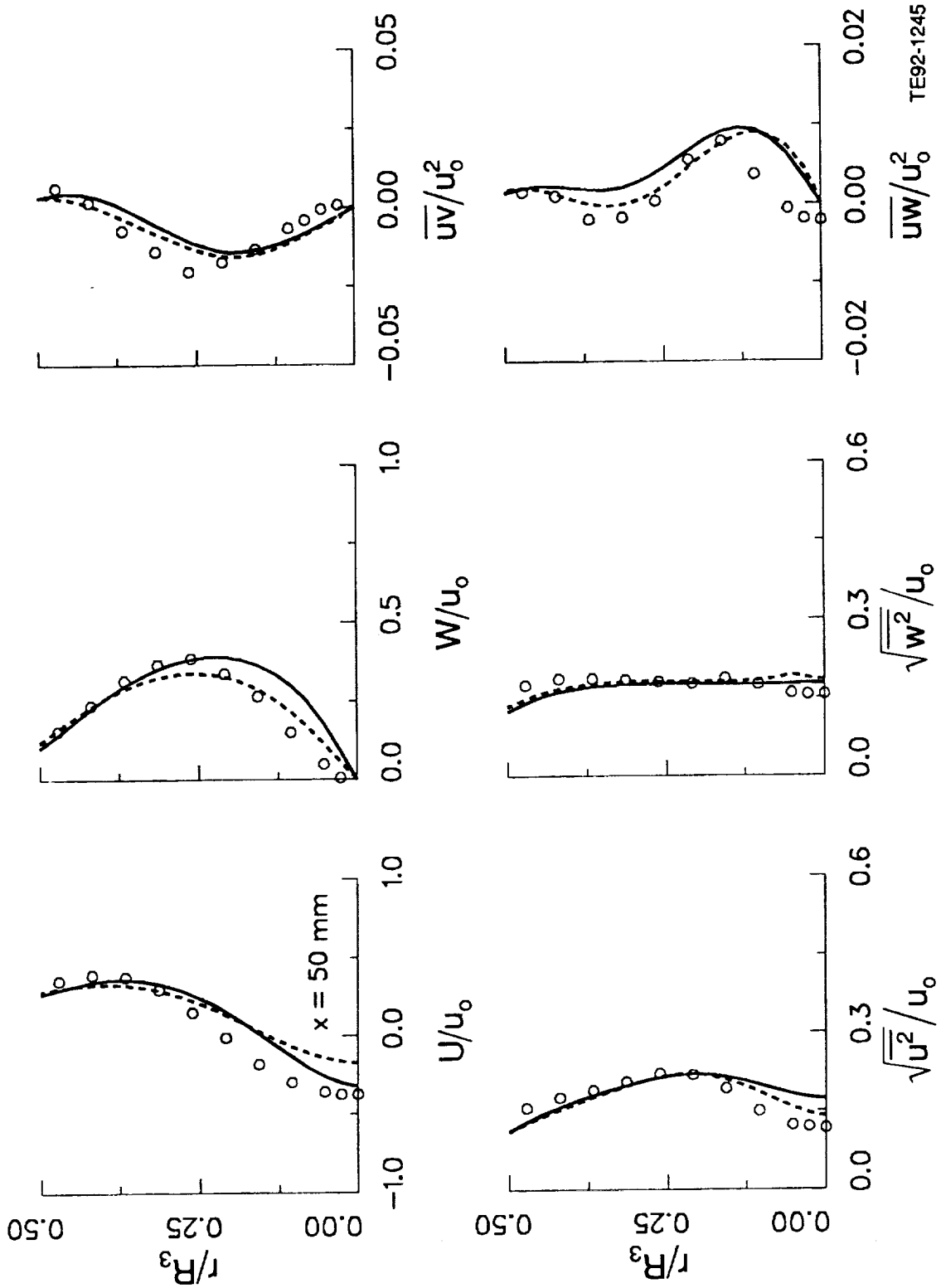


Figure 6.3.2-24. Comparison of the predicted mean and turbulence quantities by ASM and DSM with data.

6.4 COAXIAL JETS

6.4.1 Unconfined Coaxial Jets

For the present study, an unconfined flow configuration was selected, operating with an axial jet injector surrounded by a nonswirling annular jet, as shown in Figure 6.4.1-1. In this configuration, the injector was directed vertically downward within a 457 mm² wire mesh screen. The flow conditions used for the case considered are given in Table 6.4-I. The jet center (diameter, D = 24.1 mm) is surrounded by an annular jet with the inner and outer diameters of 29 mm and 36.7 mm, respectively. The effective area ratio and axial velocity ratio of the annular jet to the center jet are 0.87 and 1.8, respectively. Data were obtained at eight axial stations 2, 15, 25, 35, 50, 75, 150, and 300 mm from the exit plane of the injector. At each axial station, between 10 and 20 radial points were scanned as determined by the desired level of profile resolution.

The computations for coaxial jets can be made using a parabolic marching procedure if the radial pressure gradients are small. Such a situation occurs if velocities in the two streams are comparable or the inner streams are faster and if the swirl is weak. However, if the swirl is strong and/or the outer stream is significantly faster, the radial pressure gradients become significant and a region of reverse flow develops. The ultimate goal is to extend this study to swirling flow analyses. Therefore, a calculation procedure based on elliptic flows was used. The discretization equations are obtained using a control volume approach (Patankar, 1980). Three different numerical schemes were tested for the convection and diffusion terms in the transport equations. The schemes used are the hybrid scheme (Patankar, 1980), the power-law differencing scheme (Patankar, 1980), and the flux-spline differencing scheme (Varejao, 1979).

A calculation procedure for elliptic flow requires boundary conditions on all boundaries of the computational domain. Four kinds of boundaries need consideration, namely, inlet, axis of symmetry, outlet, and the entrainment boundary. At the inlet boundary, which was located at the first measurement plane, the measured profiles of U and V were prescribed. The k-profile was obtained from the measured Reynolds stresses. These profiles are shown in Figure 6.4.1-2. This kinetic energy distribution and the measured shear stress profile were used to derive the ε values at the inlet plane through the following relationship

$$\epsilon = \frac{C_{\mu} k^2}{(-\overline{uv})} \left(\frac{\partial U}{\partial r} \right) \quad (69)$$

Table 6.4-I.
Unconfined coaxial jets experimental conditions at 2 mm downstream of pipe exit.

Parameter	Single-phase flow	Particle-laden flow	
		Air	Particles
Inner jet			
Centerline velocity (m/s)	4.64	4.76	4.20
Density, ρ ₁ (kg/m ³)	1.178	1.178	2500.0
Mass flow rate, m ₁ (kg/s)	0.0021	0.0021	0.00042
Reynolds number, Re = 4m ₁ /πμ ₁ D*	6000	6000	
Ratio of particle-to-gas mass flow rate, LR		0.2	
Annular jet			
Maximum velocity (m/s)	6.60	6.60	
Density, ρ ₁ (kg/m ³)	1.178	1.178	
Mass flow rate, m ₂ (kg/s)	0.0033	0.0033	

*D = 0.0241 m

At the axis of symmetry, the radial velocity and the radial gradients of other variables are set to zero. At the outlet, axial diffusion is neglected for all variables. Along the entrainment boundary, which was placed sufficiently far from the axis of symmetry, the quantity (rV) was assumed constant. In addition, the axial velocity U was assumed zero and k and ϵ were assigned arbitrarily low values yielding an eddy viscosity, $\mu_t = 10\mu$.

The computational mesh used for all calculations consisted of 76×69 nonuniformly distributed grid points in the axial (x) and radial (r) directions (Figure 6.4.1-3). The tabulated x and r grid coordinates are shown in Table 6.4-II. A finer grid spacing was used near the inlet, centerline, and in the shear layer. The computational domain extended from the first measurement plane, located downstream of the nozzle exit at a distance of 2.0 mm, to 40 inner jet diameters downstream of the nozzle exit. In the radial direction, the entrainment boundary was placed at a distance of six jet diameters from the axis of symmetry. The convergence criterion used to terminate the iterations was the absolute sums of the mass and momentum residuals at all internal grid points, normalized by inlet mass and momentum fluxes, less than 5×10^{-3} . The numerical results were obtained using two turbulence models with various differencing schemes. The calculated mean and turbulence quantities are compared with the measurement at selected stations.

6.4.1.1 The k - ϵ Turbulence Model

The effect of different discretization schemes is shown by comparing the predicted axial velocity profiles at three streamwise locations, namely, $x = 15, 35,$ and 75 mm. The velocity profiles are presented in Figure 6.4.1-4. It is noted that, except for some minor differences, all three schemes for the convective terms yield nearly identical results. In earlier studies (Patankar et al, 1987; Varejao, 1979), it was shown that in the region of high Peclet number the flux-spline results are more accurate than those from the power-law scheme. The fact that for the present situation there are no significant differences between results from these schemes indicates that the results are grid independent. The differences between the hybrid and the power-law schemes are attributed to the different treatments of the diffusion terms. The computed results at the selected axial stations compare reasonably well with the experimental data. The computations consistently show sharper gradients than the experiment at the points of the maximum and minimum velocity.

Figure 6.4.1-5 shows the kinetic energy profiles at three axial locations. The experimental kinetic energy profiles were derived from the measured Reynolds stresses. In these figures, results from the power-law scheme and the flux-spline scheme have been shown. Again, the two sets of computations are in close agreement with each other. Most of the differences are seen in the regions of steep gradients where the flux-spline results are expected to be more accurate. The agreement between the predicted and experimental values of kinetic energy is not as good as that for the axial velocity. Even though the trends are similar, the predicted kinetic energy levels are smaller than those derived from the measurements.

Since the present calculations are essentially free of numerical diffusion, the discrepancies between the experimental data and the predictions can be attributed to two sources, improper boundary conditions at the inlet plane and the deficiencies of the turbulence model. As regards the inlet conditions, all quantities except the dissipation rate were prescribed from the experiment. The ϵ values, however, were derived from the measured shear stresses and the mean velocity gradients. The uncertainties in the measurements and in the evaluation of the velocity gradients may lead to errors in the ϵ values which would adversely affect the calculations at downstream locations.

Numerical experiments indicate that the inlet ϵ profile is the single most important factor in predicting the maximum values of mean and turbulence quantities, provided a reasonable inlet kinetic energy distribution is available. To study the sensitivity to inlet ϵ profile, calculations were also made using an alternative ϵ distribution, which were derived from the turbulent kinetic energy and an assigned length scale distribution (3% of the radius). The inlet ϵ profiles for both cases are shown in Figure 6.4.1-6. The major differences between these two conditions are near the centerline region, however, the peak values

Table 6.4-II.
Confined coaxial jets grid definition.

STREAMWISE COORDINATES OF THE GRID

I	DX	X	XU
1	0.000E+00	0.000E+00	0.000E+00
2	1.050E-03	1.050E-03	0.000E+00
3	2.200E-03	3.250E-03	2.100E-03
4	2.400E-03	5.650E-03	4.400E-03
5	2.600E-03	8.250E-03	6.900E-03
6	2.800E-03	1.105E-02	9.600E-03
7	3.075E-03	1.412E-02	1.250E-02
8	3.550E-03	1.767E-02	1.575E-02
9	4.225E-03	2.190E-02	1.960E-02
10	4.950E-03	2.685E-02	2.420E-02
11	5.550E-03	3.240E-02	2.950E-02
12	6.000E-03	3.840E-02	3.530E-02
13	6.475E-03	4.487E-02	4.150E-02
14	6.950E-03	5.182E-02	4.825E-02
15	7.175E-03	5.900E-02	5.540E-02
16	7.225E-03	6.622E-02	6.260E-02
17	7.275E-03	7.350E-02	6.985E-02
18	7.300E-03	8.080E-02	7.715E-02
19	7.300E-03	8.810E-02	8.445E-02
20	7.300E-03	9.540E-02	9.175E-02
21	7.300E-03	1.027E-01	9.905E-02
22	7.300E-03	1.100E-01	1.063E-01
23	7.300E-03	1.173E-01	1.136E-01
24	7.300E-03	1.246E-01	1.209E-01
25	7.300E-03	1.319E-01	1.282E-01
26	7.300E-03	1.392E-01	1.355E-01
27	7.300E-03	1.465E-01	1.428E-01
28	7.300E-03	1.538E-01	1.501E-01
29	7.300E-03	1.611E-01	1.574E-01
30	7.300E-03	1.684E-01	1.647E-01
31	7.300E-03	1.757E-01	1.720E-01
32	7.300E-03	1.830E-01	1.793E-01
33	7.300E-03	1.903E-01	1.866E-01
34	7.300E-03	1.976E-01	1.939E-01
35	7.300E-03	2.049E-01	2.012E-01
36	7.300E-03	2.122E-01	2.085E-01
37	7.300E-03	2.195E-01	2.158E-01
38	7.300E-03	2.268E-01	2.231E-01
39	7.300E-03	2.341E-01	2.304E-01
40	7.300E-03	2.414E-01	2.377E-01
41	7.300E-03	2.487E-01	2.450E-01
42	7.300E-03	2.560E-01	2.523E-01
43	7.300E-03	2.633E-01	2.596E-01
44	7.300E-03	2.706E-01	2.670E-01
45	7.300E-03	2.779E-01	2.742E-01
46	7.300E-03	2.852E-01	2.815E-01
47	7.350E-03	2.925E-01	2.888E-01
48	7.575E-03	3.001E-01	2.962E-01

PART 1 OF 3
TE92-1246

Table 6.4-II (cont).

49	7.875E-03	3.080E-01	3.040E-01
50	8.000E-03	3.160E-01	3.120E-01
51	8.000E-03	3.240E-01	3.200E-01
52	8.000E-03	3.320E-01	3.280E-01
53	8.500E-03	3.405E-01	3.360E-01
54	9.500E-03	3.500E-01	3.450E-01
55	1.000E-02	3.600E-01	3.550E-01
56	1.000E-02	3.700E-01	3.650E-01
57	1.250E-02	3.825E-01	3.750E-01
58	1.750E-02	4.000E-01	3.900E-01
59	2.000E-02	4.200E-01	4.100E-01
60	2.000E-02	4.400E-01	4.300E-01
61	2.000E-02	4.600E-01	4.500E-01
62	2.000E-02	4.800E-01	4.700E-01
63	2.250E-02	5.025E-01	4.900E-01
64	2.750E-02	5.300E-01	5.150E-01
65	3.000E-02	5.600E-01	5.450E-01
66	3.000E-02	5.900E-01	5.750E-01
67	3.250E-02	6.225E-01	6.050E-01
68	3.750E-02	6.600E-01	6.400E-01
69	4.000E-02	7.000E-01	6.800E-01
70	4.000E-02	7.400E-01	7.200E-01
71	4.000E-02	7.800E-01	7.600E-01
72	4.000E-02	8.200E-01	8.000E-01
73	4.000E-02	8.600E-01	8.400E-01
74	4.000E-02	9.000E-01	8.800E-01
75	5.000E-02	9.500E-01	9.200E-01
76	3.000E-02	9.800E-01	9.800E-01

TRANSVERS COORDINATES OF THE GRID

J	DY	Y	YV
1	0.000E+00	0.000E+00	0.000E+00
2	3.750E-04	3.750E-04	0.000E+00
3	7.500E-04	1.125E-03	7.500E-04
4	8.750E-04	2.000E-03	1.500E-03
5	1.000E-03	3.000E-03	2.500E-03
6	1.000E-03	4.000E-03	3.500E-03
7	1.000E-03	5.000E-03	4.500E-03
8	1.000E-03	6.000E-03	5.500E-03
9	1.000E-03	7.000E-03	6.500E-03
10	1.000E-03	8.000E-03	7.500E-03
11	1.000E-03	9.000E-03	8.500E-03
12	1.000E-03	1.000E-02	9.500E-03
13	1.000E-03	1.100E-02	1.050E-02
14	8.750E-04	1.187E-02	1.150E-02
15	6.250E-04	1.250E-02	1.225E-02
16	5.000E-04	1.300E-02	1.275E-02

PART 2 OF 3
TE92-1246

Table 6.4-II (cont).

17	5.000E-04	1.350E-02	1.325E-02
18	6.250E-04	1.412E-02	1.375E-02
19	8.750E-04	1.500E-02	1.450E-02
20	1.000E-03	1.600E-02	1.550E-02
21	1.000E-03	1.700E-02	1.650E-02
22	1.000E-03	1.800E-02	1.750E-02
23	1.000E-03	1.900E-02	1.850E-02
24	9.800E-04	1.998E-02	1.950E-02
25	1.047E-03	2.103E-02	2.046E-02
26	1.300E-03	2.233E-02	2.159E-02
27	1.563E-03	2.389E-02	2.306E-02
28	1.735E-03	2.562E-02	2.472E-02
29	1.875E-03	2.750E-02	2.653E-02
30	1.995E-03	2.950E-02	2.847E-02
31	2.100E-03	3.159E-02	3.052E-02
32	2.192E-03	3.379E-02	3.267E-02
33	2.275E-03	3.606E-02	3.490E-02
34	2.353E-03	3.841E-02	3.722E-02
35	2.425E-03	4.084E-02	3.961E-02
36	2.495E-03	4.333E-02	4.207E-02
37	2.557E-03	4.589E-02	4.460E-02
38	2.615E-03	4.851E-02	4.719E-02
39	2.672E-03	5.118E-02	4.983E-02
40	2.725E-03	5.390E-02	5.253E-02
41	2.777E-03	5.668E-02	5.528E-02
42	2.830E-03	5.951E-02	5.808E-02
43	2.877E-03	6.239E-02	6.094E-02
44	2.922E-03	6.531E-02	6.384E-02
45	2.967E-03	6.828E-02	6.678E-02
46	3.010E-03	7.129E-02	6.977E-02
47	3.050E-03	7.434E-02	7.280E-02
48	3.090E-03	7.743E-02	7.587E-02
49	3.128E-03	8.056E-02	7.898E-02
50	3.165E-03	8.372E-02	8.213E-02
51	3.205E-03	8.693E-02	8.531E-02
52	3.240E-03	9.017E-02	8.854E-02
53	3.272E-03	9.344E-02	9.179E-02
54	3.313E-03	9.675E-02	9.508E-02
55	3.357E-03	1.001E-01	9.842E-02
56	3.390E-03	1.035E-01	1.018E-01
57	3.400E-03	1.069E-01	1.052E-01
58	3.425E-03	1.103E-01	1.086E-01
59	3.475E-03	1.138E-01	1.120E-01
60	3.500E-03	1.173E-01	1.155E-01
61	3.500E-03	1.208E-01	1.190E-01
62	3.525E-03	1.243E-01	1.225E-01
63	3.575E-03	1.279E-01	1.261E-01
64	3.625E-03	1.315E-01	1.297E-01
65	3.650E-03	1.352E-01	1.333E-01
66	3.650E-03	1.388E-01	1.370E-01
67	3.700E-03	1.425E-01	1.406E-01
68	4.675E-03	1.472E-01	1.444E-01
69	2.800E-03	1.500E-01	1.500E-01

PART 3 OF 3
TE92-1246

are about the same. The predicted results of mean axial velocity and turbulent kinetic energy at an axial location of 15 mm are shown in Figure 6.4.1-7. The results show that the turbulent kinetic energy has decreased due to an excessive inlet dissipation rate in the inner region. On the other hand, the mean velocity is not affected significantly. This can be attributed to the fact that the maximum value of the inlet ϵ in the annular region has not been changed considerably.

6.4.1.2 The Algebraic Second-Moment Closure

In this section, the predictions using the ASM have been compared with those from the k - ϵ model. Similar to the trends observed in the k - ϵ model calculations, the effect of various discretization schemes on the ASM results was found to be rather insignificant. Consequently, results from different schemes will be shown only for some cases. The predicted mean axial velocity profiles from the ASM and k - ϵ models have been compared in Figure 6.4.1-8. These results were obtained using the flux-spline discretization scheme. The use of ASM improves the overall agreement between the predictions and the experimental data. The major differences between the two turbulence models are seen in the regions where a maxima or a minima occurs in the velocity profiles.

The predicted turbulent shear stress from the ASM has been compared with the experimental data in Figure 6.4.1-9. Here, results from the power-law differencing scheme have also been included to assess the numerical accuracy of the results. Both discretization schemes give nearly identical results, indicating that the solution is grid independent. The positive peak in the shear stress profile corresponds to the shear layer between the two streams and the negative peak corresponds to the shear layer associated with the expansion. The agreement between the calculation and the experimental data is good, although the peak values are not well predicted.

The normal stresses at different axial locations are shown in Figure 6.4.1-10. Again, results from both the power-law and flux-spline schemes have been included. The two schemes perform essentially to the same level except for minor differences in the peak values. The differences between the calculated and experimental results are most significant in the case of the normal stresses. The experimental data indicate a faster mixing within the shear layer is predicted by the model.

Comparisons of the radial and tangential Reynolds stress components with the measurements are presented in Figures 6.4.1-11 and 6.4.1-12. Essentially, the same trends are observed for v^2 and w^2 profiles. The peak values of the w^2 , however, are reported higher. Such behavior has been correctly predicted by the ASM calculation. In addition, the maximum values are overpredicted for u^2 , underpredicted for v^2 , and closely predicted for w^2 . This clearly indicates the lack of performance of the pressure-strain model. One reason for this could be that the constant C_2 used is not suitable for complex turbulent flows. Since C_2 is determined from simple turbulent flows in local equilibrium, it would be more appropriate for equilibrium ASM than for nonequilibrium ASM. Another reason could be the incorrect modeling of the mean strain part of the pressure-strain term. It is very important to model the mean strain tensor correctly. Either the mean strain effects are not modeled at all or they should be accounted for properly (Nikjooy and So, 1987). Near the centerline region, substantial differences are observed between the model predictions and the experimental data. The discrepancies are attributed to inaccurate anisotropic diffusivity in momentum as well as k and ϵ equations, an improper model used for the pressure-strain term, and the shortcoming of the algebraic stress model in predicting the normal stress components. Overall, the algebraic stress model can do a better job of predicting the shear stress components than the normal stresses.

Numerical calculations were also performed starting from 15 mm downstream of the nozzle exit where no reverse flow occurred. This allowed the application of parabolic calculations with very fine grid to achieve numerically accurate solutions. The experimental profiles of mean and turbulence quantities at $x = 15$ mm were used as initial conditions for the parabolic calculations. The inlet turbulence dissipation rate profile was derived from Equation 69.

The k - ϵ turbulence model was applied first for a single-phase coaxial jet calculation to establish the suitability of the model before introducing two-phase effects. The predicted mean axial velocity, turbulent kinetic energy, and shear stress profiles at the various axial stations, 15 (inlet plane), 25, 35, 50, 75, 150, and 300 mm, are shown in Figure 6.4.1-13 and have been normalized by the inner jet pipe radius and local centerline velocity.

The k - ϵ model yields good overall agreement with velocity measurements, however, the discrepancies are high for the kinetic energy distribution. The underpredicted values of the kinetic energy of turbulence are more obvious in the regions where the flow changes rapidly, in the developing shear layer between the two jets (first region) and where the shear layer reaches the centerline (second region).

In the first region, the mixing layer between the two flows produced by the inner and outer streams is changing from a thin layer characterized by a high shear stress to a self-similar shear flow where the shear stress is relatively small. In both regions, the flow possesses two significant rate-of-strain components resulting from the velocity gradients in both the axial and radial directions. This type of flow is classified as complex shear flow, which is difficult to predict by using the standard version of the k - ϵ model.

The distribution of the turbulent shear stress and its dependence on the mean velocity gradient are also shown in Figure 6.4.1-13. According to the eddy-viscosity hypotheses, the sign of the shear stress and the velocity gradient is clearly consistent across the flow field. The positive shear stress in the inner jet region indicates that the flow still bears the characteristics of the upstream pipe flow, the gradient of mean axial velocity is still negative but approaching zero. The distribution of k and uv reach their more familiar shapes (as in a single free jet) when the mixing takes place across the entire flow and the mean axial velocity gradient becomes negative across the entire jet.

The gas-phase rms velocities are shown in Figure 6.4.1-14. It is assumed that turbulent kinetic energy redistributes with $u^2 = k$, $v^2 = w^2$. The shapes of the three components have maximum values just behind the nozzle wall and minimum values at the central axis. But in the farther downstream region where the mixing layer merges with the central axis, the rms profiles take a uniform shape like that observed in fully developed jet flows. Figure 6.4.1-14 also shows that the radial rms velocity component, v^2 , has almost the same value of the axial component.

The k - ϵ model is extended to particle-laden jets' situations. The mass loading, defined as the ratio of particle-to-gas mass flow rate of the inner jet at the inlet plane, $LR = 0.2$, was considered. To distinguish between the effects of mean and fluctuating gas velocity on particle transport, predictions were compared using ST and DT treatments to the measured data.

Figure 6.4.1-15 presents the mean axial velocity, kinetic energy, and shear stress of the carrier phase. The high velocity of the external stream, compared to that of the central jet, causes a rapid increase in the axial velocity of the inner jet downstream of the exit plane. Because of this transfer of mass and momentum from the external to the internal stream, the carrier-phase velocity distribution where the particles exist becomes different from that of the axisymmetric jet flow case. This change in air velocity affects particle velocity, which is discussed in connection with Figure 6.4.1-15.

The present particle loading is fairly small in terms of altering the carrier-phase flow field (Mostafa and Mongia, 1988). However, comparison of the last two planes in Figure 6.4.1-15 with those of Figure 6.4.1-13 shows some reductions in turbulence kinetic energy and shear stress in the near centerline region where the particles exist. This turbulence modulation is caused mainly by the fluctuating relative velocity between the particles and the carrier phase. Particles generally cause a reduction in gas turbulence and an increase in the dissipation rate of that energy. This phenomenon was simulated in the present study by introducing extra terms into the turbulence kinetic energy and its dissipation rate equations. Increasing the particle loading increases the turbulence modulation, as recently measured by Fleckhaus et al

(1987). Figure 6.4.1-15 shows that the present mathematical model yields fairly good agreement with the experimental data.

Figure 6.4.1-16 presents the measured values of the three components of fluctuating velocity of the carrier phase when glass beads are present. The effect of the particles on the radial and azimuthal components is higher than that on the axial component. This condition may be attributed to the differences in the mean velocity strain profiles and to the small ratio of particle-to-gas velocity fluctuation. According to Fleckhaus et al (1987), the smaller the ratio of particle-to-gas velocity fluctuation, the higher is turbulence attenuation. This observation supports the postulate that particles increase the level of anisotropy and shows the need for detailed measurements of mean and fluctuating components of the two phases under different flow conditions.

Figure 6.4.1-17 presents the data of the mean axial particle velocity. It also compares the predictions of the ST and DT treatments to the experimental data. The mean particle velocity profile is uniform over the entire cross section of the flow field. This behavior is different from that observed in round jet flow measurements and could be attributed to rapid mixing between inner and outer jets, which subject the particles to a more uniform gas velocity distribution. This jet mixing process creates a strong negative radial velocity in the jet's outer region and causes the particle-number density to become narrower than the corresponding profile for axisymmetric round jet flows. Figure 6.4.1-17 also shows that the ST provides good predictions compared to the experimental data, whereas the DT performs quite poorly at the downstream stations. That is, a particle moves radially because of its initial mean radial velocity and/or the mean radial gas velocity, both of which are very small compared to the axial component. This effect explains the narrow distribution of particle mean axial velocity and number density predicted by DT.

Figure 6.4.1-18 presents the measurements of the three components of fluctuating particle velocity and indicates the extent to which ST allows reasonable calculations. Although DT ignores these components entirely, ST simulates these particle-velocity fluctuations as a response to the carrier-phase components. The agreement between predictions and data is less than satisfactory at the last station, which could be attributed to the limitations of the assumptions embedded in the ST formation. Figure 6.4.1-18 also shows the high anisotropy of particle turbulent quantities that increase the anisotropy level of the carrier phase discussed in the analysis of Figure 6.4.1-16.

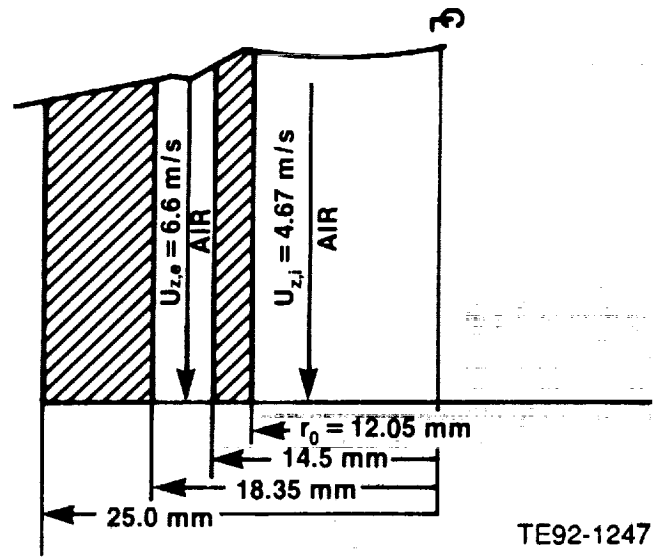
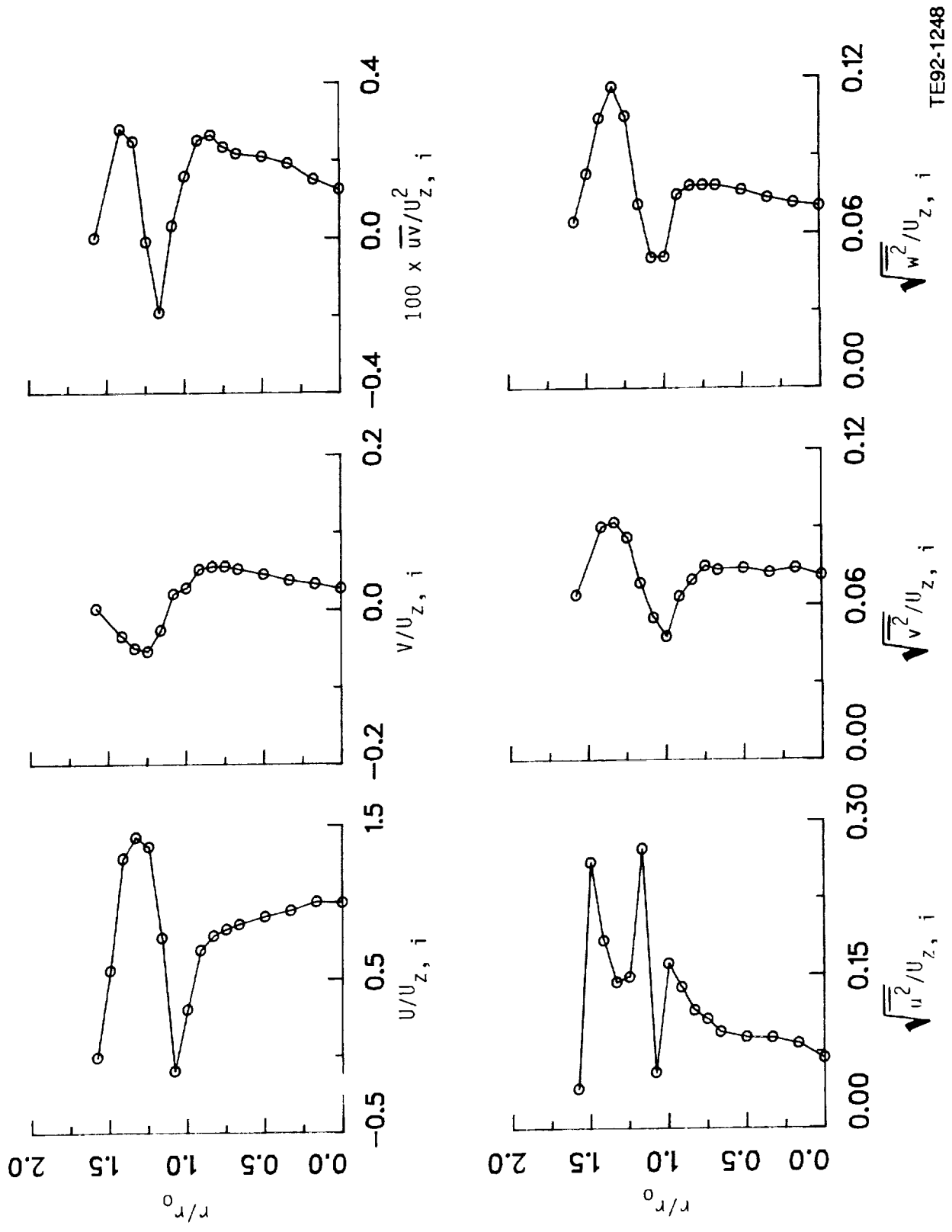
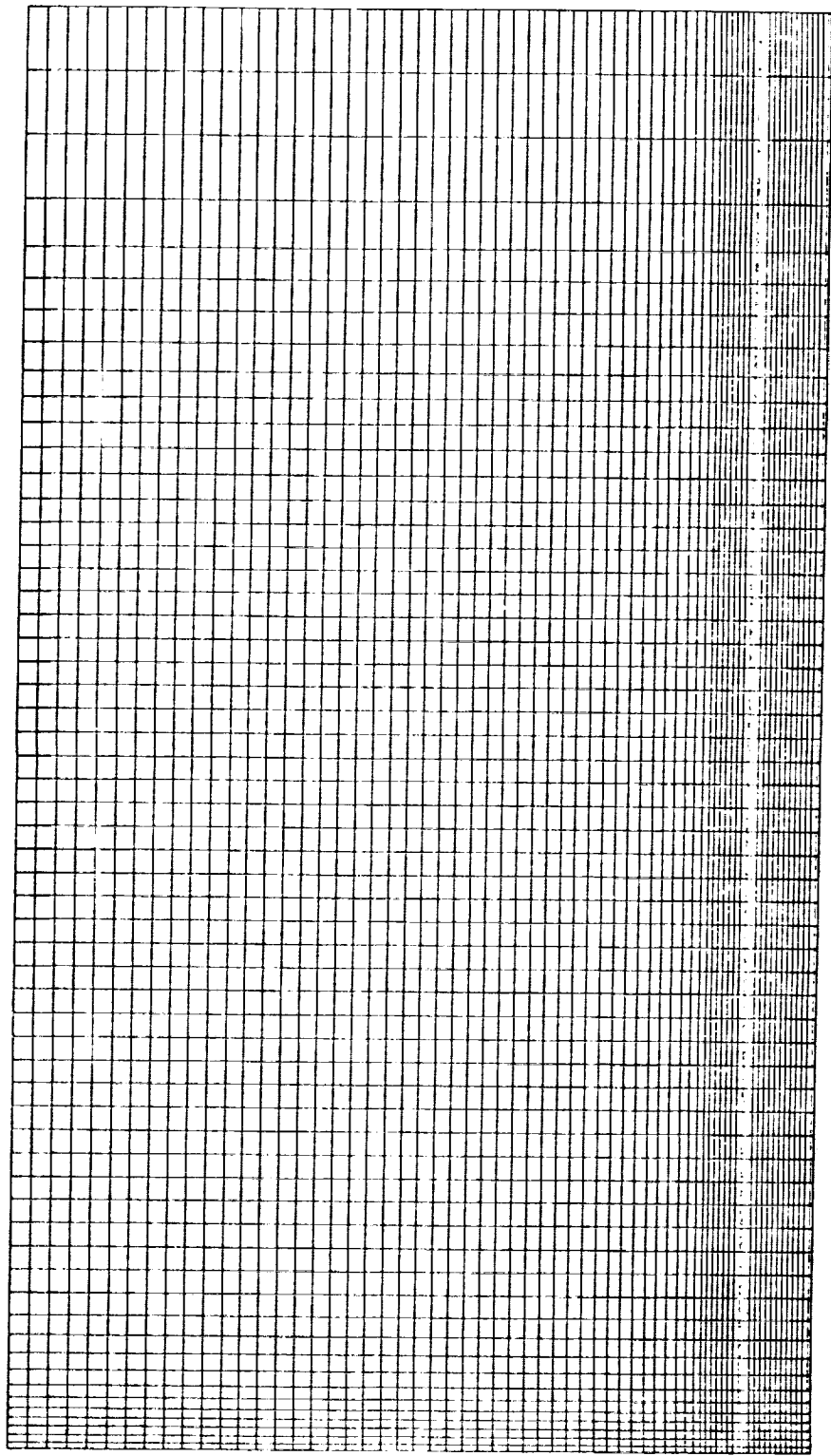


Figure 6.4.1-1. Unconfined coaxial jets geometry.



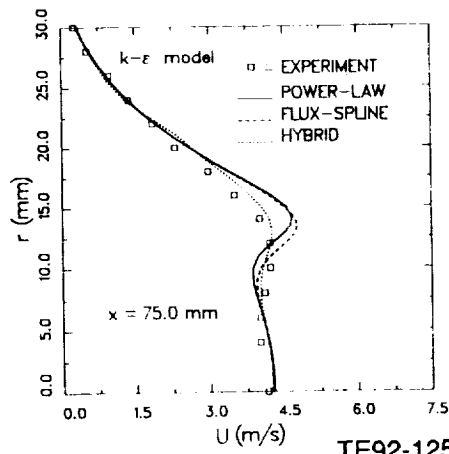
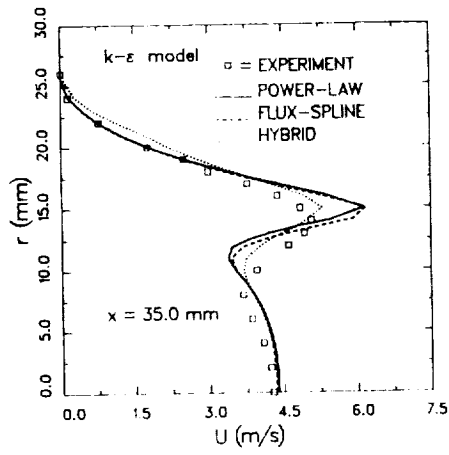
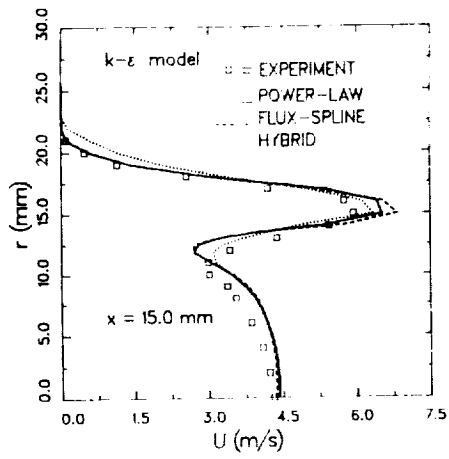
TE92-1248

Figure 6.4.1-2. Measured profiles at the inlet plane ($x = 2 \text{ mm}$).



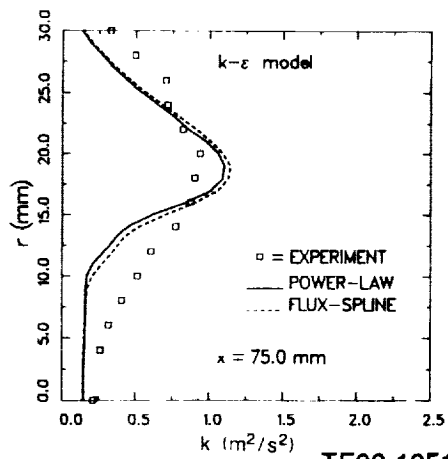
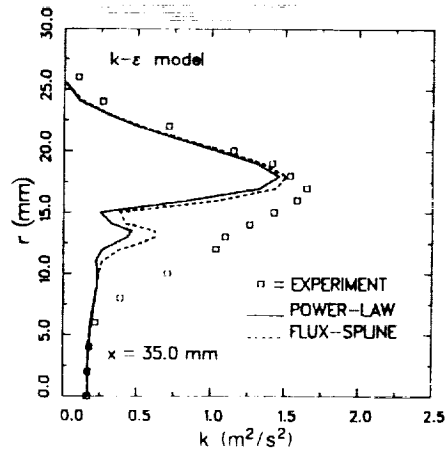
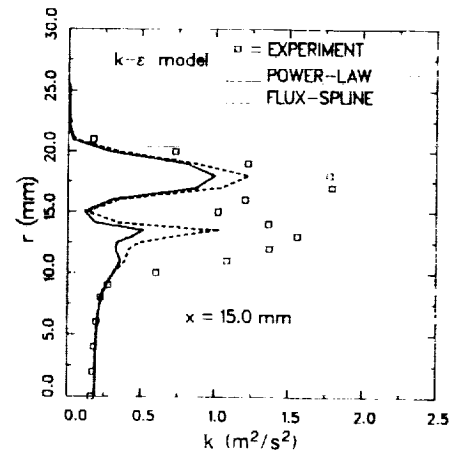
TE92-1249

Figure 6.4.1-3. Unconfined coaxial jets grid layout.



TE92-1250

Figure 6.4.1-4. Comparison of measurements with mean axial velocity calculations for unconfined coaxial jets.



TE92-1251

Figure 6.4.1-5. Comparison of measurements with turbulent kinetic energy calculations.

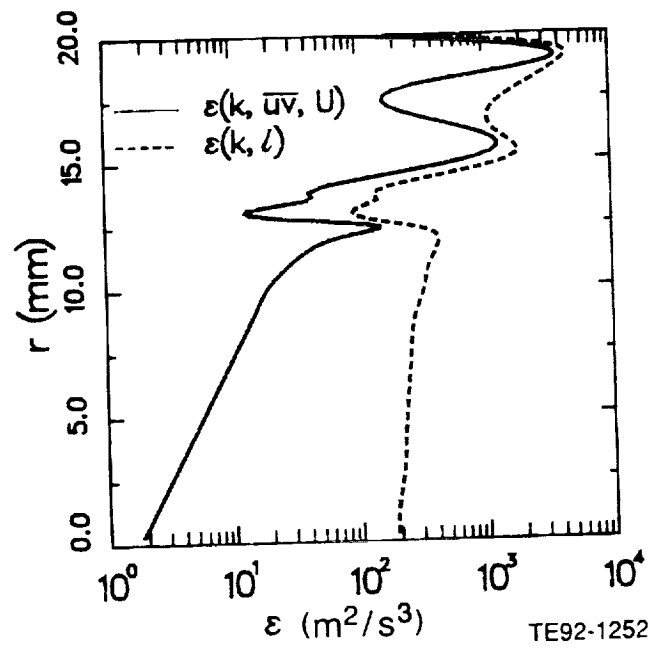


Figure 6.4.1-6. Inlet dissipation rate profiles.

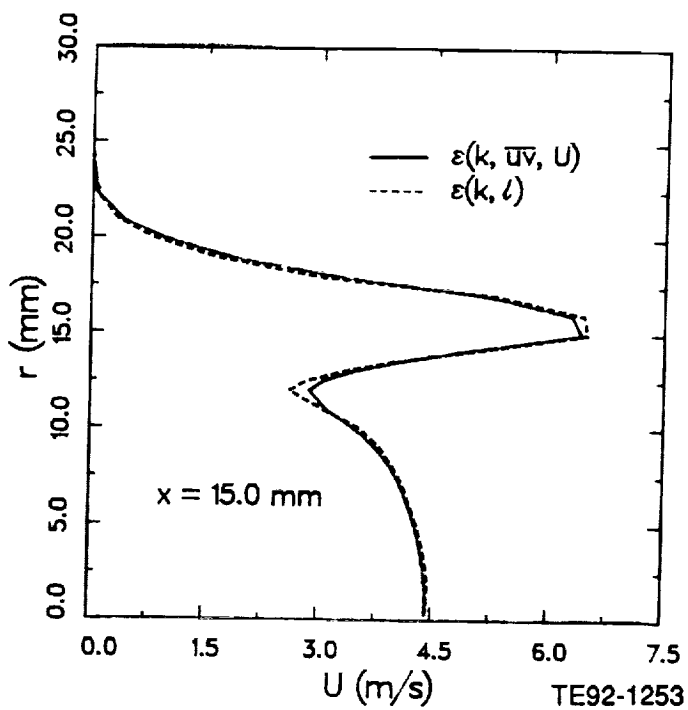
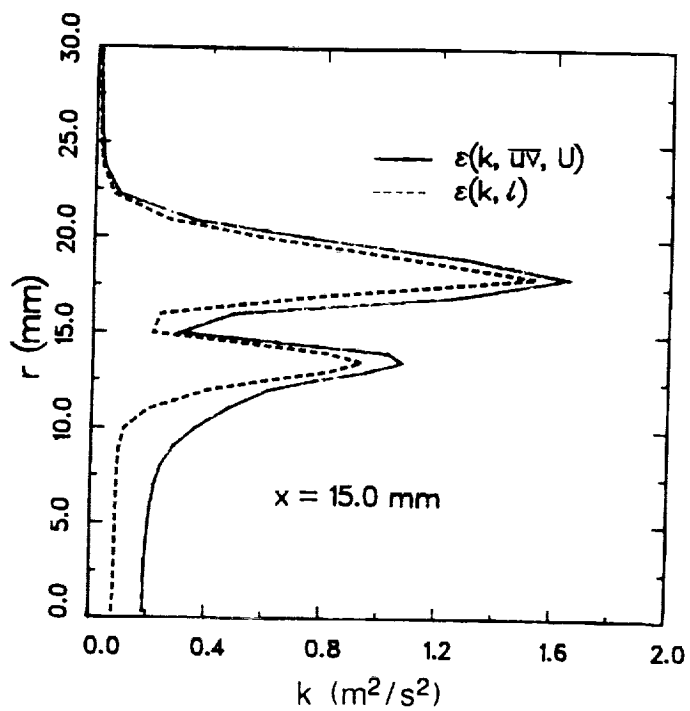
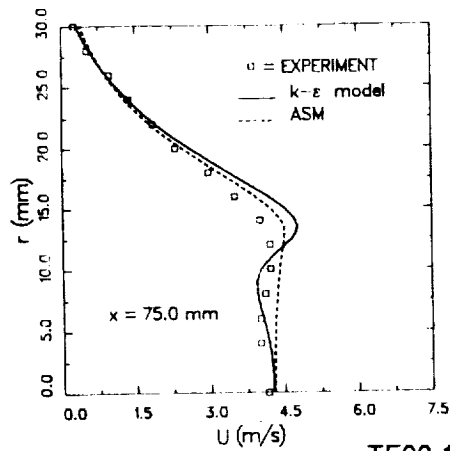
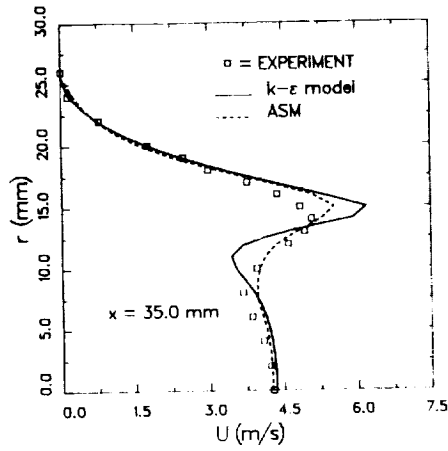
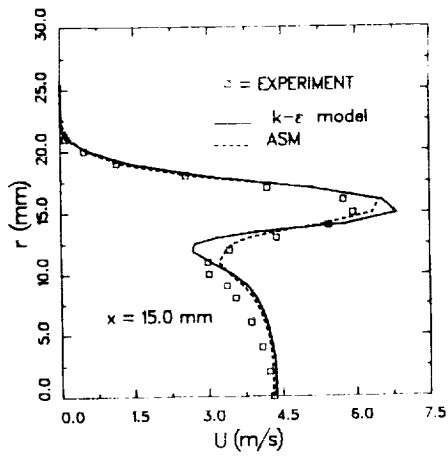
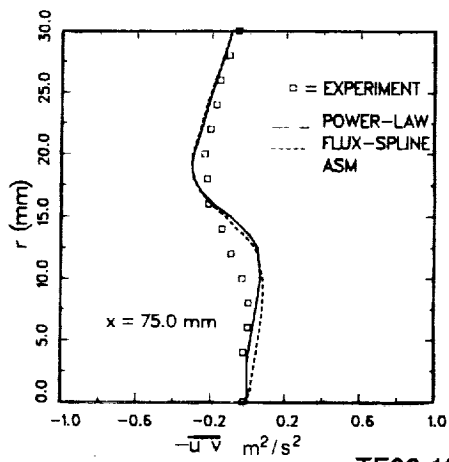
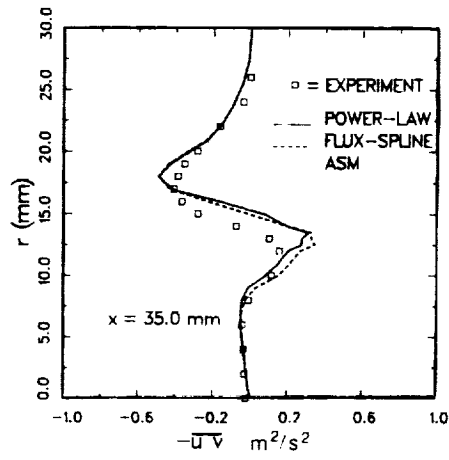
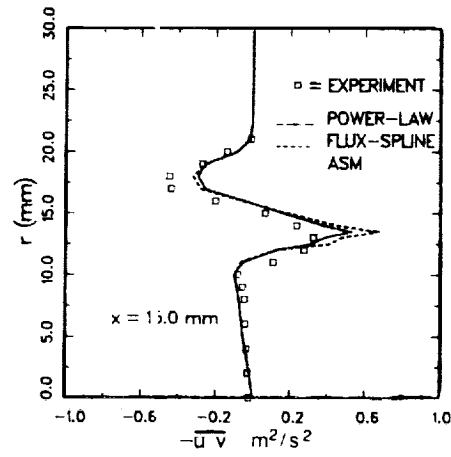


Figure 6.4.1-7. Profiles of mean axial velocity and turbulent kinetic energy using different inlet turbulent dissipation rate.



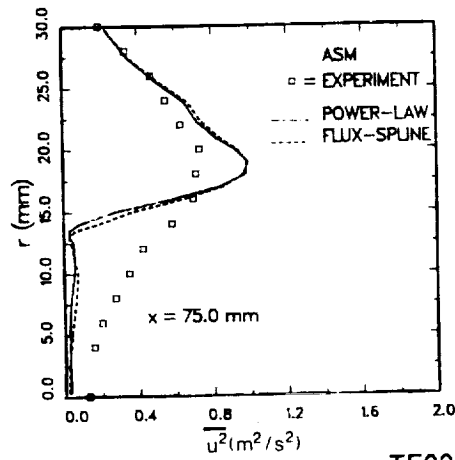
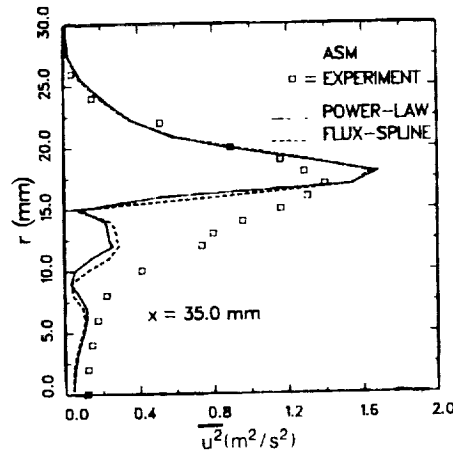
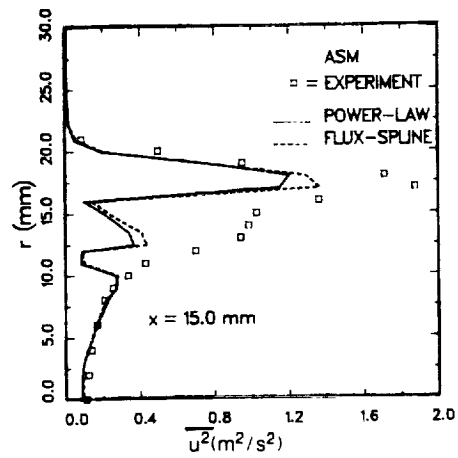
TE92-1254

Figure 6.4.1-8. Comparison of the $k-\epsilon$ and the ASM predictions of axial velocity using flux-spline with measurements.



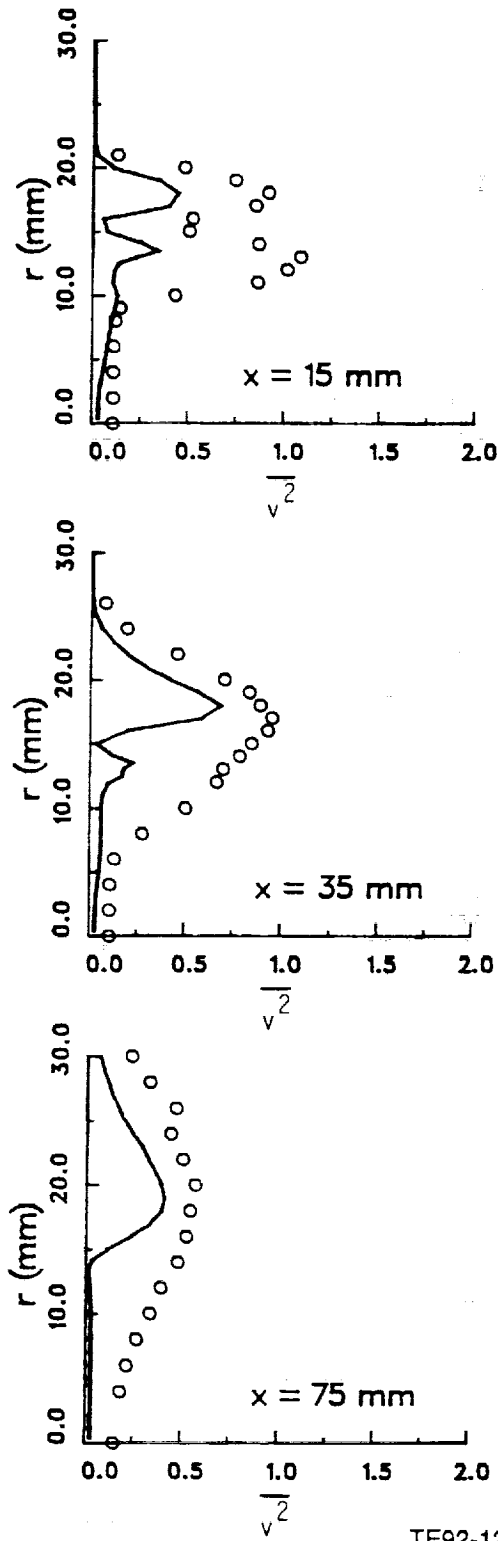
TE92-1255

Figure 6.4.1-9. Comparison of the ASM prediction of turbulent shear stress with data.



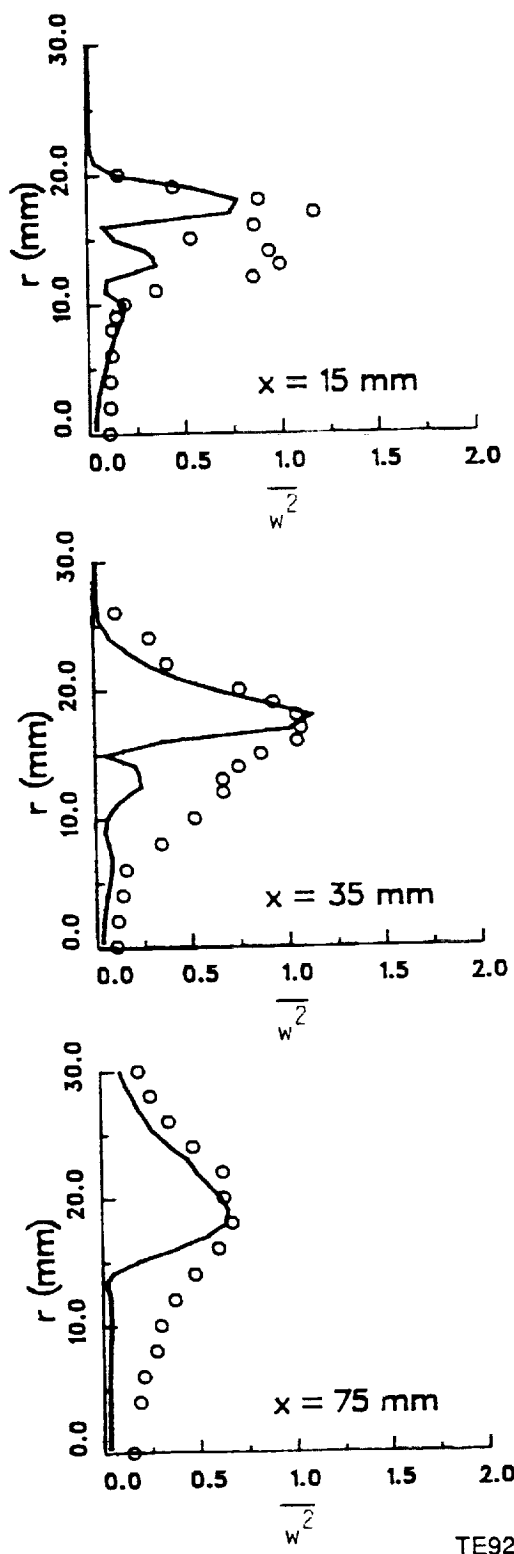
TE92-1256

Figure 6.4.1-10. Comparison of the ASM prediction of axial normal stress with data.



TE92-1257

Figure 6.4.1-11. Comparison of the ASM prediction of radial normal stress with data.



TE92-1258

Figure 6.4.1-12. Comparison of the ASM prediction of tangential normal stress with data.

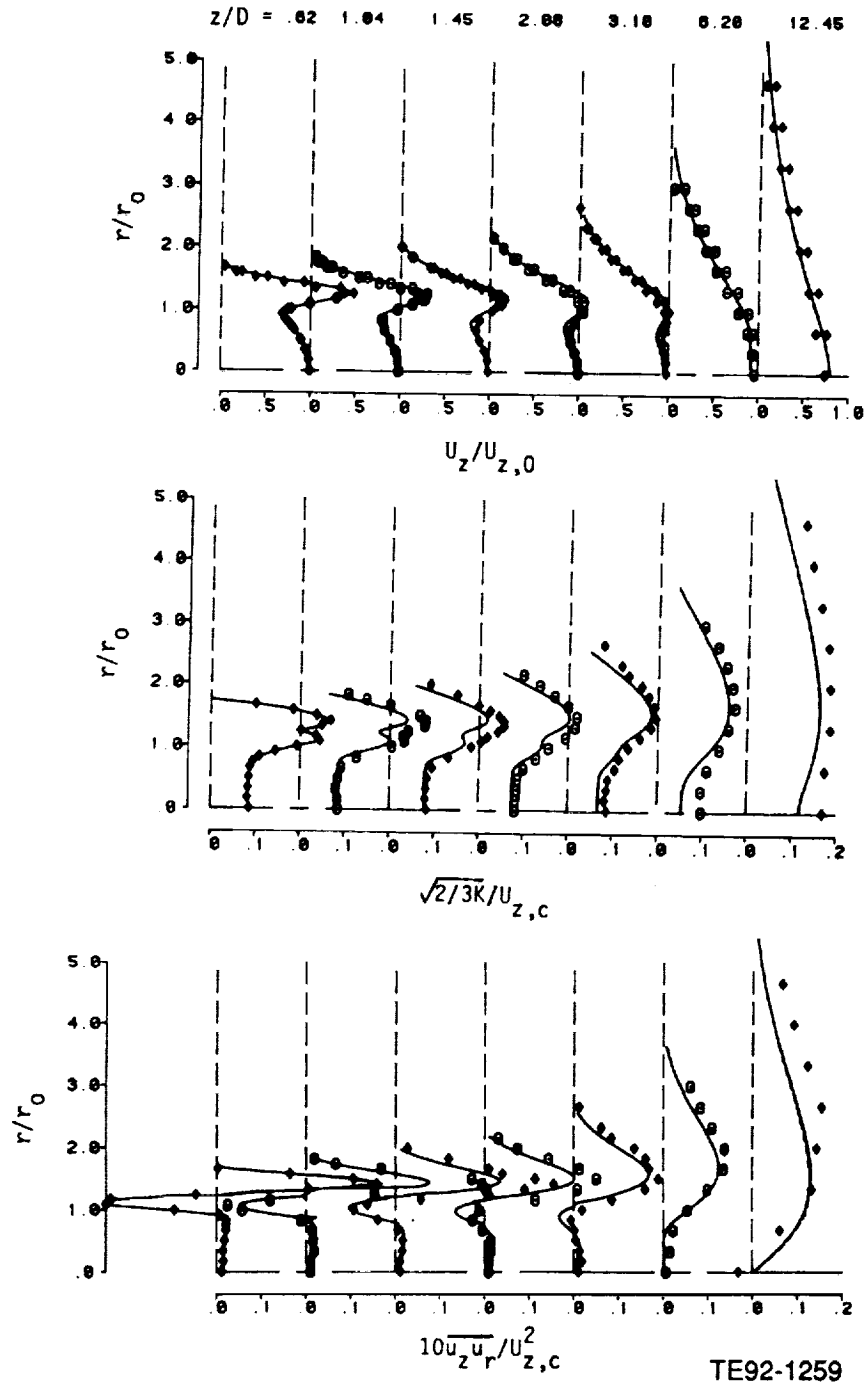


Figure 6.4.1-13. Radial profiles of normalized mean axial velocity, turbulent kinetic energy, and shear stress for the single-phase coaxial jets.

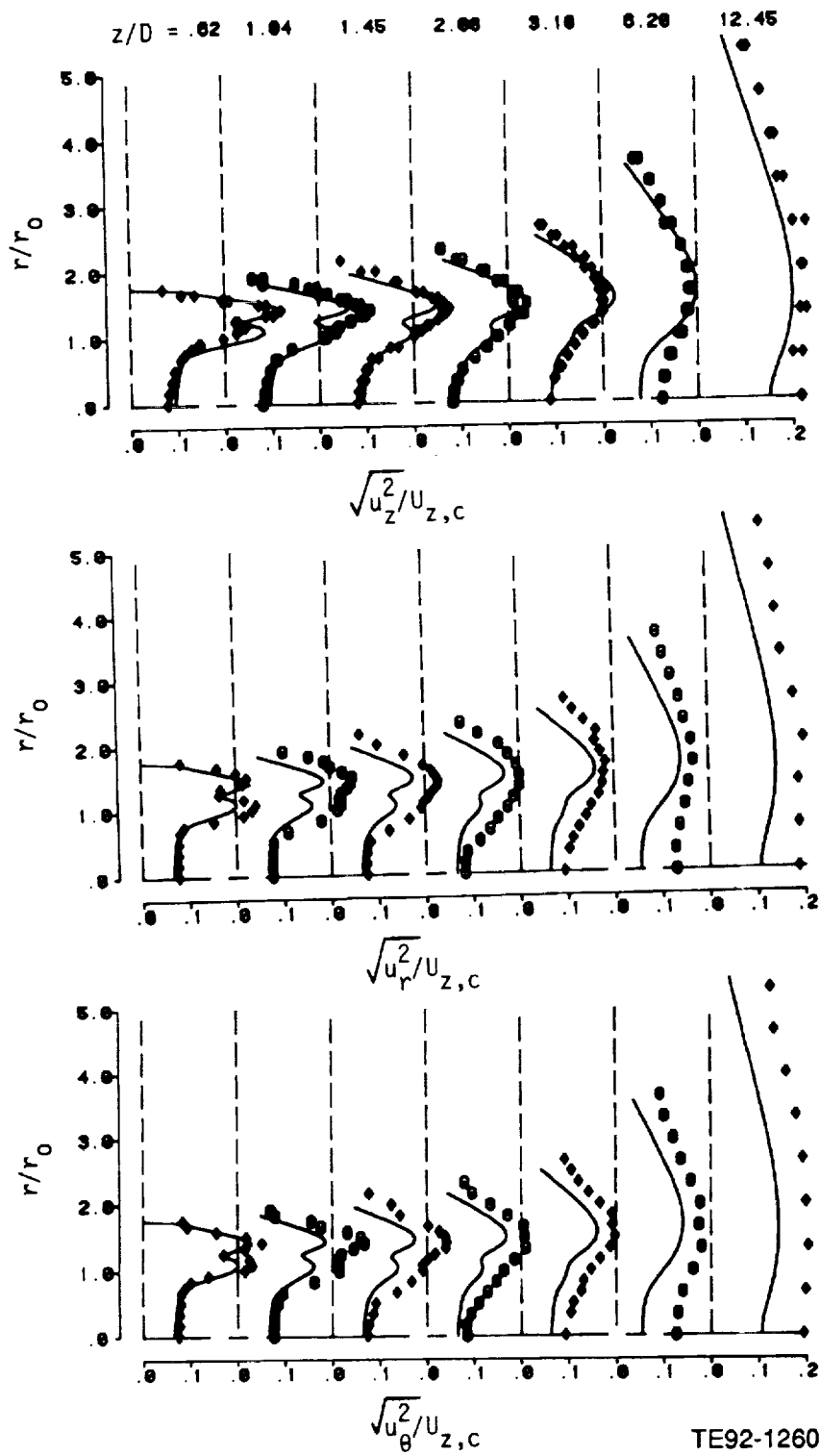


Figure 6.4.1-14. Radial profile of normalized rms velocity components for the single-phase coaxial jets.

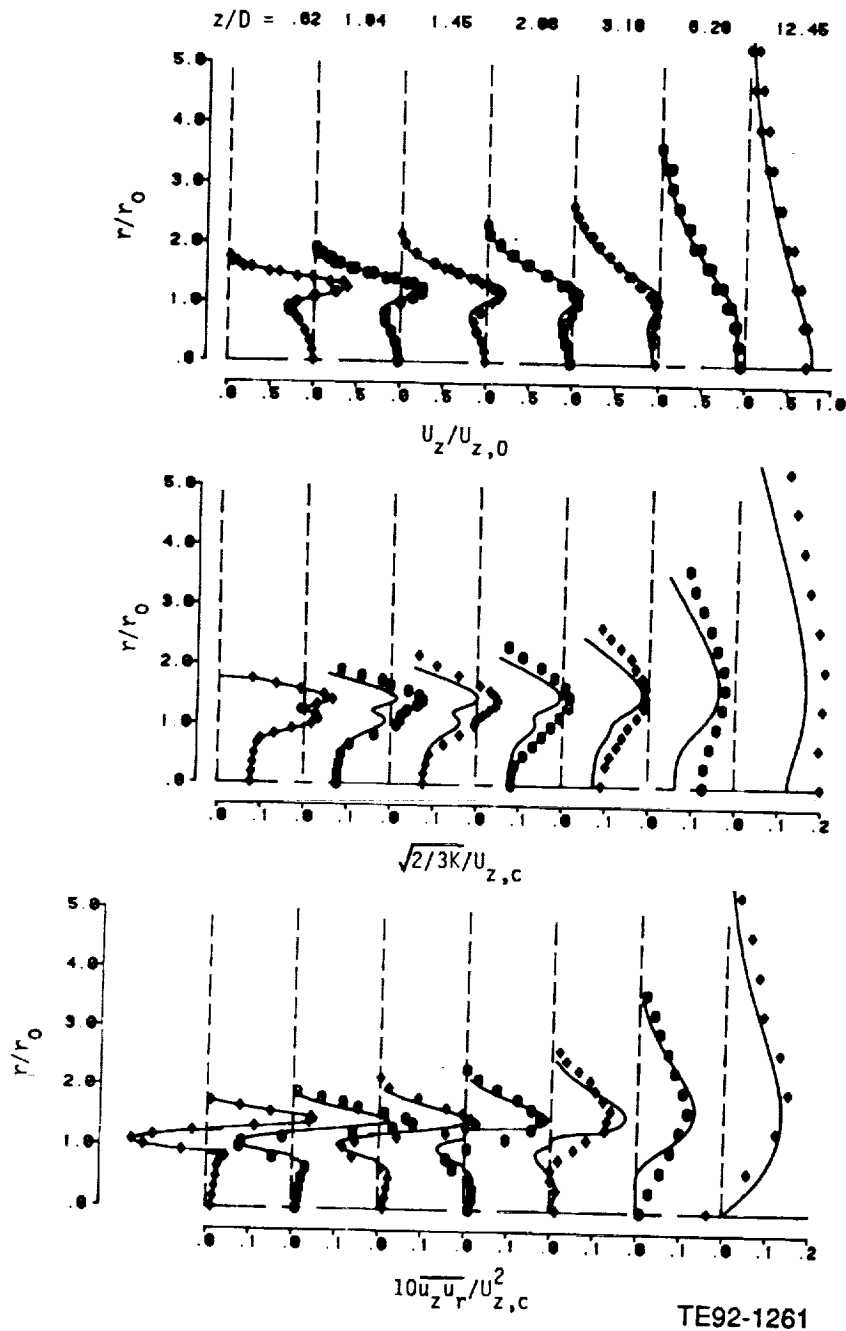


Figure 6.4.1-15. Radial profiles of normalized mean axial velocity, turbulent kinetic energy, and shear stress for the particle-laden coaxial jets.

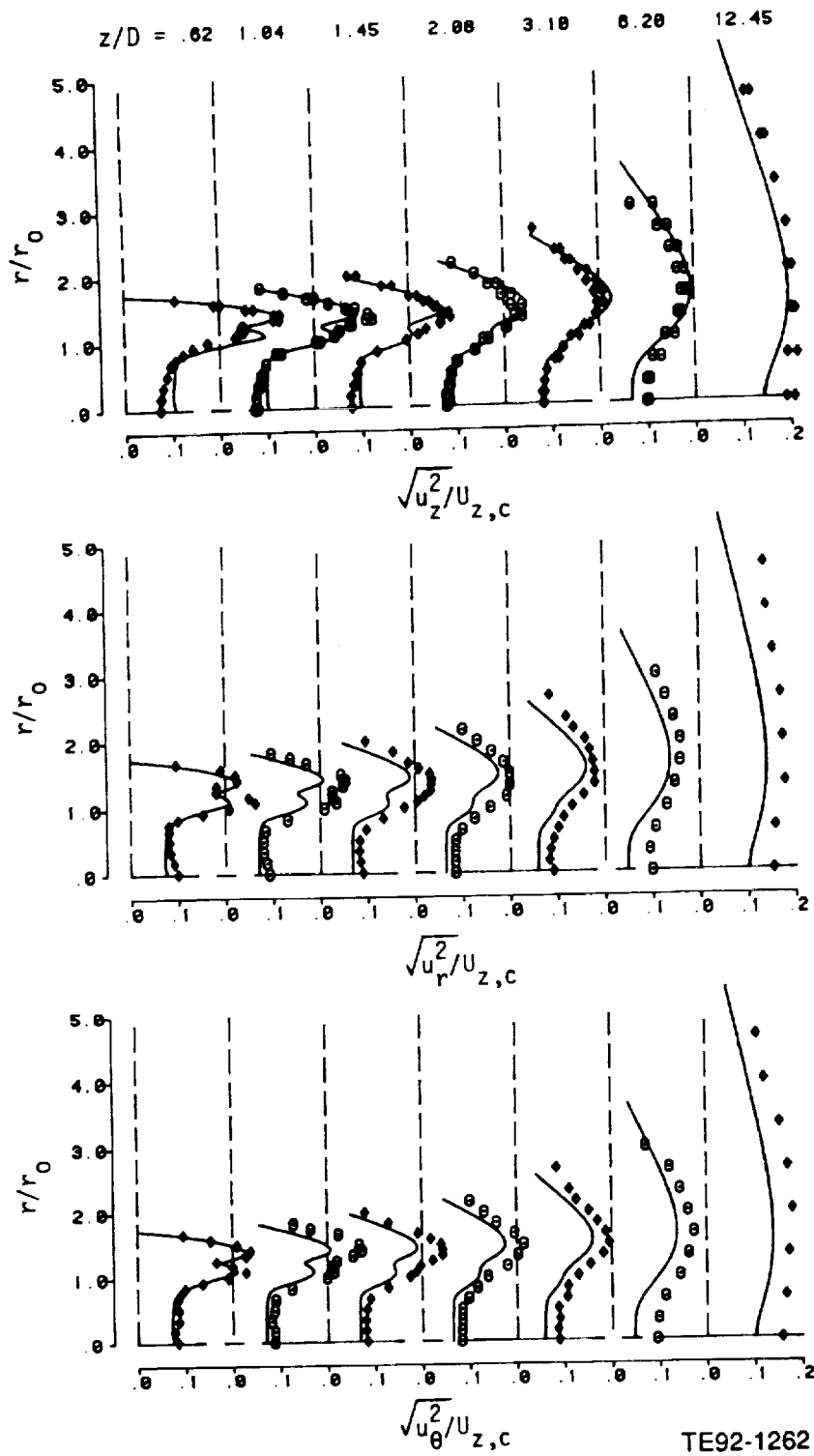


Figure 6.4.1-16. Measurements of rms gas velocity component for the particle-laden coaxial jets.

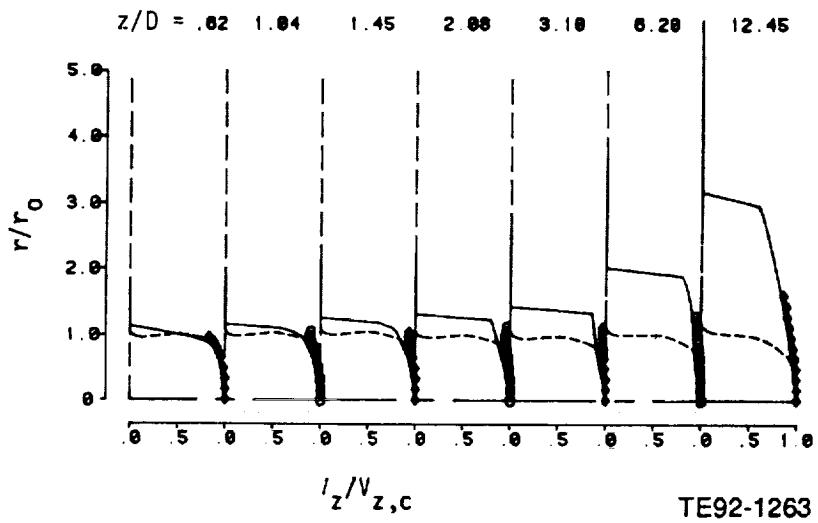


Figure 6.4.1-17. Radial profiles of normalized particle axial velocity.

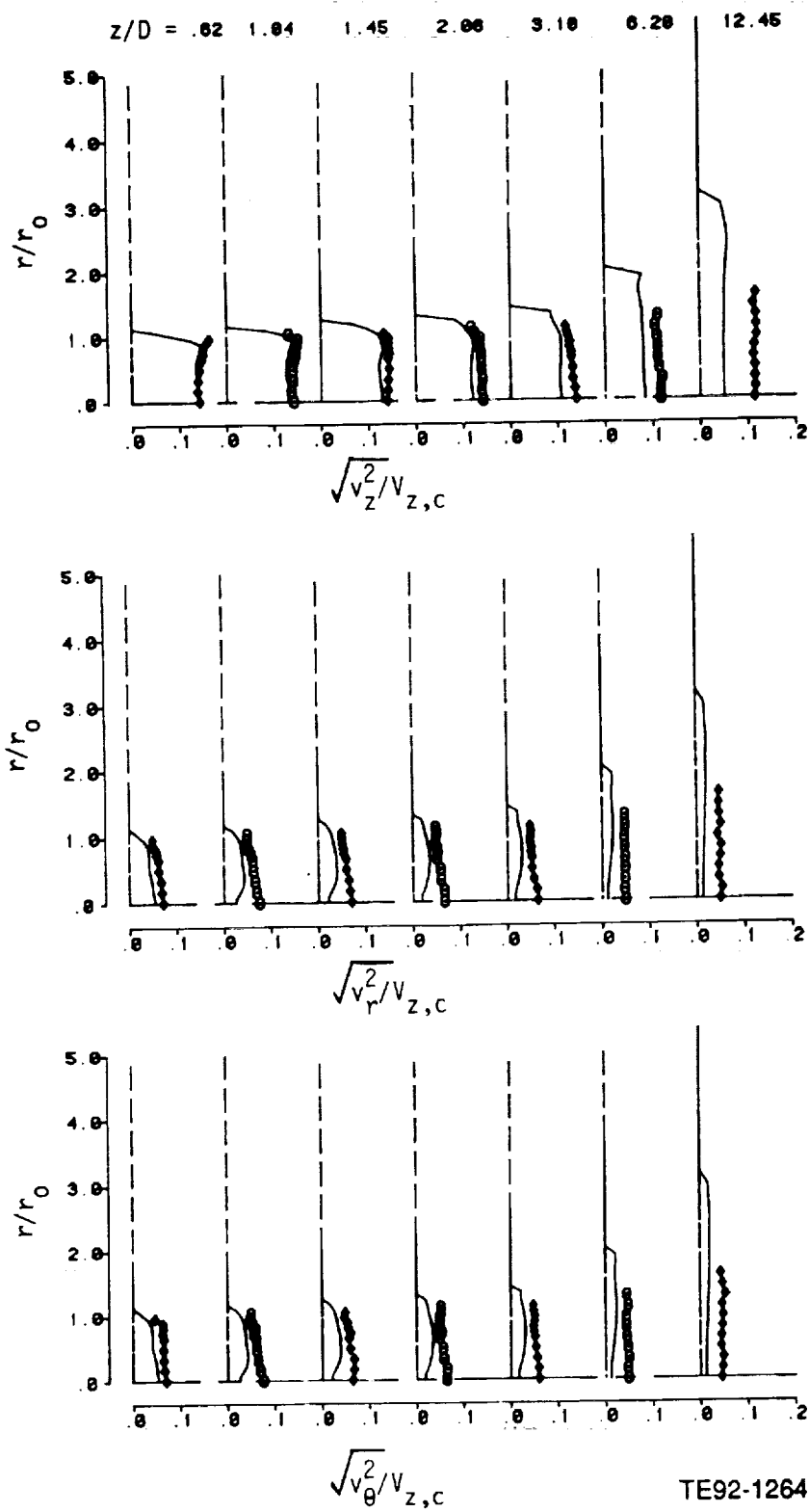


Figure 6.4.1-18. Radial profiles of rms of particle velocity components.

6.4.2 Confined Coaxial Jets

In this section comparison of computational results with data is presented for coaxial flow with and without particle beads. For the present study, a confined flow configuration was selected. In this configuration, the injector was directed vertically downward. The experimental test parameters are summarized in Table 6.4-III, and the sketch of the test section is shown in Figure 6.4.2-1.

The set of governing partial differential equations apply for nonswirling continuous (carrier) phase flow consist of equations for continuity, axial (x) and radial (r) momenta, ϵ , and four Reynolds stress components. The finite volume approach (Patankar, 1980) is used to reduce the continuous equations to a set of coupled discrete equations. The numerical solutions are obtained using the flux-spline differencing scheme (FSDS) (Varejao, 1979).

The elliptic nature of transfer equations requires that boundary conditions be specified on the four sides of the solution domain. Four kinds of boundaries, inlet, axis of symmetry, wall, and the outlet, need consideration. At the inlet boundary, which is located at the first measurement plane ($x = 4$ mm), the measured profiles of U, V, W, u^2, v^2, w^2 , and uv are applied. The inlet dissipation rate is prescribed based on the assumption of constant length scale and the turbulent kinetic energy, namely

$$\epsilon = \frac{K^{1.5}}{0.2 R_3} \quad (70)$$

where R_3 ($R_3 = 76$ mm) is the pipe radius. The macrolength scale of $0.2 R_3$ was estimated through the sensitivity analysis.

At the axis of symmetry, the radial velocity, shear stresses, and the radial gradients of other variables are set to zero. All streamwise gradients are presumed zero in the exit plane of the calculation domain except for axial velocity which needs to be corrected to satisfy integral mass balance. The conventional logarithmic law, which is based on the local equilibrium assumption, is applied to determine the wall shear stress component. The shear stress is then used as the boundary condition for U momentum and uv equations. The boundary conditions for normal stresses are imposed through the modifications of their production terms using the new calculated wall shear stress value.

Table 6.4-III.
Confined coaxial jets experimental conditions at 4 mm downstream of nozzle exit.

Continuous phase	
Medium	Air
Density, ρ	1.17 Kg/m ³
Inner jet mass flow rate, m_1	0.0021 Kg/s
Annular jet mass flow rate, m_2	0.0033 kg/s
Dilute jet mass flow rate, m_3	0.0272 kg/s
Averaged velocity of inner jet, U_0	3.935 m/s
Discrete phase	
Medium	Glass beads
Density, ρ_p	2500 kg/m ³
Beads diameter, D_p	105 μ m
Centerline velocity	4.2 m/s
Centerline beads rate	90 1/s
Mass flow rate	0.00193 kg/s
Mass loading beads to air, LR	0.925

The coupled equations and boundary conditions are solved numerically in a sequential manner using the staggered grids for velocities and shear stresses. The main advantage of staggering the locations of stresses is to enhance the numerical stability, a result of high coupling between the shear stresses and related mean strains. The iteration sequence employs the SIMPLER algorithm (Patankar, 1980) to handle the coupling between the continuity and momentum equations. The algebraic equations are solved using a line-by-line TDMA.

The ordinary differential equations describing the dispersed phase are solved using forward numerical integration. The calculations start from the first measurement plane ($x = 4$ mm) where the mean and fluctuation velocity profiles of particles and their rates of injection are available. At the wall, particles are assumed to bounce back with an angle of reflection equal to the angle of incidence.

Numerical iterations are performed over the continuous and dispersed phases until the absolute sums of the normalized mass and momentum of the carrier phase at all internal grid points, and the change of the particle source terms, are less than 10^{-5} .

A nonuniform grid of 61×57 in the axial and radial directions is used for continuous phase calculations (Figure 6.4.2-2). A finer grid spacing is assigned near the inlet, centerline, and in the shear layer. The computational domain extends from the first experimental location ($x = 4$ mm) to 300 mm downstream of the jet exit. Since the measured flow does not show any x dependence at $x > 250$ mm, the specified condition $\partial/\partial x = 0$ at the exit plane of the calculation domain is reasonable. The discrete phase calculation also starts from the same axial location, i.e., $x = 4$ mm. Four thousand particles distributed at forty radial locations are used for ST treatment.

The present calculations have been made using the flux-spline differencing scheme and the calculated results are essentially free of numerical diffusion. Therefore, the discrepancy between the experimental data and the prediction can be attributed to two sources, improper boundary conditions at the inlet plane and the deficiency of the turbulence model. As regards the inlet conditions, all quantities except the dissipation rate (ϵ) were prescribed from the measurement. These profiles are shown in Figure 6.4.2-3 and have been normalized by the inner jet averaged velocity (U_0) and the pipe radius (R_3). Above $r/R_3 > 0.5$, the flow field is similar to plug flow condition created by the strong coflow. This region is not the focus of the study and has not been shown in the presented figures. The uncertainties in the derivation of inlet ϵ profile would adversely affect the calculation at downstream locations. It was shown, however, that the use of inlet ϵ derived from the constant length-scale assumption can result in a better prediction (Nikjooy and Mongia, 1991).

Comparison of the normalized axial mean velocity profiles for single-phase flow with experimental data along the streamwise direction is presented in Figure 6.4.2-4. These results were obtained from the $k-\epsilon$ model. The predictions are in very good agreement with measured values. There are some discrepancies near the maximum flow region which can be due to the higher radial diffusion process. The flow discharging from the inner pipe has a flat velocity profile which decelerates gradually due to the pressure effects. Comparisons of the turbulent shear stress and kinetic energy are shown in Figures 6.4.2-5 and 6.4.2-6. The $k-\epsilon$ model overestimated the maximum level of the turbulent kinetic energy near the nozzle exit, however, the agreement between the calculated shear stress and data is excellent. It seems that the overpredicting of turbulent kinetic energy in the upstream region resulted in higher effective diffusion, which is responsible for underestimating the peak velocities. At about $x = 150$ mm both flow streams have been completely mixed. The agreement between the predicted and experimental values of kinetic energy is not as good as that for the axial velocity. Even though the trends are similar, the predicted kinetic energy is smaller than that derived from the measurements in downstream regions.

Comparison of the mean and turbulence quantities by the DSM closure with the measured values is presented in Figures 6.4.2-7 through 6.4.2-11. The predicted mean velocity profiles are in excellent agreement with the data. The peak and centerline velocities were very well predicted. The pressure-strain correla-

tion model used for these calculations is just based on the return-to-isotropy model ($C_1 = 5.0$, $C_2 = 0.0$). The differences between the calculated and experimental results are most significant in the case of the normal stresses. The maximum axial turbulence intensity has been overpredicted in most of the flow region, however, the trend was accurately predicted. This behavior resulted in underprediction of the maximum values of other rms components, especially the radial fluctuation. Essentially, the same trends are observed for radial and tangential stress components. The discrepancies between the model and data clearly indicate the lack of performance of the pressure-strain model. One reason for this could be the lack of an appropriate model for the "rapid part" which was not considered here. The turbulent shear stress was accurately predicted. The negative peak in the shear stress profile corresponds to the shear layer between the two streams and the positive peak corresponds to the shear layer associated with the expansion.

Comparisons of the normalized mean axial velocity and Reynolds stress predicted by DSM and ASM closures with the measured values are presented in Figures 6.4.2-12 through 6.4.2-16. The calculated velocity fields predicted by both models are very similar at downstream locations. Some differences are observed between the two models in the maximum and expansion zones at upstream regions. Overall, the ASM prediction is in good agreement with data. Examination of the calculated rms profiles indicates that the DSM's results mimic the experimental data better at all stations. A wide disparity exists between the measured normal Reynolds stresses and the ASM's results, especially in the peak zone. As regards the turbulent shear stress, the ASM underpredicted the maximum and minimum data points in upstream locations. The predicted turbulent kinetic energy by the k - ϵ , DSM, and ASM (Figure 6.4.2-17) shows that the DSM simulated the data better than other models.

The calculation for a particle-laden jet was also performed over the same computational domain and the same grid distribution was used. The inlet conditions, except the dissipation rate (ϵ) were specified from the experimental data. These profiles are shown in Figure 6.4.2-18 and have been normalized by the inner jet averaged velocity (U_0), particles flux at the centerline (N_0), and the pipe radius (R_3). The inlet dissipation rate is prescribed based on the assumption of constant length scale and the turbulent kinetic energy.

The normalized axial component of mean velocity by DSM at different streamwise locations is shown in Figure 6.4.2-19. The predicted result is in excellent agreement with the experimental data. The velocity profiles are quite flat near the centerline. The measurement shows that the centerline velocity initially decreases about 10% from the inlet plan to station $x = 25$ mm. The deceleration in axial velocity probably results from the pressure effect. The predicted pressure distribution shows a negative radial gradient favoring an outward motion of the flow. As a result, the axial velocity is slowing down to satisfy the mass conservation. The centerline velocity at subsequent streamwise locations then increases, indicating the momentum transfer from the annular jet to the core region. It should be mentioned that the choice of model constants in the pressure redistribution term has been found to be effective especially on the turbulence field (Nikjooy and Mongia, 1991). The case of coaxial jets was also calculated for $C_1 = 1.5$ and $C_2 = 0.6$ in the ϕ_{jj} model. The prediction however was in large discrepancy with the data.

Comparisons of the normalized rms velocity components predicted by DSM closure with the measured values are presented in Figures 6.4.2-20, 6.4.2-21, and 6.4.2-22. Near the injector exit, e.g. $x < 15$ mm, the axial rms peaks at two radial locations correspond to the sharp decrease in the mean velocity. The production of turbulent kinetic energy is increased at these locations, consistent with the maximum turbulent intensity profiles observed in the measurement. Overall, the calculated $\sqrt{u^2}$ profiles are in good agreement with the data. The peak values are slightly overpredicted at some locations. This behavior resulted in underprediction of the maximum values of other rms components, especially the radial fluctuation. The discrepancy observed in the turbulence field between the prediction and the measurement is related in large to the deficiency of the pressure-strain model. The turbulence quantities however were all well predicted near the centerline. At downstream locations, turbulent intensities are relatively uniform across the pipe, indicating a well-mixed flow condition. As regards the turbulent shear stress, uv , the cal-

culated profiles are very similar to the data behavior (Figure 6.4.2-23). The results demonstrate that the dispersed phase had no significant effects on the continuous phase.

Predicted and measured mean particle velocities along the axis are shown in Figures 6.4.2-24 and 6.4.2-25. The calculated velocities are based on the particles' mass flow rate weighted averages. Only a portion of the entire radial section where particles could be found are presented. The predicted axial values are in good agreement with data. Despite the variations observed in the gas phase velocity near the centerline, the particle velocity shows almost no change. This is related to the fact that the particle dynamic relaxation time (τ_d) is very large compared to the turbulent characteristic time (τ). The reason for large τ_d is found in the large particle-to-gas density ratio (2500:1.17). This clearly shows that the inertia force is responsible for the particles' motion and the effects of drag force are marginal. The predicted profiles of mean radial velocity of particles are in qualitative agreement with the data. The radial velocity component however is at least one order of magnitude smaller than the axial component. It is therefore reasonable to believe that their quantitative disagreement would not severely affect other results.

The agreements between the predicted and measured fluctuating velocities of the particles are not favorable in downstream locations (Figures 6.4.2-26, 6.4.2-27, and 6.4.2-28). The data show similar radial and tangential fluctuation components. On the other hand, the axial rms value is about 1.5 times larger than others. The model has successfully predicted the anisotropy feature of the dispersed flow field. However, all three components are predicted to be lower than the data. The results for the normalized particle number density are illustrated in Figure 6.4.2-29. The reference value used for normalization is the particle number density on the centerline at the inlet plane ($x = 4$ mm). The predicted profiles presented here also represent the particles' mass flow rate per unit area or mass flux. The predicted mass flux is in reasonable agreement with data at upstream locations ($x < 35$ mm). However, the calculation shows a larger spread of the particles at the downstream region. As a result, the particles mass flux is underpredicted in the central region of the flow at those places. Although the gas phase was well-mixed downstream of the flow field, the particles will tend to accumulate near the centerline. The reasons can be due to the lack of lift force, which was discarded from the interfacial force term.

In the present study, the Reynolds equations have been extended to calculate two-phase turbulent flow without evaporation. The selected model used in this study is the extension of those desired for constant density single-phase turbulent flow. Therefore, some of the discrepancies observed in the results are related to this matter. However, the errors arising from the inlet dissipation rate profile and/or the model constants used in the pressure redistribution term should not be overlooked. Overall, the mean and turbulence fields associated with the continuous phase were reasonably well predicted by DSM. The gas appeared to be unaffected by the particles' motion. The discrete phase results are also encouraging. The discrepancies observed in the fluctuation velocities and the mass flux profiles for the particles are more clear in the downstream region where the carrier phase flow is well mixed. However, the particles still tend to accumulate near the centerline region. This shortcoming may be removed by including the effects of the lift force into the carrier phase equations.

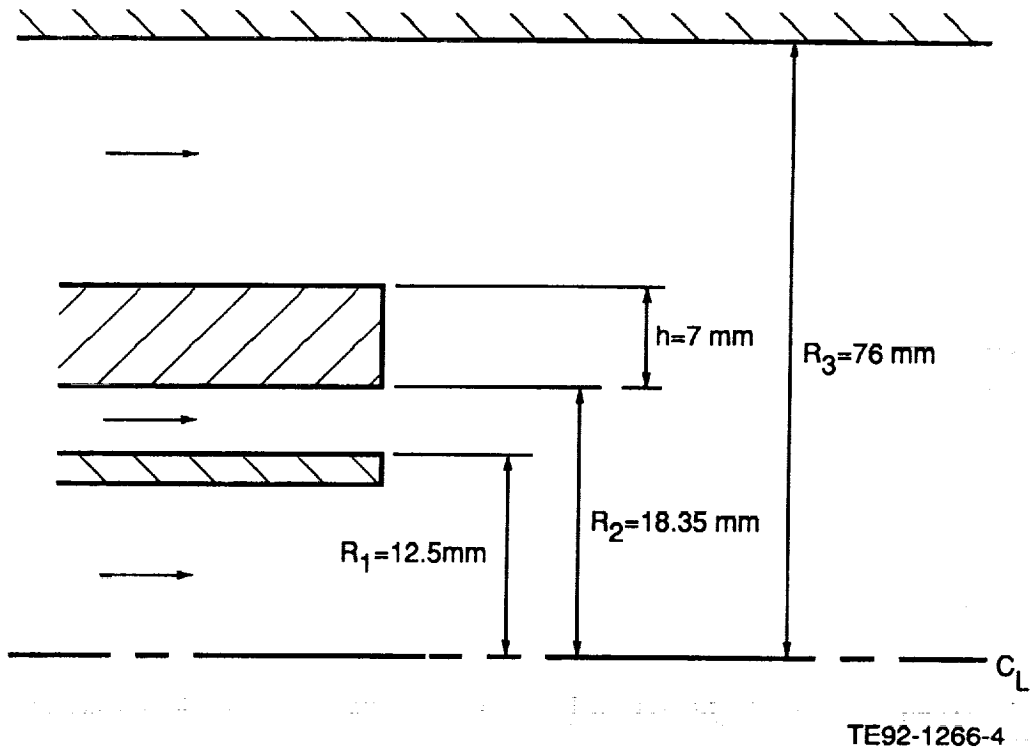
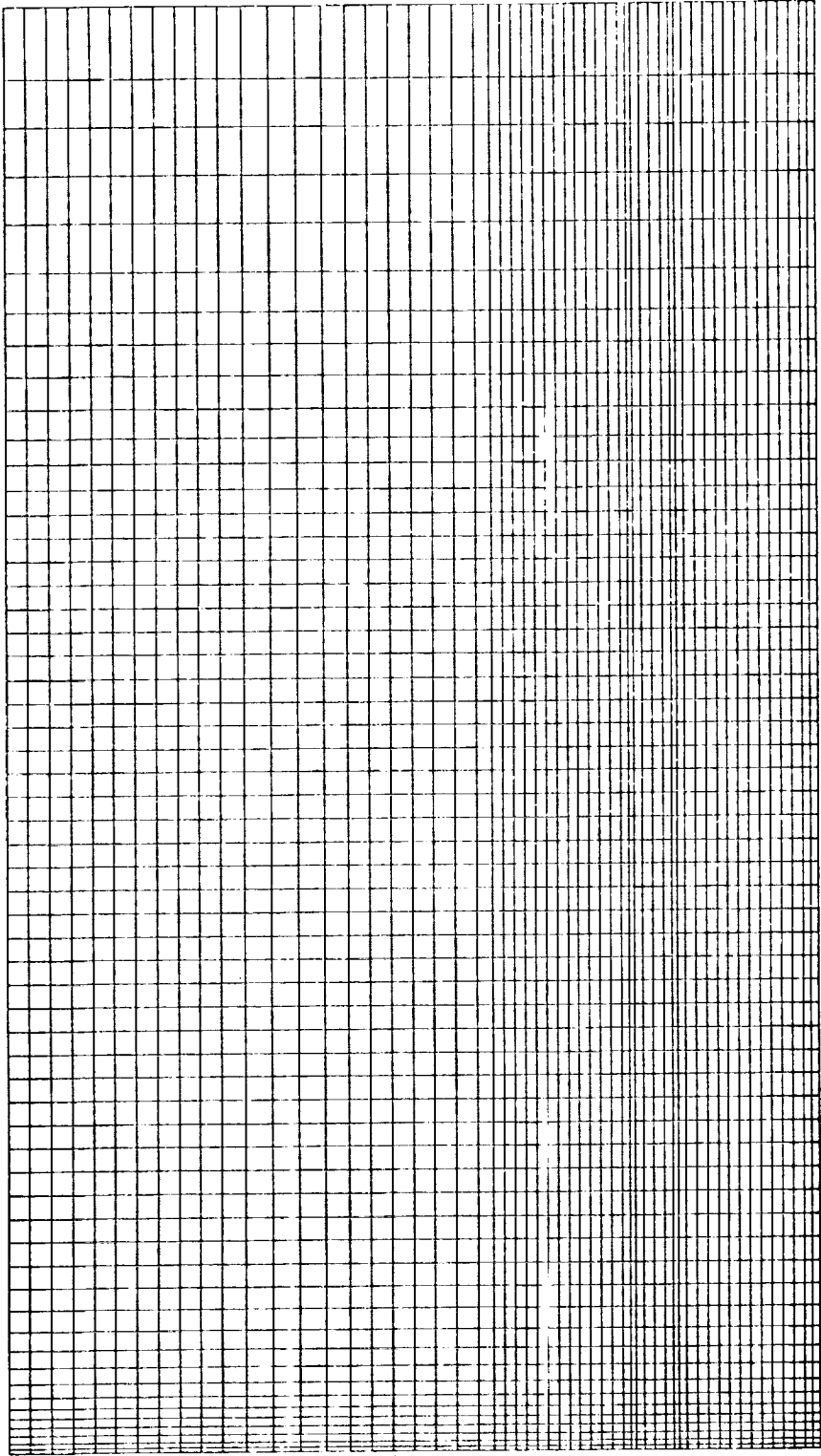


Figure 6.4.2-1. Confined coaxial jets – geometrical details.



TE92-1267

Figure 6.4.2-2. Confined coaxial jets - grid layout.

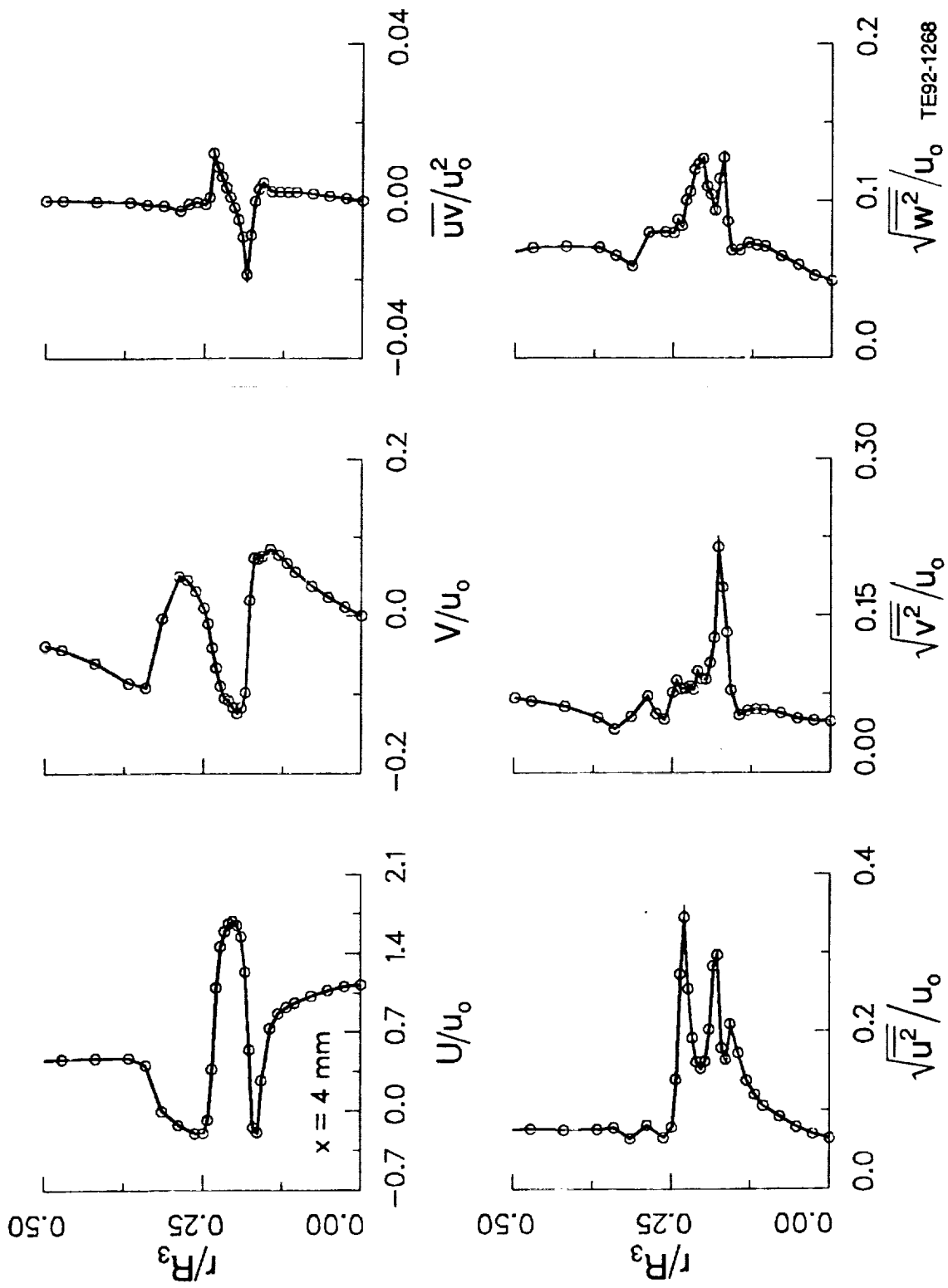
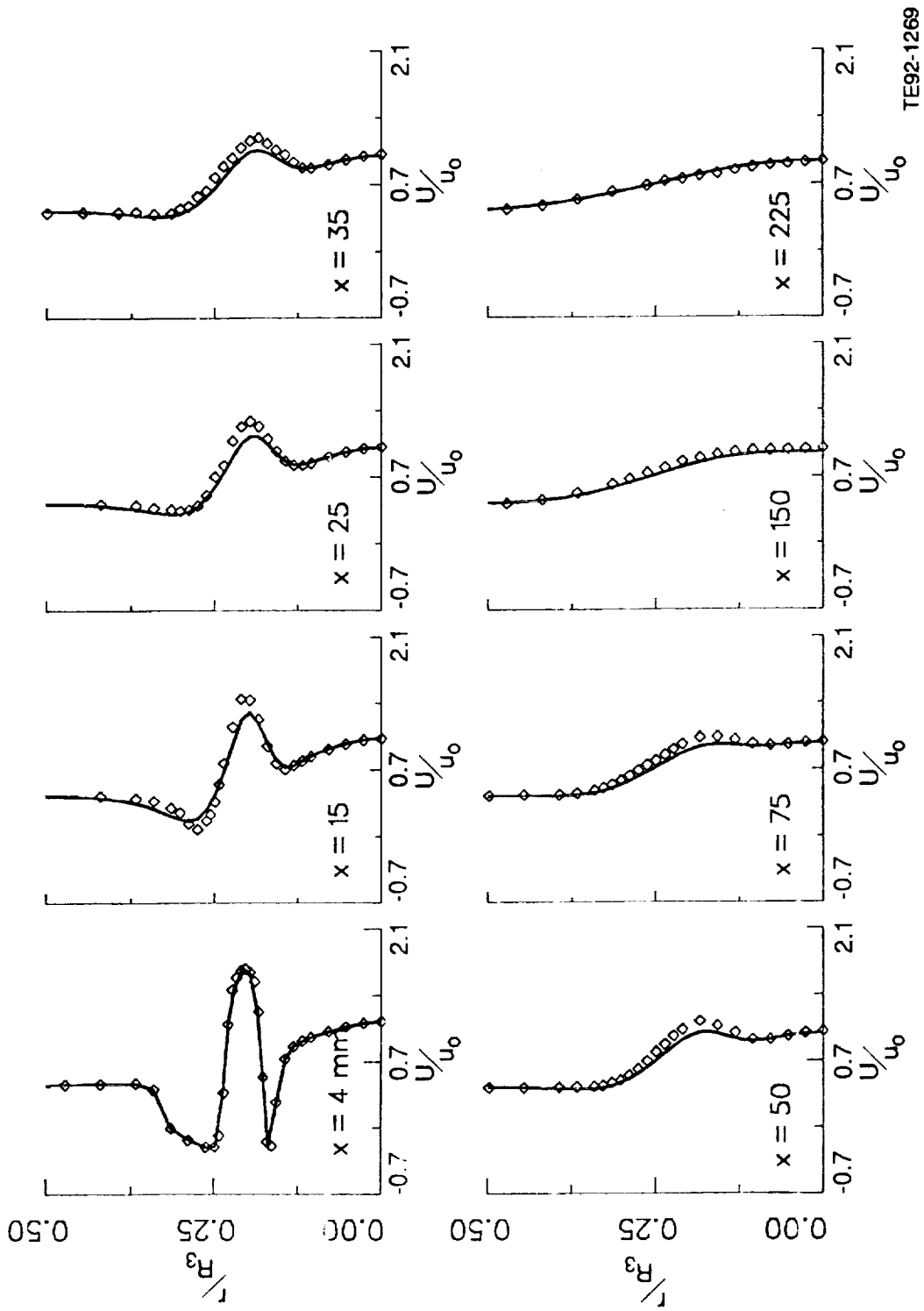


Figure 6.4.2-3. Measured profiles at the inlet plane ($x = 4 \text{ mm}$).



TE92-1269

Figure 6.4.2-4. Comparison of predicted mean axial velocity by $k-\epsilon$ model with data.

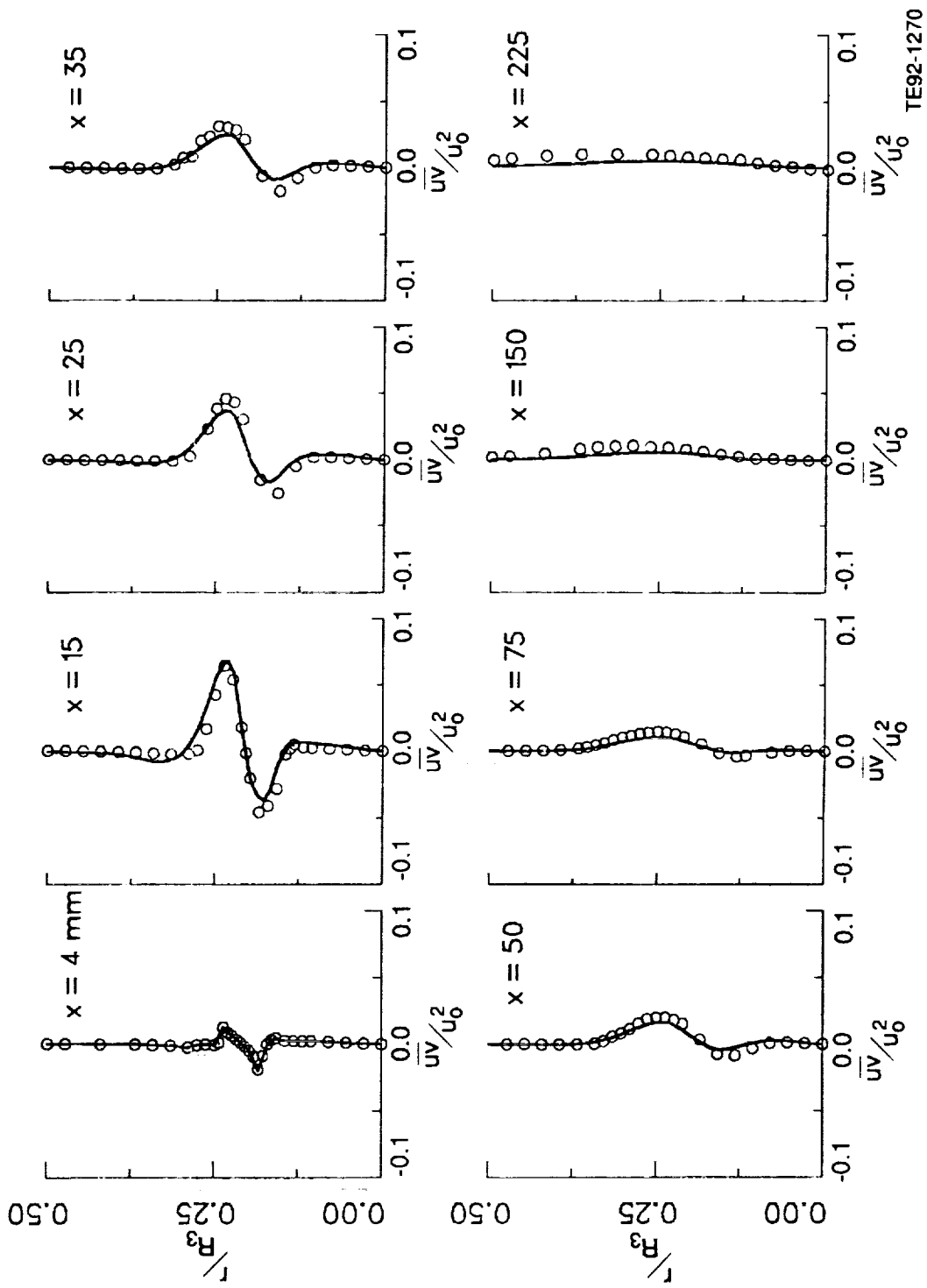


Figure 6.4.2-5. Comparison of predicted turbulent shear stress by $k-\epsilon$ model with data.

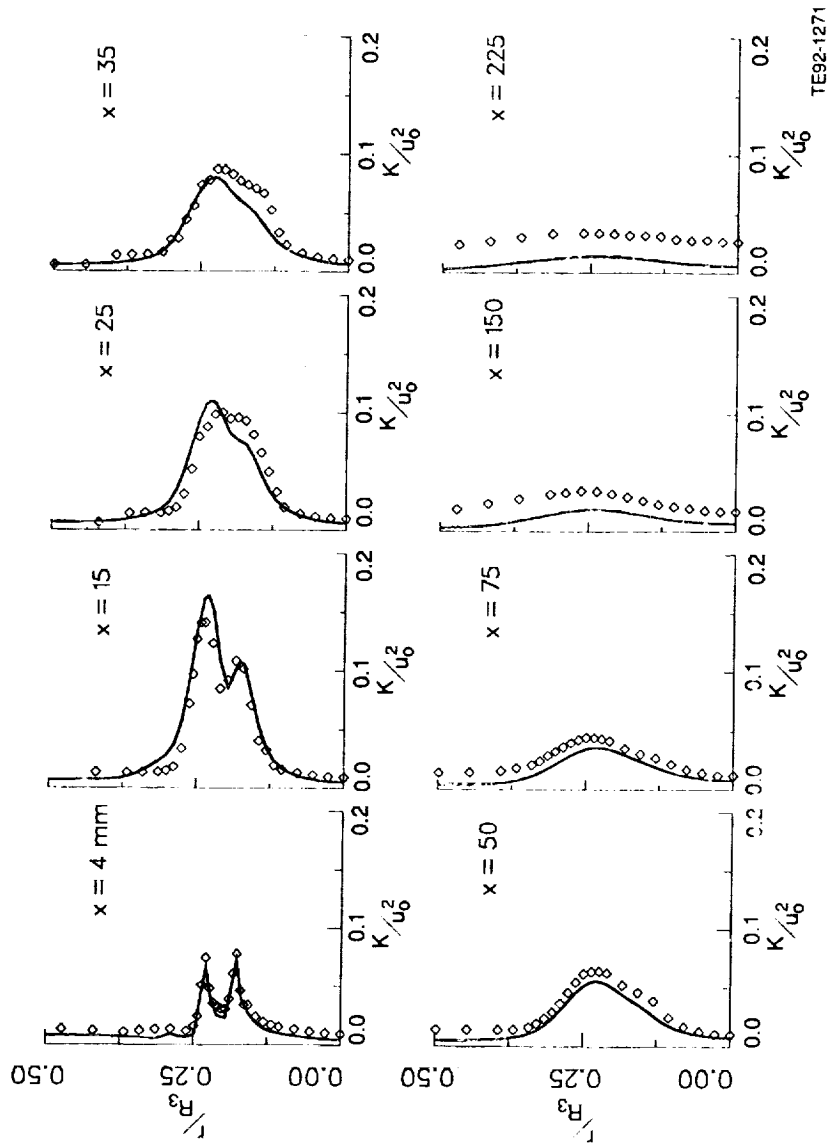
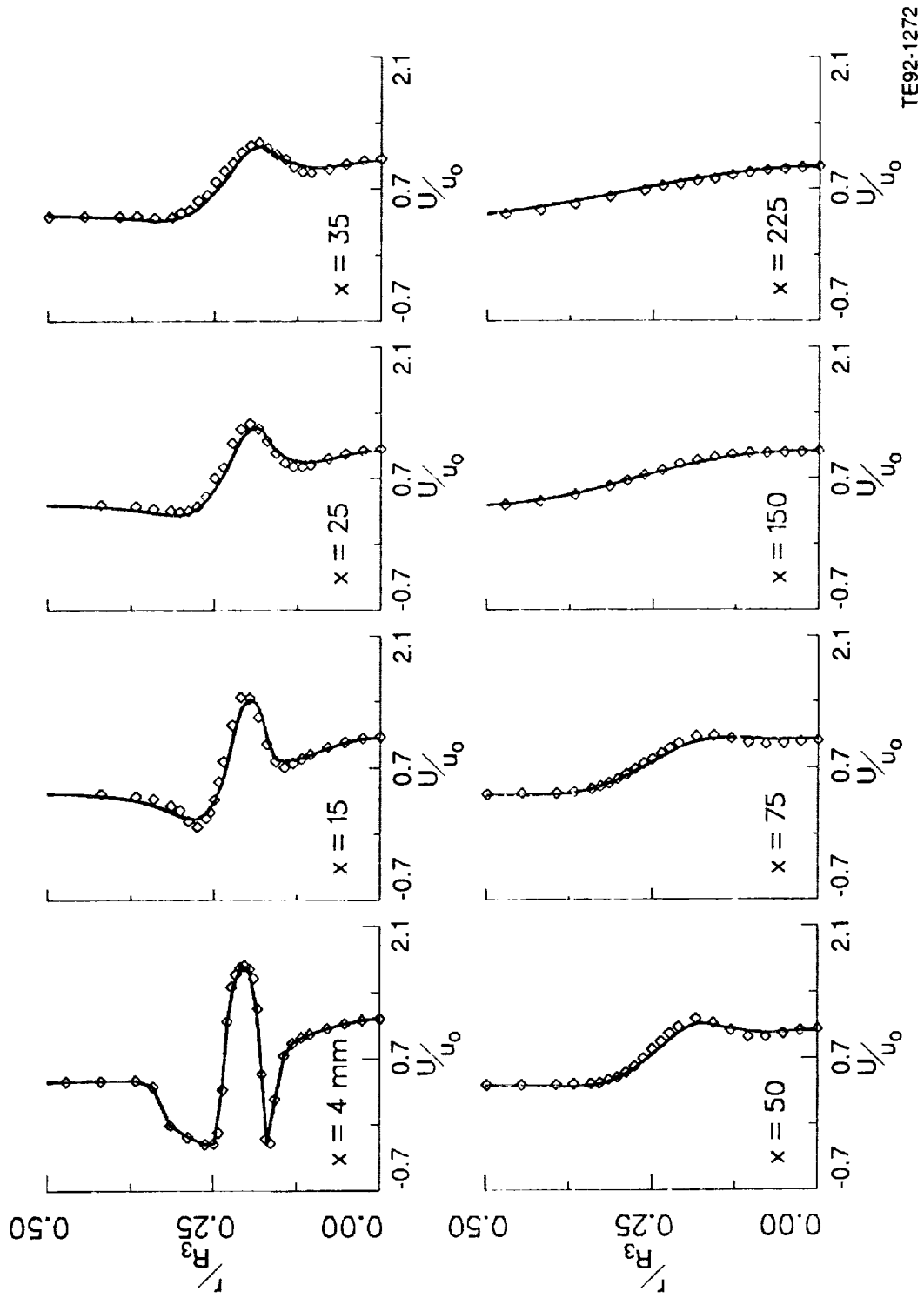
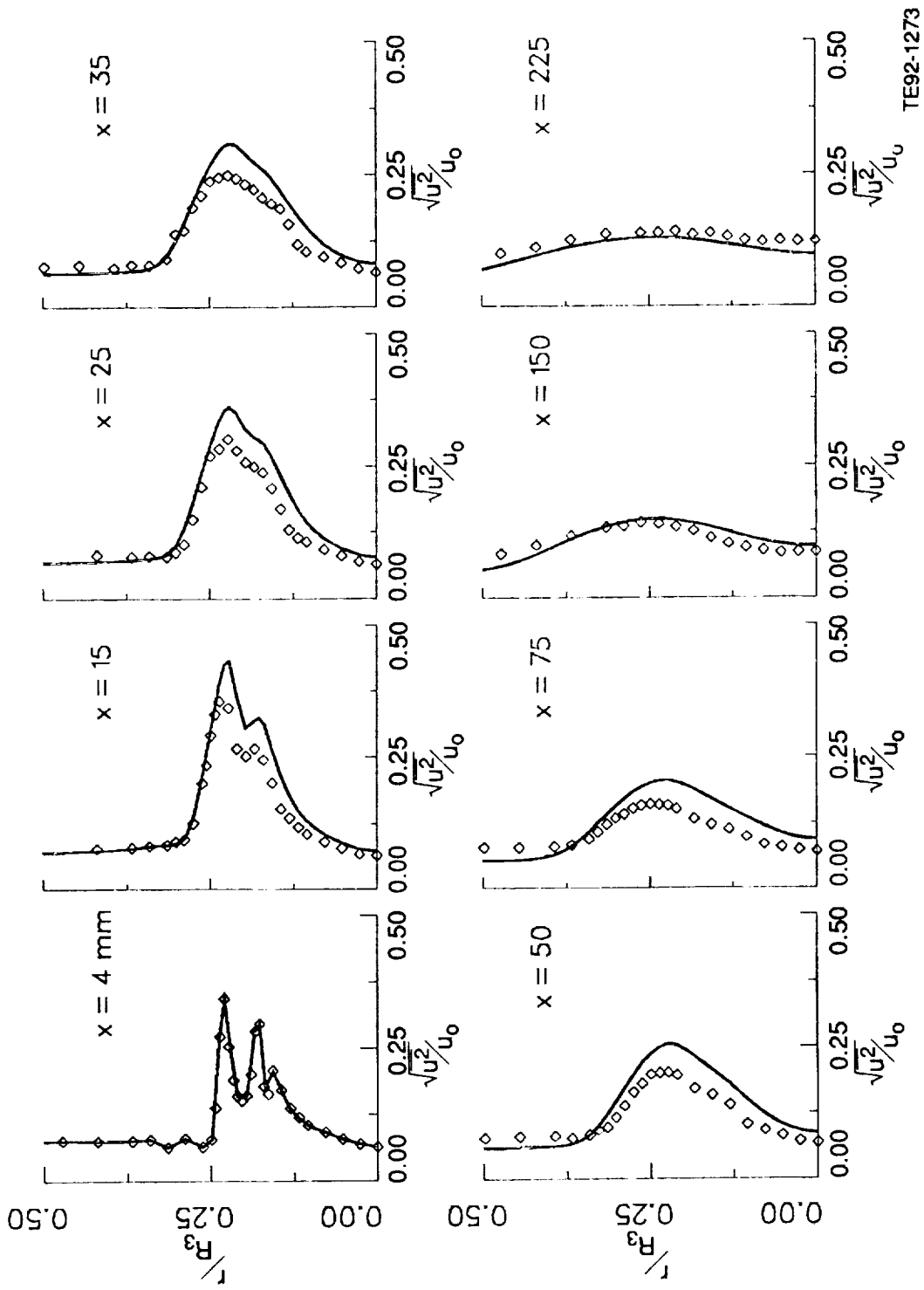


Figure 6.4.2-6. Comparison of predicted turbulent kinetic energy by $k-\epsilon$ model with data.



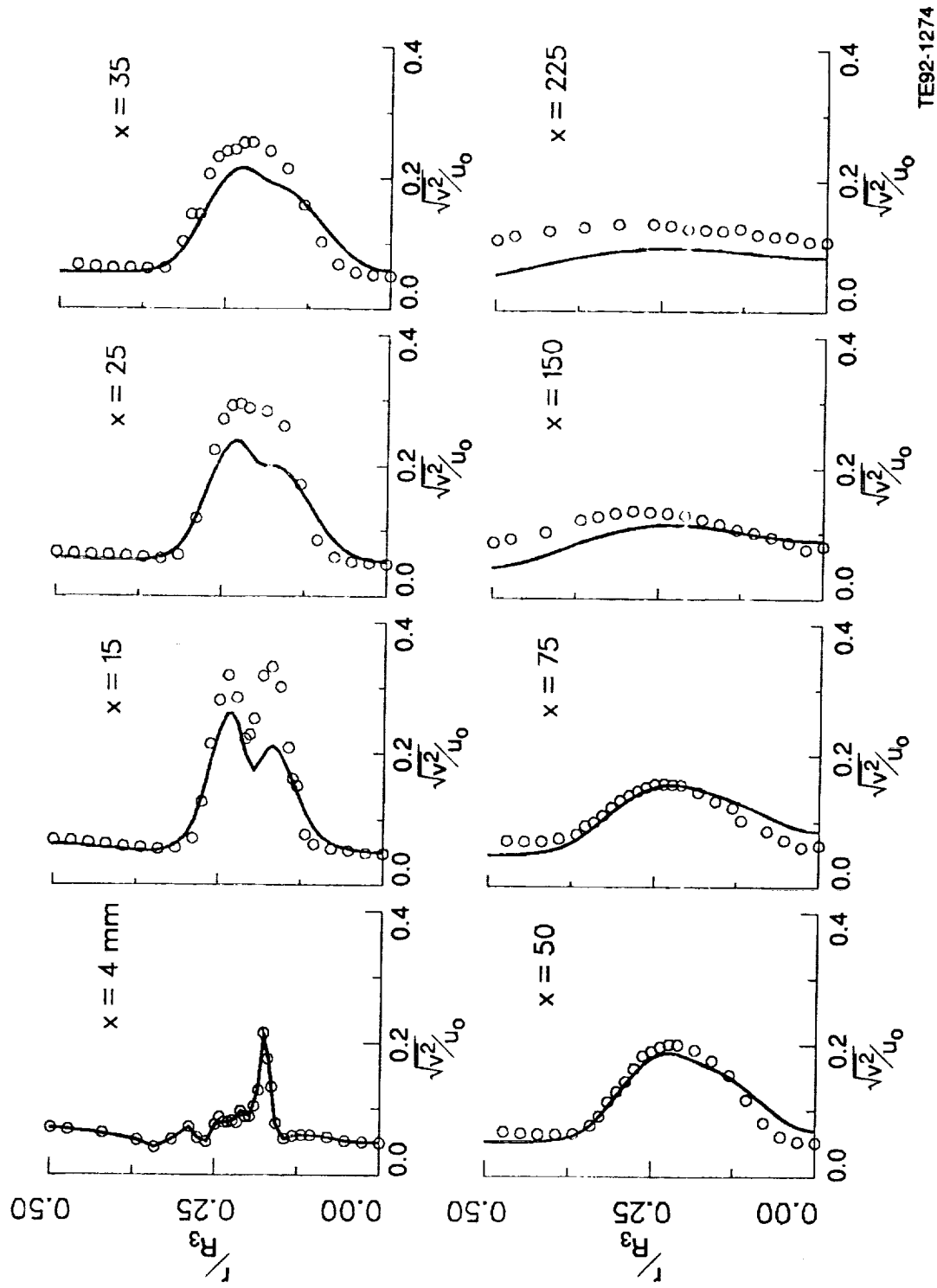
TE92-1272

Figure 6.4.2-7. Comparison of predicted mean axial velocity by DSM with data.



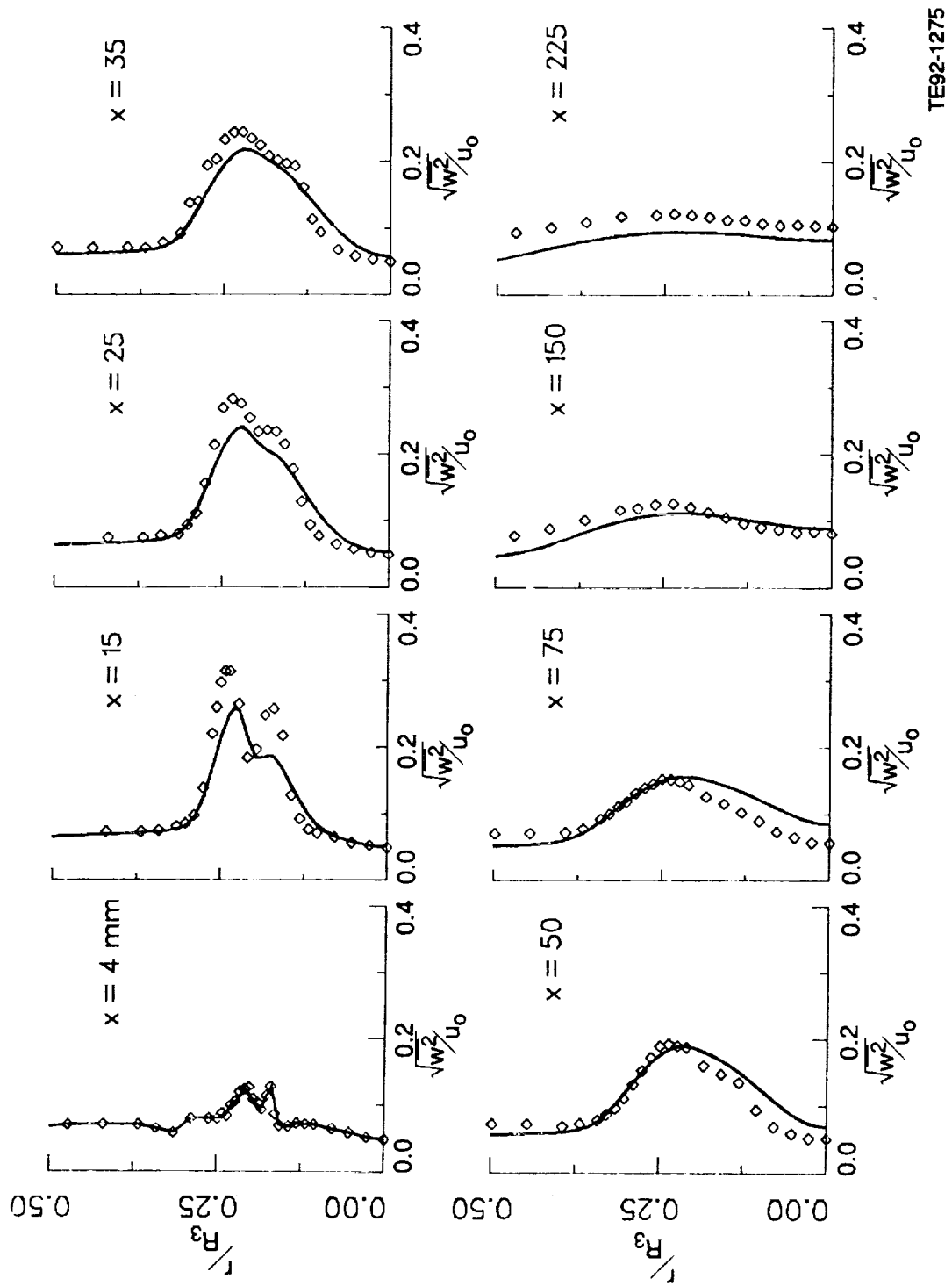
TE92-1273

Figure 6.4.2-8. Comparison of predicted axial rms velocity by DSM with data.



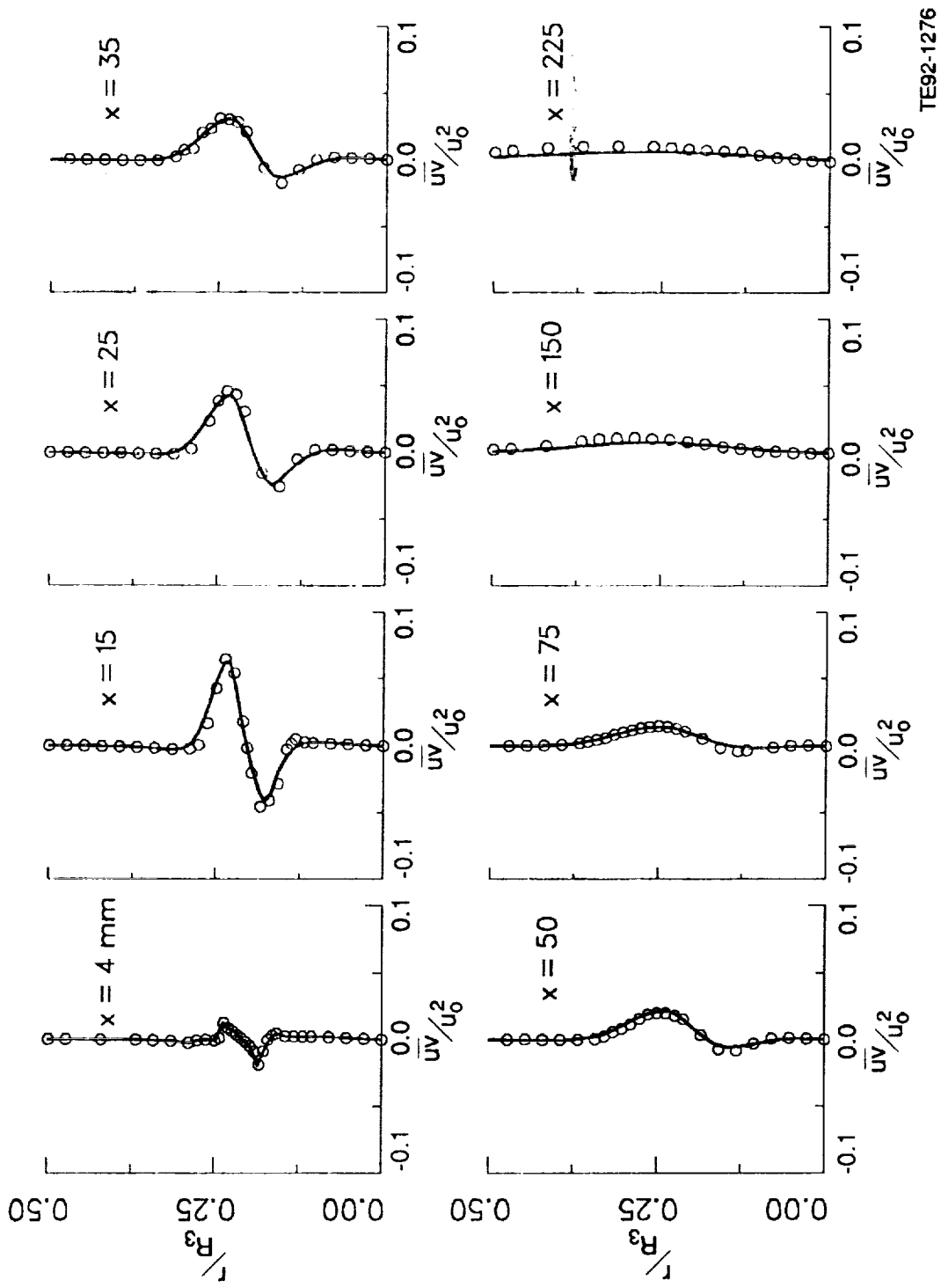
TE92-1274

Figure 6.4.2-9. Comparison of predicted radial rms velocity by DSM with data.



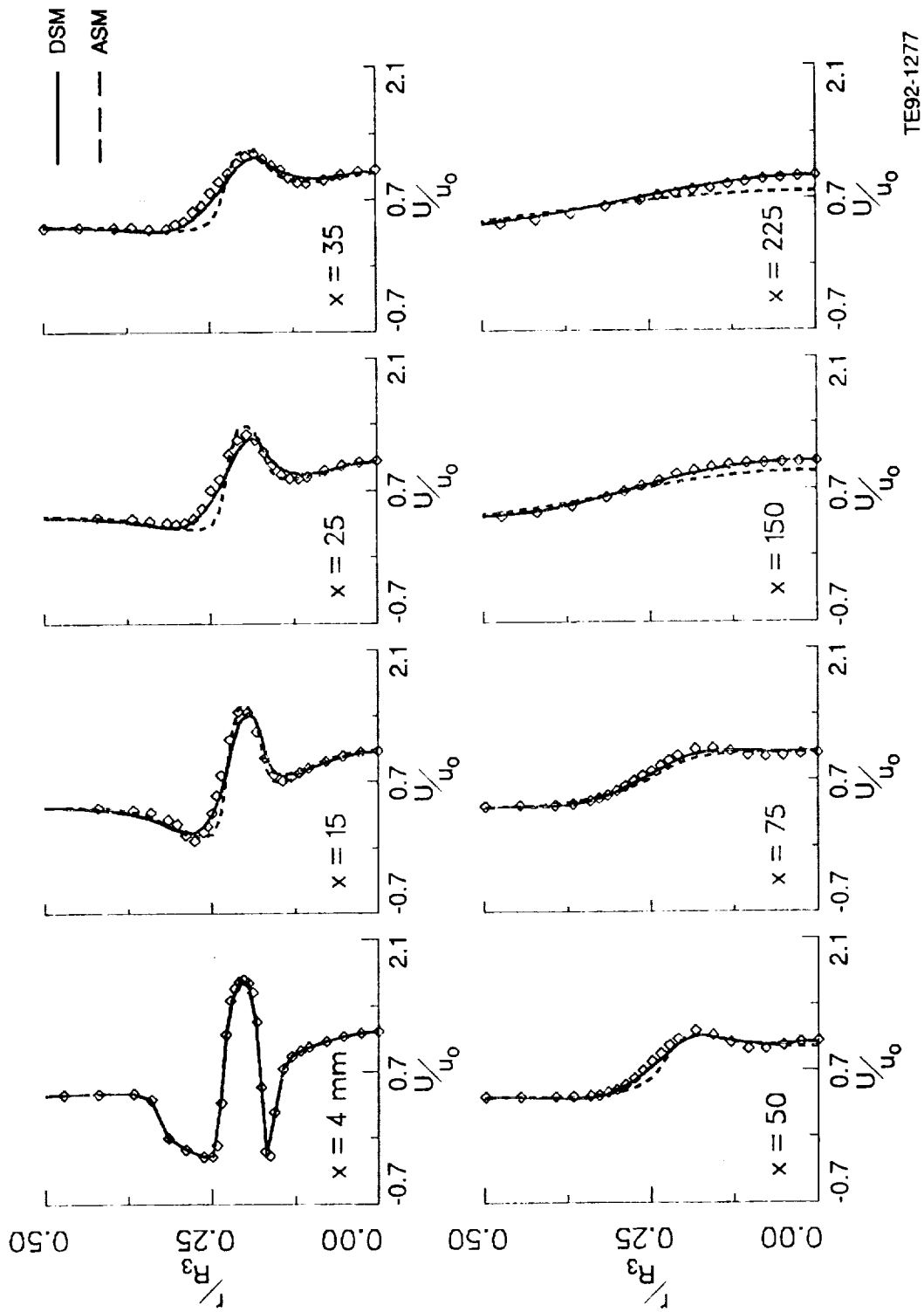
TE92-1275

Figure 6.4.2-10. Comparison of predicted tangential rms velocity by DSM with data.



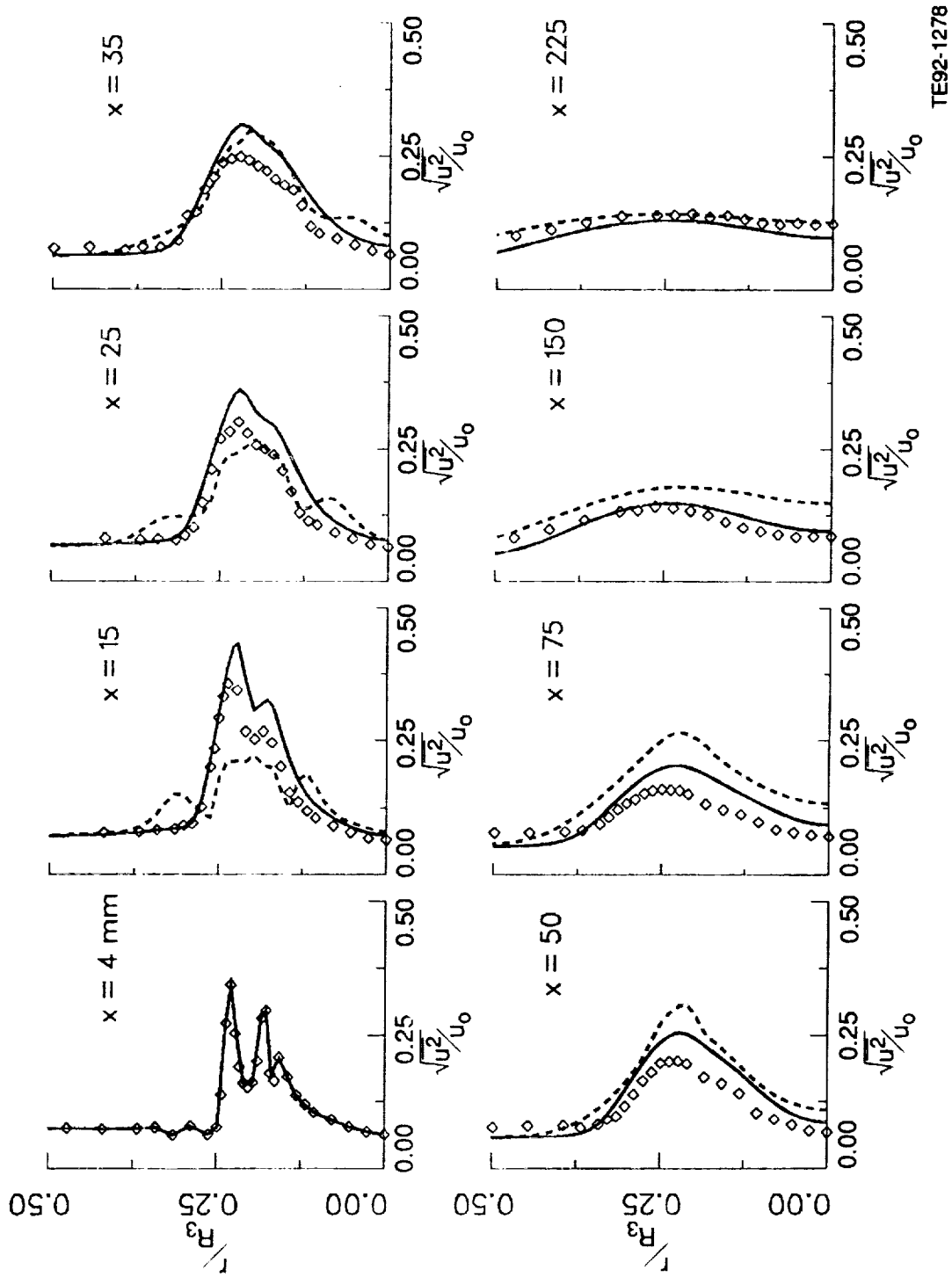
TE92-1276

Figure 6.4.2-11. Comparison of predicted turbulent shear stress by DSM with data.



TE92-1277

Figure 6.4.2-12. Comparison of predicted mean axial velocity by DSM and ASM with data.



TE92-1278

Figure 6.4.2-13. Comparison of predicted axial rms velocity by DSM and ASM with data.

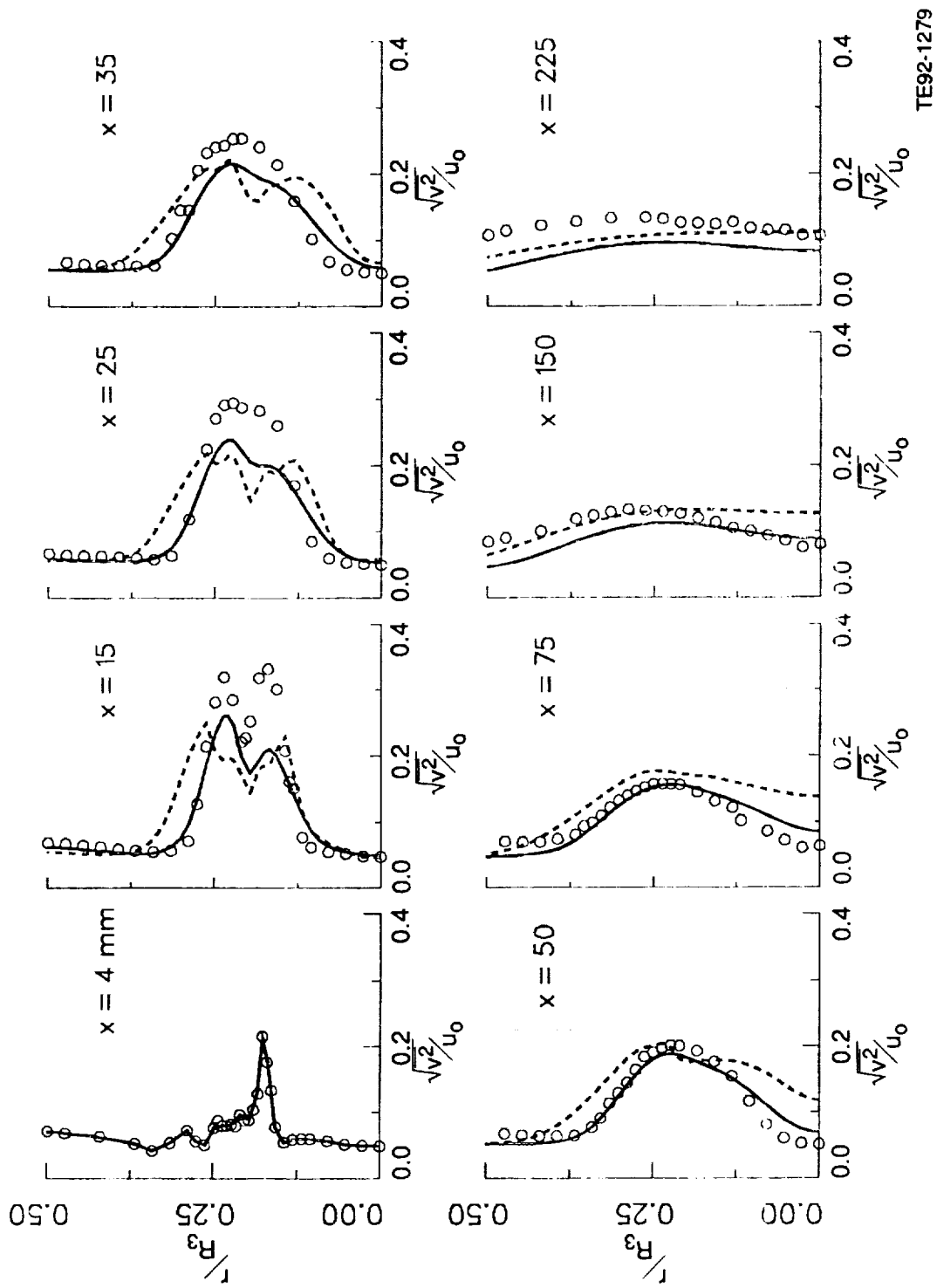


Figure 6.4.2-14. Comparison of predicted radial rms velocity by DSM and ASM with data.

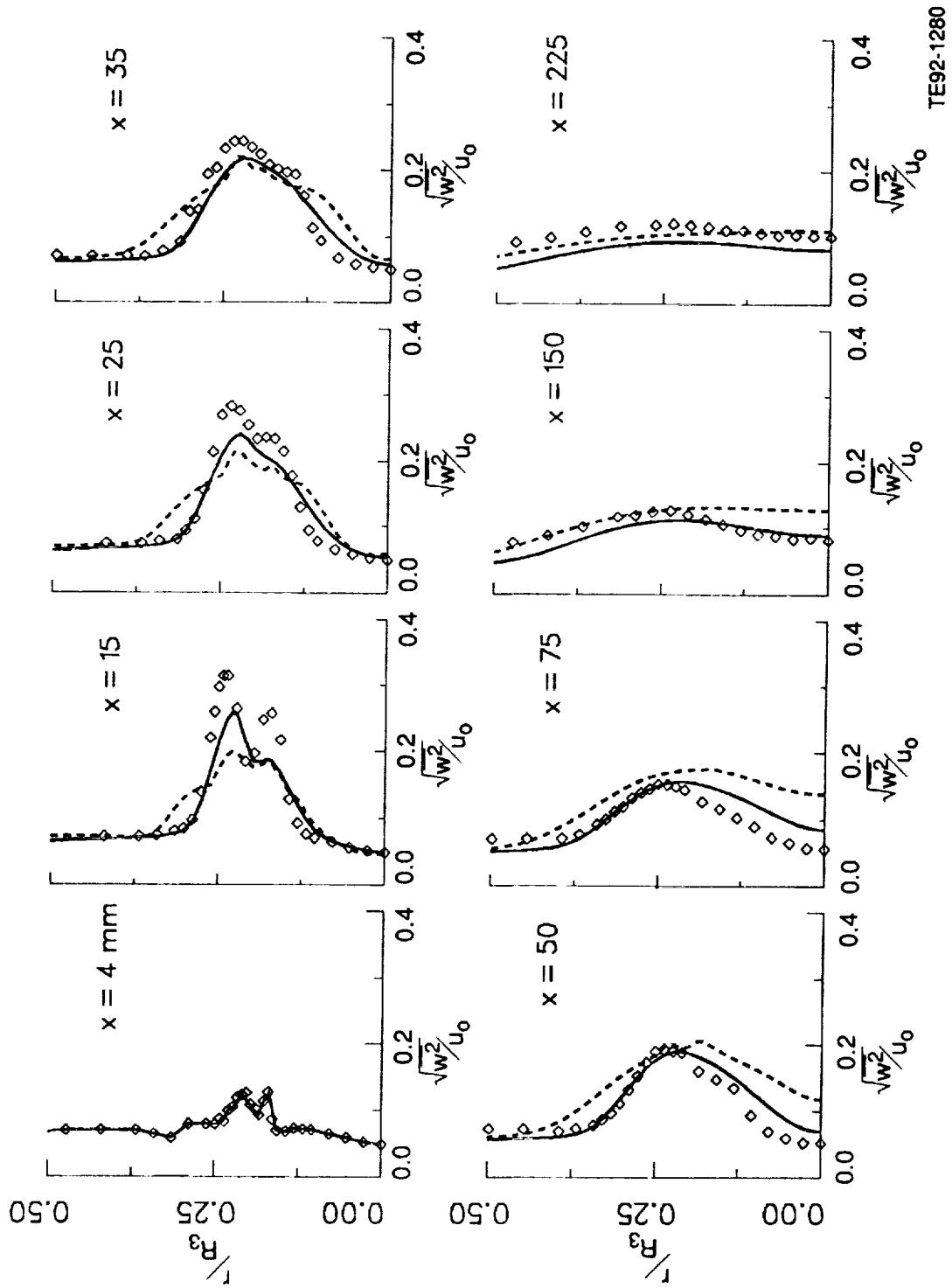
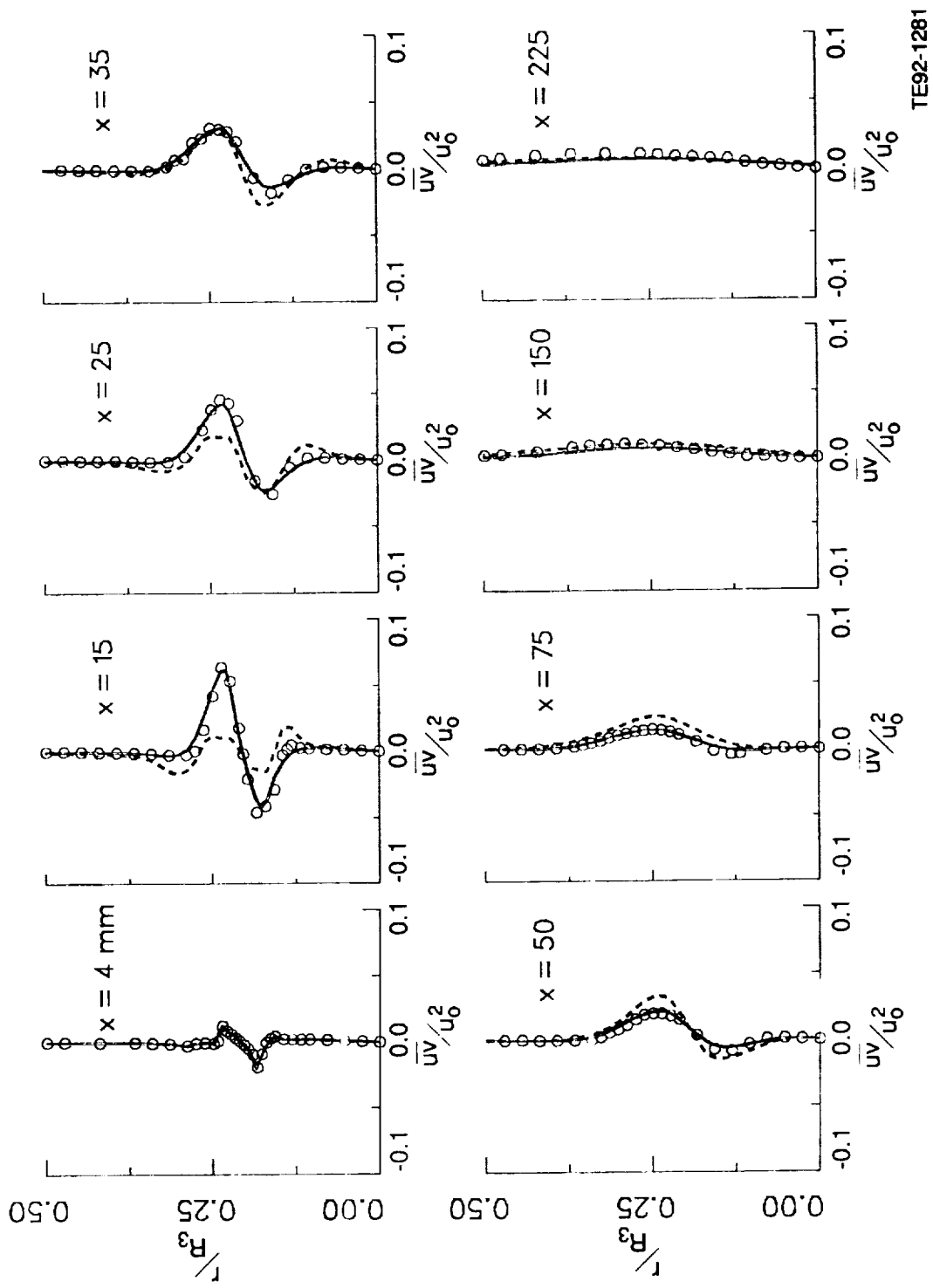


Figure 6.4.2-15. Comparison of predicted tangential rms velocity by DSM and ASM with data.



TE92-1281

Figure 6.4.2-16. Comparison of predicted turbulent shear stress profiles by DSM and ASM with data.

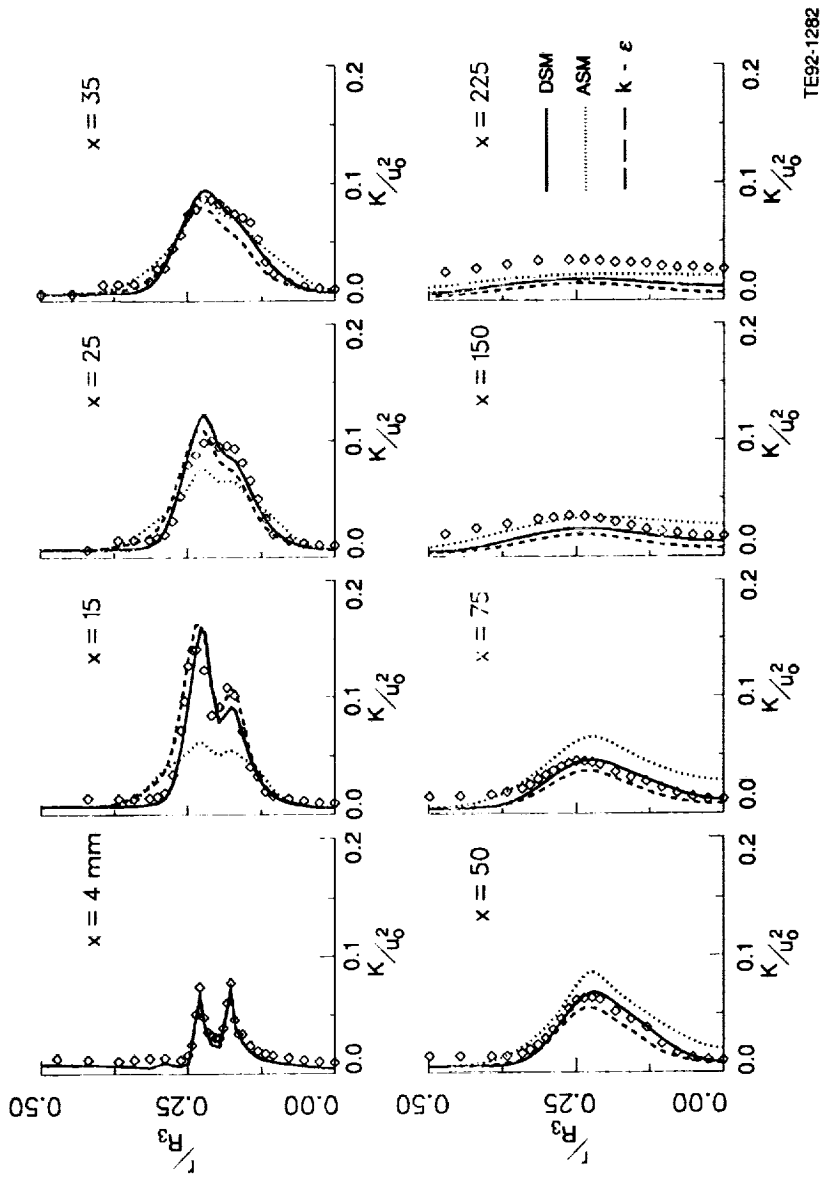


Figure 6.4.2-17. Comparison of predicted turbulent kinetic energy by $k-\epsilon$, DSM, and ASM with data.

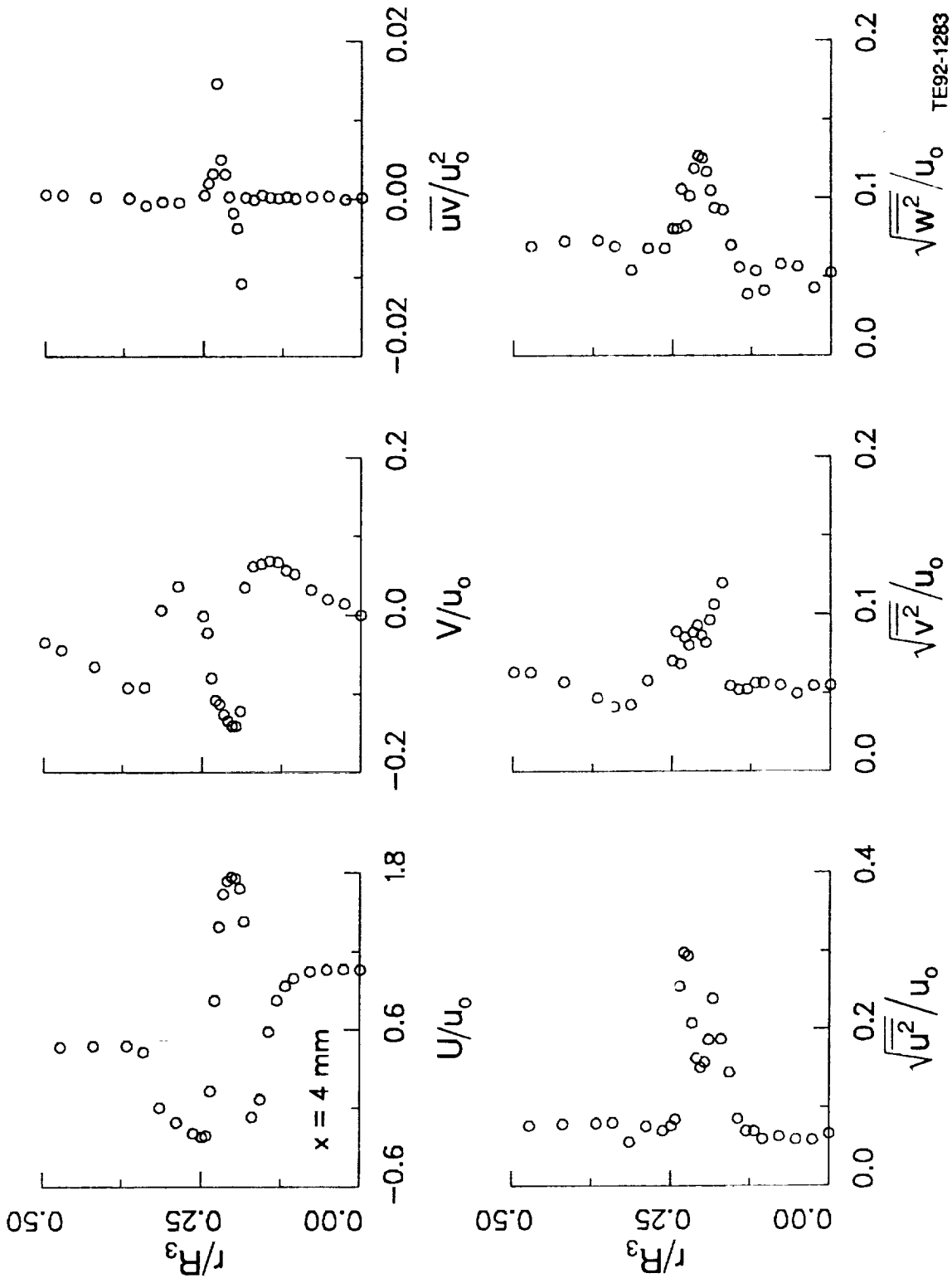


Figure 6.4.2-18. Measured profiles at the inlet plane ($x = 4 \text{ mm}$) (1 of 2).

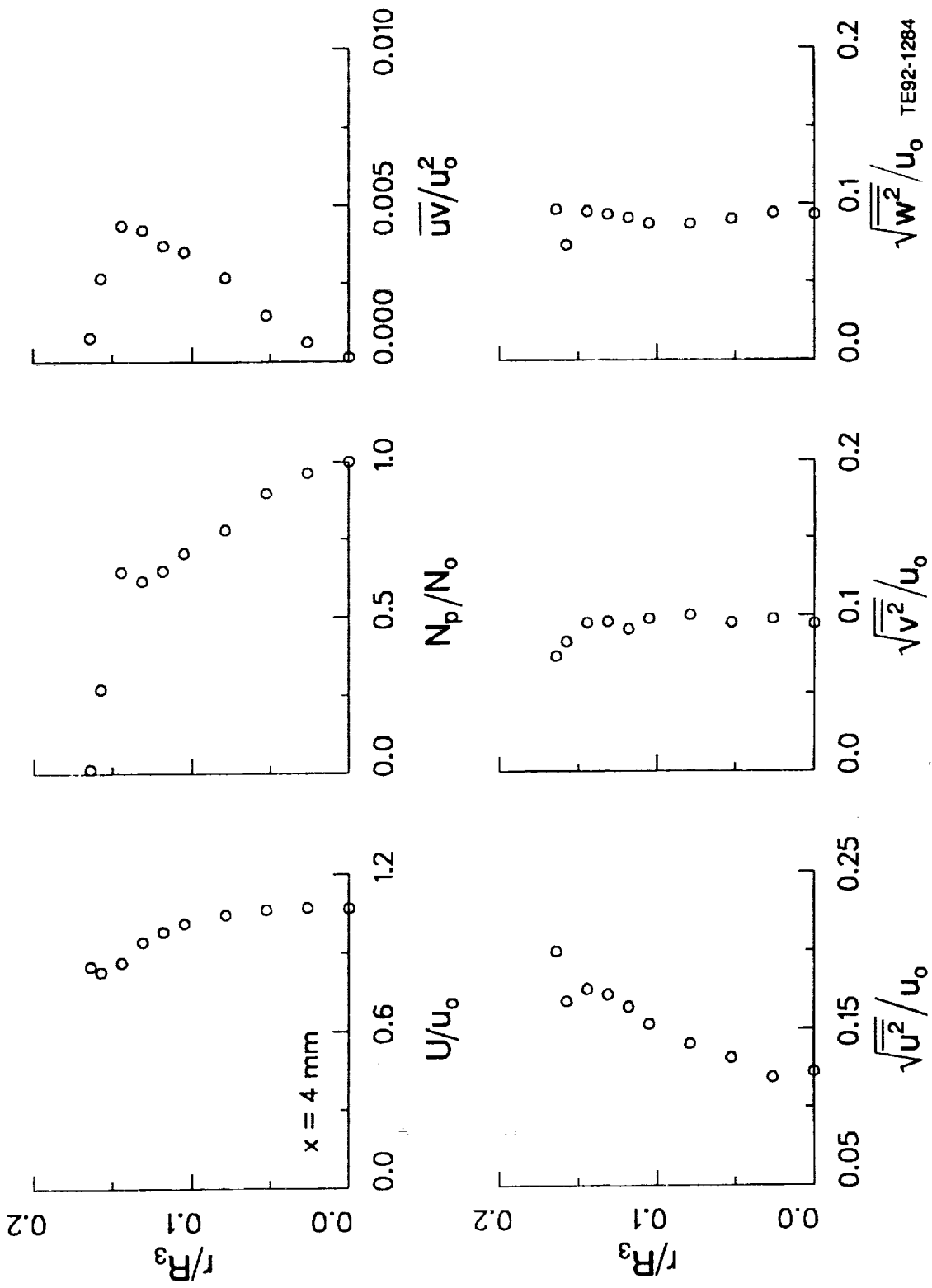


Figure 6.4.2-18. Measured profiles at the inlet plane (x = 4 mm) (2 of 2).

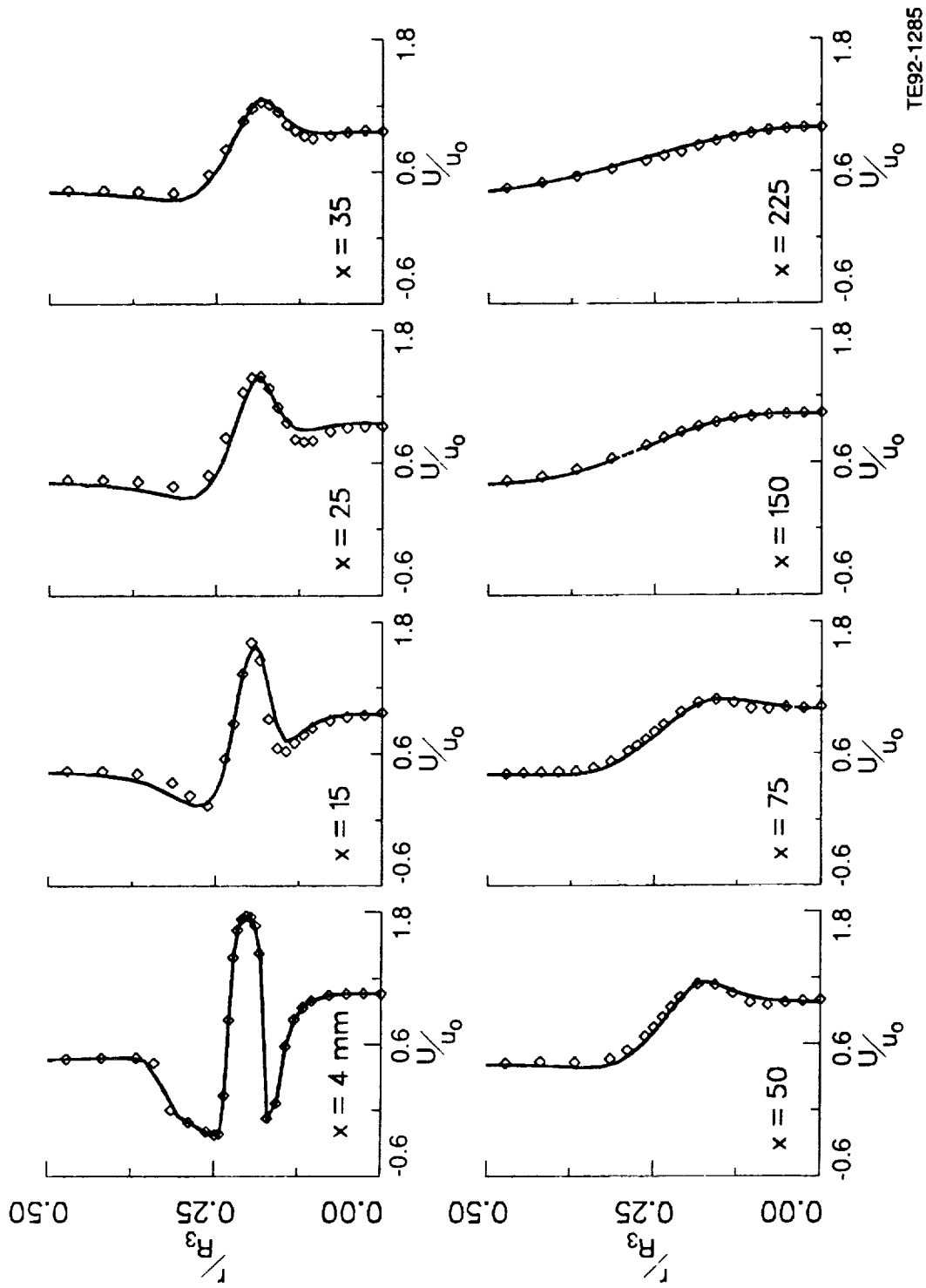
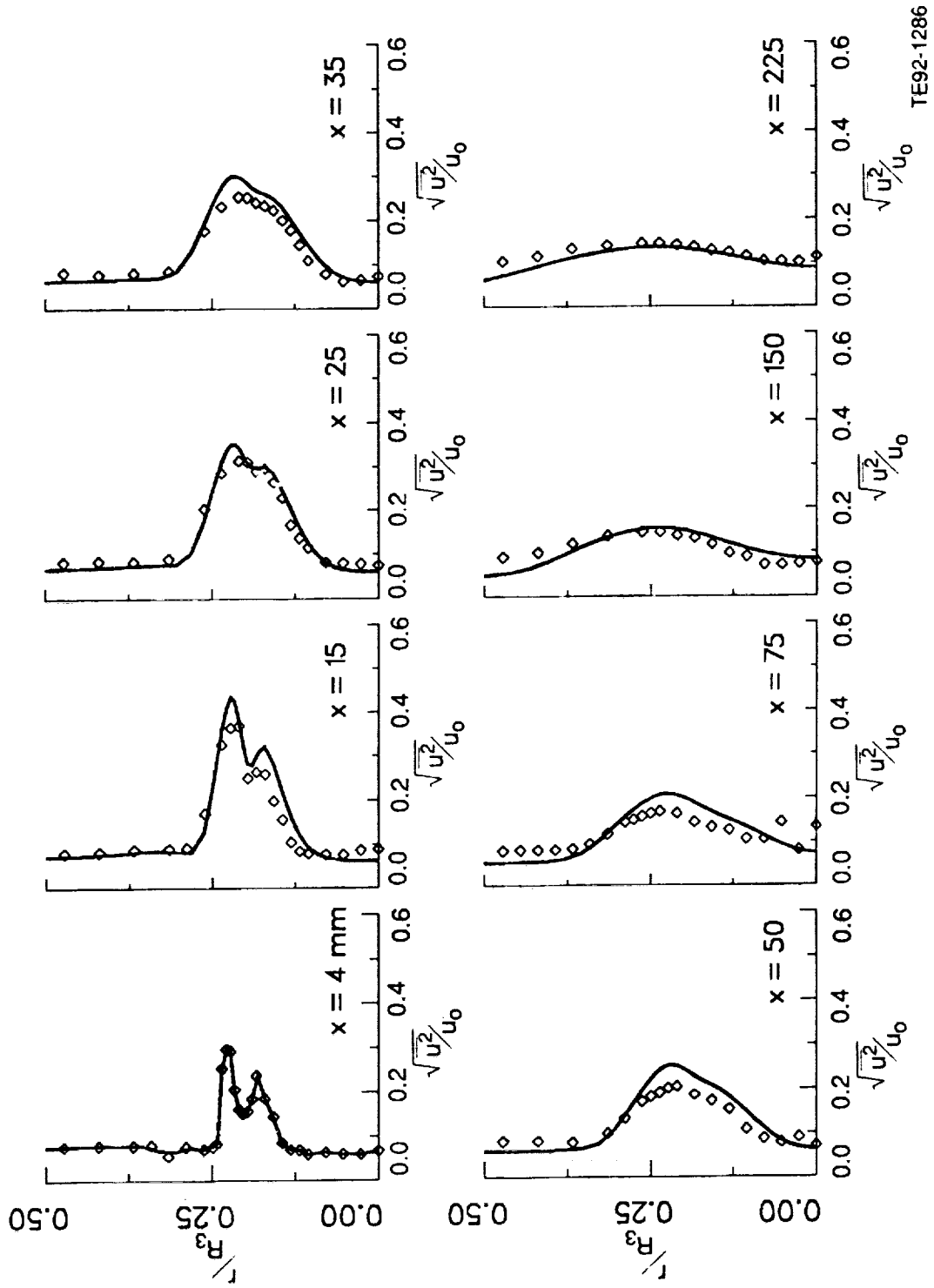
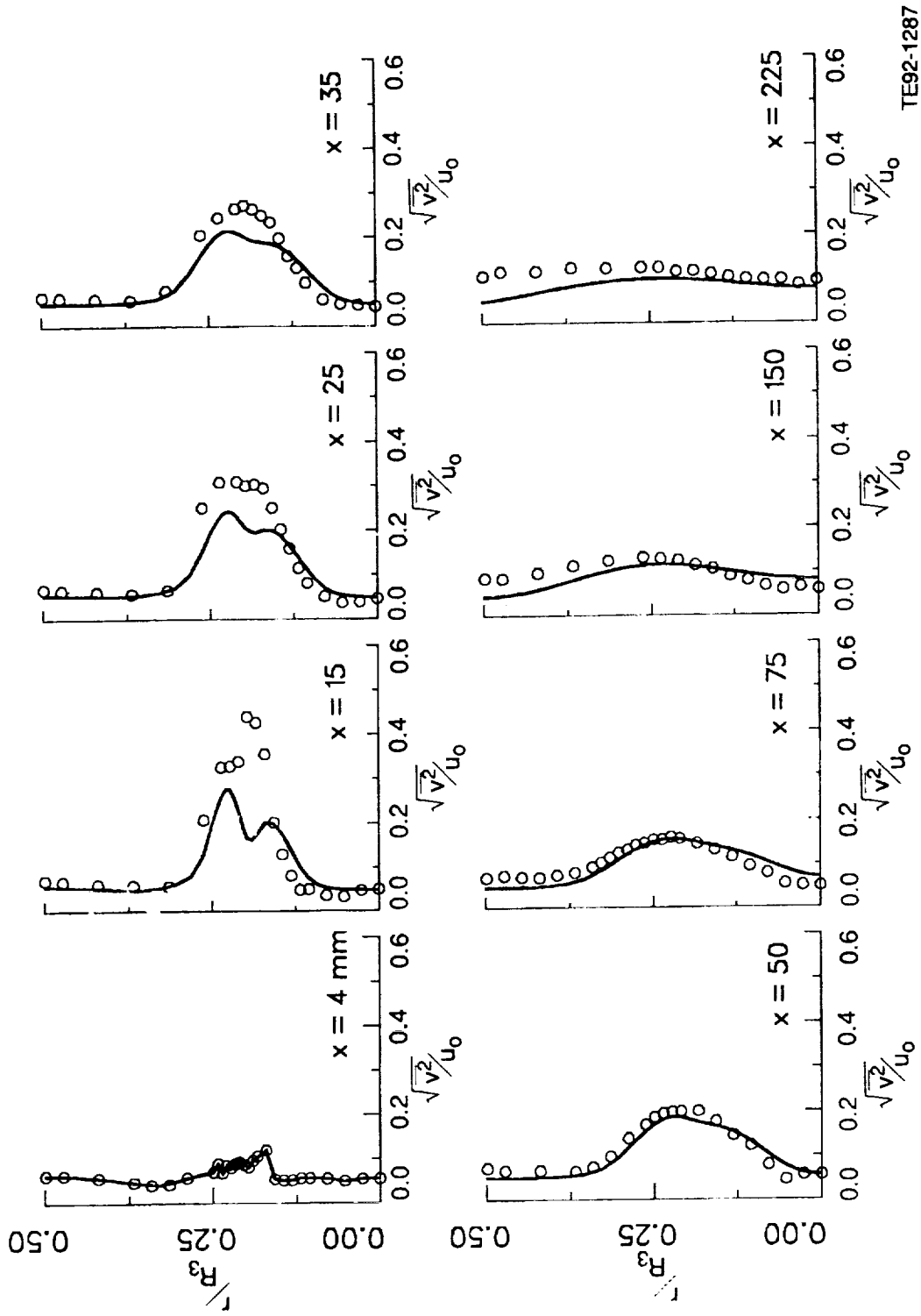


Figure 6.4.2-19. Comparison of calculated normalized mean axial velocity of the continuous phase by DSM with data.



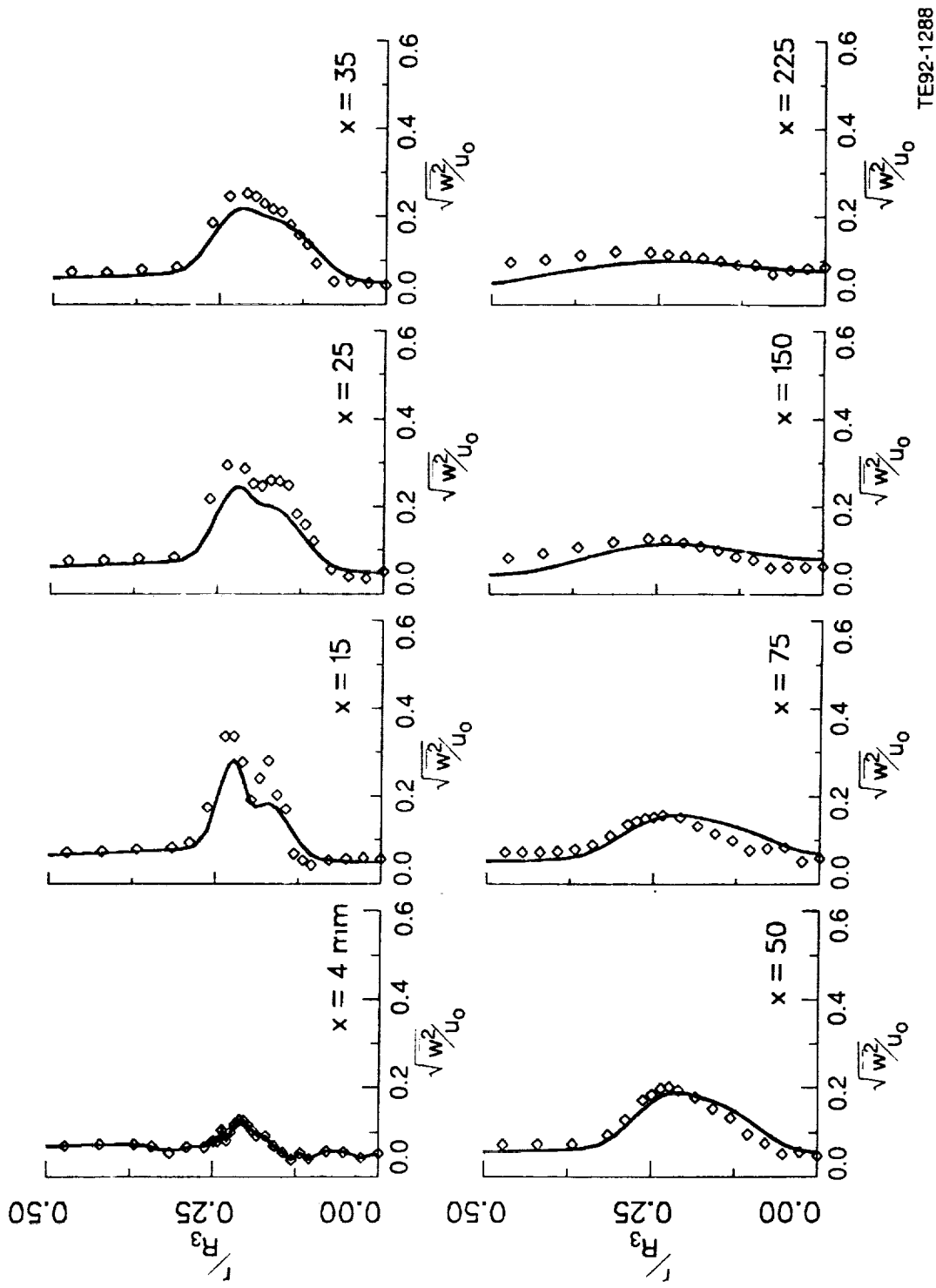
TE92-1286

Figure 6.4.2-20. Comparison of calculated normalized streamwise turbulence intensity of continuous phase by DSM with data.



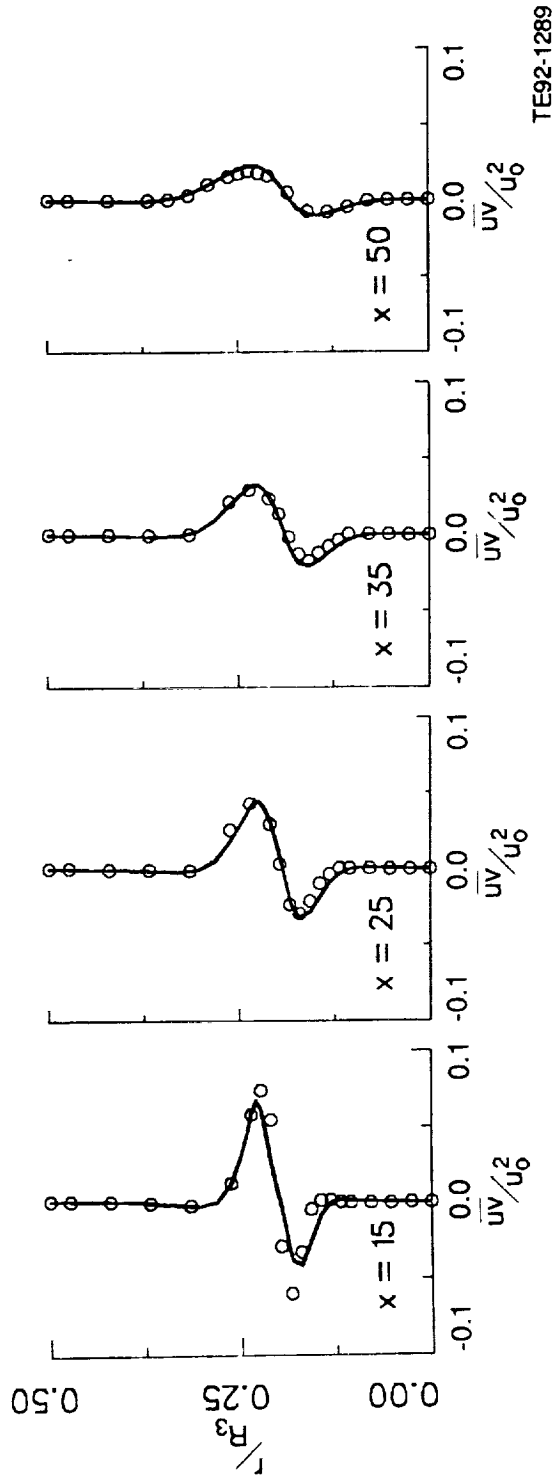
TE92-1287

Figure 6.4.2-21. Comparison of calculated normalized radial turbulence intensity of continuous phase by DSM with data.



TE92-1288

Figure 6.4.2-22. Comparison of calculated normalized tangential turbulence intensity of continuous phase by DSM with data.



TE92-1289

Figure 6.4.2-23. Comparison of calculated normalized shear stress of continuous phase by DSM with data.

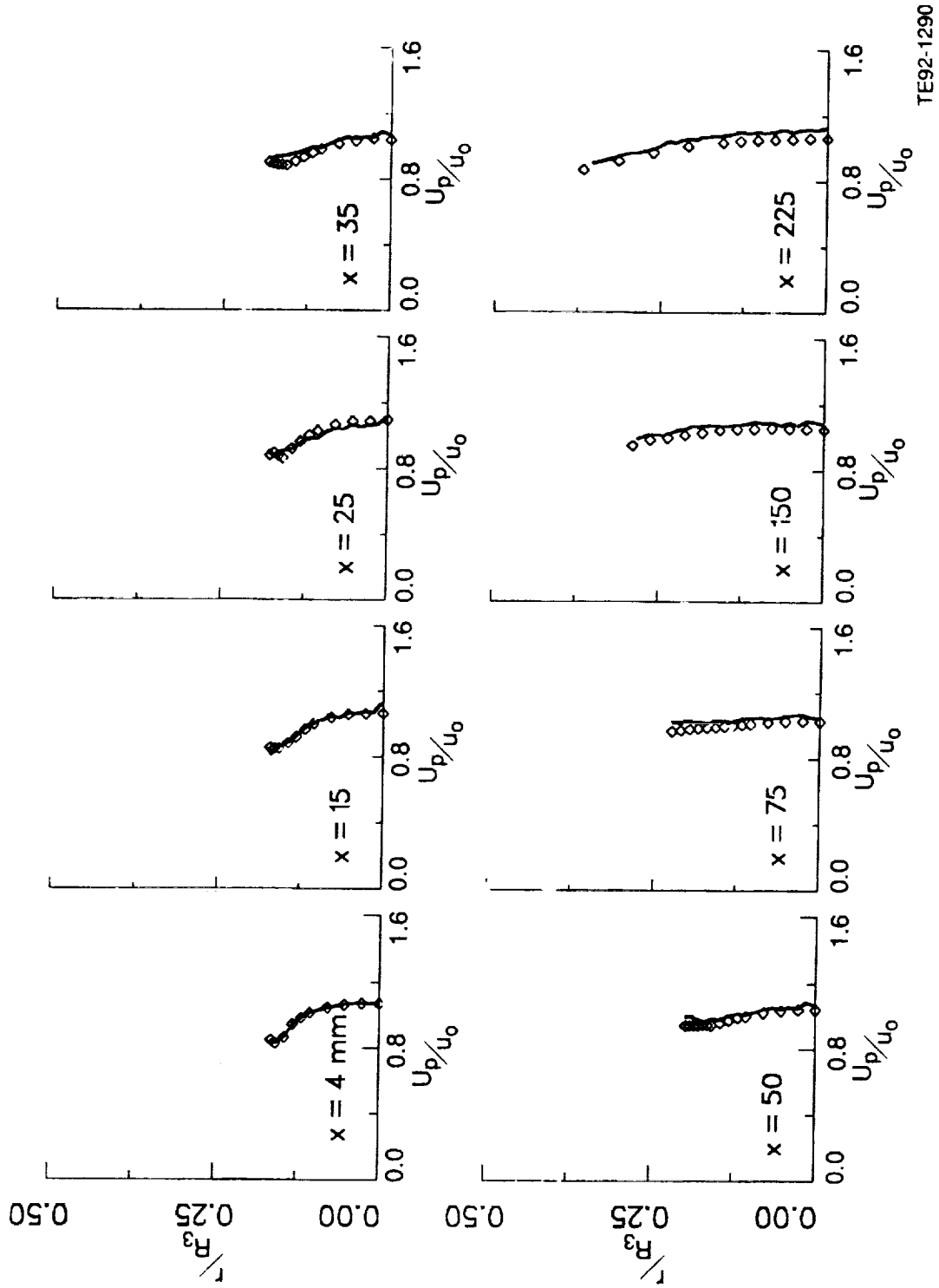
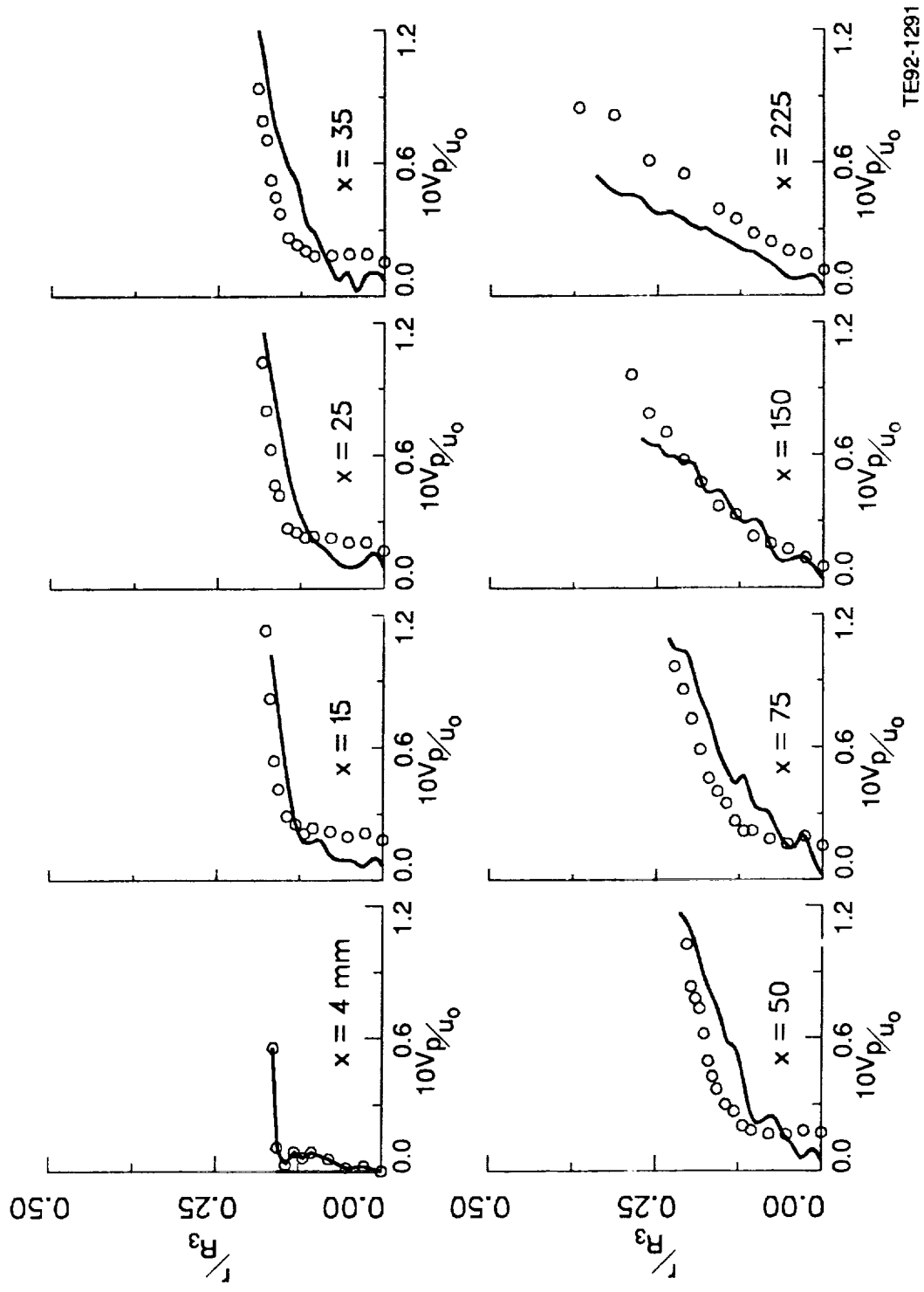
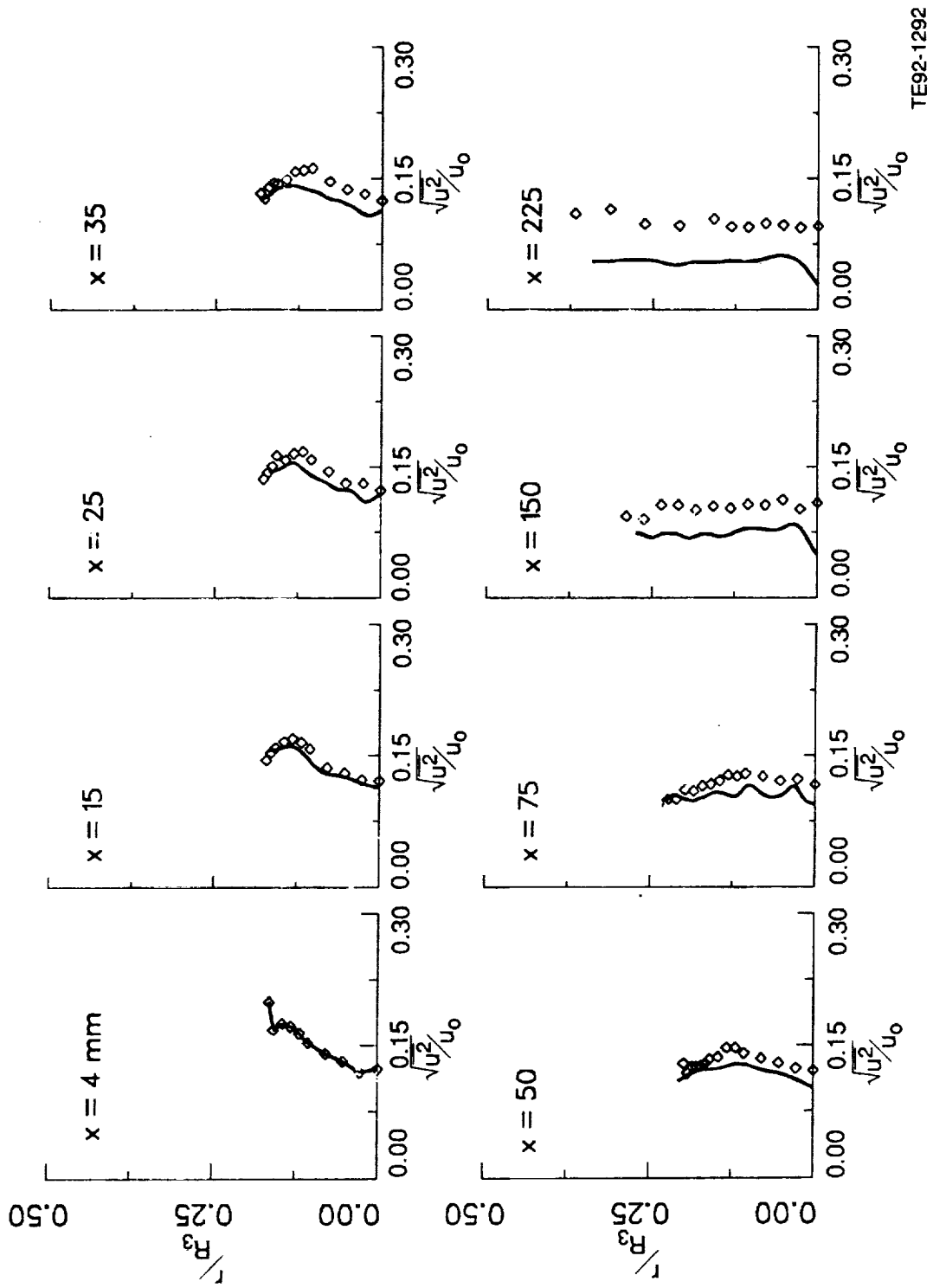


Figure 6.4.2-24. Comparison of calculated normalized mean axial velocity of dispersed phase (U_p) by DSM with data.



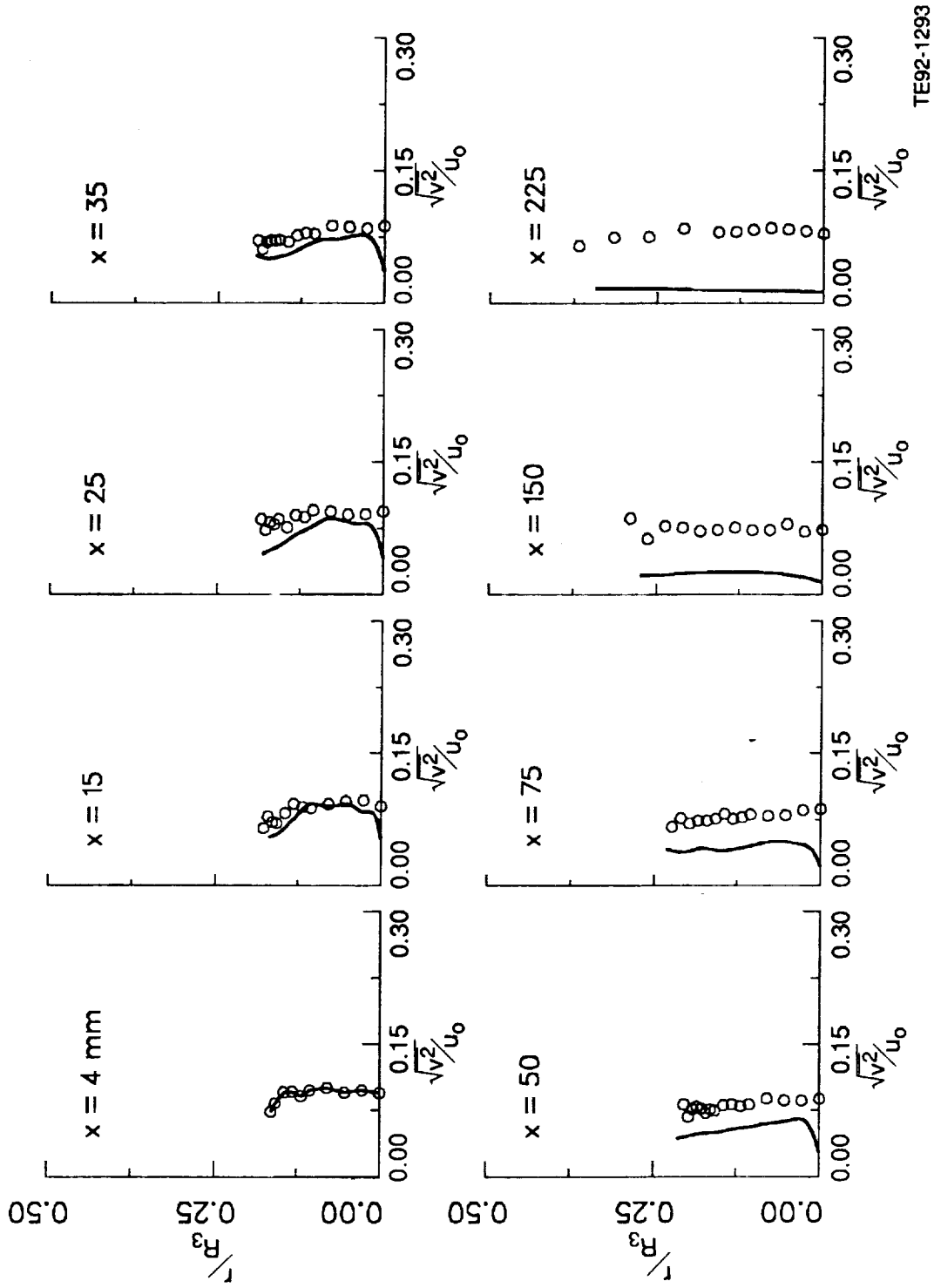
TE92-1291

Figure 6.4.2-25. Comparison of calculated normalized mean radial velocity of dispersed phase (V_ρ) by DSM with data.



TE92-1292

Figure 6.4.2-26. Comparison of calculated normalized streamwise turbulence intensity of dispersed phase by DSM with data.



TE92-1293

Figure 6.4.2-27. Comparison of calculated normalized radial turbulence intensity of dispersed phase by DSM with data.

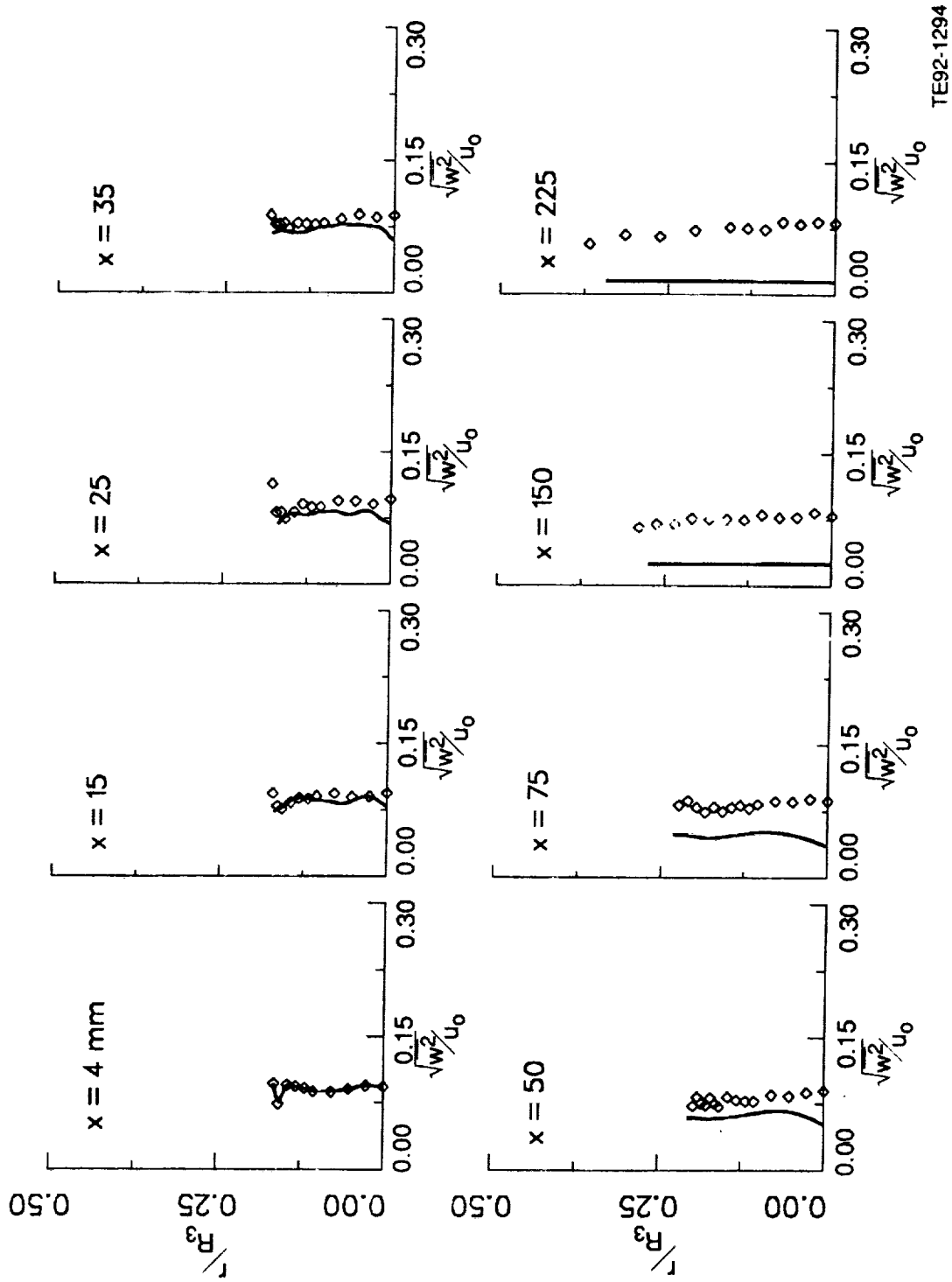
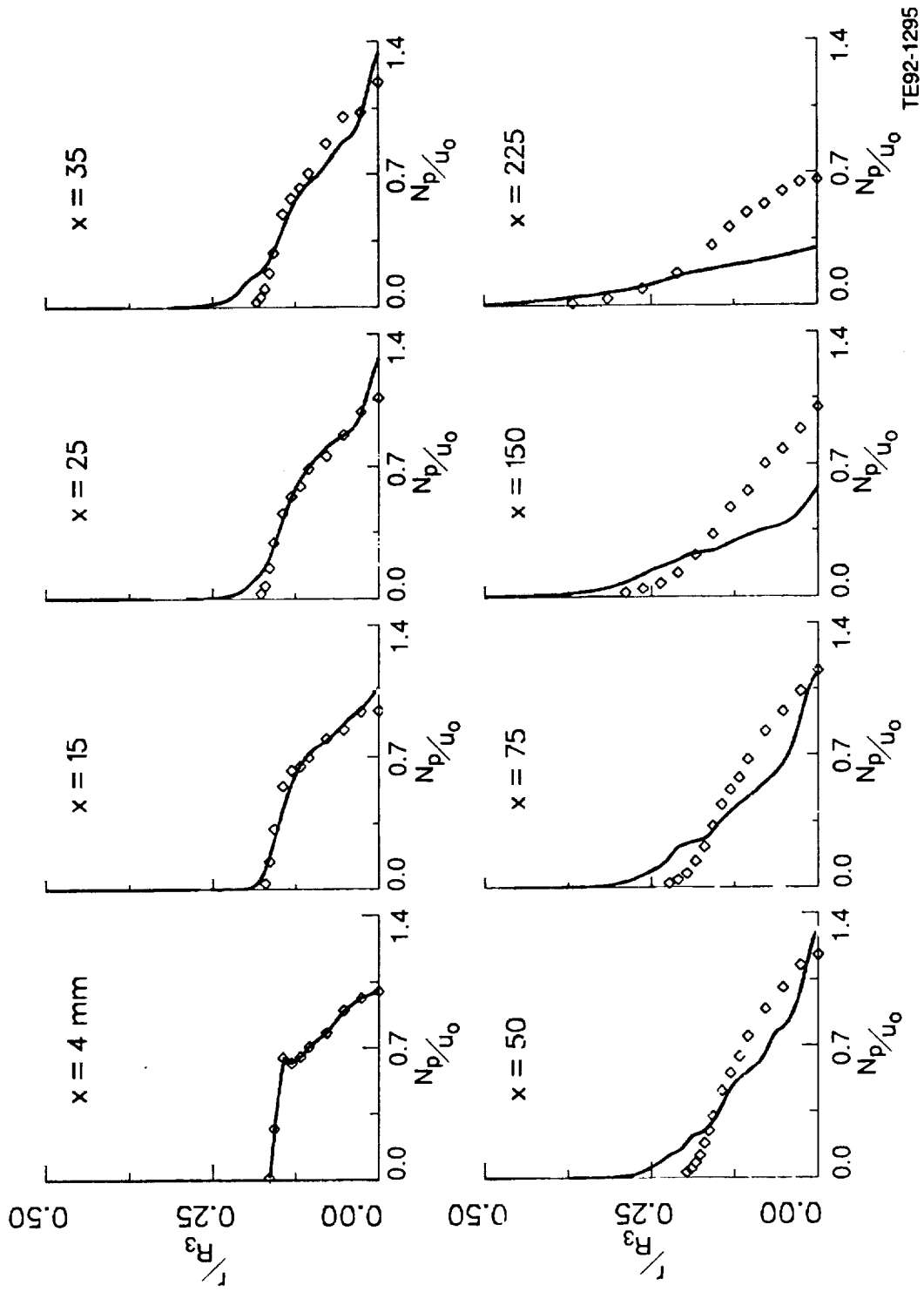


Figure 6.4.2-28. Comparison of calculated normalized tangential turbulence intensity of dispersed phase by DSM with data.



TE92-1295

Figure 6.4.2-29. Number density distribution.

6.5 UNCONFINED COAXIAL JETS WITH SWIRLING ANNULAR FLOW

In this section, computations for unconfined axisymmetric swirling coaxial jets are reported. In this configuration, an axial jet injector surrounded by a swirling annular jet, as shown in Figure 6.5-1, was directed vertically downward within a 457 mm² wire mesh screen. The entire test assembly was surrounded by a flexible plastic enclosure. This helped damp-out extraneous room drafts, and more importantly, allowed uniform seeding of the entrained air, thereby permitting unbiased measurements in the outer region. Data were obtained at eight axial stations 4, 15, 25, 35, 50, 75, 100, and 150 mm from the exit plane of the injector. At each axial station, between 10 and 20 radial points were scanned. The flow conditions used for this case are given in Table 6.5-I. The center jet (diameter, $D = 24.1$ mm) is surrounded by an annular jet with the inner and outer diameters of 29 and 36.7 mm, respectively. The effective area and axial velocity ratios of the annular jet to the center jet are 0.87 and 1.8, respectively.

The control-volume approach was applied to discretize the governing equations. To minimize the effects of false diffusion, numerical solutions have been obtained using a flux-spline scheme for the convection and diffusion terms in the transport equations on a fine grid. The computational mesh used for all calculations consisted of 76 x 69 nonuniformly distributed grid points in the axial and radial directions. A finer grid spacing was used near the inlet and the centerline in the shear layer and within the recirculation zone (Figure 6.5-2). The tabulated axial (x) and radial (r) grid points are shown in Table 6.5-II. The computational domain extended from the first measurement plane, located downstream of the nozzle exit at a distance of 3.0 mm, to 40 inner jet diameters downstream of the nozzle exit.

A calculation procedure for elliptic flow requires boundary conditions on all boundaries of the computational domain. Four kinds of boundaries, namely inlet, axis of symmetry, outlet, and the entrainment boundary, need consideration. At the inlet boundary, which was located at the first measurement plane, the measured profiles of mean velocity and Reynolds stress components were prescribed. These profiles are shown in Figure 6.5-3. The k -profile was obtained from the measured Reynolds stresses. This kinetic energy distribution was used to derive the ϵ values at the inlet plane through the relationship

$$\epsilon = \frac{K^{1.5}}{0.2 D_j} \quad (71)$$

where D_j is the inner jet diameter. This approach is based on the assumption of constant length scale.

At the axis of symmetry, shear stresses and radial gradients of other variables are set to zero. At the outlet, axial diffusion is neglected for all variables. In the radial direction, the entrainment boundary was placed at a distance of six jet diameters from the axis of symmetry. Along the entrainment boundary, the quantity (rV) was assumed constant. In addition, the axial velocity U and tangential velocity W were assumed zero. Turbulent kinetic energy and its dissipation rate were assigned arbitrarily low values yielding an eddy viscosity, $\mu_t = 10 \mu$.

Table 6.5-I.
Unconfined swirling coaxial jets experimental conditions.

Average inner velocity, m/s	3.9
Average annular velocity, m/s	7.1
Centerline velocity U_c , m/s	3.93
Density ρ , kg/m ³	1.178
Inner jet mass flow rate, m_1 , kg/m ³	0.0021
Annular jet mass flow rate, m_2 , kg/m ³	0.0033
Reynolds number, $Re = 4m_1/\rho\mu D$	5712
Swirl angle, deg	60

Table 6.5-II.
Unconfined swirling coaxial jets grid definition.

STREAMWISE COORDINATES OF THE GRID

I	DX	X	XU
1	0.000E+00	0.000E+00	0.000E+00
2	7.750E-04	7.750E-04	0.000E+00
3	1.625E-03	2.400E-03	1.550E-03
4	2.050E-03	4.450E-03	3.250E-03
5	2.500E-03	6.950E-03	5.650E-03
6	2.700E-03	9.650E-03	8.250E-03
7	2.938E-03	1.259E-02	1.105E-02
8	3.313E-03	1.590E-02	1.413E-02
9	3.888E-03	1.979E-02	1.768E-02
10	4.588E-03	2.438E-02	2.190E-02
11	5.250E-03	2.963E-02	2.685E-02
12	5.775E-03	3.540E-02	3.240E-02
13	6.238E-03	4.164E-02	3.840E-02
14	6.713E-03	4.835E-02	4.488E-02
15	7.063E-03	5.541E-02	5.183E-02
16	7.200E-03	6.261E-02	5.900E-02
17	7.250E-03	6.986E-02	6.623E-02
18	7.288E-03	7.715E-02	7.350E-02
19	7.300E-03	8.445E-02	8.080E-02
20	7.300E-03	9.175E-02	8.810E-02
21	7.288E-03	9.904E-02	9.540E-02
22	7.275E-03	1.063E-01	1.027E-01
23	7.288E-03	1.136E-01	1.100E-01
24	7.300E-03	1.209E-01	1.173E-01
25	7.300E-03	1.282E-01	1.246E-01
26	7.300E-03	1.355E-01	1.319E-01
27	7.300E-03	1.428E-01	1.392E-01
28	7.300E-03	1.501E-01	1.465E-01
29	7.300E-03	1.574E-01	1.538E-01
30	7.300E-03	1.647E-01	1.611E-01
31	7.300E-03	1.720E-01	1.684E-01
32	7.300E-03	1.793E-01	1.757E-01
33	7.300E-03	1.866E-01	1.830E-01
34	7.300E-03	1.939E-01	1.903E-01
35	7.300E-03	2.012E-01	1.976E-01
36	7.300E-03	2.085E-01	2.049E-01
37	7.300E-03	2.158E-01	2.122E-01
38	7.300E-03	2.231E-01	2.195E-01
39	7.200E-03	2.303E-01	2.268E-01
40	7.200E-03	2.375E-01	2.339E-01
41	7.400E-03	2.449E-01	2.412E-01
42	7.400E-03	2.523E-01	2.487E-01
43	7.325E-03	2.596E-01	2.560E-01
44	7.325E-03	2.670E-01	2.633E-01
45	7.275E-03	2.742E-01	2.706E-01
46	7.275E-03	2.815E-01	2.779E-01
47	7.300E-03	2.888E-01	2.852E-01
48	7.450E-03	2.963E-01	2.925E-01

PART 1 OF 3
TE92-1296

Table 6.5-II (cont).

49	7.775E-03	3.040E-01	3.001E-01
50	7.975E-03	3.120E-01	3.080E-01
51	8.500E-03	3.205E-01	3.160E-01
52	9.500E-03	3.300E-01	3.250E-01
53	1.000E-02	3.400E-01	3.350E-01
54	1.000E-02	3.500E-01	3.450E-01
55	1.125E-02	3.613E-01	3.550E-01
56	1.375E-02	3.750E-01	3.675E-01
57	1.500E-02	3.900E-01	3.825E-01
58	1.500E-02	4.050E-01	3.975E-01
59	1.500E-02	4.200E-01	4.125E-01
60	1.500E-02	4.350E-01	4.275E-01
61	7.500E-03	4.425E-01	4.425E-01

TRANSVERS COORDINATES OF THE GRID

J	DY	Y	YV
1	0.000E+00	5.000E-04	0.000E+00
2	2.500E-04	7.500E-04	5.000E-04
3	7.500E-04	1.500E-03	1.000E-03
4	1.000E-03	2.500E-03	2.000E-03
5	1.000E-03	3.500E-03	3.000E-03
6	1.000E-03	4.500E-03	4.000E-03
7	1.000E-03	5.500E-03	5.000E-03
8	1.000E-03	6.500E-03	6.000E-03
9	1.000E-03	7.500E-03	7.000E-03
10	1.000E-03	8.500E-03	8.000E-03
11	1.000E-03	9.500E-03	9.000E-03
12	1.000E-03	1.050E-02	1.000E-02
13	1.000E-03	1.150E-02	1.100E-02
14	1.000E-03	1.250E-02	1.200E-02
15	7.500E-04	1.325E-02	1.300E-02
16	5.000E-04	1.375E-02	1.350E-02
17	5.000E-04	1.425E-02	1.400E-02
18	5.000E-04	1.475E-02	1.450E-02
19	5.000E-04	1.525E-02	1.500E-02
20	5.000E-04	1.575E-02	1.550E-02
21	5.000E-04	1.625E-02	1.600E-02
22	5.000E-04	1.675E-02	1.650E-02
23	5.000E-04	1.725E-02	1.700E-02
24	5.000E-04	1.775E-02	1.750E-02
25	5.000E-04	1.825E-02	1.800E-02
26	5.000E-04	1.875E-02	1.850E-02
27	5.000E-04	1.925E-02	1.900E-02
28	5.000E-04	1.975E-02	1.950E-02
29	7.500E-04	2.050E-02	2.000E-02
30	1.000E-03	2.150E-02	2.100E-02
31	1.000E-03	2.250E-02	2.200E-02
32	1.000E-03	2.350E-02	2.300E-02

PART 2 OF 3
TE92-1206

Table 6.5-II (cont).

33	1.000E-03	2.450E-02	2.400E-02
34	1.000E-03	2.550E-02	2.500E-02
35	1.000E-03	2.650E-02	2.600E-02
36	1.000E-03	2.750E-02	2.700E-02
37	1.000E-03	2.850E-02	2.800E-02
38	1.000E-03	2.950E-02	2.900E-02
39	1.500E-03	3.100E-02	3.000E-02
40	2.000E-03	3.300E-02	3.200E-02
41	2.500E-03	3.550E-02	3.400E-02
42	3.000E-03	3.850E-02	3.700E-02
43	3.000E-03	4.150E-02	4.000E-02
44	3.000E-03	4.450E-02	4.300E-02
45	3.500E-03	4.800E-02	4.600E-02
46	4.000E-03	5.200E-02	5.000E-02
47	4.500E-03	5.650E-02	5.400E-02
48	5.000E-03	6.150E-02	5.900E-02
49	5.000E-03	6.650E-02	6.400E-02
50	5.000E-03	7.150E-02	6.900E-02
51	5.000E-03	7.650E-02	7.400E-02
52	5.000E-03	8.150E-02	7.900E-02
53	5.000E-03	8.650E-02	8.400E-02
54	5.000E-03	9.150E-02	8.900E-02
55	5.000E-03	9.650E-02	9.400E-02
56	5.500E-03	1.020E-01	9.900E-02
57	5.500E-03	1.075E-01	1.050E-01
58	5.000E-03	1.125E-01	1.100E-01
59	5.000E-03	1.175E-01	1.150E-01
60	5.000E-03	1.225E-01	1.200E-01
61	5.000E-03	1.275E-01	1.250E-01
62	5.000E-03	1.325E-01	1.300E-01
63	5.000E-03	1.375E-01	1.350E-01
64	5.000E-03	1.425E-01	1.400E-01
65	5.000E-03	1.475E-01	1.450E-01
66	2.500E-03	1.500E-01	1.500E-01

PART 3 OF 3
TE92-1296

Predictions of mean and turbulence fields obtained from the k - ϵ model are discussed first. Comparison of the calculated mean axial and tangential (azimuthal) velocity profiles with the experimental data is presented in Figures 6.5-4 and 6.5-5. In this case, the k - ϵ model fails to display the size and strength of the experimental recirculation zone. The k - ϵ model mimics the data trend reasonably well away from the symmetry axis, however, the peaks were slightly underpredicted. The underprediction for a centerline velocity stems from the incorrect representation of the turbulent diffusion process. The radial normal stress is particularly important in the upstream region and, as a consequence, the isotropic viscosity hypothesis is inadequate. The k - ϵ model prediction of tangential velocity is in relatively good agreement with data. The calculated profiles are in accordance with the data trend, although the maximum values are slightly overpredicted. At the farthest downstream locations, the measured tangential profiles are skewed toward the centerline, however, the k - ϵ model fails to demonstrate such a behavior.

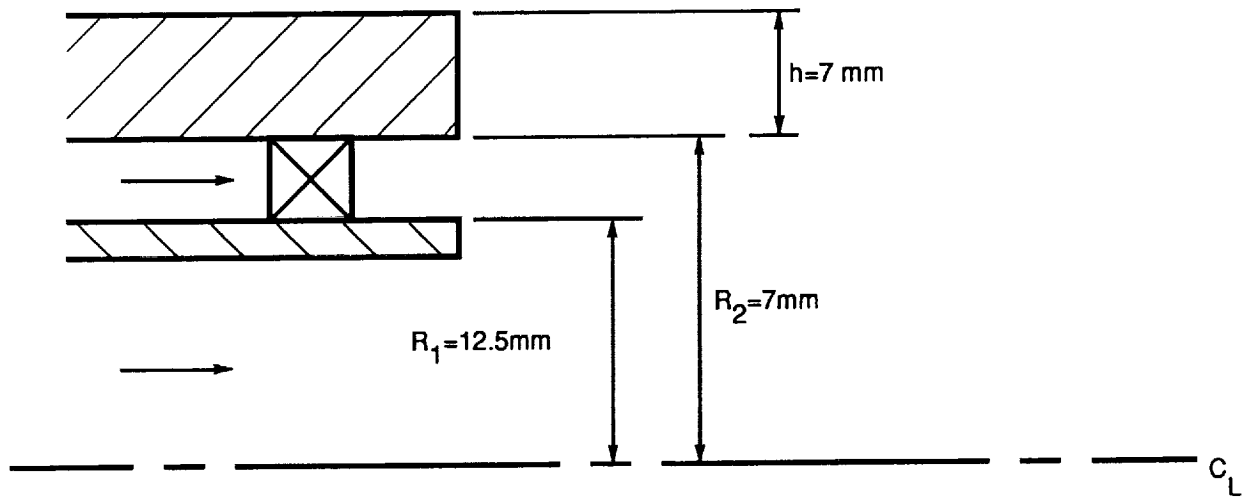
Comparison of the predicted turbulent kinetic energy, k , with the data is shown in Figure 6.5-6. The agreement between the predicted and experimental values of k is not as good as that for the velocity. The discrepancies near the centerline region can be attributed to the lack of well-predicted velocity field, inadequacy of the eddy viscosity hypothesis, and turbulent kinetic dissipation rate, ϵ . The inlet distribution of length scale has a significant effect on the ϵ distribution in the upstream region where the diffusion terms have a large effect on the mean velocity, it has no significant effect in the downstream region where the diffusion effects are small. The k - ϵ model tends to connect the dissipation rate too strongly to the local

mean velocity field (Habib and Whitelaw, 1979) which is inappropriate since the dissipation occurs in the finest scales of motion, and these do not reflect the local mean strain field. The predicted turbulent shear stress, uv , profiles have been compared with the experimental data in Figure 6.5-7. The negative peak in the shear stress profile corresponds to the shear layer between the two streams and the positive peak corresponds to the shear layer associated with the expansion. The agreement between the calculation and the experimental data is good, although the peak values are not well predicted.

Having demonstrated the results of the $k-\epsilon$ model, attention is now turned to the performance of the DSM closure. Results of the mean velocity components obtained from the $k-\epsilon$ model and the DSM are compared with the experimental data (Figures 6.5-8 and 6.5-9). A wide disparity exists between the models' prediction of the axial velocity near the centerline. It is evident that there are substantial differences in the capability of the various models to promote or hinder formation of the recirculation zone. It is clear that the proper turbulence model is dependent on the location within the flow field. With regard to the comparison between measurements and calculations, the predictions by DSM seem to be slightly better for tangential velocity and the central recirculation zone, whereas those by $k-\epsilon$ model are closer to experimental data for maximum velocity. An examination of the calculated Reynolds stresses (Figures 6.5-10, 6.5-11, and 6.5-12) indicates that the relative performance of the model is dependent on the flow region. The results show differences especially in the prediction of the centerline values in the developing region.

The reason can be attributed to the inlet dissipation rate distribution. Numerical study indicates that the inlet ϵ profile is a very important factor in predicting the maximum values of mean and turbulence quantities. In general, the DSM closure maintains the correct shape of Reynolds stress profiles which are consistent with the behavior of the mean velocity field.

Comparisons of calculated shear stresses with data are shown in Figures 6.5-13 and 6.5-14. In comparison with the data, the predicted values are in good agreement in the developed region, however, the locations of the maxima and minima have been shifted in the developing region of the flow field. In the outer part of the recirculation zone, where the effect of entrainment is more pronounced, and near the axis of symmetry, where the velocity gradient is negligible in the radial direction, the discrepancies between the $k-\epsilon$ model and DSM results are in fact diminished.



TE92-1297-4

Figure 6.5-1. Unconfined axisymmetric swirling coaxial jets geometry.

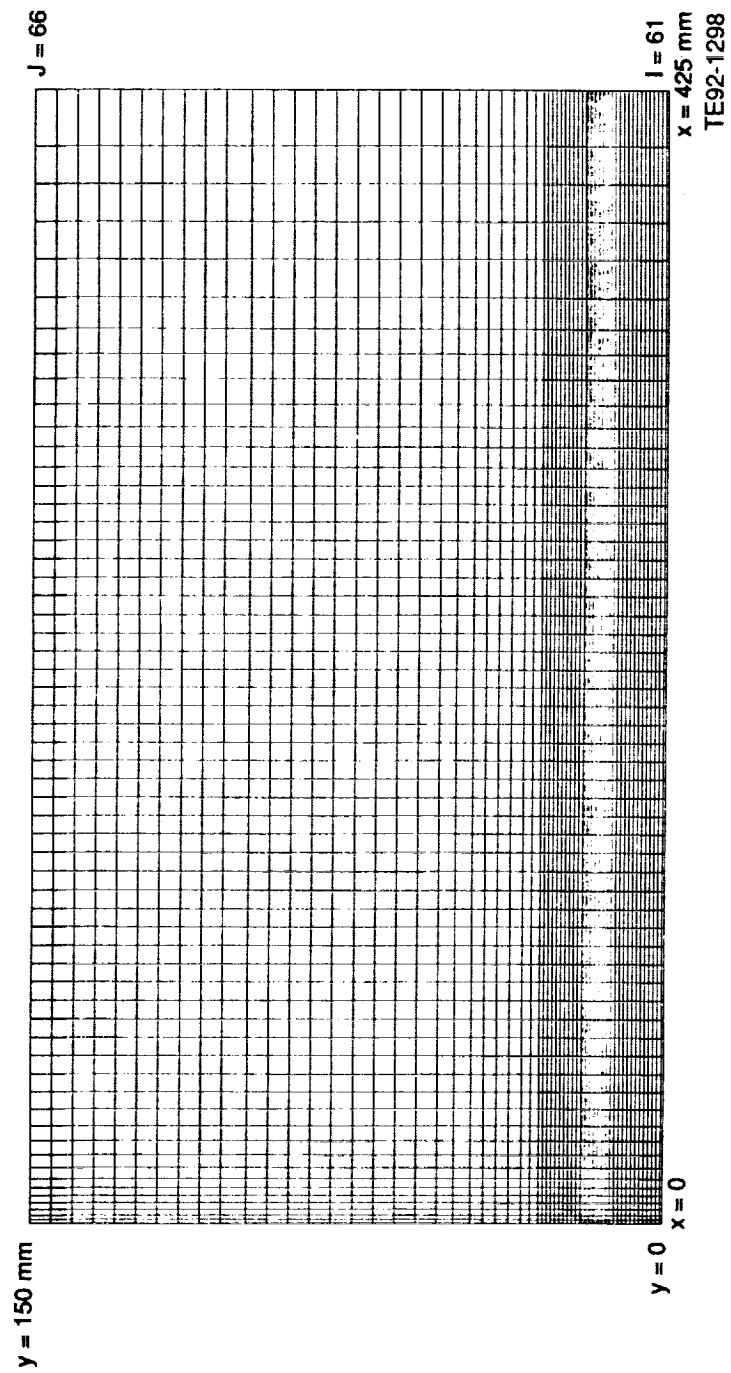


Figure 6.5-2. Unconfined swirling coaxial jets grid layout.

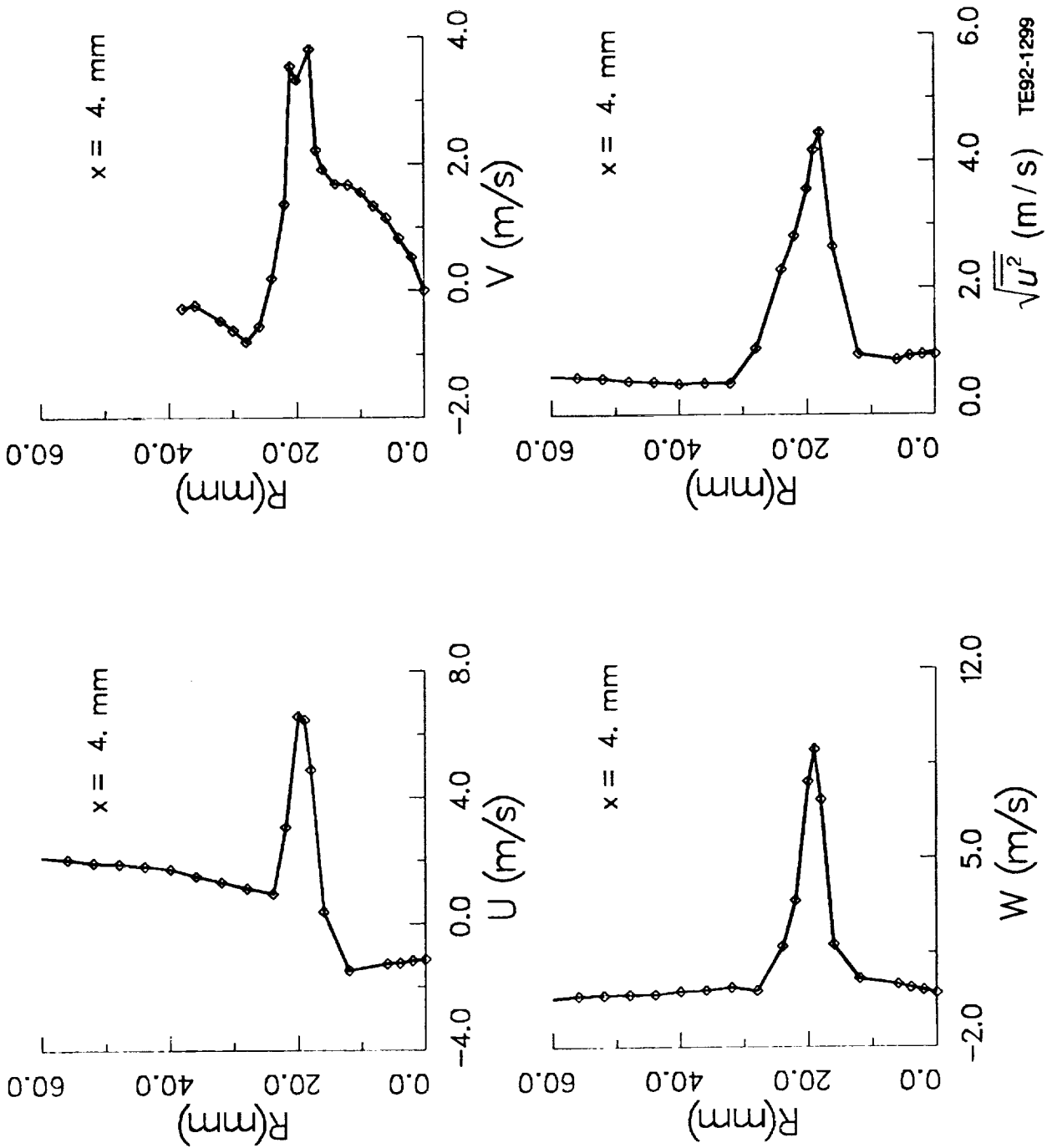


Figure 6.5-3. Measured profiles at the inlet plane ($x = 4 \text{ mm}$) (1 of 2).

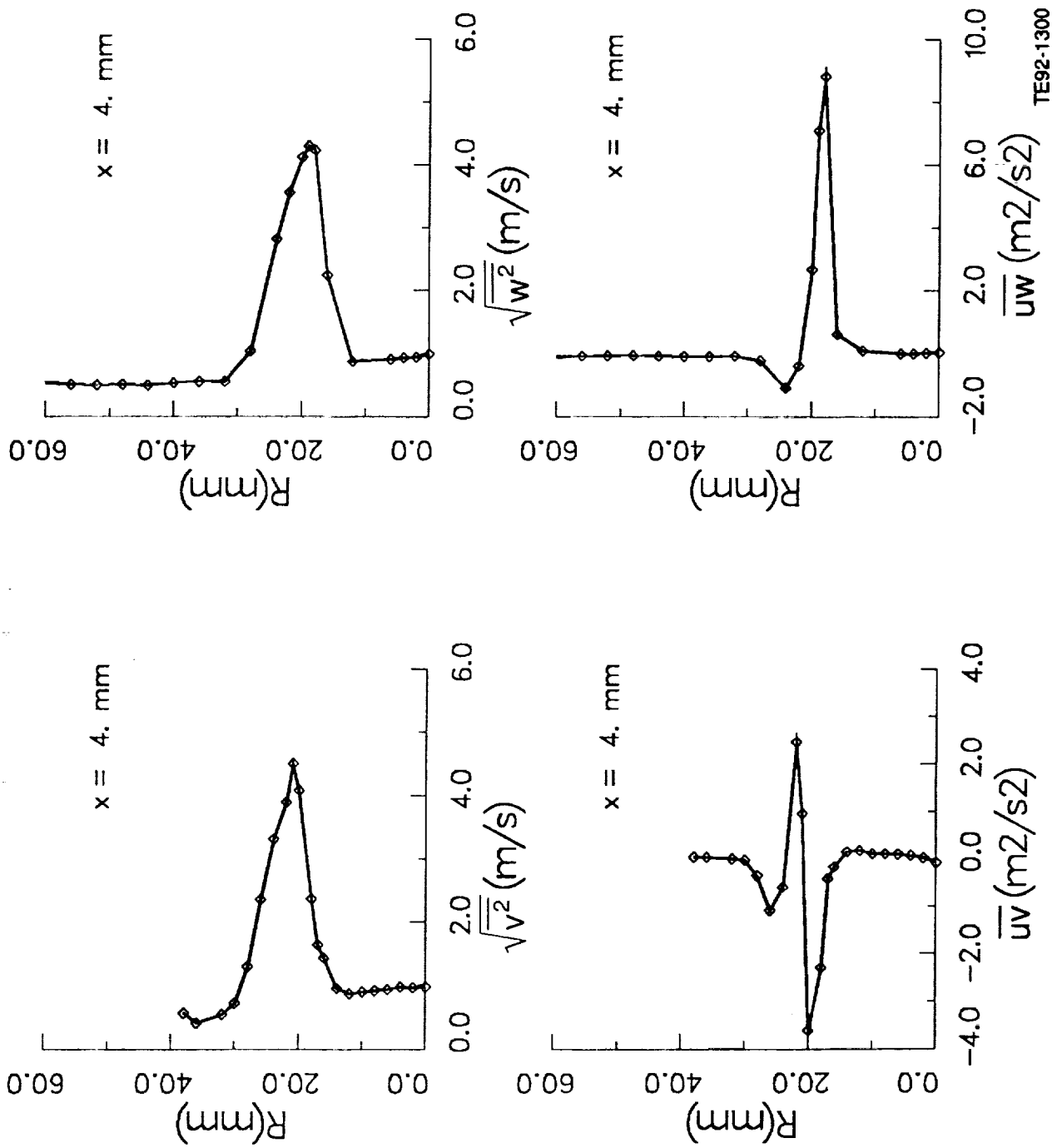


Figure 6.5-3. Measured profiles at the inlet plane ($x = 4 \text{ mm}$) (2 of 2).

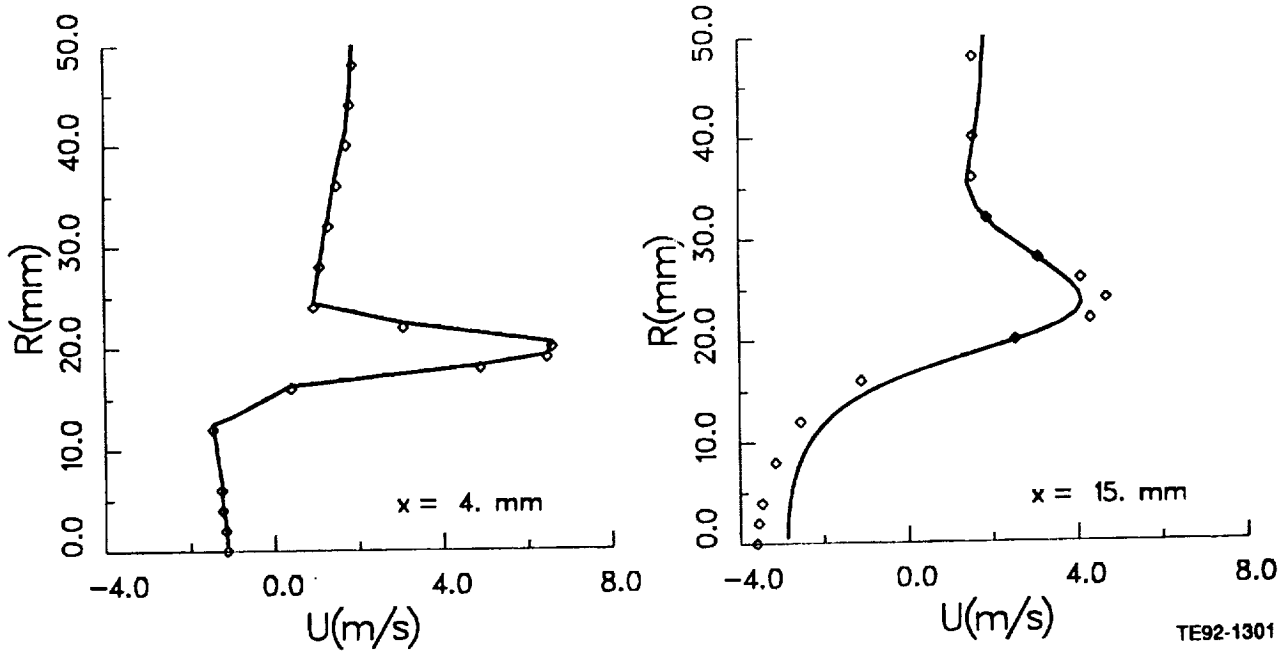


Figure 6.5-4. Comparison of calculated mean axial velocity by $k-\epsilon$ model with data (1 of 4).

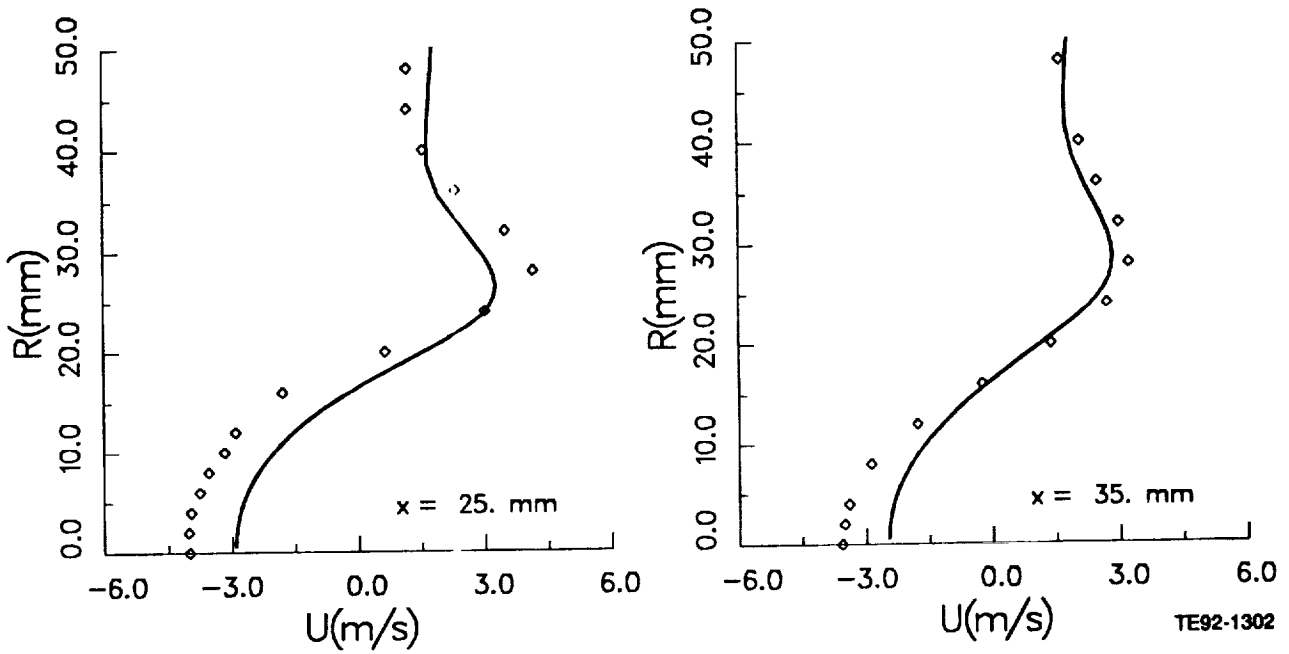


Figure 6.5-4. Comparison of calculated mean axial velocity by $k-\epsilon$ model with data (2 of 4).

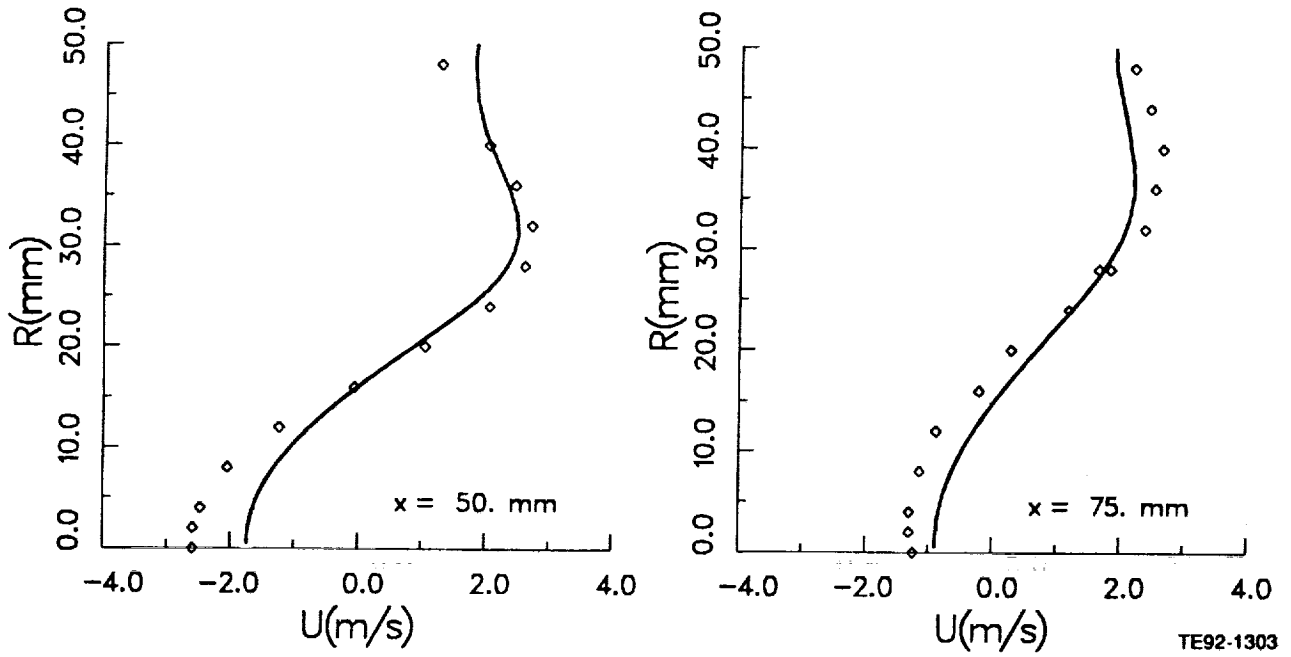


Figure 6.5-4. Comparison of calculated mean axial velocity by $k-\epsilon$ model with data (3 of 4).

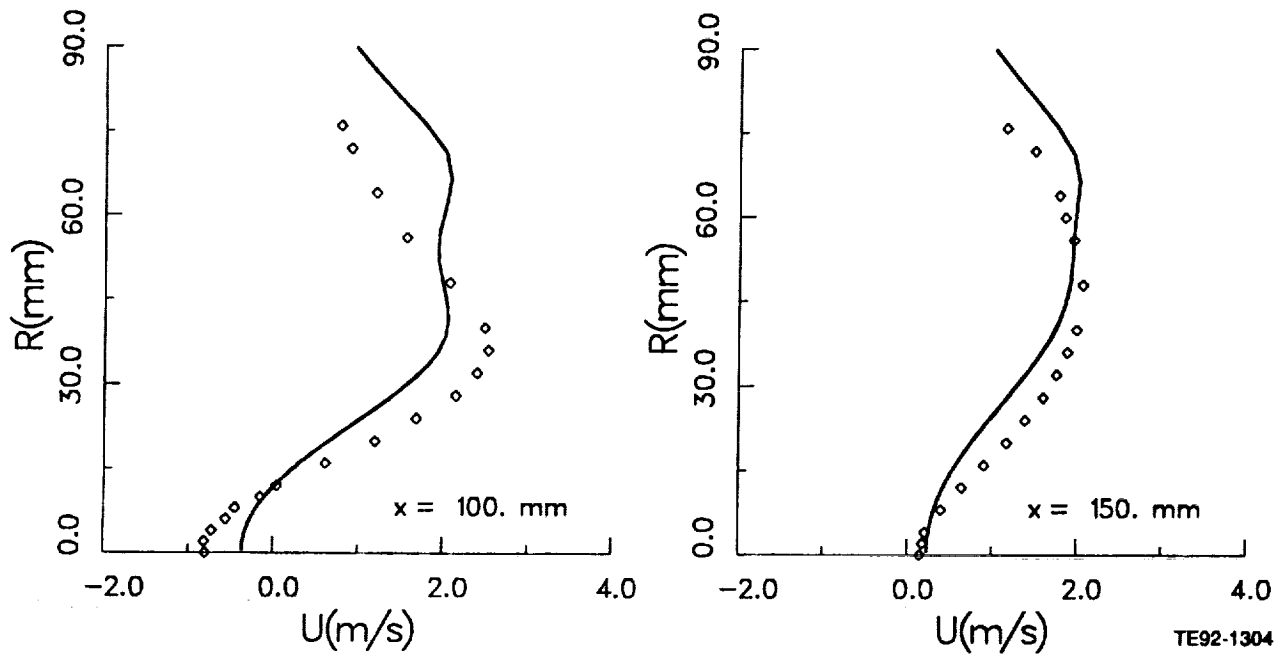
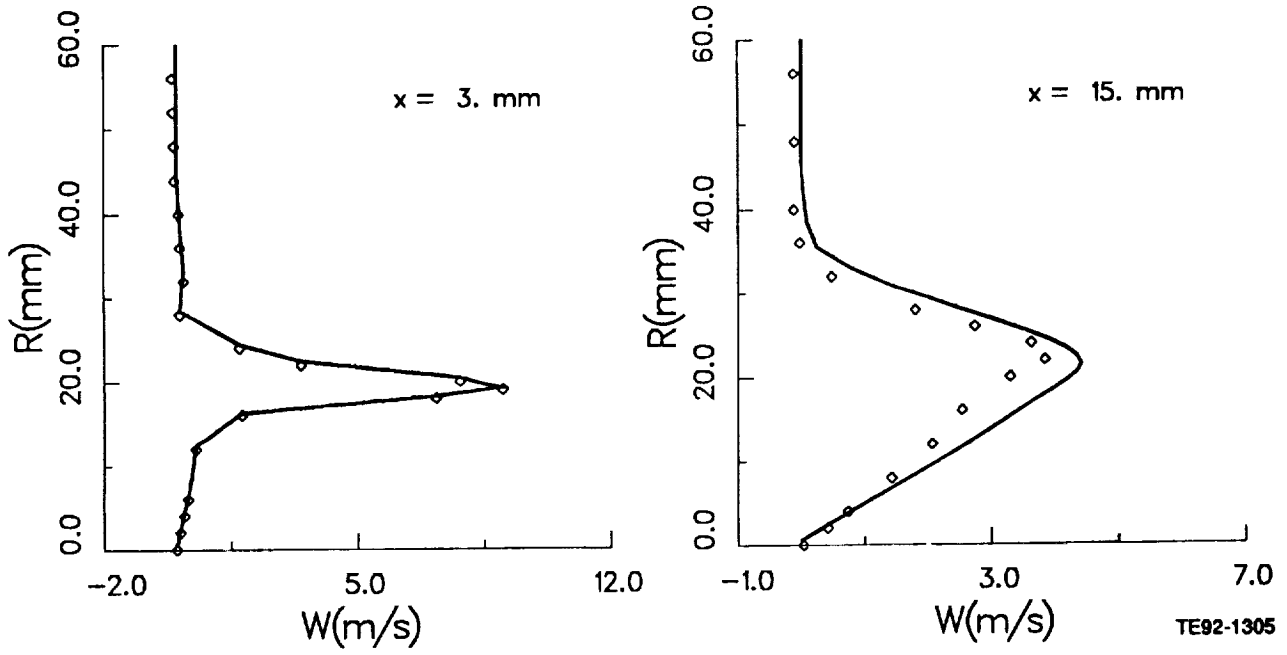
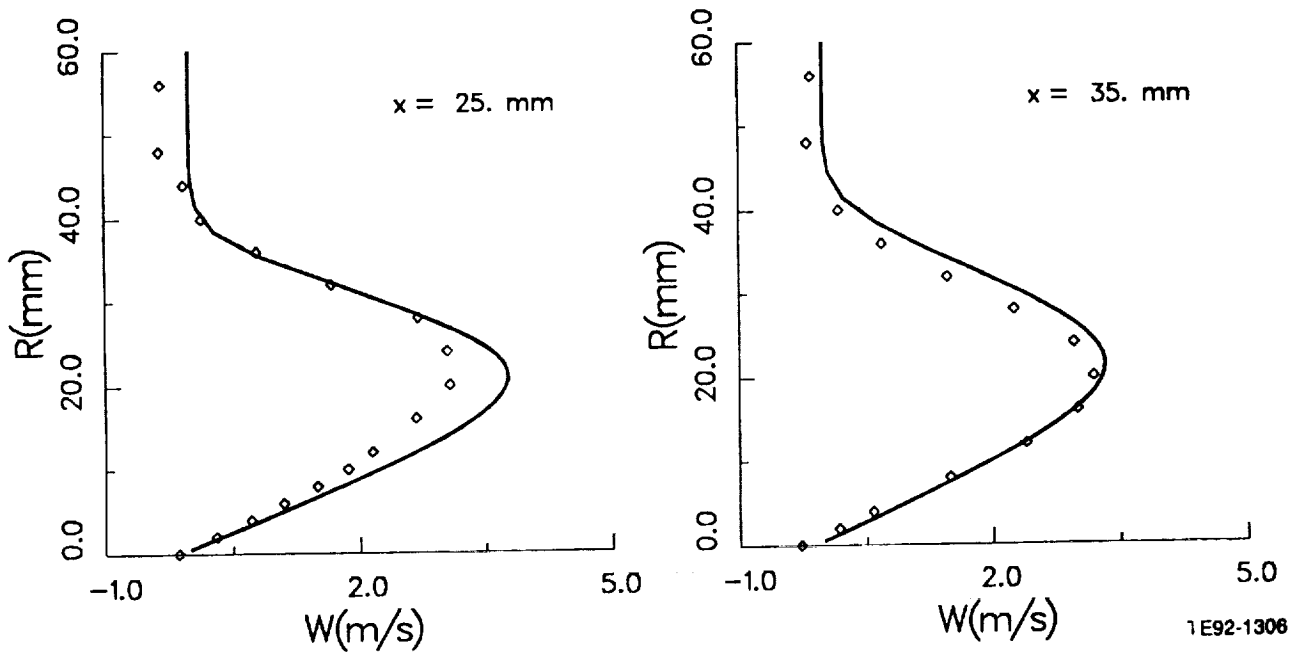


Figure 6.5-4. Comparison of calculated mean axial velocity by $k-\epsilon$ model with data (4 of 4).



TE92-1305

Figure 6.5-5. Comparison of calculated mean tangential velocity by k- ϵ model with data (1 of 4).



1E92-1306

Figure 6.5-5. Comparison of calculated mean tangential velocity by k- ϵ model with data (2 of 4).

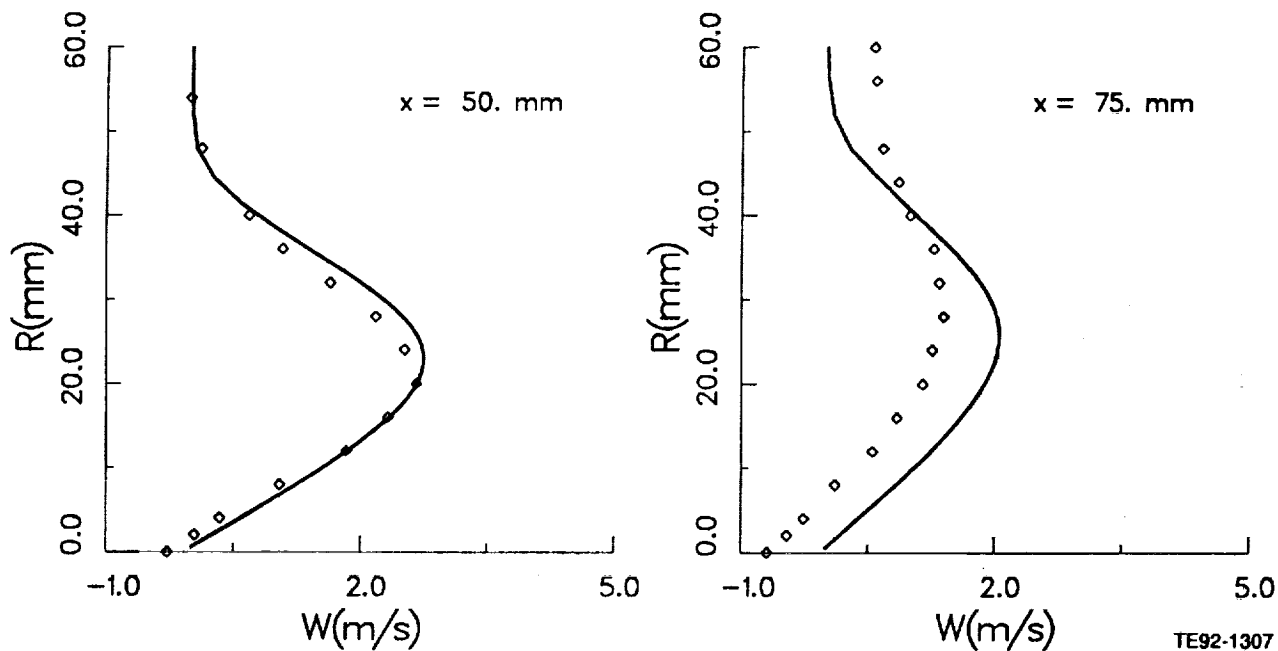


Figure 6.5-5. Comparison of calculated mean tangential velocity by $k-\epsilon$ model with data (3 of 4).

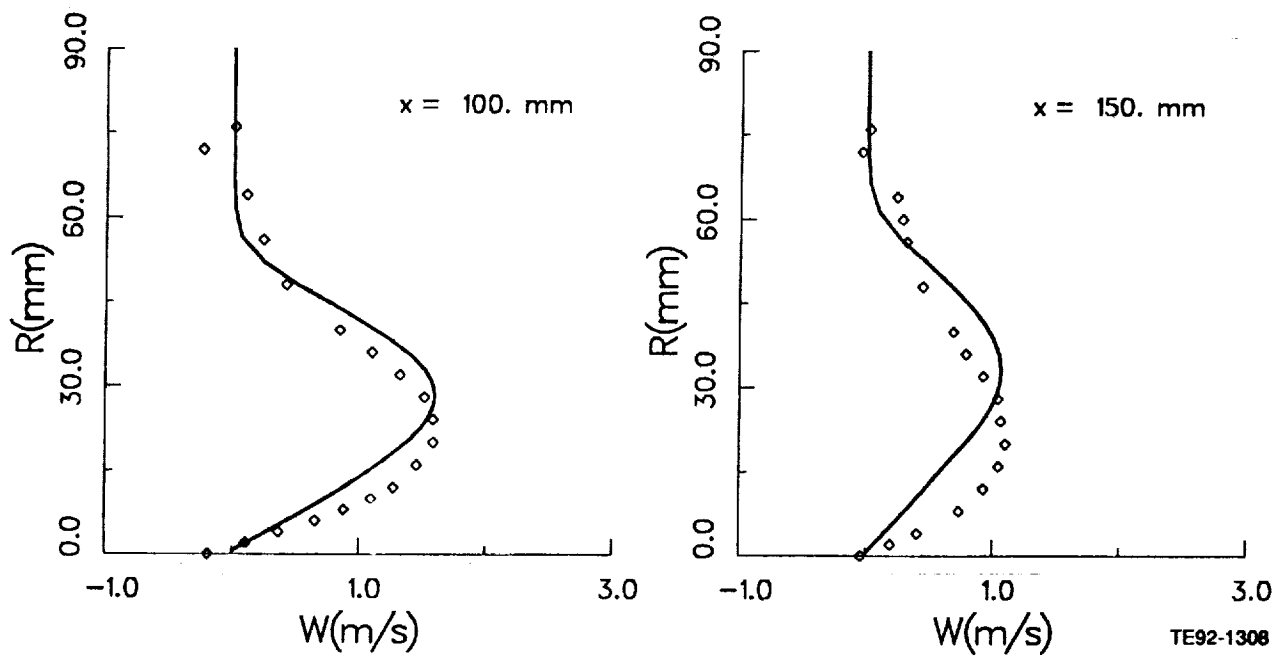


Figure 6.5-5. Comparison of calculated mean tangential velocity by $k-\epsilon$ model with data (4 of 4).

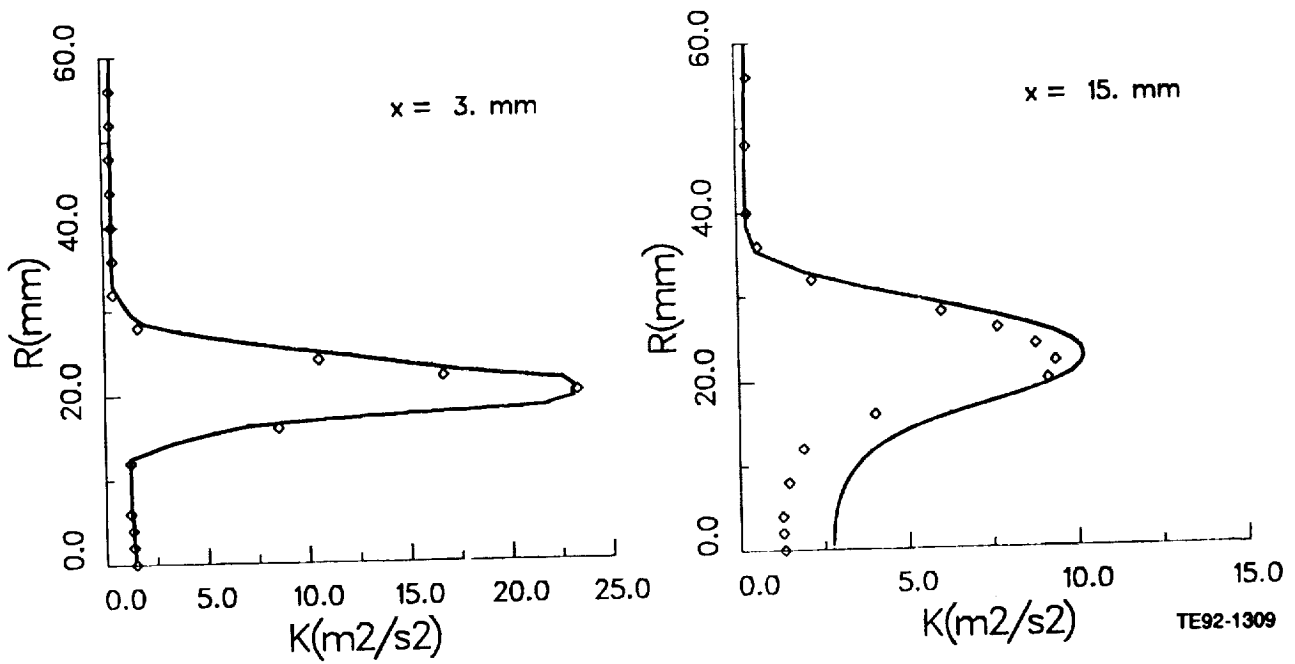


Figure 6.5-6. Comparison of predicted turbulent kinetic energy by k - ϵ model with measurement (1 of 4).

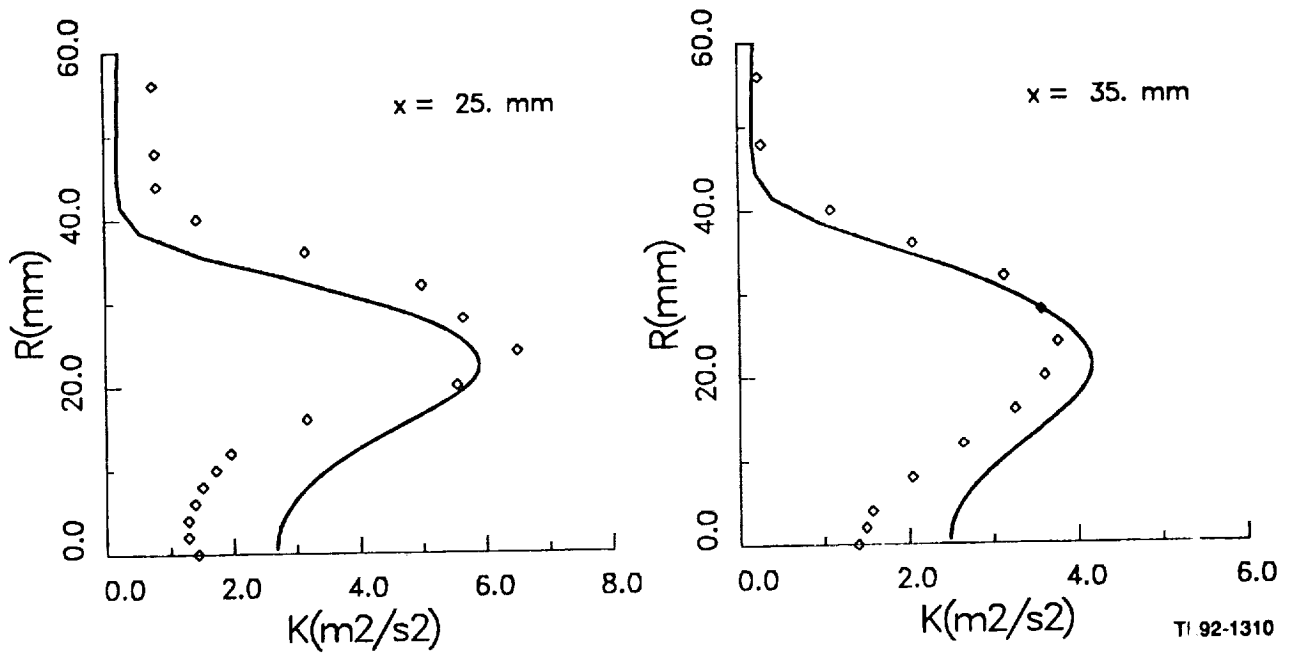


Figure 6.5-6. Comparison of predicted turbulent kinetic energy by k - ϵ model with measurement (2 of 4).

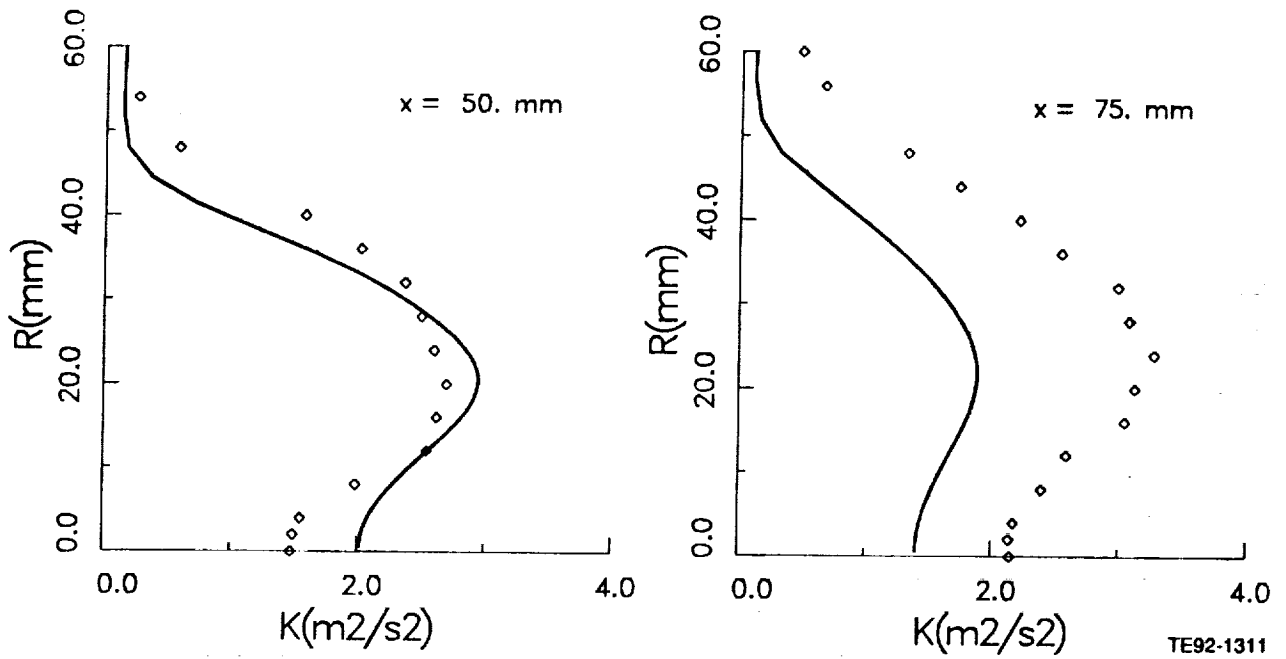


Figure 6.5-6. Comparison of predicted turbulent kinetic energy by $k-\epsilon$ model with measurement (3 of 4).

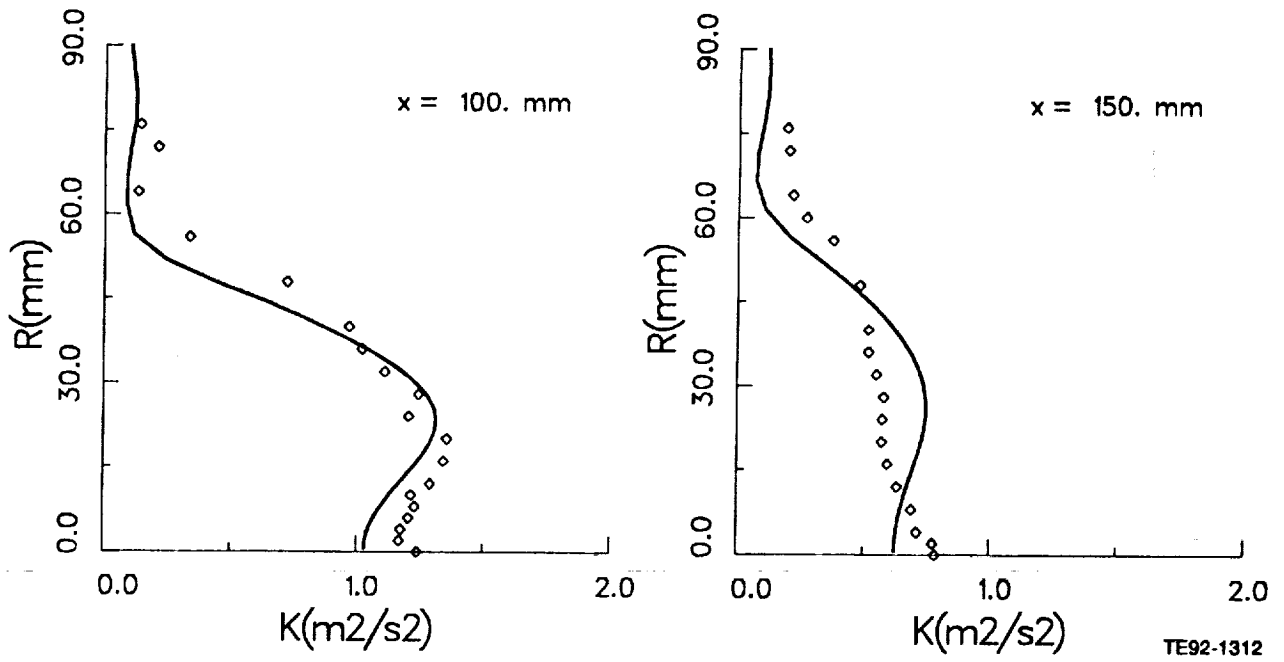


Figure 6.5-6. Comparison of predicted turbulent kinetic energy by $k-\epsilon$ model with measurement (4 of 4).

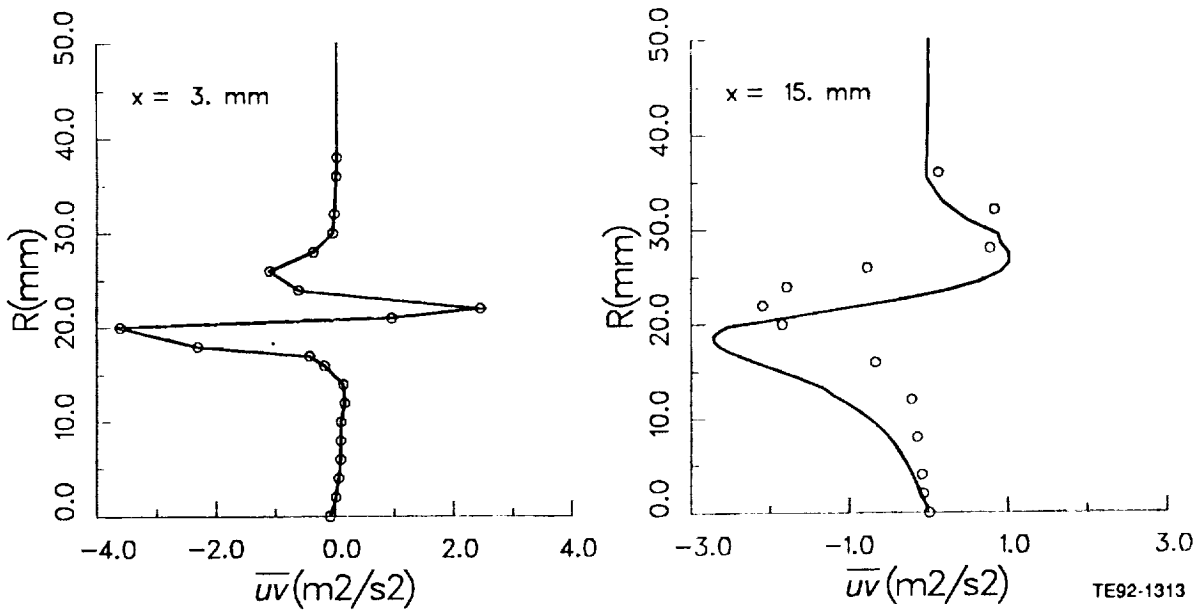


Figure 6.5-7. Comparison of predicted turbulent shear stress by $k-\epsilon$ model with data (1 of 4).

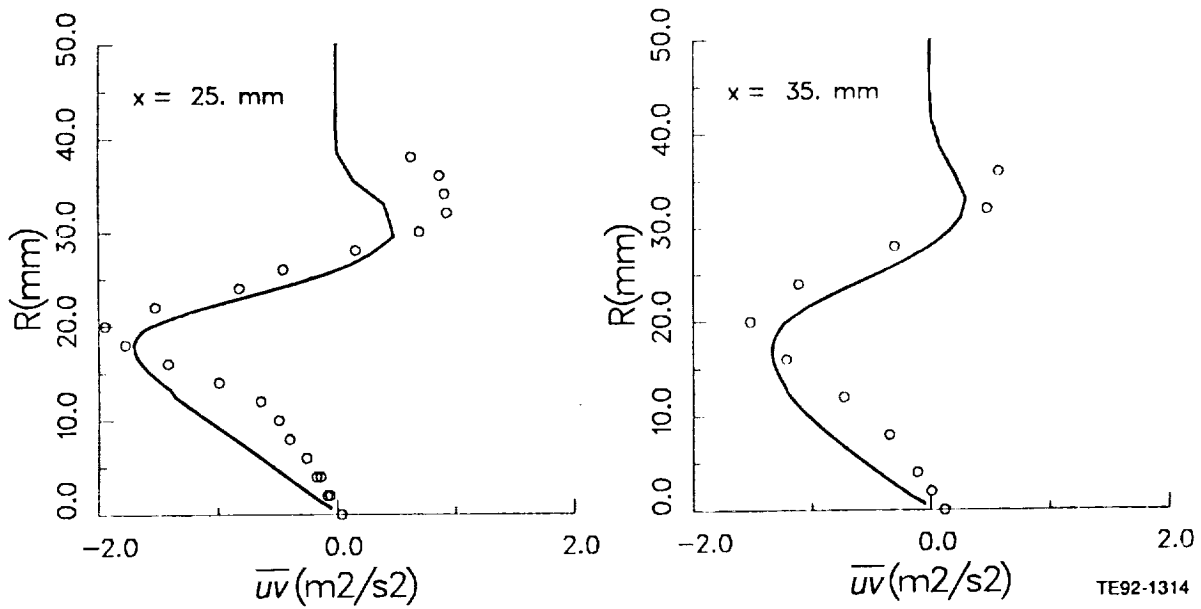


Figure 6.5-7. Comparison of predicted turbulent shear stress by $k-\epsilon$ model with data (2 of 4).

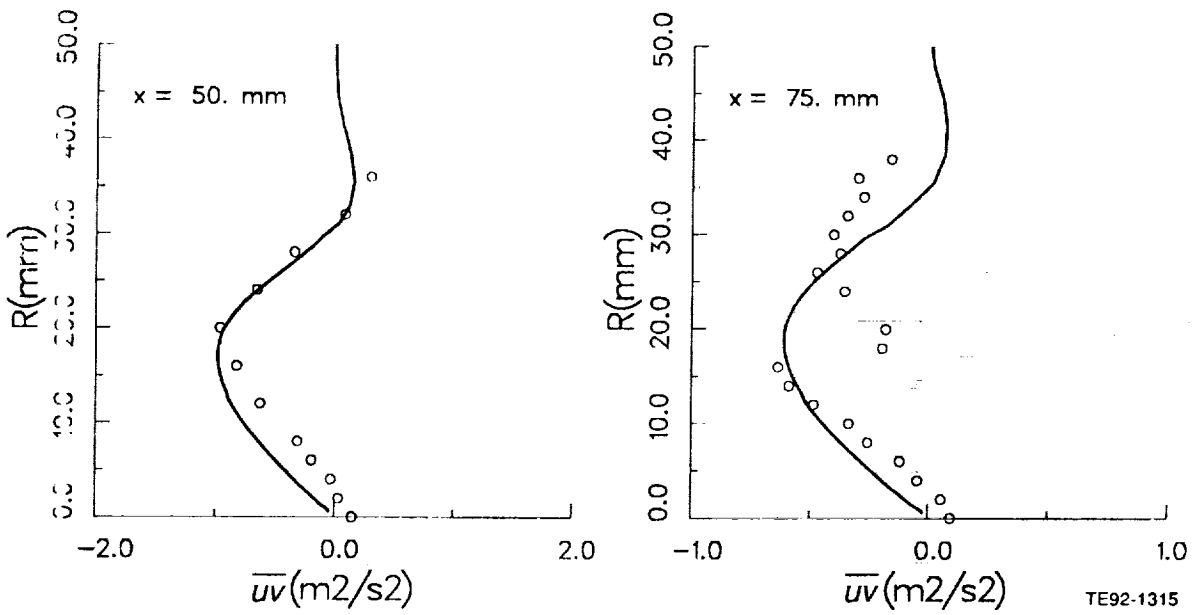


Figure 6.5-7. Comparison of predicted turbulent shear stress by $k-\epsilon$ model with data (3 of 4).

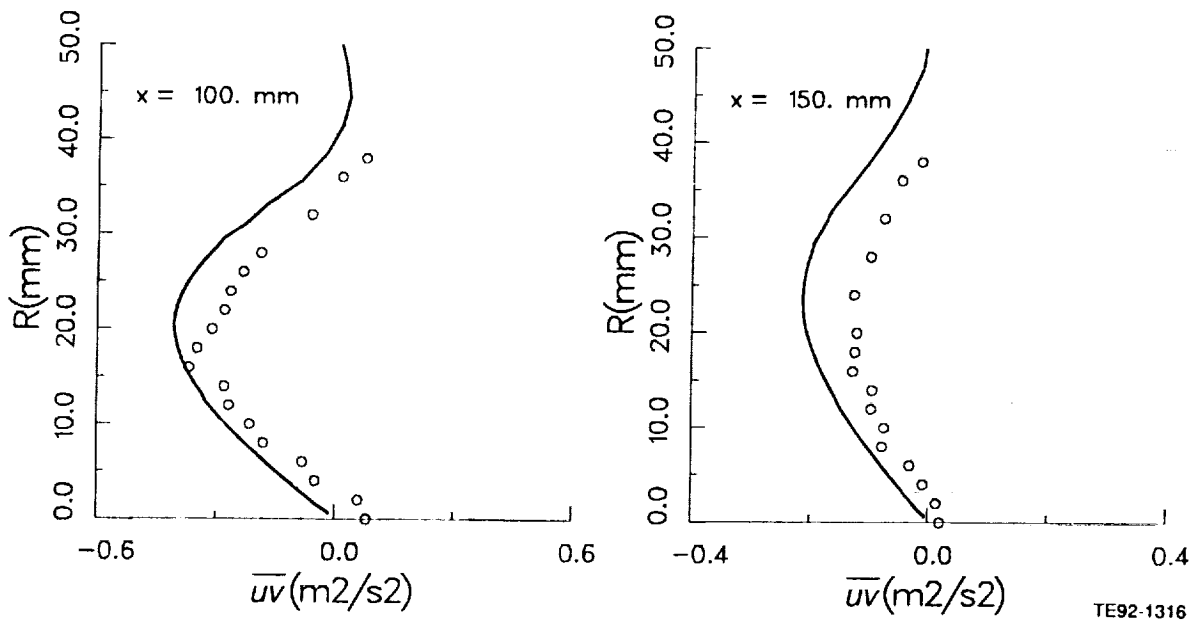


Figure 6.5-7. Comparison of predicted turbulent shear stress by $k-\epsilon$ model with data (4 of 4).

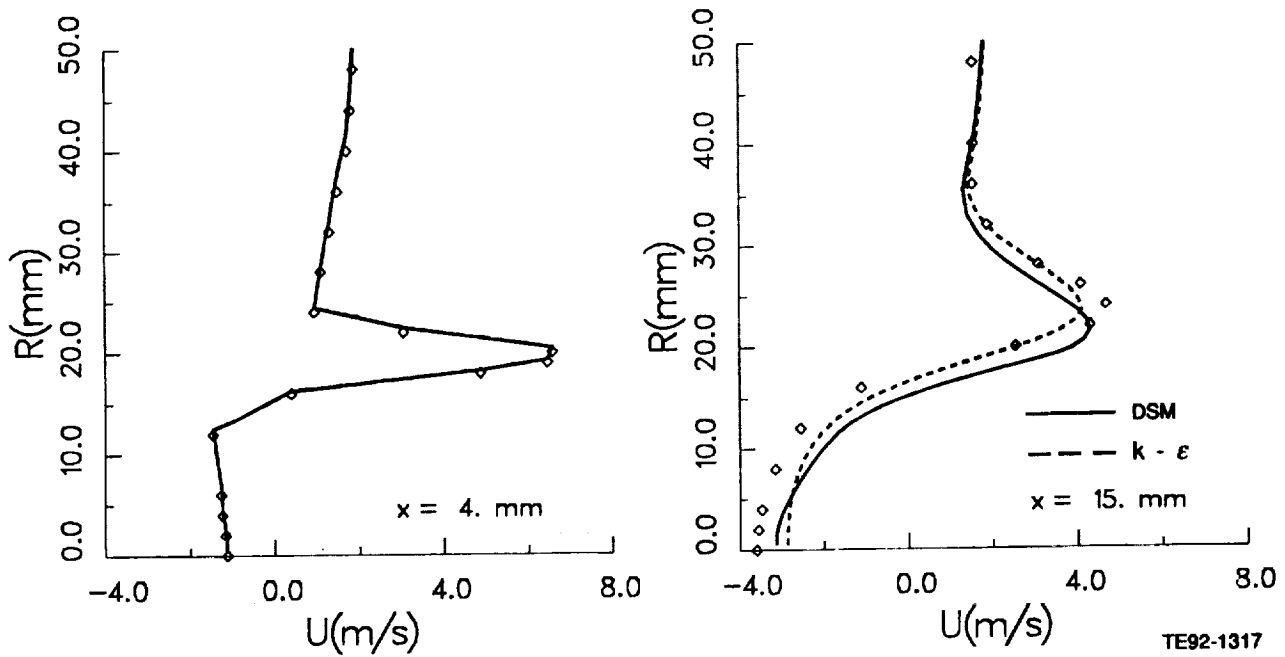


Figure 6.5-8. Comparison of calculated mean axial velocity by $k-\epsilon$ and DSM with data (1 of 4).

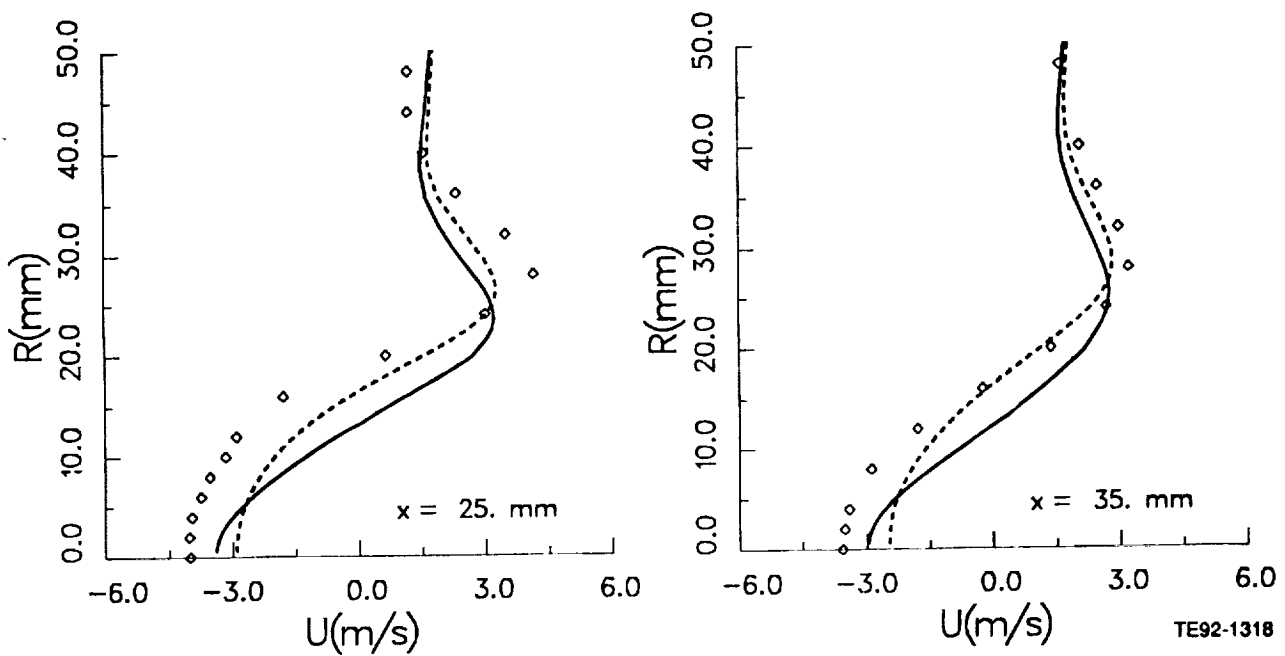


Figure 6.5-8. Comparison of calculated mean axial velocity by $k-\epsilon$ and DSM with data (2 of 4).

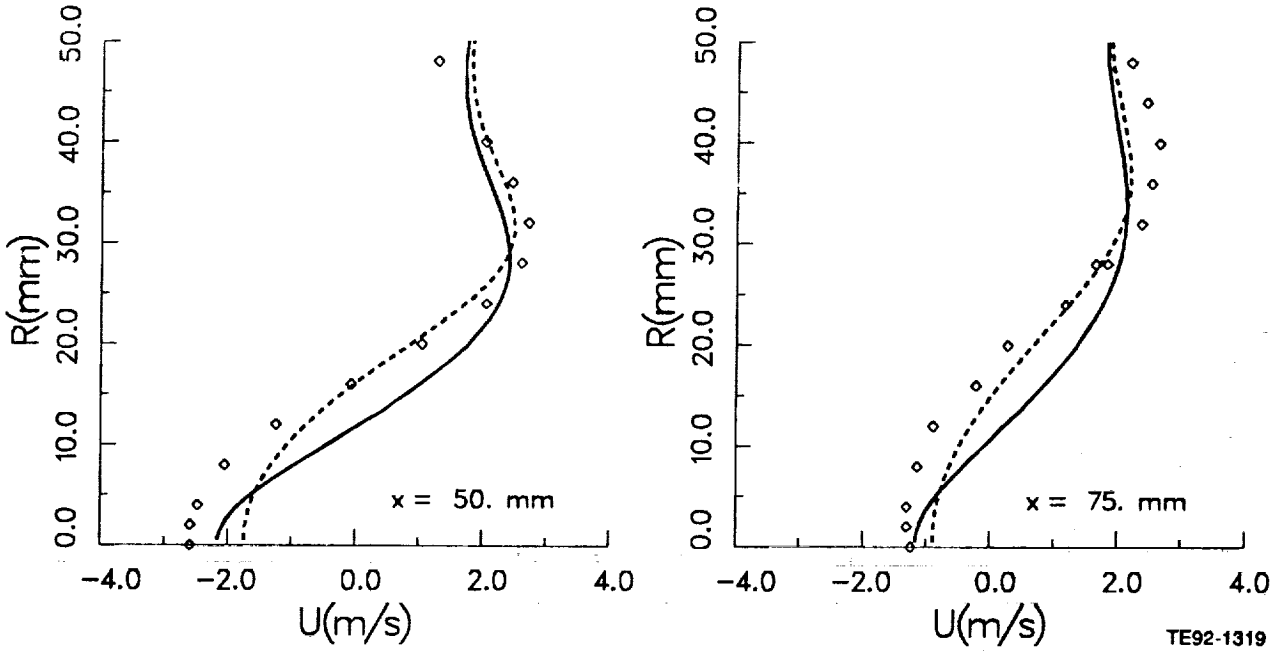


Figure 6.5-8. Comparison of calculated mean axial velocity by $k-\epsilon$ and DSM with data (3 of 4).

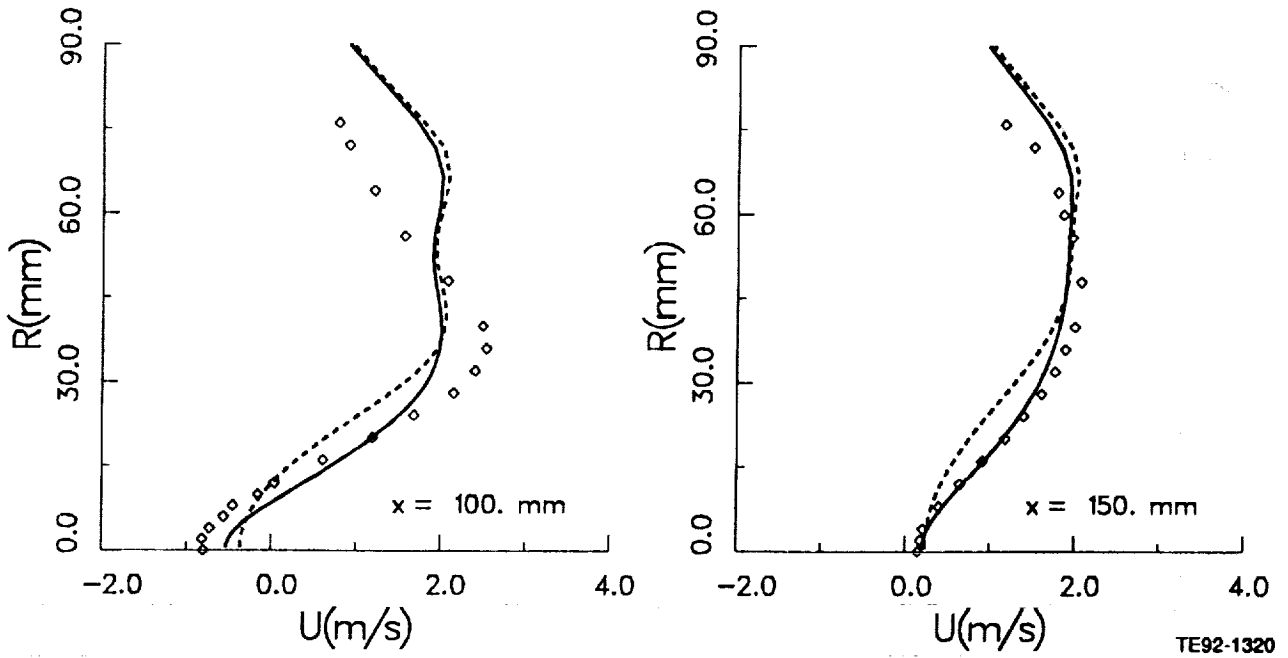


Figure 6.5-8. Comparison of calculated mean axial velocity by $k-\epsilon$ and DSM with data (4 of 4).

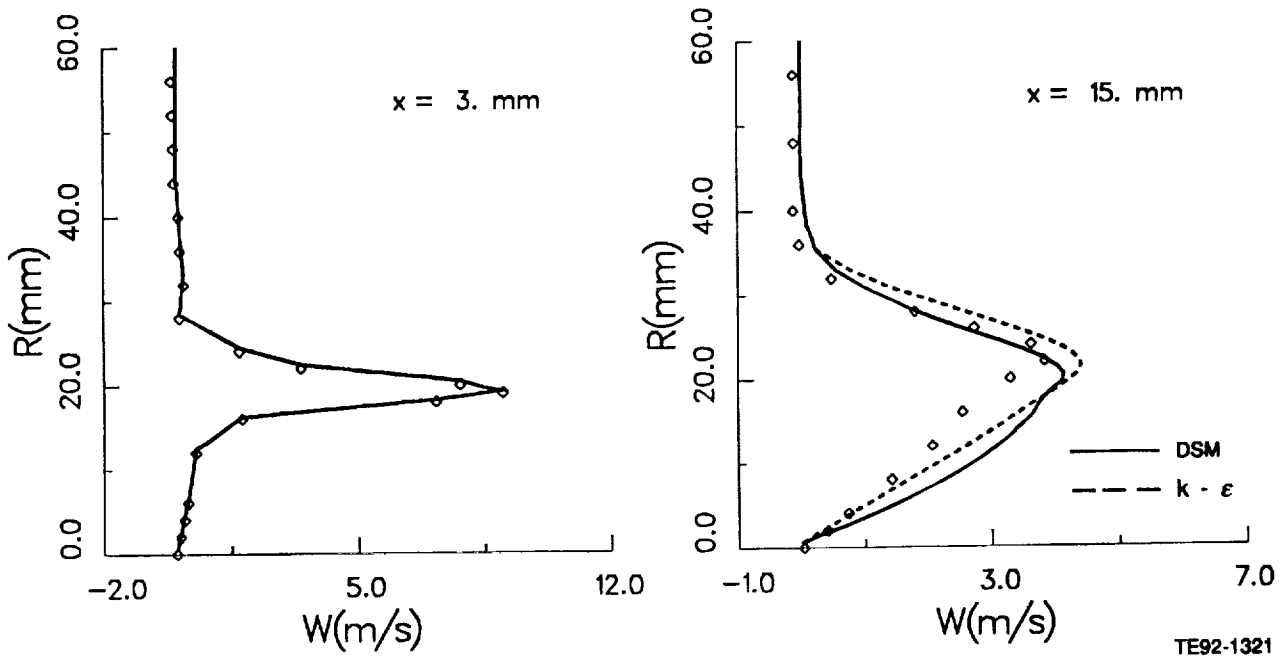


Figure 6.5-9. Comparison of calculated mean tangential velocity by k-ε and DSM with data (1 of 4).

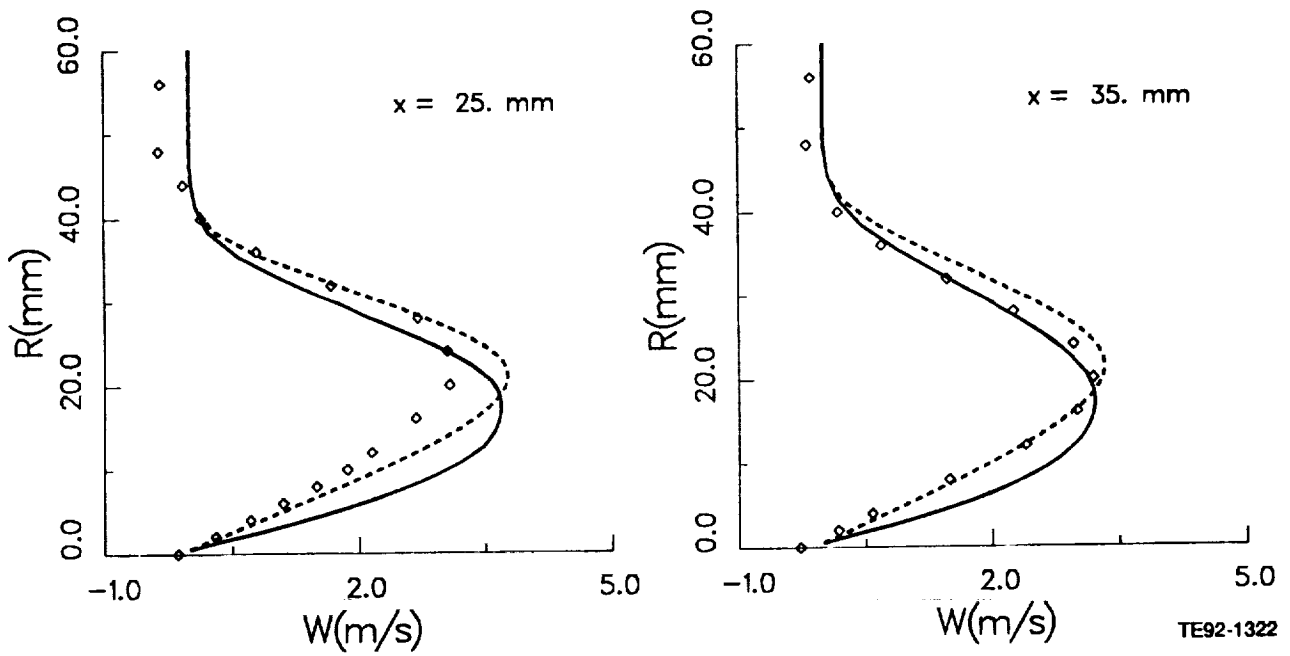


Figure 6.5-9. Comparison of calculated mean tangential velocity by k-ε and DSM with data (2 of 4).

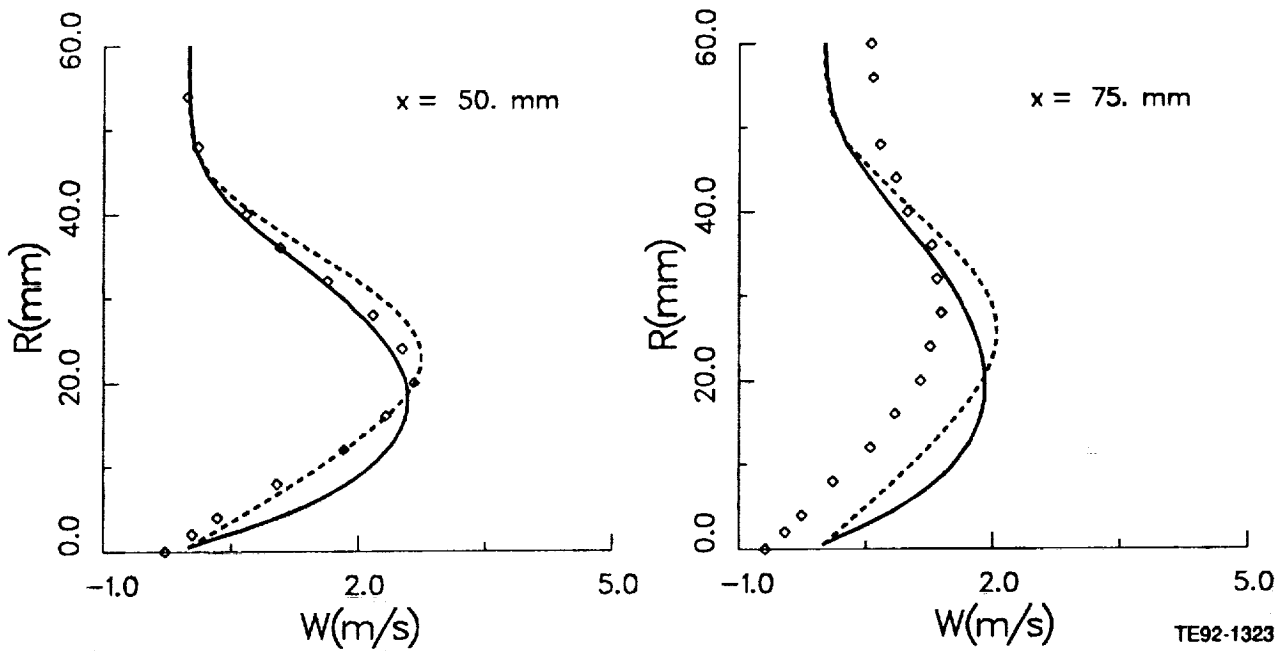


Figure 6.5-9. Comparison of calculated mean tangential velocity by $k-\epsilon$ and DSM with data (3 of 4).

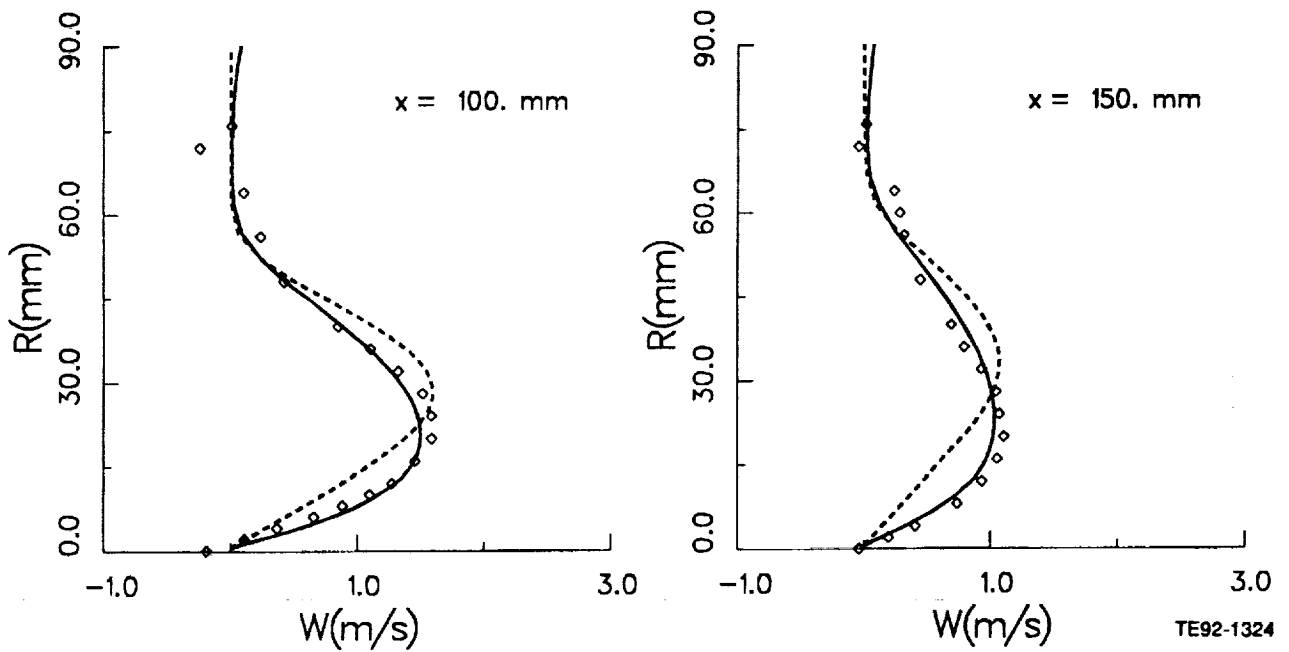


Figure 6.5-9. Comparison of calculated mean tangential velocity by $k-\epsilon$ and DSM with data (4 of 4).

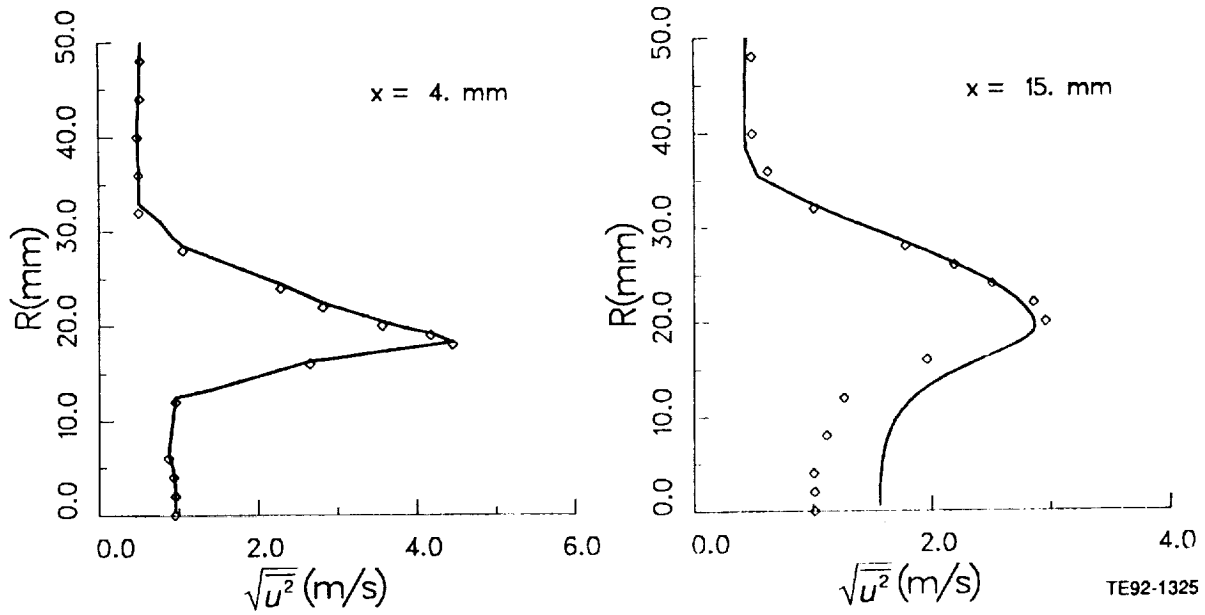


Figure 6.5-10. Comparison of calculated axial rms velocity component by DSM with data (1 of 4).

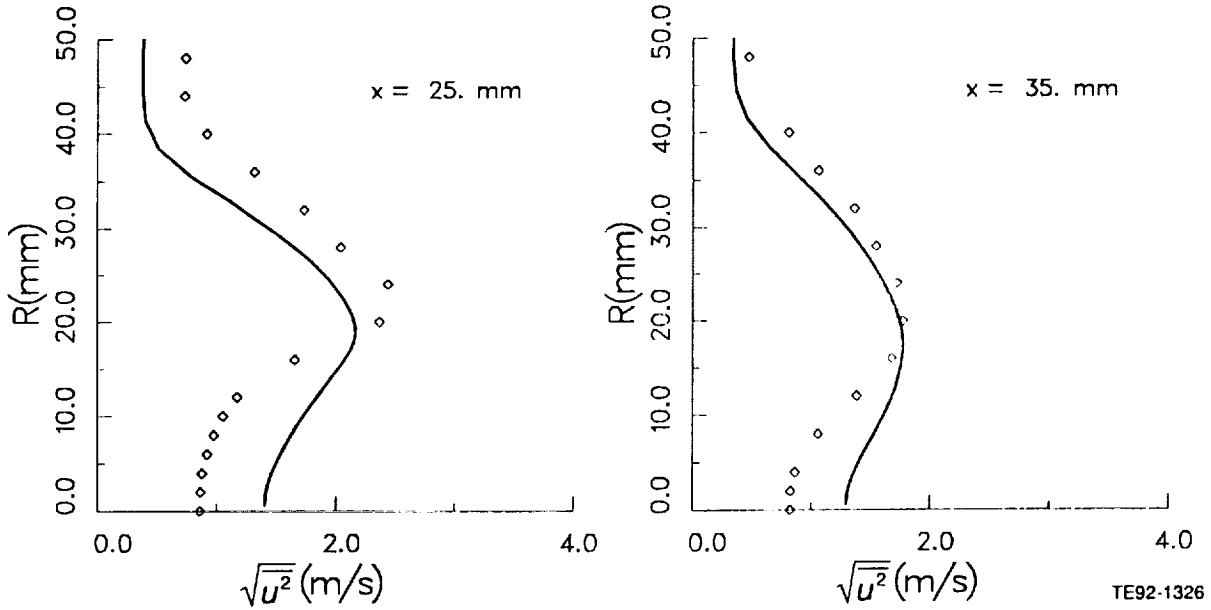


Figure 6.5-10. Comparison of calculated axial rms velocity component by DSM with data (2 of 4).

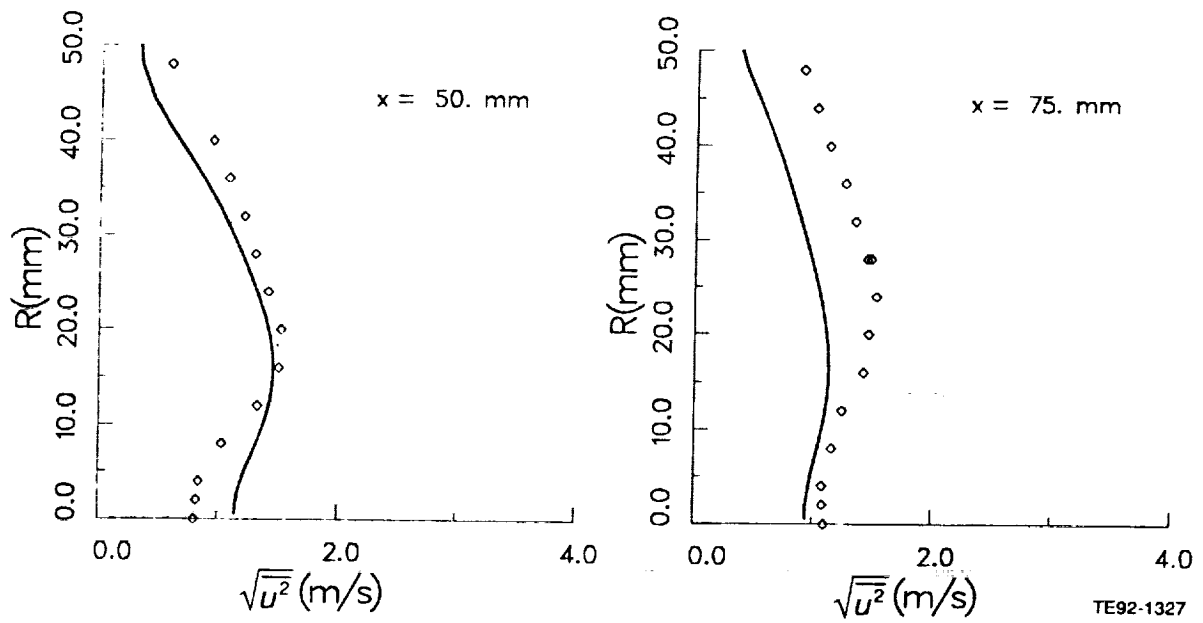


Figure 6.5-10. Comparison of calculated axial rms velocity component by DSM with data (3 of 4).

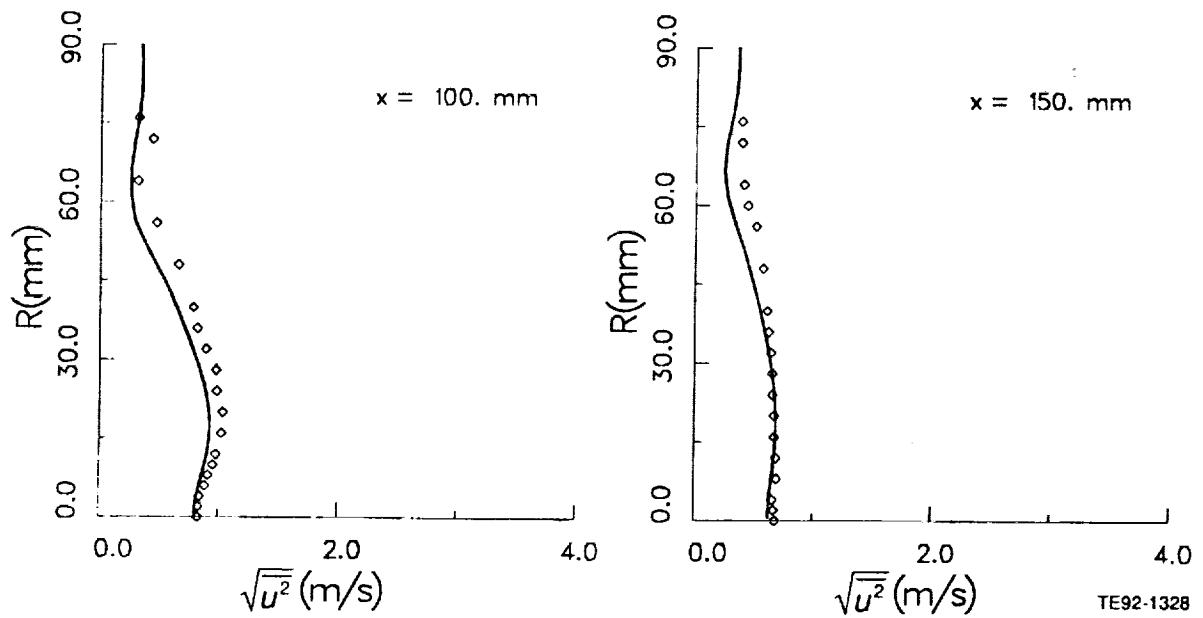


Figure 6.5-10. Comparison of calculated axial rms velocity component by DSM with data (4 of 4).

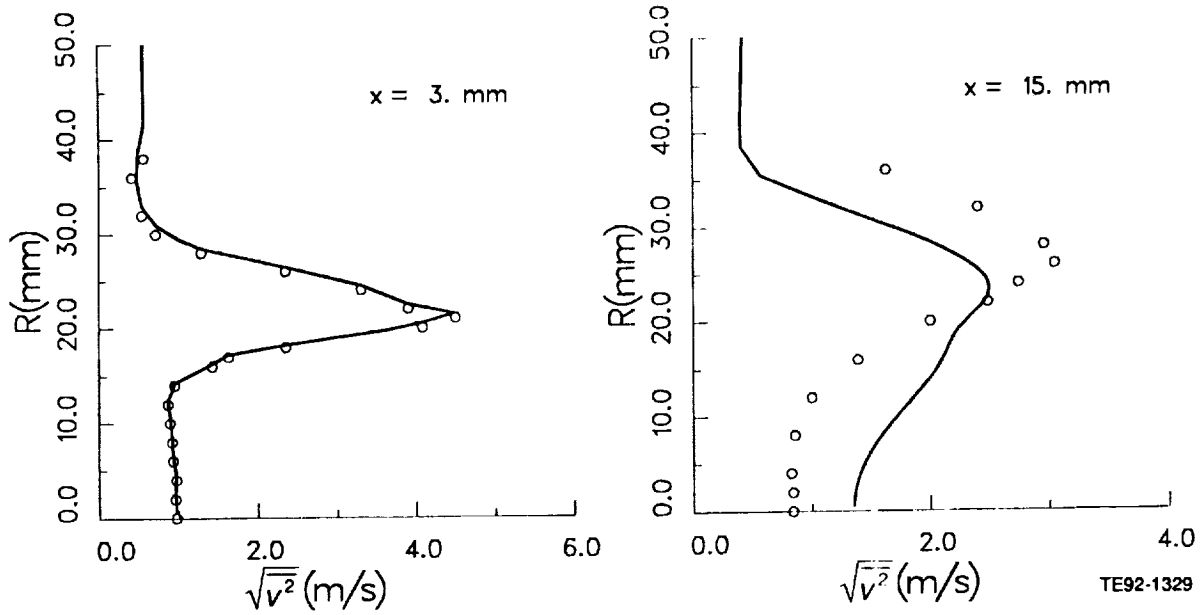


Figure 6.5-11. Comparison of calculated radial rms velocity component by DSM with data (1 of 4).

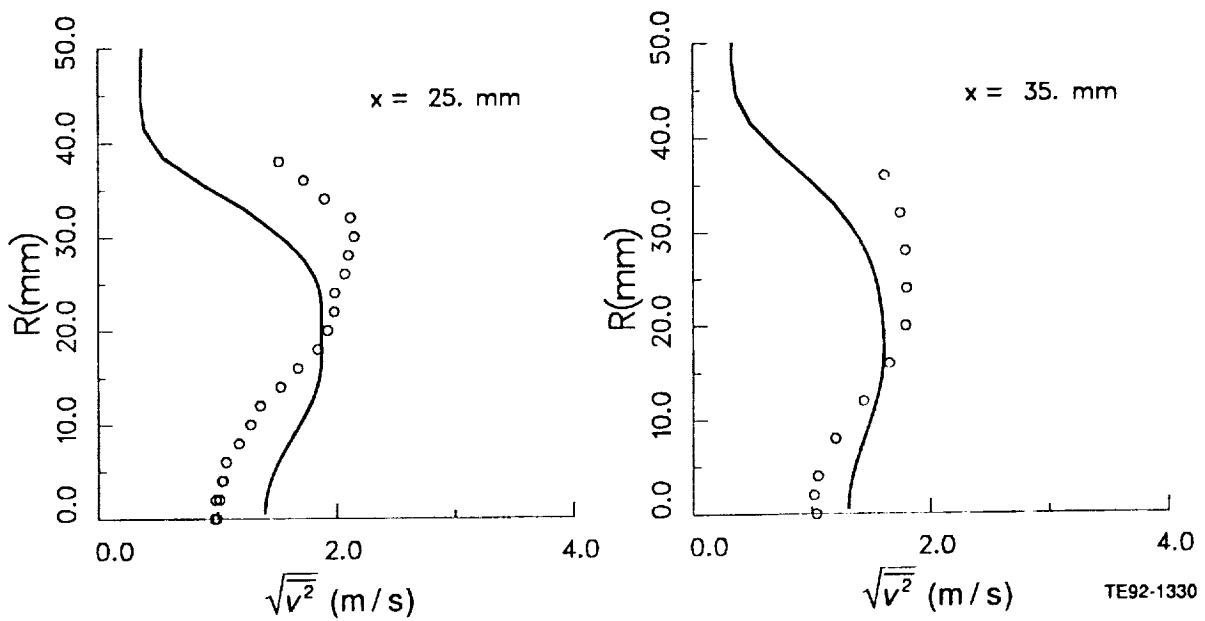


Figure 6.5-11. Comparison of calculated radial rms velocity component by DSM with data (2 of 4).

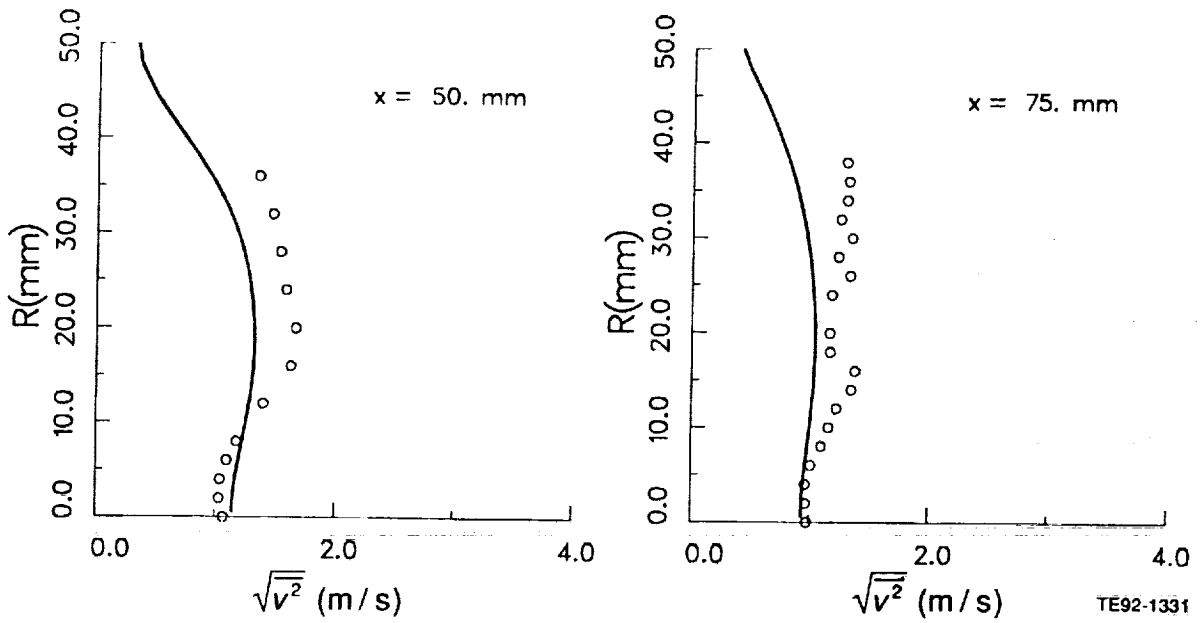


Figure 6.5-11. Comparison of calculated radial rms velocity component by DSM with data (3 of 4).

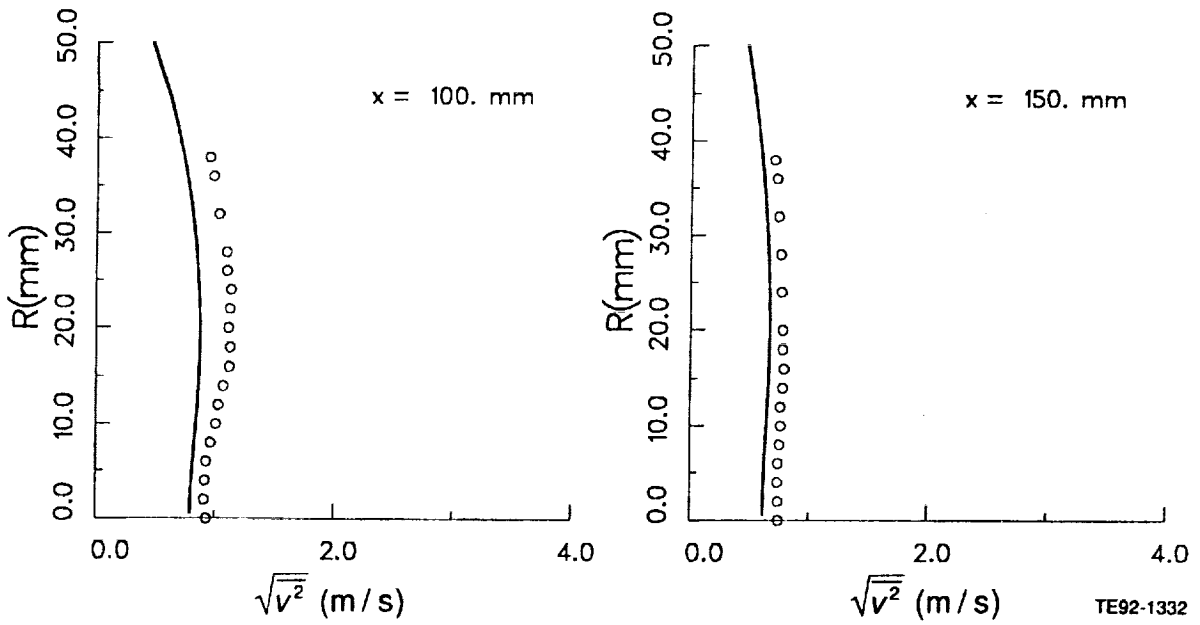


Figure 6.5-11. Comparison of calculated radial rms velocity component by DSM with data (4 of 4).

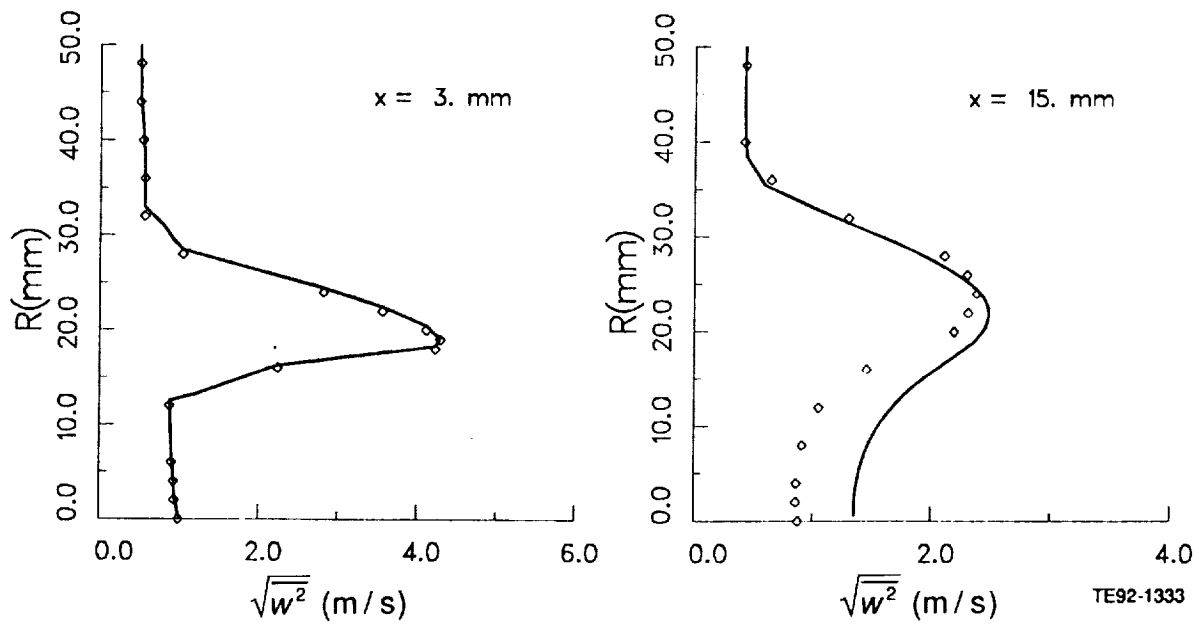


Figure 6.5-12. Comparison of calculated tangential rms velocity component by DSM with data (1 of 4).

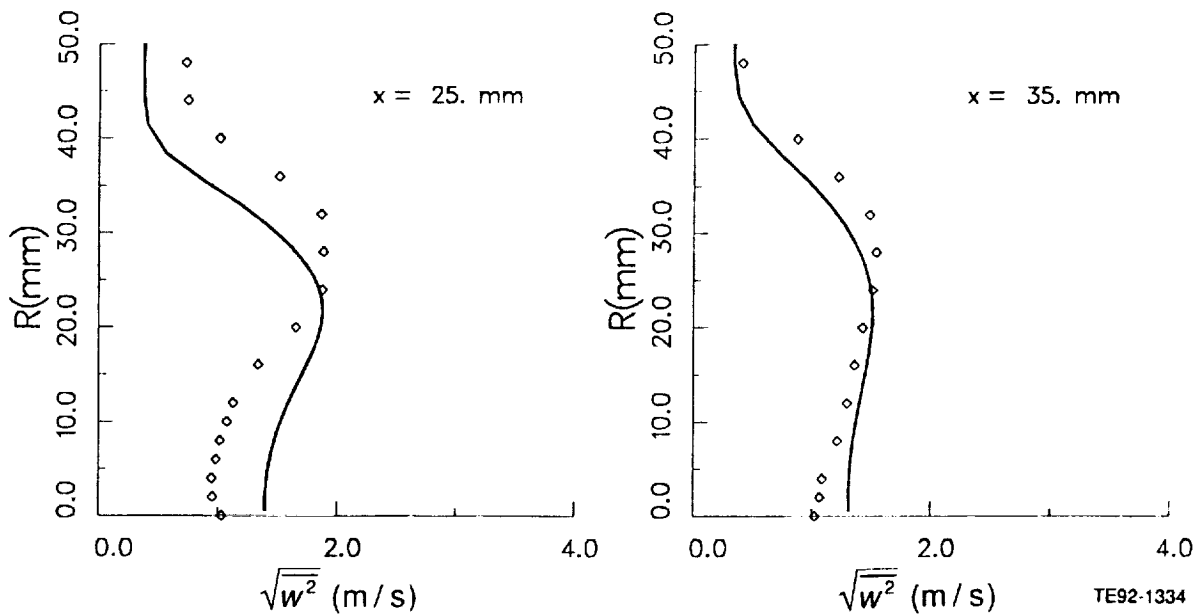


Figure 6.5-12. Comparison of calculated tangential rms velocity component by DSM with data (2 of 4).

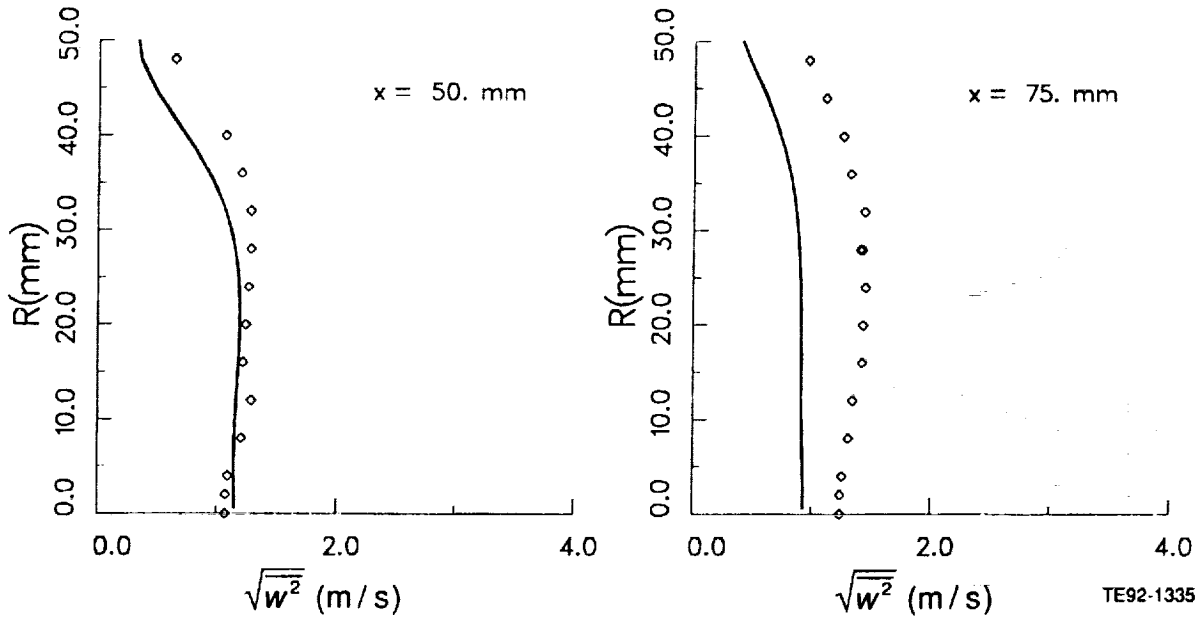


Figure 6.5-12. Comparison of calculated tangential rms velocity component by DSM with data (3 of 4).

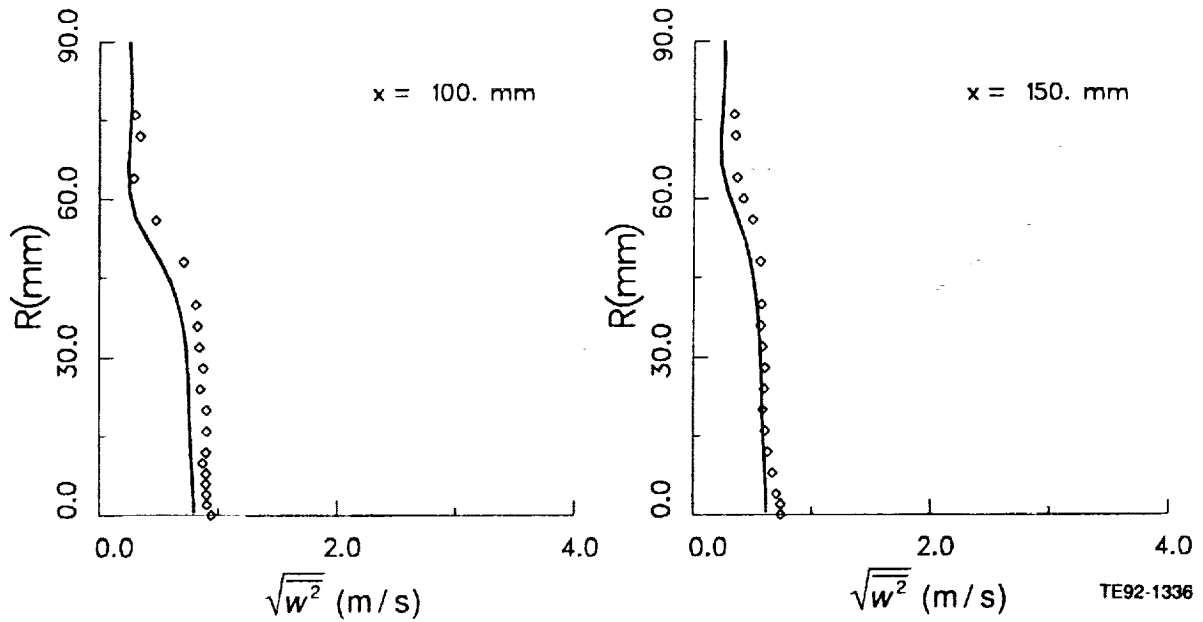
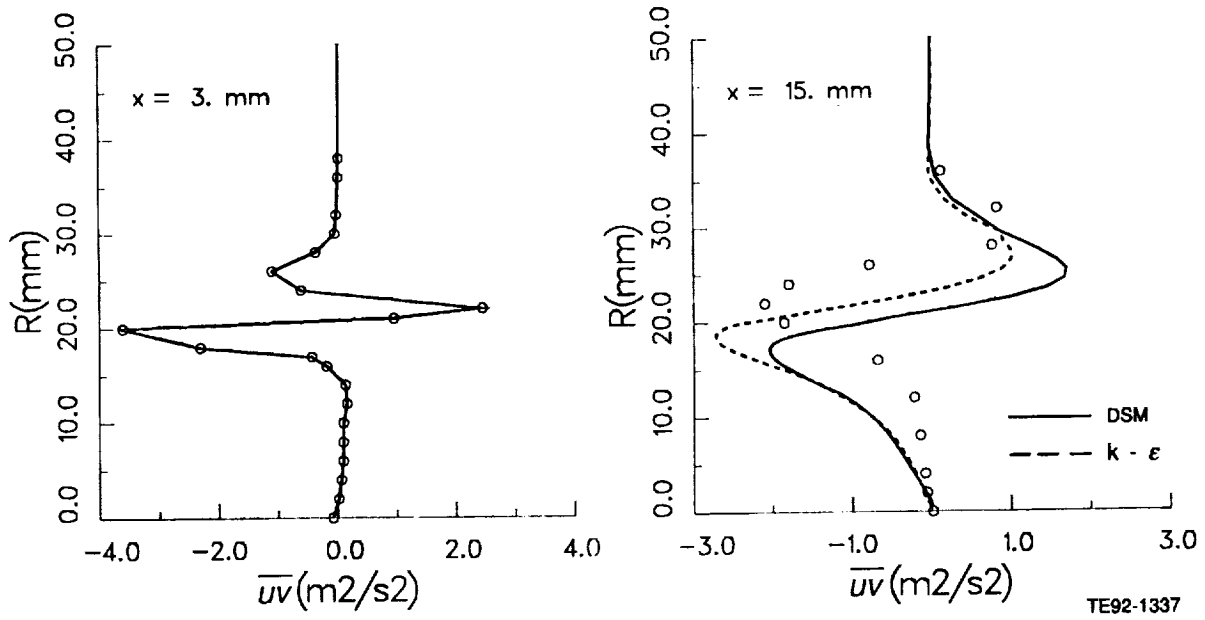
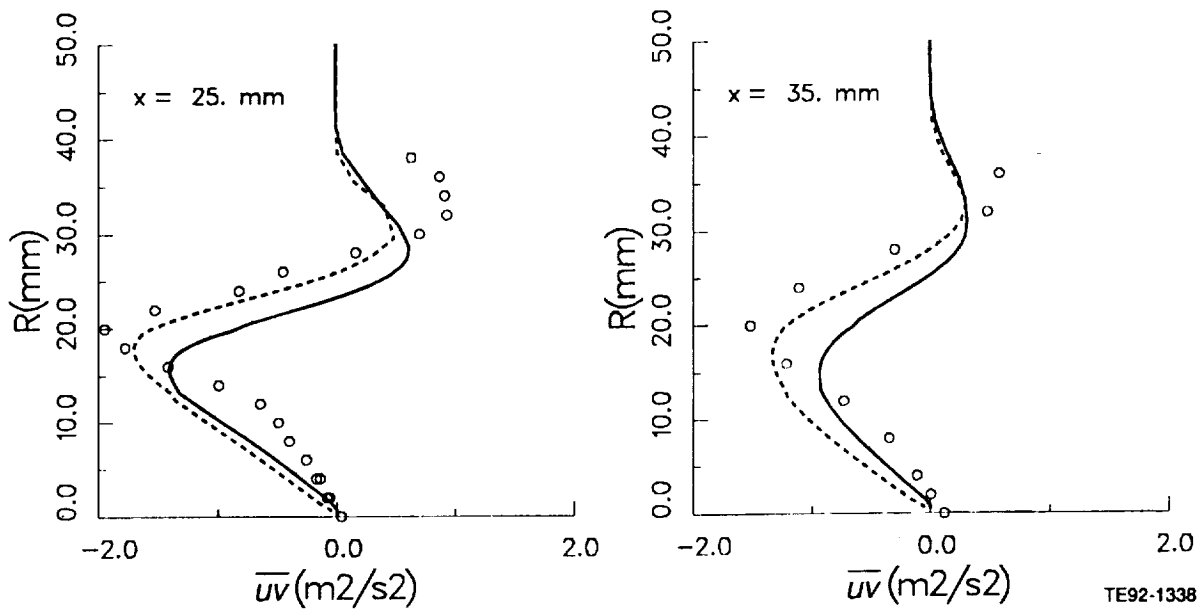


Figure 6.5-12. Comparison of calculated tangential rms velocity component by DSM with data (4 of 4).



TE92-1337

Figure 6.5-13. Comparison of calculated uv profiles by $k-\epsilon$ and DSM with data (1 of 4).



TE92-1338

Figure 6.5-13. Comparison of calculated uv profiles by $k-\epsilon$ and DSM with data (2 of 4).

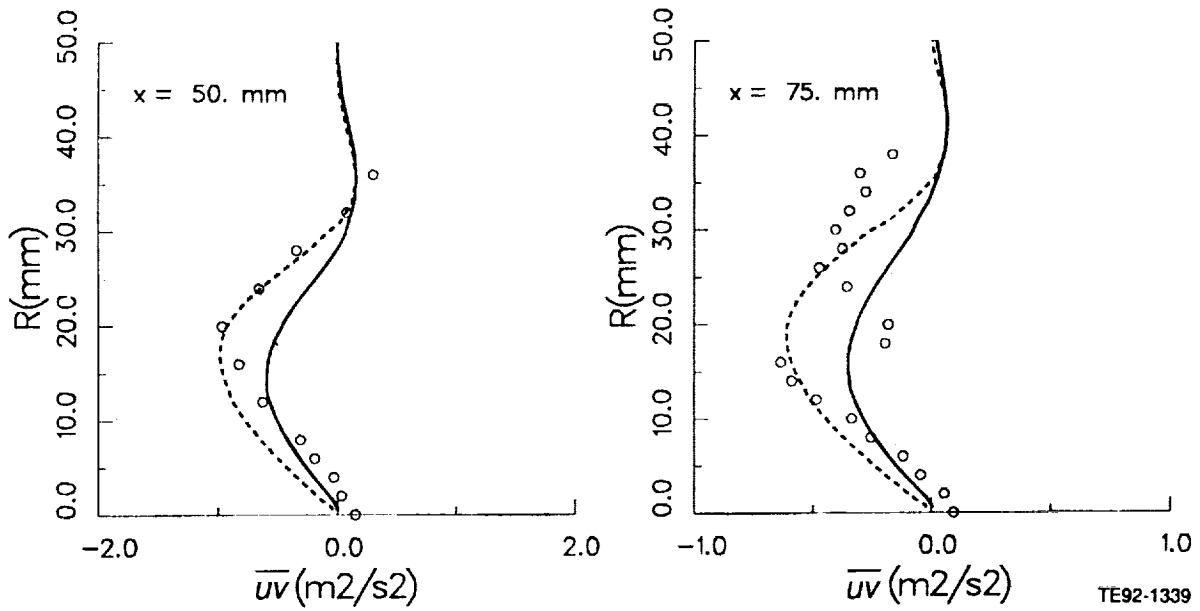


Figure 6.5-13. Comparison of calculated \overline{uv} profiles by $k-\epsilon$ and DSM with data (3 of 4).

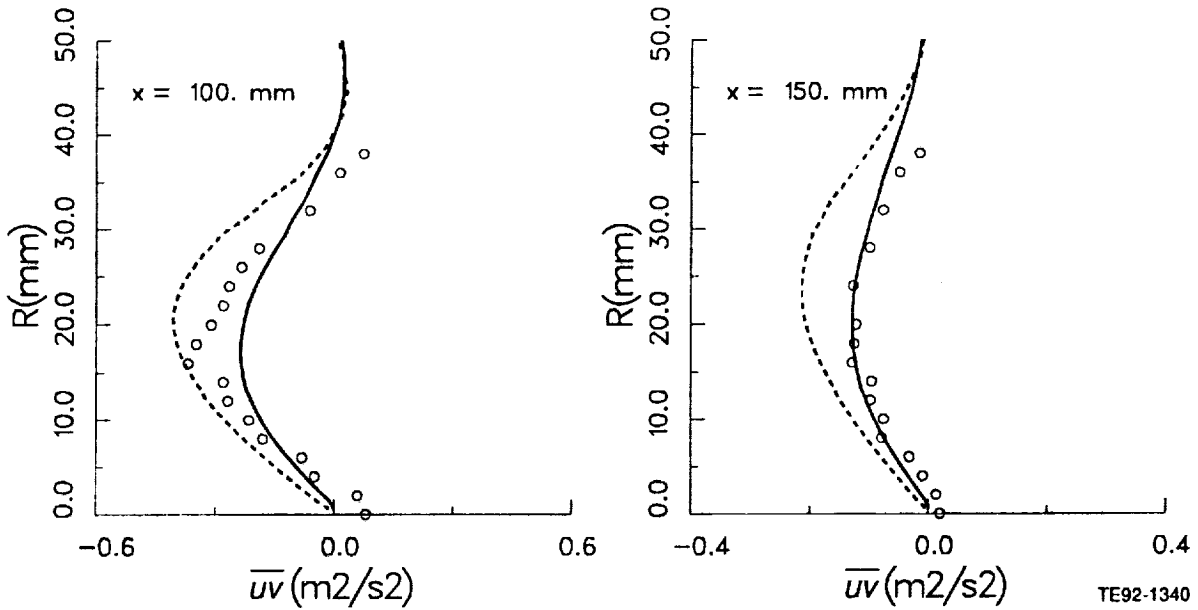
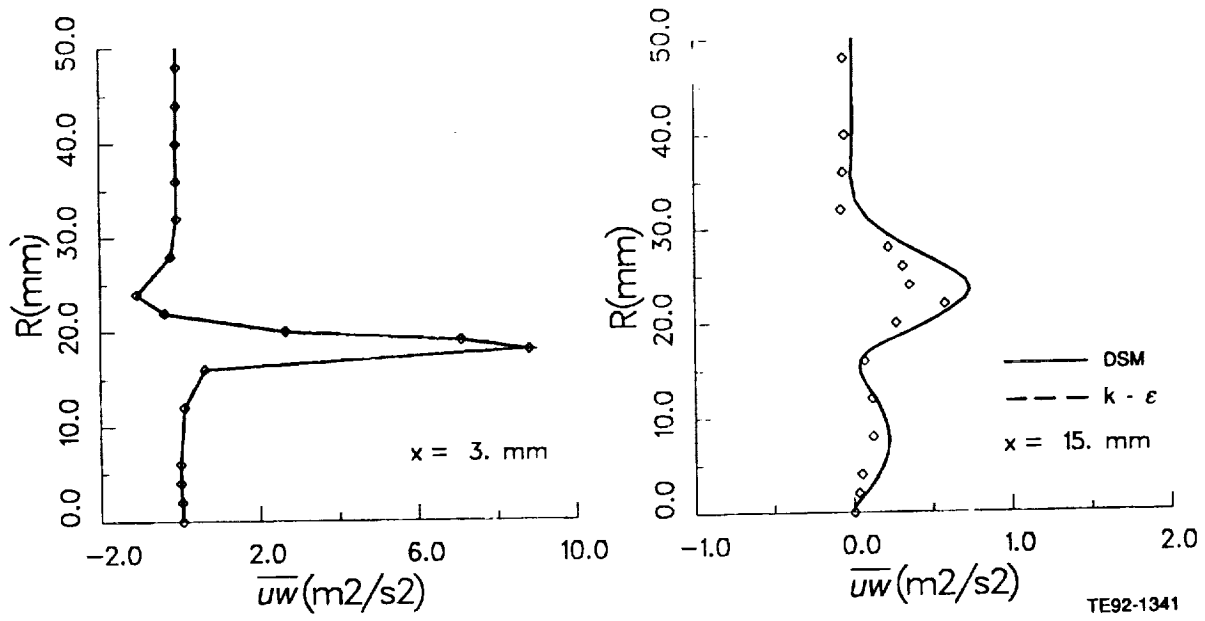
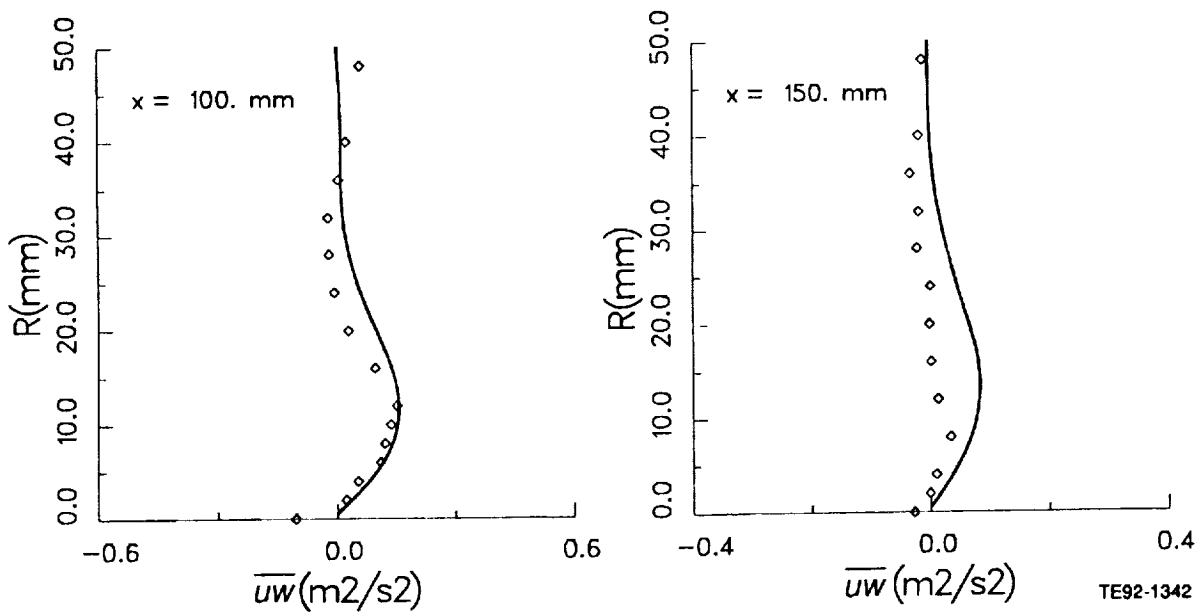


Figure 6.5-13. Comparison of calculated \overline{uv} profiles by $k-\epsilon$ and DSM with data (4 of 4).



TE92-1341

Figure 6.5-14. Comparison of calculated uw profiles by DSM with data (1 of 4).



TE92-1342

Figure 6.5-14. Comparison of calculated uw profiles by DSM with data (2 of 4).

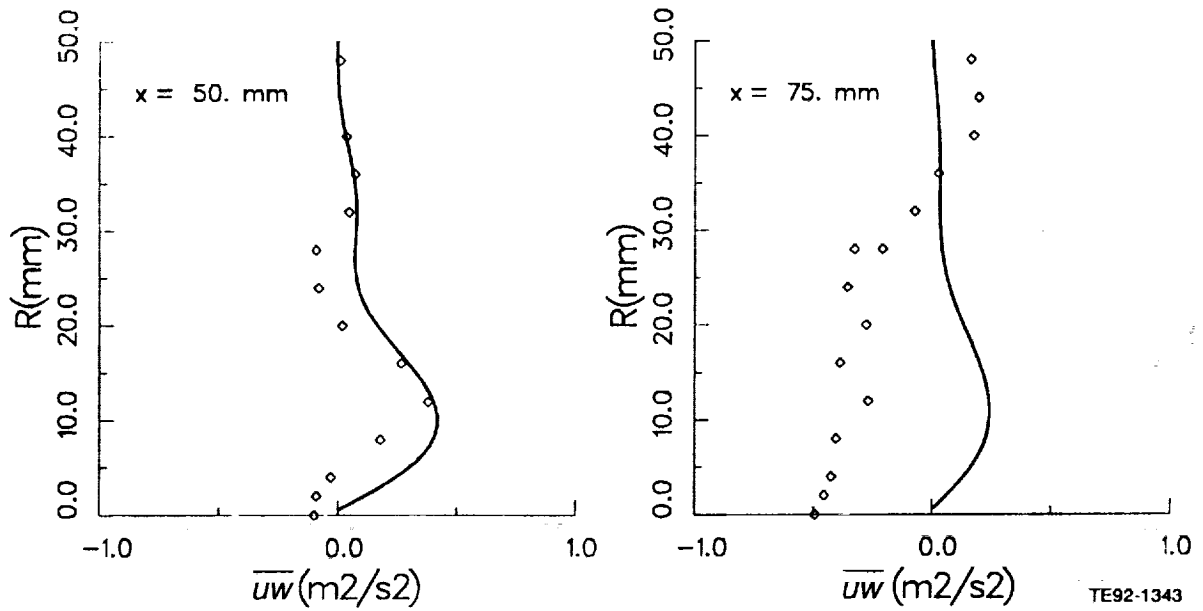


Figure 6.5-14. Comparison of calculated \overline{uw} profiles by DSM with data (3 of 4).

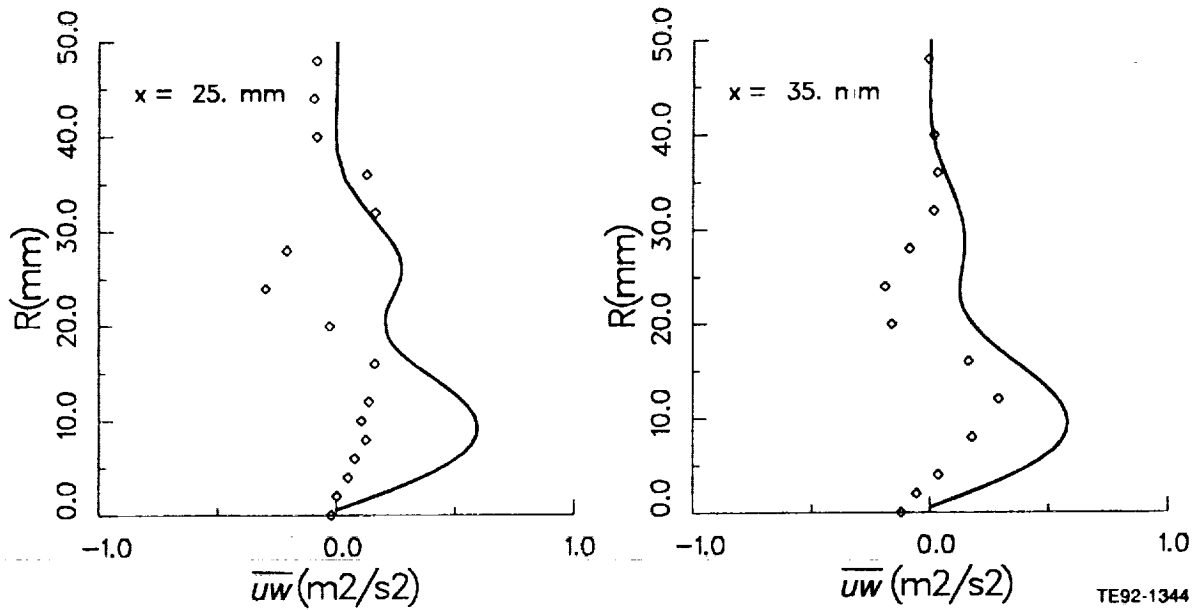


Figure 6.5-14. Comparison of calculated \overline{uw} profiles by DSM with data (4 of 4).

6.6 AIRBLAST INJECTOR

In this section, computations for the single-phase flow exhausted from the airblast injector are reported. In this configuration, unconfined atomizer flow with coflow was directed vertically downward within a 457 mm² wire mesh screen. The entire test assembly was surrounded by a flexible plastic enclosure. Data were obtained at six axial locations 25, 35, 50, 75, 150, and 300 mm from the exit plane of the injector. The details of the injector geometry are shown in Figure 6.6-1.

The set of governing partial differential equations applied to swirling flow consists of equations for continuity, axial, radial, and azimuthal momenta, ϵ , and six Reynolds stress components. The finite volume approach (Patankar, 1980) is used to reduce the continuous equations to a set of coupled discrete equations. The numerical solutions are obtained using the flux-spline differencing scheme (Varejao, 1979).

A calculation procedure for elliptic flow requires boundary conditions on all boundaries of the computational domain. Four kinds of boundaries need consideration, namely inlet, axis of symmetry, outlet, and entrainment. At the inlet boundary, which was located at the first measurement plane, the measured profiles of U , V , W , and the Reynolds stresses were prescribed. The k profile was obtained from the measured normal stresses (Figure 6.6-2). The kinetic energy distribution and the measured shear stress profile were used to derive the inlet dissipation rate values (Equation 69).

At the axis of symmetry, the radial velocity, shear stresses, and the radial gradients of other variables are set to zero. All streamwise gradients are presumed zero in the exit plane of the calculation domain. Along the entrainment boundary, which was placed sufficiently far from the axis of symmetry, the quantity rV was assumed constant. In addition, the axial velocity U was assumed zero, and k and ϵ were assigned arbitrarily low values yielding an eddy viscosity, $\mu_t = 10\mu$.

The coupled equations and boundary conditions are solved numerically in a sequential manner using the staggered grids for velocities and shear stresses. The main advantage of staggering the locations of stresses is to enhance the numerical stability, a result of high coupling between the shear stresses and the related mean strains. The iteration sequence employs the SIMPLER algorithm (Patankar, 1980) to handle the coupling between the continuity and momentum equations. The algebraic equations are solved using a line-by-line TDMA.

A nonuniform grid of 61 \times 57 in the axial and radial directions is used for computations (Figure 6.6-3). A finer grid spacing is assigned near the inlet, centerline, and in the shear layer. The tabulated axial (x) and radial (r) grid points are presented in Table 6.6-I. The computational domain extends from the first experimental location at $x = 25$ mm to 450 mm downstream of the jet exit. Since the measured flow does not show any x dependence at $x > 300$ mm, the specified condition $\partial/\partial x = 0$ at the exit plane of calculation domain is reasonable.

The presented calculations have been made using the flux-spline differencing scheme and the calculated results are essentially free of false diffusion. Therefore, the discrepancy between the experimental data and the prediction can be related to either the improper inlet boundary conditions or the deficiency of the turbulence model. As regards the inlet conditions, all quantities except the dissipation rate (ϵ) were prescribed from the measurement. The uncertainties in the derivation of the inlet ϵ profile would adversely affect the calculation at downstream locations.

Predictions of mean and turbulence fields obtained from the DSM are discussed first. Comparison of the calculated mean axial velocity profiles with the experimental data is presented in Figure 6.6-4. In this case, the DSM closure mimics the data trend reasonably well. The DSM closure prediction of axial velocity is in relatively good agreement with the data. The calculated profiles are in accordance with the data trend, although the centerline velocity values are underpredicted. The differences between the model

Table 6.6-I.
Airblast injector flow grid definition.

STREAMWISE COORDINATES OF THE GRID

I	DX	X	XU
1	0.000E+00	0.000E+00	0.000E+00
2	7.750E-04	7.750E-04	0.000E+00
3	1.625E-03	2.400E-03	1.550E-03
4	2.050E-03	4.450E-03	3.250E-03
5	2.500E-03	6.950E-03	5.650E-03
6	2.700E-03	9.650E-03	8.250E-03
7	2.937E-03	1.259E-02	1.105E-02
8	3.313E-03	1.590E-02	1.412E-02
9	3.888E-03	1.979E-02	1.768E-02
10	4.587E-03	2.437E-02	2.190E-02
11	5.250E-03	2.962E-02	2.685E-02
12	5.775E-03	3.540E-02	3.240E-02
13	6.238E-03	4.164E-02	3.840E-02
14	6.712E-03	4.835E-02	4.487E-02
15	7.062E-03	5.541E-02	5.182E-02
16	7.200E-03	6.261E-02	5.900E-02
17	7.250E-03	6.986E-02	6.622E-02
18	7.288E-03	7.715E-02	7.350E-02
19	7.300E-03	8.445E-02	8.080E-02
20	7.300E-03	9.175E-02	8.810E-02
21	7.288E-03	9.904E-02	9.540E-02
22	7.275E-03	1.063E-01	1.027E-01
23	7.288E-03	1.136E-01	1.099E-01
24	7.300E-03	1.209E-01	1.172E-01
25	7.300E-03	1.282E-01	1.245E-01
26	7.300E-03	1.355E-01	1.318E-01
27	7.300E-03	1.428E-01	1.391E-01
28	7.300E-03	1.501E-01	1.464E-01
29	7.300E-03	1.574E-01	1.537E-01
30	7.300E-03	1.647E-01	1.610E-01
31	7.300E-03	1.720E-01	1.683E-01
32	7.300E-03	1.793E-01	1.756E-01
33	7.300E-03	1.866E-01	1.829E-01
34	7.300E-03	1.939E-01	1.902E-01
35	7.300E-03	2.012E-01	1.975E-01
36	7.300E-03	2.085E-01	2.048E-01
37	7.300E-03	2.158E-01	2.121E-01
38	7.300E-03	2.231E-01	2.194E-01
39	7.200E-03	2.303E-01	2.267E-01
40	7.200E-03	2.375E-01	2.338E-01
41	7.400E-03	2.449E-01	2.411E-01
42	7.400E-03	2.523E-01	2.486E-01
43	7.325E-03	2.596E-01	2.559E-01
44	7.325E-03	2.669E-01	2.633E-01
45	7.275E-03	2.742E-01	2.706E-01
46	7.275E-03	2.815E-01	2.778E-01
47	7.300E-03	2.888E-01	2.851E-01

Table 6.6-I.
Airblast injector flow grid definition (cont).

48	7.450E-03	2.962E-01	2.925E-01
49	7.775E-03	3.040E-01	3.001E-01
50	7.975E-03	3.120E-01	3.080E-01
51	8.500E-03	3.205E-01	3.160E-01
52	9.500E-03	3.300E-01	3.250E-01
53	1.000E-02	3.400E-01	3.350E-01
54	1.000E-02	3.500E-01	3.450E-01
55	1.125E-02	3.612E-01	3.550E-01
56	1.375E-02	3.750E-01	3.675E-01
57	1.500E-02	3.900E-01	3.825E-01
58	1.500E-02	4.050E-01	3.975E-01
59	1.500E-02	4.200E-01	4.125E-01
60	1.500E-02	4.350E-01	4.275E-01
61	7.500E-03	4.425E-01	4.425E-01

TRANSVERS COORDINATES OF THE GRID

J	DY	Y	YV
1	0.000E+00	5.000E-04	0.000E+00
2	2.500E-04	7.500E-04	5.000E-04
3	7.500E-04	1.500E-03	1.000E-03
4	1.000E-03	2.500E-03	2.000E-03
5	1.000E-03	3.500E-03	3.000E-03
6	1.000E-03	4.500E-03	4.000E-03
7	1.000E-03	5.500E-03	5.000E-03
8	1.000E-03	6.500E-03	6.000E-03
9	1.000E-03	7.500E-03	7.000E-03
10	1.000E-03	8.500E-03	8.000E-03
11	1.000E-03	9.500E-03	9.000E-03
12	1.000E-03	1.050E-02	1.000E-02
13	1.000E-03	1.150E-02	1.100E-02
14	1.000E-03	1.250E-02	1.200E-02
15	1.000E-03	1.350E-02	1.300E-02
16	1.000E-03	1.450E-02	1.400E-02
17	1.000E-03	1.550E-02	1.500E-02
18	1.000E-03	1.650E-02	1.600E-02
19	1.000E-03	1.750E-02	1.700E-02
20	1.000E-03	1.850E-02	1.800E-02
21	1.000E-03	1.950E-02	1.900E-02
22	1.000E-03	2.050E-02	2.000E-02
23	1.000E-03	2.150E-02	2.100E-02
24	1.000E-03	2.250E-02	2.200E-02
25	1.000E-03	2.350E-02	2.300E-02
26	1.000E-03	2.450E-02	2.400E-02
27	1.000E-03	2.550E-02	2.500E-02
28	1.000E-03	2.650E-02	2.600E-02
29	1.000E-03	2.750E-02	2.700E-02
30	1.000E-03	2.850E-02	2.800E-02
31	1.000E-03	2.950E-02	2.900E-02

Table 6.6-I.
Airblast injector flow grid definition (cont).

32	1.000E-03	3.050E-02	3.000E-02
33	1.000E-03	3.150E-02	3.100E-02
34	1.000E-03	3.250E-02	3.200E-02
35	1.500E-03	3.400E-02	3.300E-02
36	2.000E-03	3.600E-02	3.500E-02
37	2.000E-03	3.800E-02	3.700E-02
38	2.000E-03	4.000E-02	3.900E-02
39	2.000E-03	4.200E-02	4.100E-02
40	2.000E-03	4.400E-02	4.300E-02
41	2.000E-03	4.600E-02	4.500E-02
42	2.000E-03	4.800E-02	4.700E-02
43	2.000E-03	5.000E-02	4.900E-02
44	2.000E-03	5.200E-02	5.100E-02
45	2.000E-03	5.400E-02	5.300E-02
46	2.000E-03	5.600E-02	5.500E-02
47	2.000E-03	5.800E-02	5.700E-02
48	2.000E-03	6.000E-02	5.900E-02
49	2.000E-03	6.200E-02	6.100E-02
50	2.000E-03	6.400E-02	6.300E-02
51	2.000E-03	6.600E-02	6.500E-02
52	2.000E-03	6.800E-02	6.700E-02
53	2.000E-03	7.000E-02	6.900E-02
54	2.000E-03	7.200E-02	7.100E-02
55	2.000E-03	7.400E-02	7.300E-02
56	1.500E-03	7.550E-02	7.500E-02
57	5.000E-04	7.600E-02	7.600E-02

and data become more severe in the developing region. The discrepancies are due to the insufficient diffusion process caused by underprediction of radial normal stress component. At downstream, the calculated velocity field is in good agreement with data, however some minor discrepancies appear in that zone.

Comparisons of the predicted turbulence intensities from the DSM closure are shown in Figures 6.6-5, 6.6-6, and 6.6-7. The differences between the calculated and experimental results are significant in the case of the normal stresses. The maximum axial turbulence intensity has been underpredicted in most of the flow region, however, the trend was accurately predicted. The same trends are observed for all normal stress components. The discrepancies between the model and data clearly indicate the lack of performance of the pressure-strain model. One reason for this could be the lack of an appropriate model for the rapid part, which was not considered here. The predicted turbulent shear stress from the DSM has been compared with the experimental data in Figure 6.6-8. The positive peak in the shear stress profile corresponds to the shear layer between the two streams. The agreement between the calculation and the experimental data is relatively good, although the peak values are not well predicted.

The $k-\epsilon$ turbulence model was also applied for the same configuration to establish the suitability of the model. The predicted mean axial velocity, turbulent kinetic energy, and shear profiles at the various axial stations are shown in Figures 6.6-9, 6.6-10, and 6.6-11. The predictions of axial velocity profiles are in fair agreement with the data. The velocity profiles are relatively flat near the centerline. The maximum velocity occurs near the centerline which constantly decreases. The deceleration in axial velocity is due to the pressure effects. The agreement between the predicted and experimental values of kinetic energy is as good as that for the axial velocity. Even though the trends are similar, the predicted kinetic energy levels are smaller than those derived from the measurements. As regards the turbulent shear stress, the calculated profiles only qualitatively agree with the experimental data. The predictions are not as good as those calculated by the DSM closure.

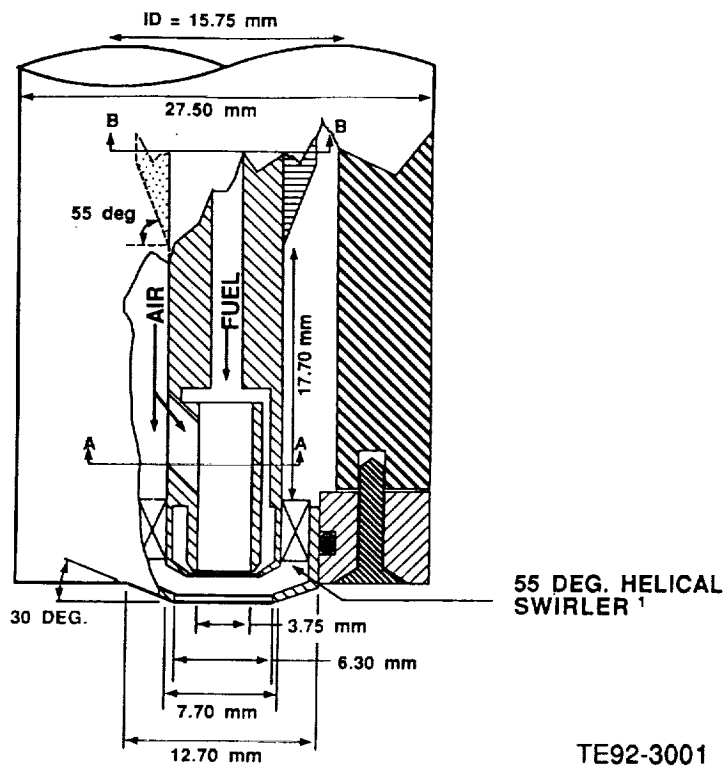
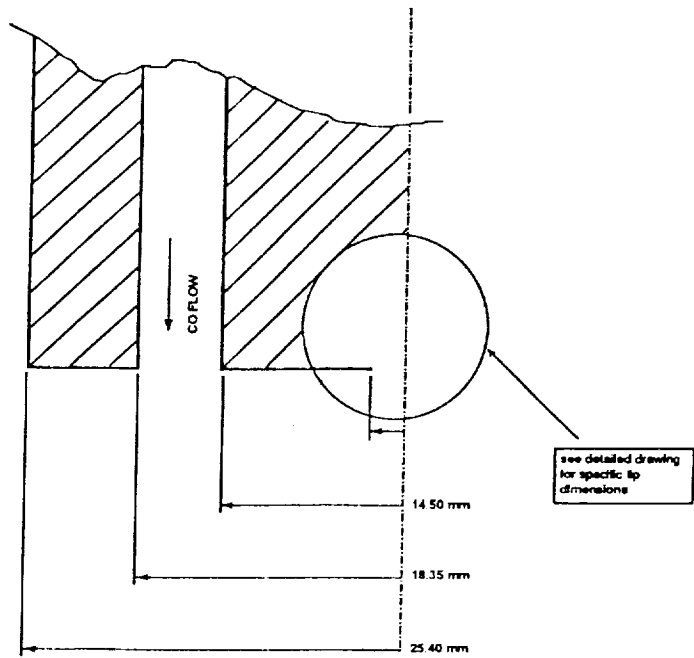


Figure 6.6-1. Airblast injector flow configuration.

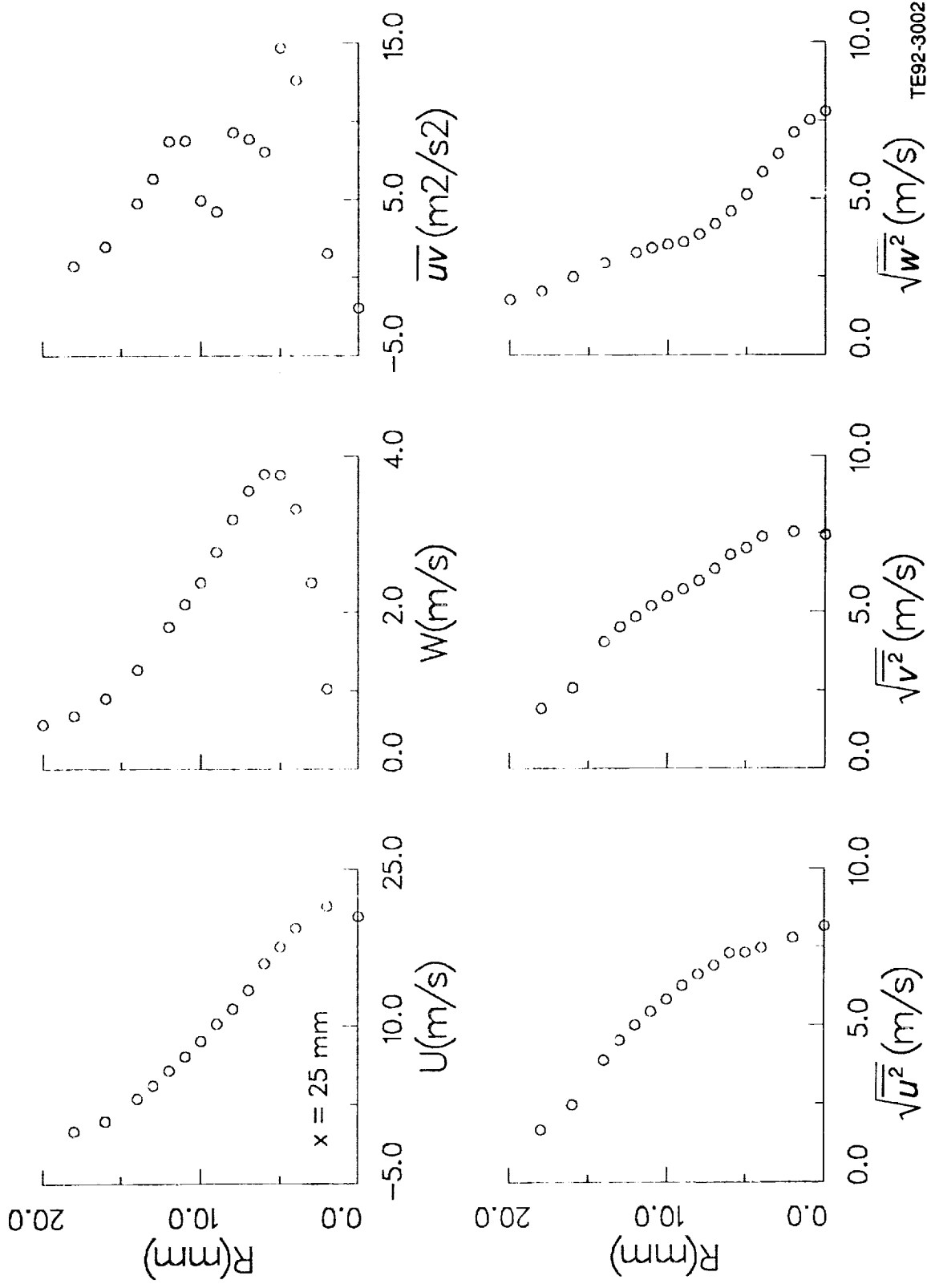
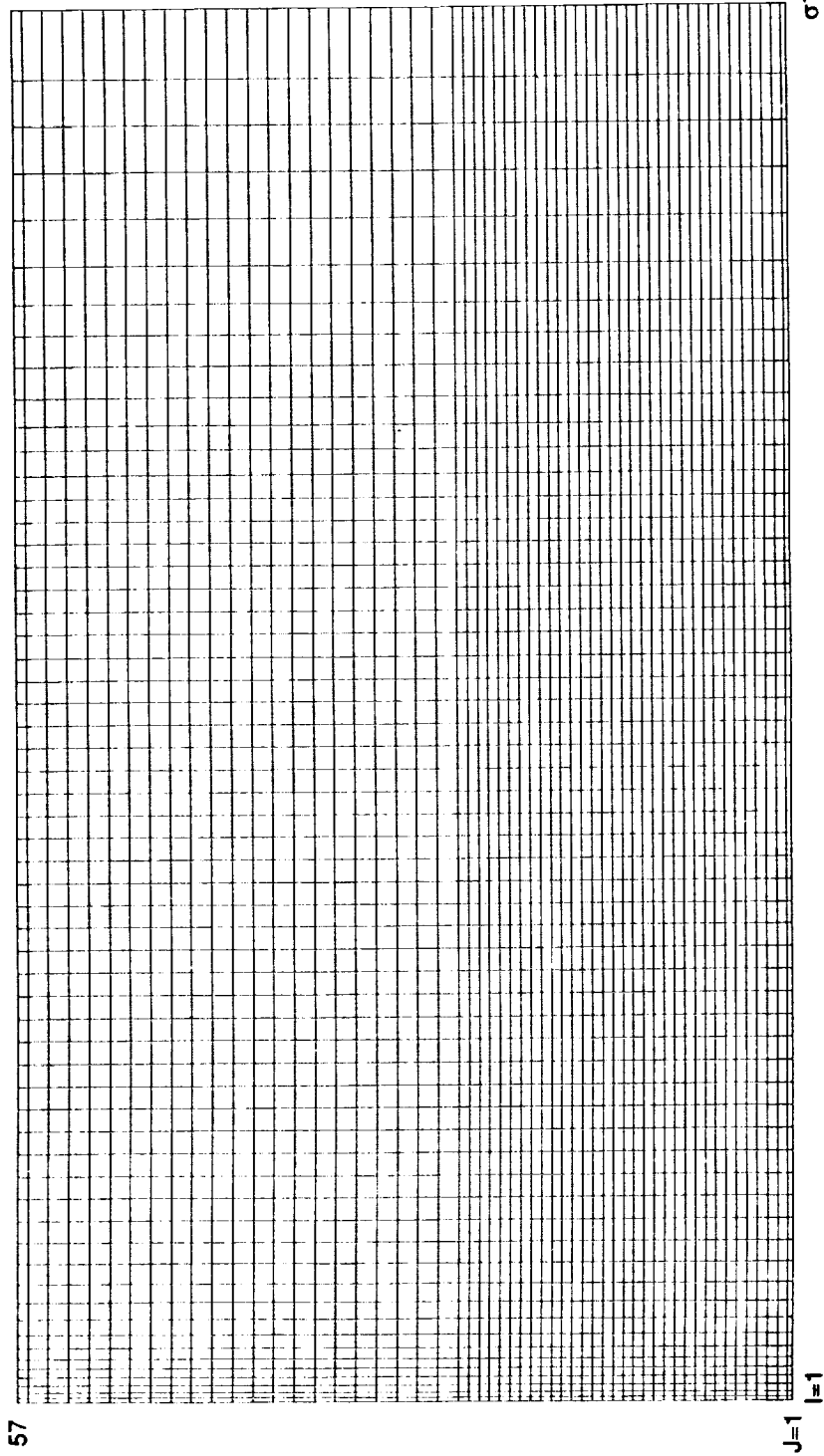
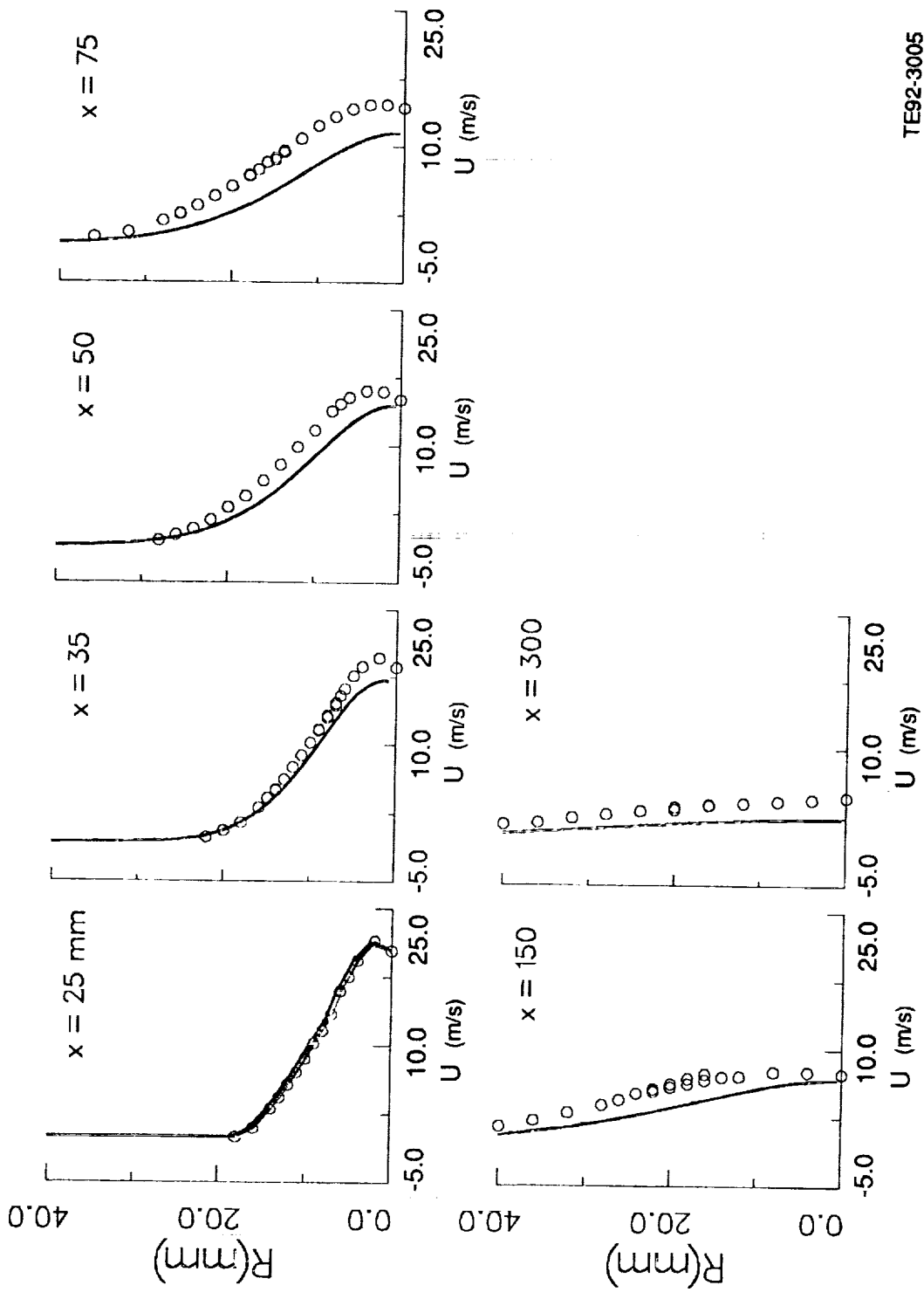


Figure 6.6-2. Airblast injector flow inlet conditions.



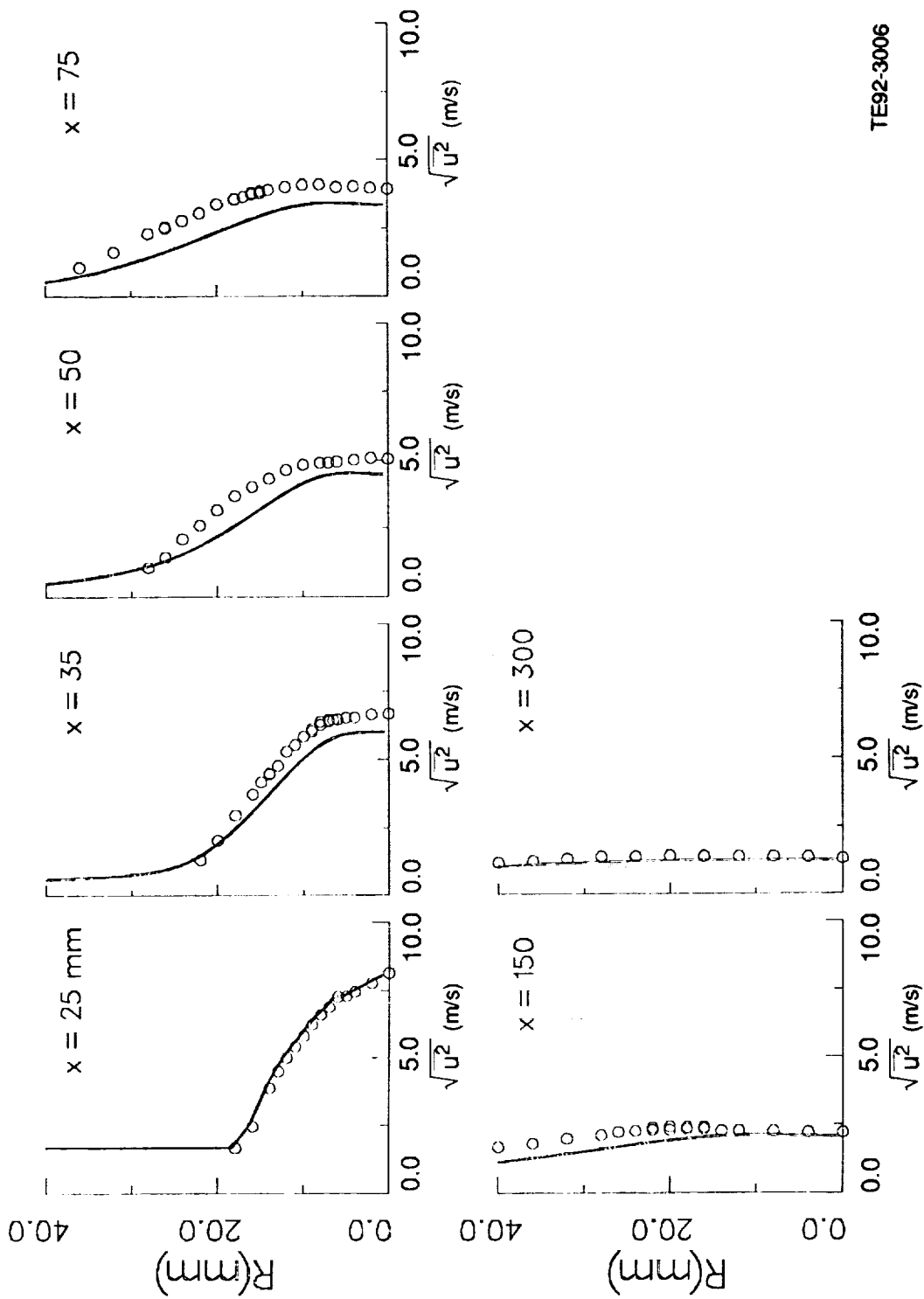
TE92-3003

Figure 6.6-3. Airblast injector flow grid layout.



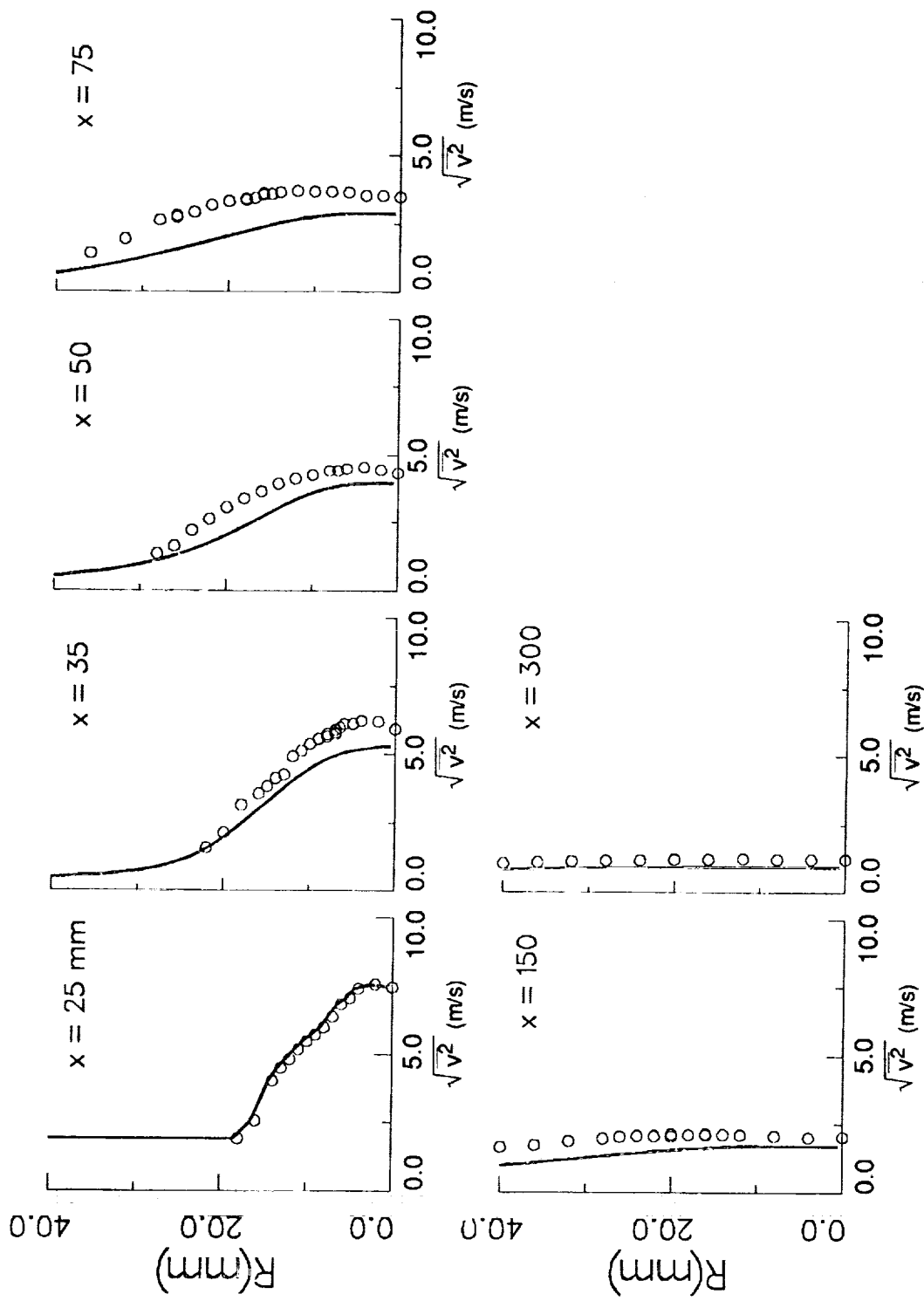
TE92-3005

Figure 6.6-4. Comparison of calculated mean axial velocity profiles by DSM with data.



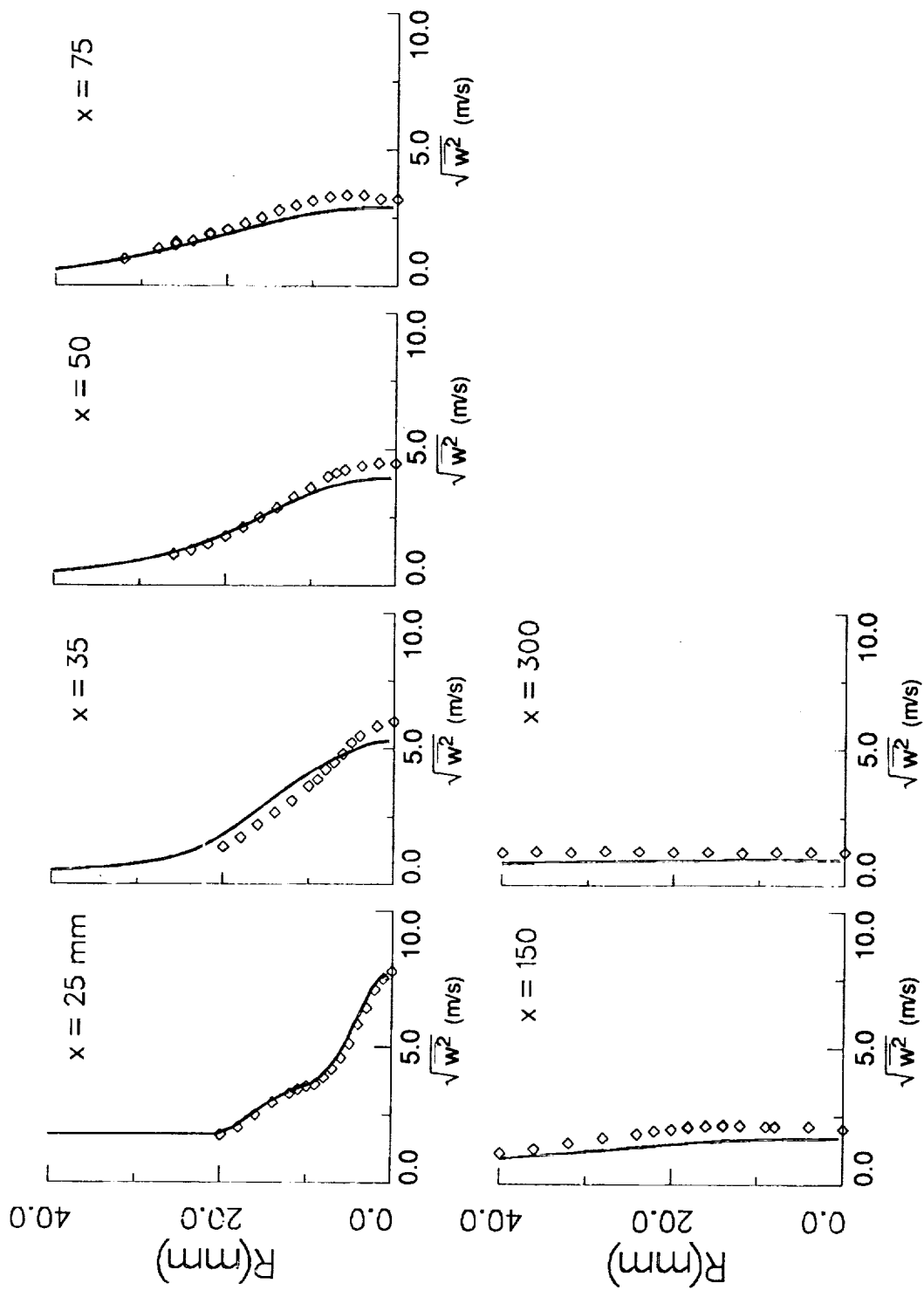
TE92-3006

Figure 6.6-5. Comparison of calculated rms axial velocity profiles by DSM with data.



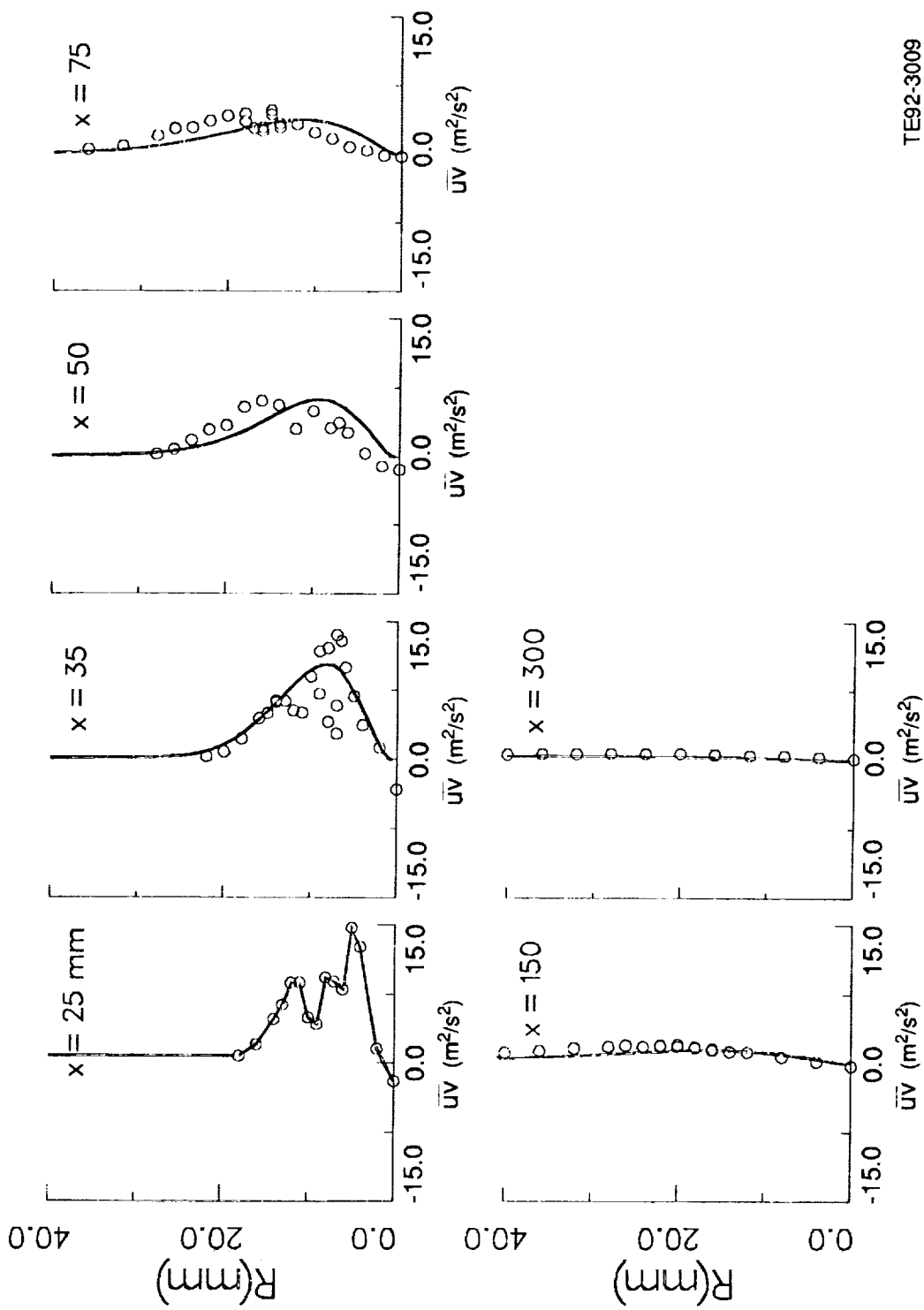
TE92-3007

Figure 6.6-6. Comparison of calculated rms radial velocity profiles by DSM with data.



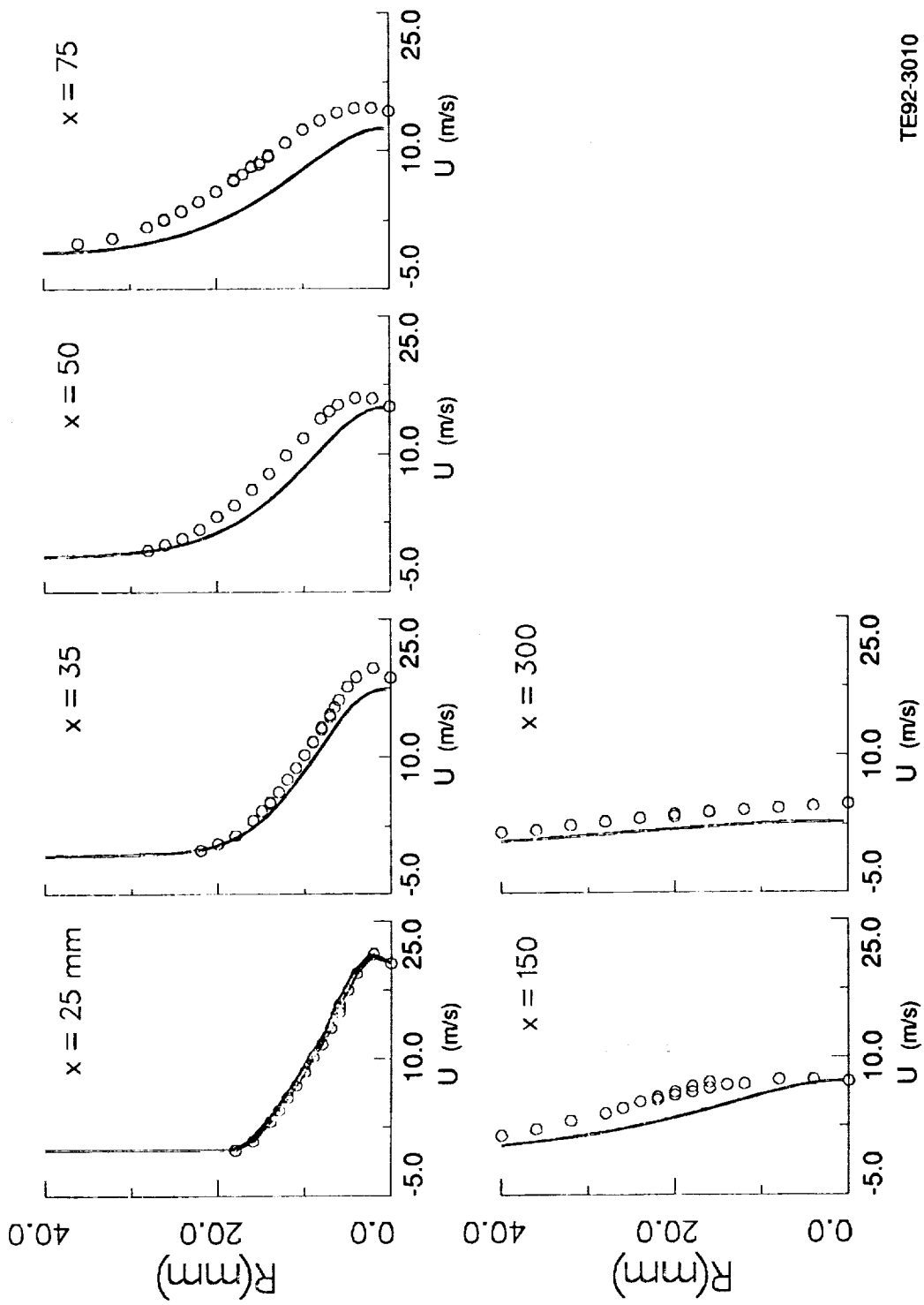
TE92-3008

Figure 6.6-7. Comparison of calculated rms tangential velocity profiles by DSM with data.



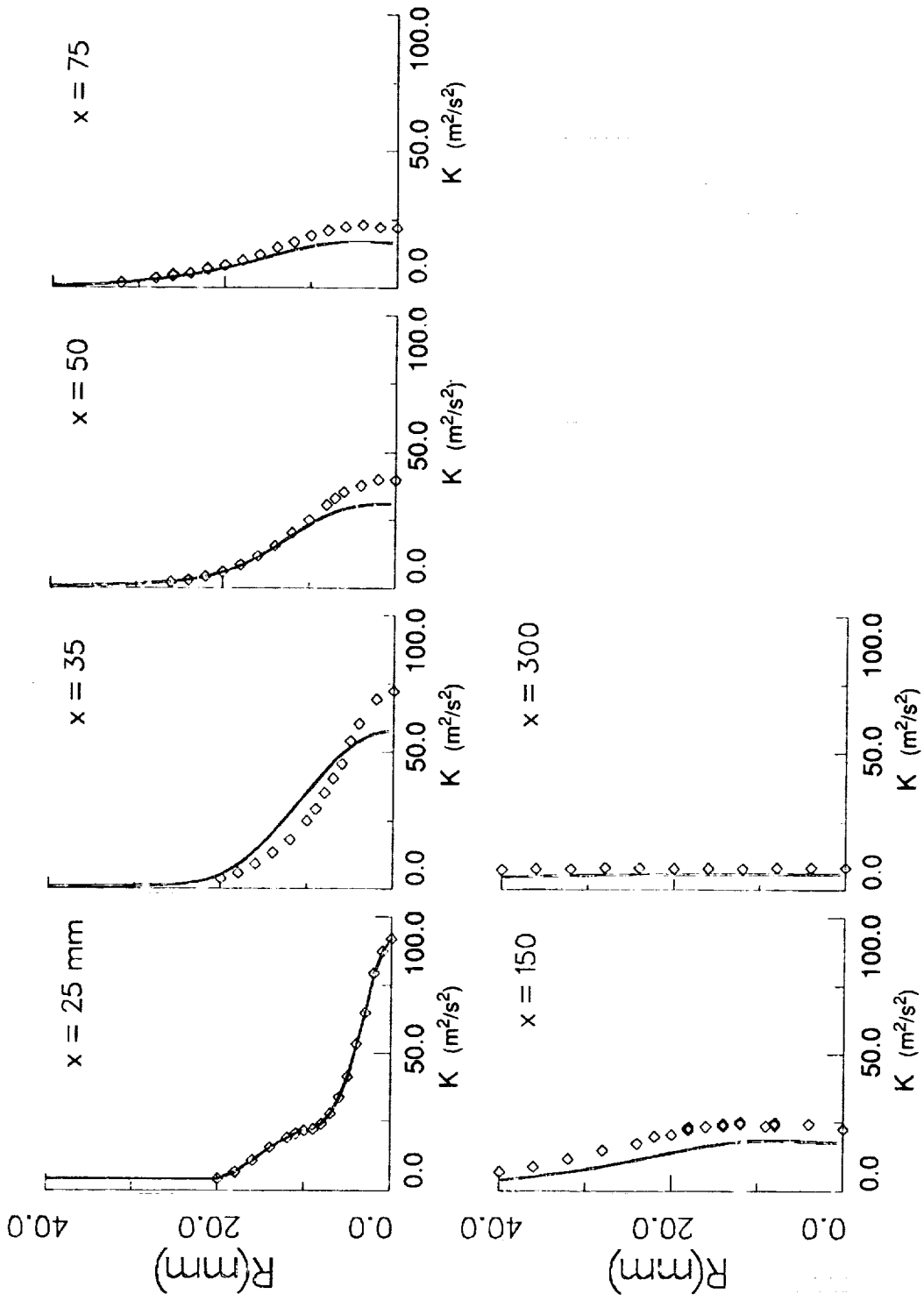
TE92-3009

Figure 6.6-8. Comparison of calculated shear stress profiles by DSM with data.



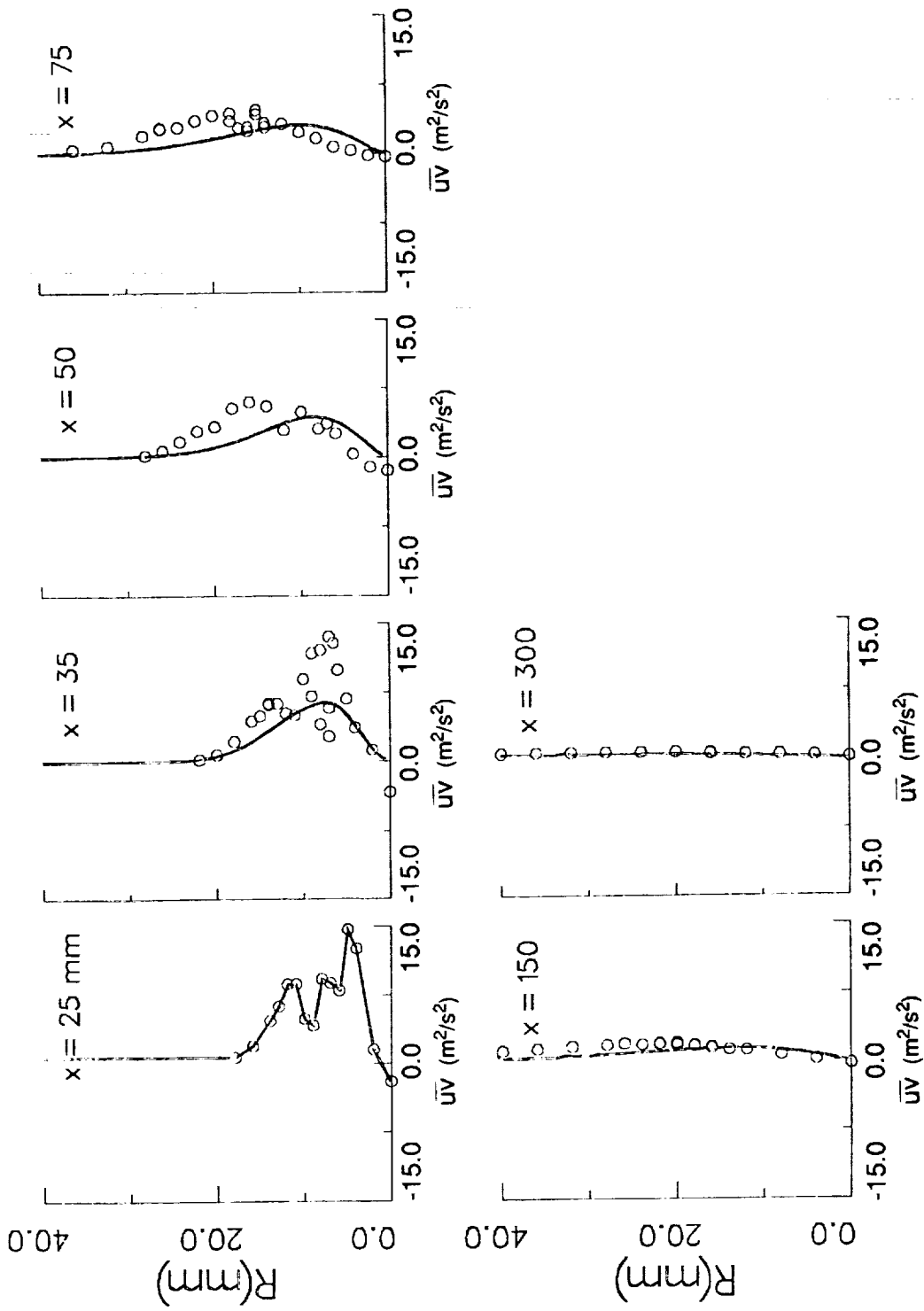
TE92-3010

Figure 6.6-9. Comparison of calculated mean axial velocity profiles by $k-\epsilon$ with data.



TE92-3011

Figure 6.6-10. Comparison of calculated turbulent kinetic energy profiles by $k-\epsilon$ with data.



TE92-3012

Figure 6.6-11. Comparison of calculated turbulent shear stress profiles by k- ϵ with data.

REFERENCES

- Bulzan, D. L., Shuen, J. S., and Faeth, G. M., 1987, "Particle Laden Swirling Free Jets: Measurements and Predictions," AIAA Paper 87-0303, January.
- Donaldson, C. du P., 1969, "A Computer Study of Boundary Layer Transition," *AIAA Journal*, Vol 7, p 271.
- Fleckhaus, D., Hishida, D., and Maeda, M., 1987, "Effect of Laden Solid Particles on the Turbulent Flow Structure of a Round Free Jet," *Experiments in Fluids*, Vol 5, pp 323-333.
- Gibson, M. M. and Younis, A. B., 1986, "Calculation of Swirling Jets with a Reynolds Stress Closure," *Phys Fl*, Vol 29, pp 38-48.
- Habib, M. A. and Whitelaw, J. H., 1979, "Velocity Characteristics of a Confined Coaxial Jets," *Journal of Fluid Engng*, Vol 101, pp 521-529.
- Launder, B. E., 1989, "Second-Moment Closure and its Use in Modeling Turbulent Industrial Flow," *International Journal of Num Meth Fl*, Vol 9, pp 963-985.
- Mostafa, A. A. and Elghobashi, S. E., 1985, "A Two-Equation Turbulence Model for Jet Flows Laden with Vaporizing Droplets," *International Journal of Multiphase Flows*, Vol 11, No. 4, July-August, pp 515-533.
- Mostafa, A. A. and Mongia, H. C., 1987, "On the Modeling of Turbulent Evaporating Sprays: Eulerian Versus Langrangian Approach," *International Journal of Heat and Mass Transfer*, Vol 30, December, pp 2583-2593.
- Mostafa, A. A. and Mongia, H. C., 1988, "On the Interaction of Particles and Turbulent Fluid Flows," *Int. J. Heat Mass Transfer*, 31 (10), 2063, 2075.
- Naot, D., Shavit, A., and Wolfshtein, M., 1970, "Interactions Between Components of the Turbulent Velocity Correlation Tensor," *Israel J. Tech.*, 8, 259-269.
- Nikjooy, M. and So, R. M. C., 1987, "On the Modeling of Non-Reactive and Reactive Turbulent Combustor Flows," NASA-CR 4041.
- Nikjooy, M. and Mongia, H. C., 1991, "A Second-Order Modeling Study of Confined Swirling Flow," *International Journal of Heat and Fluid Flow*, Vol 12, No. 1, March, pp 12-19.
- Patankar, S. V., 1980, *Numerical Heat Transfer and Fluid Flows*, Hemisphere, New York.
- Patankar, S. V., Karki, K. C., and Mongia, H. C., 1987, "Development and Evaluation of Improved Numerical Schemes for Recirculating Flows," AIAA-87-0061.
- Shuen, J. S., Chen, L. D., and Faeth, G. M., 1983, "Predictions of the Structure of Turbulent Particle-Laden Round Jets," *AIAA Journal*, Vol 21, November, pp 1483-1484.
- Spalding, D. B., 1978, "GENMIX: A General Computer Program for Two-Dimensional Parabolic Phenomena," Pergamon, Oxford, England.
- Sturgess, G. J., Syed, S. A., and McManus, K. R., 1983, "Importance of Inlet Boundary Conditions for Numerical Simulation of Combustor Flows," AIAA, 83-1263.
- Varejao, L. M. C., 1979, *Flux-Spline Method for Heat, Mass, and Momentum Transfer*, Ph.D. thesis, University of Minnesota.

TABLE OF CONTENTS

<u>Section</u>	<u>Title</u>	<u>Page</u>
VII	Concluding Remarks and Recommendations.....	655
7.1	Summary of the Present Work	655
7.2	Recommendation	655

VII. CONCLUDING REMARKS AND RECOMMENDATIONS

7.1 SUMMARY OF THE PRESENT WORK

A combined experimental/analytical investigation was conducted to validate conventional and improved turbulent and spray models. A systematic experimental program was conducted to collect benchmark quality data for the mean and fluctuating quantities in the developing region of single-phase and particle-laden flows with two mass loading ratios. Detailed velocity measurements were made using phase/Doppler equipment. A detailed specification of the flow parameters in the upstream region was provided. These are used as inlet conditions to start the computations. The test problems used ranges from simple flows to more complex flows to encompass the range of complexities involved in combustion flows. These are

- single round jet
- single annular jet
- single swirling annular jet
- coaxial jets
- coaxial jets with swirling annular flow
- airblast injector

Closure of the Reynolds equation was achieved by three different levels of models: k - ϵ , algebraic second-moment (ASM), and differential second-moment (DSM) closure. Effects of pressure-strain correlation models on these closure were also investigated. For turbulent particle-laden jet flow, the closure was affected by extending constant-density single-phase turbulence models to the continuous (carrier) phase of two-phase flow. The dispersed (discrete) phase was treated by both deterministic and stochastic-Lagrangian technique.

To reduce the effect of numerical (false) diffusion on the predicted results, the linear flux-spline scheme was used to solve several two-dimensional flows. For a given number of grid points, the flux-spline scheme produces results that are superior to those from the (lower-order) power-law differencing scheme. In addition, it has the potential of providing a grid independent solution without requiring an excessive number of grid points.

Models employing transport equations for the individual turbulent stress components simulate the turbulent processes more realistically and are, therefore, potentially more general compared to the simpler models. It should be noted that the effectiveness of turbulence model predictions could be obscured to some extent by competing factors: boundary conditions, oscillatory phenomena, and numerical diffusion. A significant contribution from any of the aforementioned factors tends to invalidate conclusions regarding the superiority or inferiority of a given turbulence model. The turbulence model cannot compensate for inadequacy in this area.

7.2 RECOMMENDATION

Although some of the models described in this study, and in particular the k - ϵ model, have been shown to work well in many situations, there is much room for further development. The ϵ -equation in its present form appears not to be sufficiently universal and should be improved. As observed by many, this equation is responsible for performance of most models. Ideas to use several length-scale equations for different directions or different processes are promising and should be developed further.

The model assumptions for the pressure-strain correlation are also not very satisfactory and need improvement. Proposals for the behavior of Φ_{ij} in homogeneous flows have only gone further than that of Rotta's linear model by including further terms in a series expansion about the isotropic homogeneous

state. However, optimization of the coefficients of the terms in the expansion on the basis of available experimental data is a very difficult task indeed.

It seems unlikely that any serious proposal for Φ_{ij1} will be made in the near future, and emphasis should be placed on developing a better approximation for Φ_{ij2} .

The derivation and validation of higher-order closure schemes holds the greatest potential for turbulence model improvement for strongly swirling flows. Efforts to find a stable and higher order (order of terms retained in an equivalent Taylor series expansion) differencing scheme that can eliminate numerical diffusion should continue. This is especially important in the case of two-phase and/or reacting flows because of the coupled nonlinearities which exist between the chemical and fluid mechanical processes.

An intensive submodel validation and development efforts, especially for the ASM closure, DSM closure, and stochastic spray model in conjunction with probability distribution function (PDF) approach should be continued.

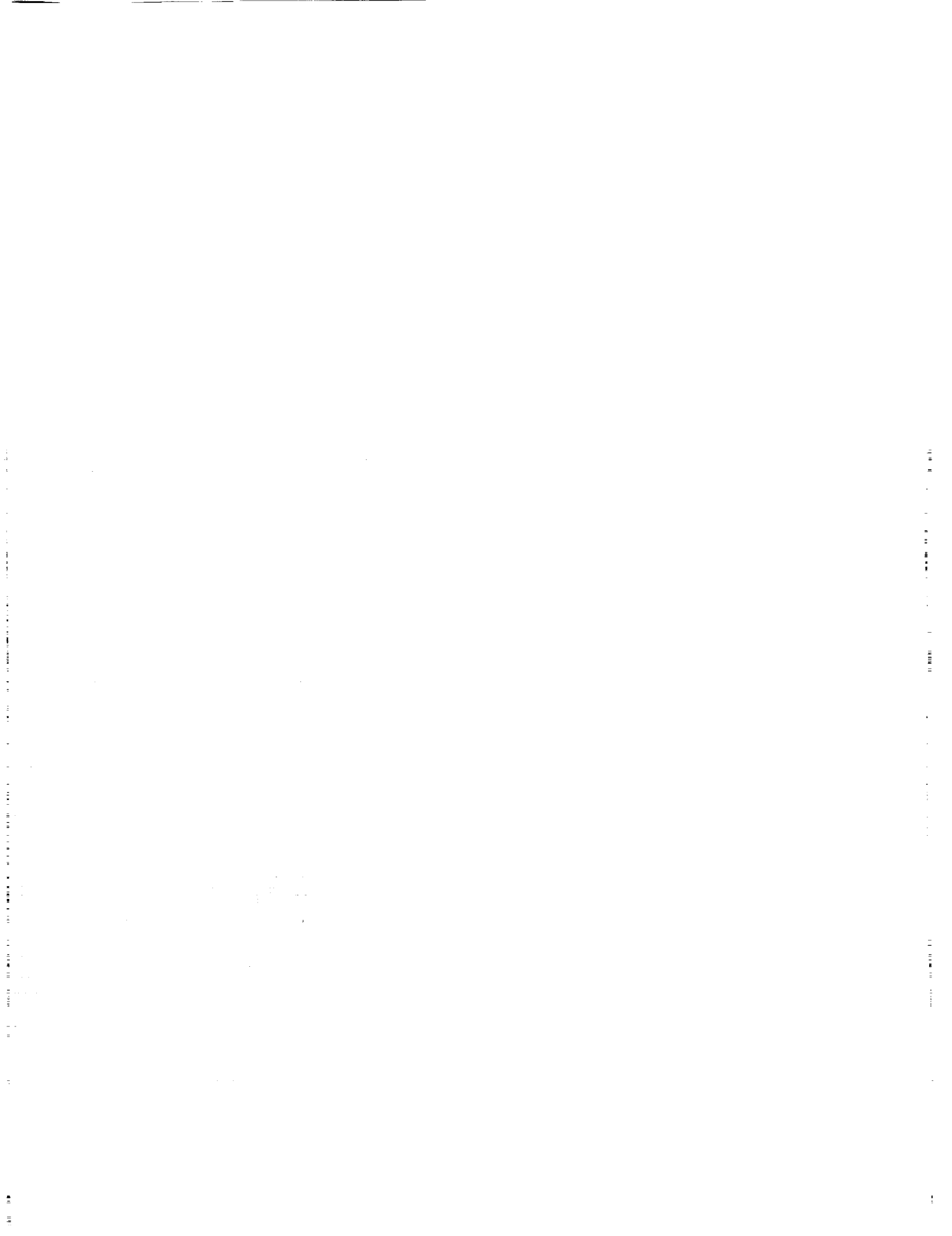
Unfortunately, in many instances there is a lack of quality data relevant to gas turbine combustion. Many modeling assumptions are similar to the constant-density, Reynolds stress closure. Therefore, further experiments with more emphasis on turbulent scalar fluxes and density correlations are needed to support or to improve these assumptions.

TABLE OF CONTENTS

<u>Section</u>	<u>Title</u>	<u>Page</u>
Appendix A	Turbulent Flow Equations for the k- ϵ Model	659
Appendix B	Turbulent Flow Equations for DSM Closure	663
Appendix C	Publications Partially Supported by the List of this Study	669



APPENDICES



APPENDIX A

TURBULENT FLOW EQUATIONS FOR THE k - ϵ MODEL

PRECEDING PAGE BLANK NOT FILMED



TURBULENT FLOW EQUATIONS FOR THE k-ε MODEL

The transport equations presented in the previous sections reduce in axisymmetric coordinates (x, r) to the following:

Continuity Equation

$$\frac{\partial}{\partial X} (r\rho U) + \frac{\partial}{\partial r} (r\rho V) = 0 \quad (\text{A1})$$

x - Momentum Equation

$$\frac{1}{r} \left[\frac{\partial}{\partial X} (r\rho UU) + \frac{\partial}{\partial r} (r\rho VU) \right] = -\frac{\partial P}{\partial X} + \frac{1}{r} \left[\frac{\partial}{\partial X} (2r\mu_T \frac{\partial U}{\partial X}) + \frac{\partial}{\partial r} [r\mu_T (\frac{\partial U}{\partial r} + \frac{\partial V}{\partial X})] \right] - \frac{2}{3} \frac{\partial}{\partial X} (\bar{\rho}k) \quad (\text{A2})$$

r - Momentum

$$\frac{1}{r} \left[\frac{\partial}{\partial X} (r\rho UV) + \frac{\partial}{\partial r} (r\rho VV) \right] = -\frac{\partial P}{\partial r} - 2\mu_T \frac{V}{r^2} + \rho \frac{W^2}{r} + \frac{1}{r} \left[\frac{\partial}{\partial X} [r\mu_T (\frac{\partial V}{\partial X} + \frac{\partial U}{\partial r})] + \frac{\partial}{\partial r} (2r\mu_T \frac{\partial V}{\partial r}) \right] - \frac{2}{3} \frac{\partial}{\partial r} (\rho k) \quad (\text{A3})$$

θ - Momentum

$$\frac{1}{r} \left[\frac{\partial}{\partial X} (r\rho UW) + \frac{\partial}{\partial r} (r\rho VW) \right] = -\mu_T \frac{W}{r^2} - \rho \frac{VW}{r} - \frac{W}{r} \frac{\partial}{\partial r} \mu_T \quad (\text{A4})$$

k - Transport Equation

$$\frac{1}{r} \left[\frac{\partial}{\partial X} (r\rho Uk) + \frac{\partial}{\partial r} (r\rho Vk) \right] = P_k - \rho \epsilon + \frac{1}{r} \left[\frac{\partial}{\partial X} [r(\frac{\mu_t}{\sigma_k} + \mu) \frac{\partial k}{\partial X}] + \frac{\partial}{\partial r} [r(\frac{\mu_r}{\sigma_k} + \mu) \frac{\partial k}{\partial r}] \right] \quad (\text{A5})$$

ε - Transport Equation

$$\frac{1}{r} \left[\frac{\partial}{\partial X} (r\rho U\epsilon) + \frac{\partial}{\partial r} (r\rho V\epsilon) \right] = C_{\epsilon 1} \frac{\epsilon P_k}{k} - C_{\epsilon 2} \rho \frac{\epsilon^2}{k} + \frac{1}{r} \left[\frac{\partial}{\partial X} [r(\frac{\mu_t}{\sigma_\epsilon} + \mu) \frac{\partial \epsilon}{\partial X}] + \frac{\partial}{\partial r} [r(\frac{\mu_r}{\sigma_\epsilon} + \mu) \frac{\partial \epsilon}{\partial r}] \right] \quad (\text{A6})$$

Turbulence Model

$$\mu_t = C_\mu \rho \frac{k^2}{\varepsilon} \quad (\text{A7})$$

$$\sigma_\varepsilon = \frac{k^2}{(C_{\varepsilon 2} - C_{\varepsilon 1}) \sqrt{C_\mu}} \quad (\text{A8})$$

where

$$\mu_T = \mu_t + \mu$$

$$P_k = \mu_t \left[2 \left[\left(\frac{\partial U}{\partial X} \right)^2 + \left(\frac{\partial V}{\partial r} \right)^2 + \left(\frac{V}{r} \right)^2 \right] + \left(\frac{\partial U}{\partial r} + \frac{\partial V}{\partial X} \right)^2 + \left(\frac{\partial W}{\partial X} \right)^2 + \left[r \frac{\partial}{\partial r} \left(\frac{W}{r} \right) \right]^2 \right]$$

APPENDIX B

TURBULENT FLOW EQUATIONS FOR DSM CLOSURE



TURBULENT FLOW EQUATIONS FOR DSM CLOSURE

The modeled Reynolds stress transport equations presented in the tensor notation reduce in axisymmetric coordinates (x, r) to the following equations.

Equation for $\overline{u^2}$:

$$\begin{aligned} & \frac{\partial}{\partial x} (\rho U \overline{u^2}) + \frac{1}{r} \frac{\partial}{\partial r} (r \rho V \overline{u^2}) - \frac{\partial}{\partial x} \left[(C_k \rho \frac{k}{\epsilon} \overline{u^2}) \frac{\partial \overline{u^2}}{\partial x} \right] \\ & - \frac{1}{r} \frac{\partial}{\partial r} \left[r (C_k \rho \frac{k}{\epsilon} \overline{v^2}) \frac{\partial \overline{u^2}}{\partial r} \right] = \frac{1}{r} \frac{\partial}{\partial r} \left[r (C_k \rho \frac{k}{\epsilon} \overline{uv}) \frac{\partial \overline{u^2}}{\partial x} \right] \\ & + \frac{\partial}{\partial x} \left[C_k \rho \frac{k}{\epsilon} \overline{uv} \frac{\partial \overline{u^2}}{\partial r} \right] - C_1 \rho \frac{\epsilon}{k} \left(\overline{u^2} - \frac{2}{3} k \right) \\ & + (1 - C_2) \rho \left[-2 \overline{u^2} \frac{\partial U}{\partial x} - 2 \overline{uv} \frac{\partial U}{\partial r} \right] + \frac{2}{3} (C_2 P_k - \rho \epsilon) \end{aligned} \tag{B1}$$

Equation for $\overline{v^2}$:

$$\begin{aligned} & \frac{\partial}{\partial x} (\rho U \overline{v^2}) + \frac{1}{r} \frac{\partial}{\partial r} (r \rho V \overline{v^2}) - \frac{\partial}{\partial x} \left[(C_k \rho \frac{k}{\epsilon} \overline{u^2}) \frac{\partial \overline{v^2}}{\partial x} \right] \\ & - \frac{1}{r} \frac{\partial}{\partial r} \left[r (C_k \rho \frac{k}{\epsilon} \overline{v^2}) \frac{\partial \overline{v^2}}{\partial r} \right] = \frac{\partial}{\partial x} \left[C_k \rho \frac{k}{\epsilon} \left(\overline{uv} \frac{\partial \overline{v^2}}{\partial r} - 2 \overline{uw} \frac{\overline{vw}}{r} \right) \right] \\ & + \frac{1}{r} \frac{\partial}{\partial r} \left[r C_k \rho \frac{k}{\epsilon} \left(\overline{uv} \frac{\partial \overline{v^2}}{\partial x} - 2 \overline{vw} \frac{\overline{vw}}{r} \right) \right] + 2 \rho \overline{vw} \frac{W}{r} \\ & - \frac{2}{r} C_k \rho \frac{k}{\epsilon} \left[\overline{uw} \frac{\partial \overline{vw}}{\partial x} + \overline{vw} \frac{\partial \overline{vw}}{\partial r} + \overline{w^2} \frac{\overline{v^2} - \overline{w^2}}{r} \right] \\ & - C_1 \rho \frac{\epsilon}{K} \left(\overline{v^2} - \frac{2}{3} K \right) + (1 - C_2) \rho \left[-2 \overline{uv} \frac{\partial V}{\partial x} - 2 \overline{v^2} \frac{\partial V}{\partial r} + 2 \overline{vw} \frac{W}{r} \right] + \frac{2}{3} (C_2 P_k - \rho \epsilon) \end{aligned} \tag{B2}$$

Equation for $\overline{w^2}$:

$$\begin{aligned}
 & \frac{\partial}{\partial x} (\rho U \overline{w^2}) + \frac{1}{r} \frac{\partial}{\partial r} (r \rho V \overline{w^2}) - \frac{\partial}{\partial x} \left[(C_k \rho \frac{k}{\epsilon} \overline{u^2}) \frac{\partial \overline{w^2}}{\partial x} \right] \\
 & - \frac{1}{r} \frac{\partial}{\partial r} \left[r (C_k \rho \frac{k}{\epsilon} \overline{v^2}) \frac{\partial \overline{w^2}}{\partial r} \right] = \frac{\partial}{\partial x} \left[C_k \rho \frac{k}{\epsilon} \left(\overline{uv} \frac{\partial \overline{w^2}}{\partial r} - 2 \overline{uw} \frac{\overline{vw}}{r} \right) \right] \\
 & + \frac{1}{r} \frac{\partial}{\partial r} \left[r C_k \rho \frac{k}{\epsilon} \left(\overline{uv} \frac{\partial \overline{w^2}}{\partial x} + 2 \overline{vw} \cdot \frac{\overline{vw}}{r} \right) \right] - 2 \rho \overline{vw} \frac{W}{r} \\
 & + \frac{2}{r} C_k \rho \frac{k}{\epsilon} \left[\overline{uw} \frac{\partial \overline{vw}}{\partial x} + \overline{vw} \frac{\partial \overline{vw}}{\partial r} + \overline{w^2} \frac{\overline{v^2} - \overline{w^2}}{r} \right] \\
 & - C_1 \rho \frac{\epsilon}{K} \left(\overline{w^2} - \frac{2}{3} K \right) + (1 - C_2) \rho \left[-2 \overline{uw} \frac{\partial W}{\partial x} - 2 \overline{vw} \frac{\partial W}{\partial r} - 2 \overline{w^2} \frac{V}{r} \right] + \frac{2}{3} (C_2 P_k - \rho \epsilon)
 \end{aligned} \tag{B3}$$

Equation for \overline{uv} :

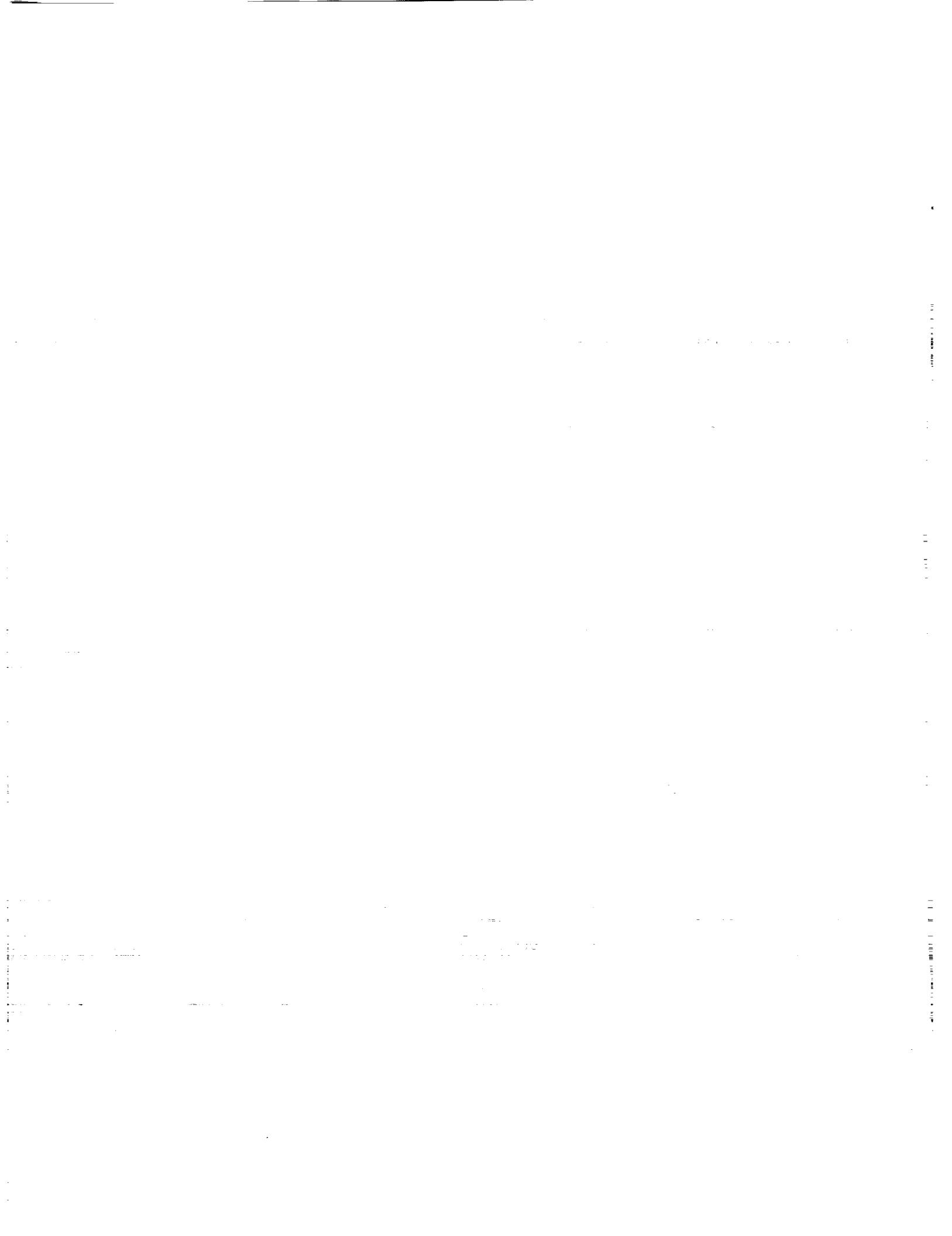
$$\begin{aligned}
 & \frac{\partial}{\partial x} (\rho U \overline{uv}) + \frac{1}{r} \frac{\partial}{\partial r} (r \rho V \overline{uv}) - \frac{\partial}{\partial x} \left[(C_k \rho \frac{K}{\epsilon} \overline{u^2}) \frac{\partial \overline{uv}}{\partial x} \right] \\
 & - \frac{1}{r} \frac{\partial}{\partial r} \left[r (C_k \rho \frac{k}{\epsilon} \overline{v^2}) \frac{\partial \overline{uv}}{\partial r} \right] = \frac{\partial}{\partial x} \left[\rho C_k \frac{k}{\epsilon} \left(\overline{uv} \frac{\partial \overline{uv}}{\partial r} - \overline{uw} \frac{\overline{uw}}{r} \right) \right] \\
 & + \frac{1}{r} \frac{\partial}{\partial r} \left[r C_k \rho \frac{k}{\epsilon} \left(\overline{uv} \frac{\partial \overline{uv}}{\partial x} - \overline{vw} \frac{\overline{uw}}{r} \right) \right] + \rho \overline{uw} \frac{W}{r} \\
 & - \frac{1}{r} C_k \rho \frac{k}{\epsilon} \left[\overline{uw} \frac{\partial \overline{uw}}{\partial x} + \overline{vw} \frac{\partial \overline{uw}}{\partial r} + \overline{w^2} \frac{\overline{uv}}{r} \right] - C_1 \rho \frac{\epsilon}{k} \overline{uv} \\
 & + (1 - C_2) \rho \left[-\overline{u^2} \frac{\partial V}{\partial x} - \overline{uv} \frac{\partial V}{\partial r} + \overline{uw} \frac{W}{r} - \overline{uv} \frac{\partial U}{\partial x} - \overline{v^2} \frac{\partial U}{\partial r} \right]
 \end{aligned} \tag{B4}$$

Equation for \overline{vw} :

$$\begin{aligned}
 & \frac{\partial}{\partial x} (\rho U \overline{vw}) + \frac{1}{r} \frac{\partial}{\partial r} (r \rho V \overline{vw}) - \frac{\partial}{\partial x} \left[\left(C_k \rho \frac{k}{\epsilon} \overline{u^2} \right) \frac{\partial \overline{vw}}{\partial x} \right] \\
 & - \frac{1}{r} \frac{\partial}{\partial r} \left[r \left(C_k \rho \frac{k}{\epsilon} \overline{v^2} \right) \frac{\partial \overline{vw}}{\partial r} \right] = \frac{\partial}{\partial x} \left[C_k \rho \frac{k}{\epsilon} \left(\overline{uv} \frac{\partial \overline{vw}}{\partial r} + \overline{uw} \frac{\overline{v^2} - \overline{w^2}}{r} \right) \right] \\
 & + \frac{1}{r} \frac{\partial}{\partial r} \left[r C_k \rho \frac{k}{\epsilon} \left(\overline{vw} \frac{\overline{v^2} - \overline{w^2}}{r} + \overline{uv} \frac{\partial \overline{vw}}{\partial x} \right) \right] \\
 & + \frac{1}{r} C_k \rho \frac{k}{\epsilon} \left[\overline{vw} \frac{\partial}{\partial r} (\overline{v^2} - \overline{w^2}) - 4 \overline{w^2} \frac{\overline{vw}}{r} + \overline{uw} \frac{\partial}{\partial x} (\overline{v^2} - \overline{w^2}) \right] \\
 & - C_1 \rho \frac{\epsilon}{k} \overline{vw} + (1 - C_2) \rho \left[-\overline{uv} \frac{\partial W}{\partial x} - \overline{v^2} \frac{\partial W}{\partial r} + \overline{vw} \frac{\partial U}{\partial x} + \overline{w^2} \frac{W}{r} - \overline{uw} \frac{\partial V}{\partial x} \right] - \rho (\overline{v^2} - \overline{w^2}) \frac{W}{r} \quad (B5)
 \end{aligned}$$

Equation for \overline{uw} :

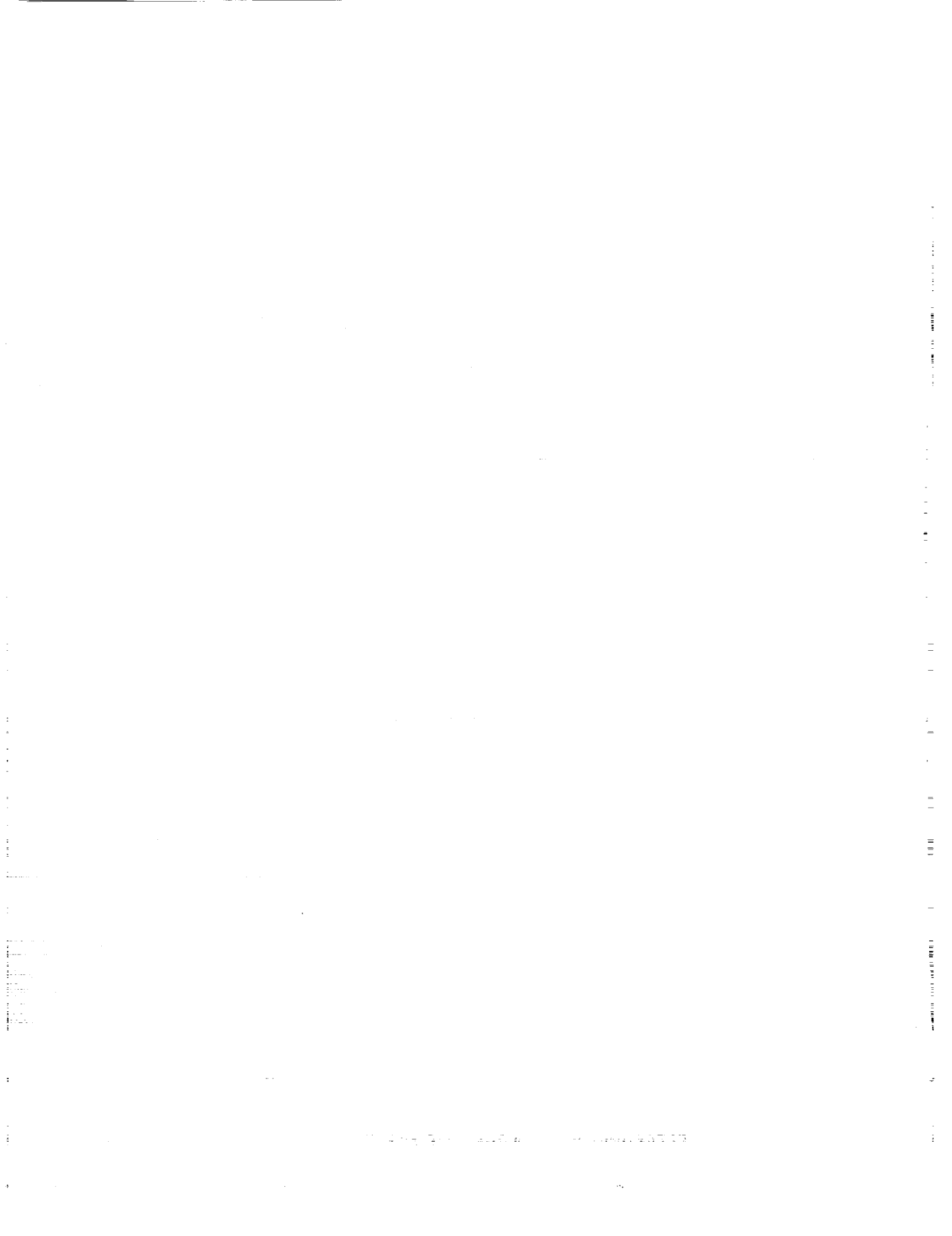
$$\begin{aligned}
 & \frac{\partial}{\partial x} (\rho U \overline{uw}) + \frac{1}{r} \frac{\partial}{\partial r} (r \rho V \overline{uw}) - \frac{\partial}{\partial x} \left[\left(C_k \rho \frac{k}{\epsilon} \overline{u^2} \right) \frac{\partial \overline{uw}}{\partial x} \right] \\
 & - \frac{1}{r} \frac{\partial}{\partial r} \left[r \left(C_k \rho \frac{k}{\epsilon} \overline{v^2} \right) \frac{\partial \overline{uw}}{\partial r} \right] = \frac{\partial}{\partial x} \left[C_k \rho \frac{k}{\epsilon} \left(\overline{uv} \frac{\partial \overline{uw}}{\partial r} + \overline{uw} \frac{\overline{uv}}{r} \right) \right] \\
 & + \frac{1}{r} \frac{\partial}{\partial r} \left[r C_k \rho \frac{k}{\epsilon} \left(\overline{uv} \frac{\partial \overline{uw}}{\partial x} + \overline{vw} \frac{\overline{uv}}{r} \right) \right] \\
 & + \frac{1}{r} C_k \rho \frac{k}{\epsilon} \left[\overline{uw} \frac{\partial \overline{uv}}{\partial x} + \overline{vw} \frac{\partial \overline{uv}}{\partial r} - \overline{w^2} \frac{\overline{uw}}{r} \right] - \rho \overline{uv} \frac{W}{r} \\
 & - C_1 \rho \frac{\epsilon}{K} \overline{uw} + (1 - C_2) \rho \left[-\overline{u^2} \frac{\partial W}{\partial x} - \overline{uv} \frac{\partial W}{\partial r} - \overline{vw} \frac{\partial U}{\partial x} + \overline{uw} \frac{\partial V}{\partial r} \right] \quad (B6)
 \end{aligned}$$



APPENDIX C

PUBLICATIONS PARTIALLY SUPPORTED BY THE LIST OF THIS STUDY

PRECEDING PAGE BLANK NOT FILMED



PUBLICATIONS PARTIALLY SUPPORTED BY THE LIST OF THIS STUDY

1. McDonell, V. G., 1987, *Development and Assessment of a Facility to Provide Benchmark Quality Data in Two-Phase Flows*, Master's Thesis, University of California, Irvine.
2. McDonell, V. G. and Samuelsen, G. S., 1988, "Application of Two-Component Phase-Doppler Interferometry to the Measurement of Particle Size, Mass Flux, and Velocities in Two-Phase Flows," *Twenty-Second Symposium (International) on Combustion*, The Combustion Institute, Pittsburgh, PA, pp 1961-1971.
3. McDonell, V. G. and Samuelsen, G. S., 1988, "Evolution of the Two-Phase Flow in the Near Field of an Air-Blast Atomizer Under Reacting and Unreacting Conditions," Presented at the 4th International Symposium on Applications of Laser Anemometry to Fluid Mechanics, Lisbon, Portugal.
4. McDonell, V. G. and Samuelsen, G. S., 1988, "Measurement of the Two-Phase Flow in the Near Field of an Air-Blast Atomizer Under Reacting and Non-Reacting Conditions," *Proceedings, Applications of Laser Anemometry to Fluid Mechanics*, Springer-Verlag.
5. McDonell, V. G. and Samuelsen, G. S., 1988, "Sensitivity Assessment of a Phase Doppler Interferometer to User Controlled Settings," to appear in Hirleman, E. D., Bachalo, W. D., and Felton, P. G., (editors), *Liquid Particle Size Measurement Techniques: 2nd Volume, ASTM STP 1083*, American Society for Testing and Materials, Philadelphia, PA, 1990, pp. 170-189.
6. McDonell, V. G. and Samuelsen, G. S., 1988, "Symmetry Assessment of a Gas Turbine Air-Blast Atomizer -- Influence of the Continuous and Dispersed Phases," *Proceedings of the 4th International Conference on Liquid Atomization and Spray Systems*, Sendai, Japan.
7. Nikjooy, M., Karki, K. C., Mongia, H. C., McDonell, V. G., and Samuelsen, G. S., 1988, "k- ϵ Turbulence Model Assessment with Reduced Numerical Diffusion for Coaxial Jets," AIAA-88-0342.
8. Mostafa, A. A., Mongia, H. C., McDonell, V. G., and Samuelsen, G. S., 1989, "Evolution of Particle-Laden Jet Flows: A Theoretical and Experimental Study," *AIAA J.* Vol. 27, No. 2, pp. 167-183 (also AIAA paper 87-2181).
9. Nikjooy, M., Karki, K. C., Mongia, H. C., McDonell, V. G., and Samuelsen, G. S., 1989, "A Numerical and Experimental Study of Coaxial Jets," *Int. J. Heat and Fluid Flow*, Vol. 10, No. 3, pp. 253-261.
10. Nikjooy, M., Mongia, H. C., Samuelsen, G. S., and McDonell, V. G., 1989, "A Numerical and Experimental Study of Confined Swirling Jets," AIAA-89-2898.
11. McDonell, V. G., 1990, "Evolution of Droplet/Gas Phase Interaction in Polydisperse Reacting and Nonreacting Sprays," Ph.D. Thesis, University of California at Irvine.
12. McDonell, V. G., Cameron, C. D., and Samuelsen, G. S., 1990, "Symmetry Assessment of an Air-Blast Atomizer Spray," *Journal of Propulsion and Power*, Vol. 6, No. 4, pp 375-381 (AIAA Paper 87-2136).
13. McDonell, V. G. and Samuelsen, G. S., 1990, "Influence of the Continuous and Dispersed Phases on the Symmetry of a Gas Turbine Air-Blast Atomizer," *ASME J. Engr. Gas Turbines and Power*, 112, 44.
14. McDonell, V. G. and Samuelsen, G. S., 1990, "Application of Laser Interferometry to the Study Droplet/Gas Phase Interaction and Behavior in Liquid Spray Combustion Systems," *Combust. Sci. and Tech.*, 74, 343.

15. Mostafa, A. A., Mongia, H. C., McDonell, V. G., and Samuelsen, G. S., 1990, "An Experimental and Numerical Study of Particle-Laden Coaxial Jet Flows," *Int. J. Heat and Fluid Flow*, Vol. 11, No. 2, pp. 90-97.
16. Nikjooy, M., Mongia, H. C., McDonell, V. G., and Samuelsen, G. S., 1990, "Calculations of Particle-Laden Flows by Second Moment Closures," AIAA Paper 90-1858.
17. McDonell, V. G. and Samuelsen, G. S., 1991, "Gas and Drop Behavior in Reacting and Non-Reacting Air-Blast Atomizer Sprays," *Journal of Propulsion and Power*, 7, 684.
18. Nikjooy, M. and Mongia, H. C., 1991, "A Second-Order Modeling Study of Confined Swirling Flow," *Int. J. Heat and Fluid*, Vol. 12, No. 1, pp. 12-19.
19. Nikjooy, M., Mongia, H. C., McDonell, V. G., and Samuelsen, G. S., 1991, "Calculations of Particle-Laden Flows by Second-Moment Closures," AIAA-91-0082.



REPORT DOCUMENTATION PAGE

Form Approved
OMB No. 0704-0188

Public reporting burden for this collection of information is estimated to average 1 hour per response, including the time for reviewing instructions, searching existing data sources, gathering and maintaining the data needed, and completing and reviewing the collection of information. Send comments regarding this burden estimate or any other aspect of this collection of information, including suggestions for reducing this burden, to Washington Headquarters Services, Directorate for Information Operations and Reports, 1215 Jefferson Davis Highway, Suite 1204, Arlington, VA 22202-4302, and to the Office of Management and Budget, Paperwork Reduction Project (0704-0188), Washington, DC 20503

1. AGENCY USE ONLY (Leave blank)		2. REPORT DATE March 1993	3. REPORT TYPE AND DATES COVERED Final Contractor Report	
4. TITLE AND SUBTITLE Fuel Injector – Air Swirl Characterization Aerothermal Modeling Phase II Final Report – Volume II			5. FUNDING NUMBERS WU-505-62-52 NAS3-24350	
6. AUTHOR(S) M. Nikjooy, H.C. Mongia, V.G. McDonell, and G.S. Samuelsen				
7. PERFORMING ORGANIZATION NAME(S) AND ADDRESS(ES) Allison Gas Turbine Division General Motors Corporation P.O. Box 420 Indianapolis, Indiana 40206-0420			8. PERFORMING ORGANIZATION REPORT NUMBER E-7593	
9. SPONSORING/MONITORING AGENCY NAMES(S) AND ADDRESS(ES) National Aeronautics and Space Administration Lewis Research Center Cleveland, Ohio 44135-3191			10. SPONSORING/MONITORING AGENCY REPORT NUMBER NASA CR-189193	
11. SUPPLEMENTARY NOTES Project Manager, James D. Holdeman, (216) 433-5846.				
12a. DISTRIBUTION/AVAILABILITY STATEMENT Unclassified - Unlimited Subject Category 07			12b. DISTRIBUTION CODE	
13. ABSTRACT (Maximum 200 words) A well integrated experimental/analytical investigation was conducted to provide benchmark quality data relevant to prefilming type airblast fuel nozzle and its interaction with combustor dome air swirler. The experimental investigation included a systematic study of both single-phase flows that involved single and twin co-axial jets with and without swirl. A two-component Phase Doppler Particle Analyzer (PDPA) equipment was used to document the interaction of single and co-axial air jets with glass beads that simulate nonevaporating spray and simultaneously avoid the complexities associated with fuel atomization processes and attendant issues about the specification of relevant boundary conditions. The interaction of jets with methanol spray produced by practical airblast nozzle was also documented in the spatial domain of practical interest. Model assessment activities included the use of three turbulence models (k-ε, algebraic Lagrangian treatment of the dispersed phase, and advanced numerical schemes. Although qualitatively good comparison with data was obtained for most of the cases investigated, the model deficiencies in regard to modeled dissipation rate transport equation, single length scale, pressure-strain correlation and other critical closure issues need to be resolved before one can achieve the degree of accuracy required to analytically design combustion systems.				
14. SUBJECT TERMS Fuel nozzles; Swirling flows; Gas turbine combustion; Experimental data; Turbulent flow model validation; Two-phase flows; Turbulence modeling			15. NUMBER OF PAGES 308	
			16. PRICE CODE A14	
17. SECURITY CLASSIFICATION OF REPORT Unclassified	18. SECURITY CLASSIFICATION OF THIS PAGE Unclassified	19. SECURITY CLASSIFICATION OF ABSTRACT Unclassified	20. LIMITATION OF ABSTRACT	